LOW-ENERGY, HIGH-RESOLUTION, VARIABLE ANGLE ELECTRON IMPACT SPECTROSCOPY

Thesis by

James Kinsey Rice

In Partial Fulfillment of the Requirements

For the Degree of

Doctor of Philosophy

California Institute of Technology

Pasadena, California

1969

(Submitted September 9, 1968)

ACKNOWLEDGMENTS

I wish to express my sincere appreciation to Professor Aron Kuppermann for suggesting this research project and for the advice and encouragement which he generously offered throughout the course of this investigation.

The invaluable help of Sandor Trajmar in the initial stages of design and construction as well as his continuing collaboration is gratefully acknowledged.

Much of my insight into both the experimental and theoretical aspects of this project has been obtained through interactions with fellow students. In particular, I wish to thank Oakley Crawford and Lonne Lane for their instruction in mechanical engineering and high vacuum technology, Dave Cartwright and Merle Riley for their assistance in computer programming, and Don Truhlar for his help in many of the theoretical and computation aspects of this study.

Special thanks are extended to Bill Schuelke and Villy Jorgensen who, along with other machinists at the California Institute of Technology, made possible the construction of this apparatus. I am also indebted to Drs. J. Arol Simpson and Chris Kuyatt of the National Bureau of Standards for very helpful information about the design of their instruments.

Financial support from the Atomic Energy Commission and the National Science Foundation is gratefully acknowledged.

Finally, but with the most affection, I thank my wife, Linda, for her continuing enthusiasm and unfailing encouragement.

ABSTRACT

A low-energy, variable angle, high-resolution, electron-impact spectrometer has been designed, constructed, and put into operation. Its performance is discussed and is found to compare favorably with that of similar instruments[24, 25, 35b].

The differential scattering cross sections (DCS) for the electron-impact excitation of helium and five molecules (N_2, CO, H_2, C_2H_2, and C_2H_4) have been measured as a function of incident electron kinetic energy (from about 20 to 60 eV) and scattering angle (from about -30° to +80°) with a resolution of 0.04 to 0.15 eV. These studies included the observation of twenty-nine electronically excited states, including 12 singlet → triplet transitions.

Comparisons of these results with presently available theoretical predictions have indicated the inadequacy of the latter. In addition, a theoretical calculation of the exchange excitation of ethylene ($\tilde{X}^1A_g \rightarrow \tilde{a}^3B_{1u}$) by electron-impact is carried out via the Ochkur-Rudge approximation[58, 62] and is compared with experiment.

The vibrational structure within several electronic bands has been resolved, and the relative vibrational intensities have been compared with optical and calculated relative Franck-Condon factors. Discrepancies, due to underlying forbidden transitions, have been noted in H_2, acetylene, and ethylene.

Some general "spectroscopic rules" for the identification of spin-forbidden excitations observed by electron-impact are presented. These rules are derived from an examination of the angular dependencies of the differential cross sections for twenty-six known transitions. On this basis, one state in N_2 ($E^3\Sigma_g^+$) has been unequivocally identified as a triplet, and two previously unknown low-lying triplet states in C_2H_2 at 5.2 eV and 6.1 eV have been detected and characterized.

TABLE OF CONTENTS

1. INTRODUCTION

The collision of an electron with an isolated atom or molecule can have a number of outcomes. Among them are the transfer of translational energy, diffraction, electron exchange, excitation or deexcitation of internal states of the target, ionization, negative ion formation, molecular fragmentation, or a combination of several of these. For any case, the quantity which characterizes the scattering process is known as the cross section. Phenomenologically, the cross section for the occurence of a certain type of event during a collision is equal to the number of these events per unit time per target particle divided by the current density (particles per unit time per unit area) of incident electrons relative to the target[1a]. As a consequence of this definition, the cross section has the units of area per target particle.

The cross section per unit solid angle for the particular process in which an electron collides with the target and then scatters into a given direction (defined by spherical polar angles θ, φ) is called the "differential scattering cross section" (hereafter abbreviated as DCS) and has the units of area per solid angle per target particle. The corresponding "total cross section" is the integral of the DCS over all scattering directions θ, φ. If we define a spherical polar coordinate system whose z axis lies along the incident beam direction, then the scattering angle θ is the colattitude of this coordinate system and φ is the azimuth (or longitude). If the target particles are randomly oriented with respect to the incident

beam direction (as is the case under our experimental conditions), then the DCS will not depend on φ.

There are two general classes of collision phenomena which can be studied by the detection of the scattered electrons:

(1) elastic scattering, in which the incident electron does not transfer any of its kinetic energy to internal energy states of the target, and

(2) inelastic scattering, in which it does.

In particular, the present investigation is concerned with the use of electron impact as a spectroscopic tool for the study of electronically excited states of atomic and molecular species in the gas phase.

In essence, the experimental method involves the production of a monochromatic beam of electrons (incident beam), the passage of this beam through a gaseous sample of the target particles (at a pressure of about 10^{-3} torr), and the measurement of the scattered electron intensity as a function of the incident electron energy, scattering angle, and energy-loss (the kinetic energy lost by the incident electron through an inelastic collision).

Under the experimental conditions employed here, each detected electron has been scattered by at most one target particle (over 90% of the incident beam is not scattered at all). Thus, each energy-loss is equal to one particular excitation energy of the target. Further, a measurement of the angular dependence of the intensity of scattered electrons with a given energy-loss (i. e. the distribution of scattered electrons which have caused a particular electronic

transition in the target) can provide the basis for an identification of the excited state.

The use of electrons to induce these transitions offers two significant advantages over the use of photons:

(1) It is no more difficult to measure energy-losses (and hence molecular excitations) corresponding to the extreme vacuum UV (wavelengths shorter than 500 Å) than those in the visible region. This is certainly not the case for optical methods.

(2) Many of the normal optical selection rules[2] governing the relative probability of observing different excitations can be broken by a judicious choice of incident electron energy and scattering angle. In particular, low-energy electrons (within a few tens of eV's of the excitation threshold) can be quite effective in causing transitions between states of different spin multiplicity (total spin angular momentum $S \rightarrow S \pm 1$) through the mechanism of electron exchange excitation. This exchange process involves the interchange of the incident electron and one of the bound ones. These transitions are highly forbidden under photon impact in the absence of appreciable spin-orbit coupling. In addition, the probability of producing transitions which are optically symmetry-forbidden can often be dramatically increased by the use of low-energy electrons.

To illustrate these marked differences, table 1.-1 presents a comparison of relative optical transition probabilities with ones obtained by electron impact for three transitions in helium. The

TABLE 1.-1

A comparison of some relative electron-impact excitation probabilities in helium with typical optical transition probabilities. $P_{opt.}$ is the relative optical excitation probability; $P^{T}_{elec.}$ is the relative electron-impact excitation probability for an incident energy of 35 eV; and $P_{elec.}(\theta)$ is the relative probability for electrons to scatter at an angle θ after causing the excitation for an incident energy of 35 eV.

Transition	Type	$P_{opt.}$	$P^{T}_{elec.}$	$P_{elec.}(\theta)$[d]	
				$\theta = 0°$	$\theta = 70°$
$1^1S \rightarrow 2^1P$	electric dipole allowed	1[a]	1[a]	1[a]	1[a]
$1^1S \rightarrow 2^1S$	electric dipole forbidden, electric quadrupole allowed.	$10^{-5} - 10^{-8}$[b]	.18[c]	0.40	.21
$1^1S \rightarrow 2^3P$	spin-forbidden, electric dipole allowed.	$< 10^{-8}$	.12[e]	.023	1.3

[a] The relative probability of this transition is taken as unity.

[b] Reference (2a), p 54. [c] Reference (42). [d] Present research, section 5.2. [e] Reference (43).

relative probability of exciting the 2^1P level (optically allowed transition) is taken as unity. The last two columns in the table give the relative probabilities for electrons which have caused a particular excitation to be scattered by a given angle θ.

To be sure, optical techniques offer some important advantages such as better resolution (about two or three orders of magnitude better in the visible region, but comparable in the vacuum UV), the ability to work with solid and liquid samples, and a well developed practical theory with which to interpret experimental results. It will become apparent that it is the lack of this latter feature in low-energy electron impact which seriously complicates its application.

The purpose of the research described here was to design, construct, and operate an electron-impact spectrometer which could use the electron-impact method of molecular excitation to obtain information about molecular excited states. A brief historical review of the experimental development of electron scattering is presented in section 2. A discussion of some of the more relevant aspects of scattering theory is given in section 3 along with an application to the electron-impact excitation of the $\tilde{a}\,^3B_{1u}$ state of ethylene. The design, construction, operation, and performance of the spectrometer is discussed in section 4. Section 5 contains the experimental results obtained for six systems--helium, molecular nitrogen, carbon monoxide, molecular hydrogen, acetylene, and ethylene. Finally, section 6 presents some empirical rules for the identification of states excited via electron impact.

2. HISTORICAL DEVELOPMENT

In 1914 Franck and Hertz[3] initiated the field of electron-impact spectroscopy with their classic experiments on the measurement of energy-losses of electron swarms in atomic gases. However, it was not until 1927 that Dymond[4] carried out the first measurements of the angular distribution of inelastically scattered electrons. At about this same time, Oppenheimer[5] pointed out the possibility of an electron exchange mechanism whereby optically spin-forbidden transitions could be produced. During the next few years, until the middle 1930's, the study of electron-impact phenomena reached a peak only to be followed by two decades of relative inactivity. A comprehensive review of this early work has been presented by Massey and Burhop[6].

Since the late 1950's, there has been a renewed and increasing interest in this field, due possibly to the development of more sophisticated experimental techniques and a heightened awareness of the importance of electron-molecule (atom) interactions in radiation chemistry, upper-atmosphere phenomena, and plasma physics. A more recent review of electron collision processes can be found in the book by McDaniel[7].

At present there are essentially two methods used to study molecular excited states through electron-impact excitation and the detection of the scattered electrons. One method, introduced by Schulz[8] and usually denoted the "trapped-electron" method, involves the use of an incident electron beam of variable kinetic energy E and

the detection of only those electrons which have lost nearly all of their kinetic energy through single collisions with the target particles. If W is a particular molecular excitation threshold, then a scattered signal is obtained for $E \approx W$. This signal, which contains contributions from electrons scattered at all angles, is proportional to the total excitation cross section in the vicinity of the excitation threshold. Since total cross sections for optically-forbidden transitions are usually steeper at threshold than those for allowed ones,[6a] the "threshold excitation spectra" obtained by this method are often dominated by spin- and symmetry-forbidden transitions.

This method has been applied to several systems by Schulz[9] and Bowman and Miller[10]. Recently, relatively high resolution data have been obtained by Brongersma and Oosterhoff[11], Dowell and Sharp[12], and Compton, et al.[13]. However, the possibility of negative ion formation and the uncertainties in energy scale calibration and threshold behavior complicate the identification of the excited state.

The other electron scattering method involves the use of an incident electron beam of fixed (or variable) energy E and the detection of electrons which have been scattered by single collisons with the target in a particular θ, φ direction (or range of angles) after undergoing a particular energy-loss (E - W). Although it has been recognized for some time that the angular dependence of the scattered electron intensity for a particular energy-loss is sensitive to the nature of the transition giving rise to it[6b], very little data

have yet been obtained about these distributions. Most of the experiments have been performed at fixed angles (or a fixed range of angles), usually near 0° or 90°.

Lassettre and coworkers[14] were among the pioneers in the field of electron-impact spectroscopy. The bulk of their work has been on relatively small molecules with incident electron energies above 200 eV and scattering angles below about 20°. Rather than attempt a complete review of their work, we will summarize only those studies relevant to the systems studied here (He, N_2, H_2, CO, C_2H_2, C_2H_4). The results of their early work on these molecules[14b] generally agreed with optical absorption measurements and indicated the validity of the Born approximation at low scattering angles and high incident energies. Of especial interest, Silverman and Lassettre[15] showed that the ratio of the intensity of the $1^1S \rightarrow 2^1S$ transition (dipole-forbidden, quadrupole-allowed) to that of the $1^1S \rightarrow 2^1P$ transition (dipole-allowed) in helium varied from about .08 at $\theta = 3.8°$ to 0.9 at $\theta = 15.3°$ for 500 eV incident electrons. Also Lassettre and Krasnow[16] verified the forbidden nature of the $X^1\Sigma_g^+ \rightarrow a^1\Pi_g$ transition (electric dipole-forbidden; magnetic dipole and electric quadrupole-allowed) in N_2 by the angular dependence ($\theta \leq 10°$) of the scattered electrons at ~500 eV incident energy.

More detailed studies[17] of N_2, at incident energies as low as 60 eV, revealed two additional electric-dipole forbidden transitions at 11.87 eV and 12.26 eV in addition to the $X \rightarrow a^1\Pi_g$ one. The upper states for both transitions were assigned as $^1\Sigma_g^+$. The one corres-

ponding to the 12.26 eV transition has also been assigned as $^1\Sigma_g^+$ by Dressler[18] from optical absorption studies. While the assignment of the 11.87 eV transition agrees with the Penning ionization results of Cermák[19], it disagrees with the E $^3\Sigma_g^+$ assignment presented by Heideman, et al.[20] based on studies at lower electron-impact energies. We have resolved this controversy with the results given in section 5.3.

A study of CO at an incident energy of 200 eV and $\theta \leq 2°$ has also been reported[21]. These results agreed quite well with UV absorption spectra except for an anomalously intense transition at 12.79 eV. At lower incident energies (30-60 eV) Skerbele, et al.[22] have resolved several singlet → triplet transitions in both N_2 and CO. However, they pointed out that in a survey of 16 additional polyatomic molecules at incident energies as low as 35 eV, they failed to observe any singlet → triplet transitions. The results of our research indicate that the restriction of their observations to small scattering angles was probably responsible for this failure.

In addition to the investigations mentioned above, Ross and Lassettre[23] have obtained high resolution energy-loss spectra of C_2H_4. Their results generally agreed with optical absorption measurements although the lowest singlet → triplet transition in ethylene was not observed while evidence of a quadrupole-allowed transition near 7.45 eV was obtained.

Several years ago, Simpson[24] constructed a high-resolution, $\theta = 0°$, electron-impact spectrometer. This instrument and a later model[25] (variable angle) provided the basis for the design of the

spectrometer described here. The work of this group with the 0° instrument has been confined to impact energies below 100 eV. Although their early investigations of He[26], H_2[27], and C_2H_4[26] did not reveal any singlet → triplet transitions at impact energies as low as 30 eV, improvements in the apparatus led to the detection of several such transitions in He[28], N_2[29], and H_2[30]. Their measurements of the forward scattering intensity ratios of several transitions in He[28] and the angular dependence[31] (0° → 60°) of electrons scattered after causing the $1^1S \rightarrow 2^3S$, 2^1S, and 2^1P transitions are compared with the results of this research in section 5.2. Recently, their variable angle instrument was also used to measure the scattered electron distributions ($0° \leq \theta \leq 20°$) for these same three excitations in He at impact energies of 100 eV to 400 eV[32]. A large part of their work is presently directed toward the study of resonance phenomena[33] and instrument design[34].

Kuppermann and Raff[35] obtained energy-loss spectra for He, Ar, H_2, and C_2H_4 with impact energies on the order of 50 eV and an instrument geometry which collected electrons scattered in the range $22° \leq \theta \leq 112°$ (with 90° favored), $0 \leq \varphi \leq 2\pi$. Under these conditions, singlet → triplet transitions were prominent features in the reported spectra. They were the first to detect triplet states by energy analysis of the scattered electrons. In particular, they observed the $\tilde{X}\,^1A_{1g} \rightarrow \tilde{a}\,^3B_{1u}$ transition in ethylene via electron impact for the first time.

Doering[36] has investigated the 90° scattering of low-energy electrons by He, N_2, C_2H_4, and C_6H_6. He confirmed the singlet → triplet transition in C_2H_4 mentioned above and observed spin-forbidden transitions in He, N_2, and C_6H_6 as well.

Recently, Ehrhardt and coworkers[37] have put into operation an elegant electron-impact spectrometer in which the target is a molecular beam. Although this instrument has been used primarily for the study of resonances, one measurement[37b] of the angular distribution (7° → 110°) of electrons causing the $1^1S \rightarrow 2^3S$ transition in helium can be compared with the present results (section 5.2).

Finally, the $\theta = 0°$ energy-loss spectra of H_2[38], N_2[39], and C_2H_4[40] have been obtained at very high incident energies ($\sim$ 35 KeV) with good resolution ($\sim$ 0.03 eV). Under these conditions (high energy, low angle), the Born approximation seems quite reliable and, as expected, these spectra are nearly identical with UV absorption spectra.

It is quite interesting to note that in general the relative vibrational intensities within a given electronic excited state as determined via electron-impact have been found to be the same as those obtained by optical absorption studies (or accurate calculations)[41]. This includes the results of threshold excitation methods as well as energy-loss determinations--regardless of the molecular species, scattering angle, or incident energy (but excludes the cases in which excitation occurs via a temporary negative ion). The theoretical implications of this result are discussed in section 3.

3. THEORETICAL DESCRIPTION OF SCATTERING

3.1. Introduction

The cross section for a particular outcome of the collision of an electron and a complex "particle" CP has been defined in section 1. In this section, we present some of the methods which can be applied to the calculation of these quantities from first principles with particular emphasis on electronic excitation.

In the elastic or inelastic scattering of electrons, a small part δE of an electron's kinetic energy E_e in the laboratory system is transformed into laboratory kinetic energy of CP. Namely, for elastic scattering

$$\frac{\delta E}{E_e} \approx \frac{4m}{M} \sin^2 \frac{\theta}{2} \qquad (3\text{-}1)$$

and for inelastic scattering events

$$\frac{\delta E}{E_e} \approx \frac{2m}{M}\left[1 - \frac{W}{2E_e} - \sqrt{1 - \frac{W}{E_e}} \cos\theta\right]. \qquad (3\text{-}2)$$

m is the mass of the electron, M is the mass of CP, θ is the angle between the incident and scattered electron (scattering angle), and W is the energy lost by the incident electron to internal states of CP. Equations (3-1) and (3-2) can be derived from the conservation of total energy and momentum during the collision. For a single collision process, such as we study, $\frac{\delta E}{E_e}$ is $\sim 10^{-4}$ while the relative electron beam resolution is only $\sim 10^{-3}$. Neither translational energy transfer nor cooperative scattering phenomena, such as electron-diffraction[6c], will be explicitly considered. In addition, only

those aspects of scattering theory which are particularly relevant to this investigation will be discussed in any detail. There are a number of good reference works available which review both the theoretical[1,44-47] and experimental[6,47] aspects of electron scattering phenomena.

3.2. Formal Description

The time evolution of a dynamical state $\Psi_I^T(t)$ of the electron-CP system is given by the time-dependent Schröedinger equation

$$i\hbar \frac{\partial \Psi_I^T(t)}{\partial t} = \hat{H}_T \Psi_I^T(t) \qquad (3\text{-}3)$$

where the subscript I specifies the initial conditions of this state, $\hat{H}_T$ is the total Hamiltonian operator, and $\hbar$ is Planck's constant divided by 2π. Since $\hat{H}_T$ is time-independent in the absence of any fields external to the electron-CP system, it is reasonable to use a time-independent formalism. Since the total energy E is conserved during the collision, $\Psi_I^T(t)$ must represent a state of constant $\langle E \rangle \equiv \langle \Psi_I^T(t) | \hat{H}_T | \Psi_I^T(t) \rangle$ (time is not included in this integration). $\Psi_I^T(t)$ can be factored into a time dependent part F(t) and a part Ψ_I, depending only on the coordinates of configuration space (since $\hat{H}_T$ is independent of time) as

$$\Psi_I^T(t) = \Psi_I F(t) \qquad \text{where}$$

$$\langle \Psi_I^T(t) | \Psi_I^T(t) \rangle = \langle \Psi_I | \Psi_I \rangle |F(t)|^2 = 1 \quad ,$$

$$\langle E \rangle = \langle \Psi_I \hat{H}_T \Psi_I \rangle |F(t)|^2 \quad , \quad \text{and}$$

$$\frac{\hat{H}_T \Psi_I}{\Psi_I} = \frac{i\hbar}{F} \frac{\partial F(t)}{\partial t} = \text{const.}$$

Combining these relations yields the steady state Schröedinger equation for Ψ_I,

$$(\hat{H}_T - \langle E \rangle)\Psi_I = 0. \qquad (3\text{-}4)$$

As an example of the application of (3-4), we shall consider the case in which an electron collides with a stationary target CP containing N-1 electrons and N′ nuclei.

The total Hamiltonian for this system is given by

$$\hat{H}_T = \hat{T}_a + \hat{T}_b + V_{aa} + V_{ab} + V_{bb} \qquad (3\text{-}5)$$

in which

$$\hat{T}_a = -\frac{\hbar^2}{2m} \sum_{k=1}^{N} \nabla_k^2 ;$$

$$\hat{T}_b = -\frac{\hbar^2}{2} \sum_{j=1}^{N'} \nabla_j^2 / M_j ;$$

$$V_{aa} = e^2 \sum_{\ell > k}^{N} \sum_{k=1}^{N} \frac{1}{r_{\ell k}} ;$$

$$V_{ab} = -e^2 \sum_{k=1}^{N} \sum_{j=1}^{N'} \frac{Z_j}{|\underset{\sim}{r}_k - \underset{\sim}{R}_j|} ;$$

$$V_{bb} = e^2 \sum_{j>i}^{N'} \sum_{i=1}^{N'} \frac{Z_j Z_i}{R_{ji}} \quad ;$$

$$\nabla_k^2 = \frac{1}{r_k^2} \frac{\partial}{\partial r_k} \left(r_k^2 \frac{\partial}{\partial r_k}\right) + \frac{1}{r_k^2 \sin\theta_k} \frac{\partial}{\partial \theta_k} \left(\sin\theta_k \frac{\partial}{\partial \theta_k}\right)$$

$$+ \frac{1}{r_k^2 \sin^2\theta_k} \frac{\partial^2}{\partial \varphi_k^2} \quad ;$$

∇_j^2 is the same as ∇_k^2 except that $(r_k, \theta_k, \varphi_k)$ are replaced by $(R_k, \theta_j, \varphi_j)$; m and $\underset{\sim}{r}_k$ are the mass and position, respectively, of the k^{th} electron; M_j, $|e|Z_j$, and $\underset{\sim}{R}_j$ are the mass, charge, and position, respectively, of the j^{th} nucleus; $r_{\ell k} \equiv |\underset{\sim}{r}_\ell - \underset{\sim}{r}_k|$; and $R_{ji} \equiv |\underset{\sim}{R}_j - \underset{\sim}{R}_i|$. It will be assumed that the center of mass (CM) of the electron + CP system coincides with that of CP, that the CM of CP is the origin of the coordinates used above (and hence, the CM motion will be neglected), and that $\hat{H}_T$ does not depend on electron or nuclear spin.

$\hat{H}_T$ can be separated into two parts, one representing the bound system CP and another the free electron and its coulombic interactions with CP. One particular separation is

$$\hat{H}_T = \frac{\hbar^2}{2m} \nabla_1^2 + \hat{H}_{1CP} + V_{1CP} \qquad (3\text{-}6)$$

where

$$V_{1CP} = e^2 \sum_{k=2}^{N} \frac{1}{r_{1k}} - e^2 \sum_{j=1}^{N'} \frac{Z_j}{|\underset{\sim}{r}_1 - \underset{\sim}{R}_j|} \quad \text{and}$$

$$\hat{H}_{1CP} = \hat{H}_T - V_{1CP} + \frac{\hbar^2}{2m} \nabla_1^2 \quad .$$

There is nothing unique about the separation (3-6), i. e. any electron can be "free" and the remainder bound.

$\hat{H}_{1CP}$ has a set of eigenfunctions which can be factored into a spatial part times a spin part (since $\hat{H}_{1CP}$ is independent of spin). The spatial functions are given by the equation

$$\hat{H}_{1CP}\,\Phi_n(\underset{\sim}{r}_2,\ldots\underset{\sim}{r}_n;\underset{\sim}{R}) = \epsilon_n\Phi_n(\underset{\sim}{r}_2,\ldots\underset{\sim}{r}_n;\underset{\sim}{R}) \qquad (3\text{-}7)$$

where ϵ_n is the energy of the state Φ_n (depending on the coordinates of all the nuclei $\underset{\sim}{R}$ and electrons $\underset{\sim}{r}$ except those of electron 1) and n represents the complete set of spatial quantum numbers which identifies this state.

We next construct a set of electronic spin wave functions $\mathcal{S}_{SS_z}(2,\ldots,N)$ for the N - 1 electrons of CP. These functions satisfy the eigenvalue equations

$$\hat{S}^2\mathcal{S}_{SS_z} = S(S+1)\mathcal{S}_{SS_z} \qquad (3\text{-}8a)$$

$$\hat{S}_z\mathcal{S}_{SS_z} = S_z\mathcal{S}_{SS_z} \qquad (3\text{-}8b)$$

where S is the total spin angular momentum of these N - 1 electrons and S_z is the z component. The wave functions $\psi_{\underset{\sim}{n}}$ which are simultaneous eigenfunctions of $\hat{H}_{1CP}$, $\hat{S}^2$, and $\hat{S}_z$ are obtained by multiplying Φ_n by $\mathcal{S}_{SS_z}$ [48].

$$\psi_{\underset{\sim}{n}}(\underset{\sim}{r}_2,\ldots\underset{\sim}{r}_N;\underset{\sim}{R}) = \Phi_n(\underset{\sim}{r}_2,\ldots\underset{\sim}{r}_N;\underset{\sim}{R})\,\mathcal{S}_{S'S_z'}(2,\ldots N)$$

$$\hat{H}_{1CP}\,\psi_{\underset{\sim}{n}} = E_n\psi_{\underset{\sim}{n}} \qquad (3\text{-}9)$$

where $\underset{\sim}{n} = (n, s', s_z')$ *represents the required set of space and spin* quantum numbers and $(\underset{\sim}{\tau}_2, \ldots \underset{\sim}{\tau}_N)$ are the electronic space and spin coordinates. The set of functions $\psi_{\underset{\sim}{n}}$ will be constructed so that they satisfy the Pauli principle[49a] (i. e., they are antisymmetric with respect to an interchange of all coordinates of any two electrons) and are orthonormal:

$$< \psi_{\underset{\sim}{n}}^{*} (\underset{\sim}{\tau}_2, \ldots \underset{\sim}{\tau}_N; \underset{\sim}{R}) \psi_{\underset{\sim}{m}} (\underset{\sim}{\tau}_2, \ldots \underset{\sim}{\tau}_N; \underset{\sim}{R}) >_{(1)} = \delta_{\underset{\sim}{n}\,\underset{\sim}{m}}. \qquad (3\text{-}10)$$

$< >_{(1)}$ represents an integration over all space and spin coordinates except those of electron 1.

If the incident and scattered electron have momenta $\hbar \underset{\sim}{k}_o$ and $\hbar \underset{\sim}{k}_n$, respectively, the total energy E of equation (3-4) is given by

$$E = \frac{\hbar^2}{2m} k_o^2 + E_o = \frac{\hbar^2}{2m} k_n^2 + E_n \qquad (3\text{-}11)$$

where E_o and E_n are the energies of CP before and after the collision, respectively. The scattering angle in this case is $\theta \equiv$ arc cos $(\underset{\sim}{k}_o \cdot \underset{\sim}{k}_n / k_o k_n)$.

Thus, E of (3-4) is specified and the desired solutions $\Psi_I (\underset{\sim}{\tau}_1, \underset{\sim}{\tau}_2, \ldots \underset{\sim}{\tau}_N; \underset{\sim}{R})$ will not only be eigenfunctions of $\hat{H}_T$ but must also satisfy certain boundary conditions dictated by the experimental arrangement.

For simplicity we shall consider an idealized experiment in which electrons of well defined momentum $\hbar \underset{\sim}{k}_o$ strike the target molecules CP which are characterized by a specific initial state

$\psi_{\underset{\sim}{o}}$. The electrons emanating from the scattering region, either unscattered or scattered leaving the molecules in one of their states $\psi_{\underset{\sim}{n}}$, are detected after they have traveled a distance D which is large compared to the range d of V_{1CP} ($D/d \sim 10^7$). As a result, the asymptotic (near the detector) form of Ψ_I can be reasonably represented by a linear combination of solutions to (3-4) with $V_{1CP} = 0$, i.e., a plane wave times $\psi_{\underset{\sim}{o}}$ to represent the unscattered beam, and outgoing spherical waves times the various $\psi_{\underset{\sim}{n}}$'s to represent the scattered electrons. In addition, the antisymmetry requirement of the Pauli principle and the indistinguishability of the electrons should be included in the boundary condition for Ψ_I. One convenient way to accomplish this is to define a permutation operator $P_{1\ell}$ which, when operating on an N electron function, exchanges the ℓ^{th} electron with the first. The desired asymptotic form of Ψ_I, including electron exchange, is

$$\Psi_I \underset{D \to \infty}{\sim} \sum_{\underset{\sim}{n}=o}^{\infty} (1 - \Sigma_{op})\{[e^{i\underset{\sim}{k}_o \cdot \underset{\sim}{r}_1}\delta_{on} + \zeta_{\underset{\sim}{o}\underset{\sim}{n}}(\theta_1, \varphi_1) \times \frac{e^{ik_n r_1}}{r_1}] s_n(1)\psi_{\underset{\sim}{n}}(\underset{\sim}{\tau}_2, \ldots \underset{\sim}{\tau}_n; \underset{\sim}{R})\} . \qquad (3\text{-}12)$$

$\Sigma_{op} \equiv \sum_{\ell=2}^{N} P_{1\ell}$, $\sum_{\underset{\sim}{n}=o}^{\infty}$ represents a sum over the discrete states plus an integral over the continium states of CP, $s_n(\ell)$ is the normalized spin wavefunction (either α or β)[49b] of the ℓ^{th} "free"

electron, and $\zeta_{\underset{\sim}{o}\,\underset{\sim}{n}}(\theta_\ell, \varphi_\ell)$ is the scattering amplitude for each possible outcome of the collision (each $\underset{\sim}{o} \rightarrow \underset{\sim}{n}$ transition of CP). We will not explicitly consider ionization (two or more outgoing electrons) or negative ion formation (no outgoing electrons).

From (3-11) one notes that k_n is imaginary for $(E_n - E_o) > \frac{\hbar^2}{2m} k_o^2$. Consequently, the terms in (3-12) corresponding to the excitation of states which are not accessible by energy conservation decay exponentially with r and contribute negligibly to the detected scattering. Nevertheless, these terms must be included for mathematical completeness.

It can be shown[1b] that the cross section per unit solid angle (DCS defined in section 1) for an electron to be scattered into the (θ, φ) direction leaving CP in its $\underset{\sim}{n}^{th}$ state is

$$\sigma_{on}(k_o, \theta, \varphi) = \frac{k_n}{k_o} \left| \zeta_{\underset{\sim}{o}\,\underset{\sim}{n}}(\theta, \varphi) \right|^2 . \qquad (3\text{-}13)$$

The total collision cross section $Q_{on}(k_o)$ for the $\underset{\sim}{o} \rightarrow \underset{\sim}{n}$ transition in CP is obtained by the integration of (3-13) over all θ and φ:

$$Q_{on}(k_o) = \int_0^{2\pi} d\varphi \int_0^{\pi} \sin\theta \; \sigma_{on}(k_o, \theta, \varphi)\, d\theta . \qquad (3\text{-}14)$$

From an examination of the required asymptotic from (3-12), it appears that a simplification of the problem can be obtained by expanding Ψ_I in terms of the functions $\psi_{\underset{\sim}{n}}$ (presumably known). This expansion must also be antisymmetric and can be written as

$$\Psi_I = \sum_{\underset{\sim}{n}=0}^{\infty} (1 - \Sigma_{op}) \{ G_{\underset{\sim}{n}}(\underset{\sim}{\tau}_1) \psi_{\underset{\sim}{n}}(\underset{\sim}{\tau}_2, \cdots \underset{\sim}{\tau}_N; \underset{\sim}{R}) \} \qquad (3\text{-}15)$$

where $G_{\underset{\sim}{n}}(\underset{\sim}{\tau}_\ell)$ is an unknown function depending on the space and spin coordinates of the ℓ^{th} electron (see reference 50). Substitution of (3-15) into (3-4) yields

$$\sum_{\underset{\sim}{n}=0}^{\infty} (\hat{H}_T - E)(1 - \Sigma_{op}) \{ G_{\underset{\sim}{n}}(\underset{\sim}{\tau}_1) \psi_{\underset{\sim}{n}}(\underset{\sim}{\tau}_2, \cdots \underset{\sim}{\tau}_N, \underset{\sim}{R}) \} = 0. \qquad (3\text{-}16)$$

Since $\hat{H}_T$ is completely symmetric in the coordinates of the electrons, $\hat{H}_T$ and Σ_{op} commute. If in addition one uses the separation of $\hat{H}_T$ indicated in (3-6) with conditions (3-9) and (3-11), (3-16) becomes

$$\sum_{\underset{\sim}{n}=0}^{\infty} (1 - \Sigma_{op}) \{ [\nabla_1^2 + k_n^2 - \frac{2m}{\hbar^2} V_{1CP}]$$

$$\times [G_{\underset{\sim}{n}}(\underset{\sim}{\tau}_1) \psi_{\underset{\sim}{n}}(\underset{\sim}{\tau}_2, \cdots \underset{\sim}{\tau}_N; \underset{\sim}{R})] \} = 0 \qquad (3\text{-}17)$$

After multiplying (3-17) by $\psi^*_{\underset{\sim}{m}}(\underset{\sim}{\tau}_2, \cdots \underset{\sim}{\tau}_N; \underset{\sim}{R})$ and integrating over all of the space and spin coordinates except those of electron 1, one obtains

$$(\nabla_1^2 + k_{\underset{\sim}{m}}^2) G_{\underset{\sim}{m}}(\underset{\sim}{\tau}_1) = \sum_{n=0}^{\infty} U_{\underset{\sim}{m}\,\underset{\sim}{n}}(\underset{\sim}{\tau}_1) G_{\underset{\sim}{n}}(\underset{\sim}{\tau}_1)$$

(3-18)

$$+ (N-1) \sum_{\underset{\sim}{n}=o}^{\infty} \int \langle \psi_{\underset{\sim}{m}}^{*}(\underset{\sim}{\tau}_2, \cdots, \underset{\sim}{\tau}_N; \underset{\sim}{R}) \psi_{\underset{\sim}{n}}(\underset{\sim}{\tau}_1, \underset{\sim}{\tau}_3, \cdots \underset{\sim}{\tau}_N; R) \hat{L}_2 G_{\underset{\sim}{n}}(\underset{\sim}{\tau}_2) \rangle_{(1)},$$

where $$\hat{L}_2 \equiv [\nabla_2^2 + k_n^2 - \frac{2m}{\hbar^2} V_{2CP}],$$

$$U_{\underset{\sim}{m}\,\underset{\sim}{n}}(\underset{\sim}{\tau}_1) \equiv \frac{2m}{\hbar^2} \langle \psi_{\underset{\sim}{m}}^{*}(\underset{\sim}{\tau}_2, \cdots \underset{\sim}{\tau}_N; \underset{\sim}{R}) V_{1CP} \psi_{\underset{\sim}{n}}(\underset{\sim}{\tau}_2, \cdots \underset{\sim}{\tau}_N; \underset{\sim}{R} \rangle_{(1)},$$

and the operations indicated by Σ_{op} have been carried out. If this infinite set of coupled integro-differential equations can be solved for the $G_{\underset{\sim}{n}}(\underset{\sim}{\tau})$ with asymptotic forms

$$G_{\underset{\sim}{n}}(\underset{\sim}{\tau}) \underset{r \to \infty}{\sim} e^{i \underset{\sim}{k}_o \cdot \underset{\sim}{r}} \delta_{on} s_o + \zeta_{\underset{\sim}{o}\,\underset{\sim}{n}}(\theta, \varphi) \frac{e^{ik_n r}}{r} s_n \qquad (3\text{-}19)$$

then the scattering problem is solved.

3.3. Approximations

3.3.1. Close-Coupling

In practice, one cannot solve an infinite system of coupled equations without some sort of simplification. The least restrictive approximation which renders (3-18) soluble (in principle) is to confine the expansion (3-15) to a finite set of basis functions which are considered to be most important for the scattering process. This is known as the close-coupling approximation. However, the inclusion of many states is extremely laborious for even a relatively simple system in which CP is atomic hydrogen. The most extensive coupling scheme yet employed for this system[51] included the 1s, 2s, 2p, 3s, 3p, and 3d atomic hydrogen states.

There is an additional complication for systems in which CP contains more than one electron since the exact wave functions $\psi_{\underset{\sim}{n}}$ are not known analytically. Burke, et al.[52] have carried out the most complete close-coupling calculation for the case in which CP is helium. They used five states--1^1S, 2^1S, 2^3S, 2^1P, 2^3P--approximated by Hartree-Fock atomic wave functions.

3.3.2. Two State

A somewhat more drastic approximation that one may make is to assume that only the initial ($\psi_{\underset{\sim}{o}}$) and final ($\psi_{\underset{\sim}{n}}$) states of CP are important in expansion (3-15). In effect, one neglects all terms in (3-18) which do not directly couple $\underset{\sim}{o} \rightarrow \underset{\sim}{o}$, $\underset{\sim}{n} \rightarrow \underset{\sim}{n}$, or $\underset{\sim}{o} \rightarrow \underset{\sim}{n}$, assuming that the coupling between the $\underset{\sim}{o}$, $\underset{\sim}{n}$ states and all others is negligibly weak. For this case, (3-18) reduces to two coupled integro-differential equations

$$[\nabla_1^2 + k_o^2 - U_{\underset{\sim}{o}\underset{\sim}{o}}] G_{\underset{\sim}{o}}(\underset{\sim}{r}_1) = U_{\underset{\sim}{o}\underset{\sim}{n}}(\underset{\sim}{r}_1) G_{\underset{\sim}{n}}(\underset{\sim}{r}_1) \tag{3-20a}$$

$$+ (N-1) \langle \psi_{\underset{\sim}{o}}^*(\underset{\sim}{r}_2, \cdots \underset{\sim}{r}_N; \underset{\sim}{R}) \psi_{\underset{\sim}{o}}(\underset{\sim}{r}_1, \underset{\sim}{r}_3, \cdots \underset{\sim}{r}_N; \underset{\sim}{R}) \hat{L}_2 G_{\underset{\sim}{o}}(\underset{\sim}{r}_2) \rangle_{(1)}$$

$$+ (N-1) \langle \psi_{\underset{\sim}{o}}^*(\underset{\sim}{r}_2, \cdots \underset{\sim}{r}_N; \underset{\sim}{R}) \psi_{\underset{\sim}{n}}(\underset{\sim}{r}_1, \underset{\sim}{r}_3, \cdots, \underset{\sim}{r}_N; \underset{\sim}{R}) \hat{L}_2 G_{\underset{\sim}{n}}(\underset{\sim}{r}_2) \rangle_{(1)}$$

and

$$[\nabla_1^2 + k_n^2 - U_{\underset{\sim}{n}\underset{\sim}{n}}] G_{\underset{\sim}{n}}(\underset{\sim}{r}_1) = U_{\underset{\sim}{n}\underset{\sim}{o}}(\underset{\sim}{r}_1) G_{\underset{\sim}{o}}(\underset{\sim}{r}_1) \tag{3-20b}$$

$$+ (N-1) \langle \psi_{\underset{\sim}{n}}^*(\underset{\sim}{r}_2, \cdots \underset{\sim}{r}_N; \underset{\sim}{R}) \psi_{\underset{\sim}{o}}(\underset{\sim}{r}_1, \underset{\sim}{r}_3, \cdots \underset{\sim}{r}_N; \underset{\sim}{R}) \hat{L}_2 G_{\underset{\sim}{o}}(\underset{\sim}{r}_2) \rangle_{(1)}$$

$$+ (N-1) < \psi_{\underset{\sim}{n}}^{*}(\underset{\sim}{\tau}_2, \cdots \underset{\sim}{\tau}_N; \underset{\sim}{R})\, \psi_{\underset{\sim}{n}}(\underset{\sim}{\tau}_1, \underset{\sim}{\tau}_3, \cdots \underset{\sim}{\tau}_N; \underset{\sim}{R})\, \hat{L}_2\, G_{\underset{\sim}{n}}(\underset{\sim}{\tau}_2) >_{(1)} .$$

This approach has been applied to a number of cases[53] and seems appropriate for transitions between states with a small energy difference (for example, the resonance ns → np transitions of alkali metals) at low impact energies.

3.3.3. Distorted Wave

If it is further assumed that the back coupling between the initial and final states is negligible (terms which couple $\underset{\sim}{o} \rightarrow \underset{\sim}{n}$ are dropped from (3-20), then (3-20a)) becomes

$$[\nabla_1^2 + k_o^2 - U_{\underset{\sim}{o}\underset{\sim}{o}}]\, G_{\underset{\sim}{o}}(\underset{\sim}{\tau}_1) \tag{3-21}$$

$$= (N-1) < \psi_{\underset{\sim}{o}}^{*}(\underset{\sim}{\tau}_2, \cdots \underset{\sim}{\tau}_N; \underset{\sim}{R})\, \psi_{\underset{\sim}{o}}(\underset{\sim}{\tau}_1, \underset{\sim}{\tau}_3, \cdots \underset{\sim}{\tau}_N; \underset{\sim}{R})\, \hat{L}_2\, G_{\underset{\sim}{o}}(\underset{\sim}{\tau}_2) >_{(1)}$$

The solution $\tilde{G}_{\underset{\sim}{o}}(\underset{\sim}{\tau})$ of (3-21) with the asymptotic form

$$\tilde{G}_{\underset{\sim}{o}}(\underset{\sim}{\tau}) \underset{r \rightarrow \infty}{\sim} (e^{i \underset{\sim}{k}_o \cdot \underset{\sim}{r}} + \tilde{\xi}_{\underset{\sim}{o}\underset{\sim}{o}}(\theta, \varphi) \frac{e^{i k_o r}}{r}) s_o \tag{3-22}$$

is substituted into (3-20b) to give the inhomogeneous integro-differential equation

$$[\nabla_1^2 + k_n^2 - U_{\underset{\sim}{n}\underset{\sim}{n}}]\, G_{\underset{\sim}{n}}(\underset{\sim}{\tau}_1) = U_{\underset{\sim}{n}\underset{\sim}{o}}(\underset{\sim}{\tau}_1)\, \tilde{G}_{\underset{\sim}{o}}(\underset{\sim}{\tau}_1) \tag{3-23}$$

$$+ (N-1) < \psi_{\underset{\sim}{n}}^{*}(\underset{\sim}{\tau}_2, \cdots \underset{\sim}{\tau}_N; \underset{\sim}{R})\, \psi_{\underset{\sim}{o}}(\underset{\sim}{\tau}_1, \underset{\sim}{\tau}_3, \cdots \underset{\sim}{\tau}_N; \underset{\sim}{R})\, \hat{L}_2\, \tilde{G}_{\underset{\sim}{o}}(\underset{\sim}{\tau}_2) >_{(1)}$$

$$+ (N - 1) \langle \psi_{\underset{\sim}{n}}^{*}(\underset{\sim}{\tau}_2, \cdots \underset{\sim}{\tau}_N; \underset{\sim}{R}) \psi_{\underset{\sim}{n}}(\underset{\sim}{\tau}_1, \underset{\sim}{\tau}_3, \cdots \underset{\sim}{\tau}_N; \underset{\sim}{R}) \hat{L}_2 G_{\underset{\sim}{n}}(\underset{\sim}{\tau}_2) \rangle_{(1)} \quad .$$

If $\tilde{G}_{\underset{\sim}{n}}(\underset{\sim}{\tau}_1)$ is the proper solution of the homogeneous equation corresponding to (3-23) (terms containing $\tilde{G}_{\underset{\sim}{o}}$ are set equal to 0) with the asymptotic form

$$\tilde{G}_{\underset{\sim}{n}}(\underset{\sim}{\tau}) \underset{r \to \infty}{\sim} (e^{i \underset{\sim}{k}_n \cdot \underset{\sim}{r}} + \tilde{\zeta}_{\underset{\sim}{o}\underset{\sim}{n}}(\theta, \varphi) \frac{e^{i k_n r}}{r}) s_n \,, \tag{3-24}$$

then it can be shown[44a] that the scattering amplitude in the asymptotic form (3-19) of $G_{\underset{\sim}{n}}(\underset{\sim}{\tau})$ is given by

$$\zeta_{\underset{\sim}{o}\underset{\sim}{n}}(\theta, \varphi) = -\frac{1}{4\pi} \int \{ \tilde{G}_{\underset{\sim}{n}}(\underset{\sim}{\tau}_1, \pi - \Theta) [U_{\underset{\sim}{n}\underset{\sim}{o}}(\underset{\sim}{\tau}_1) \tilde{G}_{\underset{\sim}{o}}(\underset{\sim}{\tau}_1) + \tag{3-25}$$

$$+ (N - 1) \langle \psi_{\underset{\sim}{n}}^{*}(\underset{\sim}{\tau}_2, \cdots \underset{\sim}{\tau}_N; \underset{\sim}{R}) \psi_{\underset{\sim}{o}}(\underset{\sim}{\tau}_1, \underset{\sim}{\tau}_3, \cdots \underset{\sim}{\tau}_N; \underset{\sim}{R}) \hat{L}_2 \tilde{G}_{\underset{\sim}{o}}(\underset{\sim}{\tau}_2) \rangle_{(1)}] \} d\underset{\sim}{\tau}_1$$

where $\cos \Theta = \cos \theta \cos \theta_1 + \sin \theta \sin \theta_1 \cos (\varphi - \varphi_1)$.

This method is denoted as the distorted wave method since the free electron is represented by functions which are distorted by the static fields of CP before and after the excitation. In another sense, this procedure simply assumes that all inelastic processes are negligible compared to the elastic one (i.e., all $\zeta_{\underset{\sim}{o}\underset{\sim}{n}}(\underset{\sim}{n} \neq \underset{\sim}{o}) \ll \zeta_{\underset{\sim}{o}\underset{\sim}{o}}$ in (3-12) and hence only $G_{\underset{\sim}{o}}$ is needed in (3-15). This situation is usually obtained at higher impact energies.

Calculations using this method have been performed for atomic hydrogen[54], helium[55], and a few other systems[53].

3.3.4. Born-Oppenheimer

3.3.4.1. Scattering amplitude

The Born-Oppenheimer approximation[56] results if, in addition to the previous approximations, we assume that all scattering (elastic and inelastic) is a small perturbation on the incident and scattered plane waves (i.e., that $\tilde{\zeta}_{\underset{\sim}{o}\underset{\sim}{o}}$ and $\tilde{\zeta}_{\underset{\sim}{o}\underset{\sim}{n}}$ can be neglected in equations (3-22) and (3-24)). If $\tilde{G}_{\underset{\sim}{o}}$ and $\tilde{G}_{\underset{\sim}{n}}$ in equation (3-25) are replaced by undistorted plane waves times one electron spin wave functions, then the scattering amplitude is given by

$$\zeta_{\underset{\sim}{o}\underset{\sim}{n}}(\theta,\varphi) = -\frac{1}{4\pi}\int\{e^{i(\underset{\sim}{k}_o-\underset{\sim}{k}_n)\cdot\underset{\sim}{r}_1}\, s_o(1)s_n^*(1)\, U_{\underset{\sim}{n}\underset{\sim}{o}}(\underset{\sim}{\tau}_1) \tag{3-26}$$

$$+(N-1)\, e^{-i\underset{\sim}{k}_n\cdot\underset{\sim}{r}_1} s_n^*(1)\langle\psi_{\underset{\sim}{n}}^*(\underset{\sim}{\tau}_2,\cdots\underset{\sim}{\tau}_N;\underset{\sim}{R})\,\psi_{\underset{\sim}{o}}(\underset{\sim}{\tau}_1,\underset{\sim}{\tau}_3,\cdots\underset{\sim}{\tau}_N;\underset{\sim}{R})$$

$$\times[\hat{L}_2\, e^{i\underset{\sim}{k}_o\cdot\underset{\sim}{r}_2} s_o(2)]\rangle_{(1)}\}\, d\underset{\sim}{\tau}_1$$

This equation can be rewritten, using the definitions of $U_{\underset{\sim}{n}\underset{\sim}{o}}$, $\psi_{\underset{\sim}{n}}$, and $\hat{L}_2$ as

$$\zeta_{\underset{\sim}{o}\underset{\sim}{n}}(\theta,\varphi) = \langle s_o(1)\mathcal{S}_{SS_z}(2,\ldots N)\, s_n^*(1)\mathcal{S}^*_{S'S_z'}(2,\ldots N)\rangle_{spin} f^B_{on}(\theta,\varphi) \tag{3-27}$$

$$-(N-1)\langle s_o(2)\mathcal{S}_{SS_z}(1,3,\ldots N)\, s_n^*(1)\mathcal{S}^*_{S'S_z'}(2,\ldots N)\rangle_{spin} g^{BO}_{on}(\theta,\varphi)$$

where

$$f^B_{on}(\theta,\varphi) \tag{3-28a}$$

$$\equiv -\frac{2\pi m}{h^2}\langle e^{i(\underset{\sim}{k}_o-\underset{\sim}{k}_n)\cdot\underset{\sim}{r}_1}\,\Phi_n^*(\underset{\sim}{r}_2,\cdots\underset{\sim}{r}_N;\underset{\sim}{R})\, V_{1CP}\,\Phi_o(\underset{\sim}{r}_2,\cdots\underset{\sim}{r}_N;\underset{\sim}{R})\rangle_{space};$$

$$g_{on}^{BO}(\theta,\varphi) \tag{3-28b}$$

$$\equiv -\frac{2\pi m}{h^2}\left\langle e^{-i\underset{\sim}{k}_n\cdot\underset{\sim}{r}_1}\Phi_n^*(\underset{\sim}{r}_2,\cdots\underset{\sim}{r}_N;\underset{\sim}{R})V_{2CP}\Phi_0(\underset{\sim}{r}_1,\underset{\sim}{r}_3,\cdots\underset{\sim}{r}_N;\underset{\sim}{R})\right.$$

$$\left.\times\left[e^{i\underset{\sim}{k}_0\cdot\underset{\sim}{r}_2}\right]\right\rangle_{space};$$

$\mathcal{S}_{S'S_z'}$ and Φ_n are the normalized space and spin wave functions, respectively, associated with each $\psi_{\underset{\sim}{n}}$; and $\langle\rangle_{spin}$ and $\langle\rangle_{space}$ represent an integration over all spin and space coordinates, respectively, of the N electrons and N′ nuclei. (3-28a) and (3-28b) correspond to the usual definitions of the Born direct and Born-Oppenheimer exchange scattering amplitudes, respectively.

The Born-Oppenheimer approximation is expected to be valid at relatively high incident energies (a few times the excitation threshold) since it is based on the assumption that there is only a weak interaction between the incident electron and the target (i. e., the probability per collision for excitation is small). Detailed discussions of the applicability of this approximation can be found elsewhere[42, 53, 57]. Usually it overestimates total cross sections within a few eV of the excitation threshold by about a factor of 10. At higher impact energies (where the probability of exchange processes approaches zero) it seems to agree with more exact calculations[57].

3.3.4.2. Spin statistics

The spin state of the N electron system (in the absence of appreciable spin-orbit coupling) before the collision $(s_o(1)\mathcal{S}_o(2,\ldots N))$ is denoted by $\mathcal{S}_{\Sigma\mu}(1,\ldots N)$ and is an eigenfunction of total spin $\hat{S}_T^2 = (\hat{S}_1 + \hat{S}_2 + \ldots \hat{S}_N)^2$ with eigenvalue Σ and of the z component $\hat{S}_{zT} = (\hat{S}_{z1} + \ldots \hat{S}_{zN})$ with eigenvalue μ. Since the interaction giving rise to the excitation is assumed independent of spin, Σ and μ are conserved. Thus, the spin state after collision $(s_n(1)\mathcal{S}_n(2,\ldots N))$ is denoted $\mathcal{S}'_{\Sigma\mu}(1,\ldots N)$ (with the same Σ and μ). There is a scattering amplitude $\underset{\sim}{\underset{\sim}{\zeta}}_{on}^{\Sigma\mu}$ associated with each value of (Σ,μ) which is computed by averaging over the experimentally accessible initial states $\mathcal{S}_{\Sigma\mu}$ and summing over the final ones $\mathcal{S}'_{\Sigma\mu}$ with the same values of Σ and μ. Since we have specifically excluded the possibility of a state with a given (Σ,μ) evolving into any state with a different (Σ,μ), the amplitudes $\underset{\sim}{\underset{\sim}{\zeta}}_{on}^{\Sigma\mu}$ cannot interfer and the DCS is given by

$$\sigma_{on}(k_o,\theta,\varphi) = \frac{k_n}{k_o} \sum_{\Sigma,\mu} p(\Sigma,\mu) \left| \underset{\sim}{\underset{\sim}{\zeta}}_{on}^{\Sigma\mu} \right|^2 . \tag{3-29}$$

$p(\Sigma,\mu)$ is the probability per collision for a spin state with Σ and μ and the sum extends over all Σ and μ which correspond to the same excitation energy of the target.

From (3-27) $\underset{\sim}{\underset{\sim}{\zeta}}_{on}^{\Sigma\mu}$ is given by

$$\begin{aligned} \underset{\sim}{\underset{\sim}{\zeta}}_{on}^{\Sigma\mu} &= \langle \mathcal{S}_{\Sigma\mu}(1,\ldots N)\, \mathcal{S}'^{*}_{\Sigma\mu}(1,\ldots N) \rangle_{spin} f_{on}^{B} \\ &- (N-1) \langle \mathcal{S}_{\Sigma\mu}(2,1,\ldots N)\, \mathcal{S}'^{*}_{\Sigma\mu}(1,\ldots N) \rangle_{spin} g_{on}^{BO} \end{aligned} \tag{3-30}$$

As specific examples for the application of (3-29) and (3-30), the scattering of electrons by atomic hydrogen and helium will be considered.

For a two electron system (electron + hydrogen atom), Σ may have the values 0 (singlet state) and 1 (triplet state) with μ values of 0 and 1, 0, -1, respectively. For each value of (Σ, μ), there is only one two-electron spin state so that $\mathcal{S}_{\Sigma\mu} = \mathcal{S}'_{\Sigma\mu}$. In this case (3-30) reduces to the simple form:

$$\begin{aligned} \underset{\sim}{\underset{o}{\underset{\sim}{\underset{n}{\zeta}}}}^{\Sigma\mu} &= \langle \mathcal{S}_{\Sigma\mu}(1,2)\, \mathcal{S}^{*}_{\Sigma\mu}(1,2) \rangle_{spin} f^{B}_{on} \\ &\quad - \langle \mathcal{S}_{\Sigma\mu}(2,1)\, \mathcal{S}^{*}_{\Sigma\mu}(1,2) \rangle_{spin} g^{BO}_{on} \\ &= f^{B}_{on} \pm g^{BO}_{on} \end{aligned} \tag{3-31}$$

where the - or + is used depending on whether $\mathcal{S}_{\Sigma\mu}$ is symmetric or antisymmetric. Since the states $(\Sigma, \mu) = (0, 0)$ are antisymmetric while those with $(\Sigma, \mu) = (1,1)$, $(1,0)$, or $(1,-1)$ are symmetric, it is easy to see from (3-31) that

$$\begin{aligned} \underset{\sim}{\underset{o}{\underset{\sim}{\underset{n}{\zeta}}}}^{0,0} &= f^{B}_{on} - g^{BO}_{on} \quad \text{and} \\ \underset{\sim}{\underset{o}{\underset{\sim}{\underset{n}{\zeta}}}}^{1,1} &= \underset{\sim}{\underset{o}{\underset{\sim}{\underset{n}{\zeta}}}}^{1,0} = \underset{\sim}{\underset{o}{\underset{\sim}{\underset{n}{\zeta}}}}^{1,-1} = f^{B}_{on} + g^{BO}_{on} \quad . \end{aligned} \tag{3-32}$$

The four $(\Sigma\mu)$ states mentioned above are all equally probable since we use an unpolarized electron beam, and no other $(\Sigma\mu)$ combinations are possible. Thus, the differential cross section as given by (3-29) is

$$\sigma_{on}(ko\ ,\theta\ ,\varphi) = \frac{k_n}{k_o}\{\frac{1}{4}\left|f^B_{on} - g^{BO}_{on}\right|^2 + \frac{3}{4}\left|f^B_{on} + g^{BO}_{on}\right|^2\} \qquad (3\text{-}33)$$

within the framework of the Born-Oppenheimer approximation.

For a three electron system (electron + helium), Σ may have the values $\frac{1}{2}$ (doublet state) and $\frac{3}{2}$ (quartet state) with μ values of $\frac{1}{2}$, $-\frac{1}{2}$ and $\frac{3}{2}$, $\frac{1}{2}$, $-\frac{1}{2}$, $-\frac{3}{2}$, respectively. Since essentially all of the helium atoms are in their singlet ground state (two electrons paired) the initial configuration (and also the final one) of the electron plus helium system must be a doublet. However, the final <u>helium</u> configuration can be either singlet or triplet. These two possible outcomes are observable as different events and, therefore, there are two amplitudes $\zeta_{\underset{\sim}{o}\underset{\sim}{n}_1}$ and $\zeta_{\underset{\sim}{o}\underset{\sim}{n}_3}$ corresponding to the singlet → singlet and singlet → triplet transitions, respectively. For helium in a singlet state and one free electron there are two possible spin states (with equal probability)

$$\mathcal{S}_{\frac{1}{2}\frac{1}{2}}(1,2,3) = \frac{1}{\sqrt{2}}\,\alpha_1\,(\alpha_2\beta_3 - \beta_2\alpha_3) \qquad \text{and}$$

$$\mathcal{S}_{\frac{1}{2}-\frac{1}{2}}(1,2,3) = \frac{1}{\sqrt{2}}\,\beta_1\,(\alpha_2\beta_3 - \beta_2\alpha_3).$$

If the final helium configuration is singlet, these sames states are also the final ones. Then one obtains $\zeta^{\frac{1}{2},\frac{1}{2}}_{\underset{\sim}{o}\underset{\sim}{n}_1}$ and $\zeta^{\frac{1}{2},-\frac{1}{2}}_{\underset{\sim}{o}\underset{\sim}{n}_1}$ from (3-30):

$$\zeta^{\frac{1}{2},\frac{1}{2}}_{\underset{\sim}{o}\underset{\sim}{n}_1} = \frac{1}{2}\langle(\alpha_1\alpha_2\beta_3 - \alpha_1\beta_2\alpha_3)(\alpha_1\alpha_2\beta_3 - \alpha_1\beta_2\alpha_3)\rangle_{spin} f^B_{on_1}$$

$$- \langle(\alpha_2\alpha_1\beta_3 - \alpha_2\beta_1\alpha_3)(\alpha_1\alpha_2\beta_3 - \alpha_1\beta_2\alpha_3)\rangle_{spin} g^{BO}_{on_1}$$

$$= f^{B}_{on_1} - g^{BO}_{on_1} \text{ and similarly,}$$

$$\underset{\sim}{\zeta}^{\frac{1}{2},-\frac{1}{2}}_{o\underset{\sim}{n}_1} = f^{B}_{on_1} - g^{BO}_{on_1} \quad .$$

Thus, the differential cross section is given by (3-29) as

$$\begin{aligned} \sigma_{on_1}(k_o, \theta, \varphi) &= \frac{k_{n_1}}{k_o}\left\{\frac{1}{2}\left|\zeta^{\frac{1}{2},\frac{1}{2}}_{on_1}\right|^2 + \frac{1}{2}\left|\zeta^{\frac{1}{2},-\frac{1}{2}}_{on_1}\right|^2\right\} \\ &= \frac{k_{n_1}}{k_o}\left|f^{B}_{on_1} - g^{BO}_{on_1}\right|^2. \end{aligned} \tag{3-34}$$

For helium in a triplet state and one free electron there are six possible spin functions, two of which have $\Sigma = \frac{1}{2}$ as required. They are

$$\mathcal{S}'_{\frac{1}{2}\frac{1}{2}}(1,2,3) = \frac{1}{\sqrt{6}}(\alpha_1\beta_2\alpha_3 + \alpha_1\alpha_2\beta_3 - 2\beta_1\alpha_2\alpha_3)$$

$$\mathcal{S}'_{\frac{1}{2}-\frac{1}{2}}(1,2,3) = \frac{1}{\sqrt{6}}(\beta_1\beta_2\alpha_3 + \beta_1\alpha_2\beta_3 - 2\alpha_1\beta_2\beta_3) \quad .$$

Then using the correct $\mathcal{S}_{\Sigma\mu}$ for each $\mathcal{S}'_{\Sigma\mu}$ (the same values of $(\Sigma\mu)$ in each), $\underset{\sim}{\zeta}^{\frac{1}{2},\pm\frac{1}{2}}_{o\underset{\sim}{n}_3}$ can be obtained from (30).

$$\begin{aligned} \underset{\sim}{\zeta}^{\frac{1}{2},\frac{1}{2}}_{o\underset{\sim}{n}_3} &= \frac{1}{\sqrt{12}}\langle(\alpha_1\alpha_2\beta_3 - \alpha_1\beta_2\alpha_3)(\alpha_1\beta_2\alpha_3 + \alpha_1\alpha_2\beta_3 - 2\beta_1\alpha_2\alpha_3)\rangle_{spin} f^{B}_{on_3} \\ &\quad - \frac{2}{\sqrt{12}}\langle(\alpha_2\alpha_1\beta_3 - \alpha_2\beta_1\alpha_3)(\alpha_1\beta_2\alpha_3 + \alpha_1\alpha_2\beta_3 - 2\beta_1\alpha_2\alpha_3)\rangle_{spin} g^{BO}_{on_3} \\ &= -\sqrt{3}\, g^{BO}_{on_3}, \text{ and} \end{aligned}$$

$\zeta^{\frac{1}{2},-\frac{1}{2}}_{\underset{\sim}{o}\underset{\sim}{n}_3} = \sqrt{3}\, g^{BO}_{on_3}$ in a similar manner.

Thus, the cross section as given by (3-29) is

$$\sigma_{on_3}(k_o, \theta, \varphi) = \frac{k_{n_3}}{k_o}\left\{\frac{1}{2}\left|-\sqrt{3}\, g^{BO}_{on_3}\right|^2 + \frac{1}{2}\left|\sqrt{3}\, g^{BO}_{on_3}\right|^2\right\}$$

$$= 3\frac{k_n}{k_o}\left|g^{BO}_{on_3}\right|^2 . \qquad (3\text{-}35)$$

3.3.4.3. Ochkur-Rudge modifications

In 1963 Ochkur[58] made a significant improvement in the Born-Oppenheimer approximation. He expanded g^{BO}_{on} in powers of $\frac{1}{k_o}$ and retained only the leading term, which varied as $\frac{1}{k_o^2}$ (the next term is of order $\frac{1}{k_o^3}$)[59]. The deletion of these higher order terms was justified by the fact that the Born direct amplitude f^B_{on} does not contain these higher order terms. The leading term can be readily obtained[53] and is given by

$$g^O_{on} = -\frac{2me^2}{\hbar^2 k_o^2}\left\langle e^{i\underset{\sim}{q}\cdot\underset{\sim}{r}_2}\, \Phi_n^*(\underset{\sim}{r}_2, \ldots \underset{\sim}{r}_N; \underset{\sim}{R})\Phi_o(\underset{\sim}{r}_2, \ldots \underset{\sim}{r}_N; \underset{\sim}{R})\right\rangle_{(1)} , \qquad (3\text{-}36)$$

where $\underset{\sim}{q} = \underset{\sim}{k}_o - \underset{\sim}{k}_n$.

At this point, we note also that f^B_{on} (equation 3-27) can be simplified. Substitution of V_{1CP} by its explicit form (3-6) and integration[60] over the coordinates of the incident electron yields

$$f_{on}^{B} = -\frac{2me^2}{\hbar^2 q^2} \langle \Phi_n^*(\underset{\sim}{r}_2, \cdots \underset{\sim}{r}_N; \underset{\sim}{R}) [\sum_{\ell=2}^{N} e^{i\underset{\sim}{q}\cdot\underset{\sim}{r}_\ell} - \sum_{j=1}^{N'} e^{i\underset{\sim}{q}\cdot\underset{\sim}{R}_j}] \Phi_o(\underset{\sim}{r}_2, \cdots \underset{\sim}{r}_N; \underset{\sim}{R}) \rangle_{(1)} \quad (3\text{-}37a)$$

If we assume that Φ can be factored into a product of an electronic and nuclear wave function[61], then for $n \neq 0$,

$$f_{on}^{B} = -\frac{2me^2}{\hbar^2 q^2}(N-1) \langle \Phi_n^* e^{i\underset{\sim}{q}\cdot\underset{\sim}{r}_2} \Phi_o \rangle_{(1)} , \quad (3\text{-}37b)$$

since all of the terms in the first sum give equal contributions and the terms of the second sum (core interaction) vanish because the electronic parts of Φ_n and Φ_o are orthogonal. It is worth noting that for elastic scattering ($n = o$), the core interaction terms must be retained in (3-37a) but that they do not appear in (3-36).

The expectation values of (3-36) and (3-37b) are the same and the scattering amplitudes differ only in the replacement of $\frac{(N-1)}{k_o^2}$ in (3-36) by $\frac{1}{q^2}$ in (3-37b). This difference leads to quite different angular dependencies as will be seen later.

Rudge[62] has pointed out that the Ochkur result is not consistent with certain variational principles. He obtained an improvement of the Ochkur result which differs only in the pre-integral factor and is given by

$$g_{on}^{OR} = -\frac{k_o^2}{[k_n - iA]^2} \; g_{on}^{O} , \quad (3\text{-}38)$$

where $A = [2mI_i]^{\frac{1}{2}}/\hbar$ and I_i is the ionization energy of the initial bound state. The Rudge result is also expected to be superior to the Ochkur one since the former is complex--a necessary[63] but not sufficient[64,57] condition for the conservation of particle flux. However, $\underset{\sim}{\zeta}_{\underset{\sim}{o}\underset{\sim}{n}}$ computed using g_{on}^{OR} does not satisfy the principle of detailed balance ($|\underset{\sim}{\zeta}_{\underset{\sim}{o}\underset{\sim}{n}}|^2 \neq |\underset{\sim}{\zeta}_{\underset{\sim}{n}\underset{\sim}{o}}|^2$) if the final state can be reached by a direct process. (Both the Ochkur and Born-Oppenheimer approximations satisfy this principle[65a].) Bely[64] has shown that this failure can be corrected if g_{on}^{OR} is replaced by its absolute value $|g_{on}^{OR}|$.

3.3.5. Comparison of Methods

Truhlar, et al.[57] have recently presented an excellent comparison of the methods discussed above (and several others) for the special case of atomic hydrogen. They included a comparison of differential as well as total scattering cross sections. In addition, calculated differential cross sections are available for the $1^1S - 2^3S$[32,66,67], $1^1S - 2^3P$[66] transitions in helium and the $1^1\Sigma_g^+ - b^3\Sigma_u^+$, $a^3\Sigma_g^+$ ones of H_2[66,68]. We know of no other inelastic differential cross section calculations apart from those using only the direct Born amplitude f_{on}^{B} [69].

It is of interest to compare the results of some of these methods with experiment for two specific cases in helium. Tables 3.3-1 and 3.3-2 present some experimental and theoretical total cross sections for the $1^1S - 2^3P$ and $1^1S - 2^3S$ transitions, respectively. Table 3.3-3 shows a comparison of differential cross

TABLE 3.3-1

Total cross sections for the $1^1S \rightarrow 2^3P$ excitation of helium in units of $10^{-2}\pi a_0^2$. The excitation threshold is 20.96 eV.

Incident Electron Energy (eV)	Experiment	Theory				
	JS[a]	MM[b]	BEM[c]	OB[d]	MR[e]	C[f]
(max)[g]	2.7(23)	15(24)	30(21)	6.8(25)	4.6(24)	4.4(25)
30	2.4	11	14	6.0	3.5	3.5
50	1.3	2.7	3.0	2.2	1.0	1.0
100	0.23	0.26	0.36	0.35	0.14	-
225	($\lesssim$.01)	0.01	0.02	0.03	-	-

[a] Experimental results, reference (43).

[b] Distorted wave method, reference (55b).

[c] Born-Oppenheimer approximation, reference (70).

[d] Ochkur approximation, reference (58b)

[e] Rudge modification of Ochkur result, reference (71).

[f] Ochkur-Rudge method, reference (66).

[g] The number in parentheses is the incident energy at which the maximum cross section is obtained.

TABLE 3.3-2

Total cross sections for the $1^1S - 2^3S$ transition of helium in units of $10^{-2}\pi a_0^2$. The excitation threshold is 19.82 eV.

Incident Electron Energy (eV)	Experiment	Theory				
	VSM[a]	MM[b]	BEM[c]	OB[d]	MR[e]	C[f]
30	-	1.50	85	6.0	6.0_5	4.7
50	-	.60	21	2.2	2.5	1.9
100	$.090_5$	-	1.6	.35	.43	-
150	$.024_3$	-	0.28	.11	.14	-
200	$.010_1$	-	0.058	.047	-	-

[a] Experimental results, reference (67b).

[b] Distorted wave approximation, reference (55a).

[c] Born-Oppenheimer approximation, reference (70).

[d] Ochkur approximation, reference (58b).

[e] Rudge modification, reference (71).

[f] Ochkur-Rudge approximation, reference (66).

TABLE 3.3-3

DCS for the $1^1S - 2^3S$ excitation of helium in units of $10^{-2}\pi a_0^2$ per steradian. The incident electron energy is 100 eV.

Scattering Angle	Experiment VSM[a]	Theory MK[b]	Theory C[c]
5°	0.19	.0045	.0019
10°	0.15	.020	.0075
15°	0.12	.051	.019
20°	0.057	.095	.038

[a] Experimental results, reference (67b).

[b] Born-Oppenheimer approximation, reference (67a).

[c] Ochkur-Rudge approximation, reference (66).

sections for the $1^1S \rightarrow 2^3S$ transition. Although the Ochkur (and Ochkur-Rudge) approximation seems to afford a remarkable improvement over the distorted wave and Born-Oppenheimer approximations for total cross sections at low energy, it fails to adequately describe the differential cross sections, either in magnitude or variation. All first order theories (Born-Oppenheimer, Ochkur-Rudge, etc.) predict a differential cross section which is peaked off 0° at sufficiently high energies for the case of the 1s → 2s exchange transition in atomic hydrogen[57]. It is interesting to note, however, that the Born-Oppenheimer approximation predicts significant forward peaking of the 1s → 2s differential cross section at lower energies for which the Ochkur approximation does not.

In the cases for which g_{on} provides a negligible contribution to $\underset{\sim}{\underset{\sim}{\zeta}}_{on}$ (high incident energy, low scattering angles, and no spin multiplicity change in the target[72]), the Born approximation (f^B_{on}) has been successful[53] in predicting differential cross sections as well as total ones. This is somewhat surprising since the Born amplitude is real and as a result cross sections derived from it necessarily violate the so called optical theorem or Born-Peierls-Placzek relation (conservation of particle flux). It can be shown[1c] simply from the Hermitian character of the Hamiltonian governing the scattering process that

$$Q_o^{total} = \frac{4\pi}{k_o} \text{Im} \{ \underset{\sim}{\underset{\sim}{\zeta}}_{oo}(0°, 0°) \} \qquad (3\text{-}39)$$

where Q_o^{total} is the total cross section for all processes with the initial state $\underset{\sim}{o}$ and $\underset{\sim\sim}{\zeta}_{\underset{\sim}{o}\,\underset{\sim}{o}}(0°,0°)$ is the forward scattering amplitude for the elastic process. If $\underset{\sim\sim}{\zeta}_{\underset{\sim}{o}\,\underset{\sim}{o}}(0°,0°)$ is replaced by $f^B_{oo}(0°,0°)$, then (3-39) implies that $Q_o^{total} = 0$ which is certainly not true. While (3-39) shows that the Born approximation is fundamentally incorrect at $(\theta,\varphi) \equiv (0°,0°)$, (3-14) indicates that its value there does not contribute to the total cross section. Further, $f^B_{\underset{\sim}{o}\,\underset{\sim}{o}}(\theta,\varphi)$ can be modified in a trivial way to satisfy (3-39), without altering the total cross section or differential ones except at $(\theta,\varphi) \equiv (0°,0°)$, by defining

$$f^{B'}_{on}(\theta,\varphi) = f^B_{on}(\theta,\varphi)\left[1 + i\,\frac{k_o Q_o^{total}}{4\pi f^B_{oo}(0°,0°)}\,\delta(\theta)\delta(\varphi)\right]. \qquad (3\text{-}40)$$

Then, from (3-13) the DCS at 0° for this modification is

$$\sigma'_{on}(k_o, 0°, 0°)$$

$$= \frac{k_n}{k_o}\left|f^B_{\underset{\sim}{o}\,\underset{\sim}{n}}(0°,0°)\right|^2\left\{1 + \frac{k_o^2}{16\pi^2}\,\frac{(Q_o^{total})^2}{[f^B_{oo}(0°,0°)]^2}\right\} \qquad (3\text{-}41$$

But $\sigma_{oo}(k_o, 0°, 0°) \cong \left|f^B_{oo}(0°,0°)\right|^2$ and at high incident energy $Q_o^{total} \cong Q_{oo}$ (total elastic). Since $\sigma_{oo}(k_o, 0°, 0°)$ is independent of k_o and $Q_{oo} \propto \frac{1}{k_o^2}$ at sufficiently high energy[44b], $k_o^2 (Q_o^{total})^2/(f^B_{oo}(0°,0°))^2 \to 0$ as $\frac{1}{k_o^2}$ for large k_o. However, calculations of forward differential scattering cross sections based on f^B_{on} at relatively low energies seem of doubtful value[73].

3.3.6. Selection Rules

General selection rules concerning electron impact excitation are quite difficult to define since all excited states are in principle coupled with the initial state (see equation (3-18)). However, at energies for which first order approximations are valid (in particular equation (3-27)), some meaningful "selection rules" can be obtained. We will consider the excitation of helium from its ground state as a specific example in order to simplify the discussion.

The DCS for transitions which do not involve a spin multiplicity charge ($1^1S \rightarrow n^1L$, where $L = S, P, \ldots$ and $n = 2, 3, \ldots$), is given (from equation(3-34)) approximately by

$$\sigma_{on_1}(k_o, \theta, \varphi)$$

$$\cong \frac{k_{n_1}}{k_o}\left[\left|f^B_{on_1}\right|^2 + \left|g^O_{on_1}\right|^2 - 2\cos\varphi_{on_1}\left(f^B_{on_1} g^O_{on_1}\right)\right] \qquad (3\text{-}42)$$

where φ_{on_1} is the relative phase angle between the direct and exchange amplitudes. φ_{on_1} is a function of k_o but not (θ, φ). From a comparison of (3-36) and (3-37) for helium, we obtain

$$g^O_{on_1} = \frac{q^2}{2k_o^2} f^B_{on_1} \qquad (3\text{-}43)$$

which implies from (3-42) that

$$\sigma_{on_1}(k_o, \theta, \varphi) \cong \frac{k_{n_1}}{k_o}\left|f^B_{on_1}\right|^2\left[1 - \frac{q^2}{k_o^2}\cos\varphi_{on_1} + \frac{q^4}{4k_o^4}\right]. \qquad (3\text{-}44)$$

Thus, in this approximation, the behavior of $f^B_{on_1}$ (equation 3-37) will determine that of σ_{on_1}.

Without loss of generality, the z_2 axis for the $\underset{\sim}{r}_2$ integration in (3-37) can be chosen along $\underset{\sim}{q}$. Further,

$$e^{i q z_2} = \sum_{\ell=0}^{\infty} \frac{(i q z_2)^{\ell}}{\ell!} \quad \text{if} \quad (q z_2)^2 < \infty. \tag{74a}$$ (3-45)

Substitution of (3-45) into (3-37) yields

$$f^{B}_{on_1} = \frac{-4me^2}{\hbar^2 q^2} \sum_{\ell=1}^{\infty} \frac{(i q)^{\ell}}{\ell!} z^{\ell}_{on_1} \tag{3-46}$$

where $z^{\ell}_{on_1} \equiv \int \phi^{*}_{n_1}(\underset{\sim}{r}_2, \underset{\sim}{r}_3)(z_2)^{\ell} \phi_o(\underset{\sim}{r}_2, \underset{\sim}{r}_3) d\underset{\sim}{r}_2 d\underset{\sim}{r}_3$.

The $z^{\ell}_{on_1}$ are the z components of the electric dipole ($\ell = 1$), quadrupole ($\ell = 2$), etc., transition moments encountered in optical spectroscopy[75]. If $\frac{\hbar^2 k_o^2}{2m} \gg E_n - E_o$, and θ^2 small, equation (3-44) becomes

$$\sigma_{on_1}(k_o, \theta, \varphi) \cong C\left\{\frac{(z^{1}_{on_1})^2}{q^2} + \frac{7}{12}(z^{2}_{on_1})^2 + \ldots\right\}\left\{1 - O(\theta^2)\right\}, \tag{3-47}$$

where $C = \left(\frac{4me^2}{\hbar^2}\right)^2$.

For dipole-allowed transitions ($1^1S \rightarrow 2^1P$ in helium for example) $z^{1}_{on_1}$ is dominant. In this case, electron impact excitation cross sections obey the usual electric-dipole selection rules of optical spectroscopy.

If a transition is electric-dipole forbidden ($z^{1}_{on_1} = 0$) but electric-quadrupole allowed ($z^{2}_{on_1} \neq 0$), then the transition is "allowed" to this same order by electron impact. The $1^1S \rightarrow n^1S$ transitions in helium are examples of this case. Note that to

$O(\theta^2)$ (and the neglect of $(z^3_{on_1})^2$, etc.) the differential cross section does not depend on either k_o or θ. It has recently been shown[32] that the $1^1S \rightarrow 2^1S$ differential cross section from 5° to 20° is relativcly independent of k_o from 150 eV to 400 eV but decreases sharply with increasing θ.

We next consider the case of exchange excitation in helium ($1^1S \rightarrow n^3L$). Equation (3-35) and the preceding analysis which led to equation (3-47) lead to

$$\sigma_{on_3}(k_o, \theta, \varphi) \cong 3C\left\{\frac{q^2}{k_o^4}\left(z^1_{on_3}\right)^2 + \frac{7}{12}\frac{q^4}{k_o^4}\left(z^2_{on_3}\right)^2 + \ldots\right\}. \tag{3-48}$$

Note that σ_{on_3} is predicted to increase with increasing θ (for small angles) for both S → S and S → P transitions. This seems to be in direct contradiction to the observed[32] behavior of the $1^1S \rightarrow 2^3S$ transition at large energies. It is also worth noting that as θ increases from 0°, the DCS for optically forbidden (spin and symmetry) transitions are enhanced relative to the allowed ones (compare equations (3-48) and (3-47)).

3.3.7. Treatment of Molecules

3.3.7.1. Diatomic molecules

The principles discussed above can be applied equally well to molecules if we continue to neglect such interactions as spin-orbit and spin-spin coupling, and magnetic and relativistic effects in the

Hamiltonian $\hat{H}_T$. This will generally be the case for small molecules containing atoms of low atomic number.

We will discuss the special case of the electron-impact excitation of diatomic molecules since it serves to illustrate most of the additional complications.

Let o, o, J, and M be the electronic, vibrational, and rotational quantum numbers for the initial molecular state (the ground electronic and vibrational state), and n, ν, J′, and M′ the corresponding final ones. The molecular wave function can be written as[61]

$$\psi_{\left(\substack{n\\ \sim\\ o}\right)}(\underset{\sim}{r}_2,\ldots\underset{\sim}{r}_N;\underset{\sim}{R}) = \Phi_{\binom{n}{o}}(\underset{\sim}{r}_2,\ldots\underset{\sim}{r}_N;\underset{\sim}{R})\,\mathcal{S}_{\binom{S'S'_z}{SS_z}}(2,\ldots N) \quad (3\text{-}49)$$

$$\Phi_{\binom{n}{o}} = \phi_{\binom{n}{o}}(\underset{\sim}{r}_2,\ldots\underset{\sim}{r}_N;R)\,\eta_{\binom{n\nu J'}{ooJ}}(R)\,Y_{\binom{J'M'}{JM}}(\chi,\emptyset)\,. \quad (3\text{-}50)$$

ϕ_o and ϕ_n are the ground and excited state electronic wave functions for a particular internuclear distance R; η_{ooJ} and $\eta_{n\nu J'}$ are the ground and excited state vibrational wave functions; Y_{JM} and $Y_{J'M'}$ are the rotational wave functions (spherical harmonics[1d]) of the initial and final rotational states; $\chi,\emptyset$ are the spherical polar angles defining the molecular orientation with respect to a space fixed axis; and the $\mathcal{S}_{\binom{S'S'_z}{SS_z}}$ are the N -1 electron spin wave functions for each state.

The Born direct scattering amplitude (f^B_{on} of equation (3-37)) and the Ochkur approximation (g^O_{on} of equation (3-36)) to the Born-

Oppenheimer exchange scattering amplitude are given by

$$f^{B}_{on}(\theta,\varphi) = \frac{-2me^2}{\hbar^2 q^2}(N-1)\int \Phi_n^* e^{i\underset{\sim}{q}\cdot\underset{\sim}{r}_2}\Phi_o d\underset{\sim}{r}_2 \ldots d\underset{\sim}{r}_N d\underset{\sim}{R} \qquad (3\text{-}51)$$

and

$$g^{O}_{on}(\theta,\varphi) = \frac{-2me^2}{\hbar^2 k_o^2}\int \Phi_n^* e^{i\underset{\sim}{q}\cdot\underset{\sim}{r}_2}\Phi_o d\underset{\sim}{r}_2 \ldots d\underset{\sim}{r}_N d\underset{\sim}{R} \qquad (3\text{-}52)$$

where $\underset{\sim}{q} = \underset{\sim}{k}_o - \underset{\sim}{k}'$

$$k' = \left[k_o^2 - \frac{2m}{\hbar^2}(E_{n\nu J'M'} - E_{ooJM})\right]^{\frac{1}{2}} .$$

$E_{n\nu J'M'}$ and E_{ooJM} are the energies of the final and initial molecular states, respectively. If $\mathcal{S}_{\Sigma\mu}$ and $\mathcal{S}'_{\Sigma\mu}$ are the initial and final total spin wave functions for the N electrons (N - 1 bound and one free), then the scattering amplitude, in direct analogy to (3-30), is

$$\underset{\sim\sim}{\zeta}^{\Sigma\mu}_{on} = \langle \mathcal{S}'^{*}_{\Sigma\mu}(1,\ldots N)\,\mathcal{S}_{\Sigma\mu}(1,\ldots N)\rangle_{spin} f^{B}_{on} - (N-1)\langle \mathcal{S}'^{*}_{\Sigma\mu}(2,1,\ldots N)\,\mathcal{S}_{\Sigma\mu}(1,\ldots N)\rangle_{spin} g^{O}_{on} . \qquad (3\text{-}53)$$

The differential cross section for a particular $(o,o,J,M) \rightarrow (n,\nu,J',M')$ transition in analogy to (3-29) is

$$\sigma_{on}(k_o,\theta,\varphi) = \frac{k'}{k_o}\sum_{2\Sigma=0}^{\infty}\sum_{\mu=-\Sigma}^{\Sigma} p(\Sigma,\mu)\left|\underset{\sim\sim}{\zeta}^{\Sigma\mu}_{on}\right|^2 . \qquad (3\text{-}54)$$

If $\mathcal{S}_{SS_z} \neq \mathcal{S}_{S'S'_z}$, f^B_{on} will not contribute to $\underset{\sim}{\underset{\sim}{\zeta}}^{\Sigma\mu}_{on}$ since the spin integral multiplying f^B_{on} in (3-53) will be zero.

Define:

$$T_{on}(k_o,\theta,\varphi;\, R,\chi,\emptyset) \equiv \int \phi^*_n(\underset{\sim}{r}_2,\ldots\underset{\sim}{r}_N;\, R)\, e^{i\underset{\sim}{q}\cdot\underset{\sim}{r}_2}\, \phi_o(\underset{\sim}{r}_2,\ldots\underset{\sim}{r}_N;\, R)\, d\underset{\sim}{r}_2\ldots d\underset{\sim}{r}_N \quad , \tag{3-55}$$

$$\Lambda^{n\nu J'}_{ooJ}(k_o,\theta,\varphi;\,\chi,\emptyset) \equiv \int \eta^*_{n\nu J'}(R)\, T_{on}\, \eta_{ooJ}(R)\, R^2\, dR \quad , \tag{3-56}$$

$$\mathcal{S} \equiv <\mathcal{S}'^*_{\Sigma\mu}(1,\ldots N)\, \mathcal{S}_{\Sigma\mu}(1,\ldots N)>_{spin} \quad ,$$

and

$$\tilde{\mathcal{S}} \equiv <\mathcal{S}'^*_{\Sigma\mu}(2,1,\ldots N)\, \mathcal{S}_{\Sigma\mu}(1,\ldots N)>_{spin}. \tag{3-57}$$

Then, $\left|\underset{\sim}{\underset{\sim}{\zeta}}^{\Sigma\mu}_{on}\right|^2$ can be written as

$$\left|\underset{\sim}{\underset{\sim}{\zeta}}^{\Sigma\mu}_{on}\right|^2 = \left(\frac{2me^2(N-1)}{\hbar^2}\right)^2 \left(\frac{\mathcal{S}}{q^2} - \frac{\tilde{\mathcal{S}}}{k_o^2}\right)^2 \left|\Gamma^{n\nu J'M'}_{ooJM}\right|^2 \tag{3-58}$$

where

$$\Gamma^{n\nu J'M'}_{ooJM}(k_o,\theta,\varphi) \equiv \int Y^*_{J'M'}(\chi,\emptyset)\, \Lambda^{n\nu J'}_{ooJ}\, Y_{JM}(\chi,\emptyset)\, \sin\chi\, d\chi\, d\emptyset \quad . \tag{3-59}$$

Under the present experimental conditions, the target molecules are initially in their ground electronic and vibrational states with room temperature (~300°K) Boltzmann distributions of rotational ones. Since we do not resolve rotational excitation and since each molecule (in a particular o, o, J, M state) scatters independently of all the others, the observed DCS for a particular o, o → n, ν transition is proportional to $I_{oo}^{n\nu}(k_o, \theta, \varphi)$ where

$$I_{oo}^{n\nu} \equiv \left\langle \sum_{J'=0}^{J'_{max}} \sum_{M'=-J'}^{J'} \left| \Gamma_{ooJM}^{n\nu J'M'} \right|^2 \right\rangle_{JM}. \qquad (3\text{-}60)$$

$\langle \rangle_{JM}$ indicates a statistical-mechanical average over the initial rotational states J, M. J'_{max} is the maximum J′ for which k′ of (3-52) remains real. The mathematical details and the assumptions involved in evaluating (3-60) are given by Cartwright and Kuppermann[76]. Their result is

$$I_{oo}^{n\nu} \cong \frac{1}{4\pi} \int \left| \Lambda_{oo}^{n\nu} \right|^2 \sin \chi \, d\chi d\emptyset \qquad (3\text{-}61)$$

where k′ is replaced by

$$k'' = \left\{ k_o^2 - \frac{2m}{\hbar^2} \left[E_{n\nu oo} - E_{oooo} \right] \right\}^{\frac{1}{2}} \qquad (3\text{-}62)$$

and the vibrational wave functions are assumed independent of J′ and J. The orientationally and rotationally averaged scattering amplitude from equation (3-58) is then

$$\left| \underset{\sim}{\underset{\sim}{\zeta}}_{on}^{\Sigma\mu} \right|_{AVG}^2 = \left[\frac{2me^2(N-1)}{\hbar^2} \right]^2 \left[\frac{\mathcal{S}''}{q^2} - \frac{\tilde{\mathcal{S}}'}{k_o^2} \right]^2 I_{oo}^{n\nu} \, . \qquad (3\text{-}63)$$

If T_{on} is a slowly varying function of R[16], it may be evaluated at R equal to the equilibrium internuclear separation R_e of the ground state and removed from the R integral of (3-56).

Then,

$$I_{oo}^{n\nu} = G_{oo}^{n\nu} \left| T_{on}(k_o, \theta, \varphi; R_e) \right|^2_{AVG} \tag{3-64}$$

where

$$\begin{aligned} &\left| T_{on}(k_o, \theta, \varphi; R) \right|^2_{AVG} \\ &= \frac{1}{4\pi} \int \left| T_{on}(k_o, \theta, \varphi; R, \chi, \emptyset) \right|^2 \sin \chi \, d\chi \, d\emptyset \end{aligned} \tag{3-65}$$

and

$$G_{oo}^{n\nu} \equiv \int \eta^*_{n\nu}(R) \, \eta_{oo}(R) \, R^2 \, dR \quad . \tag{3-66}$$

$G_{oo}^{n\nu}$ is the Franck-Condon factor[77] for the (oo) → (nν) electronic-vibrational transition. If the vibrational structure of the excited state is not resolved, $I_{oo}^{n\nu}$ must be summed over all vibrational states ν.

Since

$$\sum_{\nu = 0}^{\infty} G_{oo}^{n\nu} = 1 \tag{3-67}$$

(Franck-Condon factor sum rule[78]),

$$I_{oo}^{n} \equiv \sum_{\nu=0}^{\infty} I_{oo}^{n\nu} \cong \left| T_{on}(k_o, \theta, \varphi; R_e) \right|^2_{AVG} \tag{3-68}$$

where k'' is replaced by

$$k''' = \{k_o^2 - \frac{2m}{\hbar^2}[E_{n\nu'oo} - E_{ooo}]\}^{\frac{1}{2}} \qquad (3\text{-}69)$$

and ν' is the value of ν for which $G_{oo}^{n\nu}$ is a maximum. The validity of (3-68) depends on k_o^2 being large enough so that k'' doesn't change appreciably over the range of ν for which $G_{oo}^{n\nu}$ is not negligibly small.

It is worth emphasizing that there are three basic approximations inherent in the derivation of (3-64).

1) The ground and excited state wave functions can be factored into a product of electronic, vibrational, rotational, and electron spin parts. This is called the Born-Oppenheimer separability approximation and is an excellent approximation in cases for which spin-orbit coupling is negligible.

2) The electronic transition occurs on a time scale that is short compared to vibrational periods. This is called the Franck-Condon principle[79] and provides the justification for using the same R in both the ground and excited state wave functions. It should be a good approximation provided the excitation does not occur via a long lived negative ion.

3) The electronic transition amplitude T_{on} is a slowly varying function of R. This is a more subtle point which in general requires either empirical or numerical verification. If the vibrational structure (or overall envelope) of an electronic excitation can be observed, then the relative intensities of the vibrational transitions

can be compared with the $G_{oo}^{n\nu}$ obtained from calculations or optical spectroscopy. For all reported cases, the electron-impact and optical absorption measurements of relative intensities have agreed[41](except for transitions occurring through negative ion formation).

Since we can clearly resolve vibrational structure in the energy-loss spectra of H_2, N_2, and CO, it is worthwhile to examine more closely the relative vibrational level peak intensities to be expected from the above Franck-Condon factor considerations. For a three electron system within the framework of the Born approximation (no exchange), the differential cross section for excitation of the n^{th} electronic and ν^{th} vibrational state from the ground electronic and vibrational state is

$$\sigma_{n\nu}(k_o,\theta) = \frac{k_\nu}{k_o}\frac{16}{q^4} G_{oo}^{n\nu} \left| T_{on}(k_o,\theta,\varphi; R_e) \right|^2_{AVG} \qquad (3\text{-}70)$$

in Hartree atomic units. $\left| T_{on}(k_o,\theta,\varphi; Re) \right|^2_{AVG}$ is defined by equation (3-65), k_o and k_ν are the wave numbers of the incident and scattered electrons, respectively, and

$$q^2 = k_o^2 + k_\nu^2 - 2k_o k_\nu \cos\theta \ .$$

For small q, $e^{i\underset{\sim}{q}\cdot\underset{\sim}{r}_2}$ appearing in equation (3-55) can be expanded as in equation (3-45). In this way the energy and scattering angle dependence in $\left| T_{on} \right|^2_{AVG}$ can be factored out term by term.

For an electronic transition which is dipole allowed, equation (3-70) becomes approximately

$$\sigma_{n\nu}(k_o,\theta) \cong \frac{k_\nu}{k_o} \frac{16}{q^2} G_{oo}^{n\nu} (z_1)^2 \qquad (3\text{-}71)$$

where z_1 is the properly averaged dipole-matrix element[128] in analogy to equation (3-46). Since we measure the energy-loss spectrum at constant resolution and with a collection efficiency that is independent of energy (see section 4.4.4.3.), the ratio of the peak intensities $I_\nu/I_{\nu o}$ for two vibrational levels ν and νo is

$$\left(\frac{I_\nu}{I_{\nu o}}\right)^{\text{DIR.}}_{\text{DIPOLE}} = \frac{\sigma_{n\nu}(k_o,\theta)}{\sigma_{n\nu o}(k_o,\theta)} = C^{DD}_{\nu\nu o} \frac{G_{oo}^{n\nu}}{G_{oo}^{n\nu o}} \qquad (3\text{-}72)$$

with

$$C^{DD}_{\nu\nu o} = \frac{k_\nu}{k_{\nu o}} \frac{q_o^2}{q^2}$$

and

$$k_\nu^2 = k_o^2 - 2W_\nu$$

$$k_{\nu o}^2 = k_o^2 - 2W_{\nu o}$$

$$q_o^2 = k_o^2 + k_{\nu o}^2 - 2k_o k_{\nu o} \cos\theta$$

where W_ν and $W_{\nu o}$ are the excitation energies (in hartrees) of the ν^{th} and νo^{th} vibrational states of the upper electronic state (n), respectively.

In an analogous way, this analysis can be performed for a dipole-forbidden but quadrupole-allowed transition with the result

$$\left(\frac{I_\nu}{I_{\nu o}}\right)^{\text{DIR.}}_{\text{QUAD}} = C^{DQ}_{\nu\nu o}\ \frac{G^{n\nu}_{oo}}{G^{n\nu o}_{oo}} \tag{3-73}$$

where

$$C^{DQ}_{\nu\nu o} = \frac{k_\nu}{k_{\nu o}} \quad .$$

For the case of exchange scattering, the Ochkur approximation and the same high-energy approximations used to derive equation (3-72) yield (assuming z_1 is dominant),

$$\left(\frac{I_\nu}{I_{\nu o}}\right)^{\text{EX}}_{\text{DIPOLE}} = C^{ED}_{\nu\nu o}\ \frac{G^{n\nu}_{oo}}{G^{n\nu o}_{oo}} \tag{3-74}$$

with

$$C^{ED}_{\nu\nu o} = \frac{k_\nu}{k_{\nu o}}\ \frac{q^2}{q_o^2} \quad .$$

If $z_1 = 0$ and z_2 is dominant,

$$\left(\frac{I_\nu}{I_{\nu o}}\right)^{\text{EX}}_{\text{QUAD}} = C^{EQ}_{\nu\nu o}\ \frac{G^{n\nu}_{oo}}{G^{n\nu o}_{oo}} \tag{3-75}$$

with

$$C^{EQ}_{\nu\nu o} = \frac{k_\nu}{k_{\nu o}}\ \frac{q^4}{q_o^4} \quad .$$

The factors multiplying the Franck-Condon factor ratios in equations (3-72), (3-73), and (3-74) have been calculated for some specific cases and are given in the discussions of N_2 (section 5.3) and CO (section 5.4).

From the failure of both the Born and Ochkur approximations to reliably predict low-energy differential cross sections, it is of doubtful value to use them in determining the relation of relative peak heights to relative Franck-Condon factors.

3.3.7.2 Ethylene

In this section we apply the Ochkur approximation to the spin-forbidden $\tilde{X}\,{}^1A_{1g} \rightarrow \tilde{a}\,{}^3B_{1u}$ $(\pi \rightarrow \pi^*)$ transition[80,81a] of ethylene. This transition has been observed by both optical methods[82,83] and electron impact[84].

Within the framework of the Born-Oppenheimer separability approximation, the π electron approximation[81b] and the LCAO method[85], the ground and excited state wave functions for this transition can be written as

$$\psi_{\tilde{X}} = \phi_{\tilde{X}\pi}(\underset{\sim}{r}_2, \underset{\sim}{r}_3; \underset{\approx}{R})\, \phi_{\tilde{X}\sigma}(\underset{\sim}{r}_4, \ldots \underset{\sim}{r}_{17}; \underset{\approx}{R})\, \varphi_{\tilde{X}}(\underset{\approx}{R})\, \mathcal{S}_{00}(2, \ldots 17) \tag{3-76}$$

and

$$\psi_{\tilde{a}} = \phi_{\tilde{a}\pi}(\underset{\sim}{r}_2, \underset{\sim}{r}_3; \underset{\approx}{R})\, \phi_{\tilde{a}\sigma}(\underset{\sim}{r}_4, \ldots \underset{\sim}{r}_{17}; \underset{\approx}{R})\, \varphi_{\tilde{a}}(\underset{\approx}{R})\, \mathcal{S}_{1S'_z}(2, \ldots 17) \tag{3-77}$$

$\phi_{\tilde{x}\pi}$ and $\phi_{\tilde{a}\pi}$ are the ground and excited state wave functions for the two π electrons at fixed nuclear geometry $\underset{\sim}{R}$. $\phi_{\tilde{x}\sigma}$ and $\phi_{\tilde{a}\sigma}$ are the corresponding wave functions for the remaining electrons. $\varphi_{\tilde{x}}(\underset{\sim}{R})$ and $\varphi_{\tilde{a}}(\underset{\sim}{R})$ are the vibrational-rotational wave functions, and $\mathcal{S}_{00}$ and $\mathcal{S}_{1S'_z}$ are the normalized spin wave functions for the ground and excited states. We assume that only the two π electrons are involved in the transition so that

$$\phi_{\tilde{x}\sigma} = \phi_{\tilde{a}\sigma} \tag{3-78}$$

and the N in equation (3-58) is 3. The ground state spin wave function is a singlet (S = 0) while the excited state is a triplet (S′= 1). In analogy with helium, the DCS for the spin forbidden transition in the Ochkur approximation is

$$\sigma^{O}_{\tilde{x}\tilde{a}}(k_o,\theta,\varphi) = \frac{3k'''}{k_o} \left| g^{O}_{\tilde{x}\tilde{a}} \right|^2 \tag{3-79}$$

where

$$\left| g^{O}_{\tilde{x}\tilde{a}} \right|^2 \cong \left(\frac{2me^2}{\hbar^2 k_o^{\,2}}\right)^2 \left| T_{\tilde{x}\tilde{a}}(k_o,\theta,\varphi;R_e) \right|^2_{AVG} , \tag{3-80}$$

$$k''' = \left\{ k_o^{\,2} - \frac{2m}{\hbar^2} W \right\}^{\frac{1}{2}} , \tag{3-81}$$

$\left| T_{\tilde{x}\tilde{a}}(k_o,\theta,\varphi;R_e) \right|^2_{AVG}$ is given by equation (3-65) with

$$\begin{aligned} &T_{\tilde{x}\tilde{a}}(k_o,\theta,\varphi;R,\chi,\emptyset) \\ &= \int \phi^{*}_{\tilde{a}\pi}(\underset{\sim}{r}_2,\underset{\sim}{r}_3,R)\, e^{i\underset{\sim}{q}\cdot\underset{\sim}{r}_2}\, \phi_{\tilde{x}\pi}(\underset{\sim}{r}_2,\underset{\sim}{r}_3,R)\, d\underset{\sim}{r}_2\, d\underset{\sim}{r}_3 , \end{aligned} \tag{3-82}$$

$$\underset{\sim}{q} = \underset{\sim}{k}_o - \underset{\sim}{k}''' \quad ,$$

$$q^2 = k_o^{\,2} + (k''')^2 - 2k_o k''' \cos\theta \quad .$$

$\hbar\underset{\sim}{k}_o$ is the initial electron momentum and $\hbar\underset{\sim}{k}'''$ is the final one. R_e is the C-C equilibrium internuclear distance, $\frac{\hbar^2}{2m} k_o^{\,2}$ is the incident electron kinetic energy, $\frac{\hbar^2}{2m} k'''^{\,2}$ is the scattered electron kinetic energy, and W is the excitation energy for the peak of the transition (~4.6 eV). We have assumed that ethylene can be treated as a diatomic molecule and that the cross section (3-79) has been summed over all rotational and vibrational states (since neither is resolved). The π electron spatial wave functions for electrons 2 and 3 can be approximated by[86]

$$\begin{aligned} \phi_{\underset{\sim}{x}\pi} &= h_1(\underset{\sim}{r}_2)\, h_1(\underset{\sim}{r}_3) \\ \phi_{\underset{\sim}{a}\pi} &= \frac{1}{\sqrt{2}}\{h_1(\underset{\sim}{r}_2)\, h_2(\underset{\sim}{r}_3) - h_1(\underset{\sim}{r}_3)\, h_2(\underset{\sim}{r}_2)\} \end{aligned} \qquad (3\text{-}83)$$

where

$$\begin{aligned} h_1 &= \frac{1}{\sqrt{2}} \frac{1}{\sqrt{1+S_{ab}}} (\chi_a + \chi_b) \quad , \\ h_2 &= \frac{1}{\sqrt{2}} \frac{1}{\sqrt{1-S_{ab}}} (\chi_a - \chi_b) \quad , \end{aligned} \qquad (3\text{-}84)$$

χ_a and χ_b are P_z orbitals[49c] centered on carbon a and b, respectively;

$$\chi_{\binom{a}{b}} = \left(\frac{\gamma^5}{\pi}\right)^{\frac{1}{2}} \cos\theta_{\binom{a}{b}}\, r_{\binom{a}{b}}\, e^{-\gamma r_{\binom{a}{b}}} \quad , \qquad (3\text{-}85)$$

and S_{ab} is the overlap of the two orbitals for an internuclear $(C_a - C_b)$ distance R_c,

$$S_{ab} \equiv \int \chi_a \chi_b \, d\underset{\sim}{r} \quad . \tag{3-86}$$

Substitution of (3-83) into (3-82) yields

$$T_{\tilde{x}\tilde{a}} = -\frac{1}{2\sqrt{2}} \int \{(\chi_a(\underset{\sim}{r}_a))^2 - (\chi_b(r_b))^2\} e^{i\underset{\sim}{q}\cdot\underset{\sim}{r}} d\underset{\sim}{r} \quad , \tag{3-87}$$

where the origin of $\underset{\sim}{r}$ is centered on a line joining the two carbons and the origins of $\underset{\sim}{r}_a$ and $\underset{\sim}{r}_b$ are carbons a and b. If $\underset{\sim}{R}_a$ and $\underset{\sim}{R}_b$ are the fixed vector positions of carbons a and b with respect to the origin of $\underset{\sim}{r}$, then

$$\begin{aligned} \underset{\sim}{R}_b + \underset{\sim}{r}_b &= \underset{\sim}{r} \\ \underset{\sim}{R}_a + \underset{\sim}{r}_a &= \underset{\sim}{r} \\ \underset{\sim}{R}_a &= -\underset{\sim}{R}_b \equiv \underset{\sim}{R}_e/2 \end{aligned} \tag{3-88}$$

Substitution of (3-88) into (3-87) yields

$$\begin{aligned} & T_{\tilde{x}\tilde{a}} \\ & = \left(\frac{-i\gamma^5}{\sqrt{2\pi}}\right) \frac{\sin(\underset{\sim}{q}\cdot\underset{\sim}{R}_e/2)}{\sqrt{1 - S_{ab}^2}} \int \cos^2\theta \; r^2 \; e^{-2\gamma r} \; e^{iqr\cos\theta} r^2 dr d(\cos\theta) d\varphi \end{aligned} \tag{3-89}$$

where the z axis for the $\underset{\sim}{r}$ integration has been chosen along $\underset{\sim}{q}$. The integration of (3-89) is straightforward[74b], and we obtain

$$T_{\tilde{x}\tilde{a}} = -i\frac{64\gamma^6}{\sqrt{2}}\frac{1}{\sqrt{1-S_{ab}^2}}\frac{(4\gamma^2-5q^2)}{(4\gamma^2+q^2)^4}\sin(\underset{\sim}{q}\cdot\underset{\sim}{R}_e/2) \quad . \tag{3-90}$$

Substitution of (3-90) into (3-65) and integration over all molecular orientations gives

$$\left|T_{\tilde{x}\tilde{a}}\right|^2_{AVG} = A^2\left(\frac{4\gamma^2-5q^2}{[4\gamma^2+q^2]^4}\right)^2\left[1-\frac{\sin qR_e}{qR_e}\right] \tag{3-91}$$

where

$$A = \frac{32\gamma^6}{\sqrt{1-S_{ab}^2}} \quad .$$

The differential cross section is then obtained by substituting (3-91) into (3-80) and (3-80) into (3-79).

$$\sigma^{O}_{\tilde{x}\tilde{a}}(k_o,\theta) = B^2\frac{k'''}{k_o^5}\left(\frac{4\gamma^2-5q^2}{[4\gamma^2+q^2]^4}\right)^2\left[1-\frac{\sin qR_e}{qR_e}\right] , \tag{3-92a}$$

where

$$B = \frac{2\sqrt{3}\,Ame^2}{\hbar^2} \quad .$$

The expression for the DCS of (3-92a) can be converted to the more accurate Ochkur-Rudge expression by

$$\sigma^{OR}_{\tilde{x}\tilde{a}}(k_o,\theta) = \frac{k_o^4}{[k'''-iA]^4}\,\sigma^{O}_{\tilde{x}\tilde{a}}(k_o,\theta) \tag{3-92b}$$

(see equation 3-38)). The total cross section is given by

$$Q_{\tilde{x}\tilde{a}}(k_o) = 2\pi\int_{-1}^{1}\sigma^{OR}_{\tilde{x}\tilde{a}}\,d(\cos\theta) \quad . \tag{3-93}$$

Both the differential and total cross sections have been calculated (via equations (3-92b) and (3-93)) for

$$W = 4.6 \text{ eV}$$

$$R_e = 1.33 \text{ Å} \quad \text{(reference 81c)}$$

$$\gamma = 3.07 \text{ Å}^{-1} \quad \text{(81d)}$$

$$S_{ab} = .28 \quad \text{(81e)}$$

The results obtained for the total cross section are compared in figure 3.3-1 with the results of Ochkur and Bratsev[58b] for excitation of the 2^3P state of helium. The shapes of the cross section curves are quite similar. Figure 3.3-2 shows the threshold region of the $\tilde{x}\,^1A_{1g} \rightarrow \tilde{a}\,^3B_{1u}$ total excitation cross section along with the experimental results of Brongersma[87]. The experimental and theoretical cross section curves have similar shapes, while the discrepencies in the magnitudes are not at all unreasonable considering the approximations involved in the calculation. The angular distributions (DCS) obtained by this calculation are compared with our experimental results in section 5.7.

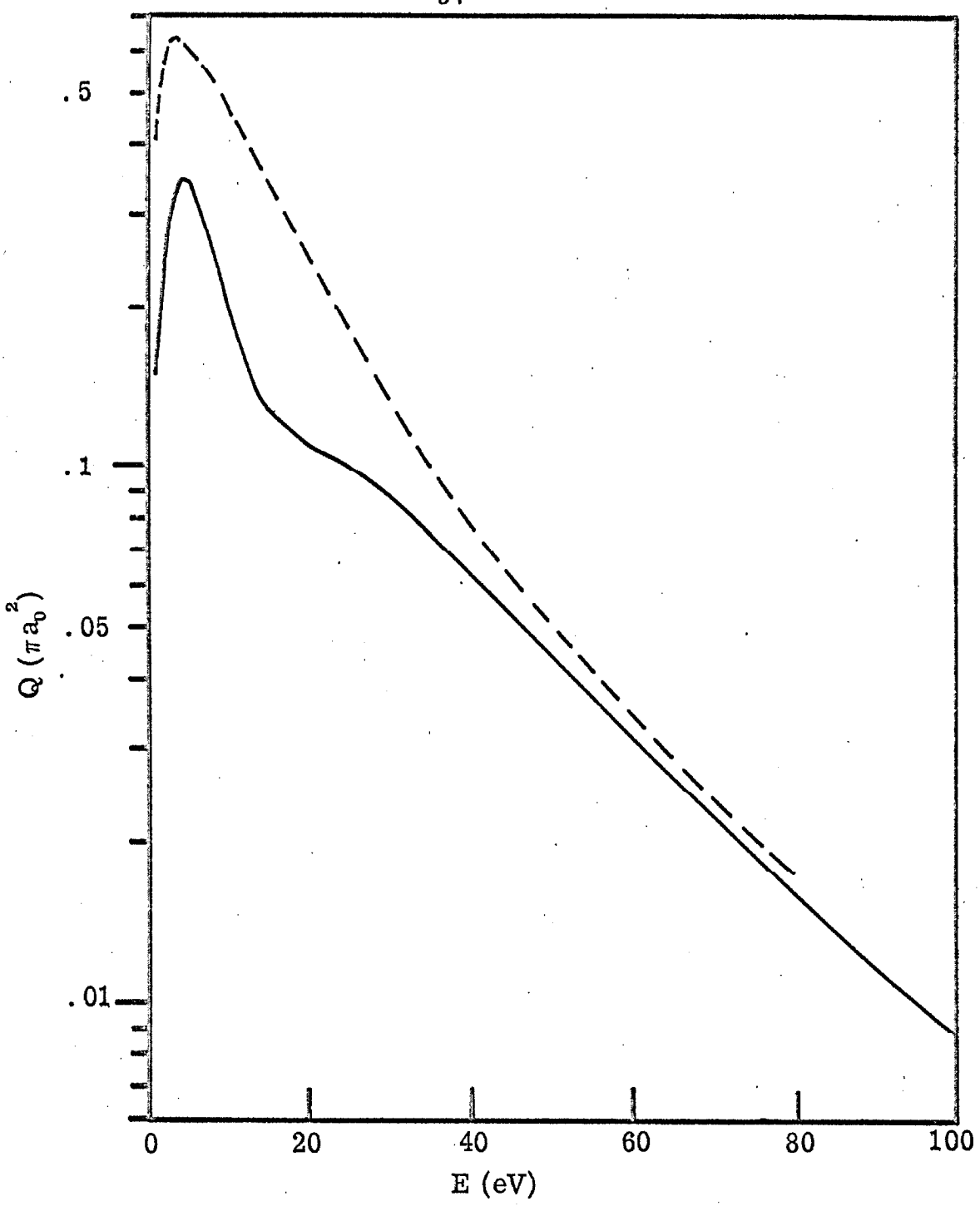

Figure 3.3-1. The total cross section Q for the $\tilde{X}\,^1A_{1g} \rightarrow \tilde{a}\,^3B_{1u}$ transition in ethylene by electron impact (solid line). E is the kinetic energy of the incident electron minus the excitation energy W = 4.6 eV. The dashed line is the calculated[58b] total cross section × 10 for excitation of the 2^3P state of helium.

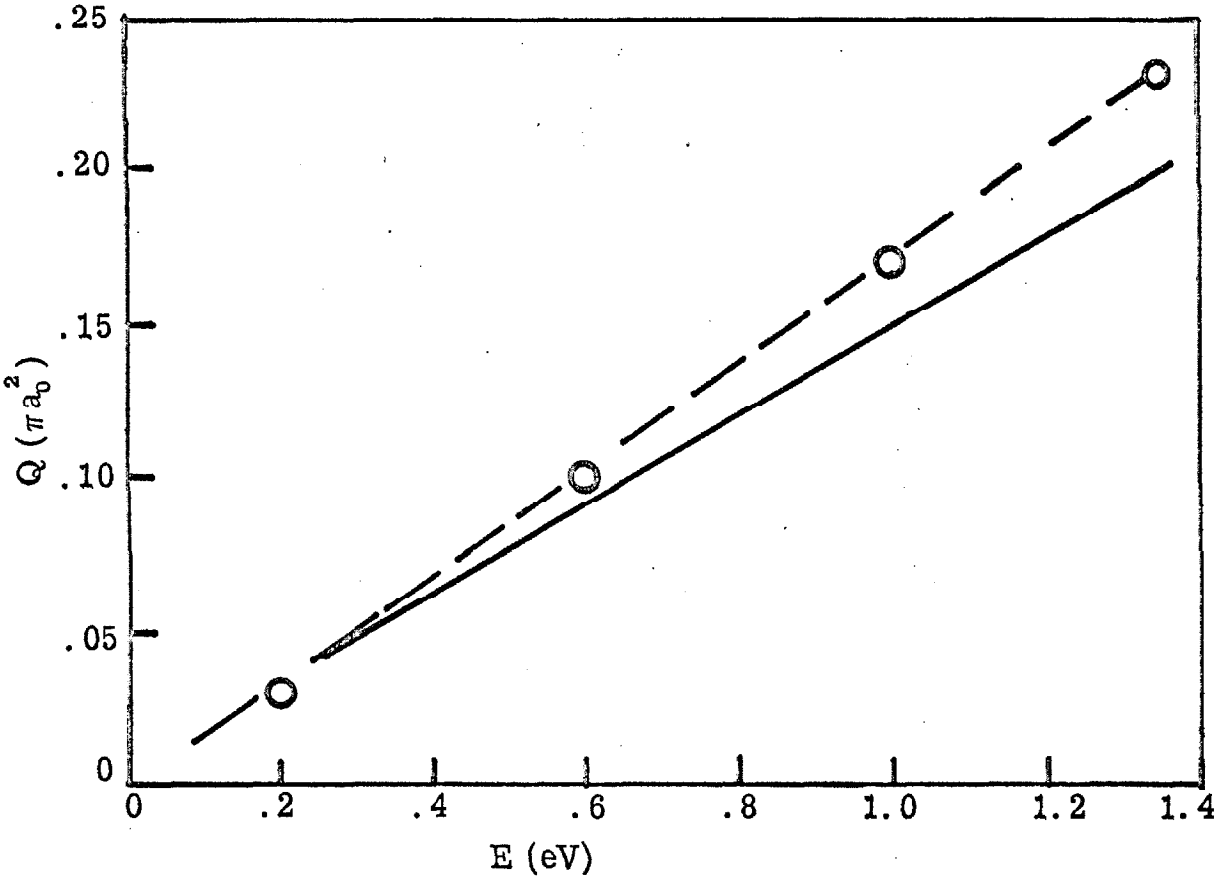

Figure 3.3-2. The total cross section Q near threshold for the $\tilde{x}\,^1A_{1g} - \tilde{a}\,^3B_{1u}$ transition in ethylene by electron impact. The solid line is the calculated behavior, and the circles are the experimental results of Brongersma[87] times $\frac{1}{2}$. The calculated slope is $0.13\pi a_0^2$/eV while the experimental one is $0.34\pi a_0^2$/eV. E is the energy above threshold.

3.4. Partial Wave Analysis

3.4.1 Introduction

The approximate first order methods discussed above are expected to be valid only at relatively high impact energies. Thus, some other approach is needed to provide at least a qualitative understanding of the angular distribution of scattered electrons for low impact energies. The method of partial waves[44c] is one such approach which has proved useful in the treatment of scattering by spherically symmetric potentials. The method involves the expansion of the total wave function in radial functions (functions of r) times spherical harmonics (functions of θ, φ). If the possibility of exchange excitation is included, the desired radial functions are solutions of an infinite set of coupled integro-differential equations similar in form to equation (3-18) for even the simplest system of an electron plus atomic hydrogen[88].

A more fruitful qualitative approach (though certainly less rigorous) is to treat the electron plus target scattering problem as if it were spherically symmetric. The differences between the direct and exchange excitation mechanisms are then included through the use of different effective electron-target interaction potentials.

For example, in a three electron system, the "potential"[44d] leading to direct excitation is in some sense proportional to the electronic matrix element

$$M_D(r_1) \propto \int \phi_n^*(\underset{\sim}{r}_2, \underset{\sim}{r}_3) \frac{1}{r_{12}} \phi_o(\underset{\sim}{r}_2, \underset{\sim}{r}_3) d\underset{\sim}{r}_2 \, d\underset{\sim}{r}_3 \qquad (3\text{-}94)$$

while that for exchange is

$$M_{EX}(r_1) \propto \int \phi_n^*(\underset{\sim}{r}_1, \underset{\sim}{r}_2) \frac{1}{r_{12}} \phi_o(\underset{\sim}{r}_2, \underset{\sim}{r}_3) d\underset{\sim}{r}_2 \, d\underset{\sim}{r}_3 \quad . \qquad (3\text{-}95)$$

$\underset{\sim}{r}_3$, $\underset{\sim}{r}_2$, and $\underset{\sim}{r}_1$ are the respective coordinates of the two initially bound electrons and the incoming one. ϕ_n and ϕ_o are the final and initial bound state spatial wave functions, respectively, of the target. $r_{12} = |\underset{\sim}{r}_1 - \underset{\sim}{r}_2|$.

The potentials M_D and M_{EX} have quite different effective ranges as indicated by their behavior for $r_1 \gg r_2, r_3$ (a case in which the incoming electron is relatively far from the target).

$\frac{1}{r_{12}}$ can be expanded as

$$\frac{1}{r_{12}} = \sum_{\ell=0}^{\infty} \frac{r_2^{\ell}}{r_1^{\ell+1}} P_\ell(\cos\theta_{12}) \quad \text{for } r_1 > r_2. \qquad (3\text{-}96)$$

The $P_\ell(\cos\theta_{12})$ are Legendre polynomials and $\cos\theta_{12} = \frac{\underset{\sim}{r}_1 \cdot \underset{\sim}{r}_2}{r_1 r_2}$.
Substitution of (3-96) into (3-94) and (3-95) yields

$$M_D(r_1) \underset{r_1 \gg r_2, r_3}{\sim} \frac{\hat{r}_1}{(r_1)^2} \cdot \int \phi_n^*(\underset{\sim}{r}_2, \underset{\sim}{r}_3) \underset{\sim}{r}_1 \phi_o(\underset{\sim}{r}_2, \underset{\sim}{r}_3) d\underset{\sim}{r}_2 \, d\underset{\sim}{r}_3 \qquad (3\text{-}97)$$

$$+ \; 0\left(\frac{1}{(r_1)^3}\right) \quad .$$

and

$$M_{EX}(r_1) \underset{r_1 \gg r_2, r_3}{\sim} \frac{1}{r_1} \int \phi_n^*(\underset{\sim}{r}_1, \underset{\sim}{r}_2)\, \phi_0(\underset{\sim}{r}_2, \underset{\sim}{r}_3)\, d\underset{\sim}{r}_2\, d\underset{\sim}{r}_3$$

$$+ \frac{\hat{r}_1}{(r_1)^2} \cdot \int \phi_n^*(\underset{\sim}{r}_1, \underset{\sim}{r}_2)\, \underset{\sim}{r}_2\, \phi_0(\underset{\sim}{r}_2, \underset{\sim}{r}_3)\, d\underset{\sim}{r}_2\, d\underset{\sim}{r}_3 \qquad (3\text{-}98)$$

$$+ 0\left(\frac{1}{r_1^3}\right) \quad ,$$

respectively, where $\hat{r}_1$ is a unit vector in the $\underset{\sim}{r}_1$ direction. However,

$$\phi_n^*(\underset{\sim}{r}_1, \underset{\sim}{r}_2) \underset{r_1 \gg r_2}{\sim} r_1^m\, e^{-\alpha_n r_1} \chi^*(\underset{\sim}{r}_2; \theta_1, \varphi_1) \qquad (3\text{-}99)$$

since $\underset{\sim}{r}_1$ is the coordinate of a bound electron in the excited state. Substitution of (3-99) into (3-98) yields

$$M_{EX}(r_1) \underset{r_1 \gg r_2, r_3}{\sim} r_1^{m-1}\, e^{-\alpha_n r_1} \int \chi^*(\underset{\sim}{r}_2; \theta_1, \varphi_1)\, \phi_0(\underset{\sim}{r}_2, \underset{\sim}{r}_3)\, d\underset{\sim}{r}_2\, d\underset{\sim}{r}_3$$

$$+ 0\left(r_1^{m-2}\, e^{-\alpha_n r_1}\right) \quad . \qquad (3\text{-}100)$$

As a result, $M_{EX}(r_1)$ is of much shorter range than $M_D(r_1)$ since the former decays exponentially while the latter decreases only as $\frac{1}{r_1^2}$.

Thus, we will apply the partial wave method rigorously to the problem of elastic scattering from a central potential. Then the angular dependence of the direct and exchange differential cross sections can be qualitatively explained in terms of the different effective ranges of the direct and exchange "potentials."

3.4.2. Elastic Scattering by a Center of Force.

The steady state Schröedinger equation for an electron of kinetic energy $\frac{\hbar^2}{2m} k^2$ (at $r = \infty$) in a potential field $V(r)$ is

$$[\nabla^2 + (k^2 - U(r))]\psi(\underset{\sim}{r}) = 0 \qquad (3\text{-}101)$$

where $U(r) = \frac{2m}{\hbar^2} V(r)$.

If the electron is assumed to be incoming along the z axis of the $\underset{\sim}{r}$ coordinate system with a momentum $\hbar \underset{\sim}{k}$ (at $r \to \infty$), then the desired solutions of (3-101) have an asymptotic form

$$\psi(r,\theta) \underset{r \to \infty}{\sim} e^{ikz} + f(\theta) \frac{e^{ikr}}{r} . \qquad (3\text{-}102)$$

(ψ is not a function of φ since $V(r)$ is spherically symmetric.)

The general solution of (3-101) is

$$\psi(r,\theta) = \frac{1}{r} \sum_{\ell = 0}^{\infty} R_\ell(r) P_\ell(\cos\theta) \qquad (3\text{-}103)$$

where $R_\ell(r)$ is a solution of

$$\frac{d^2 R_\ell(r)}{dr^2} + \left[k^2 - U(r) - \frac{\ell(\ell+1)}{r^2}\right] R_\ell(r) = 0 \qquad (3\text{-}104)$$

If $U(r)$ tends to zero faster than $\frac{1}{r}$ as $r \to \infty$, then

$$R_\ell(r) \underset{r \to \infty}{\sim} A_\ell \sin(kr + \epsilon_\ell) \qquad (3\text{-}105)$$

where A_ℓ and ϵ_ℓ are constants.

If $U(r) = 0$, the solutions $R_\ell^o(r)$ to (3-104) which are bounded at the origin, are

$$R_\ell^o(r) = B_\ell \sqrt{\frac{\pi kr}{2}}\, J_{\ell+\frac{1}{2}}(kr) \tag{3-106}$$

where B_ℓ is a constant and $J_{\ell+\frac{1}{2}}(kr)$ is a Bessels' function of the first kind. $R_\ell^o(r)$ has the asymptotic form

$$R_\ell^o(r) \underset{r\to\infty}{\sim} B_\ell \sin\left(kr - \tfrac{1}{2}\ell\pi\right) . \tag{3-107}$$

Thus, for $U(r) \neq 0$, we require

$$R_\ell(r) \underset{r\to\infty}{\sim} A_\ell \sin\left(kr - \tfrac{1}{2}\ell\pi + \eta_\ell\right) \tag{3-108}$$

so that the phase shift η_ℓ is zero for $U(r) = 0$. η_ℓ depends on k and $U(r)$.

A_ℓ is determined by first substituting (3-108) into (3-103) to obtain

$$\psi(r,\theta) \underset{r\to\infty}{\sim} \frac{1}{2ir} \sum_{\ell=0}^{\infty} \left[\left(e^{-i\ell\pi/2} e^{i\eta_\ell}\right)e^{ikr} - \left(e^{i\ell\pi/2} e^{-i\eta_\ell}\right) e^{-ikr}\right] \tag{3-109}$$

$$\times A_\ell P_\ell(\cos\theta)$$

Then (3-102) is expanded in Legendre polynomials:

$$\psi(r,\theta) \underset{r\to\infty}{\sim} \frac{1}{2ir} \sum_{\ell=0}^{\infty} \left[\left(\frac{2\ell+1}{k} + 2iC_\ell\right) e^{ikr} - \left(\frac{(2\ell+1)e^{i\ell\pi}}{k}\right) e^{-ikr}\right] \tag{3-110}$$

$$\times P_\ell(\cos\theta)$$

where

$$f(\theta) = \sum_{\ell=0}^{\infty} C_\ell P_\ell(\cos\theta) \quad . \tag{3-111}$$

Since (3-109) and (3-110) are asymptotic forms of the same function, they must be equivalent. A comparison of the coefficients of $e^{\pm ikr}$ requires

$$C_\ell = \frac{(2\ell+1)}{2ik}(e^{2i\eta_\ell} - 1) \quad . \tag{3-112}$$

The differential cross section is given by

$$\sigma(k,\theta) = |f(\theta)|^2 \tag{3-113}$$

and, thus,

$$\sigma(k,\theta) = \frac{1}{4k^2} \left| \sum_{\ell=0}^{\infty} (2\ell+1)[e^{2i\eta_\ell} - 1] P_\ell(\cos\theta) \right|^2 . \tag{3-114}$$

The phase shifts are obtained in general by numerical integration of (3-104).

It can be shown[44e], however, that

$$\eta_\ell \cong -\frac{\pi}{2} \int_0^{\infty} U(r)[J_{\ell+\frac{1}{2}}(kr)]^2 r\, dr \tag{3-115}$$

if the right hand side is small. This is a form of the Born approximation for potential scattering.

Suppose that $r^2U(r)$ has an effective range r_{max} and that within that range it never exceeds some finite value, i. e.

$$r^2|U(r)| \leq a \qquad 0 < r \leq r_{max}$$
$$= 0 \qquad r_{max} < r \quad . \tag{3-116}$$

If the impact energy is low enough so that $\frac{kr_{max}}{2} \ll 1$, then the small argument form[89] of $J_{\ell+\frac{1}{2}}$ can be used and

$$|\eta_\ell| \leq (\tfrac{\pi}{2}) \frac{a}{(\Gamma(\ell+\frac{3}{2}))^2} \int_0^{r_{max}} (\tfrac{kr}{2})^{2\ell+1} \frac{dr}{r} \tag{3-117}$$

$$= \frac{2\pi a}{(2\ell+1)^3} (\frac{kr_{max}}{2})^{2\ell+1} \frac{1}{[\Gamma(\ell+\frac{1}{2})]^2} \quad .$$

If η_ℓ is small then (3-114) implies that

$$\sigma(k,\theta) \cong \frac{1}{k^2} \left| \sum_{\ell=0}^{\infty} (2\ell+1)\eta_\ell P_\ell(\cos\theta) \right|^2 \quad . \tag{3-118}$$

Each term in the expansion is called a "partial wave" and is often designated as an S, P, D, etc. wave depending on whether $\ell = 0, 1, 2,$ etc.

Since the range (r_{max}) of the interaction leading to direct scattering is much larger than that leading to exchange, the number of η_ℓ's needed in (3-118) is greater. From the nature of Legendre polynomials, the more of them which are included in (3-118), the more sharply peaked toward $\theta = 0°$ can be the differential cross section. Thus, we expect the angular distribution of electrons scattered after causing exchange excitations to be relatively more

isotropic than that of electrons causing excitations via a direct mechanism. Indeed, this has been found to be the case[90].

Notice also that if k is lowered (lower impact energy) fewer η_ℓ's are required and both direct and exchange cross sections should become more isotropic. This also has been observed[91].

3.4.3. Data Expansion in Partial Waves

In this research we actually measure several inelastic differential cross sections, corresponding to excitation via direct and/or exchange mechanisms, over an angular range of $10° \lesssim \theta \lesssim 80°$. It would be of interest to expand these measured distributions in Legendre polynomials in an attempt to determine the c_ℓ's of an expansion such as (3-111). For a general inelastic process, the c_ℓ's do not have the simple form of (3-112) in which η_ℓ is real. This form can be preserved for the general case if

$$\eta_\ell \equiv \lambda_\ell + i\mu_\ell \tag{3-119}$$

where λ_ℓ and μ_ℓ are real[44f]. For our purposes, we assume

$$c_\ell \equiv a'_\ell e^{i b'_\ell} \tag{3-120}$$

in which a'_ℓ and b'_ℓ are real. The differential cross section for any particular inelastic process (o → n) can be written as

$$\sigma_{on}(k_o,\theta) = \frac{k_n}{k_o} |A_{on}|^2 \tag{3-121}$$

where $\frac{\hbar^2 k_o^2}{2m}$ is the energy of the incident electron, $\frac{\hbar^2 k_n^2}{2m}$ is the energy of the scattered electron, and A_{on} is the complete scattering amplitude associated with the observed process (a suitable linear combination of $\zeta_{\underset{\sim}{o}\underset{\sim}{n}}^{S,S_z}$, as discussed previously). We have neglected any φ dependence in (3-121) since we do not measure it nor do we expect it under our experimental conditions. The amplitude A_{on} can be expanded in Legendre polynomials as

$$A_{on} = \sum_{\ell=0}^{\infty} c_\ell P_\ell(\cos\theta). \tag{3-122}$$

The substitution of (3-120) into (3-122) and the result into (3-121) yields

$$\frac{\sigma_{on}(k_o,\theta)}{(a'_o)^2} = \frac{k_n}{k_o} \sum_{\ell=0}^{\infty} \sum_{m=0}^{\infty} a_\ell a_m e^{i(b_\ell - b_m)} P_\ell(\cos\theta) P_m(\cos\theta) \ , \tag{3-123}$$

where $a_\ell \equiv a'_\ell/a'_o$ and $b_\ell \equiv b'_\ell - b'_o$. These last two definitions are introduced since: (1) the experimental cross section in this case (σ_{on}^{EXP}) is related to the theoretical one (3-123) by an unknown multiplicative constant and; (2) a knowledge of σ_{on} leaves A_{on} indeterminant to within an arbitrary phase factor $e^{i\phi}$.

The product of Legendre polynomials in (3-123) can also be expanded as

$$P_\ell(\cos\theta)\,P_m(\cos\theta) = \sum_{p=0}^{\infty} D^p_{\ell m}\,P_p(\cos\theta) \qquad (3\text{-}124)$$

where

$$D^p_{\ell m} \equiv \frac{2p+1}{2}\int_{-1}^{1} P_p(\cos\theta)\,P_\ell(\cos\theta)\,P_m(\cos\theta)\,d(\cos\theta)\ .$$

Notice that $D^p_{\ell m} = D^p_{m\ell}$. It can be shown[65b] that

$$\int_{-1}^{1} P_{\ell_1}(\mu)\,P_{\ell_2}(\mu)\,P_{\ell_3}(\mu)\,d\mu = 2\begin{pmatrix}\ell_1\ell_2\ell_3\\0\,0\,0\end{pmatrix}^2 \qquad (3\text{-}125)$$

where $\begin{pmatrix}\ell_1\ell_2\ell_3\\0\,0\,0\end{pmatrix}$ is the usual Wigner 3_j symbol[92].

Thus,

$$D^p_{\ell m} = (2p+1)\begin{pmatrix}p\,\ell\,m\\0\,0\,0\end{pmatrix}^2\ . \qquad (3\text{-}126)$$

Substitution of (3-124) into (3-123) and a rearrangement of terms yields

$$\frac{\sigma_{on}(k_o,\theta)}{(a'_o)^2} = \frac{k_n}{k_o}\sum_{p=0}^{\infty} F_p\,P_p(\cos\theta) \qquad (3\text{-}127)$$

where

$$F_p \equiv \sum_{\ell=0}^{\infty} a_\ell^2\,D^p_{\ell\ell} + 4\sum_{\ell>}\sum_{m=0} a_\ell a_m\cos(b_\ell - b_m)D^p_{\ell m}\ . \qquad (3\text{-}128)$$

The experimentally determined differential cross section at each angle θ_i is related to the theoretical one by

$$\sigma^{EXP}_{on}(k_o,\theta_i) \cong C'\,\sigma_{on}(k_o,\theta_i) \qquad (3\text{-}129)$$

where C' is an unknown positive constant, depending on k_o, but not θ. In principle, the F_p's of (3-127) (and hence the a_ℓ's and b_ℓ's of (3-128)) can be determined by a least squares fit of the data to the theoretical expression (3-127). In particular, we wish to minimize the quantity

$$\gamma \equiv \sum_{s=1}^{M} [\sigma_{on}^{EXP}(k_o,\theta_s) - C'\sigma_{on}(k_o,\theta_s)]^2 (\frac{1}{\epsilon_s})^2 \qquad (3\text{-}130)$$

where ϵ_s is the relative error in the measurement at the angle θ_s, and M is the number of experimental points. It is clear that the expansion (3-127) must be truncated so that there are fewer unknowns than data points. If the number of terms retained in (3-127) is N + 1, then

$$\gamma = \sum_{s=1}^{M} [\sigma_{on}^{EXP}(k_o,\theta_s) - C \sum_{p=0}^{N} F_p P_p(\cos\theta_s)]^2 (\frac{1}{\epsilon_s})^2 \qquad (3\text{-}131)$$

where $C = C'(a_o')^2 \frac{k_n}{k_o}$.

The minimization of (3-131) was attempted in two ways.

I. γ was minimized with respect to a variation in $F_p' = CF_p$. In other words, we require

$$\frac{\partial \gamma}{\partial F_p'} = 0 \qquad \text{for } p = 0,\ldots N .$$

This implies from (3-131) that

$$\sum_{s=1}^{M} (\frac{1}{\epsilon_s})^2 [\sigma_{on}^{EXP}(\theta_s) - \sum_{p=0}^{N} F_p' P_p(\cos\theta_s) P_q(\cos\theta)] = 0 \qquad (3\text{-}132)$$

for $q = 0, \ldots N$.

The solutions F'_p to the system of equations (3-132) can be written in matrix notation as

$$\underset{\sim}{F'} = (\mathbb{P}\,\mathbb{E}\,\mathbb{P}^T)^{-1}(\mathbb{P}\,\mathbb{E}\,\underset{\sim}{\sigma}) \tag{3-133}$$

where $\underset{\sim}{F'}$ and $\underset{\sim}{\sigma}$ are column vectors with elements F'_p and $\sigma_{on}^{EXP}(\theta_s)$, respectively;

$$(\mathbb{P})_{ij} = P_i(\cos\theta_j) \; ; \qquad (\mathbb{E})_{k\ell} = \left(\frac{1}{\epsilon_k}\right)^2 \delta_{k\ell} \; ;$$

and the various indices have ranges: $(p, i) \rightarrow (0, \ldots N)$; $(j, k, \ell, s) \rightarrow (1, \ldots M)$. The matrix inversion and multiplications indicated in (3-133) were first carried out in double-precision arithmetic on an IBM 7094 computer for two test cases.

Test case (1): A set of ten "data-points" (value of the differential cross section at ten angles $\theta_s = n \times 10°$, $n = 0, \ldots 9$) was generated by assuming

$$\sigma_{on}^{EXP}(\theta_s) = \sum_{\ell=0}^{2} x_\ell P_\ell(\cos\theta_s) \tag{3-134}$$

where x_ℓ is given.

These values of $\sigma_{on}^{EXP}(\theta_s)$, each with the same relative error, were substituted into (3-133). (3-133) was then solved to obtain the F'_p's for N = 2 and 4. Table 3.4-1 summarizes the results for one set of x_ℓ's. Notice that the "data" are fit with the correct coefficients for N = 2 and that the inclusion of higher-order P_ℓ's does not affect the coefficients of the first three terms. This ideal

TABLE 3.4-1

Least squares fit of "data" from test case (1). $N + 1$ is the number of terms included in the expansion (3-127). x_ℓ is the "true" coefficient of the ℓ^{th} order Legendre polynomial while F'_ℓ is the one calculated according to equation (3-133). RMS is the root-mean-square deviation of the fit from the "data."

	x_0	x_1	x_2	x_3	x_4	RMS
	.5550	.3330	.1110	.0	.0	
N + 1	F'_0	F'_1	F'_2	F'_3	F'_4	
3	.5550	.3330	.1110	-	-	1.1×10^{-6}
5	.5550	.3330	.1110	-5.7×10^{-6}	1.1×10^{-6}	1.0×10^{-6}

behavior is to be expected.

Test case (2): In this case, a random percentage error, $-5\% \leq \epsilon_s \leq +5\%$, was added to each "data-point" of test case (1). (3-133) was solved in this case for N = 2, 4, and 6. Table 3.4-2 summarizes the results for the same set of x_ℓ's used in Table 3.4-1. Notice that in this case the addition of higher-order polynomials drastically affects the coefficients of lower-order ones.

Unfortunately, an analysis of the real data according to this method (equation (3-133)) yielded the results indicated by test case (2). Therefore, we do not feel that meaningful coefficients can be obtained in this way from our experimental data. Nevertheless, we can estimate the minimum number of terms needed in (3-122) to explain the observed angular distribution. We simply determine the minimum even value of N for which the least-squares fit (according to (3-133)) lies within the range of error in the data. The minimum number of terms this requires in (3-122) is $\frac{N}{2} + 1$.

II. Recently, Hoeper, et. al.[93] have been successful in fitting the observed low-energy elastic differential scattering cross sections of several rare gases to an expansion of the type (3-111) with c_ℓ given by (3-112). Their neglect of the imaginary part of η_ℓ (equation (3-119)) was justifiable since the electron impact energies were below the lowest inelastic threshold. Even though the extension of their method into the realm of inelastic scattering doubles the number of unknowns for the same maximum value of ℓ, it was felt that a consistent set of coefficients might be obtained

TABLE 3.4-2

Least squares fit of "data" from test case (2). Refer to the legend of table 3.4-1.

	x_0	x_1	x_2	x_3	x_4	x_5	x_6	RMS
	.5550	.3330	.1110	0.0	0.0	0.0	0.0	
	F_0'	F_1'	F_2'	F_3'	F_4'	F_5'	F_6'	
3	.5687	.2805	.1402	-	-	-	-	.025
5	4.697	-9.029	8.636	-4.376	1.079	-	-	.021
7	12.26	-35.24	53.60	-53.38	35.30	-14.34	2.811	.020

(i. e., the expansion (3-127) might converge).

The method, as outlined below, is based on the expansion of F_p (equations (3-127), (3-128)) in a Taylor series about some initial "guesses" for the a_ℓ's and b_m's (denote these by a_ℓ^o and b_m^o).

$$F_p \cong F_p^{\,o} + \sum_{\ell=1}^{N} \left(\frac{\partial F_p}{\partial a_\ell}\right)_o \Delta a_\ell + \sum_{m=1}^{N} \left(\frac{\partial F_p}{\partial b_m}\right)_o \Delta b_m \qquad (3\text{-}135)$$

where $F_p^{\,o}$ is F_p (equation (3-128)) evaluated at a_ℓ^o, b_m^o; $(\ \ )_o$ represents the derivative evaluated at a_ℓ^o, b_m^o; and $N + 1$ is the number of terms to be included in the expansion (3-127). Note that

$$\left(\frac{\partial F_p}{\partial a_\ell}\right) = 2 \sum_{m=0}^{N} a_m D^p_{m\ell} \cos(b_\ell - b_m) \qquad (3\text{-}136a)$$

and

$$\left(\frac{\partial F_p}{\partial b_\ell}\right) = 2 \sum_{m=0}^{N} a_m a_\ell D^p_{m\ell} \sin(b_m - b_\ell) \ . \qquad (3\text{-}136b)$$

F_p (as given by 3-135) is substituted into (3-131) and γ is minimized with respect to variations in C and the Δa_ℓ's and Δb_m's (except, of course for $\ell = m = 0$ for which $a_0 = 1$ and $b_0 = 0$). The best initial C (labelled C_o) is determined from the requirement that

$\frac{\partial \gamma}{\partial C} = 0$ for $\Delta a_\ell = \Delta b_\ell = 0$ for $\ell = 1, \ldots N$. It can be shown in a straightforward way that

$$C_o = \frac{\underset{\sim}{F}^{oT} \mathbb{P} \mathbb{E} \underset{\sim}{\sigma}}{\underset{\sim}{F}^{oT} \mathbb{P} \mathbb{E} \mathbb{P}^T \underset{\sim}{F}^{o}} \qquad (3\text{-}137)$$

where the matrix definitions are the same as before and $\underset{\sim}{F}^{o}$ is a column vector of elements F_p^o.

This value of C_o is substituted back into equation (3-131) and the Δa_ℓ's and Δb_ℓ's are determined from the requirements that

$$(\frac{\partial \gamma}{\partial \Delta a_\ell}) = 0 \; ; \quad (\frac{\partial \gamma}{\partial \Delta b_\ell}) = 0 \quad \text{for} \quad \ell = 1, \ldots N.$$

Again, after a little matrix algebra, we obtain

$$\begin{aligned} \Delta \underset{\sim}{x} = (\mathbb{F}^{oT}\, \mathbb{P}\, \mathbb{E}\, \mathbb{P}^T\, \mathbb{F}^o)^{-1} \{ & \frac{1}{C_o}\, \mathbb{F}^{oT}\, \mathbb{P}\, \mathbb{E}\, \underset{\sim}{\sigma} \\ & - \mathbb{F}^{oT}\, \mathbb{P}\, \mathbb{E}\, \mathbb{P}^T\, \underset{\sim}{F}^o \}. \end{aligned} \tag{3-138}$$

where $\Delta \underset{\sim}{x}$ is a column vector with 2N elements $(\Delta a_1, \ldots \Delta a_N, \Delta b_1, \ldots \Delta b_N)$ and $\mathbb{F}^o$ is a matrix in which

$$(\mathbb{F}^o)_{ij} = (\frac{\partial F_i}{\partial \Delta x_j})_o \; .$$

The solution $\Delta \underset{\sim}{x}$ of (3-138) is used to correct the initial values a_ℓ^o, b_ℓ^o as

$$a_\ell(\text{new}) = a_\ell^o(\text{initial}) + \Delta a_\ell$$

and $$b_\ell(\text{new}) = b_\ell^o(\text{initial}) + \Delta b_\ell \; .$$

These improved values are substituted back into equation (3-135) and the entire procedure is repeated. Thus, by successive iterations, the required a_ℓ's and b_ℓ's can in principle be determined from the data.

The method was first applied to a set of test "data" similar to that of test case (1) mentioned previously. In this case, however, the values of a_ℓ and b_ℓ, as determined by successive iterations of equations (3-137) and (3-138), would not converge very rapidly to the "true" values even for initial guesses which were within 1/100 of these values. Table 3.4-3 summarizes one such test case. If the initial "guess" was not within about 1/10 of the correct value, the method would not converge at all. These initial attempts were discouraging enough to forestall the further application of this method.

TABLE 3.4-3

Iterative least-squares determination of the a_ℓ's and b_ℓ's from initial "guesses" a_ℓ^o, b_ℓ^o. a_o and b_o are not varied, as discussed in the text. The value of a_ℓ (b_ℓ) obtained after the n^{th} iteration is labelled a_ℓ^n (b_ℓ^n). The "true" values are labelled a_ℓ^T (b_ℓ^T). RMS is defined in the legend of table 3.4-1.

n	a_1^n	b_1^n	RMS
0	.8710	.5010	
1	.8730	.4928	.00026
2	.8730	.4927	.00026
9	.8729	.4929	.00025
	a_1^T = .8700	b_1^T = .5000	

4. EXPERIMENTAL

4.1 Design

4.1.1. Electron Energy Analyzer

4.1.1.1 General considerations

It is essential to the aim of these experiments to distinguish between electrons that have scattered after causing molecular excitations to an energy level W_n from those causing excitations to another level W_m (n and m represent the set of quantum numbers which identifies a molecular state). Since the scattered electrons are identical except for their energy, one must provide an incident beam of kinetic energy $E_0 \pm \Delta E/2$ and must resolve the energy of the scattered beam to within $\pm \Delta E/2$ where

$$\Delta E \lesssim |W_n - W_m| \tag{4-1}$$

in order to distinguish the two excitations.

The energy distribution of electrons emitted from a thermionic cathode is given approximately by the Boltzmann equation (see section 4.4.1),

$$I(E,T) = \frac{I_o(T)}{(kT)^2} E e^{-E/kT} \tag{4-2}$$

in which $I(E,T)$ is the current carried by electrons with kinetic energy E per unit energy, $I_o(T)$ is the total current at cathode temperature T, and k is the Boltzmann constant. The full-width at half-maximum (FWHM) $\Delta E_{\frac{1}{2}}$ of this distribution is 2.54 kT. The maximum current that can be drawn from a cathode of area A and

work function ϕ_W is given by the well known Richardson-Dushman equation[94a],

$$I_{MAX}(T) \approx 120\, A\, T^2\, e^{-(\phi_W/kT)} \quad . \qquad (4\text{-}3)$$

If T is lowered in order to decrease $\Delta E_{\frac{1}{2}}$, the maximum available current $I_{MAX}(T)$ *falls faster than exponentially.* Even with low work function oxide coated cathodes ($\phi_W \approx$ 1 to 2 eV) the lower temperature limit for suitable currents is approximately 1000°K, for which $\Delta E_{\frac{1}{2}} = 0.22$ eV. While electronic energy level spacings in molecules are of the order of 1 to 10 eV, vibrational spacings are ~.01 to 0.1 eV and rotational spacings are ~ 0.001 to 0.0001 eV. Consequently, to resolve higher electronic states and vibrational states, some sort of electron energy analyzer is required to provide an incident beam of sufficiently narrow energy spread and to determine the energy of the scattered electrons.

Although any device whose transmission varies with electron energy can in principle be used as an analyzer, the most common arrangement is to use an electric and/or magnetic field configuration so that the electron trajectory through the system is a function of energy. Systems which have been successfully employed include those based on uniform magnetic fields[95]; crossed electric and magnetic fields[96,97]; and electrostatic fields between parallel plates[98], coaxial cylinders[9,99,100,101], and concentric hemispheres[21,24]. Our choice of the last type of analyzer resulted from several considerations. First, magnetic fields, which are

difficult to effectively shield from other parts of the apparatus, are not required; second, the hemispherical analyzer focuses in two directions so that axially symmetric lens systems can be used for beam propagation and control; and third, it is easy to construct, simple to operate, and has given satisfactory performance in other laboratories[24,25].

4.1.1.2. Hemispherical electrostatic energy analyzer

4.1.1.2.1. Trajectory equations

Although Purcell[102] has described the spherical sector analyzer, it is necessary to carry out a more detailed analysis for our present application. The analyzer system is shown in Figure 4.1-1. The field matching elements, denoted as Herzog numbers 1 and 2, are equipotential with the center of the gap between the concentric outer and inner hemispheres of radii R_2 and R_1, respectively. The potential field $V(R,\theta,\varphi)$ in the space between the spheres can be determined by solving Laplace's equation,

$$\nabla^2 V(R,\theta,\varphi) = 0, \tag{4-4}$$

with the boundary conditions

$$\begin{aligned} V(R_0,\theta,\varphi) &= V_0, \\ V(R_1,\theta,\varphi) - V(R_2,\theta,\varphi) &= \Delta V \end{aligned} \tag{4-5}$$

in which $R_0 = (R_1 + R_2)/2$, V_0 is the Herzog potential, and ΔV is the potential difference between the spheres. Equation (4-4) can be easily solved to yield

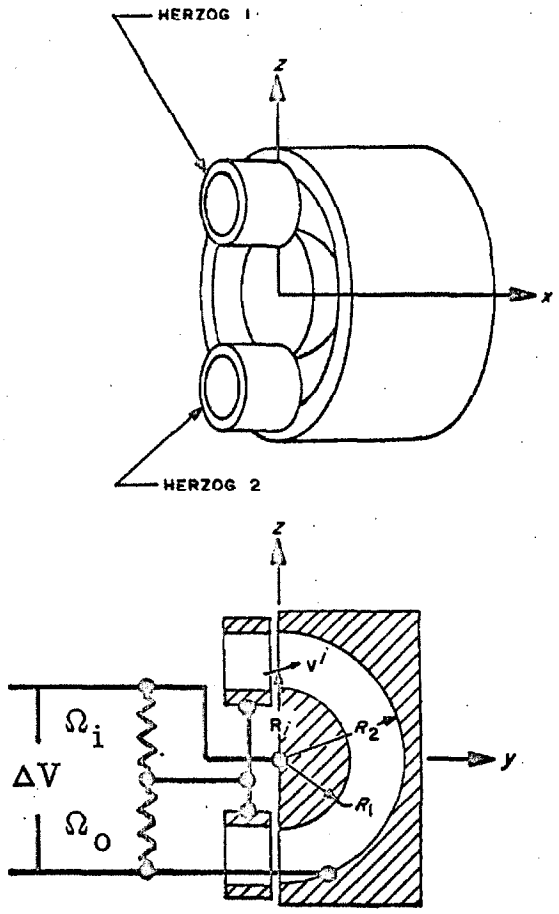

Figure 4.1-1. Diagram of the analyzer system and the coordinate system chosen for the derivation of section 4.1.1.2. The symbols are defined in the text.

$$V(R_1,\theta,\varphi) = V(R) = G\,\Delta V(1/R - 1/R_0) + V_0 \qquad (4\text{-}6)$$

where $$G = R_1R_2/(R_2 - R_1).$$

Note from (4-6) that the potentials of the inner and outer sphere with respect to the Herzogs are $R_2\Delta V/(R_2 + R_1)$ and $-R_1\Delta V/(R_2 + R_1)$, respectively. Consequently, the dividing resistors in figure 4.1-1 must obey the relation

$$\Omega_i/\Omega_0 = R_2/R_1 \quad . \qquad (4\text{-}7)$$

In the absence of "fringe-field" effects, space charge, and magnetic or extraneous electric fields, the electron-optical properties of this analyzer can be derived from the trajectory of an electron subject to V(R). The Lagrangian equations of motion for an electron between the spheres are

$$\frac{d}{dt}\left(\frac{\partial L}{\partial \dot{X}_i}\right) = \frac{\partial L}{\partial X_i} \qquad (4\text{-}8)$$

where $X_i = R, \theta$, or φ

$$\dot{X}_i = \frac{dX_i}{dt}$$

$$L = \left(\frac{m}{2}\right)\left[\dot{R}^2 + (R\dot{\theta})^2 + (R\dot{\varphi}\sin\theta)^2\right] + qV(R),$$

m = electron mass ,

q = absolute value of electron charge.

Consider an electron of initial velocity $\underset{\sim}{v}_i'$ coming from Herzog 1 and entering the gap between the spheres at a point P_i whose distance

from their center O is R_i. In crossing the boundary between Herzog 1 and the spheres, the electron velocity will in general change, both in magnitude and direction, to $\underset{\sim}{v}_i$ at time t = 0. Let us choose a coordinate system centered on O with the z axis containing P_i and the yz plane containing $\underset{\sim}{v}_i$. Then, if

$$\underset{\sim}{v}_i = \hat{j}\, v_{iy} + \hat{k}\, v_{iz}$$

(where $\hat{j}$ and $\hat{k}$ are the unit vectors in the O_y and O_z directions, respectively), the six initial conditions required to solve (4-8) are

$$\begin{aligned} R(t=0) &= R_i & \dot{R}(t=0) &= v_{iz} \\ \theta(t=0) &= 0 & \dot{\theta}(t=0) &= v_{iy}/R_i \\ \varphi(t=0) &= \pi/2 & \dot{\varphi}(t=0) &= 0\ . \end{aligned} \tag{4-9}$$

<u>φ - equation</u>

With $X_i = \varphi$, (4-8) yields

$$\varphi m R^2 \sin^2\theta = C \tag{4-10}$$

at any time $t \geq 0$ in which C is a time-independent constant (constant of the motion). The initial conditions require C = 0, hence, $\varphi m R^2 \sin^2\theta = 0$ for all $t \geq 0$. Thus,

$$\varphi(t) = 0\ , \tag{4-11}$$

(i. e. the electron remains in the same φ plane throughout its trajectory).

θ - equation

With $X_i = \theta$, (4-8) and (4-11) yield

$$mR^2\dot{\theta} = A \tag{4-12}$$

in which A is a time-independent constant. Applying the initial conditions, we find that

$$A = mR_i v_i \cos\alpha \tag{4-13}$$

where $\cos\alpha = v_{iy}/v_i$. α (which we will denote as the entrance angle) is the angle between $\underset{\sim}{v}_i$ and $\hat{j}$.

R - equation

With $X_i = R$, (4-8), (4-11), and (4-12) yield

$$\frac{d^2R}{dt^2} = \frac{2}{m}\frac{R_i^2}{R^3}E_i\cos^2\alpha - \frac{q}{m}G\frac{\Delta V}{R^2} \tag{4-14}$$

where $E_i = \frac{1}{2}m v_i^2$ is the kinetic energy of the electron just after entering the analyzer at point P_i. The substitution of $R = \frac{1}{U}$ and a change from t to θ as the independent variable gives

$$\frac{d^2U}{d\theta^2} + U = \frac{q\ \Delta V\ G}{2E_i R_i^2\cos^2\alpha} \quad . \tag{4-15}$$

After integration and application of the remaining boundary conditions, $R(\theta)$ can be expressed as

$$R(\theta) = R_i\left[\frac{qG\Delta V(1-\cos\theta)}{2E_i R_i\cos^2\alpha} + \cos\theta - \tan\alpha\sin\theta\right]^{-1} . \tag{4-16}$$

Note, however, that E_i is a function of R_i. The total electron energy before entering the analyzer is equal to its kinetic energy $E = \frac{1}{2} m(v_i')^2$ plus its potential energy $-qV_o$ in Herzog 1. This total energy is conserved through its trajectory. In particular, the electron's total energy in Herzog 1 is equal to its total energy immediately after entering the analyzer at P_i. Mathematically, this implies

$$E - qV_o = E_i - qV(R_i) \quad . \tag{4-17}$$

Substitution of E_i in (4-16) by (4-17) with (4-6) yields

$$R(\theta) = R_i\left[\frac{G(1 - \cos\theta)}{2R_i \cos^2\alpha}\left(\frac{E}{q\Delta V} + \frac{G}{R_i} - \frac{G}{R_o}\right)^{-1} + \cos\theta - \tan\alpha\sin\theta\right]^{-1} \quad . \tag{4-18}$$

ΔV is chosen so that an electron of kinetic energy E_o in Herzog 1 entering the analyzer so that $R_i = R_o$ and $\alpha = 0$ describes a circular orbit of radius R_o. Solving (4-18) for $q\Delta V$ under these conditions yields

$$q\Delta V = \frac{2E_oR_o}{G} \quad . \tag{4-19}$$

Substitution of this result into (4-18) yields

$$R(\theta) = R_i\left[\frac{R_o(1 - \cos\theta)}{2R_i \cos^2\alpha}\left(\frac{E}{2E_o} + \frac{R_o}{R_i} - 1\right)^{-1} + \cos\theta - \tan\alpha\sin\theta\right]^{-1} . \tag{4-20}$$

If $R_i = R_o$ and $E = E_o$ in (4-20), we obtain

$$R(\theta) = R_o\left[\frac{1 - \cos\theta \sin^2\alpha}{\cos^2\alpha} - \tan\alpha \sin\theta\right]^{-1} . \qquad (4\text{-}21)$$

Since we use a cylindrically symmetric electron beam, α can have a range of values centered on 0. Expanding (4-21) for small α, we obtain

$$R(\theta) = R_o\left[1 - \alpha \sin\theta + O(\alpha^2)\right]^{-1} . \qquad (4\text{-}22)$$

Thus, if $\theta = \pi$, $R(\theta = \pi)$ will be independent of the entrance angle α to order α^2. For this reason, the analyzer is chosen to be hemispherical.

At $\theta = \pi$ the electron leaves the analyzer at a distance $R_f = R(\theta=\pi)$ from the center with an exit angle α' with respect to the negative y axis. R_f and α' are given by

$$R_f = \frac{R_i \cos^2\alpha\left[1 - \eta\frac{R_i}{R_o}\right]}{1 - \cos^2\alpha\left[1 - \eta\frac{R_i}{R_o}\right]} \qquad (4\text{-}23)$$

and

$$\tan\alpha' = \frac{1}{R}\left(\frac{dR}{d\theta}\right)_{\theta=\pi} = \frac{R_f}{R_i}\tan\alpha \qquad (4\text{-}24)$$

where $\eta \equiv 1 - E/2E_o$.

Typical electron trajectories calculated from (4-20) are shown in figures 4.1-2, -3, and -4. Note from (4-23) that:

(1) Electrons with the same E and R_i entering with entrance

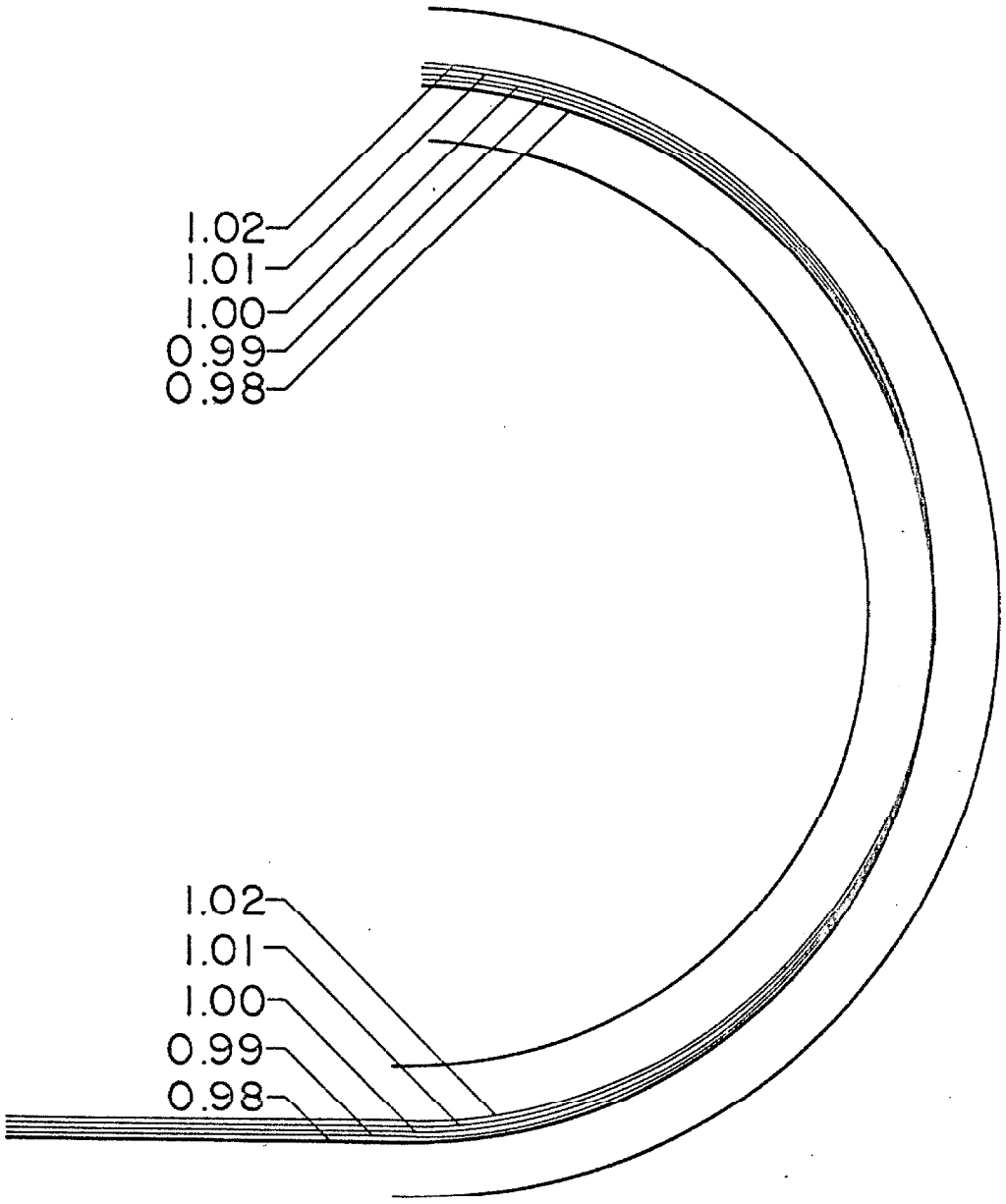

Figure 4.1-2. Electron trajectories in the yz plane (fig. 4.1-1) according to equation (4-20) for $\alpha = 0°$, $R_o = 1.00$, and $E = E_o$. The curves are for the indicated values of R_i.

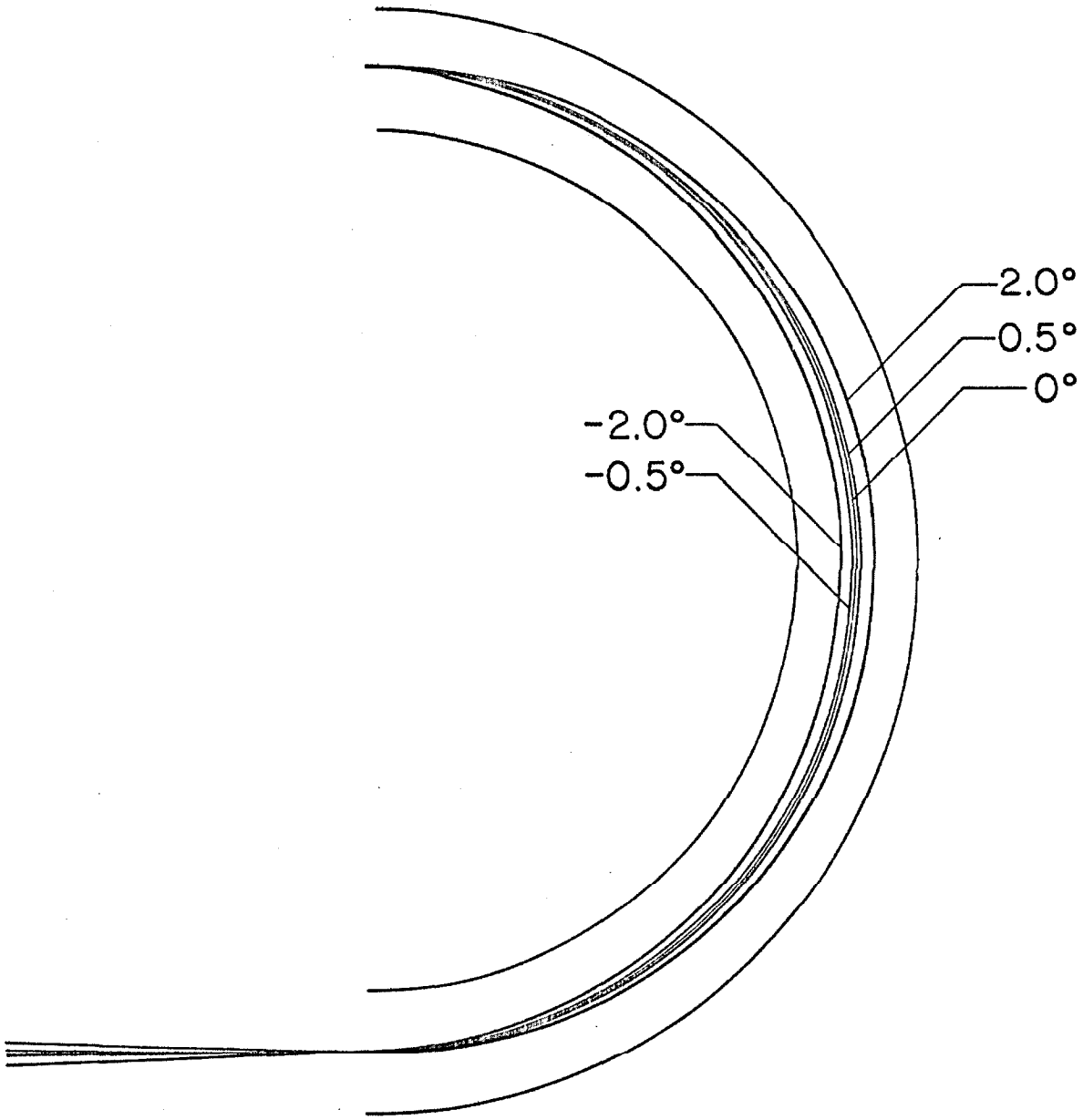

Figure 4.1-3. Electron trajectories in the yz plane (fig. 4.1-1) according to equation (4-20) for $R_o = R_i$ and $E = E_o$. The curves are for the indicated values of α.

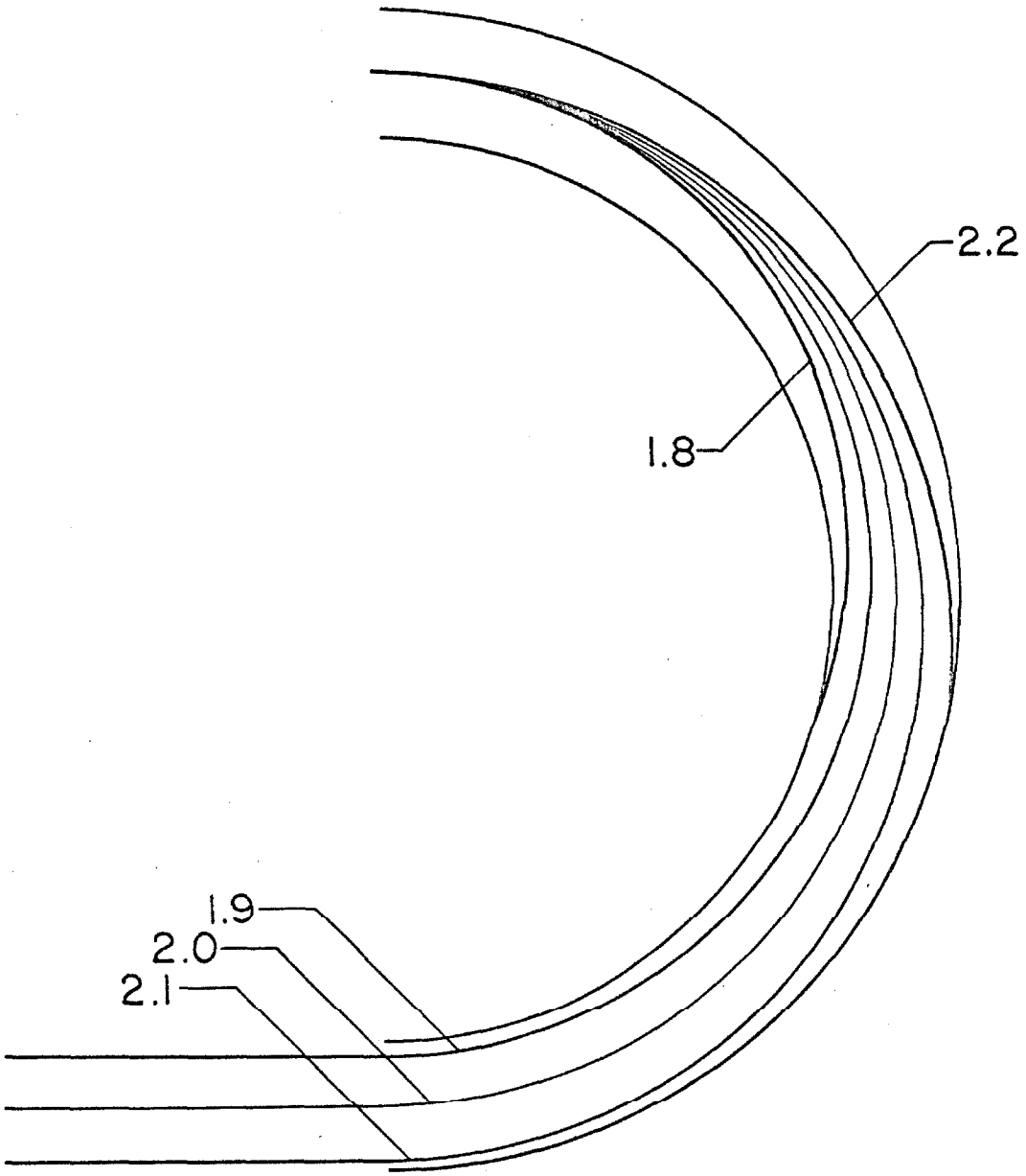

Figure 4.1-4. Electron trajectories in the yz plane (fig. 4.1-1) according to equation (4-20) for $\alpha = 0$, $E_o = 2.0$, and $R_i = R_o$. The curves are for the indicated values of E.

angles of the same absolute value (i. e. , α and $-\alpha$) exit at the same point,

(2) For small α, R_f is independent of α to order α^2, indicating first order focusing in α,

(3) Electrons with the same E, R_i, and $|\alpha|$ but which enter the analyzer in different φ planes for which $0 < \varphi < \pi$ will leave the analyzer at tne same point R_f (i. e. , focusing occurs in φ as well as in α).

4.1.1.2.2 Electron-optical properties

The electron-optical properties of this analyzer can be obtained from the total differential relation

$$dR_f = \frac{\partial R_f}{\partial R_i} dR_i + \frac{\partial R_f}{\partial E} dE + \frac{\partial R_f}{\partial \alpha} d\alpha \qquad (4\text{-}25)$$

in which $\frac{\partial R_f}{\partial R_i}$, $\frac{\partial R_f}{\partial E}$, and $\frac{\partial R_f}{\partial \alpha}$ represent the magnification, energy dispersion, and angular aberration, respectively. For small α, (4-23) reduces to

$$R_f = \frac{R_o}{\eta}\left[1 + \alpha^2\left(1 - \frac{R_o}{\eta R_i}\right)\right] - R_i \quad . \qquad (4\text{-}26)$$

Since the maximum value of α is approximately . 07 radians in the present apparatus, this is a relatively good approximation. After carrying out the indicated partial differentiation in (4-25) using (4-26), we obtain

$$\frac{dR_f}{R_o} = \left[-1 + \frac{\alpha^2 R_o^2}{\eta^2 R_i^2} \right] \frac{dR_i}{R_o} + \left[\frac{1+\alpha^2}{2\eta^2} - \frac{\alpha^2 R_o}{\eta^3 R_i} \right] \frac{dE}{E_o} + \frac{2\alpha}{\eta} \left[1 - \frac{R_o}{\eta R_i} \right] d\alpha \quad . \tag{4-27}$$

The change in R_f, ΔR_f, for a finite change in entrance conditions from those for which the hemispheres are tuned ($R_i \rightarrow R_o \pm \Delta R_i/2$, $E \rightarrow E_o \pm \Delta E/2$, $\alpha \rightarrow 0 + \alpha$) is given by the integration of (4-27) over the indicated ranges.

$$\frac{\Delta R_f}{R_o} = \left[-1 + \frac{\alpha^2}{\eta^2 (1 - \Delta R_i/2R_o)^2} \right] \frac{\Delta R_i}{R_o} + \left[\frac{2}{1 - (\frac{\Delta E}{2E_o})^2} \right] \left[1 + \alpha^2 + \frac{4\alpha^2 R_o}{R_i [1 - (\frac{\Delta E}{2E_o})^2]} \right] \frac{\Delta E}{E_o} + \left(\frac{1}{\eta} - \frac{R_o}{R_i \eta^2} \right) \alpha^2 \quad . \tag{4-28}$$

An electron beam entering the analyzer with a conical divergence angle equal to α, a diameter of ΔR_i centered at R_o, and a broad range of kinetic energies, will be dispersed so that the portion of the beam of diameter ΔR_f centered at R_o leaving the analyzer will have a maximum energy spread of ΔE as given by relation (4-28). Note that ΔE is not the same as the FWHM $\Delta E_{\frac{1}{2}}$, but is approximately the base width of the transmission line shape. The actual line

shape (and hence $\Delta E_{\frac{1}{2}}$) depends on the energy and geometrical distribution of the beam entering the analyzer as well as the exit electron optics. On the basis of experimental observations, $\Delta E_{\frac{1}{2}} \approx \Delta E/2$ and line shapes are generally Gaussian[24]. In section 4.1.1.3 a mathematical verification of these observations will be carried out.

Since the experimental conditions require $\Delta R_f/R_o$, $\Delta R_i/R_o$, and α^2 all $\ll 1$, $\Delta E/E_o$ must also be small. Rewriting (4-28) under these conditions and requiring equal entrance and exit apertures, either real or virtual, yields

$$\frac{\Delta E_{\frac{1}{2}}}{E_o} = \frac{\Delta R}{2R_o} + \frac{\alpha^2}{2} \qquad (4\text{-}29)$$

where $\Delta R = \Delta R_i = \Delta R_f$.

Another property of the analyzer which is of interest is the maximum deviation r_{max} of the beam from the central trajectory of radius R_o. For small deviations of E, R_i, and α from E_o, R_o, and 0, respectively,

$$r_{max} \approx \left| R(\theta = \pi/2) - R_o \right| . \qquad (4\text{-}30)$$

Thus, from (4-20) and (4-30) with $E = E_o \pm \Delta E/2$, $R_i = R_o \pm \Delta R/2$, and $\alpha^2 \ll 1$,

$$r_{max}/R_o = \Delta E/E_o + \sqrt{\alpha^2 + (\Delta R/2R_o + \Delta E/E_o)^2} \qquad (4\text{-}31)$$

$$+ \text{ higher order terms.}$$

4.1.1.3. Line shape

In order to assess the performance of the analyzer system and interpret the energy-loss spectrum peaks in terms of a DCS, it is important to know the characteristic instrumental line shape. Refer to figure 4.1-5 for the definitions of the coordinates associated with the following derivation. In addition, we define the quantities

I_0 ≡ the total number of electrons per second entering the analyzer;

$F(E,R,\varphi,\alpha)$ ≡ the fraction of I_0 entering at the coordinate position (R,φ) per unit area with kinetic energy E per unit energy range and an entrance angle α per unit range of α. E is the kinetic energy of the electrons when they are in Herzog 1 (at potential V_0). F is called the input function;

$N(K,R',\varphi',\alpha')$ ≡ the number of these electrons per second leaving the analyzer at (R',φ') per unit area with kinetic energy K per unit energy range and an exit angle α' per unit range of α'. K is the kinetic energy of the electrons when they are in Herzog 2 (also at potential V_0).

$i(K)$ ≡ the total number of electrons per second leaving the analyzer through a particular area with a given range of α' (determined by the electron optics at the exit of the analyzer) and with a kinetic energy K per unit energy range. This is the definition of the line shape function of a single analyzer.

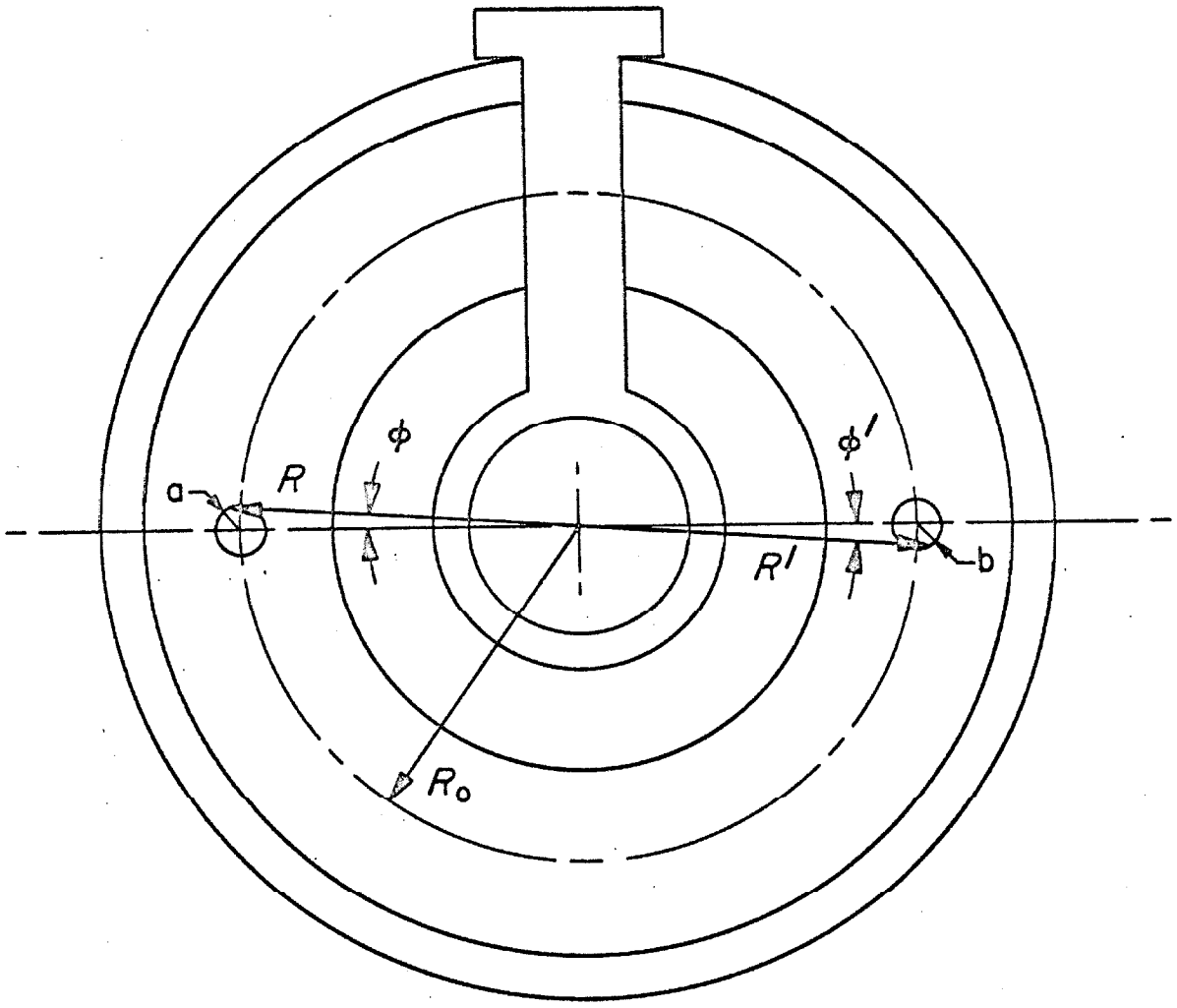

Figure 4.1-5. Front view of the analyzer (xz plane of figure 4.1-1) showing the coordinate definitions used in section 4.1.1.3. The angles φ and φ' are shown in a positive sense. The other symbols are discussed in the text.

$F(E,R,\varphi,\alpha)$ is normalized so that

$$\int_{E=0}^{\infty}\int_{R=R_1}^{R_2}\int_{\varphi=-\pi/2}^{\pi/2}\int_{\alpha=-\pi/2}^{\pi/2} F(E,R,\varphi,\alpha)R\,dE\,dR\,d\varphi\,d\alpha = 1. \tag{4-32}$$

An electron entering the analyzer at (R,φ) with kinetic energy E and a small entrance angle α will exit at (R',φ') with kinetic energy K and exit angle α' if and only if:

(1) $R = R(R',E,\alpha)$ in which R is given by (4-26) ($R \equiv R_i$, $R' \equiv R_f$),

(2) $E = K$ (conservation of energy),

(3) $\varphi = \varphi'$ (consequence of (4-11)),

(4) $\alpha = R\alpha'/R'$ (small α approximation to (4-24).

From these conditions, it follows directly that

$$N(K,R',\varphi',\alpha')$$

$$= \int_{E=0}^{\infty}\int_{R=R_1}^{R_2}\int_{\varphi=-\pi/2}^{\pi/2}\int_{\alpha=-\pi/2}^{\pi/2} \{ I_0 F(E,R,\varphi,\alpha)$$

$$\times \delta[E-K]\frac{\delta[R-R(R',E,\alpha)]}{R}\delta[\varphi-\varphi']\,\delta[\alpha-\frac{R}{R'}\alpha']\}\,R\,dE\,dR\,d\varphi\,d\alpha\,. \tag{4-33}$$

Performing the E,φ, and α integrals leaves a delta function in the integrand of the form $\delta[R-R(R',K,R\alpha'/R')]$. This function is converted to $\delta[R-R(R',K,\alpha')]$ by solving the equation $R = R(R',K,R\alpha'/R')$ for R. After performing the final R integral one obtains

$$N(K,R',\varphi',\alpha') = I_o F(K;R(R',K,\alpha');\varphi';\frac{R(R',K,\alpha')}{R'}\alpha') \quad (4\text{-}34)$$

from (4-33). Then, the line shape function is

$$i(K) = \int_{R'=R'_{min}}^{R'_{max}} \int_{\varphi'=\varphi'_{min}}^{\varphi'_{max}} \int_{\alpha'=\alpha'_{min}}^{\alpha'_{max}} N(K,R',\varphi',\alpha')\, R'\, dR' d\varphi'\, d\alpha' \quad (4\text{-}35)$$

in which the integrations are carried out over the range of beam angles (α') and area (R',φ') sampled by the exit electron optics. If the input function F were known, it would be a straightforward, albeit tedious, exercise to calculate i(K). In order to arrive at an approximate expression for i(K) that will be applicable to the present case, we will consider the following input function describing the initial electron beam (beam leaving the electron gun and entering the monochromator):

$$F(E,R,\varphi,\alpha) = A f(E)\, g(R,\varphi)\, \delta(\alpha) \quad (4\text{-}36)$$

in which (1) $\alpha = 0$ for all electrons (parallel beam),

(2)
$$f(E) = \begin{cases} \left(\frac{E-V}{kT}\right) \exp\left[-(E-V)/kT\right] & E \geq V \\ 0 & E < V \end{cases},$$

(T is the cathode temperature and k is Boltzmann's constant),

(3)

$$g(R,\varphi) = \begin{cases} e^{-(R-R_o)^2/a^2} \; e^{-R_o^2\varphi^2/a^2} & R_1 < R < R_2 \\ & -\frac{\pi}{2} < \varphi < \pi/2 \\ 0 & \text{otherwise} \end{cases}$$

(4)

$$A \cong \frac{2}{a^2\pi(kT)^2} \quad .$$

f(E) represents the expected kinetic energy distribution of the electrons in Herzog 1 due to a Boltzmann distribution of energies from a thermionic cathode after acceleration by V. The peak of f(E) occurs at $E' = V + kT$. We shall assume that the analyzer is "tuned" so that E_o (of equation (4-19) and following) equals E'.

$g(R,\varphi)$ is the geometrical beam distribution peaked at R_o and $\varphi = 0$. "a" characterizes the entrance beam diameter. We actually expect the incoming beam to be cylindrically symmetric, which $g(R,\varphi)$ is not. A symmetric distribution could be of the form,

$$\exp\{-[R_o^2 + R^2 - 2RR_o\cos\varphi]/a^2\} \quad .$$

But, for small values of φ this becomes

$$\exp[-(R-R_o)^2/a^2]\exp[-RR_o\varphi^2/a^2] \quad . \qquad (4\text{-}37)$$

Since the real beam is relatively narrow, an accurate mathematical representation would require that the characteristic beam radius "a" be much smaller than R_o. Only values of R in the region $R_o \pm a$,

for which $RR_o/a^2 \approx R_o^2/a^2$, will contribute significantly to the integral over $g(R,\varphi)$.

A is simply the normalization constant required by (4-32).

It has also been assumed that the incoming beam exhibits no correlation between its kinetic energy and geometry. This is not strictly true since the focal properties of the lenses used to form the beam are energy dependent. These approximations are quite good compared to the more fundamental assumption that all electrons obey the trajectory equation (4-20)(negligible "fringe-fields", space charge, and magnetic or electric disturbances).

From (4-26) and the preceding conditions, one obtains

$$R = R_o/(1 - K/2E_o) - R' = R(R', K, \alpha'). \qquad (4\text{-}38)$$

We obtain the line shape function i(K) from (4-34), (4-35), (4-36), and (4-38).

$$i(K) = C\, f(K)\, X(K) \qquad (4\text{-}39)$$

in which the ranges of integration for (4-35) were chosen to be $R'_{min} = R_o - b$, $R'_{max} = R_o + b$, $\varphi'_{min} = -\beta$, and $\varphi'_{max} = +\beta$. (b and β define the area of the beam collected by the exit electron optics.) C is given by

$$C = \frac{I_o}{kT} \operatorname{erf}\left(\frac{R_o \beta}{a}\right)$$

and X(K) by

$$X(K) = \frac{\sqrt{\pi}\,(K/2E_o)}{(1 - K/2E_o)} \left[\operatorname{erf} \epsilon_+ - \operatorname{erf} \epsilon_-\right]$$

$$+ \frac{a}{R_o}\left[e^{-\epsilon_+^2} - e^{-\epsilon_-^2} \right]$$

where

$$\epsilon_\pm = \frac{R_o(K/E_o - 1)}{a(1 - K/2E_o)} \pm \frac{b}{a}$$

and

$$\mathrm{erf}x = \frac{2}{\sqrt{\pi}} \int_0^x e^{-t^2}\, dt \quad .$$

In the present system the electron beam diameter entering the analyzer (characterized by "a") and that collected by the exit optics (characterized by "b") are nearly the same ($a/b \sim 1$). Also R_o is about 100 times the beam diameter (i.e., $R_o/a \sim 10^2$). Equation (4-39) can be simplified somewhat under these conditions if we consider only the "tails" of the i(K) distribution. If $K \geq 1.02\, E_o$ (note that i(K) peaks at $K = E_o$), (4-39) can be written to a good approximation as

$$i(K) \cong C G_-(K)\ e^{-\left\{\frac{[K - E_o(1 + b/2R_o)]^2}{(aE_o/2R_o)^2}\right\}} \qquad (4\text{-}40)$$

which for $K \leq 0.98\, E_o$

$$i(K) \cong C G_+(K)\ e^{-\left\{\frac{[K - E_o(1 + b/2R_o)]^2}{(aE_o/2R_o)^2}\right\}} \qquad (4\text{-}41)$$

where

$$G_\pm(K) = f(K)\left[\frac{(1/\epsilon_\pm^3 - 1/\epsilon_\pm)}{(1 - 2E_o/K)} - \frac{a}{R_o}\right] .$$

The behavior of i(K) is dominated by the exponential in these regions, and as a consequence, i(K) "tails" off approximately as a Gaussian with a FWHM of $\Delta K_{\frac{1}{2}} \approx aE_o\sqrt{\ell n 2}/R_o$. If ΔR is the geometrical FWHM of the incident beam, $\Delta R = 2a\sqrt{\ell n 2}$ and

$$\frac{\Delta E_{\frac{1}{2}}}{E_o} \cong \frac{\Delta R}{2R_o} \quad , \tag{4-42}$$

which is identical to (4-29) with $\alpha = 0$.

A comparison of the line shape calculated according to (4-39) with a Gaussian and the experimental peak shape is given in section 4.4.5.3.

4.1.1.4. Resolution

Since the energy-loss spectra obtained from the spectrometer are to be interpreted in terms of relative differential scattering cross sections, it is extremely important to assess the effects of the finite resolving power of the analyzer on these spectra.

Consider a simple target "atom" with two electronic excited states of energies $E_b > E_a$ above the ground state. It is assumed that the inherent energy width of these states is much smaller than any achievable resolution in the present instrument. Let the electron beam striking the target have a Gaussian energy distribution centered at $E_o > E_a$ or E_b and a FWHM of $\Delta E_{\frac{1}{2}}^{m}$. After scattering and passing through the selector with a FWHM of $\Delta E_{\frac{1}{2}}^{s}$, the electron beam will produce a signal I at the detector which is a function of the energy-loss E. If we assume the analyzer

has a Gaussian line shape (see section 4.1.1.3), then the observed spectrum will be a superposition of Gaussians, centered at 0, E_a, and E_b, with FWHM which are determined by the resolution of the analyzers. The detected signal at each energy-loss can then be represented mathematically as

$$I(E) = \frac{I_o}{D\sqrt{\pi}}\{ f_e\, e^{-E^2/D^2} + f_a\, e^{-(E-E_a)^2/D^2} + f_b\, e^{-(E-E_b)^2/D^2} \} . \tag{4-43}$$

$D^2 = \frac{(\Delta E_{\frac{1}{2}}^{S})^2 + (\Delta E_{\frac{1}{2}}^{m})^2}{4\,\ell n\,2}$; I_o is the total electron current reaching the detector; and f_e, f_a, and f_b are the fractions of I_o scattered elastically and inelastically leaving the "atom" in states E_a and E_b, respectively. Suppose that $E_b - E_a = W$ and that E_a^2/D^2 is so large that there is no significant overlap of the elastic peak with the inelastic ones. That portion of the energy-loss spectrum in which we are interested can be represented by an equation of the form

$$I(E) = C\{ f_a \exp(-\frac{E^2}{D^2}) + f_b \exp[-\frac{(E-W)^2}{D^2}]\} , \tag{4-44}$$

in which the elastic peak has been neglected, E_a has been taken as the energy-loss origin, and C is an energy-loss independent constant.

The slope of (4-44) is given by

$$S(E) = -\frac{2C}{D^2}\left[f_a e^{-E^2/D^2} + f_b (E - W)\, e^{-(E-W)^2/D^2}\right]. \quad (4\text{-}45)$$

If the two peaks (at energy-losses E_a and E_b) are resolved, S(E) will have three distinct zeros in the range $0 \leq E \leq W$ given by the transcendental equation

$$x\, e^{-2a^2 x} = (1 - x)\frac{f_b}{f_a}\, e^{-a^2} \quad (4\text{-}46)$$

in which $x = \frac{E}{W}$ and $a = \frac{W}{D}$.

A careful analysis of relation (4-46) reveals the following:

(1) If $W^2 < 2D^2$, then the peaks will not be resolved (i. e., only two zeros in equation (4-45)) regardless of the value of $\frac{f_b}{f_a}$. We assume $W^2 > 2D^2$ for the remainder of this discussion.

(2) If

$$\frac{f_b}{f_a} < \frac{1 + p}{1 - p}\, e^{-W^2 p/D^2} \quad (4\text{-}47)$$

where $p = (1 - \frac{2D^2}{W^2})^{\frac{1}{2}}$, the smaller feature is buried under the tail of the larger one.

(3) The range of parameters (f_a, f_b, D, and W) for which the spectrum is considered resolved (i. e., three zeros in S(E)) is given by the inequality

$$\frac{1 + p}{1 - p}\, e^{-W^2 p/D^2} < \frac{f_b}{f_a} < \frac{1 - p}{1 + p}\, e^{W^2 p/D^2} \quad (4\text{-}48)$$

As a specific example, we shall consider the problem of resolving the transitions from the ground 1^1S state of helium to

the 3^1S (state a) and 3^1P (state b) ones at an incident energy of 35 eV and a 25° scattering angle. From the data of section 5.2 (figure 5.2-1 in particular) we note that $f_b/f_a \cong 5.5$ and W = 0.16 eV (we will ignore the effect of the underlying $1^1S - 3^3P$ transition). Then, (4-48) implies that the maximum allowable $\Delta E_{\frac{1}{2}} \approx 0.11$ eV which is approximately the case in this example (figure 5.2-1). State a will be shifted in apparent energy-loss by ≈ 0.01 eV due to the overlap with state b, while b will be shifted only by $\approx .001$ eV. The peak height of a will be increased by $\sim 5\%$ due to b while the increase of b is completely negligible.

4.1.2. Electron-Optics

4.1.2.1. First stage electron-optics

4.1.2.1.1. General requirements

The design criteria for an electron gun to generate the electron beam and for the optics to transport the beam through the monochromator and into the scattering chamber are obtained by specifying the required beam conditions at the scattering chamber entrance. In turn, the optimum entrance or "incident beam" conditions are determined by the nature of the present experimental investigation.

There are five parameters which appropriately characterize the incident beam--kinetic energy, energy spread, angular divergence, diameter, and intensity. Unfortunately, they are not independently adjustable, and the final result will be a compromise

between two basically incompatible requirements at fixed energy--high current density and low angular divergence.

The electron beam kinetic energy and FWHM are to be ~ 30 eV and $\sim .03$ eV, respectively. An incident energy of 30 eV is chosen since it is within a few tens of eV's of the excitation threshold for most atomic and molecular electronically excited states. This is just the energy region in which forbidden transitions are most likely to occur (recall the discussions in section 3.). The FWHM of .03 eV is desired so that we may readily resolve vibrational structure in electronic transitions.

Since we wish to measure differential scattering cross sections, which are functions of the angle between the incident and scattered beam, the incident beam must have a relatively well defined direction. It need not be as narrow in this case as experiments at higher (>100 eV) impact energy require since low energy differential cross sections are not peaked so sharply in the forward ($\theta = 0°$) direction[6d]. An angular divergence (incident beam cone angle) of $\sim .03$ radians and diameter of ~ 0.5 mm are assumed as reasonable values since this choice can provide an angular resolution of about $2°$. Finally, the optimum beam intensity is the highest value compatible with the four other restrictions.

4.1.2.1.2. Monochromator

Since the monochromator is the current-limiting element in this case, we consider its optimal parameters first. $\Delta E_{\frac{1}{2}}$ has already been specified. Assume that the size of the monochromator (R_o) has also been fixed. Then, the electron kinctic energy in the analyzer for maximum current is determined to a certain extent by space charge[103a].

The space-charge-limited current I_s which can be transmitted through a cylindrical volume defined by two apertures of diameter d separated by a length ℓ is [104a]

$$I_s = K E^{3/2} (d/\ell)^2 \mu A \ , \qquad (4\text{-}49)$$

in which E is the electron kinetic energy in eV and K = 38.5. The beam must be launched so that in the absence of space charge it would focus to a point at the center of the volume. Figure 4.1-2 shows an example of this type of focus for the present analyzer. If that portion of the analyzer in which the beam is confined is treated as a volume of diameter ΔR and length $\ell = \pi R_o$, then from (4-49) the space-charge-limited current which can be transmitted by the analyzer is

$$I_s = (K/\pi^2) E^{3/2} (\Delta R/R_o)^2 \ . \qquad (4\text{-}50)$$

α of the relation (4-29) should equal 0 to satisfy the launching condition. Then (4-29) becomes

$$\frac{\Delta E_{\frac{1}{2}}}{E} = \frac{\Delta R}{2R_o} \tag{4-51}$$

Combining (4-50) and (4-51) yields

$$I_s \approx \frac{4K}{\pi^2} \frac{(\Delta E_{\frac{1}{2}})^2}{\sqrt{E}} \quad . \tag{4-52}$$

(4-52) indicates that the greatest space charge limited current can be obtained at the lowest mean kinetic energy (E).

This oversimplified model ignores some of the internal focusing of the monochromator. A significantly more sophisticated point of view has been taken recently by Kuyatt and Simpson[25]. In this approach, space charge spreading is considered to be the result of a negative lens in the vicinity of the minimum beam cross section, i. e., at the exit focal plane of the analyzer. After space charge spreading, the electron beam appears to come from a source smaller than the actual minimum beam diameter. Acceleration of the beam reduces the degree of space charge and allows one to obtain a real image of the apparently small source. As a result, the "effective" aperture size (ΔR) and angular spread (α) can be chosen independently[25]. (4-49) can be rewritten in terms of the beam angle $\alpha = d/\ell$ as

$$I_s = K E^{3/2} \alpha^2 \quad . \tag{4-53}$$

The maximum allowable α^2 is determined from (4-29) and is proportional to $\Delta E_{\frac{1}{2}}/E$. If $\alpha^2 = C \Delta E_{\frac{1}{2}}/E$, then

$$I_S = KC E^{\frac{1}{2}} \Delta E_{\frac{1}{2}}. \qquad (4\text{-}54)$$

(4-54) differs from (4-52) in one very significant way--increasing the mean kinetic energy in the monochromator should increase the space charge limited current. Note, however, that to maintain constant resolution with increasing E, ΔR and α must decrease. For a fixed analyzer size (R_o), and resolution ($\Delta E_{\frac{1}{2}}$), the required aperture size (ΔR) to satisfy (4-29) varies inversely with the first power of the electron kinetic energy. However, the susceptibility of the electron beam to stray magnetic fields drops off only as the inverse one-half power of the energy (refer to section 4.1.3.2.). As a result, at higher analyzing energies, the effect of magnetic disturbances becomes more severe.

In studying this space charge lens[25] model, it was found that an empirically determined anomalous energy spread factor limited the analyzer performance. Dense electron beams exhibit energy widths which are current dependent and much greater than those characterized by the cathode temperature[25]. Consequently, an optimum monochromator design must take into consideration this new factor. Since its dependence on analyzer or electron-optics geometry is not known, an "a priori" monochromator design is not possible.

Aside from these maximum current considerations, (4-29) can be used to obtain approximate design parameters. An empirical adjustment of voltages and lens elements can then be used to optimize the analyzer performance.

If ΔR is on the order of 0.05 cm and $\Delta E_{\frac{1}{2}} \sim .03$ eV, (4-29) requires

$$E_o \sim R_o \tag{4-55}$$

for E_o in eV, R_o in cm and provided that

$$\alpha^2 \ll (\Delta R/2R_o). \tag{4-56}$$

The choice of R_o (or E_o) is still arbitrary. We have chosen R_o = 2.5 cm primarily because the apparatus is then reasonably compact, adequate magnetic field compensation (section 4.3.2.) is more easily obtained, and analyzers of this same dimension have been successfully employed elsewhere[24,25]. With this choice of R_o, (4-55) requires $E_o \sim 2.5$ eV.

4.1.2.1.3. Lens system

Since the electron kinetic energy E_s at the scattering chamber is to be ~ 30 eV while E_o (the kinetic energy in the analyzer) is only ~ 2 to 3 eV, some sort of accelerating lens system is required to image the exit plane of the monochromator onto the physical aperture at the scattering chamber entrance. In this way, the low-energy electrons leaving the analyzer do not pass through any physical apertures until they have been accelerated to a much higher energy. It is believed that this will eliminate aperture scattering effects and secondary electron production at the focal planes of the analyzer. Double-aperture lenses described by Spangenberg[105] are used for this purpose because of their ease of construction and operation.

Let P be the object distance; Q the image distance; A and D the aperture separation and diameter, respectively; R_a the acceleration ratio ($R_a = E_s/E_o$); and M the magnification. We choose M = 1, A/D = 1, and require $R_a \approx 10$. This implies[105] That P/A = Q/A = 4.4. With A taken to be 3.2 mm, P = Q = 14.1 mm. The choice of A is predicated upon two considerations:

(1) the lens should be reasonably short but (2) not narrow enough to intercept any appreciable portion of the beam.

As a consequence of accelerating the beam, α_s, the beam half-angle at the scattering chamber, will differ from α, the beam half-angle at the monochromator. The beam angles and energies at these image-object planes are related by the Abbe-Helmholtz sine law[106]

$$E_s^{\frac{1}{2}} \sin \alpha_s = M E_o^{\frac{1}{2}} \sin \alpha , \qquad (4\text{-}57)$$

in which M is the Gaussian magnification. Substituting the appropriate values that have been previously determined, we find that the maximum allowable α is 0.1 radians.

Two pairs of parallel plate electrostatic deflectors were installed at the entrance to the scattering chamber to aid in "threading" the beam through this aperture.

4.1.2.1.4. Electron gun

It has been pointed out[106] that for unipotential electron guns (a cathode-anode structure with a single accelerating potential)

of axial symmetry derived from space charge limited diodes there exist both a minimum voltage and maximum width-to-length ratio γ of the space that can be saturated with electrons. If a unipotential gun is to be used for this research, it must operate at ~ 2 to 3 eV (since this is the mean electron kinetic energy required in the analyzer) and saturate a space approximately defined by $\gamma = \alpha = 6°$ (since this is the maximum desired beam divergence at the analyzer). From reference (106) it is apparent that this cannot be done. This limitation can be circumvented[107] by using a two-stage gun in which an extraction stage, based upon the immersion objective of Soa[108] and operated at a higher voltage to overcome space charge at the cathode, is followed by a deceleration stage based on the double-aperture lenses characterized by Spangenberg[105]. The design of this type of gun has been thoroughly discussed in reference (107), and we have followed the procedure outlined there.

The gun should saturate with electrons a space defined by an angle of ~6° with a beam energy of ~2.5 eV and a diameter of ~.05 cm (conditions on the beam at the entrance of the monochromator). From (4-53) the space charge limited current is found to be ~1.5 μA. The maximum achievable current density J_{max} in an electron beam at energy E with respect to the cathode is related to the current density $J_{cathode}$ at the cathode by the Langmuir equation[104b, 109]

$$J_{max}/J_{cathode} = (1 + 11,600E/T)\sin^2\gamma \quad (4\text{-}58)$$

for E in eV and T in °K. In this case $J_{max} \approx 10^3 \mu A/cm^2$, and as a result $J_{cathode}$ must exceed $3 \times 10^3 \mu A/cm^2$ for a cathode temperature of 1160°K. This value of the cathode loading is well within the capabilities of most cathode materials[103b].

The required perveance ($I/V^{3/2}$) is $\sim .009 \mu A/V^{3/2}$ for an extraction voltage of 30 V. The extraction stage is followed by a 10:1 deceleration stage identical in design to the double-aperture lens system described in section 4.1.2.1.3.

From the design graph of reference (107) this value of the perveance requires M_G (magnification of the gun) to be ~ 2. Q/d_k can be estimated by extrapolation to be ~ 22. (Q is the anode-gun image distance; d_k is the cathode-grid distance.) A grid bias (V_{grid}/V_{anode}) of $\sim .023$ is also necessary according to reference (107). Since the diameter of the emitting area of the cathode is approximately 1/2 the grid bore D_q, the final image size at the analyzer ΔR, is given by the relation

$$\Delta R = 1/2 \, D_q \, M_G \, . \qquad (4\text{-}59)$$

With $\Delta R = .05$ cm and $M_G = 2$, we obtain $D_q = .05$ cm. Once D_q has been determined, all other spacings in the Soa gun are fixed[107].

Two pairs of electrostatic deflectors have been incorporated into the gun structure to facilitate the correction of any misalignment in the beam.

4.1.2.2. Second stage electron optics

4.1.2.2.1. General requirements

The second half of the spectrometer is devoted to collecting a certain fraction of those electrons which have been scattered by an angle θ with respect to the incident beam and to determining the current of such electrons which have lost a specified amount of their initial kinetic energy as a result of the scattering process. The electron beam entering the second stage has an energy distribution consisting approximately of a superposition of Gaussian functions (refer to section 4.1.1.4.), each peaked at an energy $E_o - W_n$, where E_o is the initial beam kinetic energy and W_n is the excitation energy of a particular molecular transition. The FWHM of these peaks is determined by the monochromator and consequently the second stage energy analyzer (selector) should be chosen to have an intrinsic FWHM approximately equal to that of the monochromator. Further, this beam is usually of very low intensity ($\sim 10^{-14}$A) compared to the beam leaving the gun ($\sim 10^{-6}$A). Finally, since we are to determine differential scattering cross sections, the collected beam should have a suitably small angular divergence (approximately the same as that of the incident beam).

4.1.2.2.2. Selector

Space charge effects can be neglected due to the low current densities in the selector. Otherwise, the same considerations that were pertinent to the monochromator are applicable to the selector. The latter was chosen to be identical in construction to the mono-

chromator primarily to simplify the operation and preserve the symmetry of the apparatus.

4.1.2.2.3. Lens systems

The lens system between the scattering chamber and the selector is identical in design concept to that between the monochromator and the scattering chamber (see section 4.1.2.1.3.) with one important exception. The transmission of the entire second stage must have no overall energy-loss dependence, i.e., electrons leaving the scattering chamber with different kinetic energies (corresponding to different energy-loss processes) must be detected with the same efficiency when that particular energy-loss is being transmitted by the selector. This behavior is not quantitatively "built-in" to the present apparatus. Rather, it is to be determined empirically. We have used a three-lens system at the exit of both the scattering chamber and selector. Qualitatively, it should provide a weak lens followed by a strong one so that relatively large changes in electron kinetic energies entering or leaving the lenses do not change the eventual focal point appreciably. The experimental justification for the usefulness of this simple system is given in section 4.4.6. There are more sophisticated approaches to this problem now available[110] which may be incorporated into future modifications of this instrument.

4.1.3. External Fields

4.1.3.1. Introduction

Throughout the discussion of electron optics and analyzers (sections 4.1.1., 4.1.2.) the electrons were assumed to travel in field-free regions except for those regions in which electric fields were desired for focusing, etc. In practice, of course, electric and/or magnetic fields from television and radio stations, nearby electronic equipment, or the Earth itself may seriously affect the performance of the spectrometer. In this section, we shall attempt to assess the magnitude of these disturbances and outline methods of reducing them.

The classical force $\underset{\sim}{F}$ acting on an electron due to electric fields of strength $\underset{\sim}{\mathcal{E}}$ and magnetic fields of induction $\underset{\sim}{B}$ is given by the Lorentz force equation

$$\underset{\sim}{F} = e(\underset{\sim}{\mathcal{E}} + \underset{\sim}{v} \times \underset{\sim}{B}) \tag{4-60}$$

in which e and $\underset{\sim}{v}$ are the charge and velocity of the electron, respectively. This force can distort the electron's trajectory as well as cause an actual energy change. Since a trajectory distortion in the analyzer can be related to an apparent kinetic energy change, the kinetic energy resolution can be affected in either case. If ΔE_s is the change in the FWHM of the electron beam energy distribution due to these effects, then the inequality

$$\Delta E_s < \Delta E_{\frac{1}{2}} \tag{4-61}$$

must be satisfied for an allowable field disturbance ($\Delta E_{\frac{1}{2}}$ is the FWHM in the absence of such fields).

4.1.3.2. D.C. magnetic fields

Consider an electron with kinetic energy E, traveling in a direction perpendicular to a uniform magnetic field B, and radial field $\mathcal{E}$. From the radial force equation we obtain

$$\frac{2E}{R} = e(\mathcal{E} \pm \sqrt{\frac{2E}{m}}\, B) \tag{4-62}$$

in which R is the radius of curvature of the electron's path, ± refers to the two possible orientations of the electron's velocity vector with respect to the magnetic field direction, and m is the electron mass. Assume that $\mathcal{E}$ is the desired electric field ($\underset{\sim}{\mathcal{E}} = - \underset{\sim}{\nabla} V(R)$) within one of the hemispherical analyzers while B is an undesired magnetic field. Let $E = E_0$ be the solution of (4-62) with B = 0. If B is small (4-62) will be satisfied for another energy $E = E'$ for which

$$E' \approx E_0(1 \pm \frac{eRB}{\sqrt{2mE_0}}) \quad . \tag{4-63}$$

Then with $\Delta E_s \equiv |E' - E_0|$ and relation (4-61), B must satisfy the inequality

$$B < (\frac{\Delta E_{\frac{1}{2}}}{E_0}) \frac{\sqrt{2mE_0}}{|e|\, R} \quad . \tag{4-64}$$

(4-64) yields the rather surprising result that for constant resolution ($\Delta E_{\frac{1}{2}}$) and fixed analyzer dimensions (R), a higher

analyzing energy (E_o) requires better magnetic field compensation (i.e., lower B). This is due to the smaller effective aperture sizes (ΔR) required to maintain a constant FWHM at higher E_o in the analyzer (see section 4.1.2.1.2.). In the present case, $\Delta E_{\frac{1}{2}} \approx .03$ eV, $R_o = 2.5$ cm, and $E_o \approx 2$ eV for which relation (4-67) requires $B < 2.8 \times 10^{-2}$ gauss. Since the Earth's magnetic field is more than 10 times this value, some sort of field cancellation is necessary.

This magnetic field compensation can be provided by a set of Helmholtz coils. A pair of thin coaxial coils containing the same number of turns, carrying the same current, having the same radius, and being separated by a distance equal to their radii, will provide a nearly constant magnetic field vector directed along their axis in a small region about their midpoint. One such pair, properly oriented, could be used to partially neutralize the Earth's field in some particular region. However, in the present case, it is more convenient to use three pairs of fixed, mutually perpendicular coils. By independently varying the current in each pair, the resultant magnetic field vector, nearly constant within the desired region, can be made to point in any direction. The useful region of compensation depends on the radii of the coils, their separation, and the homogeneity of the Earth's magnetic field. Note that relay racks, vacuum equipment, etc. may cause severe local field distortions. The actual construction and performance are given in sections 4.2.2. and 4.3.2., respectively.

4.1.3.3. Radio-frequency (RF) fields

Since this apparatus was used in a region of substantial RF activity (within line-of-sight of the TV transmitters on top of Mt. Wilson), it is important to estimate the effect of these oscillatory fields on the electron beam.

An electromagnetic wave carries with it an electric field $\underset{\sim}{\mathcal{E}}$, and a magnetic field $\underset{\sim}{B}$, related by

$$\underset{\sim}{B} = \frac{1}{c}\,\hat{k} \times \underset{\sim}{\mathcal{E}} \tag{4-65}$$

in which $\hat{k}$ is a unit vector in the direction of propagation and c is the speed of light. The force exerted on an electron by such an RF field is given by substituting (4-65) into (4-60).

$$\underset{\sim}{F} = e\ \left\{\left[1 - \frac{v}{c}(\hat{k}\cdot\frac{\underset{\sim}{v}}{v})\right]\frac{\underset{\sim}{\mathcal{E}}}{\mathcal{E}} + \frac{v}{c}(\frac{\underset{\sim}{v}}{v}\cdot\frac{\underset{\sim}{\mathcal{E}}}{\mathcal{E}})\,\hat{k}\right\}\ . \tag{4-66}$$

If $v/c \ll 1$ (i.e., low energy electrons), $\underset{\sim}{F} \approx e\underset{\sim}{\mathcal{E}}$. Consequently, it is assumed that the electromagnetic wave disturbance is due entirely to an oscillating electric field of strength $\underset{\sim}{K}$, and frequency ν, of the form

$$\underset{\sim}{\mathcal{E}}(t) = \underset{\sim}{K}\cos(\nu t + \delta_\nu) \tag{4-67}$$

in which δ_ν is the phase of the field at time $t = 0$.

As a further approximation to the actual situation, consider the case of an electron of velocity $\underset{\sim}{v}_0$, and position $\underset{\sim}{R}_0$, entering a field of the type (4-67) at $t = 0$. The trajectory $\underset{\sim}{R}(t)$, of the electron is given by the equation

$$\frac{d^2\underset{\sim}{R}(t)}{dt^2} = \frac{e}{m}\underset{\sim}{K}\cos(\nu t + \delta\nu) \qquad (4\text{-}68)$$

in which radiation of the electron due to acceleration has been ignored[111]. Integration of (4-68) and application of the initial conditions yields

$$\underset{\sim}{R}(t) = \underset{\sim}{R}_o + \underset{\sim}{v}_o t$$

$$+ \frac{e\underset{\sim}{K}}{m\nu^2}[\cos\delta_\nu - \cos(\nu t + \delta_\nu) - \nu t\sin\delta_\nu] \quad . \qquad (4\text{-}69)$$

The energy $\epsilon(\delta_\nu, \nu, t)$ transferred to the electron per unit time for an initial phase δ_ν, is equal to the work done on the electron by the field per unit time or

$$\epsilon(\delta_\nu, \nu, t) = [e\underset{\sim}{K}\cos(\nu t + \delta_\nu)] \cdot [\frac{d\underset{\sim}{R}(t)}{dt}] \quad . \qquad (4\text{-}70)$$

The total energy transferred $\Delta E\ (\delta_\nu, \nu, \tau)$, in time τ, is

$$\Delta E(\delta_\nu, \nu, \tau) = \int_o^\tau \epsilon(\delta_\nu, \nu, t)dt \quad . \qquad (4\text{-}71)$$

If a random distribution of initial phases δ_ν is assumed, the average energy $\Delta E_s(\nu, \tau)$ transferred in time τ is given by

$$\Delta E_s(\nu, \tau) = \frac{1}{2\pi}\int_o^{2\pi} \Delta E(\delta_\nu, \nu, \tau)d\delta_\nu \quad . \qquad (4\text{-}72)$$

Thus, with the use of (4-69) through (4-72), we obtain

$$\Delta E_s(\nu, \tau) = 0.88 \times 10^{11}\frac{K^2}{\nu^2}(1 - \cos\nu\tau)\ \text{eV} \qquad (4\text{-}73)$$

for K in volts/meter and ν in radians/sec.

The deviations in the electron trajectory $\underset{\sim}{D}$, due to the electric field $\underset{\sim}{\mathcal{E}}$, from (4-67) are

$$\underset{\sim}{D}(\nu, \delta_\nu, t) = \frac{e\underset{\sim}{K}}{m\nu^2} [\cos \delta_\nu - \cos(\nu t + \delta_\nu) - \nu t \sin \delta_\nu] \ . \qquad (4\text{-}74)$$

For random initial phases, $\underset{\sim}{D} = 0$. However, the square root of the average squared deviation defined by

$$\overline{\Delta D(\nu, t)} = [\frac{1}{2\pi} \int_0^{2\pi} \underset{\sim}{D} \cdot \underset{\sim}{D} \, d \, \delta_\nu]^{\frac{1}{2}} \qquad (4\text{-}75)$$

is in general non-zero. In particular,

$$\overline{\Delta D(\nu, t)} = \frac{|e|K}{m\nu^2} [1 - \cos \nu t + \frac{(\nu t)^2}{2} - \nu t \sin \nu t]^{\frac{1}{2}} \ . \qquad (4\text{-}76)$$

The effect of $\overline{\Delta D}$ is to broaden the FWHM of the electron beam in a manner similar to an increase in ΔR of equation (4-29). Therefore the apparent energy change $\overline{\Delta E_s(\nu, t)}$, within the analyzer due to $\overline{\Delta D}$ is

$$\frac{\overline{\Delta E_s}}{E_o} \approx \frac{\overline{\Delta D}}{2R_o} \ . \qquad (4\text{-}77)$$

Thus,

$$\overline{\Delta E_s(\nu, t)} = 0.88 \times 10^{11} \frac{E_o K}{R_o \nu^2} [1 - \cos \nu t + \frac{(\nu t)^2}{2} - \nu t \sin \nu t]^{\frac{1}{2}} \text{ eV} \qquad (4\text{-}78)$$

for R_o in meters and E_o in eV.

As a specific example, assume $K \sim 1$ V/M (a reasonable value for nearby sources of RF signals[112]) and $\nu = 0.5 \times 10^{-6}$ cycles/sec. For $\tau = 10^{-6}$ sec (approximate time for the electron to

pass through the system), (4-73) yields

$$\Delta E_s \approx .03 \text{ eV}$$

For $\tau \approx 10^{-7}$ sec (approximate time for the electron to pass through the sphere) and $E_o = 2$ eV, (4-78) yields

$$\overline{\Delta E}_s \approx .02 \text{ eV} \quad .$$

This type of interference has been eliminated by enclosing the entire apparatus in an RF shielded enclosure (refer to section 4.2.2.).

4.2. Construction

4.2.1. Vacuum System

Since the mean free path of an electron in air at atmospheric pressure is only on the order of 10^{-4} cm, the entire spectrometer must be enclosed within a vacuum chamber. This chamber must provide a background pressure low enough so that the only electron-molecule collisions of importance occur in the scattering chamber. It should be bakeable in order to obtain better vacuum and electron-optical element surface conditions. Finally, the chamber material should have a low magnetic susceptibility to facilitate the elimination of D. C. magnetic fields along the electron path.

A non-magnetic, type 304 stainless steel vessel (refer to figure 4.2-1) was designed by us and fabricated by C. E. Howard

Figure 4.2-1. The stainless steel main vacuum chamber. Side view (left) and front view (right). (FC 1 through FC 6) flange covers; (T) flexible stainless steel connecting tube (to pumping system, figure 4.2-2); (O) location of "O"-ring groove in flange; (G) location of gold wire gasket (if used) in flange.

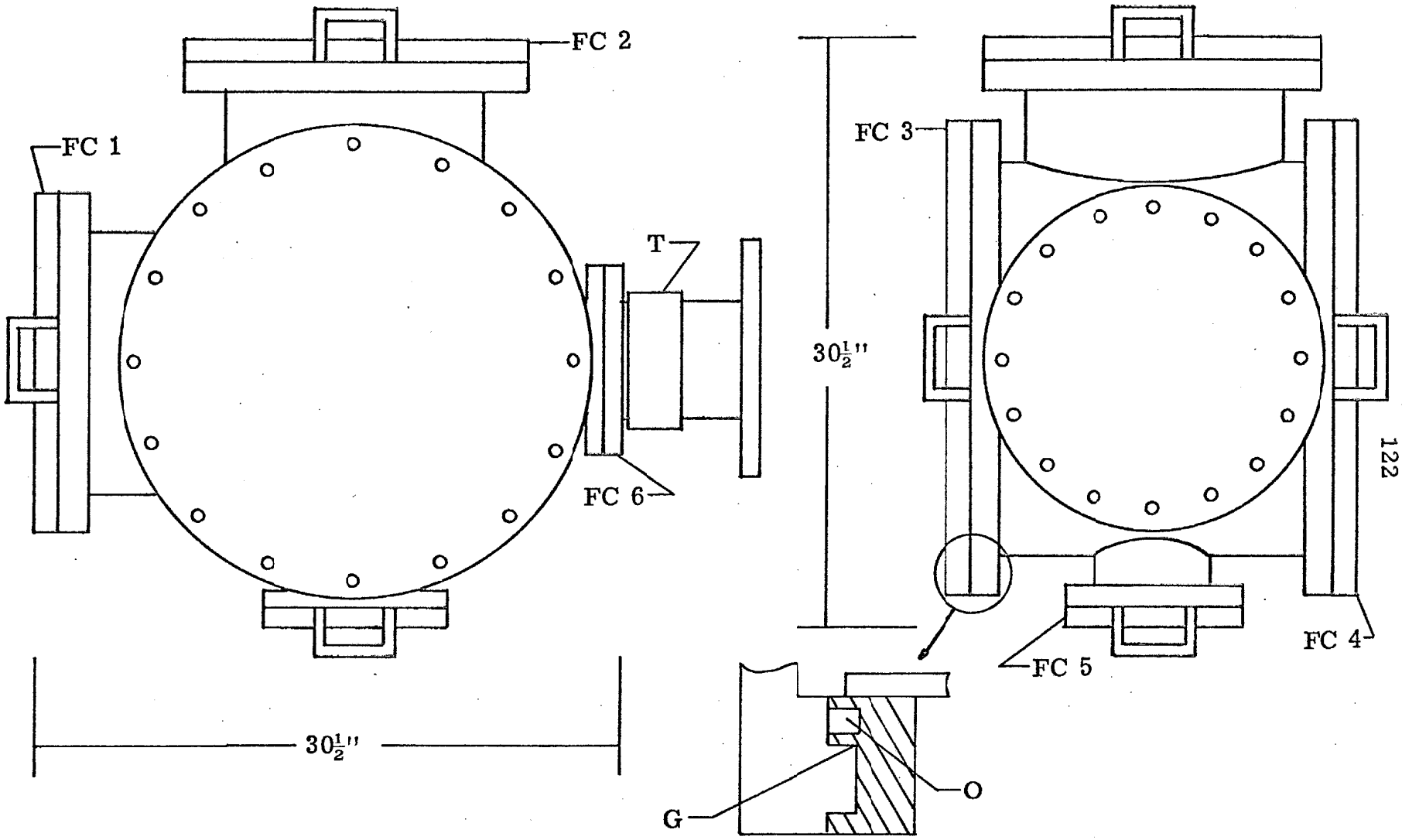
FC 2
FC 1
T
FC 6
30½"
30½"
FC 3
FC 4
FC 5
122
G
O

Corporation. The flanges are of a unique design in that either gold wire (.040" diameter) gaskets or rubber "O"-rings can be used (see insert of figure 4.2-1). Table 4.2-1 lists the various "O"-ring seals that can be used on the main chamber as well as other data about the flanges. The flange covers (FC 2, FC 3, FC 4, FC 5, FC 6) were sealed to their respective flanges with gold gaskets while a butyl-rubber "O"-ring was normally used to seal FC 1. All of the spectrometer components are mounted on this latter flange cover. The flanges and flange covers were designed to seal the gold gaskets under a pressure of 1000 lbs/linear-inch at a bakeout temperature of 450°C (if necessary).

The main chamber is evacuated through the 8" diameter flexible stainless stell tube (T) by means of a pumping system shown in figure 4.2-2. It consists (in order from the main chamber) of a Vacuum Research Corporation 10" pneumatically operated gate valve (GV); a Ladish Company 8" diameter, 90°, long radius, type 304 stainless steel elbow (E); an Edwards High Vacuum Incorporated model NTM9A, 9" liquid nitrogen cold trap (CT); an Edwards model CB9A, 9" freon cooled chevron baffle (CB 1); an Edwards model 9M3A, 9" mercury diffusion pump (DP); an Edwards, model CB 2, 2" freon cooled chevron baffle (CB 2); and an Edwards model ED500, mechanical pump (MP). The diffusion pump, baffle, and cold trap can be isolated by closing GV and the Carl Herman Associates (CHA), model Kel-122, $1\frac{1}{2}$", stainless steel bellows valve (V 1). In this way, the main chamber can be vented

TABLE 4.2-1

Construction parameters associated with the main vacuum chamber flanges.

Flange	"O"-Ring* Dimen. I.D. × Width (inches)	Gold Gasket Diam. (inches)	Bolt Circle Diam. (inches)	No. of Bolts Reqd.	Bolt Size (inches)
F 1, F 2	13.975×.275	15.250	$16\frac{1}{4}$	32	$\frac{5}{8}$-11NC×$3\frac{3}{4}$ LG.
F 3, F 4	20.955×.275	22.250	$23\frac{1}{4}$	36	$\frac{5}{8}$-11NC×4 LG.
F 5, F 6	8.975×,275	10.250	$11\frac{1}{4}$	20	$\frac{5}{8}$-11NC×$3\frac{1}{4}$ LG.

* Available from Parker Seal Co., catalog numbers 5427-84, 5-087, and 5427-74, respectively.

Figure 4.2-2. The vacuum chamber pumping system. (G 1 and G 2) ionization gages, (T 1 and T 2) thermocouple gages, (V 1) stainless steel valve, (V 2 through V 4) brass valves, (GV) aluminum gate valve, (E) stainless steel elbow, (GT) liquid nitrogen cold trap, (CB 1 and CB 2) chevron baffles, (DP) diffusion pump, (FL) fore line, (MP) mechanical pump, and (EL) exhaust line.

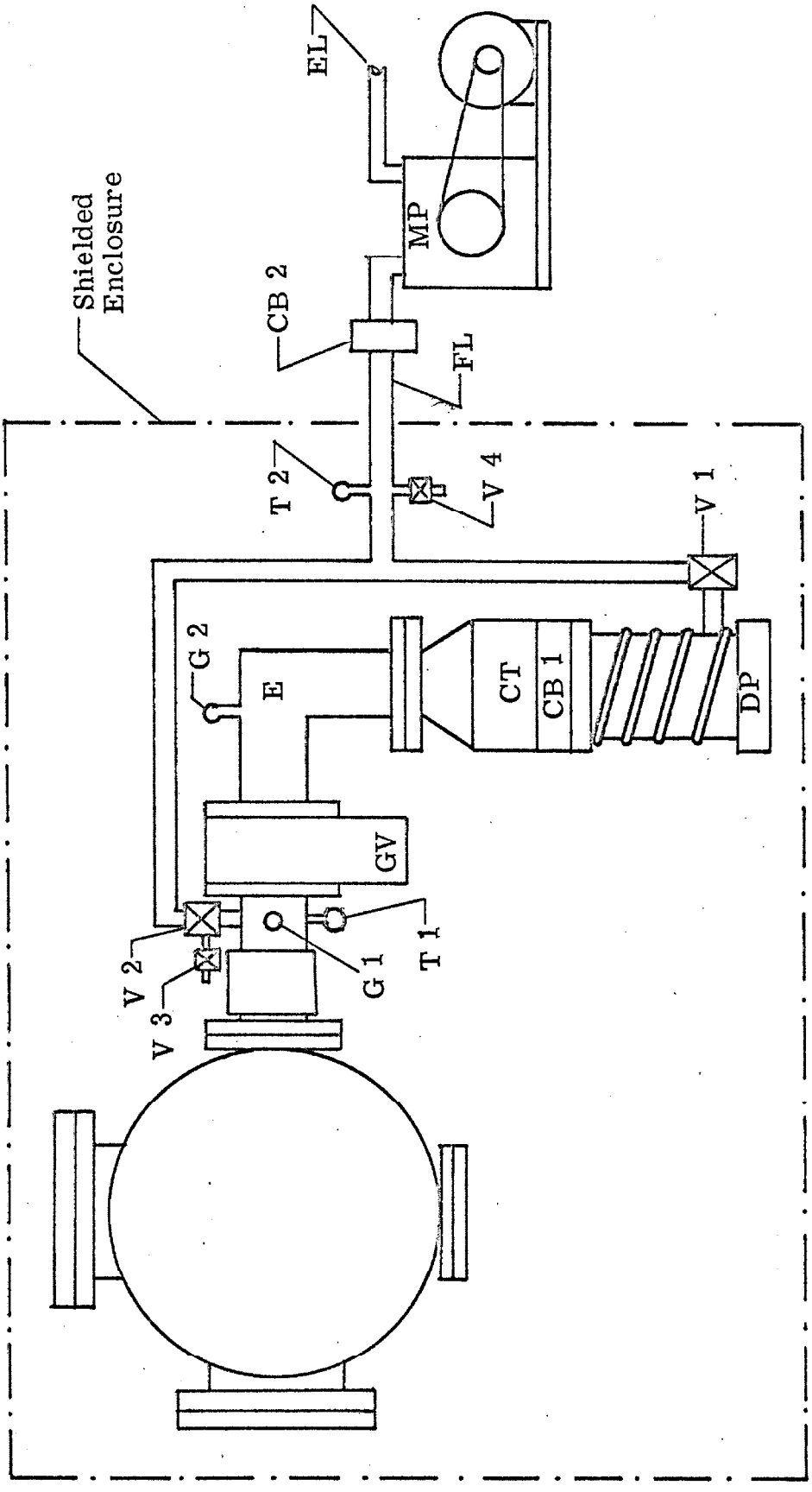
Shielded Enclosure
EL
MP
CB 2
FL
T 2
V 4
V 1
G 2
E
CT
CB 1
DP
GV
V 2
V 3
G 1
T 1

and subsequently pumped out through the CHA, model RA-12-1, $1\frac{1}{2}$" bellows valve (V 2) while the diffusion pump remains on. Thermocouple gages (Hastings, model DV-3M) are located at T 1 and T 2 while ion gages (General Electric Co., model 22GT103) are placed at G 1 and G 2. They are controlled by a Veeco thermocouple gage control unit and a G. E. ionization gage control unit, respectively. Two bellows valves (CHA, brass, $\frac{1}{2}$") are located at V 3 and V 4 for venting and leak checking. All gases pumped by the system are ducted out of the room through the exhaust line (EL).

The vacuum chamber and pumping system within the shielded enclosure are supported independently by two tables. They are constructued of 2"× 2" aluminum square tubing and have a jack screw and caster at each leg. The table supporting the vacuum chamber is 33" long by 34" wide by 29" high while the one supporting the pumping system is 58" × 34" × 35". The two compressors (which cool the baffles CB 1 and CB 2) and the mechanical pump are located outside of the shielded room.

The vacuum system is equipped with both a temperature and pressure interlock protection network. The diffusion pump will be automatically shut off and the gate valve closed if: (1) power to the mechanical pump is interrupted, (2) the diffusion pump jacket becomes too hot, or (3) the fore line pressure falls below 0. 5 torr. The gate valve will also close if power to the diffusion pump is interrupted.

4.2.2. Shielding of External Fields

4.2.2.1. Shielding of D.C. magnetic fields

In order to neutralize the Earth's magnetic field along the electron path, three pairs of Helmholtz coils were constructed and placed around the main vacuum chamber as shown in figure 4.2-3. The coils are wound on plexiglass frames designed for this purpose. Table 4.2-2 gives the construction parameters associated with these coils. Current to the windings was supplied by an Electronic Measurements, model TR 212 AMB, D. C. regulated power supply. Section 4.3.2. summarizes the performance of this system.

4.2.2.2. Shielding of RF fields

In order to shield the spectrometer from interference due to RF sources in the vicinity, most of the apparatus (including the vacuum chamber, part of the pumping system, and the electrical relay racks) was enclosed within a Topatron Incorporated, model 7322, shielded enclosure. The enclosure was originally 12' long × 8' wide × 8' high. Since these experiments were performed, it has been expanded to 12' × 12' × 8'. All feedthroughs into the enclosure (air conditioning, vacuum, water, compressed air, and electrical power) are supplied by the manufacturer and are designed not to transmit RF signals. The room has a 100 db attenuation for frequencies from 10,000 Hz to 100,000M Hz. Thus, a K value (section 4.1.3.3.) of 1 volt/meter outside the shielded room will be reduced to approximately 10^{-5} V/m within the enclosure. Since the apparatus has never been operated outside this room, it has been

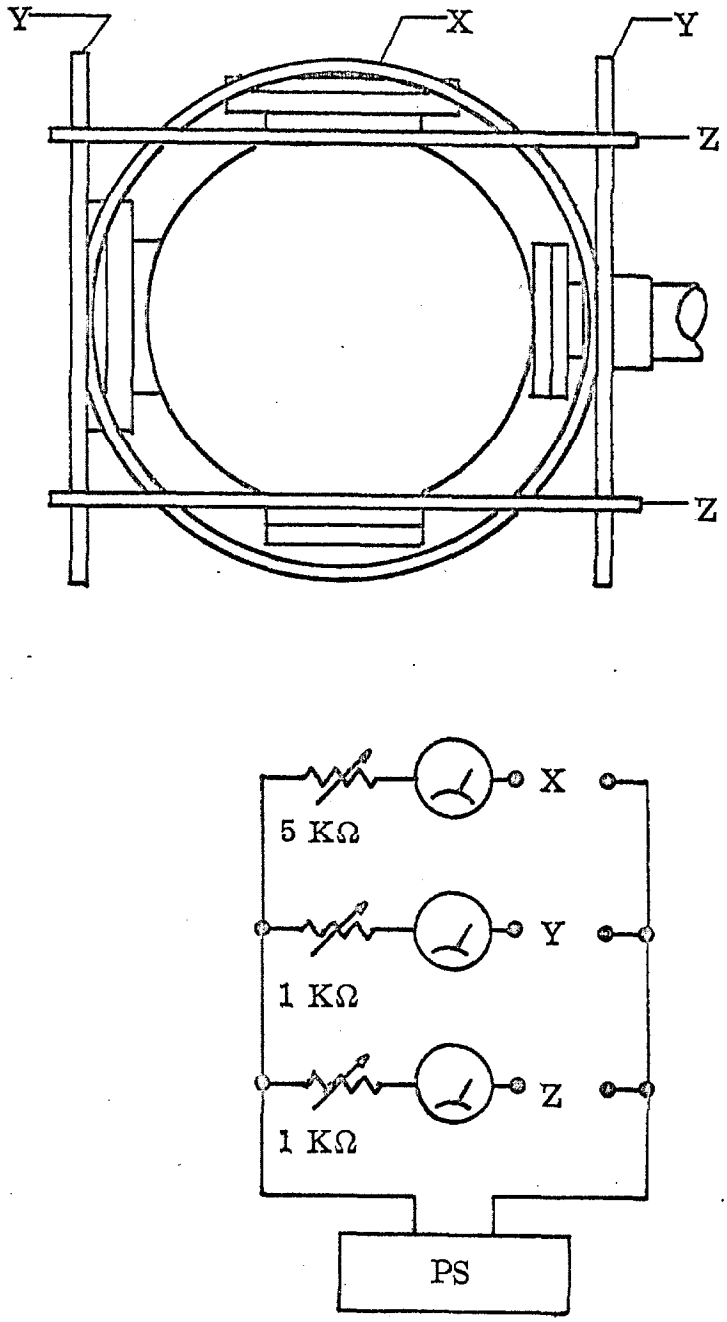

Figure 4.2-3. Orientation of the Helmholtz coils around the vacuum chamber. X, Y, and Z are the coil-pair designations. The power supply (PS) provides a constant voltage so that the current through a particular coil-pair can be varied by changing the adjustable series resistance.

TABLE 4.2-2

Construction parameters of the three pairs of Helmholtz coils.

Coil* Pair	Coil Radius cm	Coil Separation cm	Number† of Turns
X	49	54	720
Y	52	84	697
Z	55	58	662

* The coil-pair designation refers to figure 4.2-3.

† Belden magnet wire, 28 gauge, HNC Nyclad No. 8080.

impossible to empirically verify its usefulness.

4.2.3. Carriage

In order to facilitate the insertion and removal of the flange cover FC 1 (figure 4.2-1), a carriage was constructed as shown in figure 4.2-4. This carriage is a necessity since FC 1 and the spectrometer together weigh about 100 lbs. FC 1 can be bolted to the carriage, which in turn rides on two $2'' \times 2\frac{1}{2}'' \times 72''$ angle-iron rails that are clamped to the table supporting the vacuum chamber. The rails extend a sufficient length beyond the end of the table so that the spectrometer can be "wheeled" completely out of the vacuum chamber for easy access. The Helmholtz coils do not need to be removed, and the carriage with its supporting rails is easily removed from the shielded room after use. (Since the material from which it is made is highly magnetic, it must be removed when the spectrometer is to be operated.)

4.2.4. Spectrometer Components

4.2.4.1. General description

Figure 4.2-5 is a block-schematic representation of the spectrometer components. The electron beam path through the apparatus begins at the electron gun and describes an "S" shaped curve in the plane of the figure, eventually reaching the electron multiplier. This particular geometricl arrangement is chosen to reduce structural interference and to help average out the effects of constant residual fields, i.e., the electron would be deflected

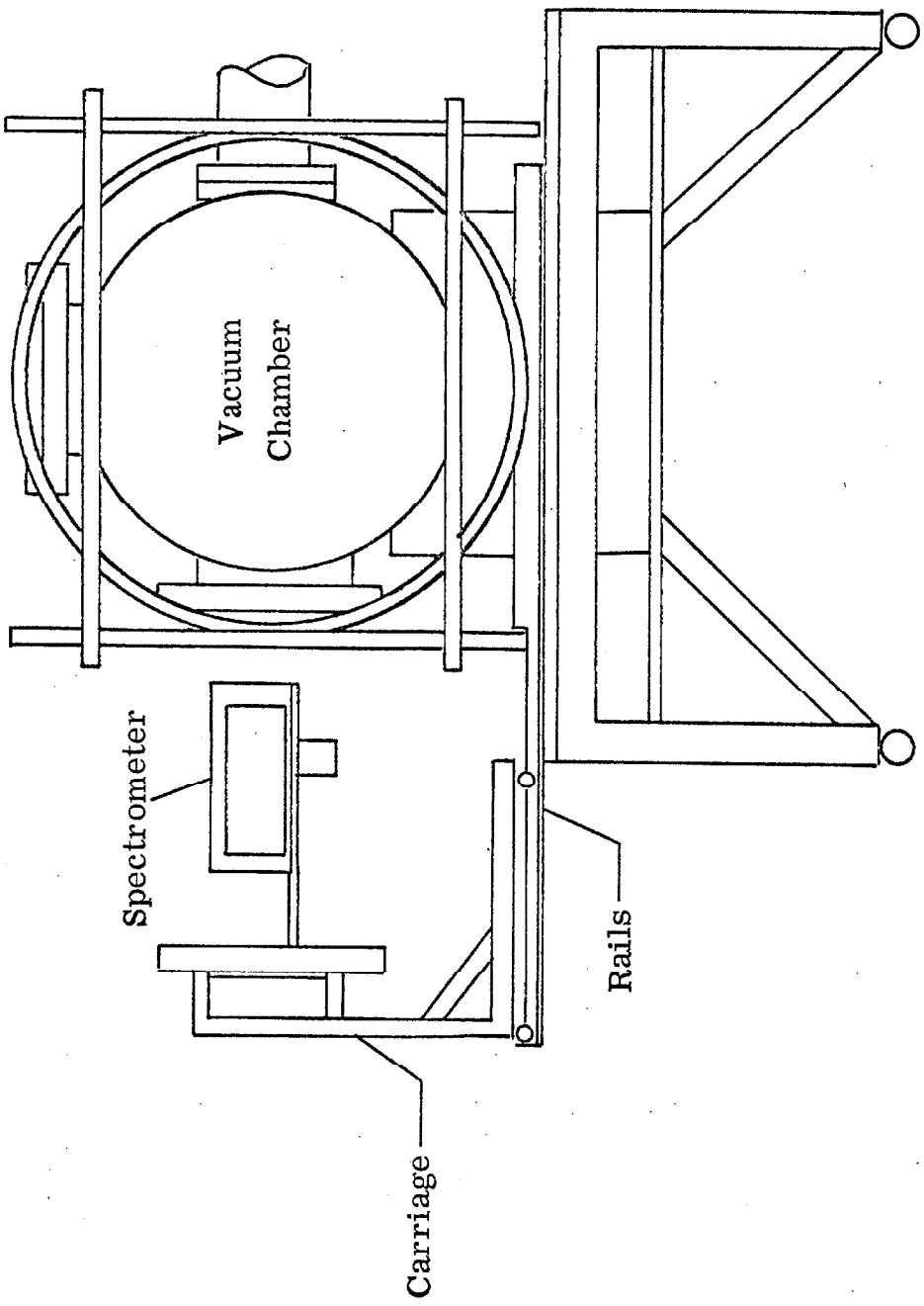

Figure 4.2-4. Carriage assembly mounted to the vacuum chamber support table (side view).

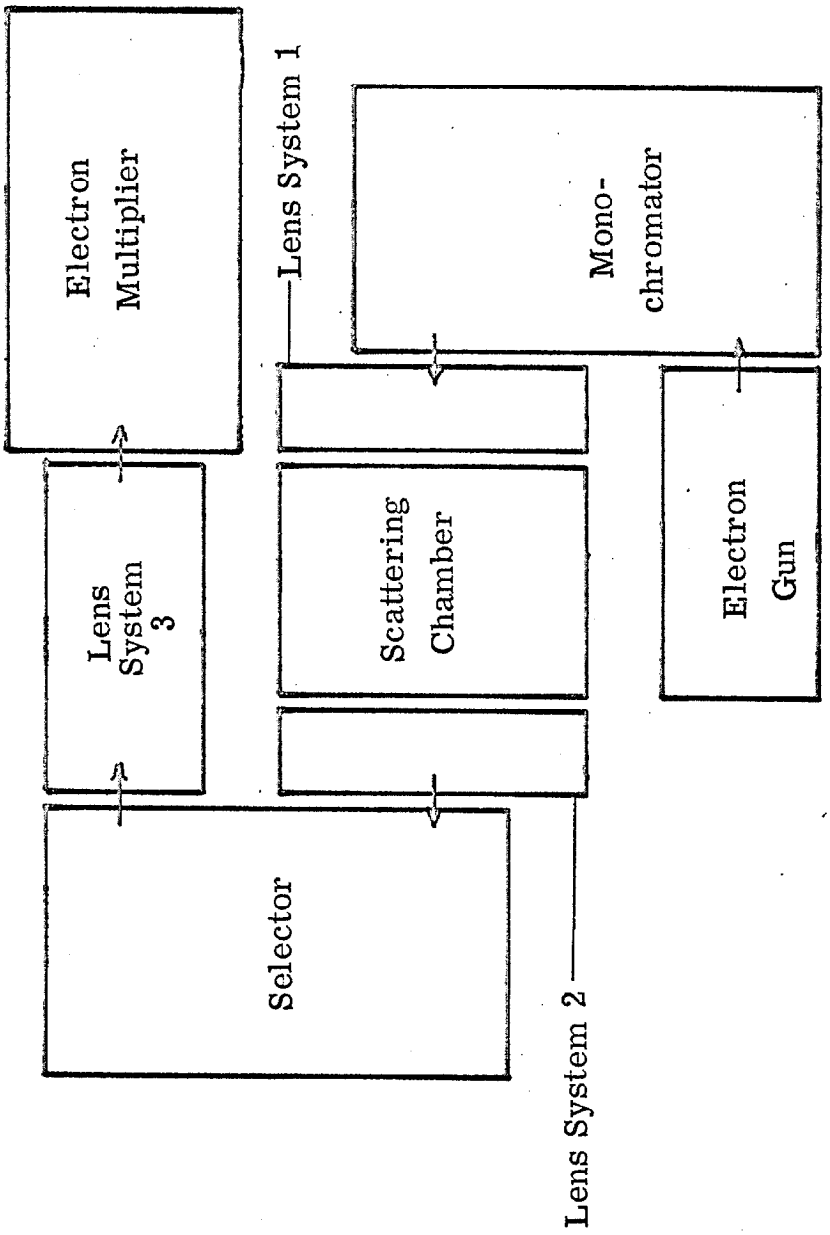

Figure 4.2-5. Block-schematic diagram of the spectrometer components. The arrows point in the direction of the electron beam.

in one direction through the first half of the "S" but would be deflected the opposite way through the second half.

The construction details of the various elements of the instrument are given in the following sections.

4.2.4.2. Electron gun

A cross-sectional view of the cylindrically symmetric electron gun is given in figure 4.2-6. The cathode housing and grid are of type 304 stainless steel, the apertures are of molybdenum, boron nitride is used for electrical insulation as indicated, and all other elements are of oxygen-free high-purity copper (OFHC). A Picker-Nuclear, No. 80-3236, .005" diameter tungsten hairpin filament is used as the electron source (cathode). The cathode, grid, and aperture A1 of the anode structure comprise the 3 element Soa gun discussed in section 4.1. Aperture A2 is included to block off much of the unwanted beam and to keep the deflectors, which aid in guiding the beam, from drawing an appreciable current. Aperture A3 defines the object of the lens system composed of elements LVL 1 and Herzog 1. (LVL stands for low-voltage-lens which is so named because under usual operating conditions its potential is within a few volts of the anode.) The image of these lenses is the entrance of the monochromator. When LVL 1 is operating at the same potential as the anode structure (note that A1, A2, and A3 are electrically connected to the anode structure while LVL 1 is not), this system operates as the simple double-aperture lens

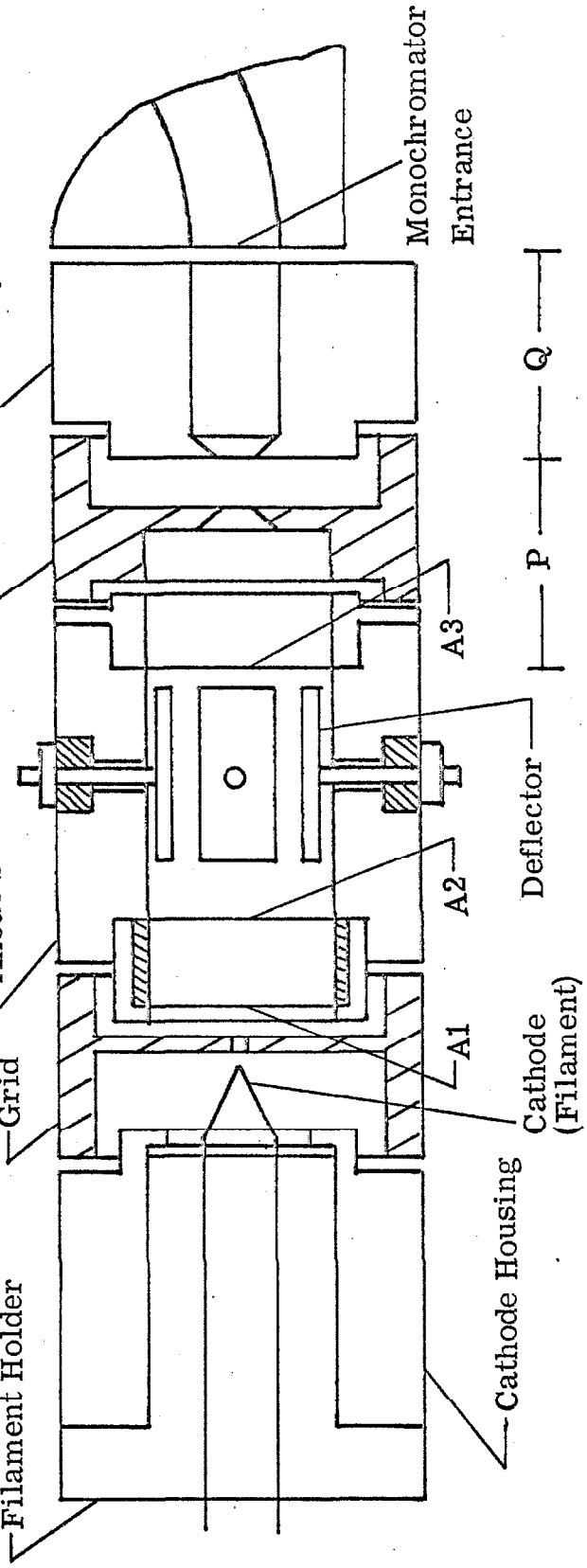

Figure 4.2-6. Cross-sectional view of the electron gun. The filament holder is of boron nitride, the cathode housing and grid are of stainless steel (type 304), and the other components are of copper (OFHC). The abbreviations are defined in the text.

discussed in section 4.1. However, the potential of LVL 1 can be varied independently to provide another degree of freedom in focusing the electron beam.

The entire gun structure is approximately 3.2" long and .985" in diameter. It is constructed of interlocking elements separated by short gaps to decrease the number of electrons which can be emitted radially while providing a reasonably open structure that can be easily outgassed. Table 4.2-3 summarizes the more important element dimensions and spacings.

4.2.4.3. Monochromator and selector

The hemispherical electrostatic energy analyzer used in this research is relatively easy to construct. It consists of an inner and outer hemisphere as shown in figure 4.2-7. The construction materials are indicated in the figure.

The analyzer is assembled as follows:

(1) the inner sphere is mounted rigidly to the inner-sphere-support bracket using the three saphire balls (.1250" ± .0001" diameter) and a machine screw;

(2)with the inner-sphere-support bracket clamped to the outer sphere, the space between the inner and outer sphere is filled with .2500" ± .0001" ball bearings;

(3) the inner-sphere-support bracket is positioned and clamped such that there is uniform contact between the inner sphere-ball bearings-outer sphere surfaces. In addition, the faces

TABLE 4.2-3

(a) Gun element dimensions

Element	Dimension (inches)	
	Bore	Thickness
Grid	.040	.040
A1	.040	.005
A2	.080	.005
A3	.030	.005
LVL 1	.125	-
Herzog 1	.125	-

(b) Gun element separations as measured between the nearest faces of the elements along the electron beam path.

Elements	Separation (inches)
Cathode - Grid	.018
Grid - A1	.080
A1 - A2	.180
A2 - A3	.700
P	.555
LVL 1 - Herzog 1	.125
Q	.555

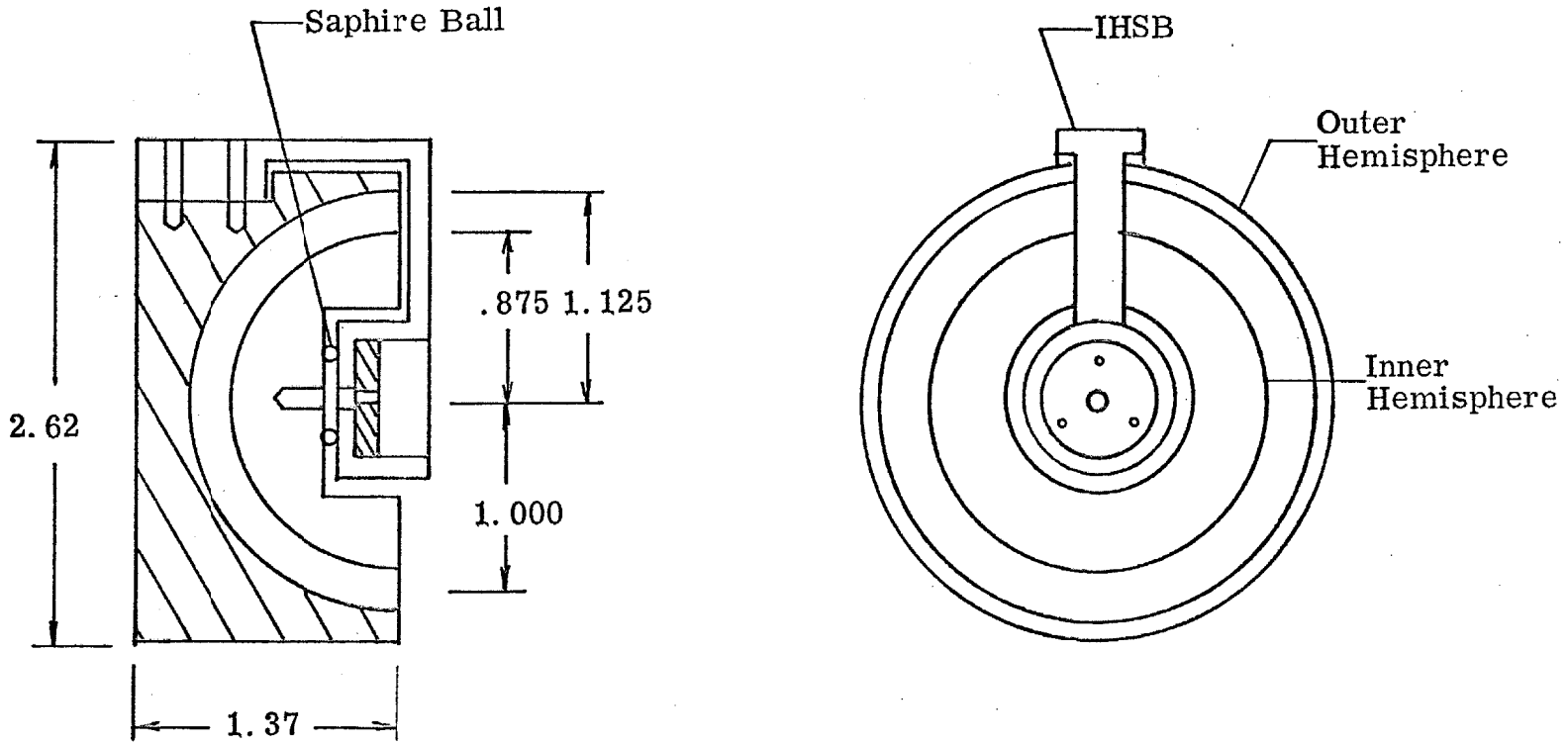

Figure 4.2-7. Front view (right) and cross-sectional side view (left) of the electrostatic energy analyzer (monochromator and selector). Dimensions are in inches. The inner hemisphere support bracket (IHSB) is of stainless steel (type 304). The hemispheres are of copper (OFHC).

of the inner and outer sphere are constrained to lie in the same plane;

(4) the bracket is drilled and screwed permanently in place. The inner sphere can be removed from the bracket and replaced to within ± .0005" of its initial position since it is accurately located by the saphire balls.

4.2.4.4. Lens system 1

The function of this lens system is to decelerate and focus a portion of the energy-dispersed electron beam leaving the monochromator onto the entrance aperture (A4) of the scattering chamber. This lens system is shown in figure 4.2-8 and consists of three basic elements--Herzog 2, LVL 2, and the scattering chamber aperture (A4)--as well as two perpendicular pairs of deflector plates for beam alignment. If LVL 2 is held at the scattering chamber potential (ground), the lens system is equivalent to the double-aperture lenses discussed in section 4.1, which image the monochromator exit on A4. The potential of LVL 2 can be varied independently to provide greater flexibility in focusing the beam as was done in the electron gun. Likewise, this lens system has an open but interlocking structure. The lens assembly is bolted to the scattering chamber support bracket. Table 4.2-4 lists the more important lens element dimensions and spacings.

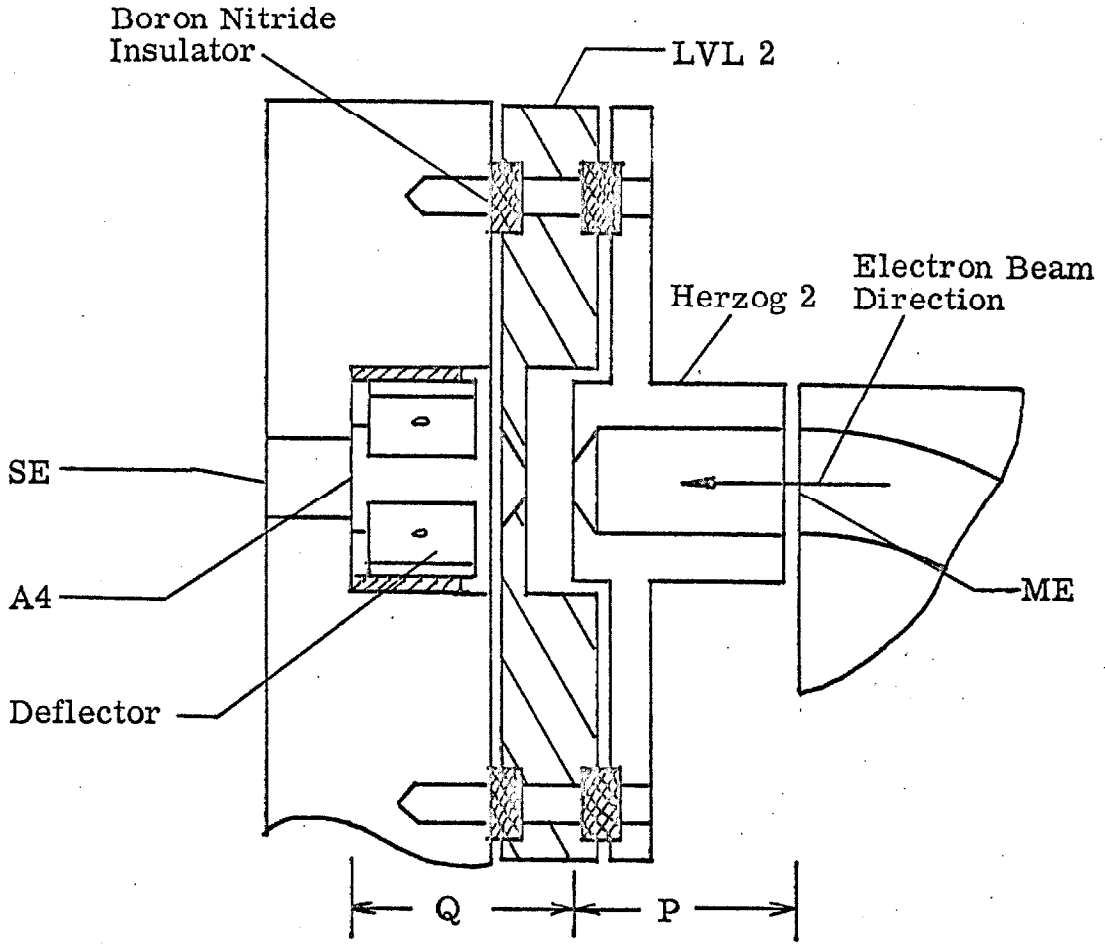

Figure 4.2-8. Cross-sectional view of lens system 1. (ME) exit of the monochromator, (SE) entrance to the scattering chamber. The other abbreviations are defined in the text.

TABLE 4.2-4

(a) Lens system 1 element dimensions.

Element	Dimension (inches)	
	Bore	Thickness
Herzog 1	.125	-
LVL 2	.125	-
A4	.020	.005

(b) Lens system 1 element separations as measured between the nearest faces of elements along the electron beam path.

Elements	Separation (inches)
Herzog 2 - LVL 2	.125
P	.555
Q	.555

4.2.4.5. Scattering chamber

The scattering chamber is designed to contain the target gas at a significantly higher pressure than that in the main vacuum chamber (10^{-2} torr compared to 10^{-7} torr, respectively). For this reason, it is completely sealed except for a sample inlet tube and the apertures through which the incident and scattered beams pass. Further, the scattering chamber is flexible so that the angle between the incident electron beam (beam leaving the monochromator) and that portion of the scattered beam we wish to detect (beam entering the selector) can be varied. This angle is defined as the scattering angle.

The complete scattering chamber assembly (figure 4.2-9) is composed of four basic units--the scattering-chamber-support bracket at the end nearest the monochromator (SCSBM), the actual bellows assembly with its three end flanges (BAF 1, BAF 2, BAF 3), the scattering-chamber-support bracket nearest the selector (SCSBS), and a remotely actuated current measuring electrode or "faraday cup" (FC).

Figure 4.2-9 gives a cross-sectional view of the scattering chamber in a plane perpendicular to the axis of rotation for a scattering angle of 30°.

Note that lens system 2 actually fits inside the SCSBS in order to bring this lens and the selector nearer to the scattering center.

Figure 4.2-9. Cross-sectional view of the scattering chamber assembly (L 2) location of lens system 2; (BCD 1) bolt-circle for the attachment of flange BAF 1 to the SCSBM; (BCD 2) bolt-circle for the attachment of BAF 2 to the SCSBS; (BCD 3) bolt-circle for the attachment of BAF 3 to the SCSBS; (FC) current measuring electrode (faraday cup, shown in the retracted position). The rotation axis (+) is perpendicular to the plane of the figure.

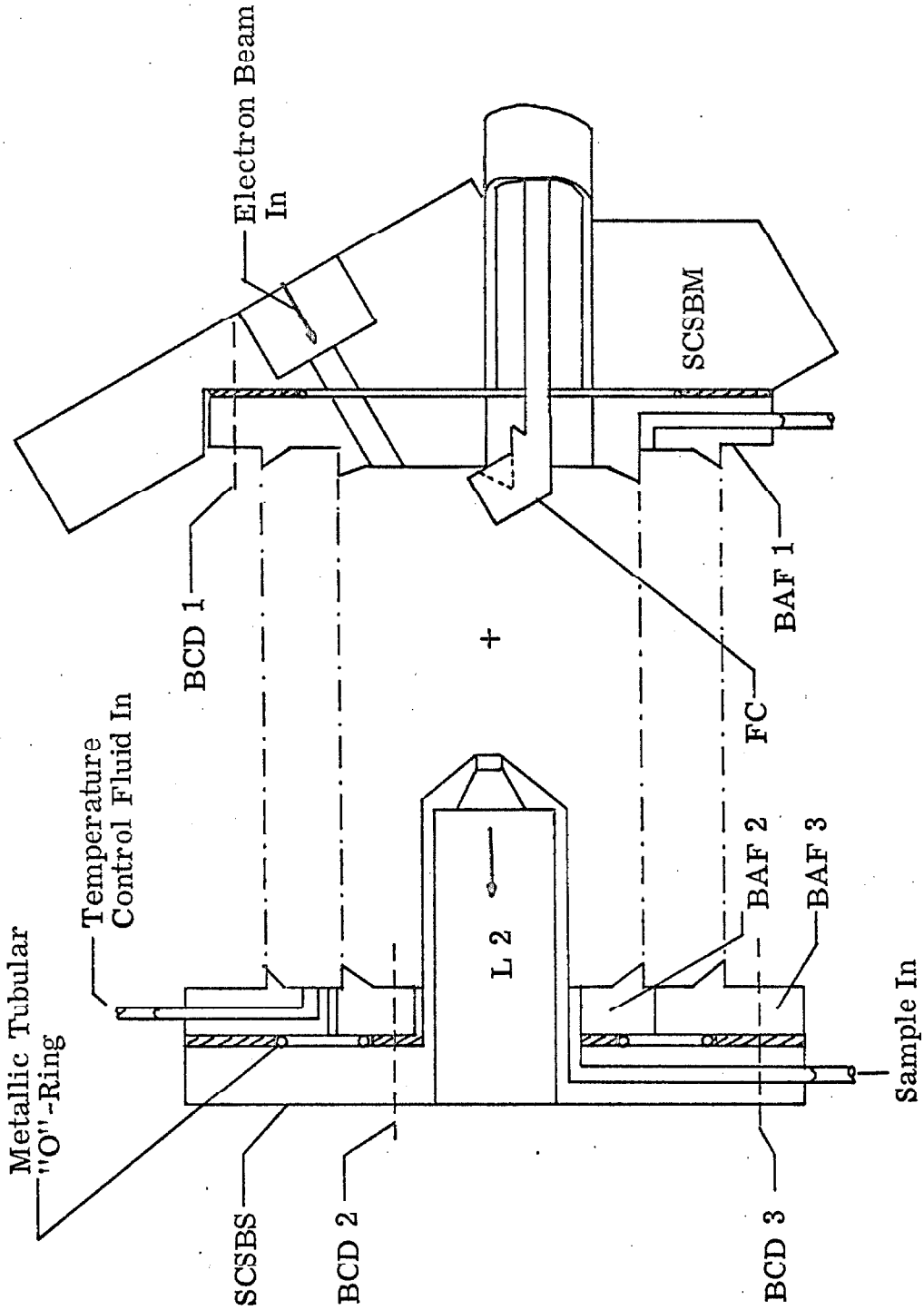
Electron Beam In
SCSBM
BCD 1
BAF 1
FC
Temperature Control Fluid In
Metallic Tubular "O"-Ring
L 2
BAF 2
BAF 3
Sample In
SCSBS
BCD 2
BCD 3

The SCSBM is made of type 304 stainless steel. The deflector plates and aperture A4 of lens system 1 are assembled within it. A4 is directly shorted to it while the deflector plates are electrically insulated by boron nitride spacers.

Because of space limitations (the distance between the monochromator and selector should be as short as practical), the bellows assembly flanges were not made thick enough to ensure a reliably vacuum tight seal using gold gaskets, which require about 1000 lbs./linear-inch. Thus, hollow tubular metallic "O"-rings made of inconel plated with silver and supplied by United Aircraft Products, Inc. were used to provide the vacuum seals between BAF 1, BAF 2, and BAF 3 and both the SCSBM and the SCSBS. These "O"-rings require less than 200 lbs./linear-inch for effective sealing since they have a cross-sectional diameter of only 1/32" and a .005" thick wall. .020" thick stainless steel spacers were used between the bellows assembly flanges and their respective support brackets to position these "O"-rings and insure that the proper amount of deformation occurred when the flanges and brackets were bolted together.

The bellows assembly, which consists of two concentric, welded bellows and flanges, was fabricated of type 345 stainless steel by Metal Bellows Corp. Each bellows consists of about 700 "S" shaped convolutions individually welded together. This results in an extremely flexible structure with the additional advantage that electrons striking the walls are effectively trapped. In a linear

bellows configuration (as in figure 4.2-9), the inner bellows has a minimum inner diameter of 1.12" and a maximum outer diameter of 1.37" while the outer bellows has a minimum inner diameter of 1.67" and a maximum outer diameter of 2.10". The scattering chamber is mounted so that the rotation axis is 1.50" from aperture A4 and .75" from aperture A5 (lens system 2). Thus, the electron path length through the target gas is approximately $2\frac{1}{4}$". One end of the bellows can be rotated by $\pm 60°$ with respect to the other about the rotation axis. However, by having the incident electron beam enter the bellows at an angle of 30° with respect to a normal to BAF 1, scattering angles from -30° to +90° can be obtained. For example, a scattering angle of 0° (the angle at which a line through A4 and A5 intersects the rotation axis)is obtained when the bellows assembly is "bent" by -30° while for a scattering angle of +30° the bellows assembly is linear. This configuration was suggested by Simpson[25].

Temperature control of the target gas contained within the inner bellows could be obtained by circulating a suitable fluid through the space between the inner and outer bellows. However, no use of this feature has been made in the present study. All data were taken at ambient (room) temperature since the substances studied so far are "permanent" gases.

The inner and outer bellows are welded to two separate concentric flanges (BAF 2, BAF 3) on the end nearest the selector. These flanges are bolted to the SCSBS.

A pneumatically operated actuator constructed of type 347 stainless steel by Metal Bellows Corporation was attached to the SCSBM. Its function is to push the copper faraday cup into the path of the incident electron beam (in order to measure its intensity) and retract the faraday cup until it is electrically shorted to BAF 1 (when scattering measurements are to be taken). The actuator is shown in figure 4.2-10. It has an overall stroke (the maximum extension under 35 lbs./sq. in. air pressure in bellows 1 minus the minimum extension with bellows 1 evacuated) of 1.00 inch. The ceramic-insulator vacuum feedthrough was supplied by Photocon Research Products. The same type of metallic tubular "O"-rings as were used above provide the required vacuum seals.

4.2.4.6. Lens system 2

The function of lens system 2 is to: (1) define the geometry (diameter and angular divergence) of the scattered beam which is to be energy analyzed by the selector, and to (2) focus this beam at the entrance of the selector in a manner that is relatively insensitive to the electron energy-loss being detected.

Lens system 2 is shown in figure 4.2-11 and consists of three basic elements--aperture A5, LVL 3, and Herzog 3. A5 is shorted directly to SCSBS while LVL 3 and Herzog 3 are electrically insulated. Table 4.2-5 lists the important lens element dimensions and spacings.

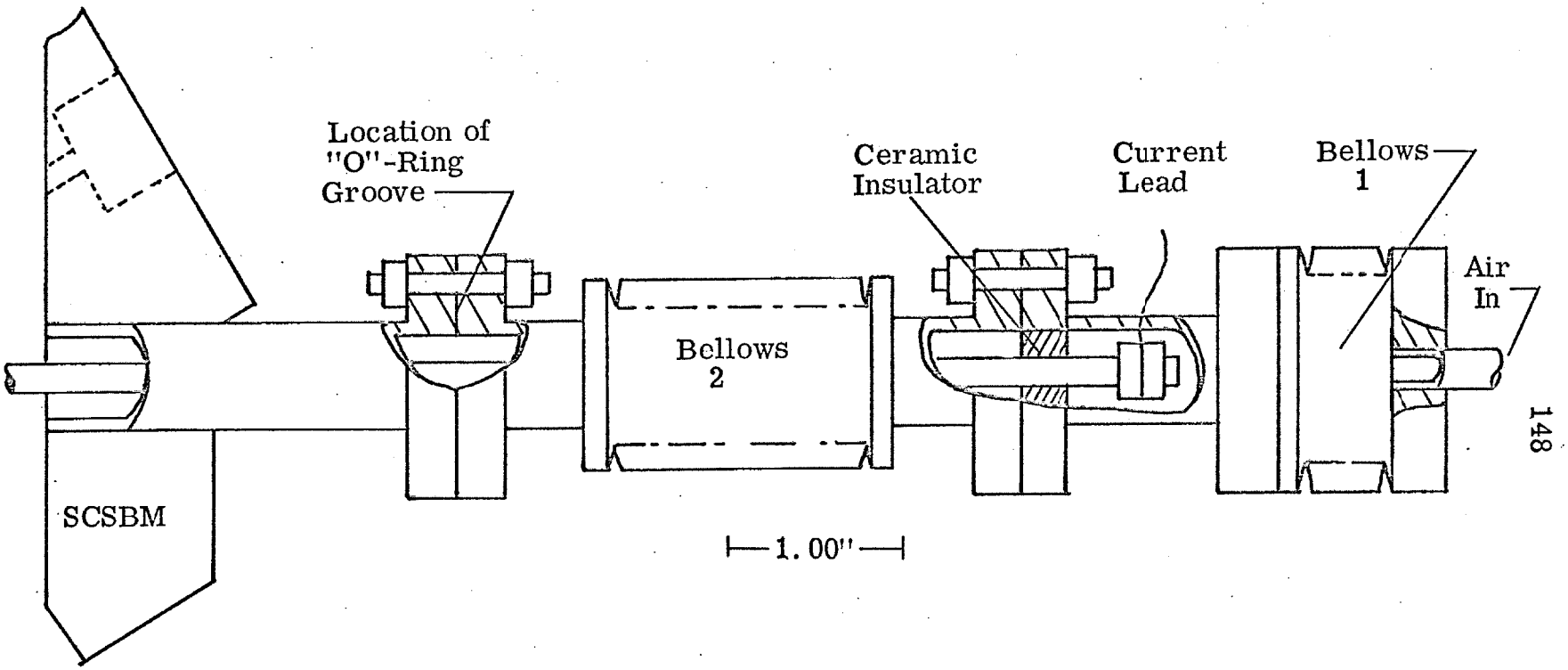

Figure 4.2-10. Cut-away view of the actuator assembly to extend and retract the faraday cup. The extreme right and left ends of the assembly are fixed relative to each other. 35 lbs/sq. inch air pressure in bellows 1 will cause it to expand and bellows 2 to contract, extending the faraday cup into the scattering chamber (figure 4.2-9).

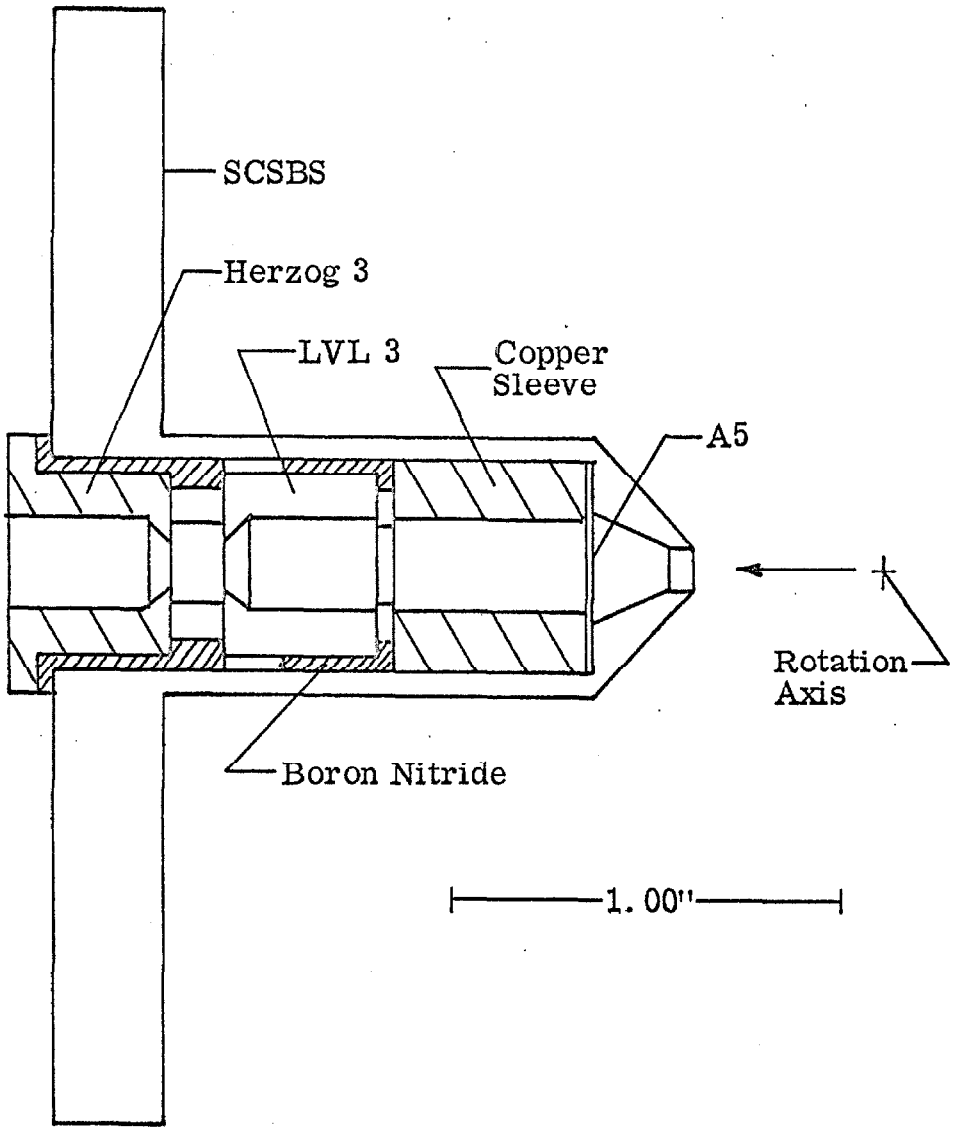

Figure 4.2-11. Cross-sectional view of lens system 2 installed in the SCSBS. The arrow points in the direction of the collected electron beam.

TABLE 4.2-5

(a) Lens system 2 element dimensions.

Element	Dimension Inches	
	Bore	Thickness
A5	.030	.005
Sleeve	.250	-
LVL 3	.125	-
Herzog 3	.125	-

(b) Lens system 2 element separations as measured between planes of minimum bore along the electron beam path.

Elements	Separation (inches)
A5 - LVL 3	.94
LVL 3 - Herzog 3	.125
Herzog 3 - Selector	.555

The boron nitride insulator-spacer elements are not quite cylindrically symmetric but are cut away along much of one side to allow for better outgassing of the lens elements.

The conical half-angle defined by this lens system is approximately .05 rad. which implies a solid angle acceptance of about 1.6×10^{-2} steradians. The realization of function (2) above depends upon the voltages applied to the lens elements and will be discussed in section 4.4.

4.2.4.7. Lens system 3

The function of lens system 3 is to focus the electron beam leaving the selector onto the first dynode of the electron multiplier. As in the other lens systems, it consists of three basic elements (as shown in figure 4.2-12)--Herzog4 and two tube lenses (TL 1, TL 2). TL 1 contains aperture A6 which, along with lens system 2, helps determine the energy resolution of the scattered beam (section 4.1.). TL 2 contains two perpendicular pairs of deflector plates to aid in aligning the beam. Table 4.2-6 summarizes the important lens element dimensions and separations. This lens system is rather long (selector to first dynode of multiplier is ~7") because the electron multiplier is too large to be moved closer to the selector.

4.2.4.8. Electron multiplier

The electron multiplier is used to detect the energy-analyzed scattered electron beam. It is a Nuclide Corporation,

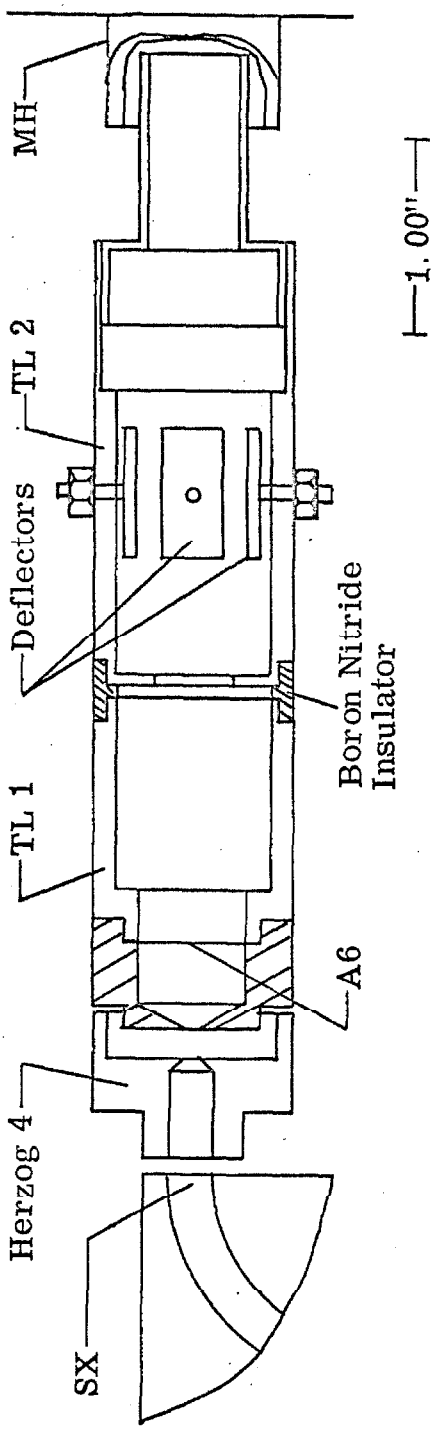

Figure 4.2-12. Cross-sectional view of lens system 3. (SX) selector exit, (MH) multiplier housing. The other abbreviations are defined in the text.

TABLE 4.2-6

(a) Lens system 3 element dimensions.

Element	Minimum Bore (inches)
Herzog 4	.125
TL 1	.125
TL 2	.30
A6	.030

(b) Lens system 3 element separations as measured between the planes of minimum bore along the electron beam path.

Elements	Separation (inches)
Selector - Herzog 4	.555
Herzog 4 - TL 1	.125
Herzog 4 - A6	.555
A6 - TL 2	1.12

model EM-2, electron multiplier, consisting of twenty copper-beryllium dynode stages in a "pie" configuration as shown in figure 4.2-13. The dynodes are assembled on inconel discs separated by ceramic washers. Bakeable 0.38 MΩ resistors (International Resistance Company, No. 00736) are used between each disc. The base of the multiplier assembly contains leads from the anode and last dynode. Leads from the first dynode and the three lens plates (in front of the first dynode) were brought out through the rear of the stainless steel enclosure around the multiplier. The enclosure interlocks with lens system 3 as shown in the figure and is wrapped with aluminum foil in addition. This was necessary to reduce the number of electrons being detected which had not passed through lens system 3. The base of the multiplier contains two $\frac{1}{4}$" diameter holes through which the multiplier (and lens system 3) is outgassed.

4.2.5. Support Structure

The spectrometer components are held in the required relative orientation to each other (refer to figure 4.2-5) in the following way, depicted in figure 4.2-14. The electron gun (EG), monochromator (M), and the SCSBM are mounted on a Pic Design Corp., model Q7-29SP, type 304 stainless steel gear wheel (GW) while the SCSBS, selector (S), lens system 3 (L 3), and the multiplier (EM) are mounted to a support frame which is rigidly attached to flange cover FC 1. The gear wheel shaft (GWS) is mounted by means of two bearings contained in the bearing

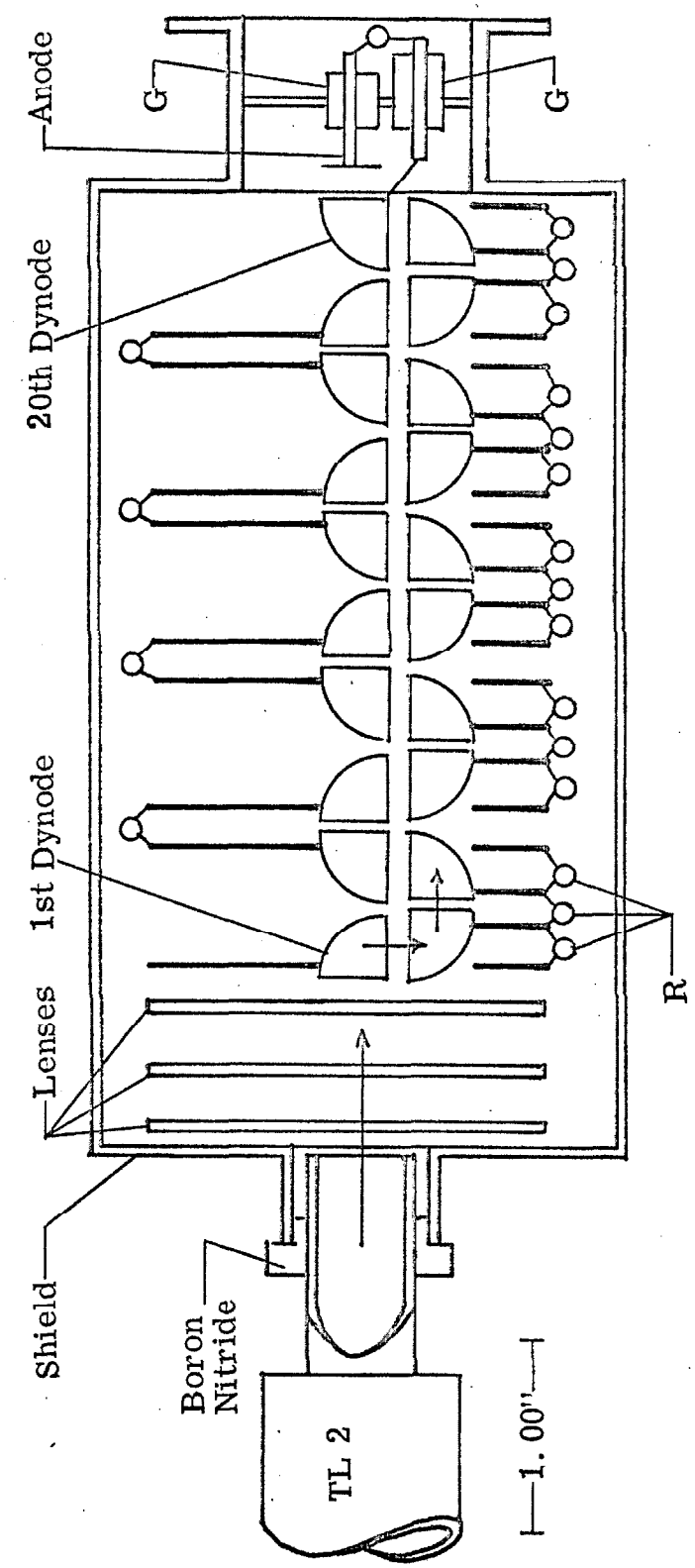

Figure 4.2-13. Cross-sectional view of the electron multiplier and its shield. (R) 0.38 MΩ bakeable resistors; (G) glass insulator; the discs supporting the dynodes are not shown to scale. The arrows indicate the direction of the incident electron and the resulting cascade.

Figure 4.2-14. Side view of the spectrometer components mounted on the support frame. The scale is approximately correct but many details have been omitted. (SF) shelf welded to FC 1, (AST) actuator support table (bolted to gear wheel), (BP) support frame base plate, (M) monochromator, (BH) bearing housing, (GWS) gear wheel shaft, (EG) electron gun, (GW) gear wheel, (S) selector, (SCB) scattering chamber bellows, (L 3) lens system 3 (mounted between sides of support frame), (EM) electron multiplier (mounted between sides of support frame), (A) faraday cup actuator, (F) support frame side plate. The other abbreviations are defined in the text.

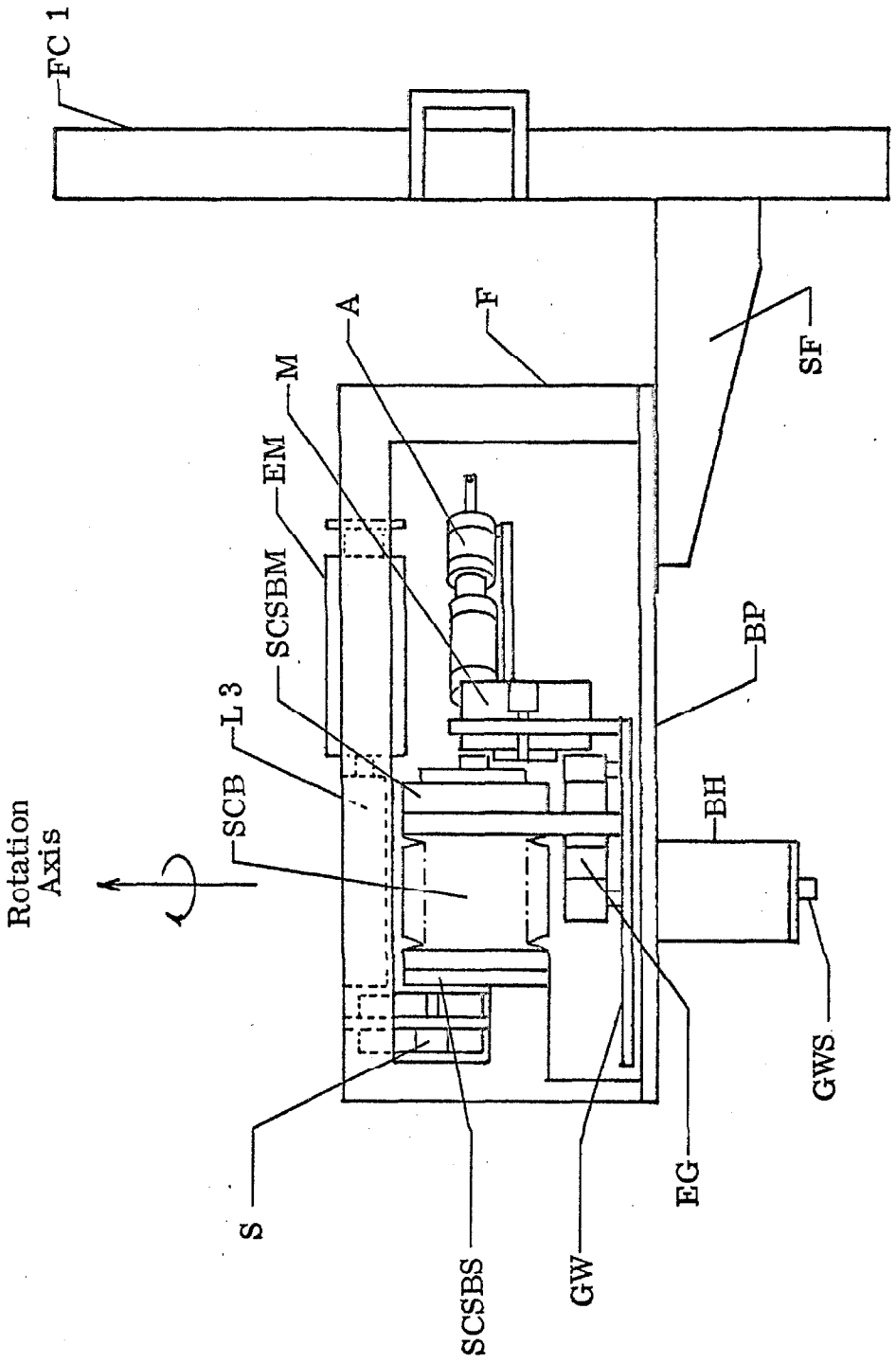
FC 1
A
F
M
EM
SCSBM
L 3
SCB
Rotation Axis
SF
BP
BH
GWS
S
SCSBS
GW
EG

housing (BH) to this same support frame. Thus, by rotating the gear wheel, the first half of the spectrometer, which produces the incident electron beam, can be rotated with respect to the second fixed half, which defines and detects a portion of the scattered beam.

The support frame is constructed from two approximately rectangular $\frac{1}{4}$" plates (F) which are welded to a $\frac{1}{4}$" thick base plate (BP) forming a rigid, box-like structure (type 304 stainless steel, electropolished). The various spectrometer components are mounted within this structure, either to the gear wheel or to the support itself. The entire unit is then bolted to a shelf (SF) that is welded to the inside of FC 1.

The actuator assembly (A) has one end rigidly attached to the SCSBM (figure 4.2-10) while its opposite end is attached to a plate (AST) extending radially from the gear wheel and bolted to it.

The electron multiplier (EM) fits between the sides of the support frame and is bolted to it. However, the multiplier shield is electrically insulated from the frame. In fact, the scattering chamber is the only spectrometer component which is internally grounded.

Figure 4.2-15 shows the monochromator and selector support brackets in more detail. The bracket for the monochromator is bolted to the gear wheel while that for the selector is bolted to the frame.

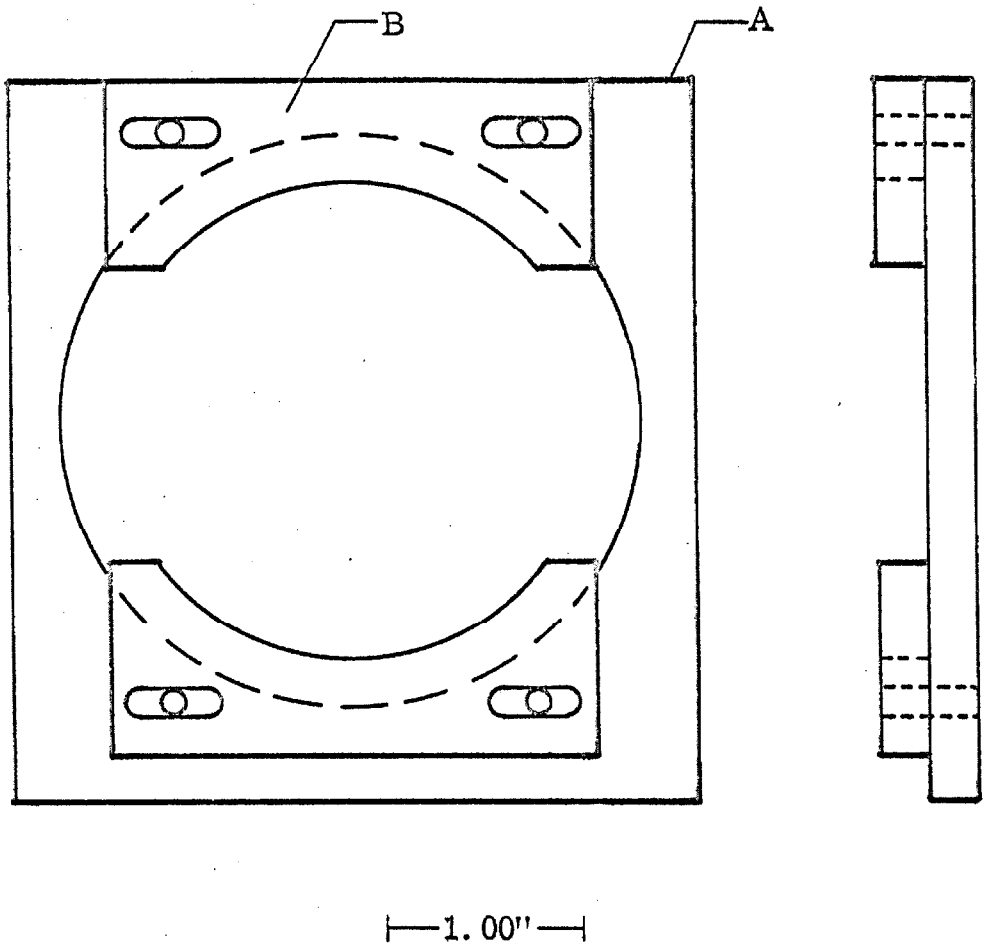

Figure 4.2-15. Front view (left) and side view (right) of the energy analyzer (selector or monochromator) support bracket. (A) stainless steel plate, (B) Boron nitride insulators which support and position the analyzer.

The electron gun and lens system 3 are mounted to the gear wheel and the support frame, respectively, by "electron-optical" benches shown in figure 4.2-16. They are identical in concept to those employed by Simpson[24].

4.2.6. Bakeout Heaters

A furnace which could enclose the main vacuum chamber was constructed for us by Kenneth C. Holloway, Inc. Its specifications are listed below:

Dimensions: $47\frac{1}{2}$" long × $39\frac{1}{2}$" wide × 44" high.

Material: Type 304 stainless steel, glass wool insulation.

Electrical: Heaters of 19 gauge, chromel-A wire; current supplied by two 220V 3-phase, 20 amp Variacs wired in a Y circuit. Total power output available is ~ 8.8 KW.

Construction: Six separate pieces including top, bottom, and four sides. Each piece is $1\frac{1}{2}$" thick, double-walled, containing the insulation.

To install the furnace, the Helmholtz coils are removed and the top, bottom, and sides of the furnace are bolted together around the chamber. The furnace is supported by the same table which supports the vacuum chamber. The gate valve and about half of the length of the tube connecting it to the main chamber (as well as the rest of the pumping system) lie outside the furnace and are kept cool (less than 80° C) during bakeout. The vacuum chamber and the components within it can be heated to more than 450° C in about

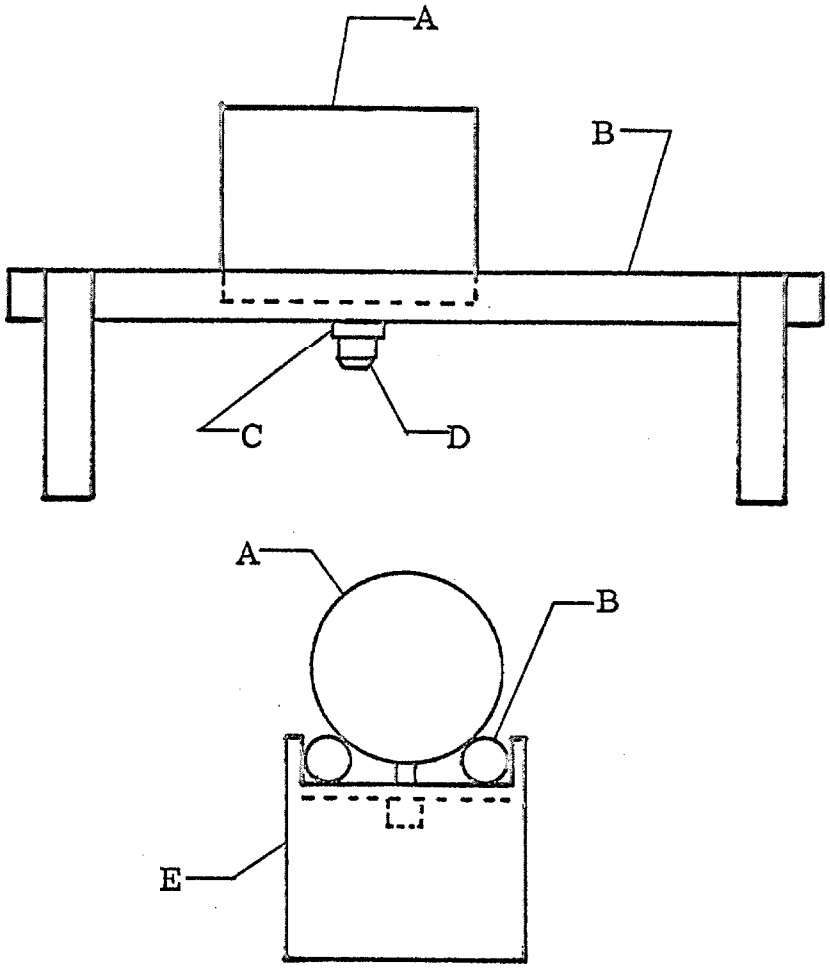

Figure 4.2-16. Side view (upper) and end view (lower) of the "electron-optical" bench support structure used to mount the electron gun and lens system 3. (A) element to be supported by bench, (B) alumina rods (.2500" ± .0001" diameter), (C) stainless steel hold-down strap which is screwed into element (A) with a No. 2-56 stainless steel machine screw (D), (E) stainless steel support for the alumina rods.

8 hours. It was found, however, that such severe overall bakeout was not necessary for acceptable apparatus performance. Instead, a small resistance heater was installed directly on some of the internal (inside the vacuum chamber) components of the spectrometer. It consists of about five feet of .020 inch diameter tungsten wire covered with thin walled ceramic tubes for electrical insulation. Several loops of this wire are clamped to the monochromator, selector, SCSBM, and SCSBS. A 20 amp. 120 V Variac is used to supply the required heating power (about 600 Watts). Iron-constantan thermocouples are mounted at several places on the spectrometer to monitor the temperature.

4.2.7. Rotary Motion

Figure 4.2-17 shows the rotary motion drive train. The gear wheel (GW), on which the electron source is normally mounted, is rotated by a Pic Design Incorporated, model Q8-2, stainless steel worm gear (WG). The worm is driven from outside the vacuum chamber by means of a CHA, model D-909, bakeable, bellows sealed rotary feedthrough (RFT). The rotary feedthrough is supplied with a Varian conflat flange, model 954-5072 for attaching it to FC 1.

The worm gear bearing housing (WGBH) contains four (two on each side of the worm) Miniature Precision Bearings, Inc., type N614, copper-beryllium, ball bearings. Two flexible connectors (FXC) are used in the drive shaft to allow for any misalignment between the rotary feedthrough and the worm gear shaft.

Figure 4.2-17. Top view of the rotary motion drive train. For clarity, none of the spectrometer components are shown. The rotation axis (RA) is perpendicular to the plane of the figure. (TC) Durrant, model 4-Y-40591-412-L-CL, turn counter, (RFT) rotary feedthrough, (GW) gear wheel, (WGBH) worm gear bearing housing, (WG) worm gear, (FXC) flexible couplings.

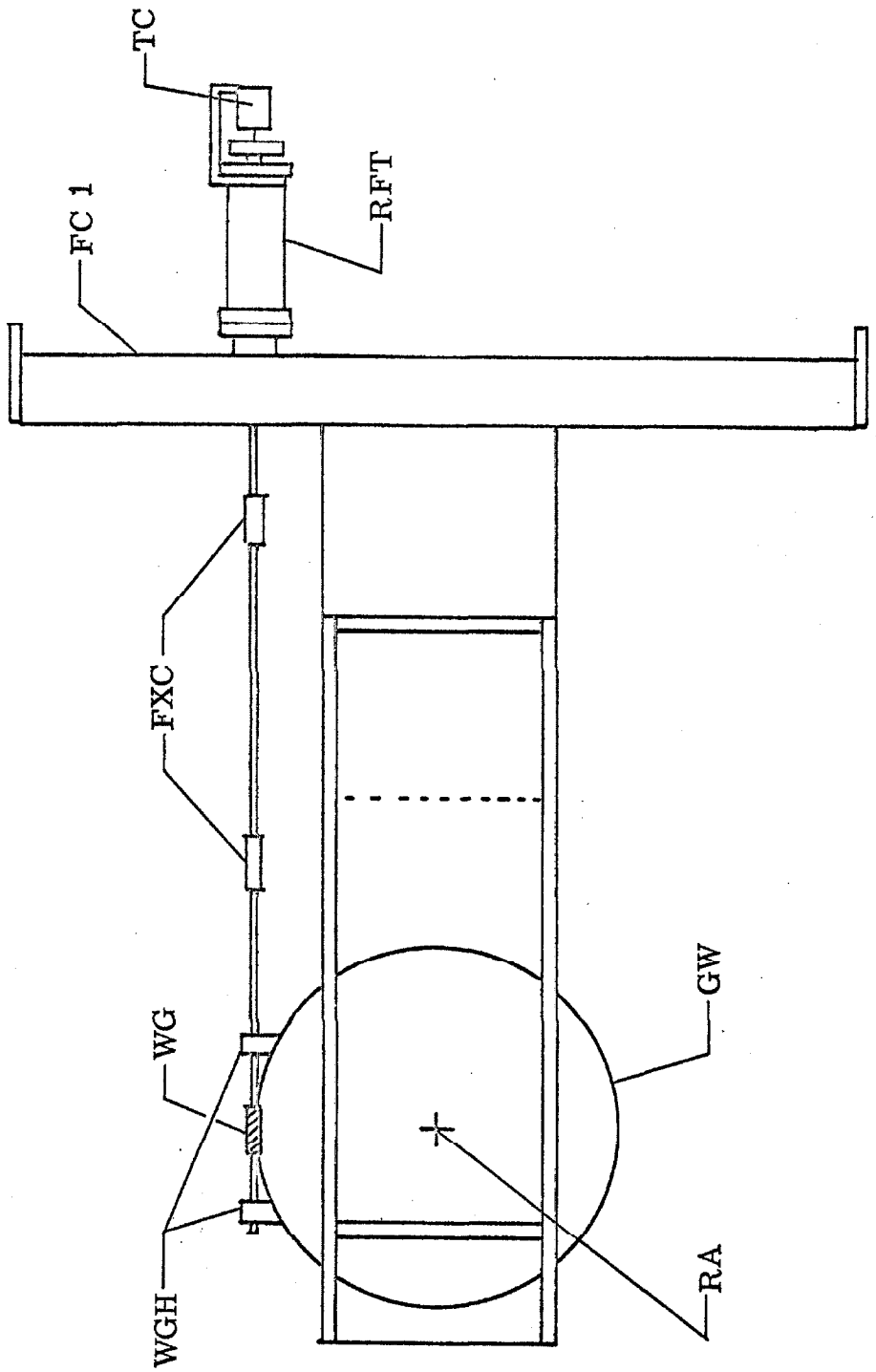
TC
RFT
FC 1
FXC
WG
WGH
GW
RA

4.2.8. Vacuum Feedthroughs

All of the feedthroughs required for the operation of the spectrometer within the vacuum chamber are installed on FC 1. The feedthrough arrangement is shown in figure 4.2-18 and table 4.2-7 gives their use and specifications. FC 1 has 8 Varian conflat flanges, model 954-5072, which seal with copper-gaskets (Varian, model 953-5014) and 6 "home-made" flanges which seal with .040" diameter gold wire. The Varian flanges are extended about 1" away from the face of FC 1 while the other flanges are staggered and extend either $1\frac{1}{2}$" or $4\frac{1}{2}$". 11-conductor, glass-wool insulated cable supplied by Sante Fe Textiles is used for wiring the components inside the chamber. All internal air and sample lines are of stainless steel supplied by U. S. Flexible Metalic Tubing, Inc. Cajon type 316 stainless steel vacuum couplings with copper gaskets are used throughout for connecting these lines in place.

4.2.9. Electrical Components

The power supplies, batteries, counting equipment, and their associated circuitry are assembled in three electrical relay racks external to the vacuum chamber but within the shielded room. Figure 4.2-19 is a block-schematic diagram showing the overall interrelation of the various electrical components. A circuit diagram for each of the components is given below (figures 4.2-20 through 4.2-26). Table 4.2-8 lists the resistors, batteries, and power supplies indicated in these figures. In addition, the potential

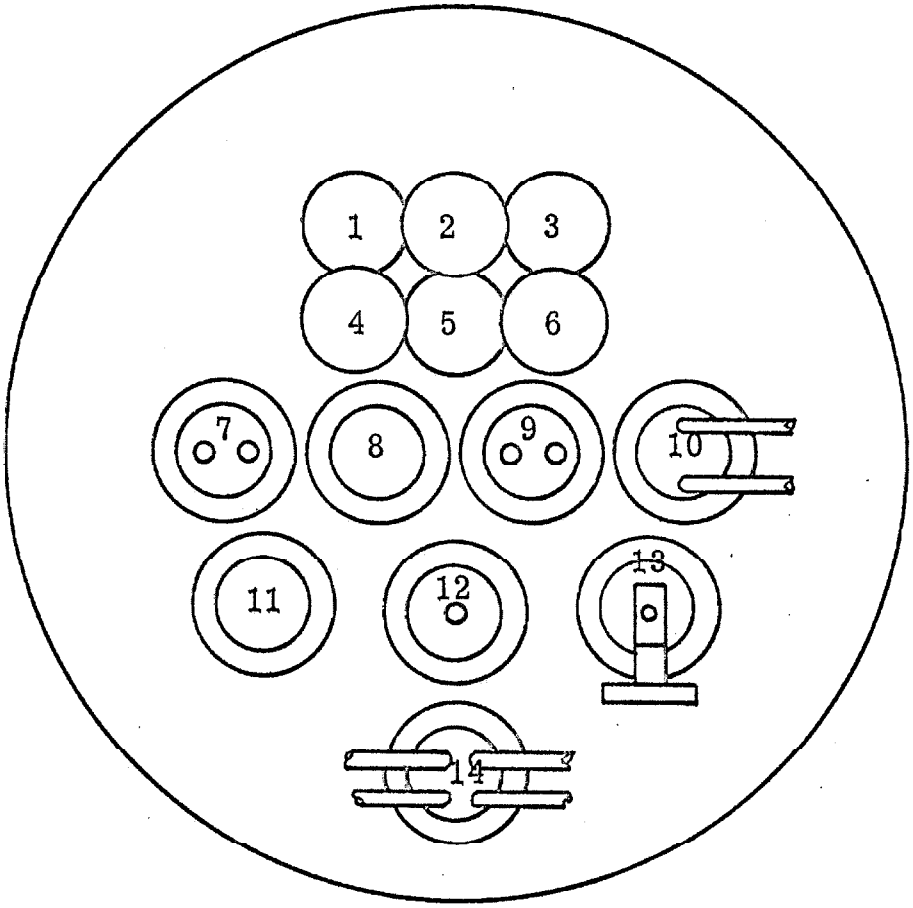

Figure 4.2-18. Front (external to vacuum chamber) view of the flange cover FC 1. Flanges 1-6 are "home-made" while 7-14 are supplied by Varian. Refer to table 4.2-7 for a list of their uses and specifications.

TABLE 4.2-7

The uses and specifications of the feedthroughs on FC 1.

Feedthrough Number (Fig. 4.1-18)	Use	Specification
1,2,3,4,6	Voltages (<100V) to spectrometer components	RCA, model J1946, 11-pin
5		Blank
7	Leads to dynodes 1 and 20 of multiplier	Cermaseal, Inc.
8	Internal bakeout heaters, thermocouples, lenses in multiplier	Varian, model 954-5013, 20-pin.
9	Leads to outer sphere of selector and faraday cup	Cermaseal, Inc.
10	Sample inlet line and air to gage port actuator	Varian conflat blank with $\frac{1}{4}$" O.D. stainless steel tubes through and welded.
11		Varian conflat blank
12	Lead to anode of multiplier	Cermaseal, Inc.
13	Rotary motion	CHA, model D-909, bellows sealed rotary feedthrough
14	Gas lines for temperature control of scattering chamber and air line to faraday cup actuator	(Same as 10)

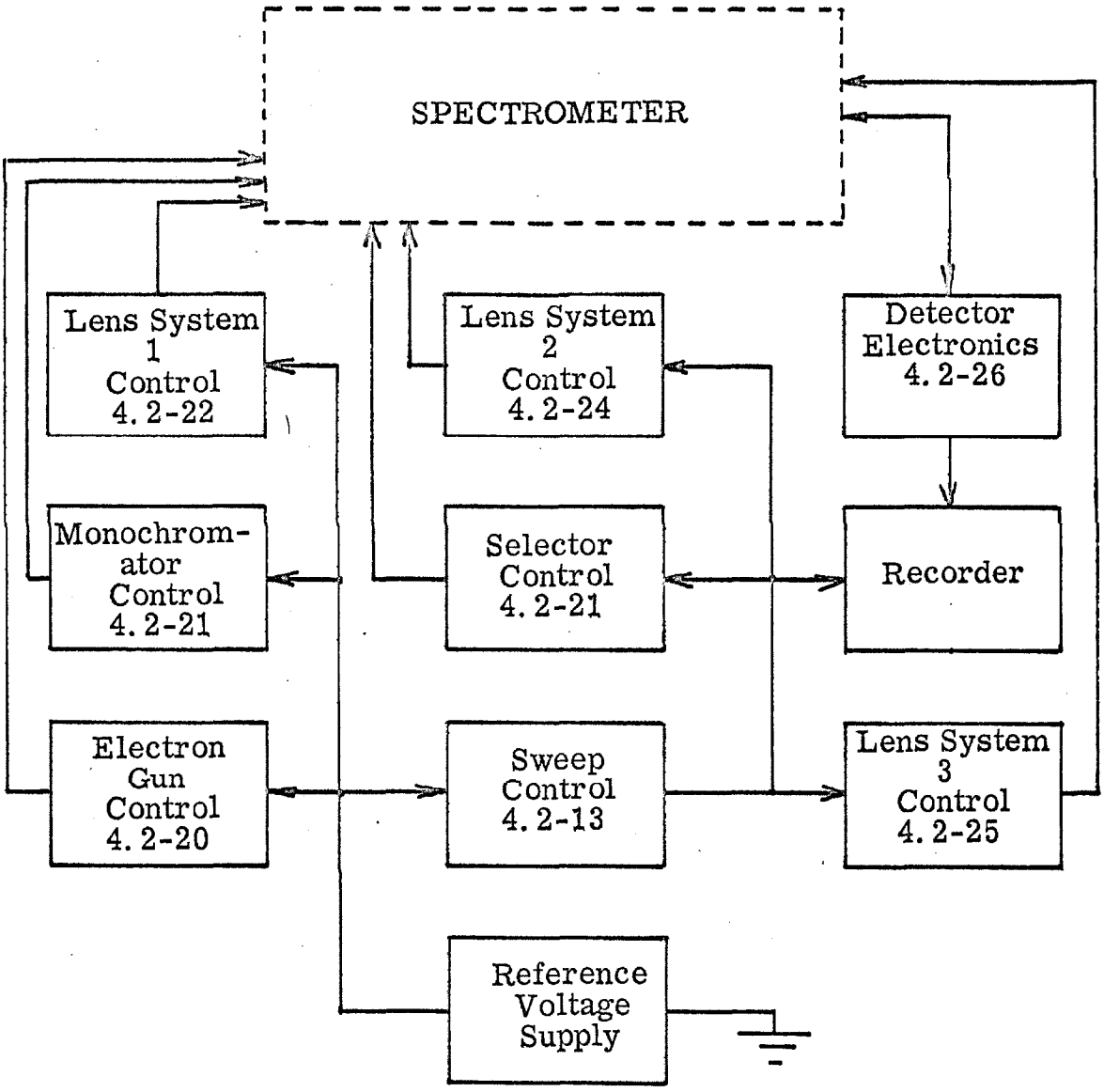

Figure 4.2-19. Block-schematic diagram of the electrical controls for the spectrometer. The dotted lines represent the vacuum wall. The arrows indicate the direction of control. The number within each box is the figure number of the circuit diagram for that control.

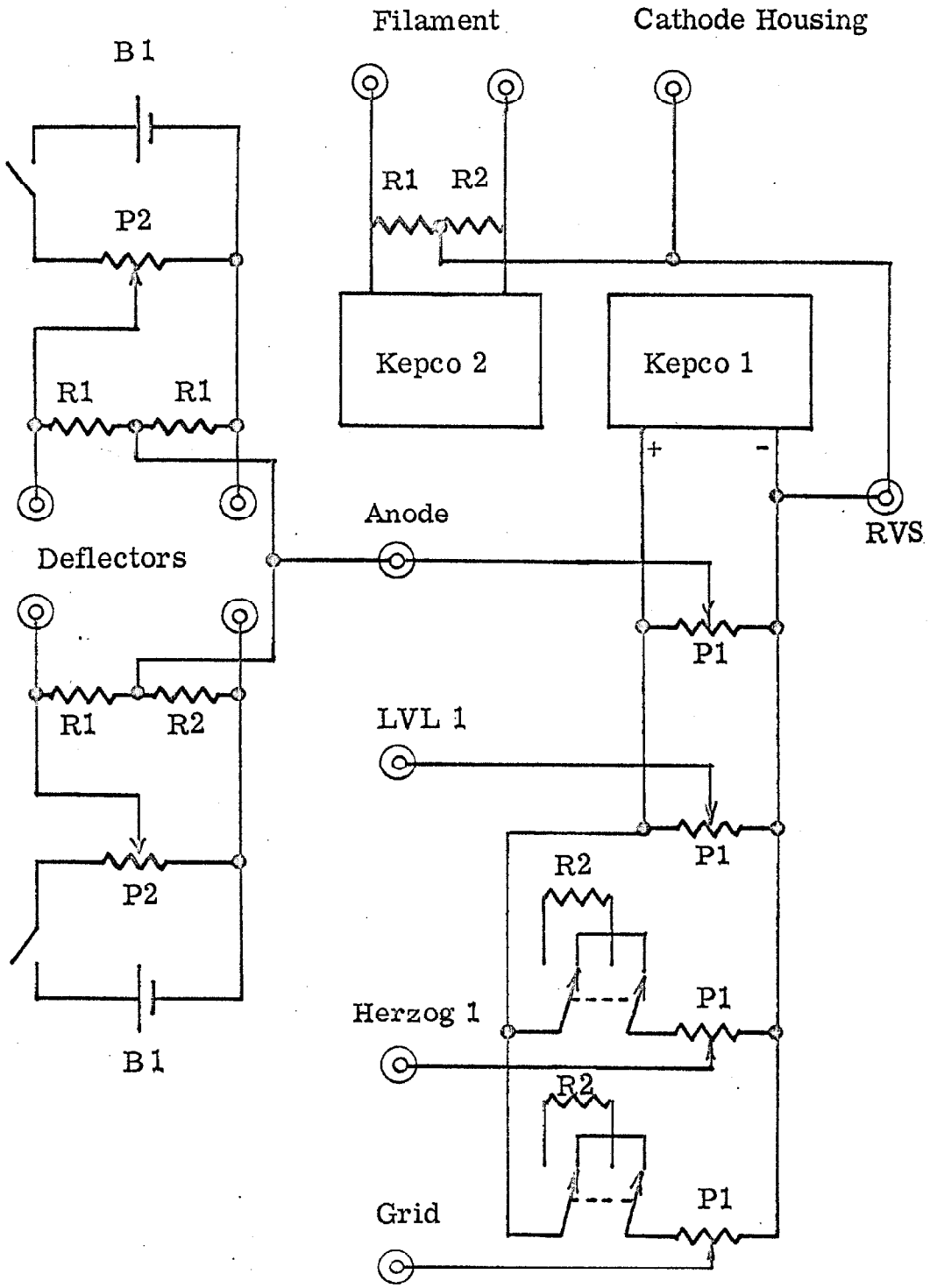

Figure 4.2-20. Circuit diagram of the electron gun control system. (RVS) reference voltage supply. The other abbreviations used for figures 4.2-20 through 4.2-26 are listed in table 4.2-8.

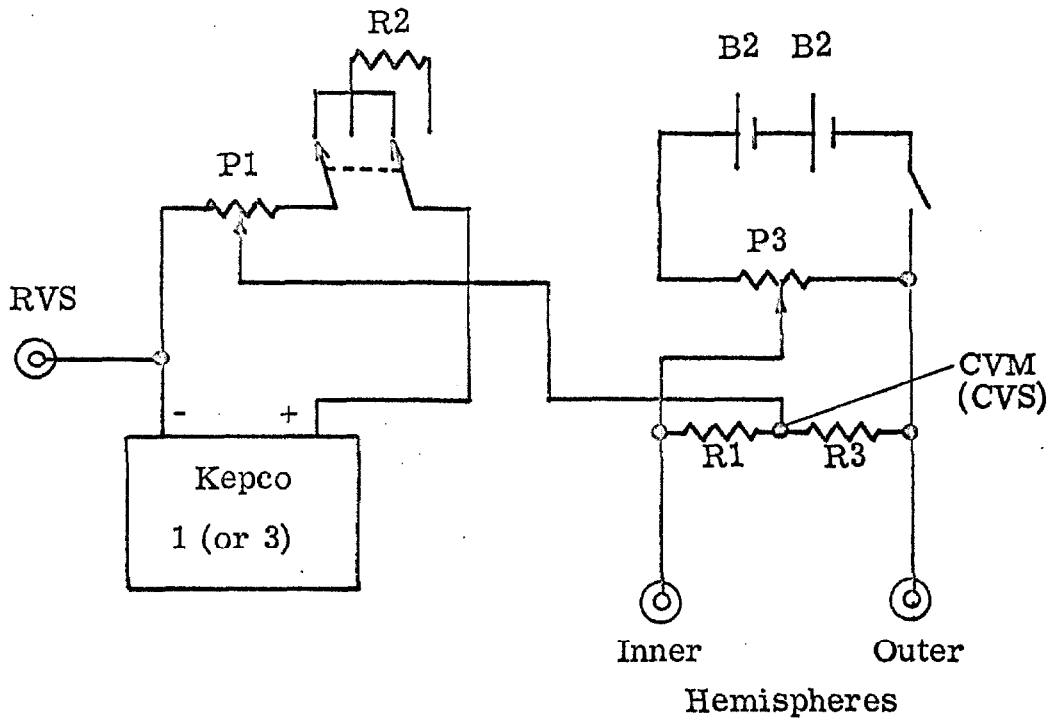

Figure 4.2-21. Circuit diagram of the energy analyzer (monochromator and selector) control unit (see table 4.2-8). R3 is adjusted to 7.9 KΩ to give the proper voltage balance with respect to CVM (CVS for the selector). See section 4.1.1.2, figure 4.1-1. (RVS) reference voltage supply. Kepco 1 is used for the monochromator system while Kepco 3 is used for the selector.

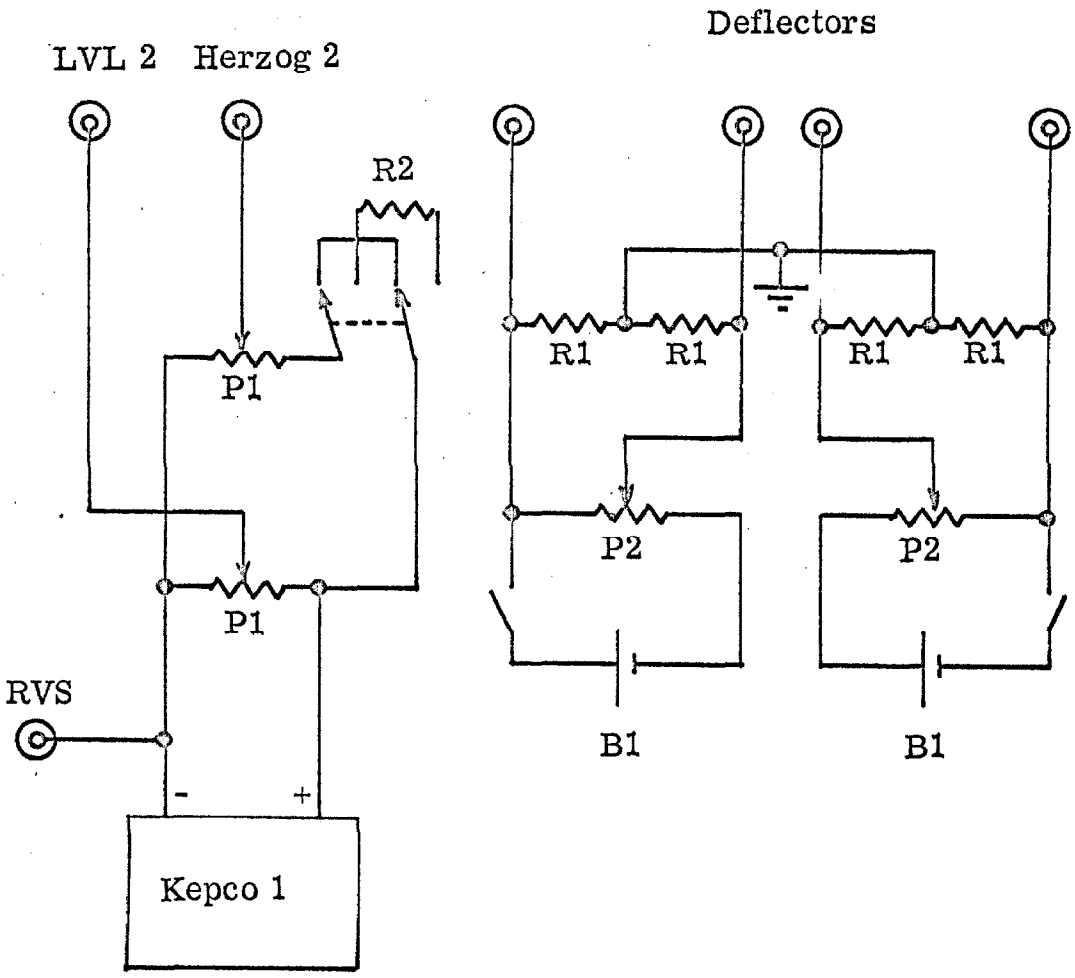

Figure 4.2-22. Circuit diagram of the control unit for lens system 1. (See table 4.2-8.)

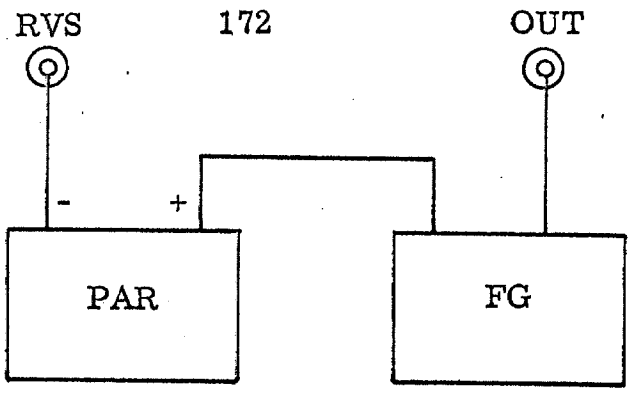

(a)

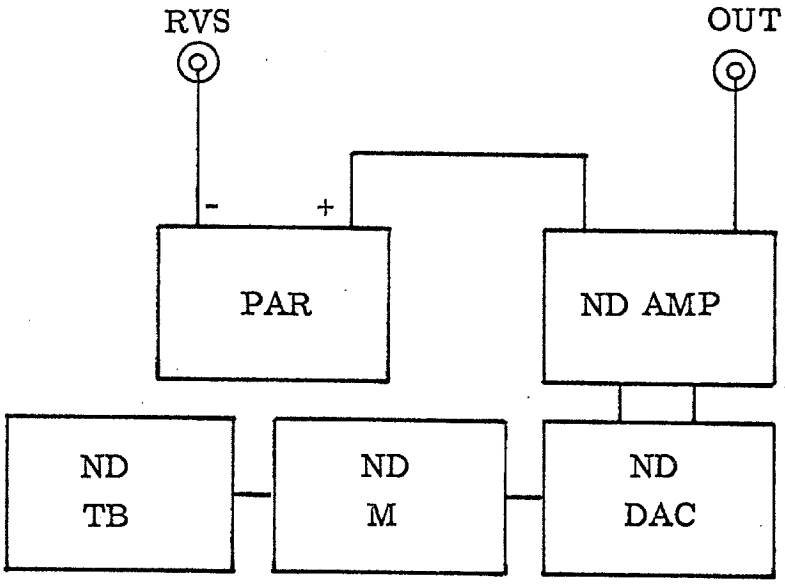

(b)

Figure 4.2-23. Block schematic diagrams of the sweep control when the function generator (FG) is used (a), and when the Nuclear Data system (ND) is used (b). The connector labelled OUT goes to the control units indicated by figure 4.2-19. (See table 4.2-8)

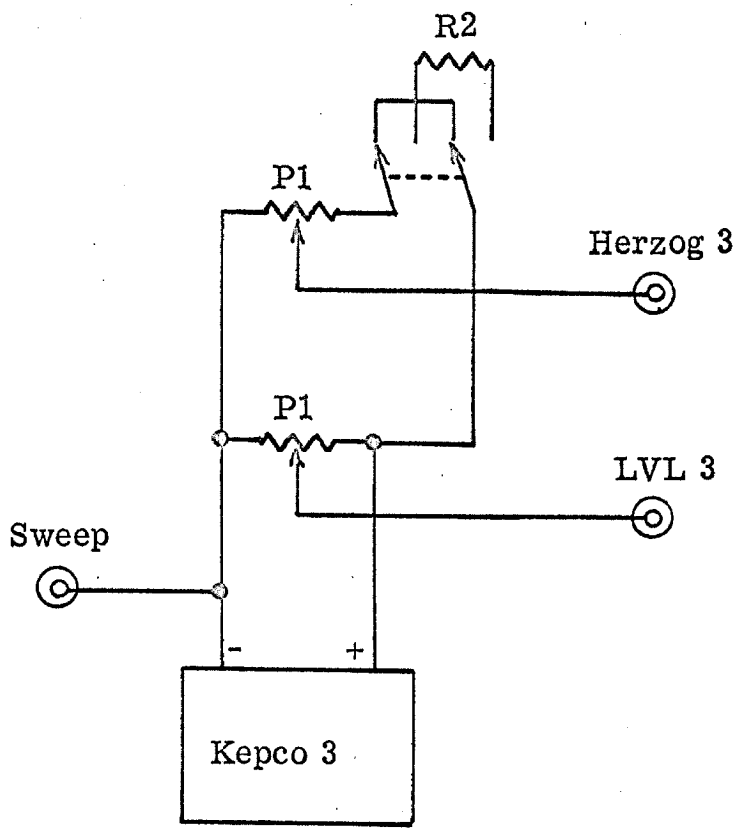

Figure 4.2-24. Circuit diagram of the lens system 2 control unit. (See table 4.2-8.)

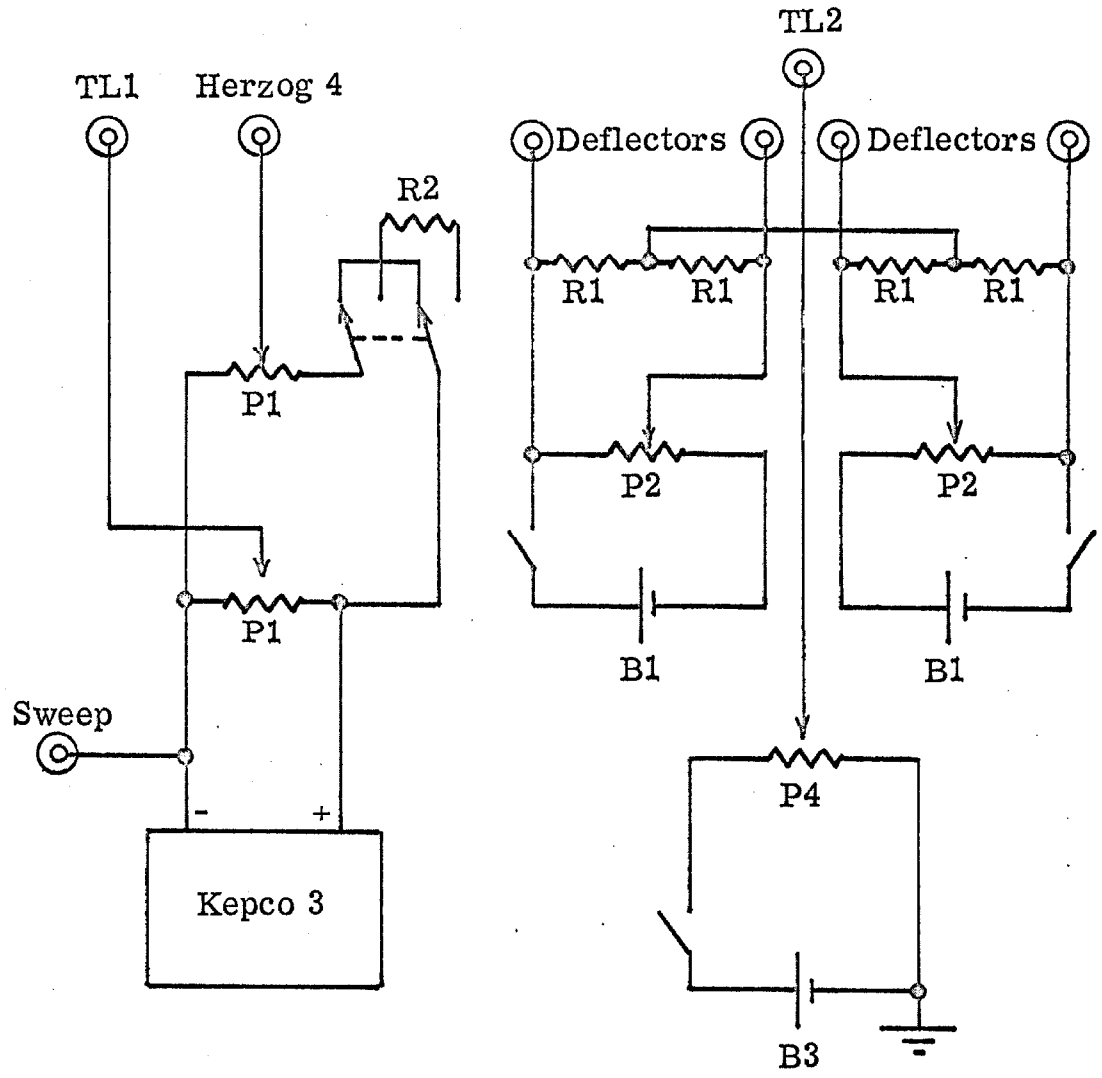

Figure 4.2-25. Circuit diagram of the lens system 3 control unit. (See table 4.2-8.)

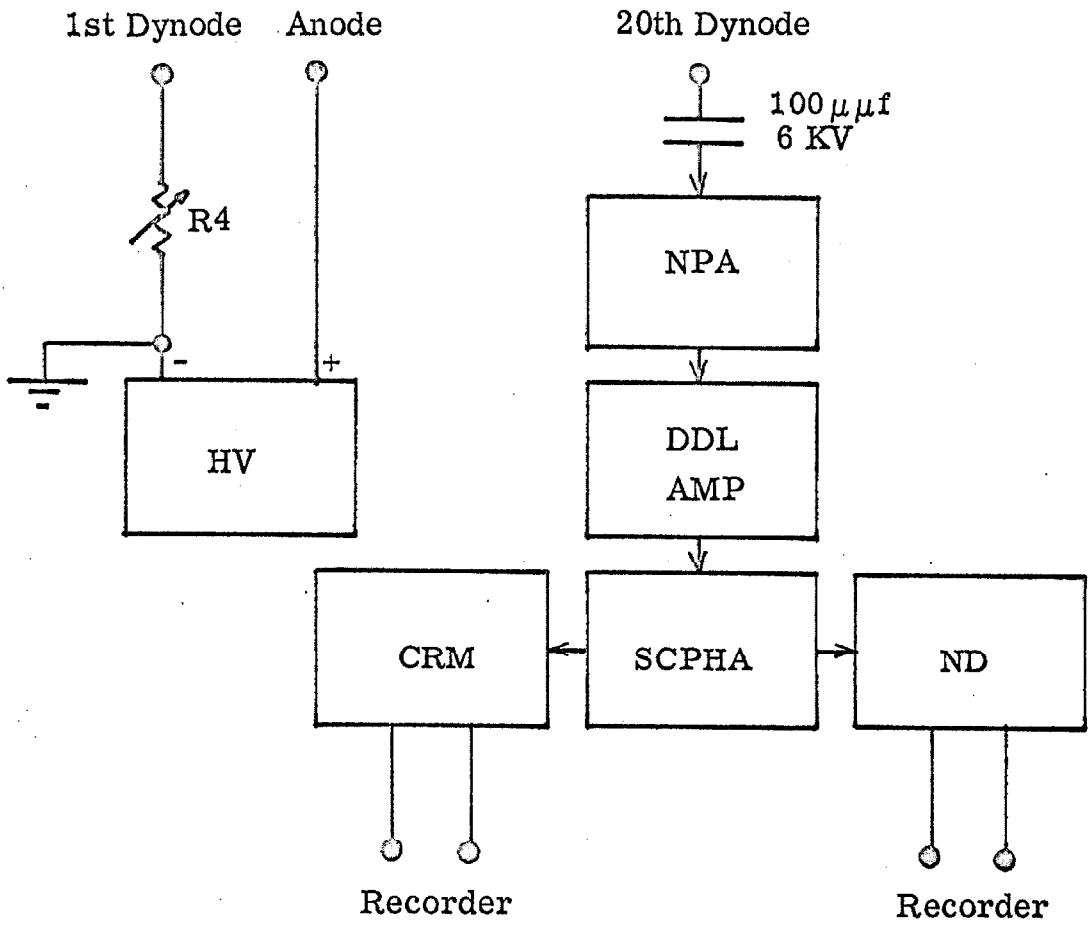

Figure 4.2-26. Block schematic of the detector electronics.

(See table 4.2-8.)

TABLE 4.2-8

Parts list for circuit diagrams 4.2-19 through 4.2-26. The first column gives the part designation as it appears in the figures. The second column gives its specification and/or manufacturer.

Part	Specification
Reference voltage supply (RVS)	Princeton Applied Research Corp., model TC 100.2BR voltage reference source. Accuracy ±.01%, stability ±.001%, resolution 100 mμV.
Recorder	Moseley, model 7001 AMR, X-Y recorder.
Kepco 1 (and 3)	Kepco, model HB2A(M), power supply. Load regulation .01%, stability .01%.
Kepco 2	Kepco, model KS36-5M, power supply (used in current regulation mode). Load regulation ±.02%.
PAR	Princeton Applied Research Corp., model TC-100.2R voltage reference supply. Accuracy ±.01%, stability ±.001%, resolution 1 mV.
FG	Exact Electronics Incorporated, type 251 function generator. 10,000 to .0001 cycles/sec.
HV	Dynamic Associates, PDI, Inc., model 1545 D.C. high voltage source. Regulation ±.001%, stability ±.02% day, resolution .01 V.
CRM	Nuclear Chicago Corp., RIDL, model 35-7B, log-linear count-rate-meter.
NPA	RIDL, model 31-1B, nuvistor pre-amplifier
DDL AMP	RIDL, model 30-23, double delay line amplifier

TABLE 4.2-8 (continued)

Part	Specification
SCPHA	RIDL, model 33-10B, single channel pulse height analyzer.
ND	Nuclear Data Corp., specially modified 1024 channel counting system.
ND AMP	Nuclear Data, model 180-014 control unit.
ND DAC	Raytheon,digital to analog converter (part of Nuclear Data system).
ND TB	Nuclear Data, model 180ITB time base generator.
ND M	Nuclear Data, model 181M, 1024 channel memory unit.
B1	Burgess, type U-15 dry cell, 22.5 V.
B2	Mallory, size D, 1.35 V mercury cell.
B3	Burgess, 300 V. B-battery.
R1	Welwyn, 1%, 10KΩ resistor.
R2	Welwyn, 1%, 90KΩ resistor.
R3	Ohmite, type U-linear, 10KΩ potentiometer.
R4	Ohmite, type U-linear, .5MΩ potentiometer.
P1	Beckman Inst., Helipot, model 7216, 10KΩ, 10 turn potentiometer.
P2	Helipot, model 5611, single turn 5KΩ potentiometer.
P3	Helipot, model 7216, 1KΩ, 10 turn potentiometer.
P4	Ohmite, type U-linear, 500KΩ potentiometer.

between any two elements could be measured with a Fairchild, model 7000, digital voltmeter. The current drawn by the elements could be measured with either a Keithley, model 600A, or a Cary, model 31, vibrating reed electrometer.

4.2.10. Sample Inlet System

The sample inlet system used in this research is shown schematically in figure 4.2-27. It is pumped by means of an Edwards, model 1SC150B mechanical pump (MP) located outside of the shielded enclosure. It can be isolated from the system by closing the Vacuum Accessories Corp., model FV-100, 1" stainless steel bellows valve (V1). V2, V3, and V4 are Nupro, model SS-6BG-SW, bakeable, $\frac{3}{8}$", stainless steel valves. A Granville Phillips, model 203001-02-011, variable leak (VL) is used to regulate the flow of sample gas to maintain the desired pressure in the scattering chamber.

A gage-port assembly (GPA) is mounted to the support frame (figure 4.2-14) inside the vacuum chamber. It contains a G.E. miniature ionization gage (IG) and an RCA, model 1946, thermocouple gage (TC) for monitoring the scattering chamber pressure. A pneumatically operated stainless steel bellows valve (BV) can be used to open one end of the gage-port assembly to the main vacuum. All fittings and tubulation are of stainless steel. The inlet system is bakeable (to about 350°C) from V1 to the main vacuum chamber.

Figure 4.2-27. Schematic diagram of the sample inlet system. (TSC) tubulation to scattering chamber; (IG) ionization gage; (TC) thermocouple (bakeable) gage; (GPA) gage port assembly; (BV) pneumatic bellows valve; (VCW) vacuum chamber wall; (V2 through V4) bakeable $\frac{3}{8}$" valves; (V1) 1" bellows valve; (VL) variable leak; (CT) liquid nitrogen cold trap; (MP) mechanical pump; (S/E) shielded enclosure wall; (EL) exhaust line.

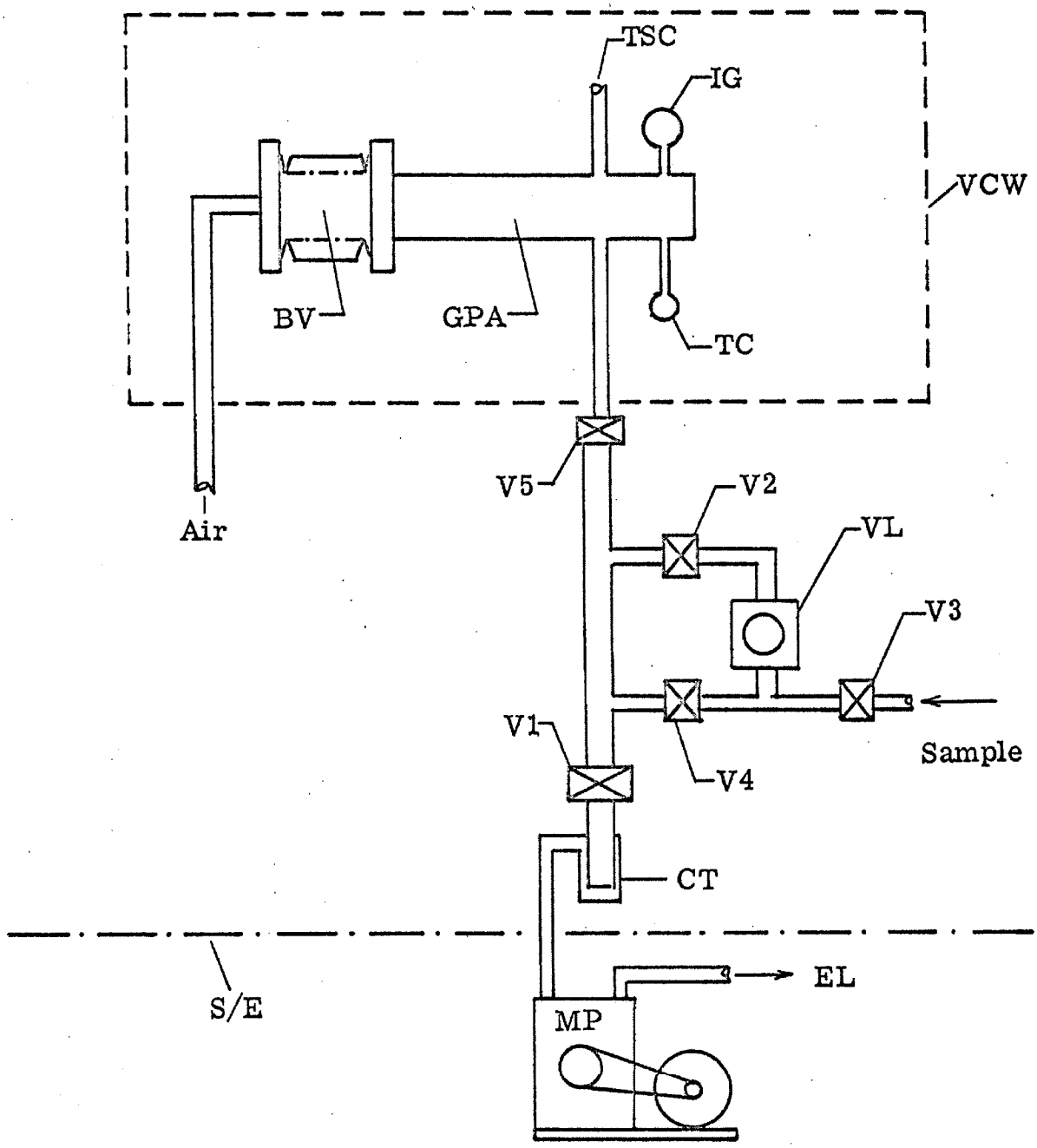
TSC
IG
VCW
BV
GPA
TC
Air
V5
V2
VL
V3
V1
V4
Sample
CT
S/E
EL
MP

4.3. Procedure

4.3.1. Pump-Down and Bake-Out

Before operating the spectrometer, the vacuum chamber must be evacuated and the internal components baked-out. A great deal of experience with this apparatus has shown that a bake-out after each exposure to air is absolutely necessary for acceptable spectrometer performance, although it has little affect on the ultimate vacuum chamber pressure.

To initiate the pump-down, valves V3 and V4 are closed (refer to figure 4.2-2), valves V1, V2, and GV are open, and the mechanical pump (MP) is started. When thermocouple (T2) indicates that the fore line pressure is below .020 torr (this usually requires 10 minutes), the two freon compressors to chill baffles CB1 and CB2 are started. After 15 minutes, GV is closed and the diffusion pump is started. By this time both T1 and T2 should indicate a pressure of 10^{-2} torr or less. 25 minutes later, the liquid nitrogen cold trap (CT) is filled. When G2 indicates a pressure of 1×10^{-6} torr (about 10 more minutes), valve V2 is closed and GV is opened. The chamber pressure usually drops to about 5×10^{-6} torr in a few seconds. After about 1 hour a background pressure of 1×10^{-6} torr is usually obtained.

At this point the internal bake-out heater is turned on at low power (200 watts) until the monochromator and selector reach about 120°C (one-half hour). The power is then increased in increments of about 100 watts every 5 minutes until 600 watts is

reached. After about 4 hours, the selector, monochromator, and scattering chamber are at approximately 250°C. The pressure, which usually rises to about 10^{-5} torr during the initial phase of the bake-out, falls back to about 10^{-6} torr. The bake-out is terminated at this point. The apparatus will return to room temperature in about ten hours with a residual pressure of about 5×10^{-8} torr. Even if the components were not baked, this value of the pressure would be obtained after about 48 hours.

4.3.2. Magnetic Field Compensation

The construction and placement of the Helmholtz coils has been discussed in section 4.2.2.1. With all spectrometer components in place (especially relay racks and power supplies), a Bell, model 120, gaussmeter and a Hall effect probe (maximum sensitivity is 1 m gauss full scale) were used to measure the residual magnetic field. By suitable adjustment of the current through the coil-pairs, the residual field was reduced to ± 5 m gauss over the entire region of the electron beam path. Table 4.3-1 gives some specific values of the field after compensation.

4.3.3. Sample Introduction

The sample inlet system has been described in section 4.2.10 and shown in figure 4.2-27. During the pump-down and bake-out (section 4.3.1) of the main chamber, valves BV, V5, V2, and V4 are kept open while valves V1 and V3 are closed. The mechanical pump is used to evacuate that part of the line below

TABLE 4.3-1

Helmholtz coil operation. I is the current through the coil-pair, $|B|$ is the residual magnetic field component in the direction of the coil-pair axis measured at the element indicated, and Δ is the rate of change of the residual magnetic field component with the current through the coil-pair.

Coil Pair	Current (mA)	$\|B\|$/m gauss		Δ (m gauss/mA)	
		Monochromator	Selector	Monochromator	Selector
X	3.3	0.5	3.5	11.1	10.8
Y	8.5	3.0	0.1	8.3	7.8
Z	10.1	3.2	5.5	12.5	9.3

V1, and the cold trap is immersed in liquid nitrogen. The inlet system is flushed several times with the gas to be studied by closing valve BV, admitting the sample through V3 until TC1 indicates about 0.5 torr, and then pumping the target gas away through V1. To obtain the desired sample pressure in the system, valves BV, V1, and V4 are closed. Valves V5, V2, and V3 are open and the gas-flow through the variable leak (VL) is adjusted to give the desired constant pressure (.001 to .010 torr) in the gage port assembly. This constant pressure is the result of a dynamic balance between the sample leaking in through VL and out through apertures A4 (fig. 4.2-8) and A5 (fig. 4.2-11).

Since the pressure monitoring gages (IG, TC1) are separated from the actual scattering region (the inside of the inner scattering chamber bellows, fig. 4.2-9) by a 0.375" I.D. × $2\frac{1}{2}$" long stainless steel tube (TSC of figure 4.2-27), the scattering chamber pressure will be somewhat lower than that indicated by the gages. An estimation of this pressure difference can be obtained from the equations and tables of Pirani and Yarwood[113].

The total conductance U_A of apertures A4 and A5 is approximately .075 liter/sec for air at 20°C if one assumes that molecular effusion conditions[113] prevail. The conductance U_T of the tube connecting the gage port assembly (at pressure P_{GPA}) and the scattering chamber (at pressure P_S) is about 2 liter/sec (see fig. 1.3 of reference 113). The throughput Q is constant throughout the system for a steady state (pressure) condition and is given by

$$Q = U(P_1 - P_2) \tag{4-79}$$

in which P_1 and P_2 are the pressures in any two regions and U is the conductance of the orifices (or tubes) separating them. In particular,

$$U_A(P_S - P_{MC}) = U_T(P_{GPA} - P_S) \tag{4-80}$$

where P_{MC} is the pressure in the main vacuum chamber ($\sim 10^{-7}$ torr) which is negligible compared to P_S ($\sim 10^{-3}$ torr). Thus, solving for P_S yields,

$$P_S \cong \frac{U_T}{U_A + U_T} P_{GPA} \quad . \tag{4-81}$$

With the values of U_T and U_A as given above, one finds that P_S is about 4% lower than P_{GPA}. Since no attempt has been made to calibrate the pressure gage used to measure P_{GPA}, this additional uncertainty is of little consequence.

4.3.4. Spectrometer Operation

4.3.4.1. Tuning

The overall objective in tuning the apparatus is to obtain the maximum electron beam intensity compatible with a given resolution (FWHM of the energy-analyzed electron beam). As yet, we have not been able to devise a step-by-step procedure which will guarantee the realization of this objective. However, by trial and error, a procedure has been developed which usually results in acceptable performance. This procedure is discussed below. Refer to figure 4.3-1 for the designations of the voltages to the various elements and to table 4.3-2 for the definitions of the abbreviations used.

Figure 4.3-1. Schematic diagram of the spectrometer components and voltage supplies. Table 4.3-2 contains the definitions of the abbreviations. The arrows indicate the direction of the electron beam.

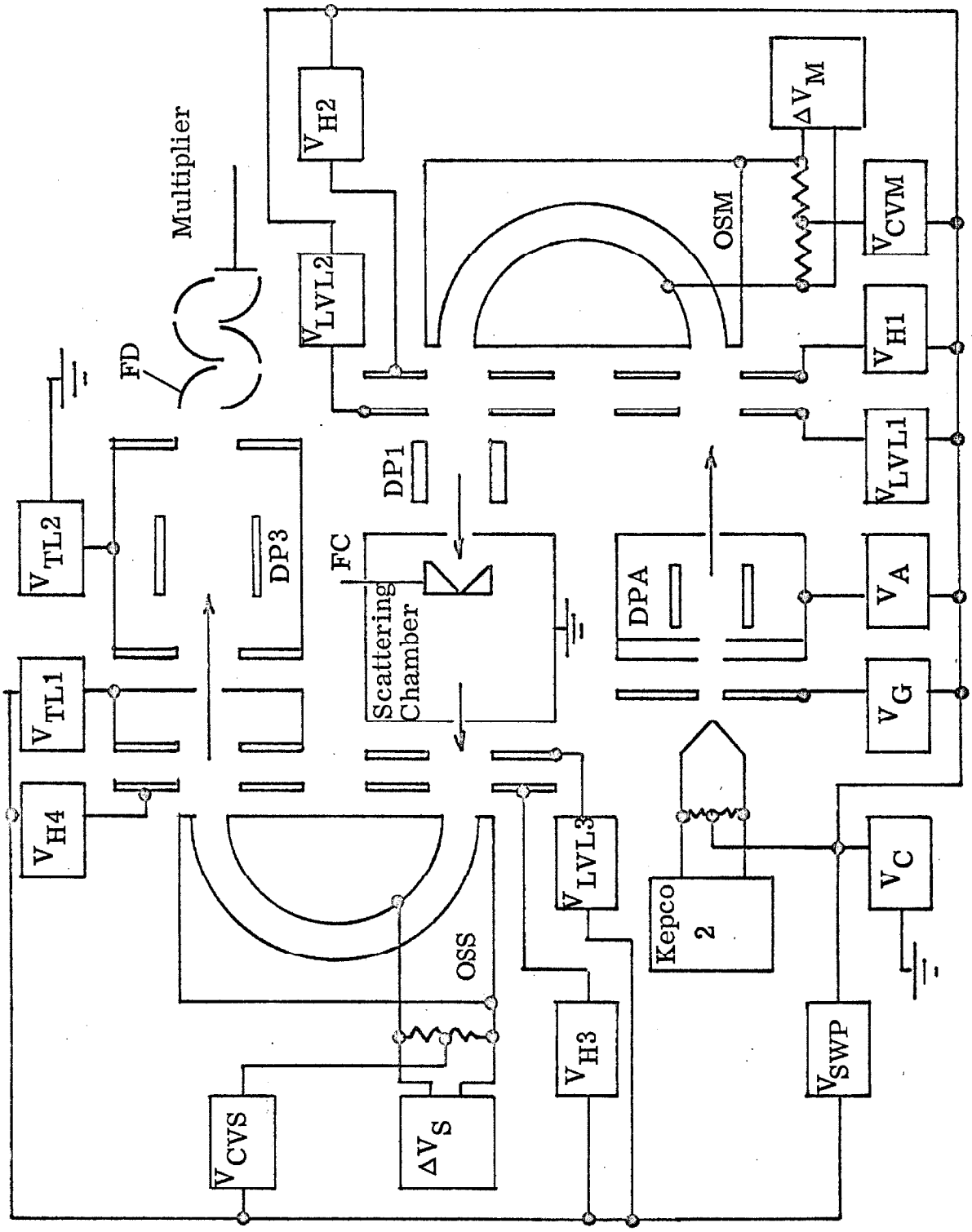
Multiplier
FD
V_{H2}
V_{LVL2}
ΔV_M
V_{CVM}
OSM
V_{H1}
V_{LVL1}
DP1
FC
Scattering Chamber
DP3
DPA
V_{TL2}
V_{TL1}
V_{H4}
V_A
V_G
V_C
V_{LVL3}
Kepco 2
OSS
V_{H3}
V_{CVS}
ΔV_S
V_{SWP}

TABLE 4.3-2

Abbreviations used for the electron-optical elements, voltages, and currents. The voltage and/or current to each element is labelled in the text by V_{SUB} and/or I_{SUB}, respectively, where SUB is the element abbreviation.

Abbreviation	Designation
C	Cathode (heating current supplied by Kepco 2, voltage supplied by reference voltage supply (RVS)).
AD	Anode. Refer to circuit diagram, fig. 4.2-20.
LVL 1 LVL 2 LVL 3	Low voltage lenses 1, 2, 3. Refer to circuit diagrams, figs. 4.2-20, 4.2-22, and 4.2-24, respectively.
H 1 H 2 H 3 H 4	Herzogs (field matching elements) 1,2,3,4. Refer to circuit diagrams, figs. 4.2-20, 4.2-22, 4.2-24, and 4.2-25, respectively.
OSM	Outer sphere of the monochromator. Refer to circuit diagram, fig. 4.2-21.
OSS	Outer sphere of the selector. Refer to circuit diagram, fig. 4.2-21.
G	Grid. Refer to circuit diagram, fig. 4.2-20.
CVM CVS	Center tap on monochromator (CVM) and selector (CVS). Refer to circuit diagram, fig. 4.2-21.
DPA	Deflector plates in anode structure. Refer to circuit diagram, fig. 4.2-20.
DP1	Deflector plates in lens system 1. Refer to circuit diagram, fig. 4.2-22.
DP3	Deflector plates in lens system 3. Refer to circuit diagram, fig. 4.2-25.
FC	Faraday cup collector in scattering chamber (pneumatically operated, see section 4.2.4.5).

TABLE 4.3-2 (Continued)

Abbreviation	Designation
ΔV_M, ΔV_S	Voltage applied across hemispheres of monochromator (ΔV_M) and selector (ΔV_S). Refer to circuit diagram, fig. 4.2-21.
FD	First dynode of electron multiplier.
V_{SWP}	Voltage applied by sweep circuit. (Voltage between points labelled "OUT" and "RVS" of fig. 4.2-23)
TL 1, TL 2	Tube lenses of lens system 3, fig. 4.2-25.

The apparatus is tuned in essentially four stages:

(1) V_C is set by the reference voltage supply to yield the desired impact energy in the scattering chamber (section 4.3.4.2); AD and LVL 1 are grounded; V_{H1} is set to the desired analyzing voltage (related to E_o of equation 4-29); the filament power supply (Kepco 2) is turned on (usually 2.3A); and I_{OSM} is maximized by adjusting V_G and V_{DPA}.

(2) Then V_{H2} and V_{CVM} are set equal to V_{H1}; LVL 2 and DP1 are grounded; and I_{FC} is maximized by adjusting ΔV_M. Next, V_{DP1} then V_{LVL1}, V_{LVL2}, and finally V_{H1}, V_{H2}, V_{AD}, V_G, V_{DP1}, V_{DPA}, and ΔV_M are adjusted for maximum I_{FC}. The optimization of this procedure is complicated by the fact that I_{FC}, as a function of the applied voltages, defines a mathematical hypersurface with many local maxima. As a result, determining the highest of these is practically impossible.

(3) To tune the second half of the spectrometer, the FC is withdrawn; $V_{SWP} = 0$; LVL 3 and H3 are grounded; and the gear wheel is rotated until the beam current to the outer sphere of the selector is maximized. Then V_{H3} is set equal to V_{CVM}. First V_{LVL3} and then all of the variable stage (1) and (2) controls are adjusted for maximum current.

(4) Next, V_{CVS} and V_{H4} are set equal to V_{CVM}; TL 1, TL 2, and the deflectors of lens system 3 (DP 3) are grounded; and the current to the first dynode (I_{FD}) of the multiplier is maximized by adjusting first ΔV_S and then all controls in this stage (except

V_{CVM} and V_{SWP}) and stages (1), (2), and (3). A typical set of operating voltages and currents are given in table 4.3-3.

4.3.4.2. Method of sweep

The energy distribution of the beam which has just been maximized in the previous section is obtained by measuring the current (I_{FD}) collected at the multiplier (detector) as a function of the sweep voltage (V_{SWP}). This can be understood as outlined below.

Let the potential of the cathode be V_C volts with respect to ground and the potentials applied to the CVS by the selector control and to the selector control by the sweep control be $+V_{CVS}$ and 0, respectively, with respect to the cathode. Thus, the kinetic energy (K.E.) distribution of the electron beam in the grounded scattering chamber will be peaked at an energy $E_C = |e|V_C$ (in the absence of "contact potentials"). Likewise, electrons of K.E. $E_{CVS} = |e|V_{CVS}$ are transmitted with the highest efficiency by the selector (E_{CVS} corresponds to E_o of equation 4-29). Since we have adjusted the selector to pass the maximum current, the electrons of K.E. E_{CVS} in the selector are the ones which had a kinetic energy E_C in the scattering chamber. Now, suppose that the sweep voltage is changed from 0 to V_{SWP} volts while all other controls are left unchanged. Electrons of K.E. E_{CVS} in the selector are still detected with the highest efficiency (recall that the electron's orbit through the analyzer depends only on its K.E. if the potential across the hemispheres remains constant), but the electrons which

TABLE 4.3-3

A typical set of voltage and current conditions.

Element	Voltage (Current)	With Respect To
V_{CAT}	-35.00	Ground
V_G	1.00	V_{CAT}
V_A	0	Ground
$V_{LVL\ 1}$	- 5.26	Ground
V_{H1}	2.02	V_{CAT}
V_{CVM}	1.82	V_{CAT}
ΔV_M	1.03	
I_{OSM}	1.3×10^{-6} A	
V_{H2}	1.82	V_{CAT}
$V_{LVL\ 2}$	- 6.24	Ground
I_{FC}	4×10^{-8} A	
$V_{LVL\ 3}$	28.25	V_{SWP}
V_{H3}	5.25	V_{SWP}
V_{CVS}	1.63	V_{SWP}
ΔV_M	.92	
V_{H4}	1.63	V_{SWP}
V_{TL1}	35.00	V_{SWP}
V_{TL2}	265	Ground
V_{FD}	265	Ground

had K.E. E_C in the scattering chamber now have K.E. $E'_{CVS} = E_{CVS} + |e|V_{SWP}$ in the selector. However, electrons of K.E. $E'_C = E_C - |e|V_{SWP}$ in the scattering chamber will have the proper K.E. (E_{CVS}) to be detected with greatest efficiency. As a result, the current measured at the detector for a given value of the sweep voltage V_{SWP} is due to electrons of K.E. $E'_C \pm \delta E$ in the scattering chamber where δE depends on the resolution of the selector. Electrons losing a portion W of their K.E. through inelastic collisions with the target molecules will be detected with peak efficiency when $|e|V_{SWP} = W$. Thus, a plot of current reaching the detector versus sweep voltage will yield an energy-loss spectrum in which the elastic processes appear as a peak at 0 volts and each inelastic process appears as a peak at $V_{SWP} = W/|e|$ volts. Since we are in effect measuring directly the difference between the incident and scattered electron K.E. (and not the actual magnitude), the contact potentials which render the value of E_C uncertain to within 1 or 2 eV cancel out.

4.3.4.3. Method of detection

If the direct or low-angle elastically scattered beam is to be measured, the signal level is usually high enough for the first dynode of the multiplier to be used as a faraday cup collector in conjunction with a Cary, model 31, vibrating reed electrometer. Otherwise, the energy-analyzed scattered beam is detected by using the electron multiplier with suitable pulse counting equipment, as shown in figure 4.2-26.

With approximately 4.5 K.V. across the multiplier resistor string, an electron with a K.E. of about 200 eV striking the 1st dynode produces several secondary electrons which are accelerated to the second dynode, etc., producing a relatively narrow (in time) pulse at the 20th dynode containing 10^7 to 10^8 electrons. This "charge" pulse is transmitted by the 100 $\mu\mu f$ blocking capacitor, converted to a voltage pulse by the nuvistor preamplifier, amplified by the double delay line amplifier, and routed into the single channel pulse height analyzer (SCPHA). The latter has variable threshold and window controls for an adjustable pulse height discrimination. If the input pulse has an amplitude greater than the threshold voltage setting and less than the threshold plus window voltage, a standard output pulse (50η sec rise time, 10 V peak, 0.5 μ sec duration) is generated. If the input pulse does not satisfy both of the above criteria, no output pulse is generated. In this way, low-level (amplifier noise, pick-up, stray electrons) and high-level (cosmic ray) pulses can be eliminated. The output pulses from the SCPHA (typically one output pulse for each electron striking the first dynode of the multiplier) can then be counted by the count-rate-meter (CRM) or the Nuclear Data 1024 channel scalar (MCS).

The CRM converts these pulses into a D.C. current proportional to the average count-rate. If the measured count-rate (number of counts/sec) is N, then from the statistical nature of the counting process the uncertainty in N (one standard deviation) is $\sqrt{N/\tau}$ where τ is the time constant (variable from 0.5 to 50 sec)

of the CRM. Thus, for low signal levels (low count-rates) τ must be made relatively large for a reasonable "statistical" accuracy. The CRM generates an output D. C. voltage that is directly proportional to the input count-rate (current) which can be used to drive the Y axis of an X-Y recorder.

The MCS, on the other hand, adds all of the pulses reaching it within a certain time interval into a designated channel of its memory. If the number of counts stored in this channel is M, the statistical uncertainty is simply $\sqrt{M}$. For lower count-rates, one must use a longer counting time in each channel to increase the relative precision of the measurement. The number of counts stored in each channel of the memory can be displayed on an oscilloscope, X-Y recorder, or punched paper tape.

4.3.4.4. Sweep-signal correlation

It has already been noted in section 4.3.4.2. that the value of the sweep voltage determines the energy-loss being detected. The variation of this sweep voltage can be obtained in two quite different ways (refer to fig. 4.2-23).

If the CRM is being used, the sweep is provided by the ramp-function output of an Exact, type 251, function generator (with an additional 10μf capacitor to reduce the lowest standard sweep-rate by a factor of 10). The PAR is used to set the voltage at which the sweep is to start. The total sweep voltage (PAR + FG) is applied simultaneously to the X axis of the recorder and to the spectrometer (as indicated in fig. 4.2-19). Since the Y axis of

the recorder is driven by the CRM output, a plot of the count-rate versus the energy-loss will be obtained directly. The relation of this count-rate to the differential scattering cross-section is discussed in section 4.4.

However, if the MCS mode of operation is used, the sweep voltage is provided by the MCS itself and is correlated to the signal as outlined below (refer to fig. 4.2-23(b)).

The output of the SCPHA is connected to the memory (ND-M) unit of the Nuclear Data system, and the pulses are counted into one of the 1024 channels. The digital-to-analog converter (ND-DAC) samples the channel number into which counts are being stored, and converts it to an analog voltage which is directly proportional to the channel number. This voltage is amplified by the ND-AMP and applied to the spectrometer as indicated in fig. 4.2-19. The time base generator (ND-TB) advances the channel number into which counts are stored by one after a preset time interval (dwell time). The ND-DAC and ND-AMP, in turn, apply a higher voltage (corresponding to the higher channel number) to the spectrometer. In this way, each channel of the memory stores counts which are correlated with a specific value of the sweep voltage (and energy-loss). Since the dwell time in each channel is the same, a plot of the number of counts in each channel versus that channel number corresponds to the count-rate versus energy-loss at a set of 1024 points.

The MCS mode of operation has one very significant advantage over the CRM mode when low count-rates are to be recorded. As noted previously (section 4.3.4.3), for the detection of low level signals by the CRM, τ must be relatively long, and, hence, the sweep rate must be very slow. Since the collection of the last part of the spectrum will occur so long after that of the first, a relatively slow drift in the beam intensity, sample pressure, or collection efficiency can cause an appreciable distortion in the energy-loss spectrum.

On the other hand, the MCS mode can be used to sweep through the entire energy-loss spectrum repetitively and quickly compared to "instrumental" drift (collecting very few counts in each channel, of course). In this way, the relative peak heights within the energy-loss spectra will not be distorted by instrumental changes, and the "statistical" accuracy can be improved by adding the counts from many sweeps. Appendix II gives a more detailed list of the MCS specifications and operation.

4.3.5. Obtaining a Spectrum

(1) The spectrometer is tuned and the gas sample is introduced into the scattering chamber as discussed in sections 4.3.4.1 and 4.3.3., respectively.

(2) The scattering angle is changed to $\sim 40°$, the multiplier high voltage and detector electronics are turned on, and the spectrometer is retuned on the elastic peak.

(3) The instrument is allowed to stabilize for about 2-8 hours, depending on the measured elastic peak drift.

(4) The desired scattering angle is set, the PAR (fig. 4.2-23) is set to the desired initial energy-loss, the voltage sweep is initiated, and the energy-loss spectrum is registered on the X-Y recorder or in the MCS memory.

4.4. Performance

4.4.1. Vacuum Characteristics

The mercury diffusion pump (section 4.2.1) is rated at a pumping speed of 1500 litre/sec (for air). However, due to the baffle, cold trap, and tubing between it and the main vacuum chamber, the pumping speed at the chamber is significantly reduced. It was calculated in the usual way[113] to be 400 ± 50 litre/sec. in the vicinity of the spectrometer. The effective pumping speed can also be determined experimentally by measuring the pressure differential between the scattering chamber and main chamber.

From the definitions and equation (4-79) of section 4.3.3,

$$S_{MC}P_{MC} = U_A(P_S - P_{MC}) , \qquad (4\text{-}82)$$

in which S_{MC} is the effective pumping speed at the main vacuum chamber. Since $P_{MC} \ll P_S$;

$$S_{MC} \approx U_A P_S / P_{MC} . \qquad (4\text{-}83)$$

U_A is known (approximately) and P_{MC} was measured for various values of P_S. From the average value of P_S/P_{MC} and U_A,

$$S_{MC} \approx 375 \text{ litre/sec} .$$

The pressure in the main chamber must be less than 2×10^{-6} torr for satisfactory operation of the spectrometer. This means that the maximum allowable sample pressure in the scattering chamber (with the present aperture dimensions and pumping speed) is about .010 torr.

4.4.2. D.C. Collector Efficiency

There are basically four elements of the spectrometer which are used routinely for D.C. current collection to assess the instrument performance--the outer spheres of the monochromator and selector, the first dynode of the multiplier, and the faraday cup in the scattering chamber. The first two of these were found to have a collection efficiency for electrons of K.E. 20 eV or higher of over 90% when the current to them was measured to ground (that is, the electrometer was connected directly between the element and ground). The efficiencies of the last two, however, exhibited pronounced dependencies on a bias voltage applied between the electrometer and ground. A typical result is shown in figure 4.4-1 for the collection of electrons with a K.E. of 35 eV by the faraday cup. This result is dependent on the beam kinetic energy and varied from 33% to 85% at 0 bias. The behavior of the first dynode was quite similar. Thus, these collectors were operated at a holding voltage sufficient

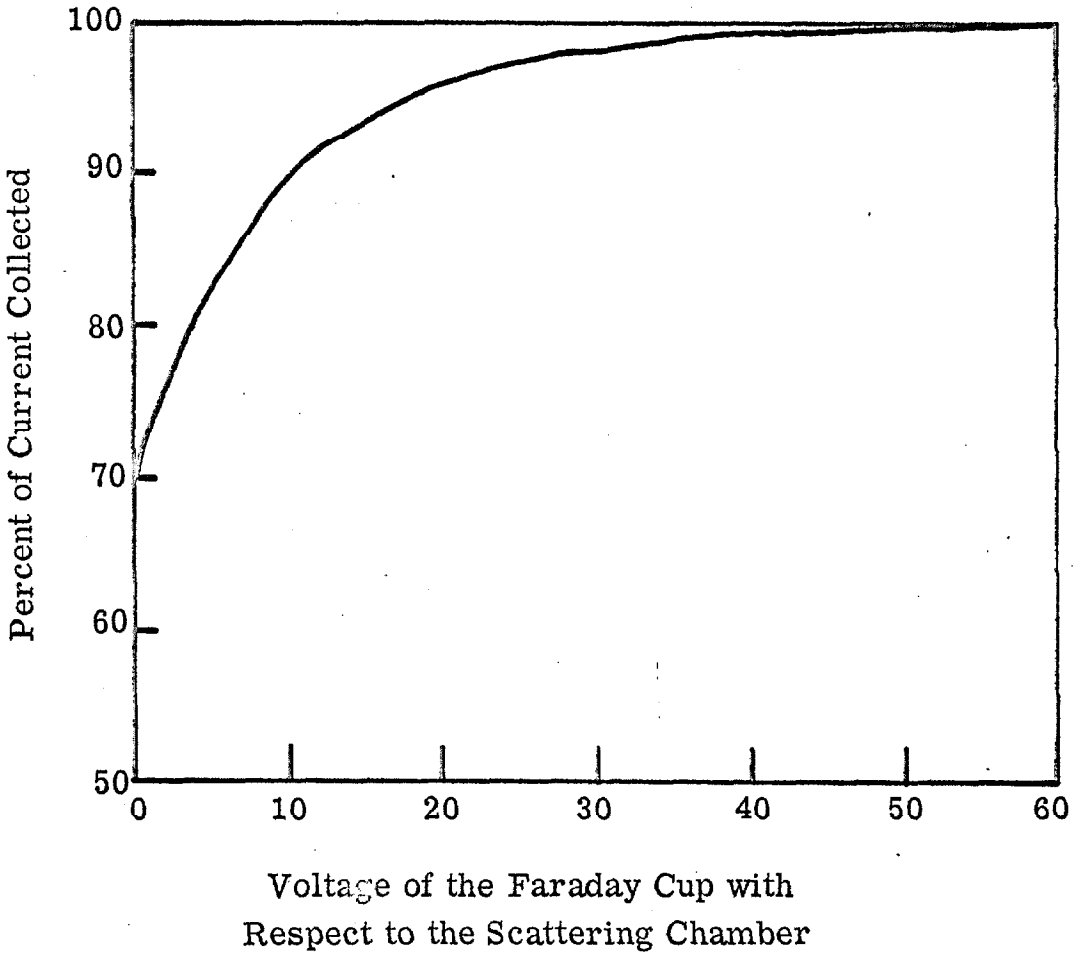

Figure 4.4-1. Collection efficiency of the scattering chamber faraday cup as a function of bias voltage. The incident beam energy and current were 35 eV and 1.2×10^{-9} A, respectively. 100% current collection was assumed at a 60 volt bias.

to collect more than 95% of the incident current.

4.4.3. Electron Beam Characteristics

4.4.3.1. Energy distribution from the gun

As a preliminary test of the operation of the gun and monochromator, the electron kinetic energy distribution leaving the gun was measured. The experimental procedure was as follows:

(1) A simple sweep circuit consisting of a battery and voltage divider (10 turn Helipot) was inserted between CVM and P1 (refer to figure 4.2-21). Herzogs number 1 and 2 were connected directly to CVM.

(2) The gun and monochromator were tuned for maximum current to the scattering chamber faraday cup (FC) with this sweep voltage equal to 0. The anode and deflectors DPA and DP 1 (fig. 4.3-1) were grounded.

(3) The current to FC (Y-axis) was measured as a function of the sweep voltage (X-axis) on an X-Y recorder with all other controls unchanged. In effect, the electron energy distribution entering the monochromator was measured with a constant resolution which was determined by observing the selector output.

If f(E) is the "true" electron energy distribution, i.e, the current per unit energy carried by electrons of kinetic energy E and g(E) is the intrinsic line shape of the monochromator (assumed to be Gaussian, refer to section 4.1), then the measured current distribution at FC will be

$$I(E) = \int_{-\infty}^{\infty} g(E - x)\, f(x)dx \tag{4-84}$$

in which E is numerically equal to the sweep circuit voltage plus an unknown constant (due to contact potentials).

If we make the usual assumptions inherent in the "free-electron" theory of metals (see reference (94b) and (114), for example), the rate at which electrons within the metal with momenta between $\underset{\sim}{p}$ and $\underset{\sim}{p} + d\underset{\sim}{p}$ strike a unit area of the surface is

$$dR = \frac{2}{mh^3} \frac{p_z dp_x dp_y dp_z}{\exp\{\frac{W - E_f}{kT} + 1\}} \tag{4-85}$$

The metal surface defines the xy plane of the coordinate system. W is the electron kinetic energy in the metal ($W = p^2/2m$) and E_f is the Fermi energy. In the absence of an external electric field, only those electrons which possess a momentum in the z direction such that

$$p_z^2/2m \geq W_f + E_f = W_a, \tag{4-86}$$

where W_f is the work function of the metal, can escape. Since W_f/kT is generally $\gg 1$, the emission current density dJ_z normal to the surface is given approximately by:

$$dJ_z = \frac{2ep_z}{mh^3} e^{-(W-E_f)/kT} dp_x dp_y dp_z \tag{4-87}$$

when (4-86) is satisfied and dJ_z equals 0 otherwise.

Nottingham[115] found that a "reflection coefficient", presumably at the metal surface, of the form

$$r(p_z) = e^{-[(p_z^2/2m - W_a)/w]} \tag{4-88}$$

(in which w is an experimental parameter equal to 0.191 eV) was required to best represent his careful retarding-potential measurements on tungsten and thoriated tungsten. Also, Hutson[116] found this reflection coefficient with the same value of w to be adequate in fitting his direct measurements of the electron kinetic energy distributions from single crystals of tungsten.

It should be noted that such a reflection function is not compatible with our present understanding of the image-force potential model of the potential barrier at the metallic surface. For example, a typical result of Belford, et al.[117] obtained by numerical integration of the Schröedinger equation for various image-force potentials is shown in figure 4.4-2 along with the experimentally derived result. The discrepancy between Nottingham's curve (N) and Belford's curve (B) may be due to a number of things, such as surface contamination and irregularities, and crystal lattice effects. The experimental situation is further complicated by the possibility of potential drops across the filament (cathode) and anomalous energy spreading[118].

Leaving the resolution of these problems to future investigators, let us proceed by incorporating a transmission function

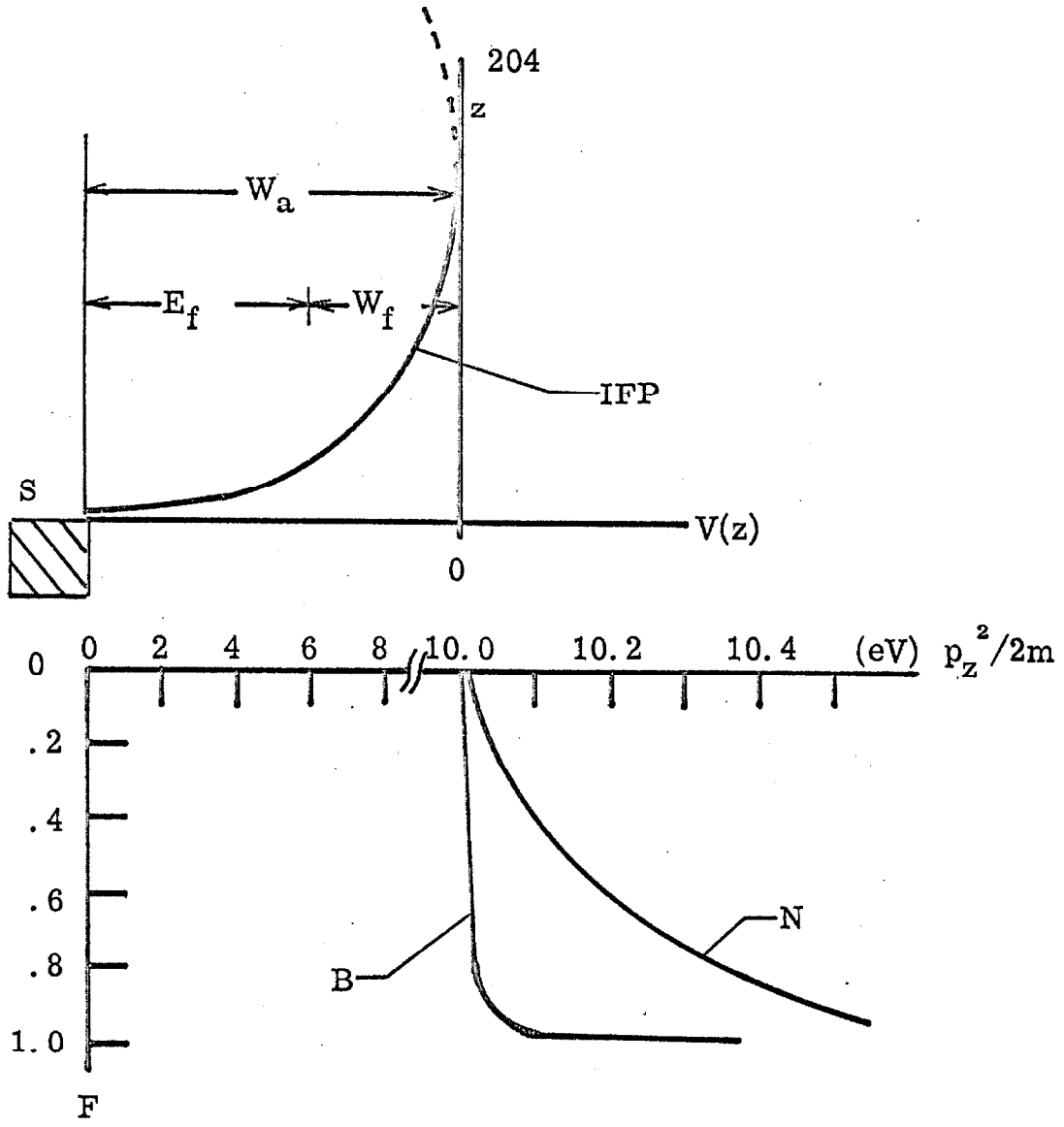

Figure 4.4-2. Schematic representation of the image-force-potential (IFP) at the metal surface and the fraction transmitted (F) according to reference (117) (B) and reference (115) (N). W_f and E_f are 4 eV and 6 eV, respectively. The potential energy scale V(z) is simply $p_z^2/2m$ - 10 eV. The dashed line continuation of the IFP line is the "bend over" which arises from draw-out electric fields. The resulting barrier is presumably responsible for quantum mechanical reflection. z measures the distance from the metal surface (S).

$$F = 1 - Ar(p_z) \tag{4-89}$$

in equation (4-87). If A = 0, F is a good approximation to the image-force-potential transmission function, while if A = 1, F is equivalent to the transmission function employed by Nottingham and Hutson.

The multiplication of (4-87) by (4-89) and conversion of the result to a distribution in laboratory kinetic energy E yields

$$dJ = \frac{8\pi me}{h^3} e^{-(E + W_f)/kT} (E + W_a) H(E)\, dE \tag{4-90}$$

after integration over φ and θ (noting relation (4-86)). In (4-90), $E = W - W_a$ and

$$H(E) = \frac{1}{2} \int_{W_a/W}^{1} [1 - A e^{-(Wx^2/w - W_a/w)}]\, dx$$

$$= \frac{1}{2} \left(\frac{E}{E + W_a}\right) \left[1 - \frac{Aw}{E} (1 - e^{-E/w})\right] .$$

Consequently, f(E) of equation (4-84) is

$$f(E) = C\, E^{-E/kT} \left[1 - \frac{Aw}{E} (1 - e^{-E/w})\right] \tag{4-91}$$

where C is a constant depending on the work function and temperature but not on E or w. If g(x) of equation (4-84) is assumed to be of the form e^{-x^2/a^2}, then performing the integration indicated by (4-84) yields

$$I(E) = D\, e^{-E/kT} \left\{ (aB_1 - w)(1 + \operatorname{erf} B_1) + \frac{a}{\sqrt{\pi}} e^{-B_1^2} \right.$$
$$\left. + Aw(1 + \operatorname{erf} B_2) \exp(-E/w + a^2/4w^2 + a^2/2wkT) \right\} \tag{4-92}$$

where $B_1 = E/a - a/2kT$

$B_2 = B_1 - a/2w$

and D is a suitable normalization constant. Notice that for values of E large compared to kT, a, and w,

$$I(E) \sim 2DE\, e^{-E/kT} \quad . \tag{4-93}$$

The effects of reflection (w, A) and finite resolving power (a) will become negligibly small. Further, a plot of lnI(E) versus E in the region where (4-93) is valid should be nearly a straight line of slope -1/kT.

The experimental energy distribution obtained from the tungsten hairpin cathode used in the present research is given in figure 4.4-3. The FWHM of the distribution is $.63_5$ eV. If (a) and (A) were 0, this half-width would imply a cathode temperature of 2900°K. The high energy tail is nearly a straight line (as expected) but its slope gives a cathode temperature of only 2560°K. This indicates that the shape in the low energy region of the curve has been distorted--possibly due either to the "reflection function" or anomalous energy broadening[118].

With the latter value of the temperature, A = 1, and a resolution of .07 eV, equation (4-92) was used to calculate the expected current distribution for w = .19 eV (solid line of figure 4.4-3). w can be changed by ± .02 eV before significant deviations from the experimental points are evident. The curve with A = 0 is shown for comparison (dashed line of fig. 4.4-3). The calculated

Figure 4.4-3. Electron kinetic energy distribution from the gun. The circles are experimental points for a primary beam energy of 35 eV and an analyzing energy of 5.0 eV. The FWHM of the monochromator output (as measured by the selector) was .07 eV. The solid curve is the calculated distribution assuming the reflection function of references (115, 116) with w = 0.19 eV. The dashed curve is the calculated distribution assuming no reflection. The cathode temperature, as determined from the slope of the high energy ($E > 1.25$ eV) tail is 2560°K.

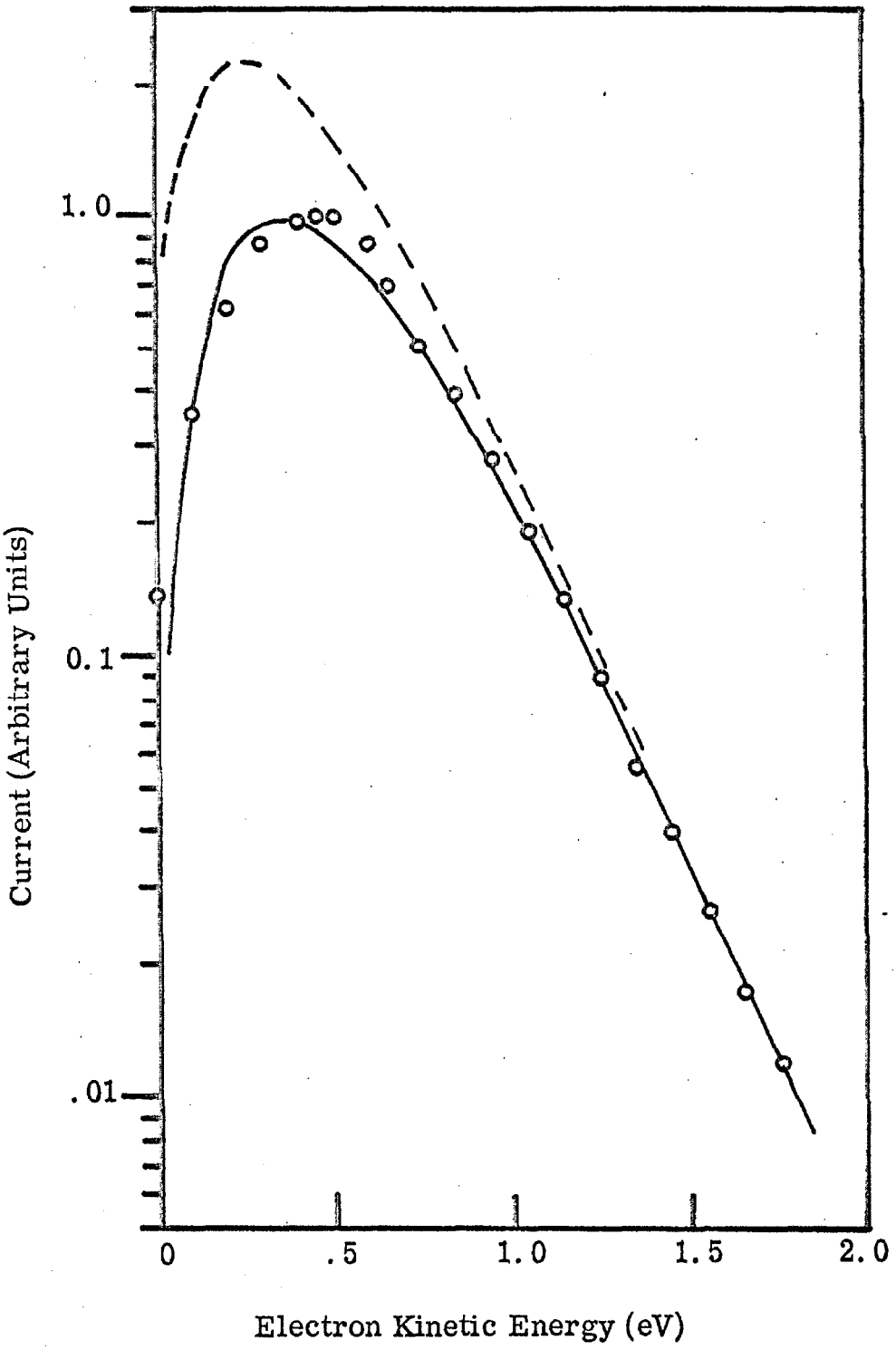
1.0
0.1
.01
Current (Arbitrary Units)
0
.5
1.0
1.5
2.0
Electron Kinetic Energy (eV)

distribution is normalized to the experimental one by assuming that the experimental points on the high energy side coincide with the calculated curve and the origin of E is determined as the point on the low energy side of the distribution where the slope is characteristic of the analyzer. Note that the position of the dashed curve is fixed with respect to that of the solid one.

The good agreement of this result with those of Nottingham and Hutson seems to preclude the importance of surface effects in view of the quite different surface preparation in the present case (none). Also, it is doubtful that the energy broadening associated with dense beams[118] is important since beam currents leaving the gun are only about 2 μA.

In summary, we can only conclude that the situation with regard to an "expected" energy distribution is indeed confusing and requires further study.

4.4.3.2. Angular divergence

Since the angular resolution of the exit end of the scattering chamber has been designed to be comparable to that of the incident beam, it is not possible to measure them separately. However, an effective overall angular resolution for the system can be determined simply by measuring the current reaching the first dynode of the multiplier as a function of the rotation angle of the gear wheel, with the scattering chamber evacuated. This has been done under many conditions. Two such profiles obtained under different beam conditions (but the same aperture geometry) are shown in figure 4.4-4.

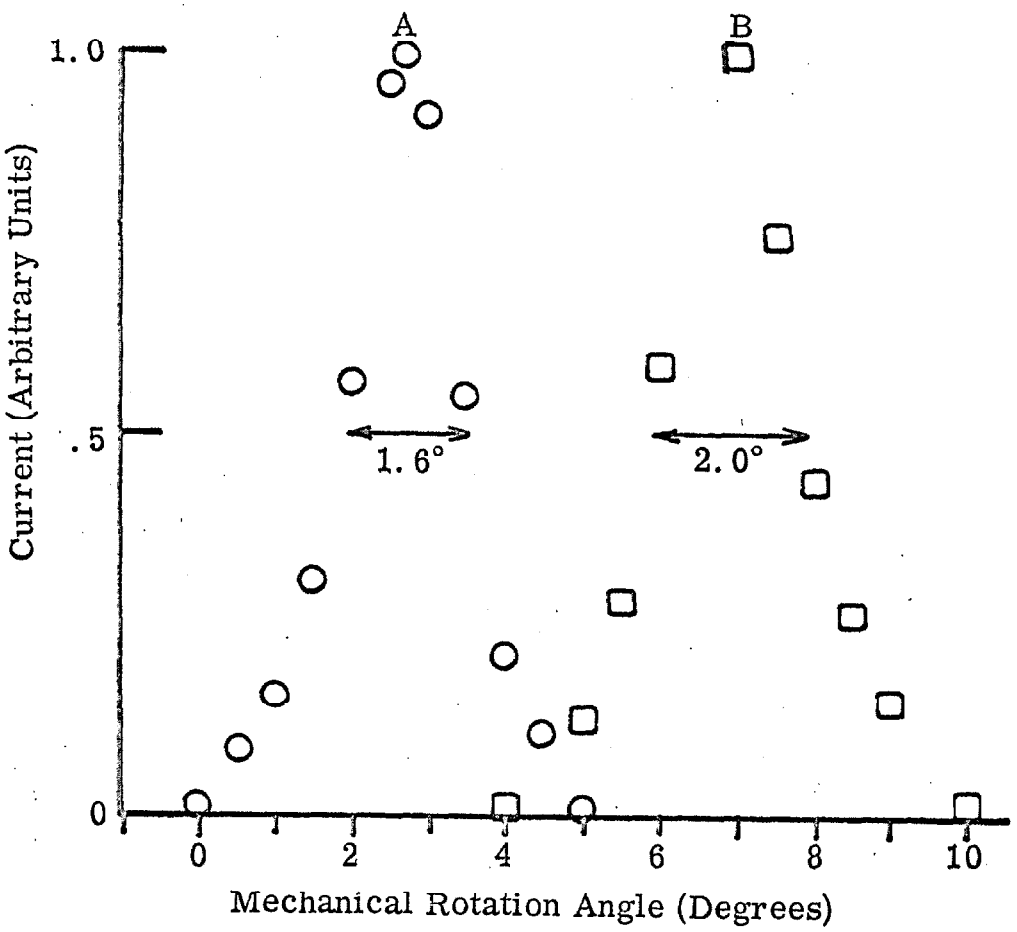

Figure 4.4-4. Effective angular profiles of the electron beam at the scattering chamber. The current is measured at the 1st dynode of the multiplier as a function of the mechanical rotation angle of the gear wheel.

	Curve A	Curve B
Incident beam energy	50 eV	30 eV
Peak current (1st dynode)	1.2×10^{-9} A	1.7×10^{-9} A
FWHM (energy distribution)	0.10 eV	0.10 eV
FWHM (angular distribution)	1.6°	2.0°
Base width (angular distribution)	5°	6°
Apertures used	Discussed in section 4.2 (same for both)	

Note that the shapes are nearly Gaussian but that the peaks occur at angles significantly different from mechanical 0°. (Mechanical 0° is the angle for which a direct "line-of-sight" was obtained through the scattering chamber and the apertures of lens systems 1 and 2. It is not possible to "see" through the chamber at a mechanical rotation angle greater than $\pm 1\frac{1}{2}°$.)

The effect of magnetic fields on the mechanical rotation angle of the direct beam was tested by using the Helmholtz coils to vary the residual field in both magnitude (from near $\lesssim 5$ m gauss to 100 m gauss) and direction (maximum field component along the X, Y, or Z coil-pair axis as well as several positions in between). Although the peak angle could be changed by $\sim 5°$, the peak symmetry was destroyed. Also, the resolution and beam current were drastically affected (unfavorably). When the residual magnetic field was ~ 5 m gauss or less, I_{FC} was found to be independent of rotation angle (as expected) from 0° – 85°. However, if the residual field was varied by enough (~ 20 m gauss) to change the beam angle by as much as 1°, I_{FC} was observed to change by 15% or more over the same angular range.

This effect (direct beam angle different from mechanical 0°) seems to be an electron-optical one. The angle of entrance into the scattering chamber is defined in part by aperture A4 but also by the position of the beam leaving the monochromator and the deflector plate voltages (fig. 4.2-8). Indeed, the angle for maximum beam current through the scattering chamber was found to depend strongly ($\pm 5°$) on these controls.

As a result, all scattering measurements were made at mechanical rotation angles below 0° as well as above. The 0° scattering angle was then defined as the angle about which the particular process was symmetric.

It is also of interest to assess what effect the angular resolution will have on the measurement of differential scattering cross sections (DCS). Suppose the instrument is set at a scattering angle θ_o. The true DCS can be expanded in a Taylor series about this angle as

$$\sigma(\theta) = \sigma(\theta_o) + \left(\frac{\partial\sigma}{\partial\theta}\right)_{\theta_o}(\theta - \theta_o) + \frac{1}{2}\left(\frac{\partial^2\sigma}{\partial\theta^2}\right)_{\theta_o}(\theta - \theta_o)^2 + \frac{1}{6}\left(\frac{\partial^3\sigma}{\partial\theta^3}\right)_{\theta_o}(\theta - \theta_o)^3 + \text{order } (\theta - \theta_o)^4 \quad . \tag{4-94}$$

If a Gaussian angular acceptance function of FWHM = $\Delta\theta_{\frac{1}{2}}$ is assumed, the measured cross section at θ_o will be

$$\sigma_{EXP}(\theta_o) = \frac{1}{\sqrt{\pi}\,A}\int_{-\infty}^{\infty} e^{-(\theta - \theta_o)^2/A^2}\,\sigma(\theta)\,d\theta \tag{4-95}$$

where

$$A^2 = \frac{\Delta\theta_{\frac{1}{2}}^{\,2}}{4\ln 2} \quad .$$

Substitution of (4-94) into (4-95) and integration yields

$$\sigma_{EXP}(\theta_o) = \sigma(\theta_o) + \frac{1}{4}A^2\left(\frac{\partial^2\sigma}{\partial\theta^2}\right)_{\theta_o} + \text{order } A^4\left(\frac{\partial^4\sigma}{\partial\theta^4}\right)_{\theta_o} \quad . \tag{4-96}$$

As one would expect, if the curvature of the DCS $(\frac{d^2\sigma}{d\theta^2})$ is small compared to the FWHM of the beam profile (in angle), the shape of the experimental cross section will agree with that of the true one.

Let us consider a specific example. Simpson, et al.[31] have measured the relative DCS for the $1^1S - 2^1P$ excitation in helium with an angular resolution of less than 1° and a beam energy of 56.5 eV. This cross section varies about as rapidly with angle as the steepest ones measured in this research. The maximum curvature occurs at about $\theta_o \approx 22°$ and, in terms of the value of the cross section at that angle,

$$(\frac{\partial^2\sigma}{\partial\theta^2}) \approx .024\,\sigma\,(22°) \text{ per (degree)}^2 .$$

Thus, with $\Delta\theta_{\frac{1}{2}} = 2°$, equation (4-96) implies that

$$\sigma_{EXP}(22°) \approx 1.009\,\sigma_S(22°)$$

where $\sigma_S\,(22°)$ is the value for the relative cross section obtained by Simpson[31]. This is a negligible distortion.

4.4.3.3. Line shape

The expected line shape from the monochromator (that is, the energy distribution of the electron beam after one energy analysis) has been previously discussed in section 4.1. Equation (4-39) has been used to calculate the line shape for several different values of the parameters involved. The resulting line shapes were then

compared with Gaussians of the same FWHM. Such a comparison is shown in figure 4.4-5 in which the solid line is the Gaussian and the circles are the calculated (equation (4-39)) values. As expected, the agreement is quite good. However, this line shape cannot be compared directly with experimental energy distributions as measured at the first dynode since a second analyzer (selector) with the same intrinsic line shape is used to measure them. Consequently the convolution of the line shape with itself should be used for the comparison. Since this is a rather tedious problem in numerical integration and since a simple Gaussian function seems adequate, the convolution of two Gaussians (which is Gaussian itself, as shown in appendix I) can be compared with experiment. Figure 4.4-6 shows such a comparison in which the solid line is a Gaussian of the same FWHM as the experimental data (circles). Again, the agreement is reasonably good.

4.4.3.4. Current versus resolution

Since the electron energy distribution from the gun (section 4.4.3.1) and the line shape of the monochromator (section 4.4.3.3) have already been determined, it is possible to estimate the current I_s one should expect at the scattering chamber. If, for mathematical simplicity, it is assumed that the monochromator passes a "slice" (of FWHM = $\Delta E_{\frac{1}{2}}$) of the current distribution of equation (4-91) centered at the peak position of that distribution, then

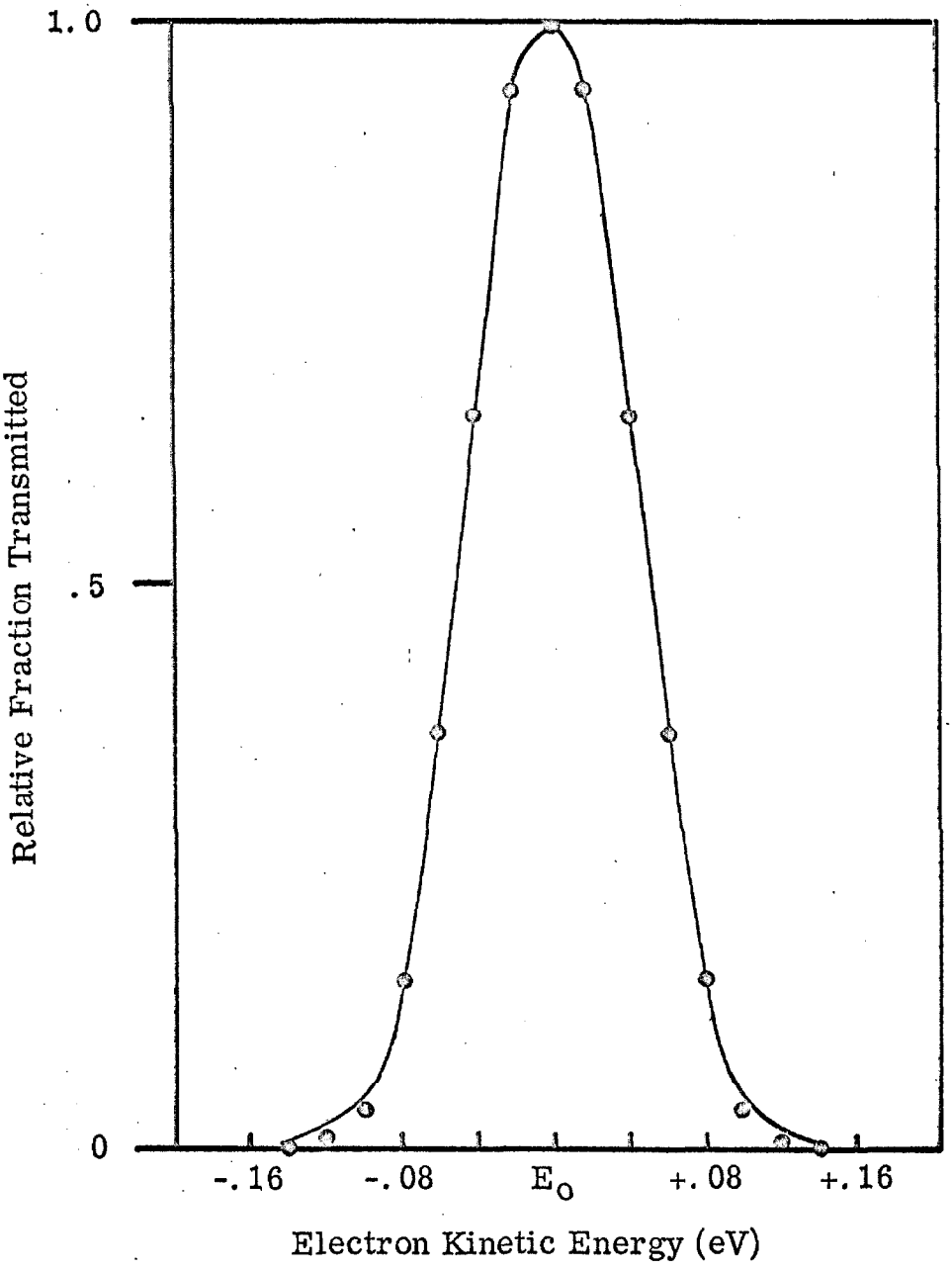

Figure 4.4-5. Comparison of the line shape calculated according to equation (4-39) (circles) and a simple Gaussian of the same FWHM (solid line). The parameters used in equation (4-39) were E_o = 10 eV, a = b = .012", R_o = 1".

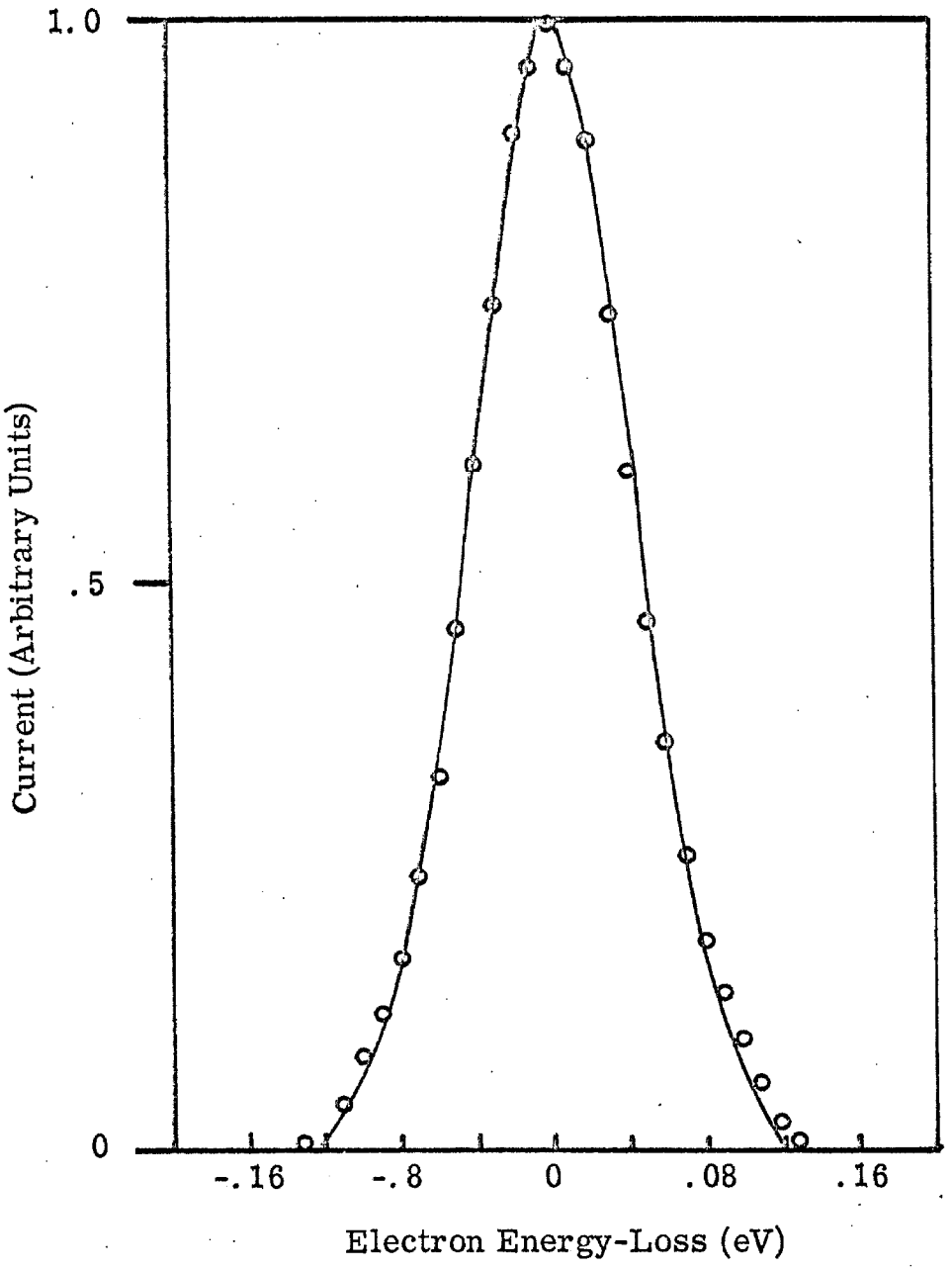

Figure 4.4-6. Comparison of the electron beam energy distribution as measured on the first dynode of the multiplier with a Gaussian of the same FWHM. 35 eV incident beam energy, 1.3×10^{-9} A peak current. The peak position is defined as 0 energy-loss.

$$I_s(\Delta E_{\frac{1}{2}}, kT) \approx \frac{I_o}{(kT)^2}\left(1 + \frac{w}{kT}\right) \int_{E_o - \frac{\Delta E_{\frac{1}{2}}}{2}}^{E_o + \frac{\Delta E_{\frac{1}{2}}}{2}} E\, e^{-E/kT}\left[1 - \frac{w}{E}\left(1 - e^{-E/w}\right)\right] dE \tag{4-97}$$

in which T is the cathode temperature in °K, I_o is the total current entering the monochromator, w is the reflection parameter and E_o is the peak of distribution (4-91). Since the cathode was ordinarily operated under the same conditions as those represented in figure 4.4-3, it will be assumed that the parameters associated with this figure may be used in (4-97), i.e., $E_o \approx 0.40$ eV, $kT \approx 0.22$ eV, and $w \approx 0.19$ eV. Integration of (4-97) yields

$$\frac{I_s}{I_o} = 2\left(1 + \frac{w}{kT}\right) e^{-E_o/kT}\left[\left(1 + \frac{E_o - w}{kT}\right) \sinh\left(\frac{\Delta E_{\frac{1}{2}}}{2kT}\right)\right.$$

$$\left. + \frac{w^2\, e^{-E_o/w}}{(kT)^2\left(1 + \frac{w}{kT}\right)} \sinh\left[\frac{\Delta E_{\frac{1}{2}}}{2}\left(\frac{1}{kT} + \frac{1}{w}\right)\right] \right. \tag{4-98}$$

$$\left. - \frac{\Delta E_{\frac{1}{2}}}{2kT} \cosh\left(\frac{\Delta E_{\frac{1}{2}}}{2kT}\right)\right] .$$

Figure 4.4-7 shows the behavior of (4-98) for the parameter values indicated above. Some typical values actually obtained for this ratio are also plotted in the figure for comparison. Table 4.4-1 gives the experimental conditions under which these data were taken. The measured fraction is considerably below the expected one. This same kind of behavior has been observed by Simpson[24]. Also, the current obtained at the scattering chamber is a steep function of

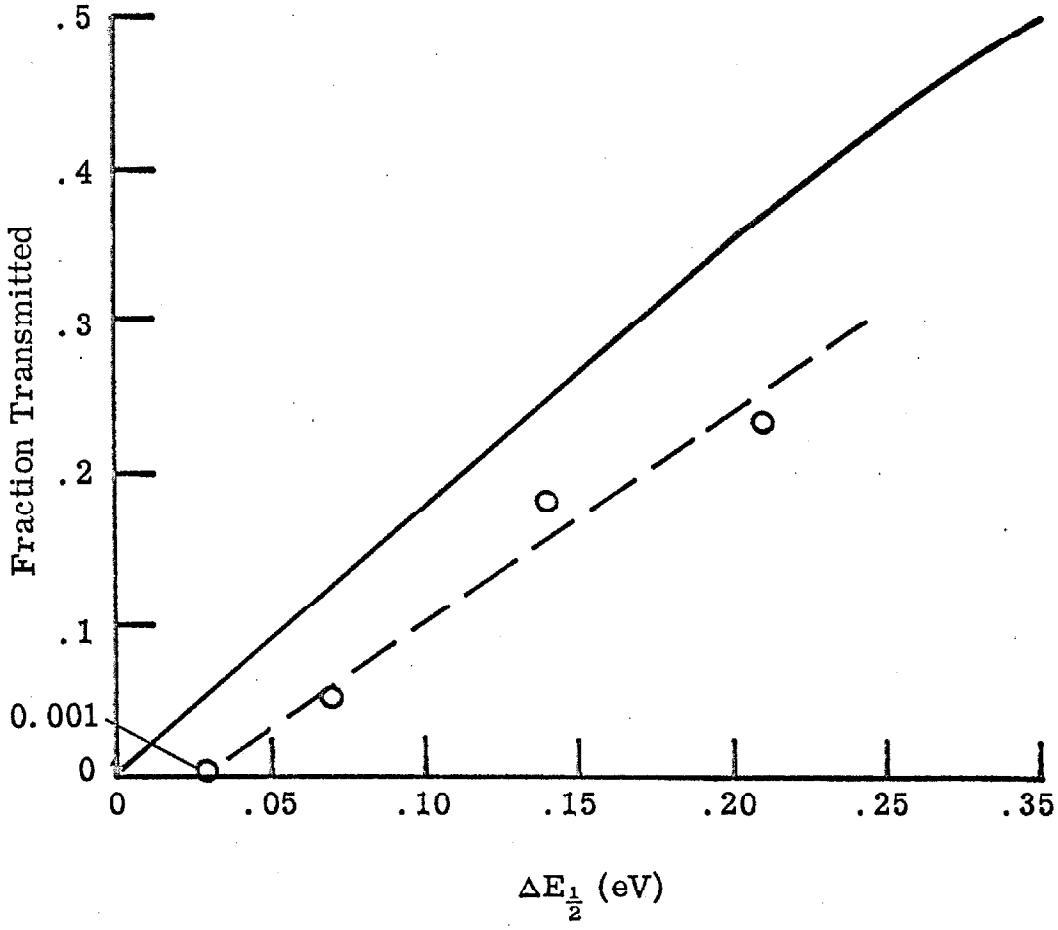

Figure 4.4-7. Fraction of the current entering the monochromator which gets into the scattering chamber. $\Delta E_{\frac{1}{2}}$ is the FWHM associated with the monochromator (FWHM as measured by the selector times 0.7). The solid curve was calculated according to equation (4-98). The circles are experimentally determined by measuring the ratio of current to the faraday cup to that leaving the gun (refer to table 4.4-1 for the operating conditions). (0.001) refers to the ordinate of the indicated point.

TABLE 4.4-1

Operating conditions for the data presented in figure 4.4-7. The spectrometer construction details are in section 4.2. The electron-optical element voltage abbreviations have been defined in table 4.3-2.

V_{RVS} (volts)	-25	-35	-35	-65
Current into monochromator (μA)	1.0	1.3	1.5	2.2
V_{CVM} (volts)	1.5	3.0	3.0	4.5
$\Delta E_{\frac{1}{2}}$ monochromator (m eV)	.03	.07	.14	.21
Current into scattering chamber (μA)	.001	.033	.27	.51

$\Delta E_{\frac{1}{2}}$. Figure 4.4-8 shows this current (curve T) for the same type of conditions under which the experimental ratios of figure 4.4-7 were determined. Curve M represents the maximum values yet observed. Maximum values reported by Kuyatt and Simpson[25] and Meyer, et al.[21] are shown for comparison. Both of these investigators used double-hemispherical analyzers but with different dimensions and different energies of operation. The former authors used analyzers of 1" mean radii and analyzing energies of ~5 eV while the latter ones used analyzers of 5" mean radii and ~200 eV analyzing energies. The maximum values we obtain compare favorably with these investigators. Also, the overall second stage collection efficiency (~ .10) defined as I_{FD}/I_{FC}, compares well with that reported by Kuyatt[25] (~.08).

4.4.3.5. Contact potential

The electron beam kinetic energy E in the scattering chamber differs from eV_c by an "effective contact potential energy" $e\bar{V}_c$, on the order of 1 or 2 eV[24]. Since the contact potential between the monochromator and scattering chamber is negligible[119] (tens of mV) on this scale, the full effect of $\bar{V}_c$ will be apparent in the monochromator. $\bar{V}_c$ includes the offset between the peak of the electron energy distribution and the zero of energy at the center tap of the cathode (~.4 eV), IR drops in the cathode circuit, and the true contact potential between the monochromator and the hot tungsten filament[24].

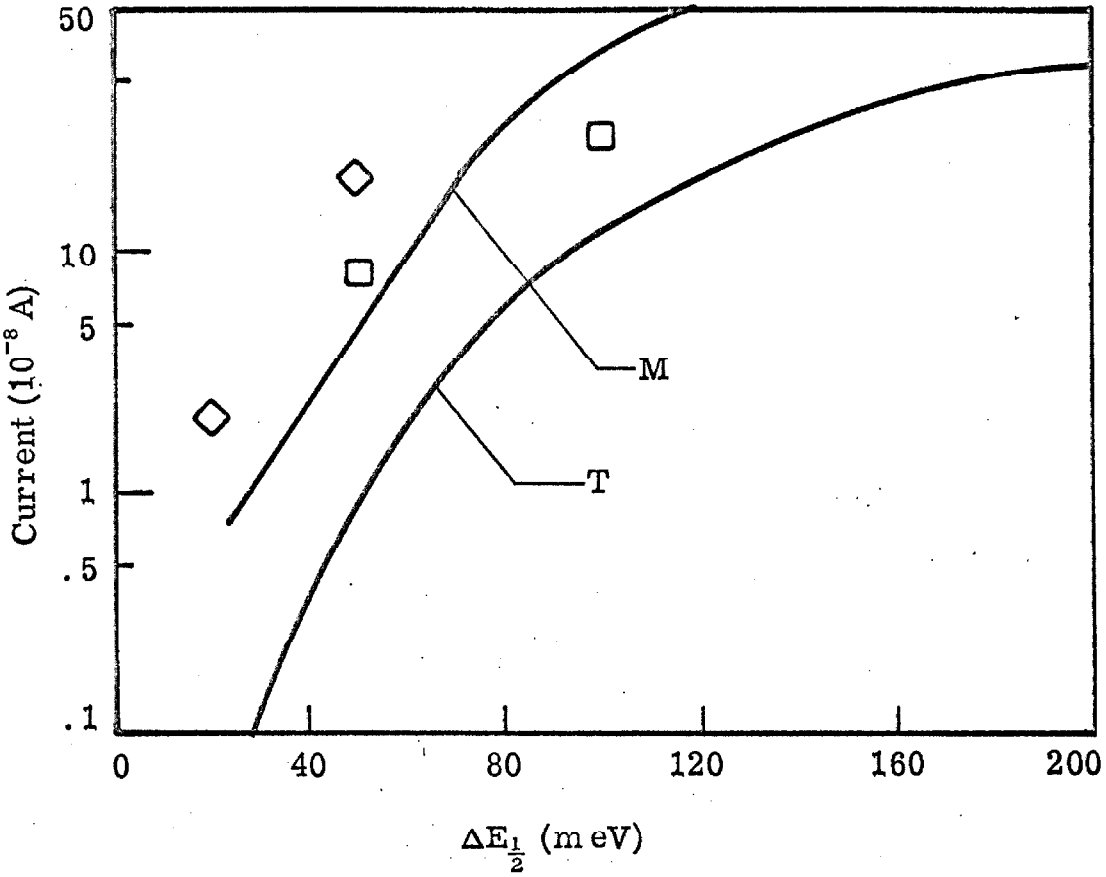

Figure 4.4-8. The variation of beam current into the scattering chamber with the resolution of the monochromator. The solid curve (T) was obtained under the conditions of fig. 4.4-7, the solid curve (M) represents values we obtained, the (◇) values are reported in reference (25); and the (□) values are the maximum ones reported in reference (21). $\Delta E_{\frac{1}{2}}$ is the FWHM of the monochromator (FWHM as measured by the selector times 0.7).

From equation (4-19), the voltage across the spheres ΔV and the kinetic energy E_o of an electron which will describe a circular orbit of radius R_o are related by $E_o = q\Delta V(\frac{R_2}{R_1} - \frac{R_1}{R_2}) = 1.91\, q\Delta V$ (in this case $R_1 = .875''$, $R_2 = 1.125''$). The true electron K.E. in the monochromator will be $qV_{CVM} + q\bar{V}_C$. Thus,

$$\bar{V}_C = 1.91\,\Delta V - V_{CVM} \quad . \tag{4-99}$$

Since ΔV and V_{CVM} are known applied voltages, $\bar{V}_C$ is determined. (Note that for a given V_{CVM}, ΔV is the voltage needed to maximize the current to the scattering chamber.) Values of $\bar{V}_C$ from .02 V to 2.3 V have been observed (usually they are $\sim$ 1 V as determined by (4-99)).

4.4.3.6. Resolution versus analyzing energy

From equation (4-29) the resolution of the monochromator should vary as

$$\Delta E_{\frac{1}{2}} \approx .01\, E_o \tag{4-100}$$

if the angular terms are negligible and the apertures are imaged properly by the lens systems. Figure 4.4-9 shows a comparison between the calculated resolution according to (4-100) (solid line) and the measured resolution (circles) of the monochromator. The effective contact potential has been incorporated into E_o. For this measurement $V_{H1} = V_{H2} = V_{CVM}$ and $V_{LVL1} = V_{LVL2} = 0$ with respect to ground. In this way the lenses which image the beam into the monochromator and scattering chamber should perform as

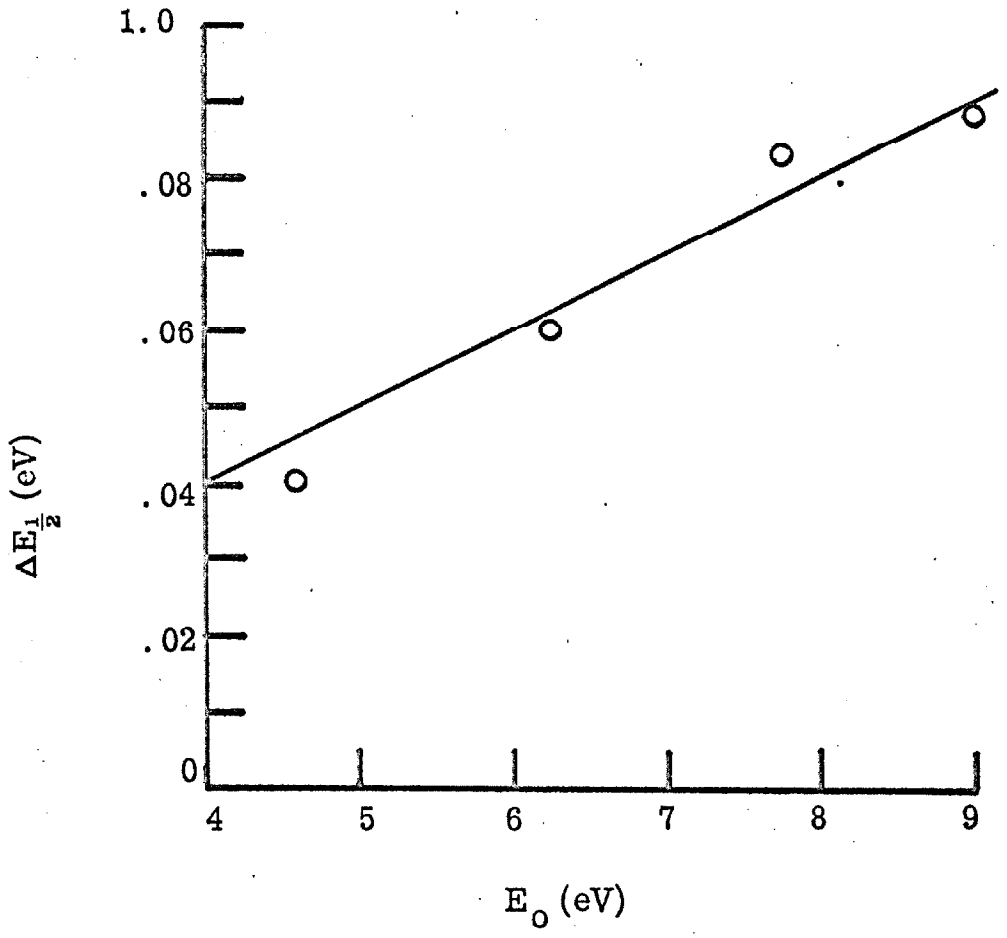

Figure 4.4-9. Variation of the resolution with the electron kinetic energy in the analyzer. $\Delta E_{\frac{1}{2}}$ is the FWHM associated with the monochromator. E_o includes the "effective contact potential" discussed in section (4.4.3.5). The solid line is calculated according to (4-100) and the circles are experimentally determined under the conditions described in the text.

initially intended. Also, the voltage ratio V_{RVS}/V_{CVM} was kept constant at about 10. The agreement is reasonably good. However, it should be noted that the beam currents into the scattering chamber obtained under these conditions were about a factor of 5 below those labelled typical in figure 4.4-8. The independent variation of V_{H1}, V_{H2}, V_{LVL1}, and V_{LVL2} evidently changes the effective image sizes which determine the monochromator resolution. It was found (see table 4.4-1) that, for a given resolution, a higher V_{RVS}/V_{CVM} ratio (~ 15) coupled with changes in the voltages above produced more intense beams than V_{RVS}/V_{CVM} ratios of about 10 with or without offsetting V_{H1}, V_{H2}, V_{LVL1}, and V_{LVL2}.

4.4.4. Relation of the Differential Scattering Cross Section to the Scattered Signal

4.4.4.1. Calculation

As previously stated, it is one of the aims of these experiments to obtain differential scattering cross sections for various molecular excitations. Thus, it is essential to relate the final signal (at the multiplier) to the cross section.

Consider the configuration depicted in figure 4.4-10. In order for an electron to get through S (and have any chance of being detected) after a single scattering event, it must scatter while in volume $V(\theta)$ at an appropriate angle χ near θ. If I_o is the total beam intensity entering the scattering chamber containing the target gas at a density ρ, the unscattered beam I_u reaching the scattering volume is given by

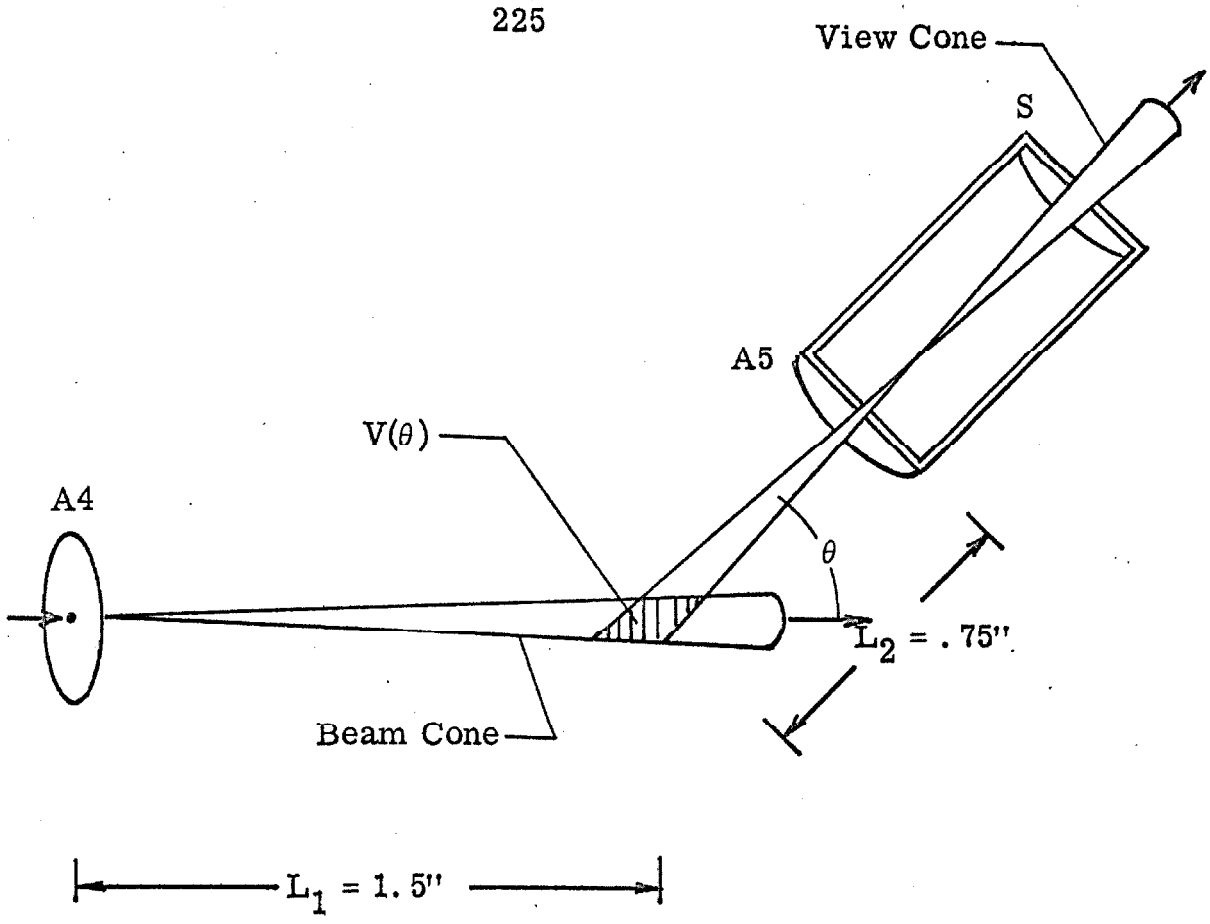

Figure 4.4-10. Schematic diagram of the incident and scattered beam configuration at a scattering angle of θ ($\sim 45°$). L_1 and L_2 are the distances from the scattering center to A4 and A5, respectively. $V(\theta)$ is the volume in which single scattering events must occur if they are to be detected.

$$I_u \cong I_o \, e^{-\bar{Q}(E_o)\rho L_1} \tag{4-101}$$

in which $\bar{Q}(E_o)$ is the average total scattering cross section for electrons in the beam and L_1 is the distance from aperture A4 to the scattering center.

$$\bar{Q}(E_o) \equiv \int_{-\infty}^{\infty} f(E_o - E)\, Q(E)\, dE \tag{4-102}$$

where Q(E) is the total cross section for all scattering processes for electrons of kinetic energy E and $f(E_o - E)$ is the incident beam energy distribution, normalized to unity and peaked at E_o.

Equation (4-101) is only approximately correct since different parts of the electron beam have different electron densities and travel different distances. Nevertheless, it is probably a very good approximation in this case.

The current $i_{SC}dE$ per unit solid angle and energy-loss due to electrons with incident energies E to E + dE, which scatter in this volume at an angle χ after losing an energy W is

$$i_{SC}dE \cong I_u \frac{V(\theta)}{A} \sigma(E, W, \chi)\, \rho\, f(E_o - E)dE \tag{4-103}$$

where $\sigma(E, W, \chi)$ is the DCS per unit solid angle and energy-loss for the particular process, and A is the cross-sectional area of the beam at the scattering center.

Since the scattered beam is attenuated approximately by a factor $e^{-\rho \bar{Q}(E_o - W)L_2}$ before reaching A5, the current $I_{SC}dE$ per unit energy-loss leaving the scattering chamber through aperture S

is then

$$I_{SC}dE \cong e^{-\rho\bar{Q}(E_o - W)L_2} dE \int_{\Omega} i_{SC}\, d\Omega, \qquad (4\text{-}104)$$

in which the Ω integration is over the range of angles accepted by the exit aperture system.

Assume that the selector is tuned to pass electrons that have lost an energy W with an efficiency $\epsilon_S(W)$. The current actually detected is then

$$I_D \cong \int_E \int_W \epsilon_1 \epsilon_S \epsilon_2 \epsilon_3 I_{SC}\, dE\, dW \quad , \qquad (4\text{-}105)$$

in which ϵ_1 is the fraction of electrons leaving S which reach the selector, ϵ_2 is the fraction of electrons through A6 (refer to fig. 4.2-12) which reach the first dynode of the multiplier, and ϵ_3 is the fraction of electrons hitting the first dynode which are actually counted. The integration is over all E and W (the distributions $f(E_o - E)$ and $\epsilon_S(W)$ are sharply peaked, thus limiting the effective range of this integration). Notice that the sweep voltage V_{SWP} is assumed constant. $\epsilon_S(W)$ can be written more explicitely as

$$\epsilon_S(W) = \epsilon_S{}^{o}(E_{SWP})\, e^{-(E_{SWP} - W)^2/\Delta^2}$$

where Δ is related to the selector resolution, $E_{SWP} = |e|V_{SWP}$, and $\epsilon_S{}^{o}(E_{SWP})$ is the fraction of electrons entering the analyzer after suffering the energy-loss $W = E_{SWP}$ which actually pass through A6.

Combining equations (4-101) through (4-105) we obtain:

$$I_D \cong I_o \frac{V(\theta)}{A} p\, e^{-\rho \bar{Q}(E_o) L_1} \int_W \int_E \int_\Omega$$

$$\times \left[\epsilon_1 \epsilon_2 \epsilon_3 \epsilon_S(W) f(E_o - E)\, \sigma(E, W, \chi)\right] \qquad (4\text{-}106)$$

$$\times \left[e^{-\rho \bar{Q}(E_o - W) L_2}\, d\Omega\, dE\, dW\right] .$$

$f(E_o - E)$ is a narrow enough distribution (FWHM $\approx$ .07 eV) so that variations in electron-optical properties (ϵ_1, ϵ_2, ϵ_3, and ϵ_S) and the variations in $\sigma(E, W, \chi)$ over the range of E for which f is appreciable are negligible in the absence of resonances[120].

The range of acceptance angles (Ω) is small enough in most cases (section 4.4.3.2) so that $\sigma(E, W, \chi)$ can be removed from the Ω integral as well as the E one and be replaced by $\sigma(E_o, W, \theta)$.

$\bar{Q}(E_o - W)$ and the various electron-optical effects vary slowly enough with W that they may be assumed constant over the range of $\epsilon_S(W)$ (about .07 eV also).

The application of the approximations discussed above and the ideal gas law to convert ρ to a sample pressure P reduce equation (106) to

$$I_D(E_{SWP}, \theta) \cong \frac{I_o V(\theta)}{AkT} \Delta\Omega P\, e^{-P/P_o}\, \epsilon(E_{SWP})\, \bar{S}(E_o, E_{SWP}, \theta) \qquad (4\text{-}107)$$

with

$$\Delta\Omega \equiv \int_\Omega d\Omega \text{ (the acceptance solid angle defined by A5}$$

and S),

$$\bar{S}(E_o, E_{SWP}, \theta)$$

$$\equiv \frac{1}{\sqrt{\pi}\,\Delta} \int_W \sigma(E_o, W, \theta)\, e^{-[E_{SWP} - W]^2/\Delta^2}\, dW \ ,$$

$$\epsilon(E_{SWP}) \equiv \epsilon_1 \epsilon_2 \epsilon_3 \epsilon_S{}^o \sqrt{\pi}\,\Delta$$

$$P_o \equiv kT/(\bar{Q}(E_o)L_1 + \bar{Q}(E_o - E_{SWP})\,L_2) \ ,$$

k is Boltzmann's constant ($\approx 1.03 \times 10^{-19}$ torr - cc/°K), and T is the sample temperature in °K.

In the following sections we shall discuss some aspects of the application of (4-107) to obtain the DCS (σ) from a measurement of I_D.

4.4.4.2. Pressure dependence

It has been pointed out[121] that double scattering events may cause serious errors in the measurement of differential scattering cross sections. This problem seems most severe for inelastic processes measured at large scattering angles and high incident energies. However, the demonstration that the pressure dependence indicated by equation (4-107) holds at every angle, for all incident energies, and for every process investigated is sufficient to insure that only single scattering events are contributing to the measured signal. Although such a complete study is indeed

sufficient, it may not be necessary. It seems more "economical" to determine the particular experimental conditions we might use for which double scattering would have the highest probability and then demonstrate that (4-107) holds in this case (i.e., that under our experimental conditions, we do not detect double scattering events).

The principal contribution to double scattering usually comes from large-angle elastic scattering in or near the scattering volume V preceded, or followed, by small-angle inelastic scattering along the view cone[121]. In particular, the current (I_2) due to electrons which have scattered twice compared to that (I_1) due to electrons which have scattered once varies approximately as

$$\frac{I_2(\theta)}{I_1(\theta)} \approx \frac{\rho \ell_{eff} < \sigma(E_o, 0, \theta')\sigma(E_o, W, \theta - \theta') >_{\theta'}}{\sigma(E_o, W, \theta)} \qquad (4\text{-}108)$$

where $\sigma(E_o, W, \theta)$ is the differential cross section for the particular inelastic process being considered, $\sigma(E_o, 0, \theta)$ is that for the elastic one, and ℓ_{eff} is an "average" scattering path length on the order of $L_1 + L_2$. $< \sigma(E_o, 0, \theta')\ \sigma(E_o, W, \theta - \theta') >_{\theta'}$ is the DCS product averaged over all possible combinations of scattering angles for the two events which would be detected as if from a single scattering event occurring within V at an angle θ.

At incident energies high enough for the Born approximation to be valid, $\sigma(E_o, W, \theta)$ is much more sharply peaked forward than is $\sigma(E_o, 0, \theta)$[122]. The principal contribution to the average in (4-108)

will come from terms in which $\theta - \theta' \approx 0$. Thus,

$$\frac{I_2(\theta)}{I_1(\theta)} \sim \rho \ell_{eff} \frac{\sigma(E_o, 0, \theta)\, \sigma(E_o, W, 0)}{\sigma(E_o, W, \theta)} \qquad (4\text{-}109)$$

under these conditions and double scattering becomes increasingly more important at higher scattering angles[121].

In the lower energy range in which we operate, the situation is not so clear. Inelastic processes, though certainly less intense, do not seem to decrease much more rapidly with angle than the elastic one. For example, the ratio of elastic to inelastic ($\tilde{X}^1\Sigma_g^+ \rightarrow \tilde{C}^1\Pi_u$) scattering in acetylene was found to be constant from $40° \rightarrow 80°$ at an impact energy of 35 eV. In addition, spin-exchange inelastic processes are often nearly isotropic, and hence the ratio of inelastic to elastic scattering is actually smallest at small angles.

For cases in which the elastic/inelastic ratio is nearly constant with angle, the value of the cross section product in (4-108) will be the same at both high and low θ'. If it is assumed that the principal contribution to the product is for $\theta' \approx 0$,

$$\frac{I_2(\theta)}{I_1(\theta)} \sim \rho \ell_{eff} \sigma(E_o, 0, 0) \quad . \qquad (4\text{-}110)$$

(4-110) implies, as expected, that double scattering will be least important in those instances for which the forward elastic DCS is lowest, regardless of the magnitude of the inelastic DCS. It also indicates that the effect is independent of angle.

Finally, there is the case of spin-exchange excitations in which $\sigma(E_o, W, \theta)$ can be assumed to be independent of angle but $\sigma(E_o, 0, \theta)$ is still forward peaked. The result (4-110) is also obtained under these conditions.

In conclusion, it seems that the relative effect of double scattering will not be highly angular dependent for low (< 50 eV) incident energies. Thus, checking relation (4-107) as a function of pressure at one high and one low angle for the most sharply forward peaked cross section should be sufficient. Parenthetically, Doering[36c] did not observe double scattering effects at 90° scattering angles and .05 torr sample pressures for low incident energies (of the order of 10-30 eV).

Finally, let us consider a specific example. The natural logarithm of (4-107) can be written as

$$\ell n \left(\frac{I_D}{I_o P}\right) = C(E_{SWP}, \theta) - P/P_o \qquad (4\text{-}111)$$

in which $C(E_{SWP}, \theta) \equiv \ell n\left\{\frac{V(\theta)\Delta\Omega}{A\,kT}\, \epsilon\,(E_{SWP})\, \bar{S}(E_o, E_{SWP}, \theta)\right\}$.

It is clear from (4-111) that a plot of $\ell n \left(\frac{I_D}{I_o P}\right)$ versus P should be a straight line of slope $-P_o^{-1}$ for single scattering. Figure 4.4-11 shows the results of such a plot for two transitions in helium ($1^1S \rightarrow 2^3P$, nearly isotropic $\sigma(E_o, W, \theta)$; $1^1S \rightarrow 2^1P$, forward peaked one) at two scattering angles (20° and 70°). The dashed line has a slope of -25 torr^{-1}. The ordinate has been shifted by an arbitrary constant for each of the four sets of data points at each angle.

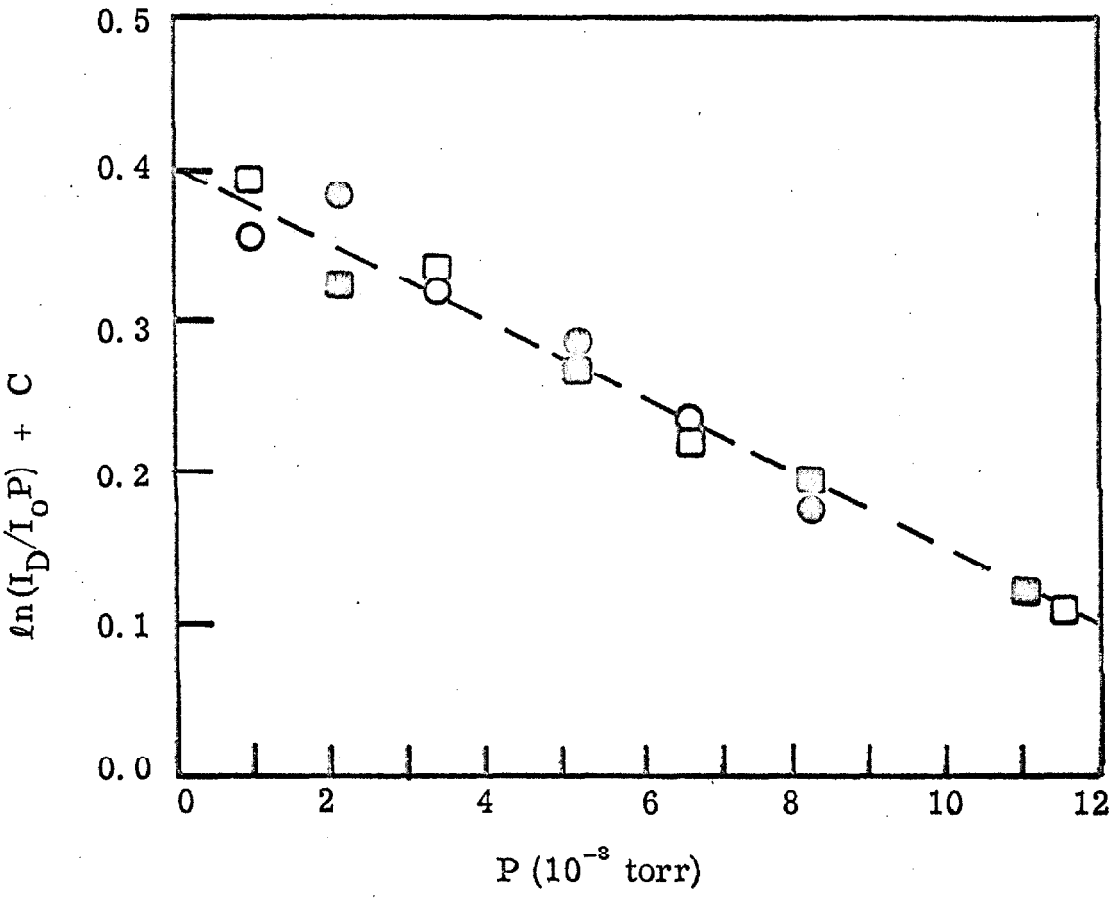

Figure 4.4-11. Demonstration of single scattering in helium. The pressure P is the reading of an uncalibrated ion-gage multiplied by 7 (to correct for the ionization efficiency difference between N_2 and He). The $\ell n\ (I_D/I_0P)$ was computed in arbitrary units for each of the four sets of data points: (○) $2^1P, \theta = 20°$; (□) $2^3P, \theta = 20°$; (⊙) $2^1P, \theta = 70°$; (▣) $2^3P, \theta = 70°$. The constant C was determined by normalizing the four data sets to the dashed line at the highest pressure side (where the signal was largest).

An attenuation in the direct beam of about 10 ± 3% was observed at 5×10^{-3} torr which indicates that $P_o \approx .05 \pm .02$ torr. P_o can also be estimated if values are assumed for the cross sections and path lengths involved. Choosing $\bar{Q}(45\text{ eV}) = 1.5\text{Å}^{(6e)}$, $\bar{Q}(24\text{ eV}) = 2.3\text{Å}^{(6e)}$, $L_1 = 3.8$ cm, and $L_2 = 1.9$ cm, implies that $P_o \approx .03$ torr (P_o was defined in equation (4-107)). Phenomenologically, P_o is the pressure (for a given apparatus, incident energy, and scattering sample) for which the mean free path of an electron in the scattering chamber is equal to the length of that chamber.

4.4.4.3. Energy-loss efficiency

Equation (4-107) was derived assuming that $\epsilon(E_{SWP})$ was a slowly varying function of E_{SWP} over a range of $\sim .07$ eV. At this point, we shall endeavor to show that ϵ is essentially independent of E_{SWP} over a range of ~ 10-20 eV. The importance of this energy-loss independence is evident from equation (4-107). At a fixed scattering angle θ and incident energy E_o, an energy-loss spectrum is obtained (refer to section 4.3.4.2) by varying V_{SWP} (and consequently E_{SWP}). In order to relate the scattered intensities (I_D) observed at different values of E_{SWP} to the effective differential cross sections $\bar{S}(E_o, E_{SWP}, \theta)$ for these values of the energy-loss, it is essential that $\frac{d\epsilon}{dE_{SWP}}$ be zero or a known function of E_{SWP}. Due to the extreme difficulty in actually measuring such a dependence, the former alternative is a practical necessity.

Consider a scattered electron beam composed of an elastically scattered (K.E. of E_o) and an inelastically scattered (K.E. of E_o - W) component. Assume that V_{LVL3}, V_{H3}, V_{CVS} ($=V_{H4}$), ΔV_S, V_{TL1}, V_{TL2}, and V_{DP3} have been adjusted for a maximum transmission of the elastically scattered component (case (1), $V_{SWP} = 0$) for a given resolution. Then change $|e|V_{SWP}$ to W (all other voltages unchanged) to transmit the inelastically scattered component (case (2)) and consider the changes, if any, in the electron-optical properties of the lenses and selector.

In case (1) the electrons are decelerated from a K.E. of E_o in the scattering chamber to $|e|V_{LVL3}$ in LVL3 while in case (2) they are decelerated from E_o - W in the scattering chamber to the same value $|e|V_{LVL3}$ in LVL3. Since the voltages of all elements from LVL3 to TL1 with respect to one another are not affected by a change in V_{SWP}, the electron-optical properties of these elements are the same for both beam components. However, the lens formed by the scattering chamber exit aperture (A5, at ground potential) and LVL3 will have different focal properties in the two cases. Likewise the lens formed by TL1 and TL2 will have a slightly different effective voltage ratio in each case. This latter effect is probably negligible since for typical cases (V_{TL2} = 250 V with respect to ground, E_o = 35 eV, W $\approx$ 15 eV, and V_{TL1} = 35 V with respect to cathode) the ratio of the K.E. in TL1 to the K.E. in TL2 would be .123 and .130 for cases (1) and (2), respectively.

The K. E. ratio between the electrons at A5 and those at LVL3 is usually near 1 (see table 4. 3. 2) for the elastic component of the beam (case (1)). For the same conditions as above, this ratio is $\approx .6$ for the inelastic component (case (2)). Both ratios are typical of weak lenses. Since the LVL-H3 pair is a relatively strong lens, (ratio ≈ 5.5) it should be much more effective in determining the image at the selector. As a result, one might expect the overall transmission to be relatively insensitive to W over a range of 10 or 20 eV. That this is indeed the case has been tested as outlined below.

The instrument is tuned for a maximum transmission of the elastically scattered current with helium in the scattering chamber. It was found that there were essentially two "modes" in which this maximum could be obtained--mode (1), in which $\frac{E_o}{|e|} \sim V_{LVL3} > V_{H3} > V_{CVS}$ as indicated in table 4. 3. 2, and mode (2), in which $\frac{E_o}{|e|} \sim V_{H3} > V_{LVL3} > V_{CVS}$. When the maximum elastic current was obtained, V_{SWP} was changed to 21. 21 V to collect the current $I_{2^1P^o}$ scattered after causing the $1^1S \rightarrow 2^1P$ (W = 21. 21 eV) transition. Then, V_{LVL3}, V_{H3}, V_{TL1}, and V_{DP3} were changed in an attempt to obtain a larger inelastically scattered current $I_{2^1P}{}^{max}$. It was assumed that the change in current would be indicative of the sensitivity of $\epsilon(E_{SWP})$ to E_{SWP} over a rather extreme range of 21. 2 eV. In other words, the smaller the percentage current change, the less ϵ varies over this range. Figure 4. 4-12 shows this

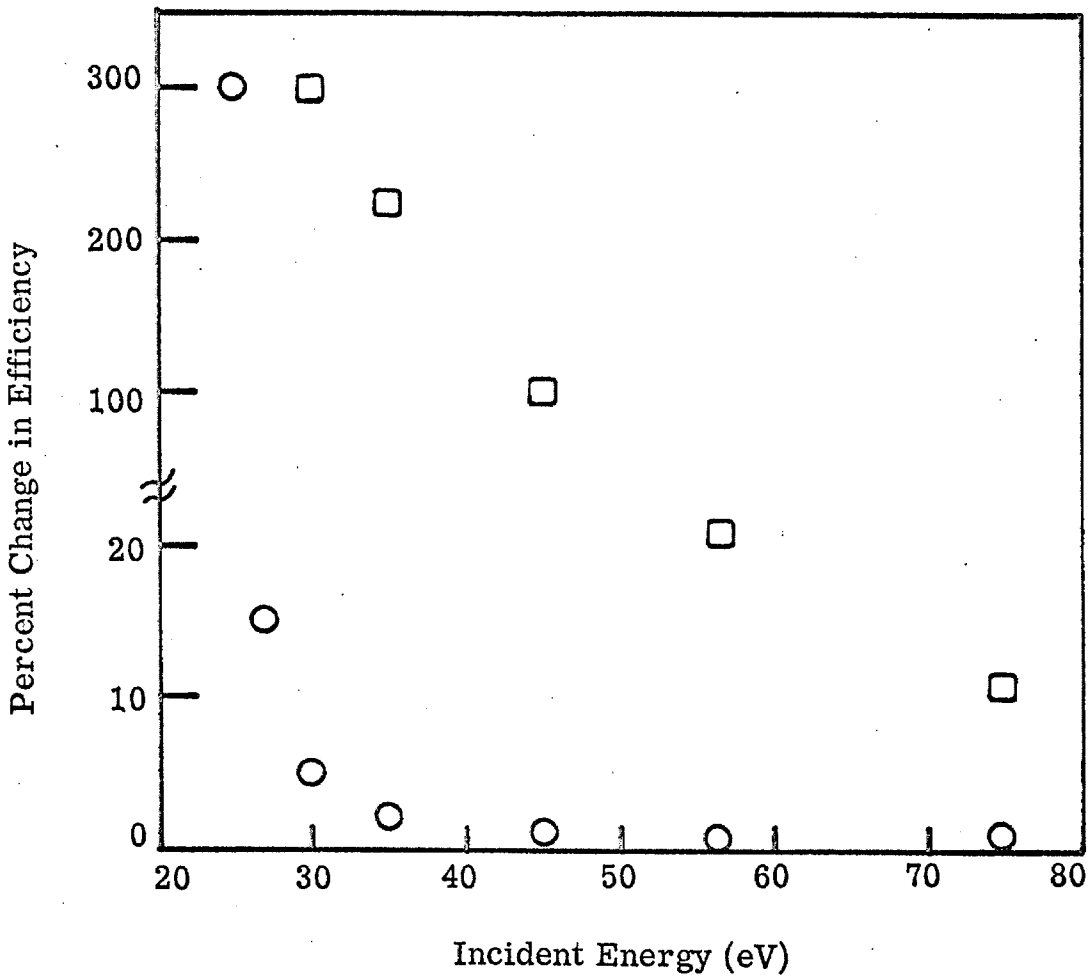

Figure 4.4-12. Percent change in efficiency for the detection of the elastic peak and the 2^1P peak (21.21 eV energy-loss) as a function of incident energy. The percent efficiency is defined as $\{(I_{2^1P}{}^{o} - I_{2^1P}{}^{max})/I_{2^1P}{}^{o}\} \times 100$. (○) mode (1) and (□) mode (2) as described in the text.

percentage change, $\{(I_{2^1P}{}^{max} - I_{2^1P}{}^{o})/I_{2^1P}{}^{o}\} \times 100$, at several incident energies for both "mode (1)" and "mode (2)" operation. Mode (2) is clearly unacceptable (as expected, since A5 - LVL3 from a strong lens in this case). Mode (1) gives acceptable performance until $(E_o - W)$ becomes less than about 7 eV. In general it was found that the instrument could be tuned such that the percentage current change as defined above was less than 3% over any 10 eV energy-loss region, provided $(E_o - W) \gtrsim 10$ eV.

4.4.4.4. Volume correction

It is apparent from figure 4.4-10 that the scattering volume is a function of the scattering angle, and further that the solid angle of acceptance $\Delta\Omega$ (defined by A5 and S) is not constant over the length of the collision volume (it is a maximum at the volume center and drops to 0 at the ends[123]). Thus, one should average the solid angle over the collision volume at each scattering angle. This would result in an effective value of scattering volume times solid angle, $(V\Delta\Omega)_{eff}$. Several calculations for experimental arrangements similar to that of figure 4.4-10 have been performed in which apertures A5 and S were assumed to be slit-slit[124], slit-hole[125], and hole-hole[126] combinations. For any particular case, the result may be expressed as

$$(V\Delta\Omega)_{eff} = \frac{B(1 + C(\theta))}{\sin\theta} \qquad (4\text{-}111)$$

where θ is the scattering angle defined by the axes of the aperture systems (θ of fig. 4.4-10), B is a constant which depends on the

geometrical arrangement, and $C(\theta)$ is a correction term which is negligible for θ large compared to the beam and view cone angles.

Since the beam and view cone angles in the present case are of the order of 4°, the quantity $(V\Delta\Omega)_{eff}$ was calculated[127] as a function of assumed beam geometries. The electron beam was considered to have a Gaussian intensity distribution of the form $e^{-\varphi^2/\alpha^2}$ where φ is the angle between a particular ray originating at A4 and the beam axis while α is the angle at which the density drops to e^{-1} of its value along the axis. For computational convenience, the intensity distribution was truncated at $\varphi = 2\alpha$. Since B (of equation (4-111)) is not important for our purposes, the values of $(V\Delta\Omega)_{eff}$ were normalized to the value obtained at $\theta = 90°$ (where $C(\theta)$ is negligible). In particular, the quantity $(V(\theta)/V(90°))_{eff}$ was determined where

$$\left[\frac{V(\theta)}{V(90°)}\right]_{eff} = \frac{(1 + C(\theta))}{\sin\theta(1+c(90°))} \cong \frac{1+C(\theta)}{\sin\theta}. \quad (4\text{-}113)$$

Figure 4.4-13 shows a plot of $C(\theta)$ for two sets of assumed conditions. In either case, the error in assuming $C(\theta) = 0$ is less than 10% above $\theta = 20°$. The difficulty with this entire approach is that the effective beam and view cone angles are not well defined. Thus, the choice of the "correct" $C(\theta)$ is somewhat arbitrary. It has been assumed that the lower curve in figure 4.4-13 corresponds to the present situation and all differential cross sections quoted have been corrected by the factor $\frac{\sin\theta}{1+C(\theta)}$. Notice that the relative behavior of

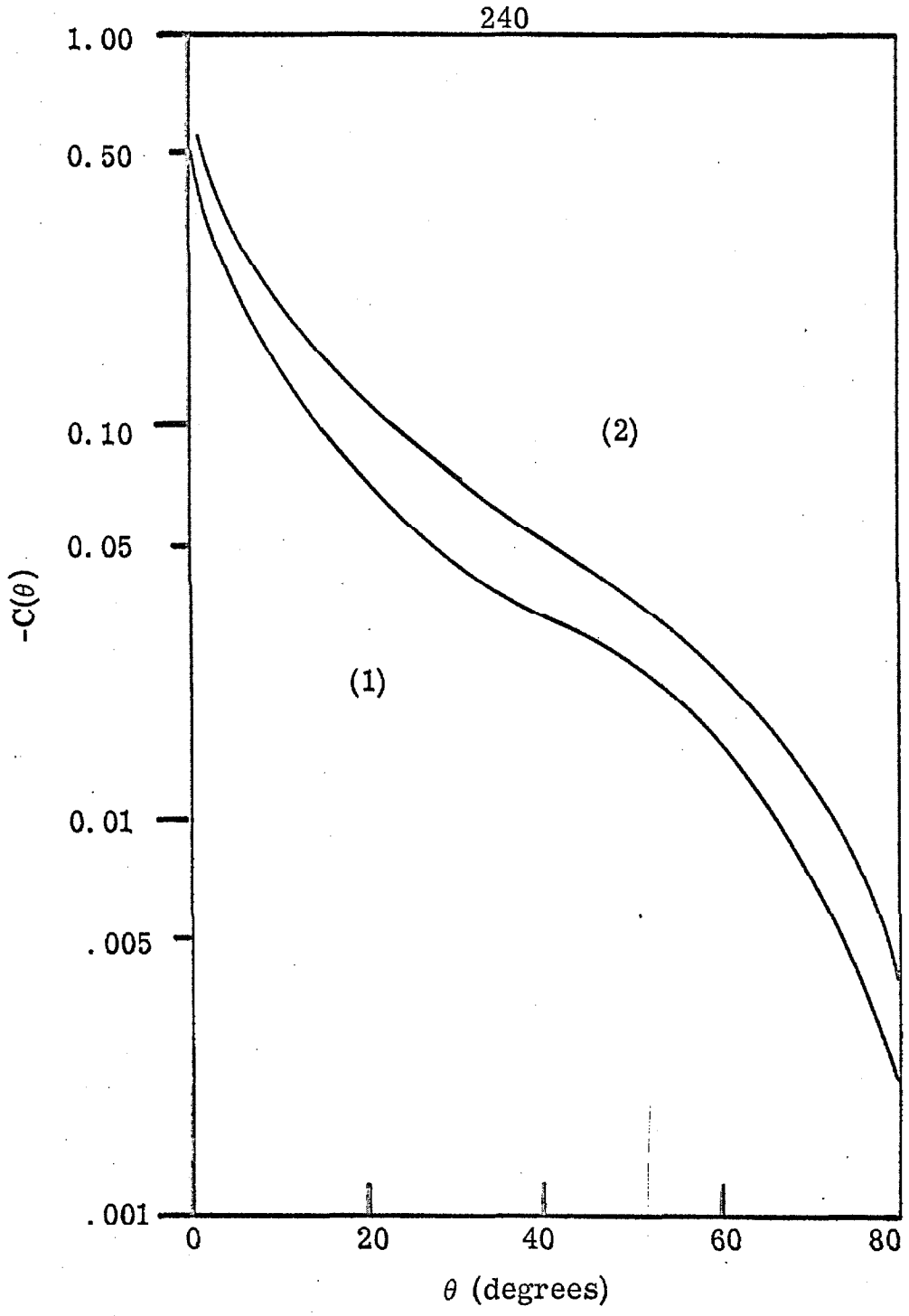

Figure 4.4-13. Plot of -C(θ) (refer to equation (4-113)) as a function of scattering angle θ for a beam cone of 4° and a view cone of 4.5°--curve (1); and a beam cone of 5° and a view cone of 3.5°--curve (2).

two differential cross sections with angle is independent of this volume correction since from (4-107) (and the arguments of section 4.4.4.3)

$$\frac{I_D(\theta, E_{SWP})}{I_D(\theta, E'_{SWP})} \cong \frac{\bar{S}(E_o, E_{SWP}, \theta)}{\bar{S}(E_o, E'_{SWP}, \theta)} \qquad (4\text{-}114)$$

Where E_{SWP} and E'_{SWP} are the two energy-losses in question.

4.4.5. Detector and Background Characteristics

The detector arrangement has already been presented in fig. 4.2-26 and its operation was discussed in section 4.3.4.3. Some of the specific parameters associated with its operation will be described in this section.

Usually, 4.5 KV is applied between the anode and first dynode of the multiplier (fig. 4.2-13) with R4 (fig. 4.2-26) adjusted to 0.4 MΩ. This implies a total load resistance for the high voltage of 8 MΩ, a current through the resistor string of about .56 mA, a first-dynode-to-ground voltage of ~ 220 V, and a stage-to-stage voltage of ~ 210 V. The gain of the multiplier under these conditions can be estimated as follows. The voltage pulse out of the DDL AMP will have an amplitude V_{OUT} where

$$V_{OUT} = G_M G_{PA} G_{AMP} \qquad (4\text{-}115)$$

in which G_M is the multiplier gain in coulombs/ incident electron, G_{PA} is the NPA gain in volts/coulomb, and G_{AMP} is the DDL AMP

voltage gain (dimensionless). For $G_{AMP} \approx 125$ and $G_{PA} \approx 10^{10}$ V/coulomb, V_{OUT} is usually about 2 to 5 V. Solving (4-115) for G_M implies that $G_M \approx$ 2 to 4×10^{-12} coulomb/incident electron or approximately 1 to 2×10^{7} electrons out per incident electron. The count-rate can be made nearly independent of the multiplier gain over about a factor of 10 change by proper adjustment of the SCPHA. The maximum count rates which can be handled by the NPA, DDL AMP, SCPHA, CRM, and ND MCS are 10^{5}, 3×10^{5}, $\sim 10^{6}$, 2×10^{4}, and $\sim 10^{6}$ counts/sec, respectively.

The background "noise" in the system can arise from three principal sources:

(1) At low scattering angles the intense direct beam can enter the selector. Even if E_{SWP} is quite different from 0 eV, a significant number of electrons can "bounce" through the selector and reach the multiplier. As expected this type of background is angle dependent, becoming completely negligible (less than 1 count/min) at angles greater than about 10°.

(2) For E_{SWP} near 0 eV, the tail of the elastic peak may contribute to the scattered signal. Since we have operated at E_{SWP} always > 3 eV, this type of background has not been observed.

(3) It was found that electrons could strike the multiplier without having passed through the scattering chamber. With all voltage controls off except V_C and the filament supply (Kepco 2), electrons could be detected. As expected, this effect was dependent on the total filament emission. With $V_C = 0$, this type of noise disappears (less than 1 count/min).

As a specific example, the total background count-rate at $\theta = 45°$ with $E_{SWP} = 15$ eV for helium (the lowest lying excited state is the 2^3S state at 19.8 eV) at a pressure of .050 torr in the scattering chamber was ~ 1.5 counts/sec, due primarily to source (3).

Under usual operating conditions, electrical noise (power supplies, amplifiers, etc.) was not detected since the SCPHA threshold was set high enough to discriminate against it (usually about 0.5 V). For example, with all spectrometer controls off except 4.5 KV to the multiplier, only 1 count was obtained in five minutes of counting.

In conclusion, it is of interest to estimate the actual numerical relation between the measured signal and the differential scattering cross section (recall equation (4-107)). If one assumes that $(\Delta\Omega)_{AVG} \approx 10^{-2}$ steradians (from lens system 2 geometry, section 4.2.4.6); $\frac{V(45°)}{A} \approx 0.5$ cm, $\epsilon \approx 0.1$ (section 4.4.3.4), a sample pressure of 10^{-2} torr (with $P/P_o \ll 1$), and a typical incident beam current of 3×10^{-8} A, then

$$I_D(E_{SWP}, 45°) \sim 3 \times 10^6 \bar{S}(E_o, E_{SWP}, 45°) \qquad (4\text{-}116)$$

where I_D is in counts/sec when $\bar{S}$ is in units of $\mathring{A}^2$/steradian. Note that (4-116) can be incorrect by an order of magnitude due to the uncertainty in the instrument parameters. If we assume the minimum detectable signal (with the CRM) to be on the order of the background (1.5 cts/sec), then the minimum detectable cross section is

approximately

$$\bar{S}(E_o, E_{SWP}, 45°) \sim .5\times 10^{-6} \text{Å}^2/\text{steradian}.$$

This detection limit can be decreased by the use of the ND MCS system to repetitively scan the feature for a long period of time. By way of comparison table 4.4-2 below lists some measured[32] DCS for an optically allowed ($1^1S \rightarrow 2^1P$), symmetry-forbidden ($1^1S \rightarrow 2^1S$), and spin-and symmetry-forbidden ($1^1S \rightarrow 2^3S$) transition in helium.

TABLE 4.4-2

DCS for three transitions in helium[32].

Incident Energy (eV)	Scattering Angle (degrees)	DCS (Å^2/steradian)		
		$1^1S \rightarrow 2^1P$	$1^1S \rightarrow 2^1S$	$1^1S \rightarrow 2^3S$
100	20	$.49\times 10^{-1}$	$.82\times 10^{-2}$	$.50\times 10^{-3}$
225	15	$.32\times 10^{-1}$	$.93\times 10^{-2}$	$.73\times 10^{-4}$

4.4.6. Energy-Loss Determination

One very important aim of this research is to obtain the positions of atomic and molecular energy levels through a measurement of the energy-losses of the scattered electrons. We have already indicated in section 4.3.4.2 that the value of the applied sweep-voltage V_{SWP} is related to the electron energy-loss being detected (W) by

$$|e|V_{SWP} = W$$

without any arbitrary constants or "contact potential" corrections. This means that the value of V_{SWP} in volts (measured by the digital voltmeter or the X-axis potentiometer of the X-Y recorder) corresponding to a particular peak in the measured energy-loss spectrum is numerically equal to the excitation energy (of the target) W in eV giving rise to that peak. The accuracy with which we can locate the energy of a specific molecular energy level depends only on the instrumental resolution (how well the peak can be separated from neighboring features) and the accuracy of our voltage measuring devices (approximately $\pm$ .001 eV for the digital voltmeter). At present, the latter limitation is negligible compared to the former in most cases.

The energy-loss spectrum of helium provides a good test for these as yet unsupported statements. (Simpson[24] suggested the method of energy-loss sweep which we use and has, of course, verified its utility for his instrument.) A comparison of the well-known

excitation energies of helium with those determined simply by measuring V_{SWP} is presented in section 5.2.3. The agreement is excellent and limited only by the resolution. These same considerations are valid as well for the molecules we studied.

5. RESULTS AND DISCUSSION

5.1. Introduction

In this section we present the results obtained for six systems: helium, molecular nitrogen, carbon monoxide, molecular hydrogen, acetylene, and ethylene.

Energy-loss spectra, where given, are unretouched X-Y recorder traces obtained from the count-rate-meter (see section 4.3.4.3). The basic data (energy-loss spectra) are obtained as follows:

(1) The instrument is "tuned" and stabilized as discussed in section 4.3.

(2) At some initial scattering angle (usually near 40°) an energy-loss spectrum is recorded.

(3) The scattering angle is increased by 10° and another energy-loss spectrum is obtained. This procedure is repeated until the entire angular range has been scanned from two to eight times.

The error bars assigned to derived quantities (such as peak height ratios and differential cross sections) are determined as follows: If $X_1, X_2, \ldots X_N$ represent a set of measurements of the same quantity, then the quoted value is $\bar{X} \pm \Delta X$ where

$$\bar{X} = \frac{1}{N} \sum_{i=1}^{N} X_i \qquad (5\text{-}1)$$

and ΔX is simply the average error,

$$\Delta X = \frac{1}{N} \sum_{i=1}^{N} |\bar{X} - X_i| \quad . \tag{5-2}$$

The error in the differential cross sections at low angles introduced by the volume correction factor (section 4.4.4.4) is not specifically indicated on the figures but we estimate it to be negligible (i.e., $\lesssim 5\%$) for angles (θ) greater than 30° and at most 20% for $\theta = 10°$.

5.2. Helium

5.2.1. Introduction

The electron-impact excitation of helium has been the subject of a great many experimental and theoretical investigations[47]. However, relatively few of these dealt specifically with the angular dependencies of inelastic differential scattering cross sections (DCS). Measurements at fixed scattering angles near 0°[129] and 90°[130] over a wide range of incident electron energies disclosed significant differences in the relative DCS for optically allowed and forbidden transitions. It was generally found that the ratios of DCS for forbidden transitions to those for allowed ones were greater for lower impact energies at a fixed scattering angle and for larger scattering angles at a fixed incident energy. The basis for this behavior is qualitatively well understood (refer to section 3) although no theoretical calculations have yet proved reliable in predicting the shape of the various inelastic DCS below about 100 eV (nor above this for exchange excitation[32]). Silverman and Lassettre[131] have shown that the Born approximation prediction of the total cross section

for the $1^1S \rightarrow 3^1P$ transition is significantly in error below about 100 eV. Vriens, et al.[32] have determined that the Born approximation is not valid for predicting DCS below about 200 eV for the $1^1S \rightarrow 2^1P$ transition nor below 400 eV for the $1^1S \rightarrow 2^1S$ one. Also they point out that the DCS for the $1^1S \rightarrow 2^3S$ transition decreases rapidly for angles greater than 5° at incident electron energies between 100 eV and 225 eV. This is in direct contradiction to the Born-Oppenheimer or Ochkur-Rudge exchange approximations (see section 3). It is interesting to note, however, that the Ochkur-Rudge approximation apparently predicts nearly the correct shape (peak near $\theta = 90°$) of the DCS for this transition at impact energies quite close to threshold[66]. It would be of interest to study this DCS as a function of incident energy to determine at what energy it begins to peak forward.

There are only three previous experimental measurements with which we can (and will) compare our results:

(1) The peak intensity ratios for several helium transitions determined by Chamberlain, et al.[27] at a 0° scattering angle and incident energies from 22 eV to 81 eV,

(2) the measurements of Simpson, et al.[31] on the shape of the $1^1S \rightarrow 2^3S$, 2^1S, and 2^1P DCS for $5° \leq \theta \leq 60°$ and 56.5 eV incident energy, and

(3) Ehrhardt and Willmann's[37b] determination of the shape of the $1^1S \rightarrow 2^3S$ DCS as a function of θ at 24 eV.

In addition, the DCS for excitations of the 2^3S, 2^1S, and 2^3P states relative to that of the 2^1P one provide essential information about the differences between the angular dependencies of scattered electron intensities for transitions which are optically spin- and/or symmetry-forbidden and those of an optically allowed one.

5.2.2. *Energy Scale Calibration*

As noted previously (section 4.4.6), the energy-loss scale is calibrated simply by tuning the instrument on the elastic peak with $V_{SWP} = 0$. The energy-loss in eV is then numerically equal to the sweep voltage without any contact potential corrections (an experimental verification of this is presented in section 5.2.3).

However, there is a contact potential associated with the incident beam (as discussed in section 4.4.3.5). In the present work, this potential was determined experimentally for helium by observing the 57.1 eV and 58.2 eV helium resonances[31]. Although this calibration of the contact potential is necessarily valid only at these particular energies (57-58 eV), it was assumed to be correct throughout the impact-energy range studied ($\sim$ 25 eV to $\sim$ 57 eV). This correction has been applied to all of the quoted impact-energies for helium.

5.2.3. Results and Discussion

Figure 5.2-1 shows an energy-loss spectrum of helium at an impact energy of 34 eV and a scattering angle (θ) of 25°. The resolution (FWHM of the elastic as well as the inelastic peaks) is

Figure 5.2-1. Energy-loss spectrum of helium. Incident beam energy (E_o) = 34 eV; incident beam current (I_o) = 3.2×10^{-8} A; scattering angle (θ) = 25°; scan rate (SR) = .010 V/sec; rate-meter time constant (TC) = .5 sec; scattering chamber pressure (P) = 3×10^{-3} torr.

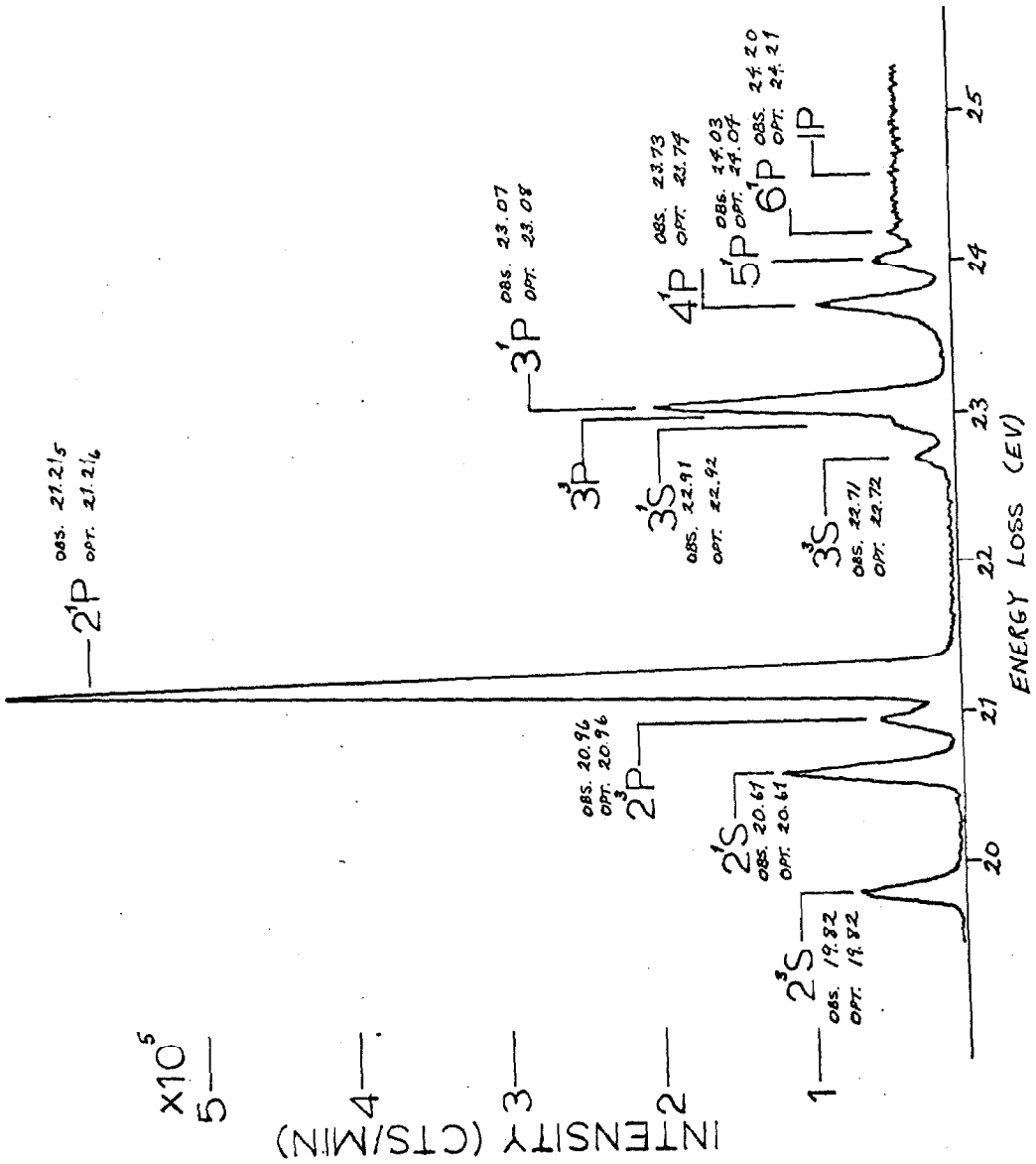
INTENSITY (CTS/MIN)
X10^5
5
4
3
2
1
ENERGY LOSS (EV)
20
21
22
23
24
25
2^3S OBS. 19.82 OPT. 19.82
2^1S OBS. 20.61 OPT. 20.61
2^3P OBS. 20.96 OPT. 20.96
2^1P OBS. 21.215 OPT. 21.214
3^3S OBS. 22.71 OPT. 22.72
3^1S OBS. 22.91 OPT. 22.92
3^3P
3^1P OBS. 23.07 OPT. 23.08
4^1P OBS. 23.73 OPT. 23.74
5^1P OBS. 24.03 OPT. 24.04
6^1P OBS. 24.20 OPT. 24.21
IP

0.10 eV, which is sufficient to clearly resolve the five lowest-lying transitions. The positions of the centers of the observed peaks are given in eV by the numbers labelled obs. Those labelled opt. were obtained from Moore's table[132] of atomic energy levels (optical data). The agreement between the obs. and opt. values is within the accuracy with which the peak positions can be determined for this resolution. In particular, the very intense 2^1P peak can be located to within .001 eV ($\sim 1\%$ of its FWHM) while the weaker and somewhat overlapping n = 3, 4, . . . , etc. levels can be determined to within .01 eV ($\sim 10\%$ of their FWHM). The pertinent instrumental settings for figure 5.2-1 are given in the figure caption.

Figure 5.2-2 shows three impact spectra of helium collected under identical conditions except for different scattering angles of 0°, 30°, and 60°. The four peaks in these spectra correspond to transitions from the 1^1S ground state to the 2^3S (spin- and symmetry-forbidden), 2^1S (symmetry-forbidden), 2^3P (spin forbidden), and 2^1P (optically allowed) states.

Since the peak shapes are not a function of angle, the respective peak heights are directly proportional to the DCS for that transition. Since the collection efficiency is not a function of energy-loss (section 4.4.4.3), it follows that the ratio of two peak intensities at the same angle is equal to the corresponding ratio of the DCS at that angle. (Note that the volume correction cancels.) Figures 5.2-3, -4, -5, and -6 contain plots of the $2^3S/2^1P$, $2^1S/2^1P$, and $2^3P/2^1P$ peak intensity ratios(and hence the DCS ratios) as a function

Figure 5.2-2. Energy-loss spectra of helium at scattering angles of $\theta = 0°$, $30°$, and $60°$. $E_o = 34$ eV, $I_o = 1 \times 10^{-8}$ A, $P = 2 \times 10^{-3}$ torr.

$\theta = 0°$ scan: SR = .010 V/sec, TC = 0.5 sec.

$\theta = 30°$ scan: SR = .005 V/sec, TC = 1 sec.

$\theta = 60°$ scan: SR = .001 V/sec, TC = 10 sec.

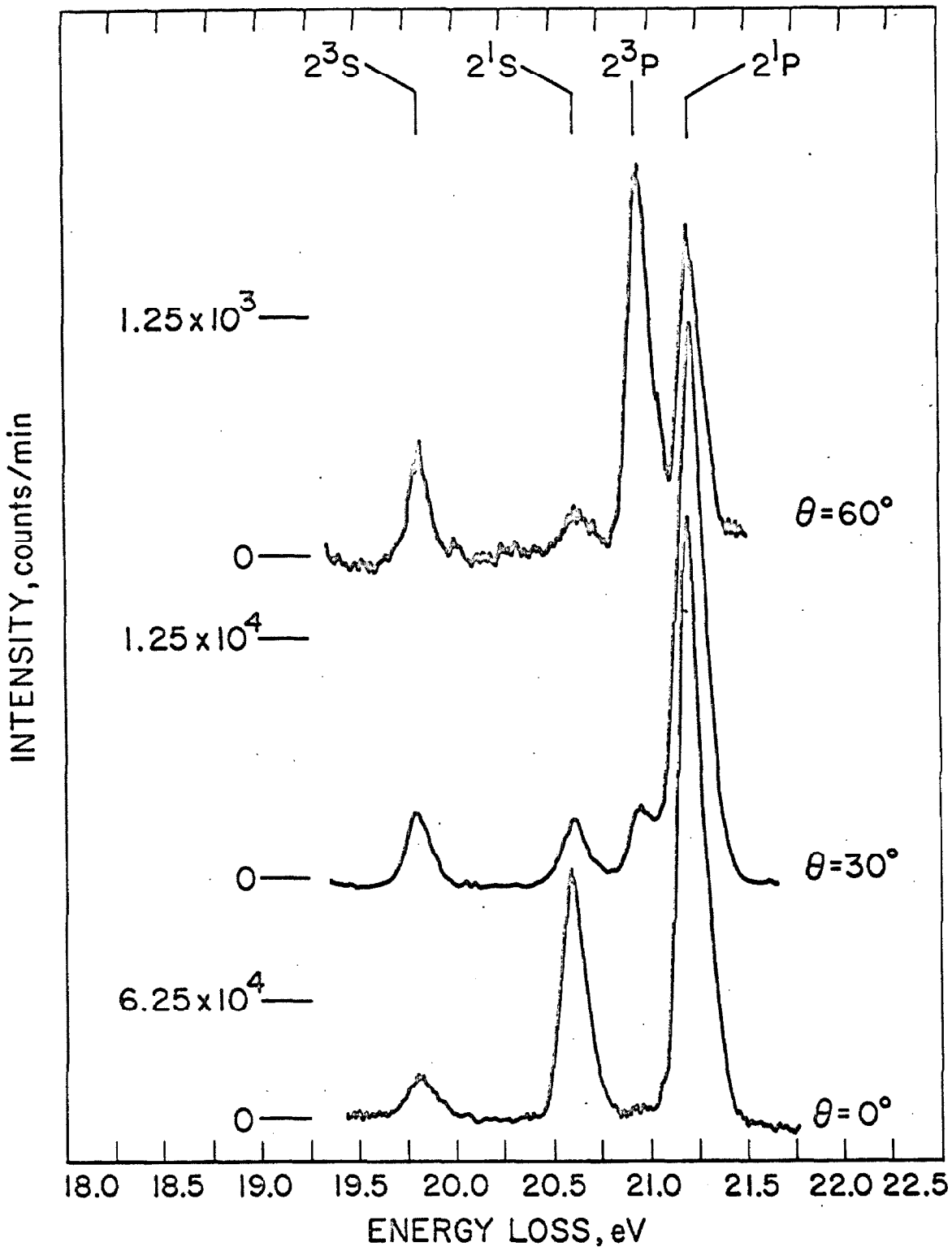
2^3S
2^1S
2^3P
2^1P
1.25×10^3
0
$\theta = 60°$
1.25×10^4
0
$\theta = 30°$
6.25×10^4
0
$\theta = 0°$
INTENSITY, counts/min
18.0 18.5 19.0 19.5 20.0 20.5 21.0 21.5 22.0 22.5
ENERGY LOSS, eV

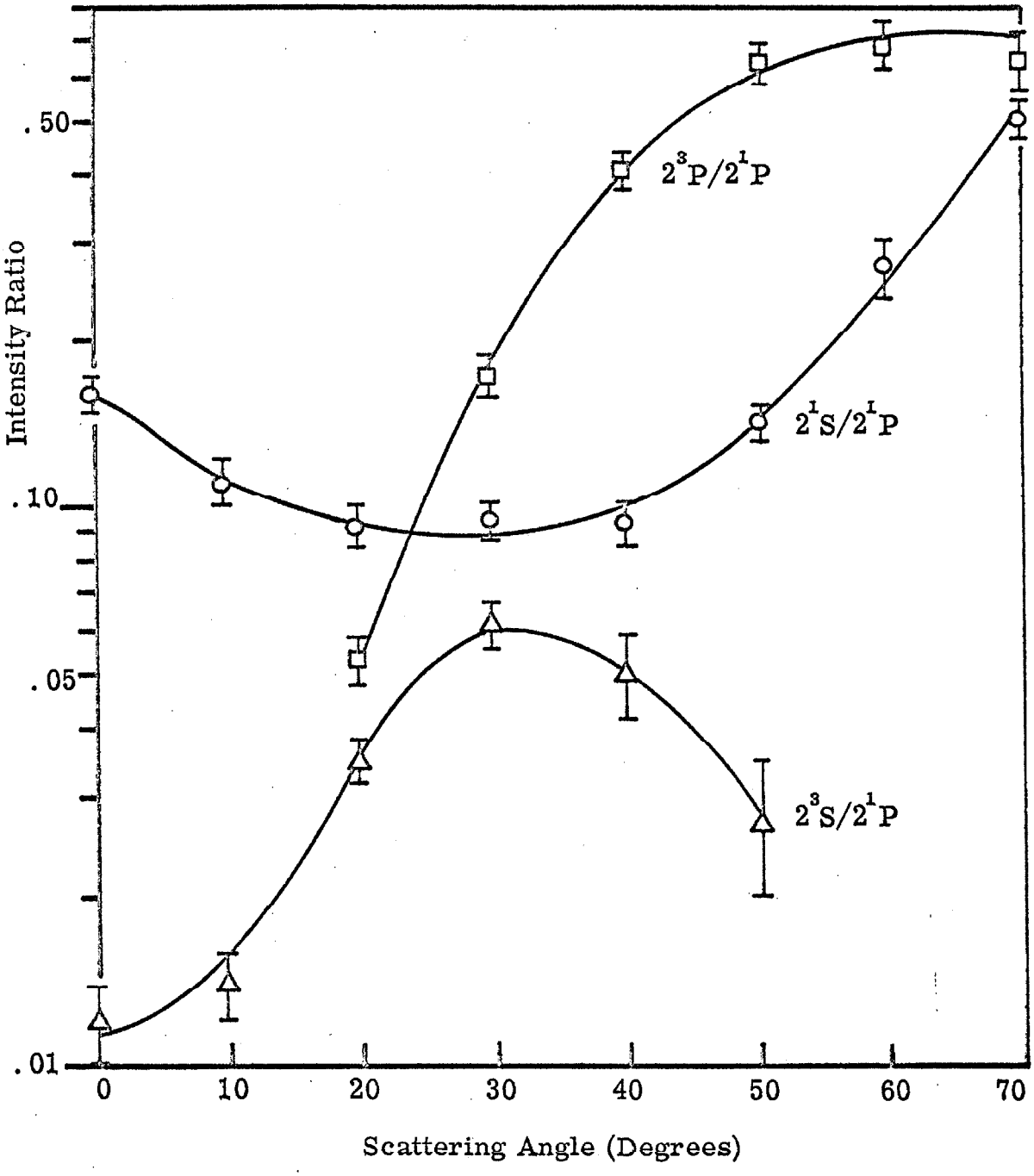

Figure 5.2-3. Ratios of intensities of the $1^1S - 2^3S$, 2^1S, and 2^3P transitions in helium to that of the $1^1S - 2^1P$ transition as a function of scattering angle. $E_o = 55.5$ eV. The average of four to six scans at each angle was used to determine the ratios.

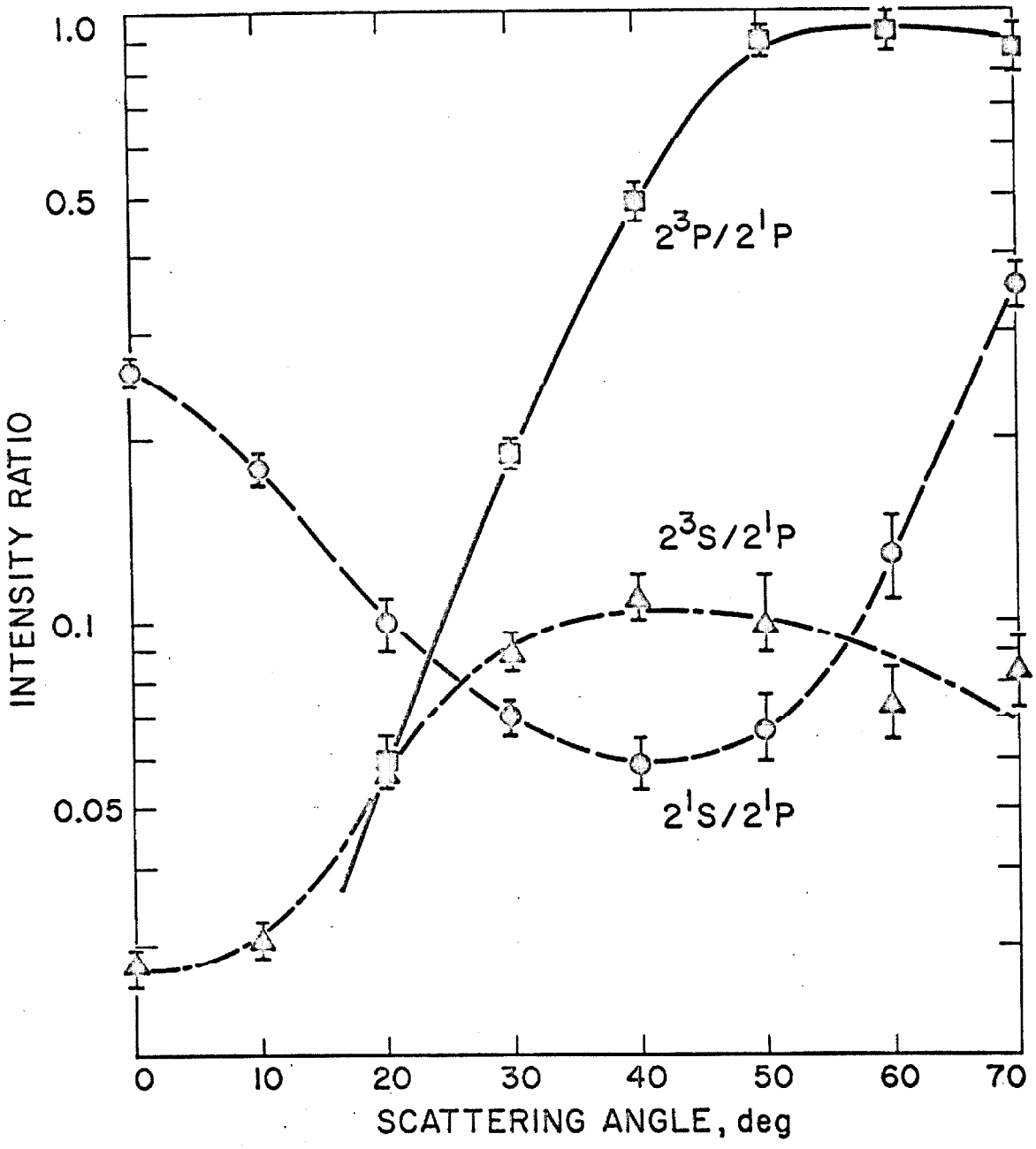

Figure 5.2-4. Same as figure 5.2-3 except that E_o = 44 eV. The average of four to five scans at each angle was used to determine the ratios.

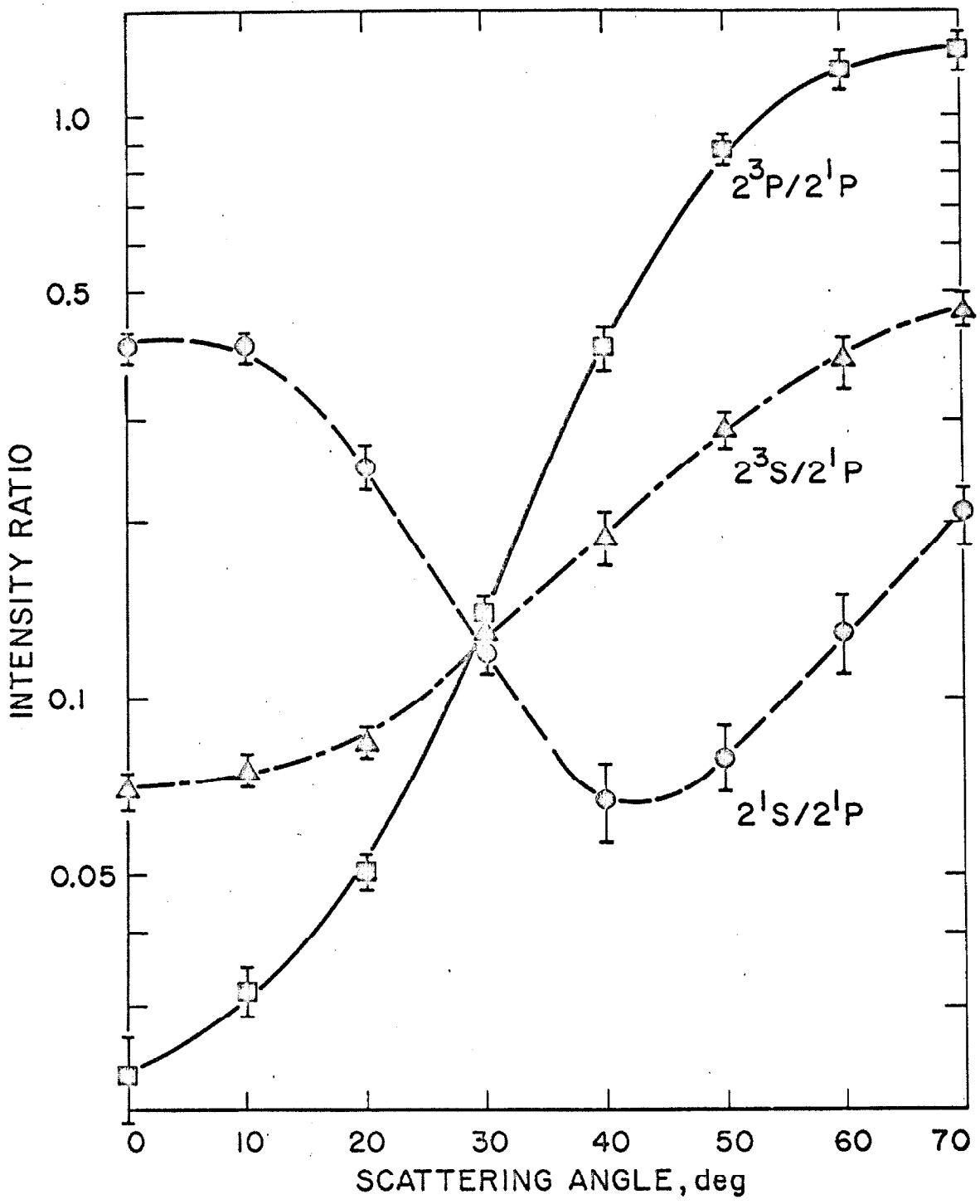

Figure 5.2-5. Same as figure 5.2-3 except that E_o = 34 eV. The average of four scans at each angle was used to determine the ratios.

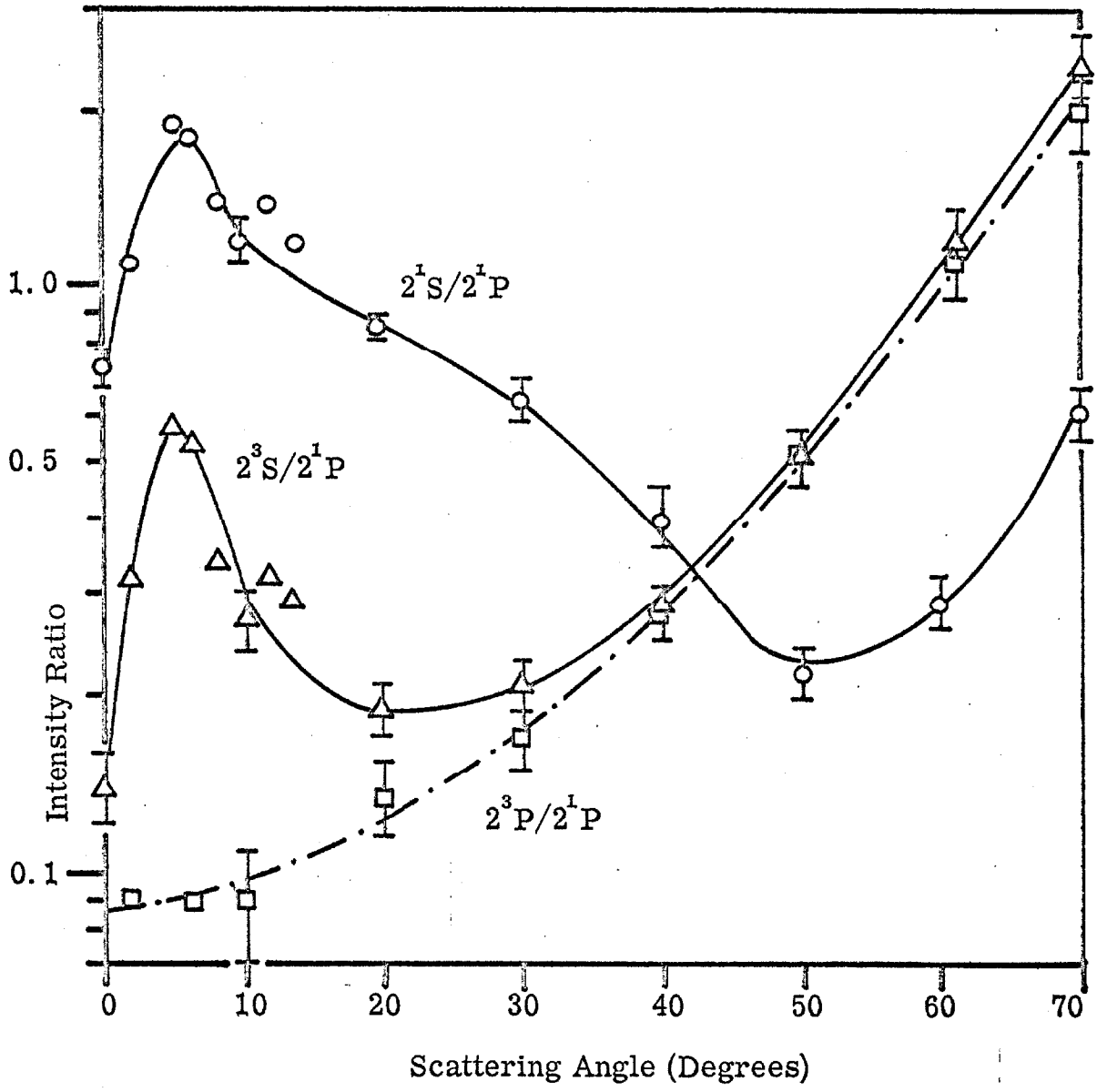

Figure 5.2-6. Same as figure 5.2-3 except that $E_o = 26.5$ (see text). The points with error bars are the average of four scans. The others are individual scans.

of scattering angle for incident electron energies of 55.5 eV, 44 eV, 34 eV, and 26 eV, respectively. The number of measurements used to determine these ratios is given in the figure captions.

Table 5.2-1 compares the $\theta = 0°$ ratios obtained in this research with those of Chamberlain, et al.[27]. The agreement is excellent except for the $2^1S/2^1P$ ratio at an impact energy of 26 eV. This difference could be satisfactorily accounted for by an inaccuracy in our incident energy calibration of about 0.5 eV at this incident energy (i.e., 26 eV should actually be 26.5 eV). Such an error is not unlikely since the calibration is performed only at ~ 60 eV. The ratios of reference (27) at an impact energy of 26.5 eV are presented in the last row of table 5.2-1.

Figure 5.2-7 shows the $3^3S/2^3S$ ratio at 34 eV as a function of θ from 10° to 70°. Within the accuracy of this determination, log $(\frac{3^3S}{2^3S})$ versus θ is a straight line. The extrapolated value of this ratio at $\theta = 0°$ is 0.15 which implies a $3^3S/2^1P$ ratio of .010. This is also in good agreement with the value (.01) from reference (27). The overall agreement serves to verify that our instrumental collection efficiency is indeed independent of energy-loss from 19.8 eV to 22.7 eV (at least to the same extent as is that of reference (27)).

Figure 5.2-8 compares the angular dependencies of the DCS for excitation of the 2^1P, 2^1S, 2^3P, and 2^3S states obtained from the present work (derived from the same energy-loss scans used for obtaining the data of table 5.2-1 and figure 5.2-3) with those of Simpson, et al.[31]. The two sets of data are normalized by setting

TABLE 5.2-1

Peak intensity ratios at $\theta = 0°$ for several transitions in helium. Column (a) contains the results of this work. Column (b) contains the results of Chamberlain, et al.[27]. The values in column (b) were obtained by plotting the ratio data of reference (27) as $\log_{10}$ (ratio) versus incident energy and fitting the points to a smooth curve. Reference (27) gives no error estimates.

Incident Energy eV	$(2^3S/2^1P) \times 100$		$(2^1S/2^1P) \times 100$		$(2^3P/2^1P) \times 100$	
	(a)	(b)	(a)	(b)	(a)	(b)
55.5	1.2 ± .2	1	16 ± 1	15	-	0
44.	2.9 ± .2	3	26 ± 2	25	-	0
34.	7.0 ± .5	7	40 ± 2	40	2.3 ± .4	2
26.	14 ± 2	14	73 ± 6	85	9 ± 2	8
26.5*		13		79		7

* Refer to text.

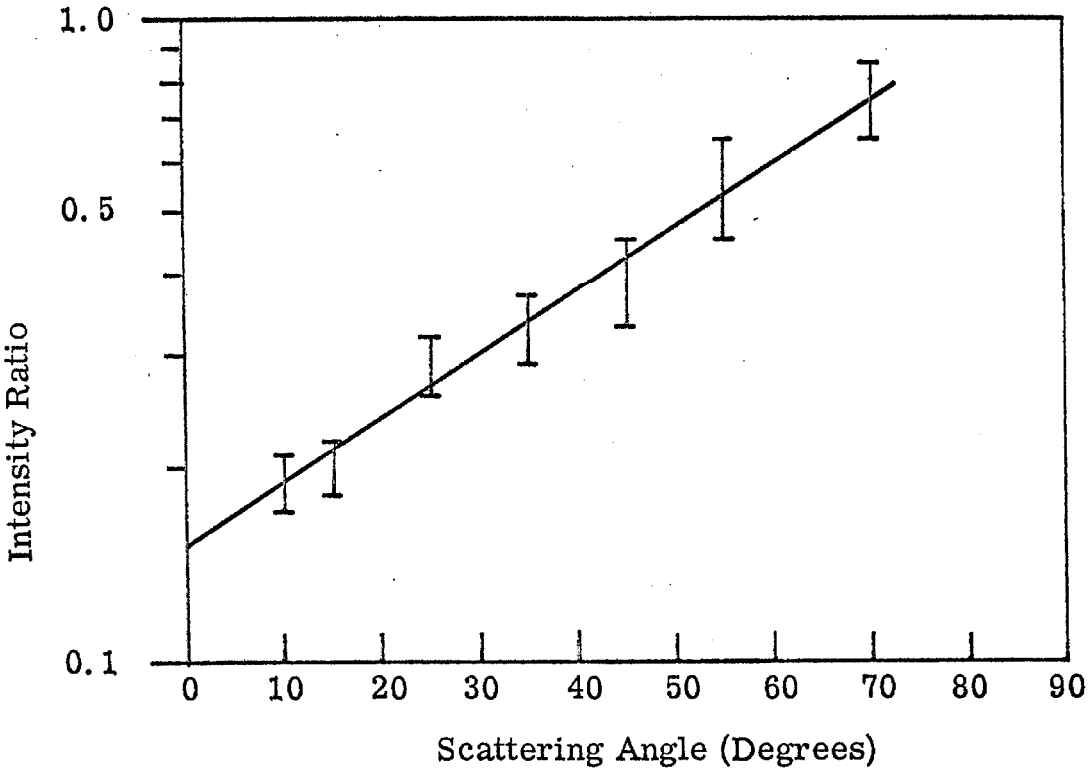

Figure 5.2-7. Ratio of intensity of the $1^1S \rightarrow 3^3S$ transition to that of the $1^1S \rightarrow 2^3S$ transition as a function of scattering angle. E_o = 34 eV. The average of three scans at each angle was used to determine the ratios. The solid line is the best straight line (average ordinate method) through the points.

Figure 5.2-8. Differential scattering cross sections (DCS) in arbitrary units for excitation of the 2^3S, 2^1S, 2^3P, and 2^1P states of helium from its 1^1S ground state. The solid line and data points are from the present research. For clarity, only a few representative error bars are shown. The dashed lines are the results of Simpson[31]. The two sets of data are normalized by setting the $1^1S \rightarrow 2^1P$ DCS equal to 30 (arbitrary units) at $\theta = 10°$. The present data may be placed on an absolute scale (see text) by multiplying the DCS of this figure by 4.7×10^{-3} (see table 5.2-2). $E_o = 55.5$ eV.

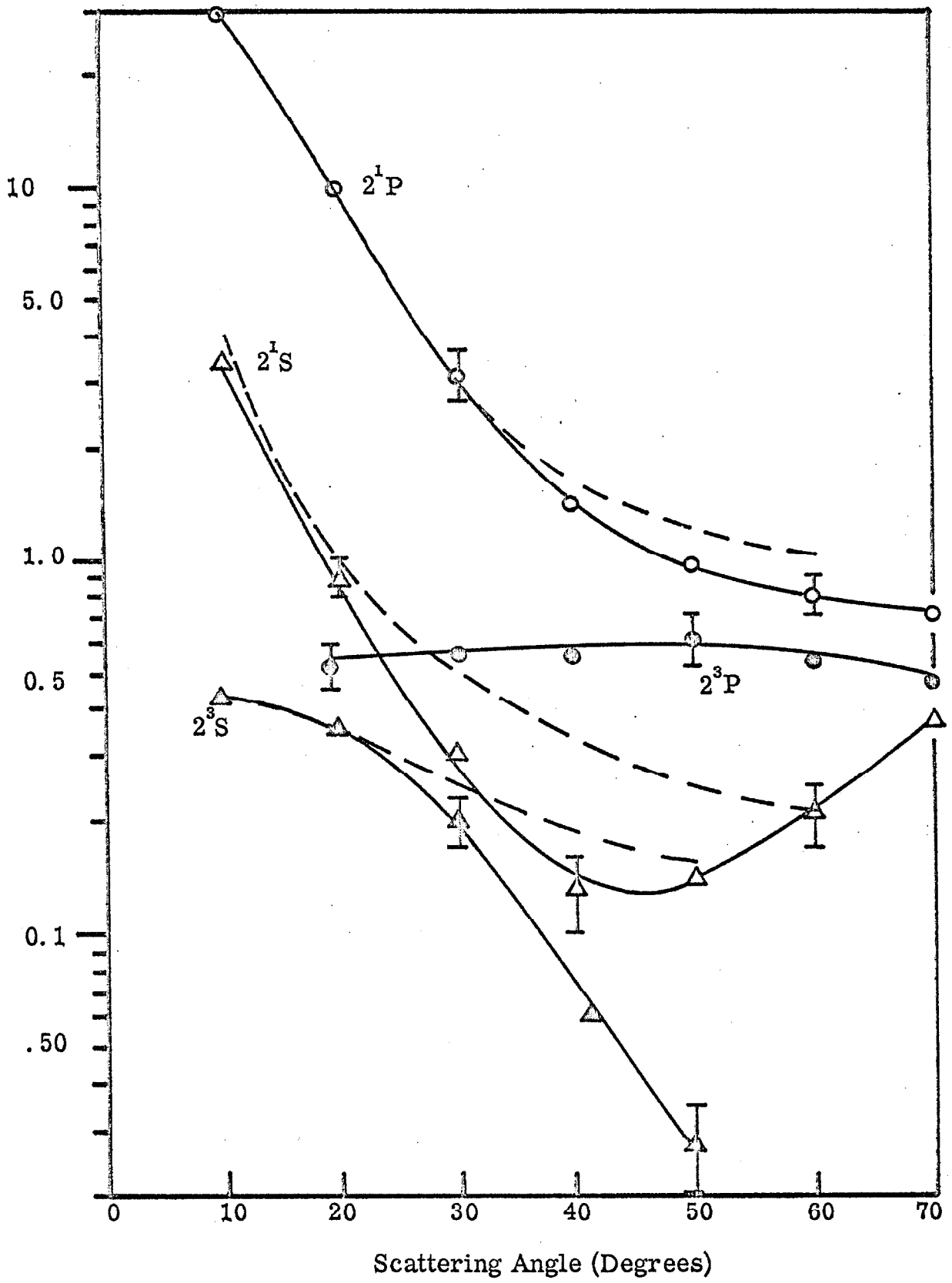
10
5.0
1.0
0.5
0.1
.50
2^1P
2^1S
2^3P
2^3S
0
10
20
30
40
50
60
70
Scattering Angle (Degrees)

the value of the DCS for excitation of the 2^1P state equal to 30 (arbitrary units) at $\theta = 10°$. The relative positions of all of the other points follow from this one requirement.

There are several factors which must be considered in comparing these data sets:

(1) They were obtained at slightly different impact energies--56.5 eV for reference (31) and 55.5 ± .2 for the present work. Since both of these impact energies are in an off-resonance portion of the helium excitation spectrum and are relatively high compared to the inelastic thresholds, this difference should not significantly alter the angular distributions.

(2) Our data are subject to an addition 20% error at $\theta = 10°$ due to the uncertainty of the beam geometry (refer to section 4.4.4.4). The data of reference (31) are not.

(3) Chamberlain, et al.[121] have suggested that it is likely that the scattering intensities of reference (31) are too high at the larger angles due to the effects of double scattering. Such effects are not important in the present research (see section 4.4.4.2).

(4) J. A. Simpson, et al.[31] give no error estimates for their data.

The agreement between this work and that of reference (31) is excellent for $\theta \leq 25°$. This is just the region in which the effects of double scattering should be least important in the data of reference (31) but the uncertainty in the proper volume correction is most significant in our data. Consequently, this good agreement indicates

that our volume correction is probably accurate to within the errors of reference (31) (unknown) and the present work (~ 10%). The discrepancies in the two data sets at higher angles could be the result of double scattering in the data of reference (31), which tends to enhance the scattered signal. Without additional details concerning the conditions under which those data were obtained, it is fruitless to speculate further.

The final experimental measurement with which we can compare our results is that of Ehrhardt and Willmann[37b]. Figure 5.2-9 shows the angular dependence of the DCS for excitation of the 2^3S state from reference (37b) and the present research at an impact energy of 24 eV. The data of reference (37b) are believed to be quite reliable. Since the target in their case is an atomic beam, the scattered intensity is directly proportional to the DCS without an angle dependent path length correction and double scattering is very unlikely. Further, they have accurately calibrated the incident beam energy (24.0 ± .05 eV for the results in fig. 5.2-9). Our results have been normalized to those of reference (37b) at $\theta = 30°$ (the volume correction for our results should be quite reliable for this angle and larger ones). The agreement is within the errors of the two measurements for scattering angles between about 10° and 50° but there is a significant deviation at higher angles. This discrepancy cannot be due to double scattering nor an improper volume correction. However, as indicated from the comparison in table 5.2-1 for an impact energy of ~ 26 eV, the incident energy in our case may be

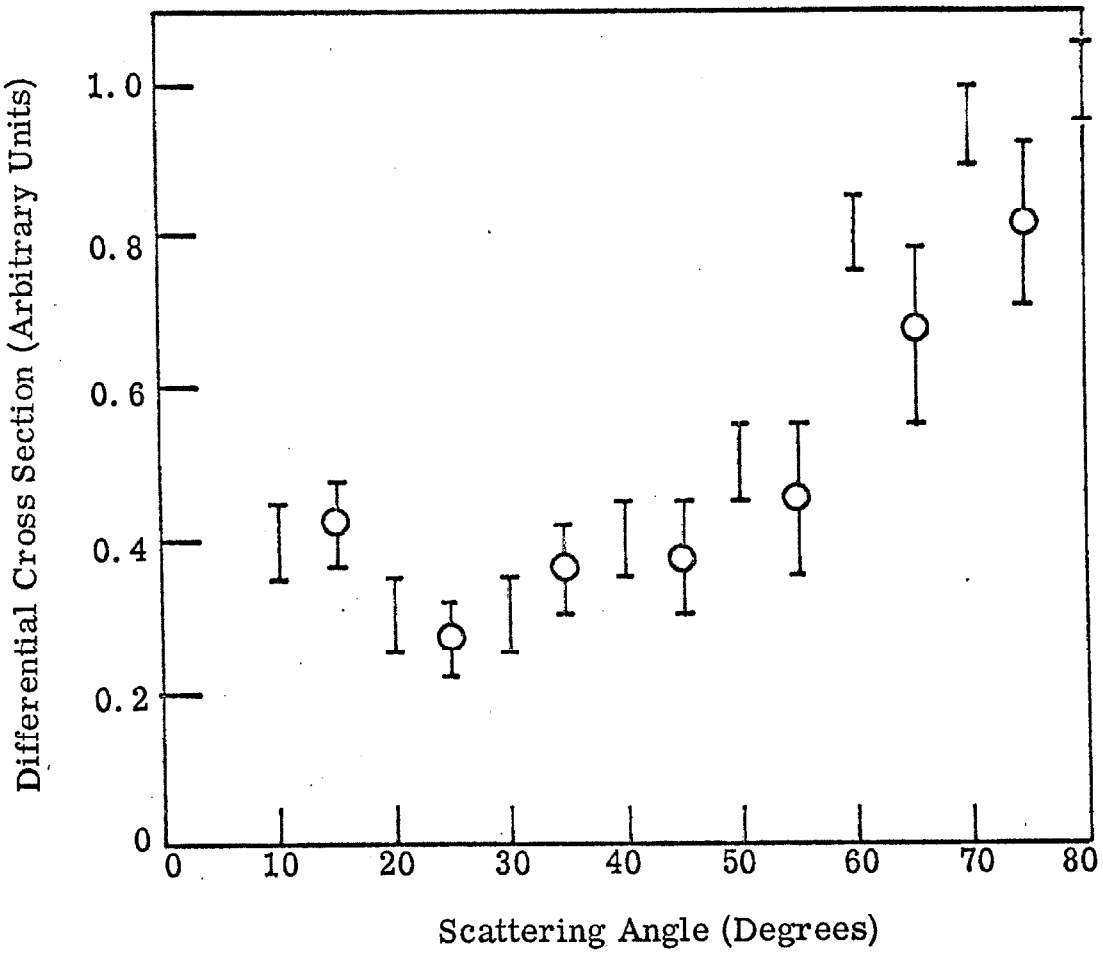

Figure 5.2-9. The $1^1S \rightarrow 2^3S$ differential scattering cross section (in arbitrary units) for helium at $E_o \approx 24$ eV. The plane error bars are the results of Ehrhardt[37b], the open circles are the present results (average of three scans at each angle). The two sets of data were normalized by setting the DCS equal to 0.30 at $\theta = 30°$. (Refer to the text for other details.)

incorrect by 0.5 eV. Unfortunately, we were not able to obtain reliable data at lower impact energies (24 eV is within 4 eV of the 2^3S excitation threshold which presents some of the difficulties discussed in section 4.4.4.3) nor do Ehrhardt and Willmann present data at higher incident energies. If we assume that the incident energy of 24 eV as determined by observation of the 57.1 eV helium resonance is inaccurate by 0.5 eV in the same sense as indicated by table 5.2-1 for the 26 eV calibration, then the "true" impact energy is probably close to 24.5 eV. Since these impact energies are so near the excitation threshold, a relatively small change in incident energy can make a large change in the angular distribution as shown in figure 5.2-10. The distributions at 22.0 eV (curve 1) and 24.0 eV (curve 2) are taken from reference (37b) while the ones at E (curve 3) ($E \cong 24.5$ if the assumptions above are correct), E + 2.0 (curve 4), and 34 eV (curve 5) are from the present work. All of the distributions have been normalized to 0.30 (arbitrary units) at $\theta = 30°$. For clarity, smooth curves have been drawn through the data points (within the error bars) and one representative error has been indicated on each curve. It is quite clear that increasing the impact energy from 22 eV to 34 eV changes the angular distribution from one that is peaked at angles greater than 70° to one that peaks at angles less than 10°. (Of course, there may be additional peaks beyond 70° which we cannot observe.) This general trend is consistent with $E \cong 24.5$ in curves 3 and 4.

Figure 5.2-10. The $1^1S - 2^3S$ differential scattering cross section (in arbitrary units) for helium. Data of reference (37b) at E_o = 22.0 eV (curve 1) and E_o = 24.0 eV (curve 2). Present results at $E_o = E$ (curve 3, see text), $E_o = E + 2$ eV (curve 4), and E_o = 34 eV (curve 5). Each curve is normalized to 0.3 arbitrary units at $\theta = 30°$ and contains one representative error bar.

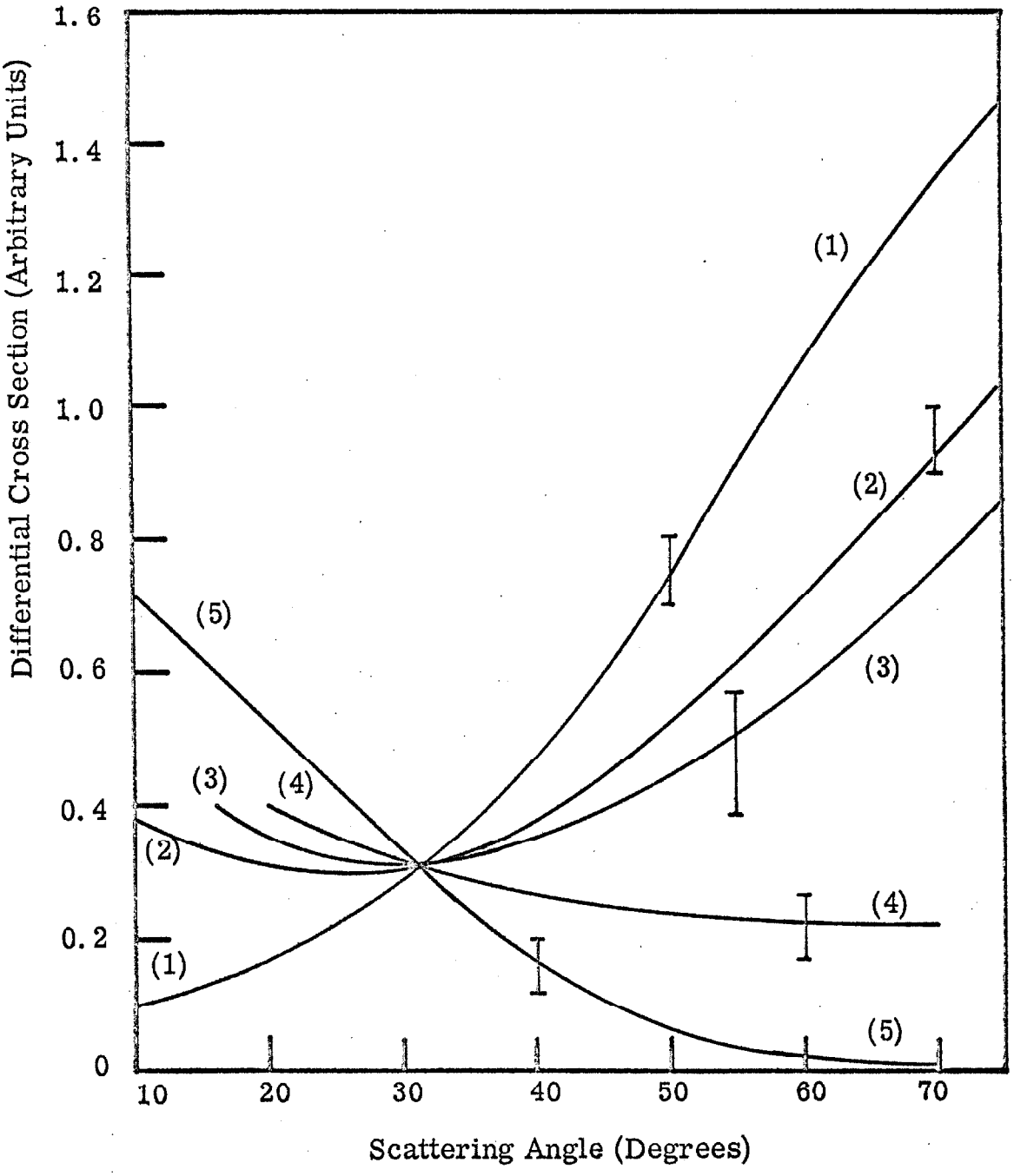
Differential Cross Section (Arbitrary Units)
1.6
1.4
1.2
1.0
0.8
0.6
0.4
0.2
0
10
20
30
40
50
60
70
Scattering Angle (Degrees)
(1)
(2)
(3)
(4)
(5)

Figures 5.2-11, -12, and -13 show the measured DCS (in arbitrary units) at 44 eV, 34 eV, and 26 (26.5 eV), respectively. These data were obtained from the same energy-loss scans which were used to derive the ratio data of table 5.2-1 and figures 5.2-4, -5, and -6.

The data in figures 5.2-8, -11, -12, and -13 can be placed on an absolute scale (but only in an approximate way) as follows. Let $\sigma^{T}_{2^1P}(E,\theta)$ be the "true" differential cross section for excitation of the 2^1P state for an incident energy E and scattering angle θ. Then, the "true" total cross section for this excitation is

$$Q^{T}_{2^1P}(E) = 2\pi \int_0^{\pi} \sigma^{T}_{2^1P}(E,\theta) \sin\theta \, d\theta \qquad (5\text{-}3)$$

Within the experimental uncertainties already discussed (section 4.4.4) the experimental DCS in "arbitrary" units is directly proportional to the "true" one:

$$\sigma^{Arb}_{2^1P}(E,\theta) = K(E)\, \sigma^{T}_{2^1P}(E,\theta) , \qquad (5\text{-}4)$$

where K(E) depends on the incident energy but not on θ. The total experimental cross section in these "arbitrary" units is

$$Q^{Arb}_{2^1P}(E) = 2\pi \int_0^{\pi} \sigma^{Arb}_{2^1P}(E,\theta) \sin\theta \, d\theta \qquad (5\text{-}5)$$

which, together with (5-3) and (5-4), gives

Figure 5.2-11. $1^1S \rightarrow 2^3S$, 2^1S, 2^3P, and 2^1P DCS (in arbitrary units) for helium. $E_o = 44$ eV. The conversion factor to place these data on an absolute scale (table 5.2-2) is $3.3 \times 10^{-3} \pi a_o^2$/arbitrary unit. For clarity, only a few representative error bars are shown.

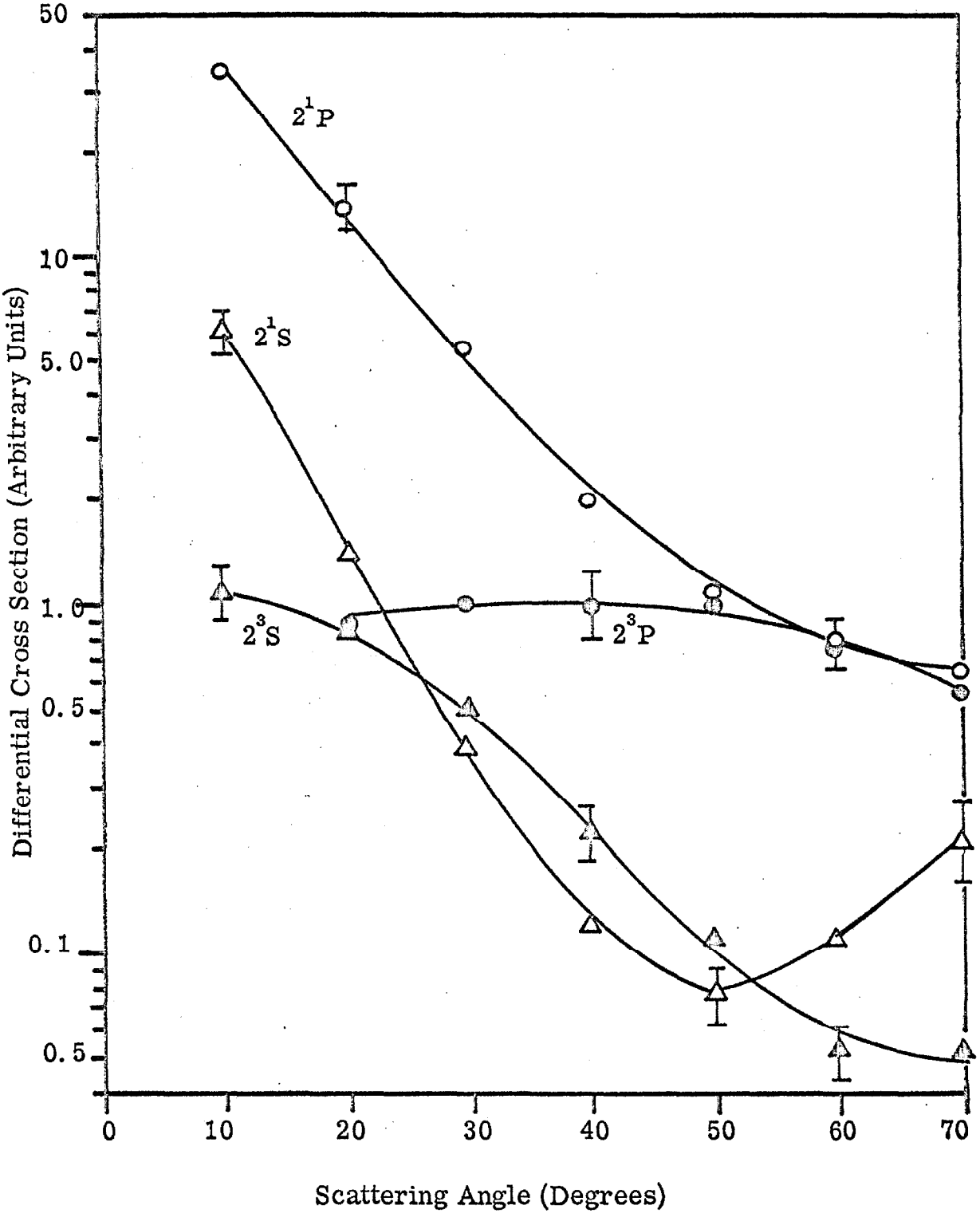
50
10
5.0
1.0
0.5
0.1
0.5
Differential Cross Section (Arbitrary Units)
2^1P
2^1S
2^3S
2^3P
0
10
20
30
40
50
60
70
Scattering Angle (Degrees)

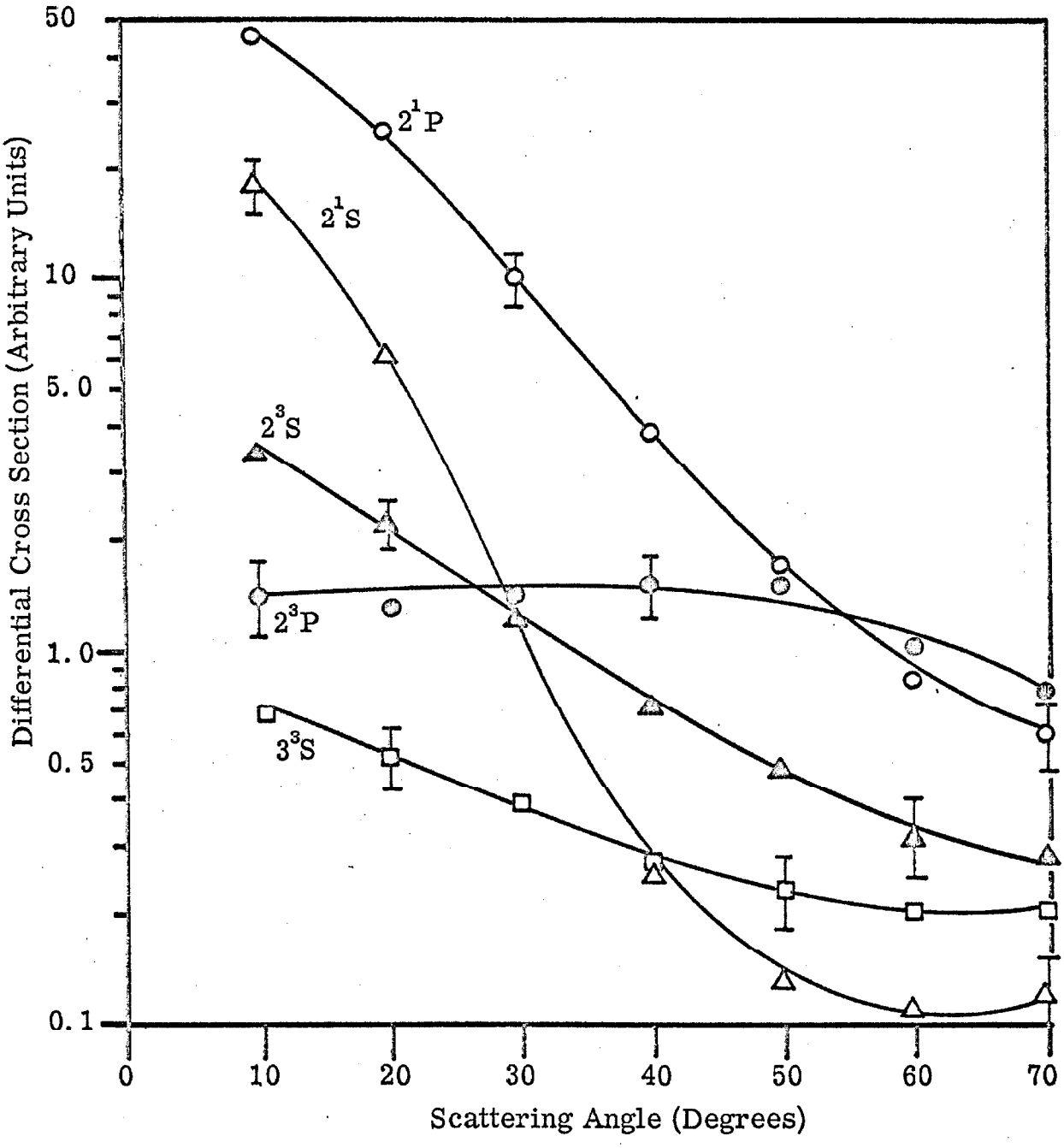

Figure 5.2-12. The same as fig. 5.2-11 except that E_o = 34 eV and the $1^1S - 3^3S$ DCS is included. Conversion factor (table 5.2-2) is $1.4 \times 10^{-3} \pi a_o^2$/arbitrary unit.

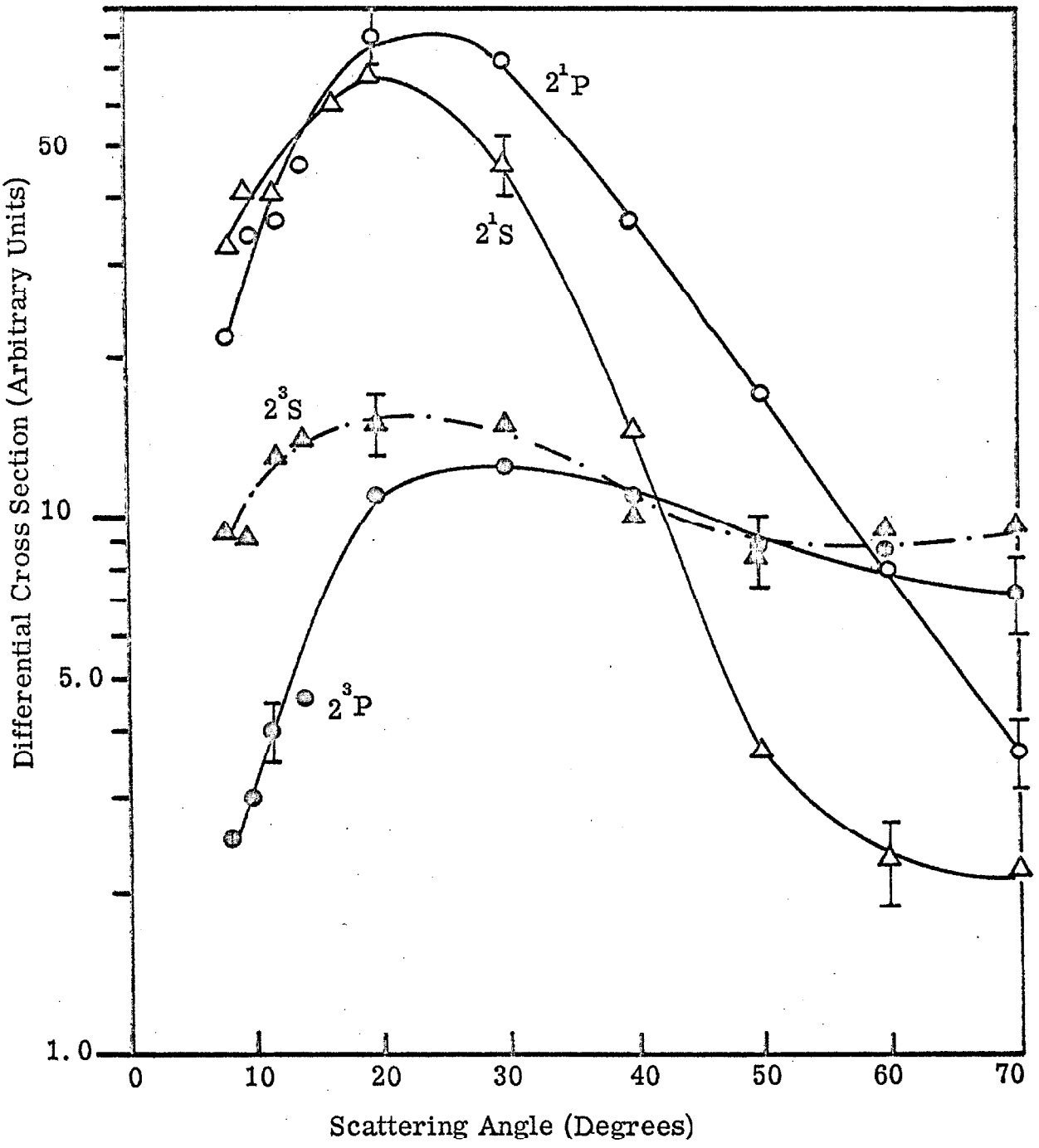

Figure 5.2-13. The same as fig. 5.2-11 except that $E_o = 26$ (26.5 eV). The conversion factor (table 5.2-2) is $1.3 \times 10^{-3} \pi a_o^2$/arbitrary unit.

$$K(E) = \frac{Q^{Arb}_{2^1P}(E)}{Q^{T}_{2^1P}(E)} \quad . \tag{5-6}$$

Reliable values of $Q^{T}_{2^1P}(E)$ for 22 eV $\leq E \leq$ 450 eV are available[43] and $Q^{Arb}_{2^1P}(E)$ can be calculated from the present data through relation (5-5). Table 5.2-2 gives the results of numerical integration of (5-5) for $\sigma^{Arb}_{2^1P}$ taken from figures 5.2-8, -11, -12, and -13. A third-order interpolation by Bessel's formula[133] was used to obtain approximately 240 "data" points from an assumed value of $\sigma^{Arb}_{2^1P}$ at $\theta = 0°$ and the $\sigma^{Arb}_{2^1P}$ values at $\theta = 10°, 20°, \ldots, 70°$ from the figures. The uncertainty of the DCS below 10° does not introduce any appreciable error in the integral (5-5) from $\theta = 0°$ to 70° because of the $\sin\theta$ weighting factor. For lack of a better method, the data were extrapolated to $\theta = 180°$ by assuming

$$\sigma^{Arb}_{2^1P}(\theta \geq 70°) = A\, e^{-\theta/\alpha} \tag{5-7}$$

where A and α were determined by $\sigma^{Arb}_{2^1P}(60°)$ and $\sigma^{Arb}_{2^1P}(70°)$. The respective values of α are given in table 5.2-2. The integral over (5-7) was performed analytically. The uncertainty in the integral (5-5) over the range $\theta = 0°$ to 70° is probably 10-15% since this is the approximate relative error in each experimental value of $\sigma^{Arb}_{2^1P}(E,\theta)$.

TABLE 5.2-2

Quantities related to the calculation of K(E). Refer to the text for the corresponding definitions. Arb stands for arbitrary units.

E (eV)	$Q^{Arb\,0}_{2^1P}$ (Arb) (eq. 5-8)	$Q^{Arb\,1}_{2^1P}$ (Arb) (eq. 5-9)	α (radians) (eq. 5-7)	$Q^{Arb\,2}_{2^1P}$ (Arb) (eq. 5-10)	$Q^{T}_{2^1P}$ $\times 10^{18}$ cm^2 (ref. 43)	$\frac{1}{K(E)}$ (πa_o^2/Arb) (eq. 5-11)	EPE (%) (eq. 5-12)
55.5 (fig. 5.2-8)	15.08	3.90	1.48	6.07	7.9	4.7×10^{-3}	23
44 (fig. 5.2-11)	19.29	2.64	.84	5.48	6.3	3.3×10^{-3}	25
34 (fig. 5.2-12)	29.66	1.76	.52	5.06	3.7	1.4×10^{-3}	23
26 (26.5) (fig. 5.2-13)	125.66	4.78	.22	30.3	1.5	1.3×10^{-4}	31

It is difficult to estimate the overall error in the calculation of $Q^{Arb}_{2^1P}$ since we have no knowledge, either theoretical or experimental, of how $\sigma^{Arb}_{2^1P}$ really varies beyond $\theta = 70°$. In order to obtain some estimate of the possible error in the integral form $\theta = 70°$ to $180°$, we have calculated this integral assuming $\sigma^{Arb}_{2^1P}(\theta \geq 70°) = \sigma^{Arb}_{2^1P}(70°)$. Thus, our estimated error in the determination of $Q^{Arb}_{2^1P}$ is simply the value of the integral between $70°$ and $180°$ assuming this constancy with respect to θ minus its value assuming the θ dependence given by (5-7) plus 12% (uncertainty in the $\theta = 0°$ to $70°$ integral). In summary, the various integral quantities in table 5.2-2 are given by:

$$Q^{Arb\,0}_{2^1P}(E, 0°\text{-}70°) = 2\pi \int_0^{70°} \sigma^{Arb}_{2^1P}(E,\theta) \sin\theta \, d\theta, \qquad (5\text{-}8)$$

$$Q^{Arb\,1}_{2^1P}(E, 70°\text{-}180°) = 2\pi A \int_{70°}^{180°} e^{-\theta/\alpha} \sin\theta \, d\theta, \qquad (5\text{-}9)$$

and

$$Q^{Arb\,2}_{2^1P}(E, 70°\text{-}180°) = 2\pi \, \sigma^{Arb}_{2^1P}(E, 70°) \int_{70°}^{180°} \sin\theta \, d\theta \, . \qquad (5\text{-}10)$$

The values of $Q^{T}_{2^1P}(E)$ are taken from reference (43). Our best estimate of K(E) (from equation (5-6)) is then

$$K(E) = \frac{Q^{Arb\,0}_{2^1P} + Q^{Arb\,1}_{2^1P}}{Q^{T}_{2^1P}} \qquad (5\text{-}11)$$

with an estimated percent error (EPE) of

$$EPE \equiv \left(\frac{Q^{Arb\,2}_{2^1P} - Q^{Arb\,1}_{2^1P}}{Q^{Arb\,0}_{2^1P} + Q^{Arb\,1}_{2^1P}} \right) \times 100 + 12\%. \qquad (5\text{-}12)$$

The results of this absolute scale calibration can be compared, at least within a factor of 2, with the absolute calculations of Heideman and Vriens[73] based on the Bethe-Born approximation, for $\sigma_{2^1P}(E, 0°)$. Table 5.2-3 summarizes this comparison. The values of $\sigma_{2^1P}(E, 0°)$ in column (a) were obtained by extrapolating the $\sigma^{Arb}_{2^1P}$ data of figures 5.2-8, -11, -12, and -13 to $\theta = 0°$ and multiplying the result by the corresponding 1/K(E) from table 5.2-2. It is evident that the resulting DCS could be incorrect by as much as a factor of 2 from a combination of the error in the extrapolation and the absolute calibration (EPE). Further, the application of a high-energy approximation to this low-energy region can introduce errors of this same magnitude[73]. The fact that the values of column (a) are lower than those of column (b) is to be expected since the Bethe-Born approximation (and all other approximations which ignore back-coupling of the states, see section 3.3.3)

TABLE 5.2-3

Zero-angle differential cross sections from this work (column a) and reference (73) (column b) for the $1^1S - 2^1P$ transition in helium. E is the incident electron energy.

E (ev)	$\sigma_{2^1P}(E, 0°)/\pi a_o^2$	
	(a)	(b)
55.5	.21	.70
44	.18	.44
34	.084	.21
(26.5)	.039	.071

consistently over estimates cross sections at lower impact energies.

There is a further theoretical comparison of interest. Cartwright[66] has calculated the DCS for the $1^1S \rightarrow 2^3S$ and 2^3P transitions in helium using the Ochkur-Rudge (OR) method. Figures 5.2-14 and -15 show the results of the present experimental work and these calculations for two different impact-energies. The agreement between the general magnitudes of the cross sections is remarkable but the lack of similarity in the shapes represents a definite failure of the OR approximation. At higher impact-energies (100 eV → 225 eV) the deviations between the experimental shapes[32] and those predicted by the OR and Born-Oppenheimer approximations[67] become even more pronounced. Finally, figure 5.2-16 shows the ratio of the DCS for excitation of the 2^3S state to that of the 2^3P state according to the OR approximation (reference (66)) and the present work. Again, the calculated ratios are of the correct order of magnitude, but their variations with θ bear little resemblance to the experimental ones.

In summary, the comparisons of this section indicate that:

(1) the data obtained with this instrument are consistent with the results of previous investigators, and

(2) the usual first order exchange approximations (OR, Born-Oppenheimer) are not reliable for predicting the detailed shape of DCS curves for excitation of the 2^3S and 2^3P states of helium in this low-energy range.

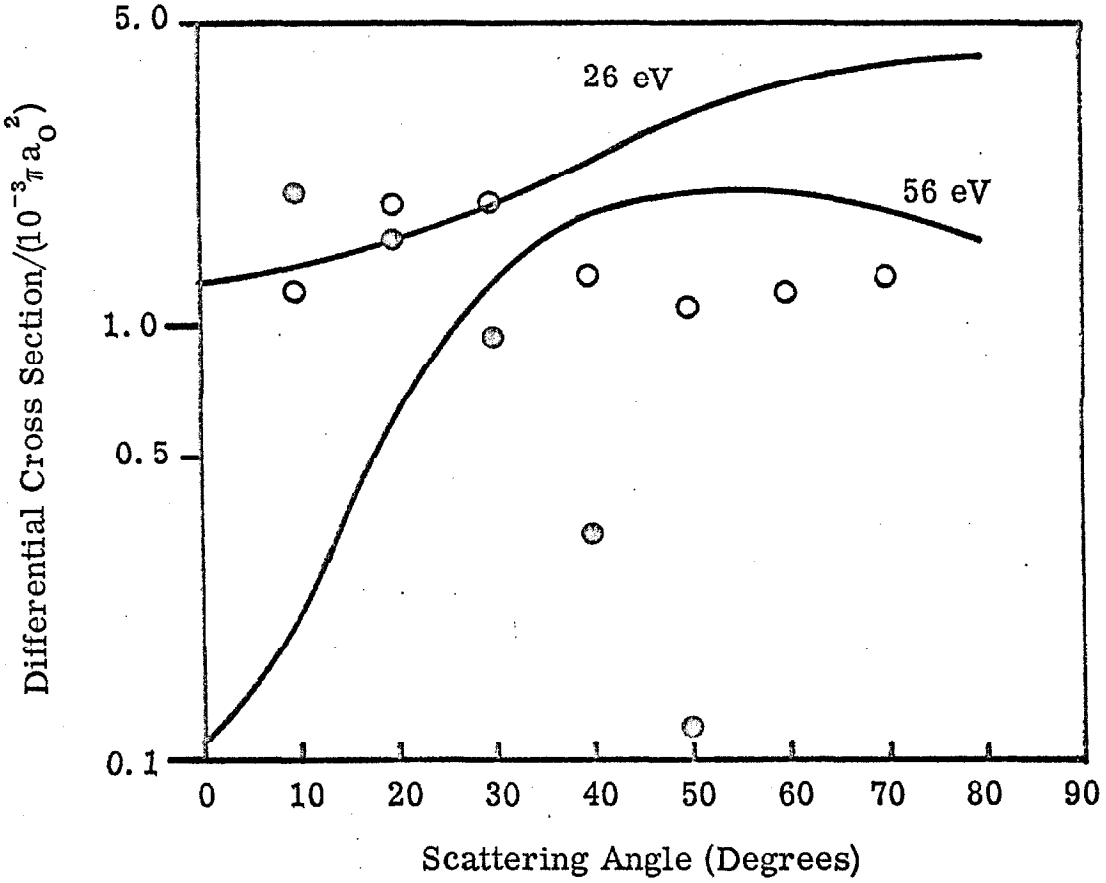

Figure 5.2-14. The $1^1S - 2^3S$ DCS for helium. The solid lines are the calculations of reference (66) at E_o = 26 eV and 56 eV. The present results are given at E_o = 26.5 eV (open circles) and at E_o = 55.5 eV (filled circles). Absolute units have been placed on the present results as discussed in the text. The relative error in the experimental data can be found in figures 5.2-8, -13.

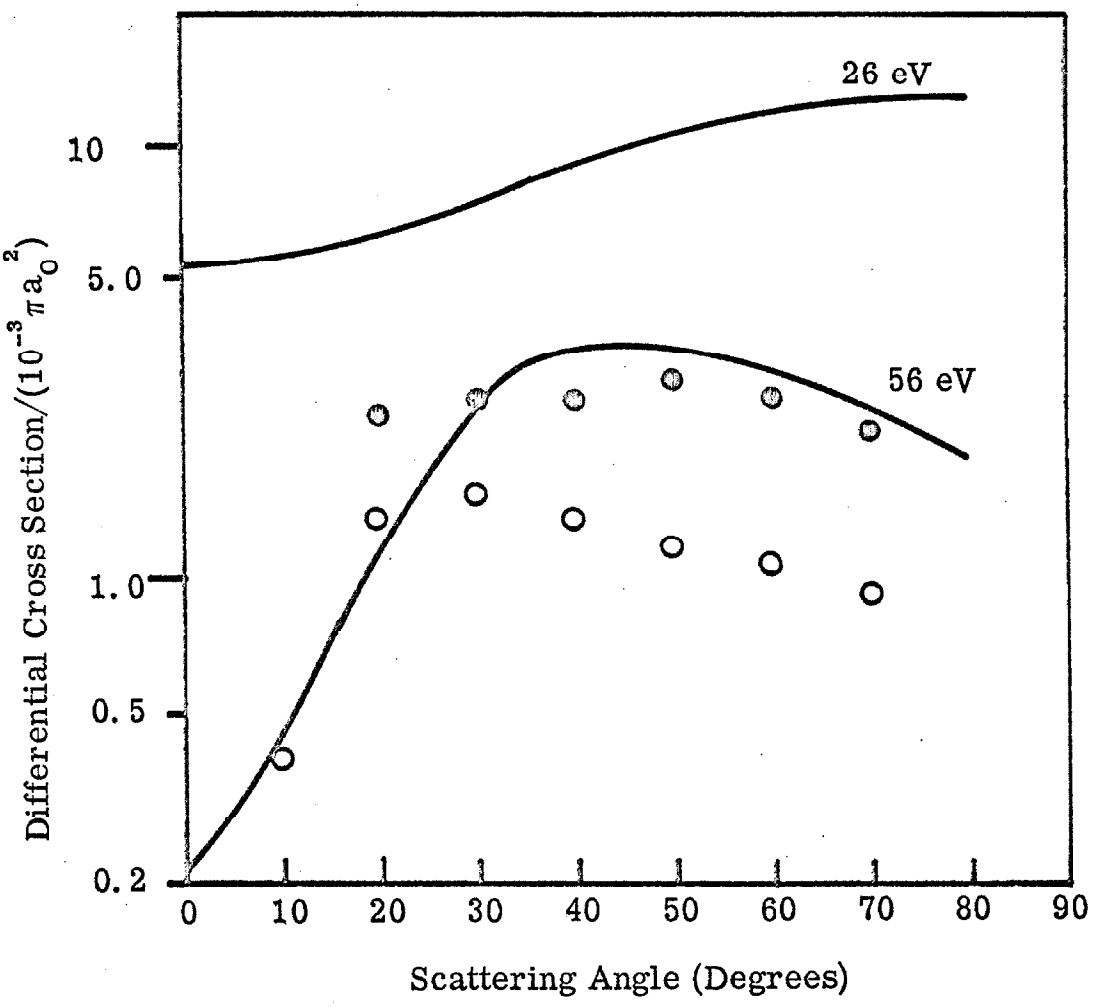

Figure 5.2-15. $1^1S - 2^3P$ DCS for helium. The solid lines are the calculations of reference (66) at E_o = 26 eV and 56 eV. The present results are given at E_o = 26.5 eV (open circles) and 55.5 eV (filled circles) and have been put on an absolute scale as discussed in the text. The relative error in the experimental data is indicated in figures 5.2-8, -13.

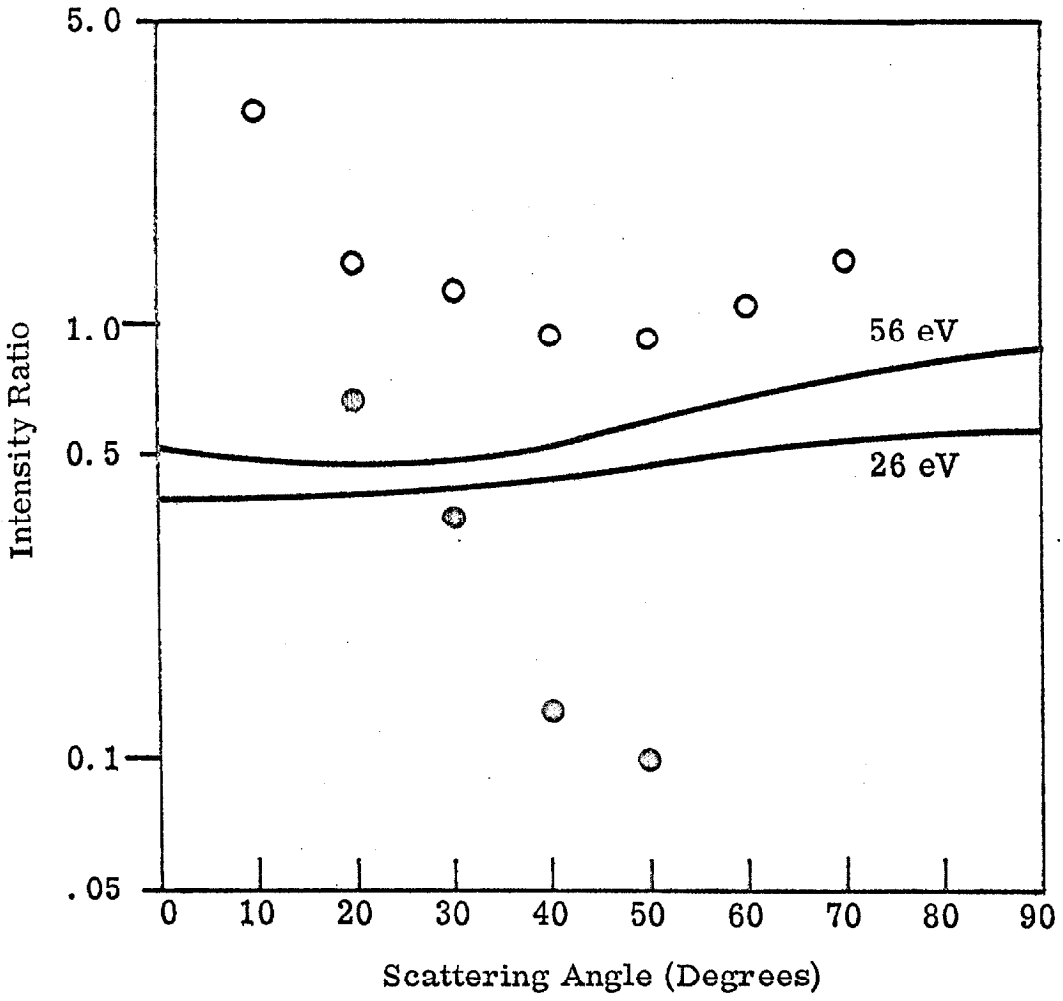

Figure 5.2-16. Ratio of intensity of the $1^1S \rightarrow 2^3S$ transition to that of the $1^1S \rightarrow 2^3P$ transition for helium. The solid lines are derived from the calculations of reference (66) at E_o = 26 eV and 56 eV. The present results are given at E_o = 26.5 eV (open circles) and 55.5 eV (filled circles). The error in the data can be obtained from figures 5.2-3, -6.

5.2.4. *Further Discussion*

As mentioned earlier, our primary concern is to use electron scattering data to determine the nature of a given transition (i. e., to determine whether it is spin- and/or symmetry-forbidden) for cases in which this information may not be available from optical studies. From our present understanding of the scattering process (refer to section 3), it is expected that the angular distribution of electrons scattered after causing optically forbidden transitions will be quite different from that of electrons causing allowed ones. These differences can be enhanced by studying the DCS ratios (rather than the DCS themselves) as a function of angle. (Further, such a study eliminates one source of experimental error, the angle dependent volume correction.)

Indeed, the DCS ratios given in figures 5.2-3, -4, -5, and -6 show such characteristic differences. The most generally consistent behavior, at all energies studied, is that of the $2^3P/2^1P$ DCS ratio (spin-forbidden only/ optically allowed). In all cases, it increases by about two orders of magnitude from $\theta = 0°$ to $70°$. The variation of the $2^3S/2^1P$ DCS ratio (spin- and symmetry-forbidden/allowed) is less uniform with changes in the incident energy. Generally, this ratio increases with increasing angles, reaching a maximum which shifts to higher angles at lower incident energies. Its maximum increase over the 0° to 70° angular range is usually significantly less than that of the $2^3P/2^1P$ ratio. Finally, the $2^1S/2^1P$ DCS ratio (symmetry-forbidden only/allowed) generally decreases with

increasing angle, reaching a broad minimum at about 40°, and thereafter increases. Silverman and Lassettre[15] have reported that the $2^1S/2^1P$ DCS ratio increases by a factor of about 10 from $\theta = 3.8°$ to $\theta = 15.3°$ at an incident energy of 500 eV. It is interesting to note that at intermediate energies (34 eV to 56 eV), this ratio decreases over the same angular range but that at 26.5 eV it increases sharply from $\theta = 0°$ to about 6° and thereafter decreases. This same effect is noted in the $2^3S/2^1P$ DCS ratio at this energy, but not in the $2^3P/2^1P$ one.

In addition to the characteristic variation of these triplet/singlet ratios with angle, they exhibit a dependence on incident energy which (in some cases) is to be expected from the considerations of section 3. As the incident energy is lowered toward threshold, spin-forbidden total cross sections are usually enhanced relative to spin allowed ones. We might expect the respective differential cross sections to vary in a similar way. Then, the triplet/singlet ratios should increase with decreasing energy more rapidly than the singlet/singlet one. This behavior is evident for $\theta = 0°$ from table 5.2-1. However, the magnitude of this effect is sensitive to the particular θ considered. Table 5.2-4 presents the ratios at $\theta = 40°$ for which the $2^3P/2^1P$ ratio is nearly constant. The enhancement with decreasing energy of the triplet/singlet ratios compared to the $2^1S/2^1P$ one is most evident in the region of low ($\theta \approx 0°$) and high ($\theta \approx 70°$) scattering angles.

TABLE 5.2-4

Peak intensity ratios in helium at $\theta = 40°$.

E_o (eV)	$2^3S/2^1P$	$2^1S/2^1P$	$2^3P/2^1P$
55.5	.050	.093	.40
44	.11	.059	.49
34	.19	.067	.40
(26.5)	.28	.40	.29*

* See reference (134).

The DCS themselves for the various transitions also show a number of interesting features. First, the 2^1S and 2^1P DCS are more sharply peaked forward than the 2^3S or 2^3P DCS (as expected). Second, as the incident energy is decreased the 2^1P and 2^3S DCS become more isotropic (recall section 3.4). The 2^3P DCS is relatively flat over a wide range of angles at all of these energies. Third, the behavior of the 2^1S DCS presents an interesting variation. At 55.5 eV it reaches a distinct minimum at about 40° while at 44 eV and 34 eV the minimum moves out to 50° and 60°, respectively, and apparently lies beyond 70° at 26.5 eV. This behavior is similar to the diffraction effects observed in both elastic and inelastic scattering from atoms[44g]. Qualitatively, the present effect can be explained as follows. Recall equation (3-114) of section 3 which relates the phase shifts η_ℓ to the angular dependence of the DCS. Suppose that $\eta_0 > \eta_1 > \eta_2 > \eta_3 >$ etc. as indicated by equation (3-117) and that $\eta_3 \cong \frac{\pi}{2}$ for a certain incident energy $\hbar^2k^2/2m$. In this case, the DCS $\sigma(k,\theta)$ will be dominated by the P_3 partial wave.

Hence,

$$\sigma(k,\theta) \simeq \text{const.} \{P_3(\cos\theta)\}^2 \quad ,$$

which has a minimum at $\theta = 40°$ (and 90°). This seems to correspond approximately to the 2^1S DCS of figure 5.2-8 at 55.5 eV. Now, suppose the incident energy is lowered. From (3-117) we expect all of the η_ℓ's to decrease. In particular, η_2 may decrease to $\simeq \frac{\pi}{2}$. Thus, at this lower impact energy

$$\sigma(k',\theta) \cong \text{const}\{P_2(\cos\theta)\}^2 \quad ,$$

which has a minimum at $\theta = 55°$. From a comparison of figures 5.2-11 and -12, this case would correspond to an incident energy intermediate between 44 eV and 34 eV. In a similar way, as the impact energy is lowered further, the first η_ℓ to reach $\sim\frac{\pi}{2}$ corresponds to a lower ℓ value and the minimum is expected to move toward larger angles. As an illustrative example, the 2^1S DCS at 55.5 eV (fig. 5.2-8) has been compared with $\{P_3(\cos\theta)\}^2$ in figure 5.2-17. Of course, partial waves other than P_3 contribute to the DCS, but the general agreement in shape is noteworthy.

Finally, the behavior of the 2^1P, 2^1S, and 2^3P DCS at 26.5 eV (fig. 5.2-13) for $\theta \lesssim 20°$ is unique in that these DCS appear to decrease markedly toward smaller angles. This effect is probably not due to a resonance, since none have been observed in this region[31,135], nor can it be explained by the preceding arguments.

5.3. Nitrogen

5.3.1. Introduction

In the excitation energy range from about 6 eV to 13 eV, N_2 exhibits a number of features which we can observe via electron impact. Table 5.3-1 lists the optical excitation energies for some of these transitions and the energy-losses at which we observe them. Notice that our values agree quite well with the optical ones.

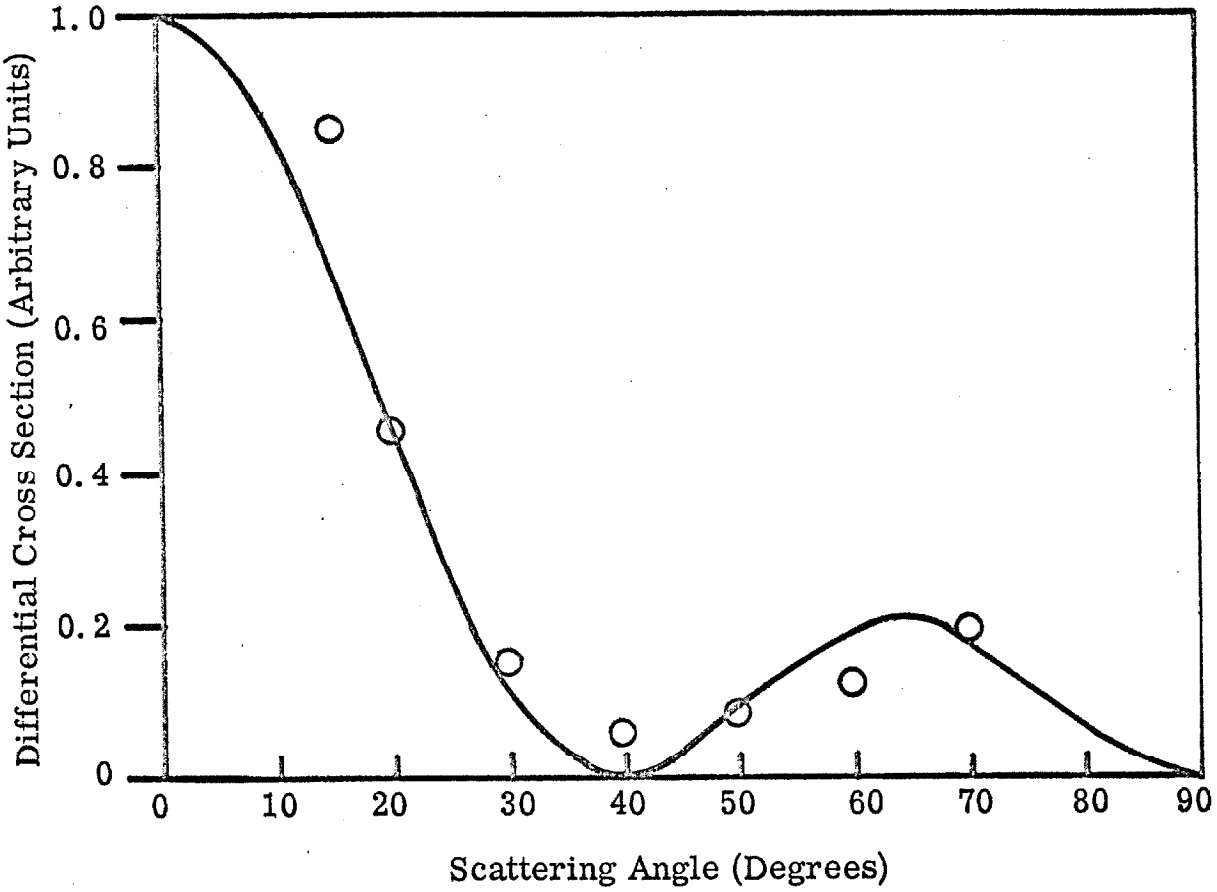

Figure 5.2-17. Comparison of the measured $1^1S \rightarrow 2^1S$ DCS of helium at $E_0 = 55.5$ eV (circles) with $|P_3(\cos\theta)|^2$ (solid line). The data have been normalized to the arbitrary value of .45 at $\theta = 20°$.

TABLE 5.3-1

Transitions from the $X^1\Sigma^+$ (ν = o) ground electronic and vibrational state of N_2 to various electronic and vibrational states in the range from 6 eV to 13.3 eV. The column labelled UES contains the upper electronic state designation, the one labelled UVS lists the upper vibrational state, OPT. EE is the optical excitation energy, and OBS.EE is the excitation energy (energy-loss) observed in the present work.

UES[a]	UVS	OPT. EE[b] (eV)	OBS. EE[c] (eV)
$A^3\Sigma_u^+$	0	6.17	-
	1	6.35	-
	2	6.52	6.50
	3	6.69	6.71
	4	6.86	6.84
	5	7.02	7.02
	6	7.18	7.19
$B^3\Pi_g$	0	7.35	7.36
	1	7.56	7.57
	2	7.77	7.77
	3	7.98	7.97
	4	8.18	8.17
	5	8.38	8.37
$a^1\Pi_g$	0	8.55	8.56
	1	8.76	8.77
	2	8.96	8.97
	3	9.16	9.16
	4	9.35	9.35
	5	9.55	9.54
	6	9.74	9.73
	7	9.92	9.91
	8	10.10	10.09
	9	10.28	10.30
	10	10.46	10.48
$C^3\Pi_u$	0	11.03	11.03
	1	11.28	11.29
	2	11.52	11.51

TABLE 5.3-1 (continued

UES[a]	UVS	OPT. EE[b] (eV)	OBS. EE[c] (eV)
$(E\,^3\Sigma_g^+)$[d]	0	11.87	11.87
$(^1\Sigma_g^+)$[e]	0	-	12.26
$b\,^1\Pi_u$	0	12.58	
	1	12.66	
	2	12.75	
	3	12.84	
	4	12.93	(12.92)[f]
$p'\,^1\Sigma_u^+$	0	12.93	
	1	13.20	(13.21)[g]

[a] State designations are taken from reference (2b) pp 551-553, except as indicated.

[b] Calculated from the data of (a) above.

[c] The observed excitation energies from this research are believed to be accurate to $\pm .01_5$ eV in most cases. The given energy-losses were determined from scans in which the feature was most clearly observed (i. e., low angles for the singlets and high ones for the triplets).

[d] This state is listed in (a) above as E. Our use of this assignment is discussed in the text.

[e] This state is not listed in (a) above. Its assignment is discussed in the text.

[f] The vibrational features are not resolved in our spectra. The peak we observe should correspond nearly to $\nu' = 4$.

TABLE 5.3-1 (continued)

[g] The vibrational structure is not resolved in our spectra. The peak position at 13.18 eV should correspond with the $\nu' = 1$ level although there may be contributions from several other states. See reference (39).

The transition from the $X^1\Sigma_g^+$ ground state of N_2 to the $b^1\Pi_u$ state is the first optically allowed one. Transitions to the lower lying states are forbidden by symmetry ($g \not\to g$, e.g., $a^1\Pi_g$, $^1\Sigma_g^+$), electron spin multiplicity ($1 \not\to 3$, e.g., $A^3\Sigma_u^+$, $C^3\Pi_u$) or both (e.g., $B^3\Pi_g$, $E^3\Sigma_g^+$). Excitation of the $p'\ ^1\Sigma_u$ (or $b^1\Pi_u$) state is electric-dipole allowed while transitions to the symmetry forbidden states are electric-quadrupole allowed. Gilmore[136] has summarized the potential energy curves for most of these states.

The electron-impact excitation of N_2 has been studied at both low and high angles at a number of incident energies. All of the electronic states of table 5.3-1 have been observed by previous investigators although the assignment of the $E^3\Sigma_g^+$ one has been in question.

Lassettre and Krasnow[16] investigated the change with scattering angle (0° to 15°) of the unresolved $X^1\Sigma_g^+ \to a^1\Pi_g$ (Lyman-Birge-Hopfield) transition at 500 eV. They found that the ratio of the DCS for excitation of the $a^1\Pi_g$ state to that of the $b^1\Pi_u$ one varied from about .05 at $\theta = 4°$ to 0.3 at $\theta = 10°$. Later these studies were extended[17c] to lower energies (60 eV) and higher resolution but at low angles ($\theta \lesssim 2.5°$). Recently, Skerbele, et al.[22a] reported high resolution spectra of N_2 at 50 eV and 36 eV ($\theta \approx 0$ to 12°). In this case, transitions to all of the electronic states of table 5.3-1 were observed although singlet → triplet transitions were a minor part of the overall spectrum.

Heideman, et al.[29] obtained energy-loss spectra for $\theta = 0°$ at incident energies of 15.7 eV and 35 eV. Neither the A nor B states were observed at either energy while the C state was evident at the lower one. Transitions to the other electronic states in table 5.3-1 could be seen at both energies.

Doering and Williams[36c] have presented lower resolution energy-loss spectra at impact energies down to 16.1 eV for $\theta = 90°$. As expected, the singlet → triplet transitions comprise a major part of the N_2 spectrum under these conditions. No vibrational structure was resolved, but transitions to the $B^3\Pi_g$, $a^1\Pi_g$, $C^3\Pi_u$, and $b^1\Pi_u$ states were evident.

The N_2 excitation spectrum has also been studied by Brongersma and Oosterhoff[11] and Compton, et al.[13] using a trapped-electron technique. Although the reported spectra of these authors are similar in appearance, their state assignments are quite different. This is probably the result of an energy calibration error in the results of Compton, et al.[13]. Brongersma[11] was able to verify the identity of the B state by resolving its vibrational structure. It is interesting to note that these threshold studies do not reveal excitations to the A or C states but are dominated by transitions to the B and E ones (all four of these states are triplets).

5.3.2. Results and Discussion

Figures 5.3-1 and -2 show energy-loss spectra of nitrogen taken at an impact energy of 40 eV (uncalibrated) and scattering angles of $\theta = 20°$ and $80°$, respectively. The low angle spectrum

Figure 5.3-1. Energy-loss spectrum of N_2. $E_o = 40$ eV, $I_o = 2 \times 10^{-8}$ A, $\theta = 20°$, SR = .01 V/sec, TC = .5 sec, $P = 1 \times 10^{-3}$ torr.

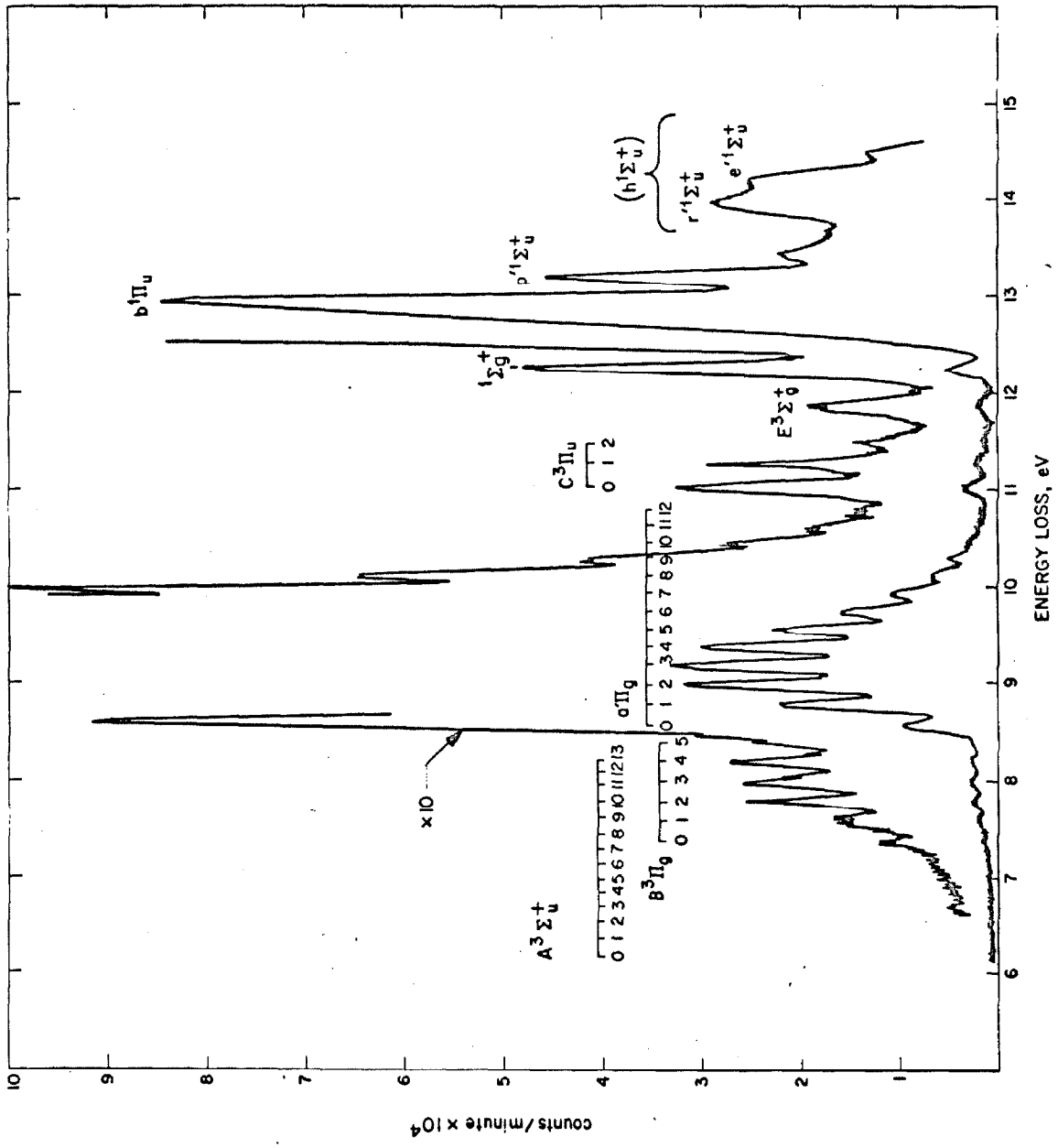
counts/minute x 10⁴
ENERGY LOSS, eV
b¹Π_u
¹Σ_g⁺
p'¹Σ_u⁺
(h¹Σ_u⁺)
r'¹Σ_u⁺
e'¹Σ_u⁺
E³Σ_g⁺
c³Π_u
a'Π_g
B³Π_g
A³Σ_u⁺
×10

Figure 5.3-2. Energy-loss spectrum of N_2. $E_o = 40$ eV, $I_o = 2 \times 10^{-8}$ A, $\theta = 80°$, SR = .002 V/sec, TC = 10 sec, P = 1×10^{-3} torr.

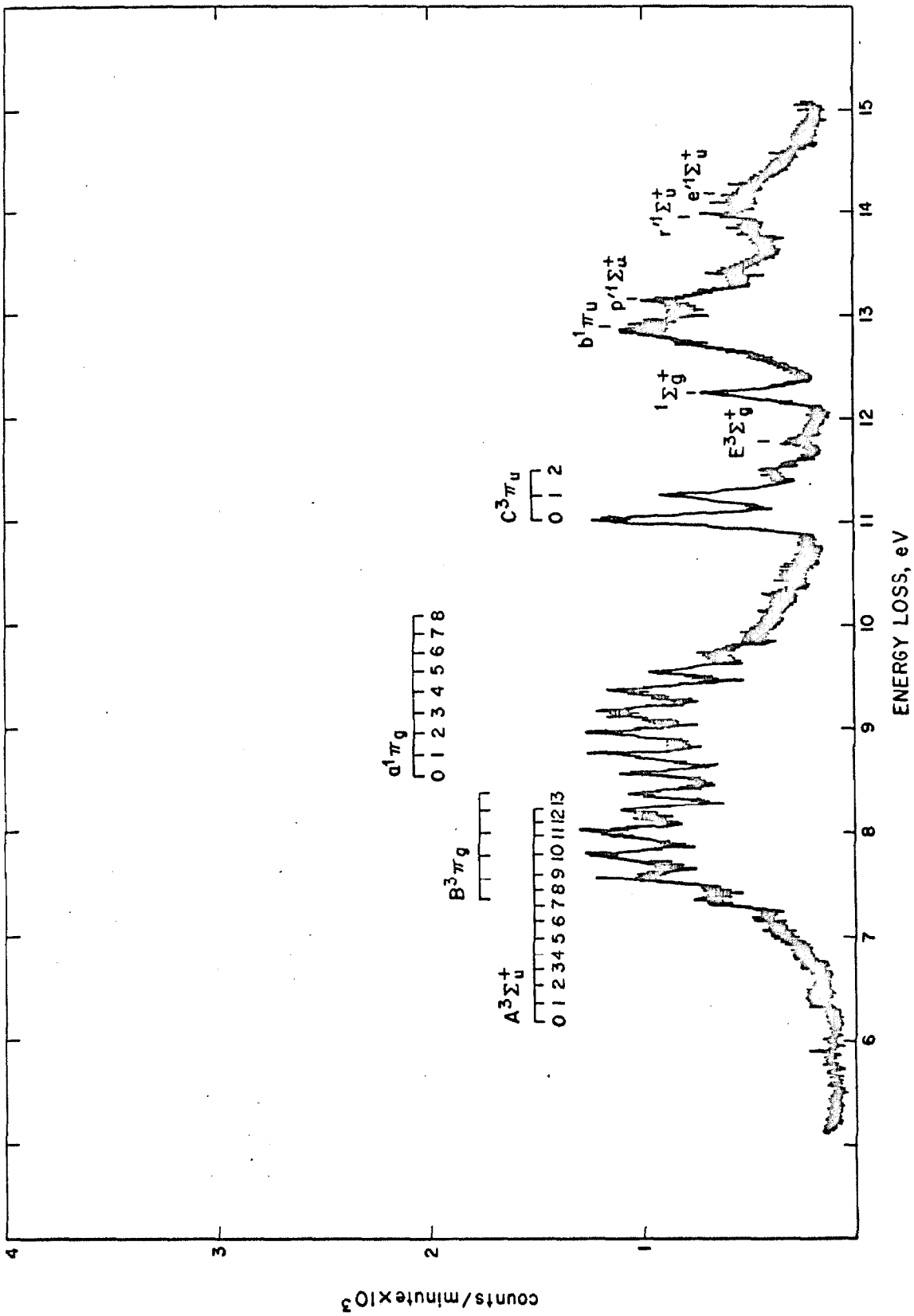
counts/minute x10³
ENERGY LOSS, eV
a¹πg
0 1 2 3 4 5 6 7 8
B³πg
A³Σu+
0 1 2 3 4 5 6 7 8 9 10 11 12 13
C³πu
0 1 2
b¹πu
p'¹Σu+
r'¹Σu+
e'¹Σu+
¹Σg+
E³Σg+

agrees with that of reference (22a) (although our resolution is not as good) while the high angle one is similar to the one of reference (36c) except that our resolution is much better. Figure 5.3-3 shows a separate scan at $\theta = 80°$ of the energy-loss region from about 6 eV to 11.5 eV. In this figure, transitions to several of the $A^3\Sigma_u^+$ vibrational levels can be weakly observed.

It is of interest to first consider the validity of the Franck-Condon factor considerations discussed in section 3.3.7.1. If they are valid, we expect the relative vibrational peak intensities (after application of the suitable correction, see section 3.3.7.1) to be (1) independent of incident energy, (2) independent of scattering angle, and (3) in accord with the results from optical measurements and reliable calculations. The $C^3\Pi_u$ state is a good "test" case since its vibrational levels are well resolved and the electronic band itself is relatively isolated. Table 5.3-2 summarizes the relative intensity data obtained in this research as well as the calculations of Benesch, et al.[137]. The error limits in the table are calculated according to equation (5-2). They do not contain a possible systematic error due to the background correction. Since the base line was determined below 6 eV, a rising background in the vicinity of 11 eV would increase the measured relative intensities. This effect would be most severe for the smallest peak, i.e., the $\nu' = 2$ one. Within the errors of this determination there is no change with scattering angle and the overall average is in reasonable agreement with the calculations[137] without the use of $C^{ED}_{\nu\nu 0}$. The

Figure 5.3-3. Energy-loss spectrum of N_2 (6 eV to 9.5 eV). E_o = 35 eV, $I_o = 3 \times 10^{-8}$ A, $\theta = 80°$, SR = .002 V/sec, TC = 10 sec, $P = 2 \times 10^{-3}$ torr.

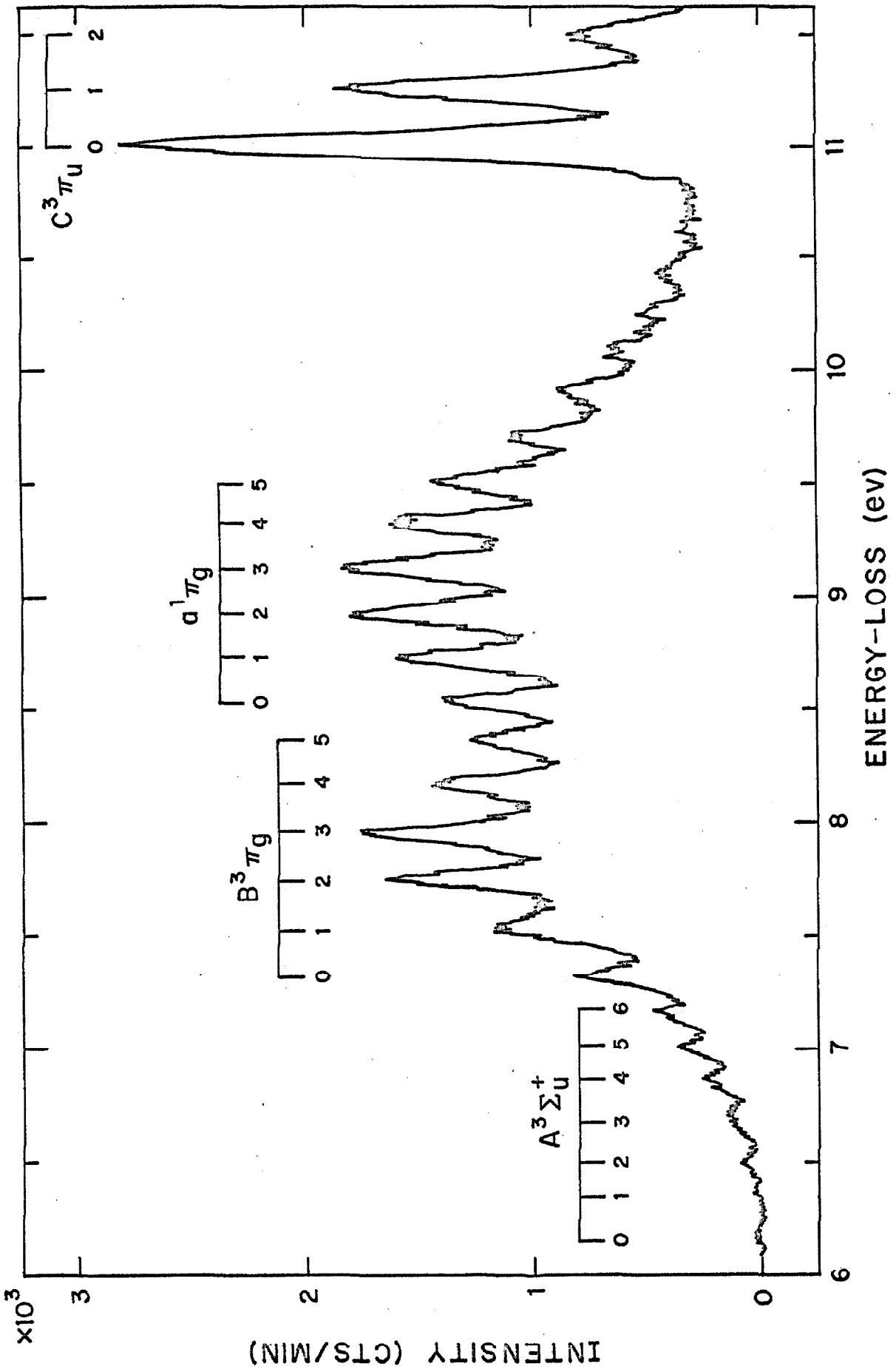
$C^3\pi_u$
$a^1\pi_g$
$B^3\pi_g$
$A^3\Sigma_u^+$
ENERGY-LOSS (eV)
INTENSITY (CTS/MIN)
x10^3

TABLE 5.3-2

Relative intensity distribution of the $X^1\Sigma_g^+(\nu = 0) \rightarrow C^3\Pi_u$ ($\nu' = 0,1,2$) transitions of N_2. The incident energy is 25 eV. The $\nu' = 0$ peak intensity is normalized to 1.00. Columns 2 and 3 contain the relative peak intensities. Columns 5 and 6 contain the factor indicated in equation (3-74) (section 3.3.7.1).

Scattering Angle (degrees)	ν' 1	ν' 2	Number of Scans	C_{10}^{ED}	C_{20}^{ED}
10	.61 ± .05	.21 ± .04	4	1.028	1.056
20	.62 ± .04	.21 ± .04	4	1.008	1.016
30	.60 ± .04	.20 ± .02	5	.997	.994
40	.59 ± .04	.22 ± .03	4	.991	.983
50	.66 ± .07	.22 ± .03	4	.989	.978
60	.68 ± .03	.24 ± .03	4	.987	.974
70	.64 ± .03	.27 ± .03	4	.986	.972
80	.68 ± .04	.27 ± .02	6	.985	.970
Average over all angles	.63 ± .03	.23 ± .02	35	.996	.993
Calculated values[a]	.558	.193			

[a] Reference (137).

precision in the measurements is not sufficient to determine whether the small trend ($\sim 4\%$) in angle, predicted by equation (3-74), is correct. If anything, this trend seems opposite to that indicated (possibly) by the data (i.e., dividing the relative intensities by C_{10}^{ED} or C_{20}^{ED} would enhance the slight deviation with angle rather than decrease it). Since the relative intensity of the $\nu' = 2$ peak is only $\sim 10\%$ larger than the calculated value, the background problem mentioned above is apparently not significant (assuming the reliability of the calculation[137]).

A similar determination was performed for an impact energy of 35 eV. An average of 28 scans at angles from 10° to 80° yielded a $\nu' = 1$ relative intensity of $0.60 \pm .03$ and a $\nu' = 2$ relative intensity of $0.21 \pm .03$. Notice that the relative intensities are also independent of incident energy (at least in this 25 - 35 eV energy range).

The relative vibrational intensities within the $a^1\Pi_g$ band have been measured by other investigators at $\theta = 0°$. We cannot reliably measure these intensities at large angles because of the overlapping $B^3\Pi_g$ state. However, six low-angle scans ($\theta \lesssim 15°$) were used to determine the relative intensities summarized in table 5.3-3. The agreement with the calculated values is quite good, except possibly for $\nu' = 0$. The $\nu' = 9$ and 10 relative intensities of this research are in better agreement with theory than those of reference (17c), presumably because the background problem encountered in that work was not evident in ours. There is an

TABLE 5.3-3

Intensity distribution in the $a^1\Pi_g$ band of N_2. The $X^1\Sigma_g^+(\nu = 0) - a^1\Pi_g(\nu' = 3)$ transition intensity is normalized to 1. $C^{DQ}_{\nu'3}$ has been calculated for an incident energy of 25 eV.

		Incident Energy (eV)				
ν'	$C^{DQ}_{\nu'3}$	400[a]	60[a]	35[b]	25 (This Research)	Calcd.[c]
0	1.019	.37 ± .03	.28 ± .02	.28	.27 ± .02	.235
1	1.012	.68 ± .04	.63 ± .05	.69	.64 ± .04	.630
2	1.006	.96 ± .07	.91 ± .03	.93	.93 ± .05	.932
3	1.00	1.00	1.00	1.00	1.00	1.00
4	.994	.83 ± .04	.85 ± .04	.84	.86 ± .03	.873
5	.998	.66 ± .01	.61 ± .05	.65	.62 ± .04	.664
6	.981	.48 ± .03	.42 ± .03	.45	.45 ± .03	.453
7	.975	.37 ± .02	.26 ± .03	.30	.28 ± .03	.287
8	.970	.27 ± .04	.17 ± .01	.22	.19 ± .02	.172
9	.965	.18 ± .01	.11 ± .01	-	.097 ± .008	.097
10	.959	.12 ± .01	(.07)	-	.04 ± .01	.054

[a] Reference (17c).

[b] Derived from the spectra of reference (29).

[c] Reference (137).

optically determined[138] set of relative intensities with which the data of table 5.3-3 can also be compared, but the relative precision of the optical measurements is too low for a meaningful comparison[139]. Again, the precision of the data is not sufficient to test the predictions of equation (3-73). The C_{03}^{DQ} value, although greater than unity, is not nearly large enough to lower the relative intensity of the $\nu' = 0$ peak by the required 10% (if this value is to agree with the calculations of reference (137)).

As mentioned in section 2, the only doubtful state assignment in this energy-loss region is that of the E one (at 11.87 eV). The state at 12.26 eV seems clearly to be a $^1\Sigma_g^+$ one[18] while the one at 11.87 eV may be either a $^1\Sigma_g^+$ (references (17a,19)) or $^3\Sigma_g^+$ (reference (29)). Meyer and Lassettre[17a] and Lassettre, et al.[17c] argue for the former (singlet) assignment primarily because they observe it at an impact energy of 400 eV. Heideman, et al.[29] prefer the latter assignment since the $\theta = 0°$ excitation function of this state is sharply peaked near threshold--a behavior indicative of a singlet → triplet transition. This disagreement can be resolved by comparing the relative angular dependencies of the DCS for excitation of the 11.87 eV and 12.26 eV states. Figure 5.3-4 shows the peak intensity ratios of the $E^3\Sigma_g^+$ (11.87 eV), $^1\Sigma_g^+$ (12.26 eV), $p'^1\Sigma_u$ (13.21 eV) and $C^3\Pi_u$ (11.03) excitations with respect to the $b^1\Pi_u$ (12.92 eV) one as a function of scattering angle from $\theta = -30°$ to $+80°$ for $E_0 = 35$ eV (uncalibrated). The $C^3\Pi_u$ intensity is the sum of the $\nu' = 0$, 1, and 2 vibrational level peak intensities while the

Figure 5.3-4. Ratios of intensities of the $X^1\Sigma_g^+ \rightarrow E^3\Sigma_g^+$ (11.87 eV), ■; $^1\Sigma_g^+$ (12.26 eV), ○; $C^3\Pi_u$ (11.03 eV), △; and $p'^1\Sigma_u^+$ (13.21 eV), □ transitions to that of the $b^1\Pi_u$ (12.92 eV) one in N_2 as a function of scattering angle. E_o = 35 eV. Peak intensities were used for the E, $^1\Sigma_g^+$, p', and b states while the sum of the $v' = 0, 1, 2$ vibrational level peak intensities was used for the C state. Each data point is an average of three to four scans at each angle. For clarity, only a few representative error bars are shown.

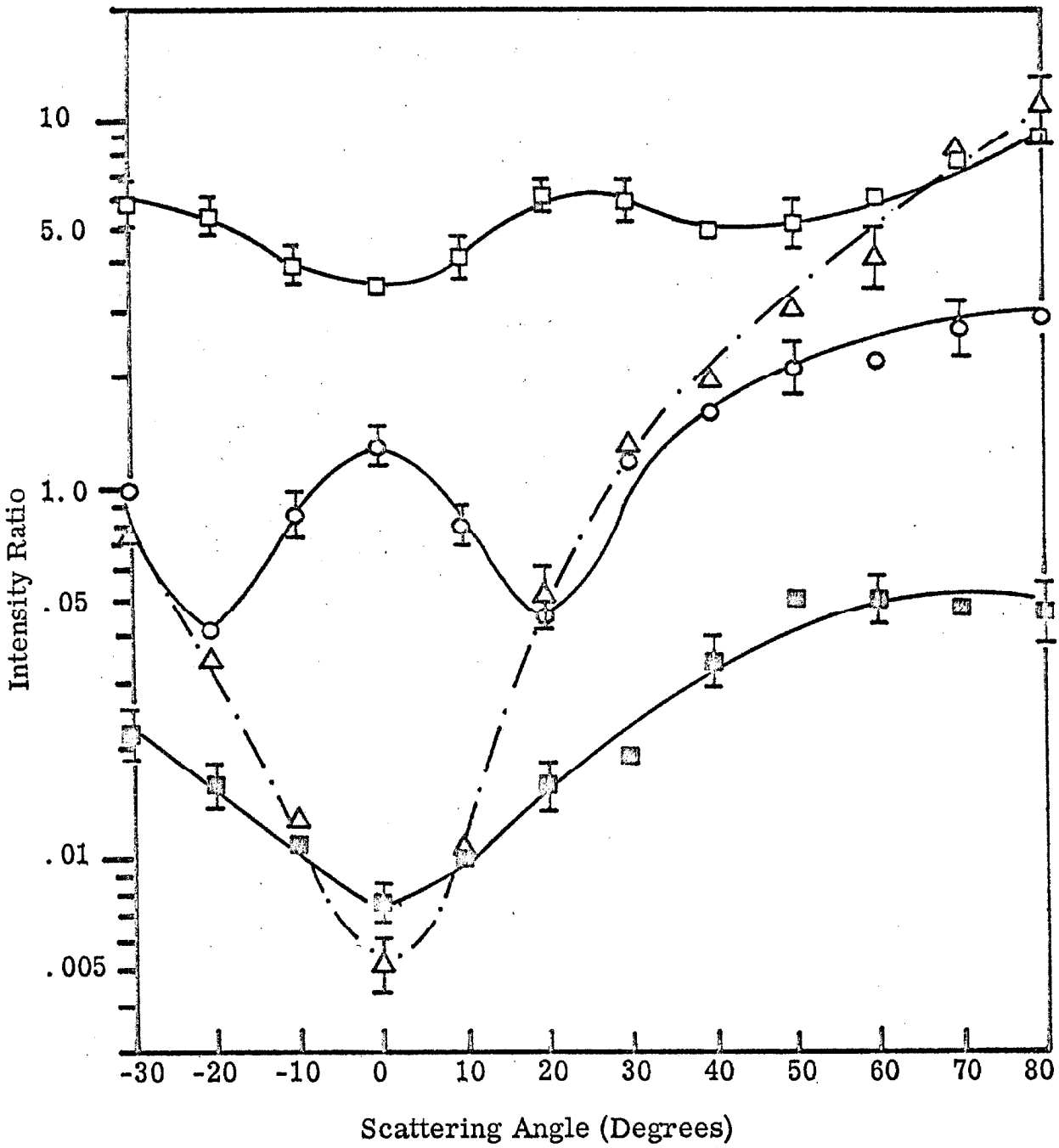
10
5.0
1.0
.05
.01
.005
Intensity Ratio
-30
-20
-10
0
10
20
30
40
50
60
70
80
Scattering Angle (Degrees)

intensity of the others are measured at their respective peaks. This figure clearly shows the expected symmetry of these ratios about $\theta = 0°$ (see section 4.4.3.2). Since the relative intensities of the vibrational levels within a given electronic band seem to be independent of angle (or incident energy), these ratios are equal to the "true" DCS ratios times a constant (independent of angle but dependent upon resolution). Of prime importance is the fact that the variation with θ of these plotted ratios is the same as that of the "true" DCS ratios. It is clear that the triplet/singlet ratios behave with θ as we expect (qualitatively) from theory and agree with our observations in helium.

The X → b transition in N_2 and the $1^1S \rightarrow 2^1P$ transition in helium are similar in that the change in orbital angular momentum ($\Delta\Lambda$) is 1 while the change in spin angular momentum (ΔS) is 0. Likewise, the X → C (N_2) and $1^1S \rightarrow 2^3P$ (He) transitions have $\Delta\Lambda = 1$ and $\Delta S = 1$. Thus, we might expect the C/b (N_2) and $2^3P/2^1P$ (He) ratios to behave in a similar manner with angle for impact energies which are higher than their corresponding threshold energies by about the same amount. A comparison of figure 5.3-4 (the incident energy is ~ 24 eV above threshold) and figure 5.2-4 (of section 5.2) shows this to be the case. In an analogous way, we expect the $^1\Sigma_g^+$ (12.26 eV)/b and $2^1S/2^1P$ ratios to exhibit similar behavior with θ. This also is evident in the comparison of these two figures. Finally, the assignment of the 11.87 eV transition as $E^3\Sigma_g^+$ is completely consistent with the similarity in the behavior of the $2^3S/2^1P$ and $E^3\Sigma_g^+$ (11.87)/b ratios ($\Delta\Lambda = 0$, $\Delta S = 1$ for both upper

states). Even if these somewhat qualitative comparisons are not convincing, it is clear from figure 5.3-4 that the 11.87 eV and 12.26 eV transitions are fundamentally different. Further, the assignment of the 11.87 eV transition as a singlet would be entirely inconsistent with our understanding of the way in which singlet/singlet and triplet/singlet ratios differ with θ. The results obtained for the isoelectronic molecule CO (see section 5.4) provide an additional justification for assigning the 11.87 eV state as a triplet.

Figure 5.3-5 shows the same peak intensity ratios of figure 5.3-4 for a lower impact energy (25 eV, uncalibrated). Note that both the E/b and C/b ratios increase by about the same amount relative to the $^1\Sigma_g^+$/b ratio. This also indicates the singlet → triplet nature of the 11.87 eV transition.

Figure 5.3-6 shows the p' $^1\Sigma_u^+$ (peak)/b $^1\Pi_u$ (peak), B $^3\Pi_g$ (ν' = 4)/b $^1\Pi_u$, and a $^1\Pi_g$ (ν' = 3)/b $^1\Pi_u$ ratios as a function of θ at 40 eV (uncalibrated). The B/b ratio behavior is nearly identical to that of the C/b one. Since the X → B and X → C transitions have $\Delta\Lambda = 1$ and $\Delta S = 1$ in common but different "even-odd" symmetries (i.e., X → B is g → g while X → C is g → u), this similarity may indicate that the latter distinction is less important in determining the angular dependence of the DCS than the former ones. However, this does not seem to be the case when $\Delta S = 0$. The $^1\Sigma_g^+$/b and p' $^1\Sigma_u^+$/b ratios both oscillate between 0° and 80° but with opposite initial slopes. Also, the a/b ratio oscillates with nearly the same frequency and phase as the p'/b one but with a larger amplitude. Note that the

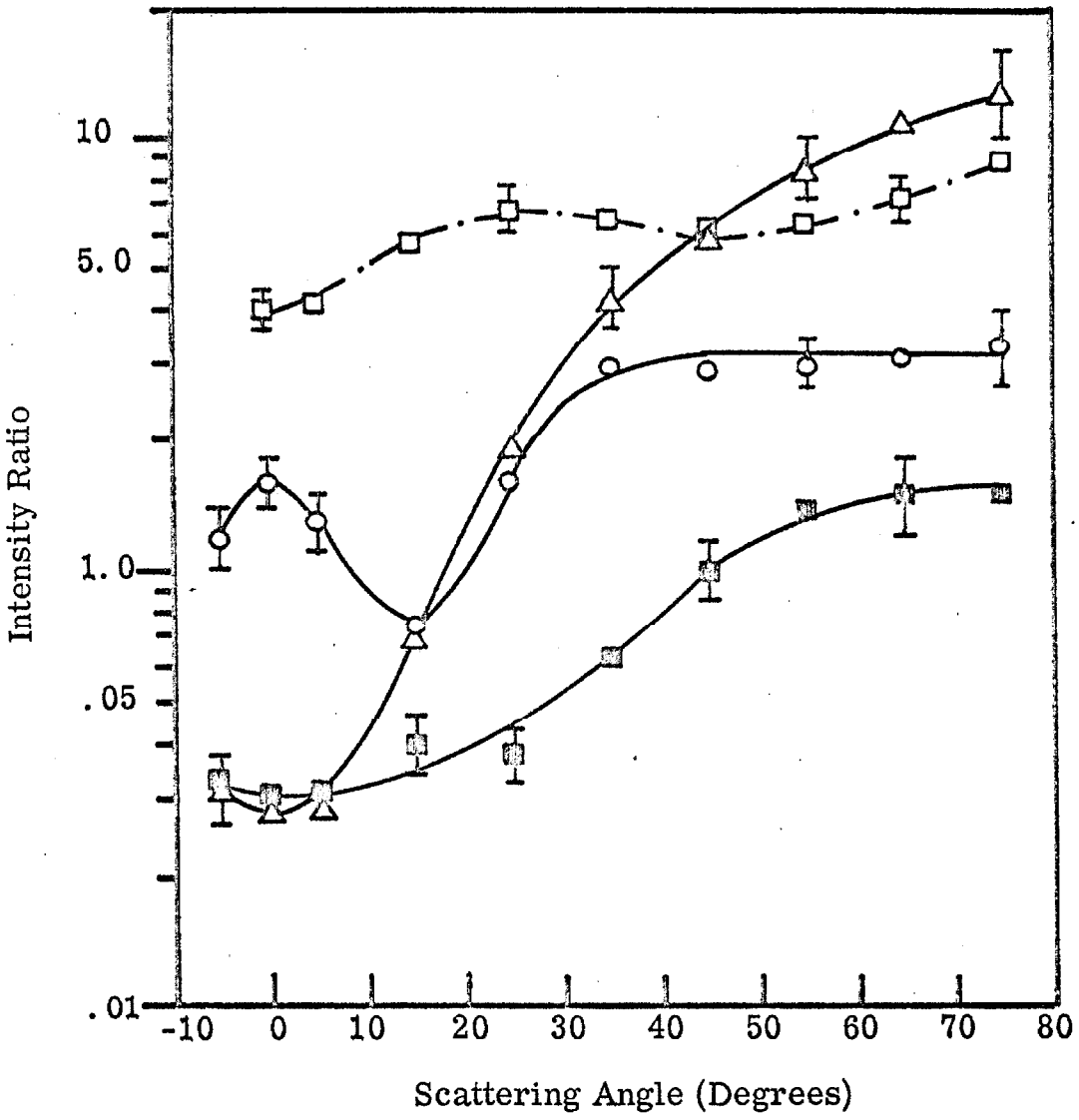

Figure 5.3-5. Ratios of intensities of the $X^1\Sigma_g^+ \rightarrow E^3\Sigma_g^+$, ■; $^1\Sigma_g^+$, ○; $C^3\Pi_u$, △; and $p'^1\Sigma_u^+$, □ transitions to that of the $b^1\Pi_u$ one in N_2 (see the caption of fig. 5.3-4). E_o = 25 eV. Each data point is an average of four to six scans (as listed in table 5.3-2).

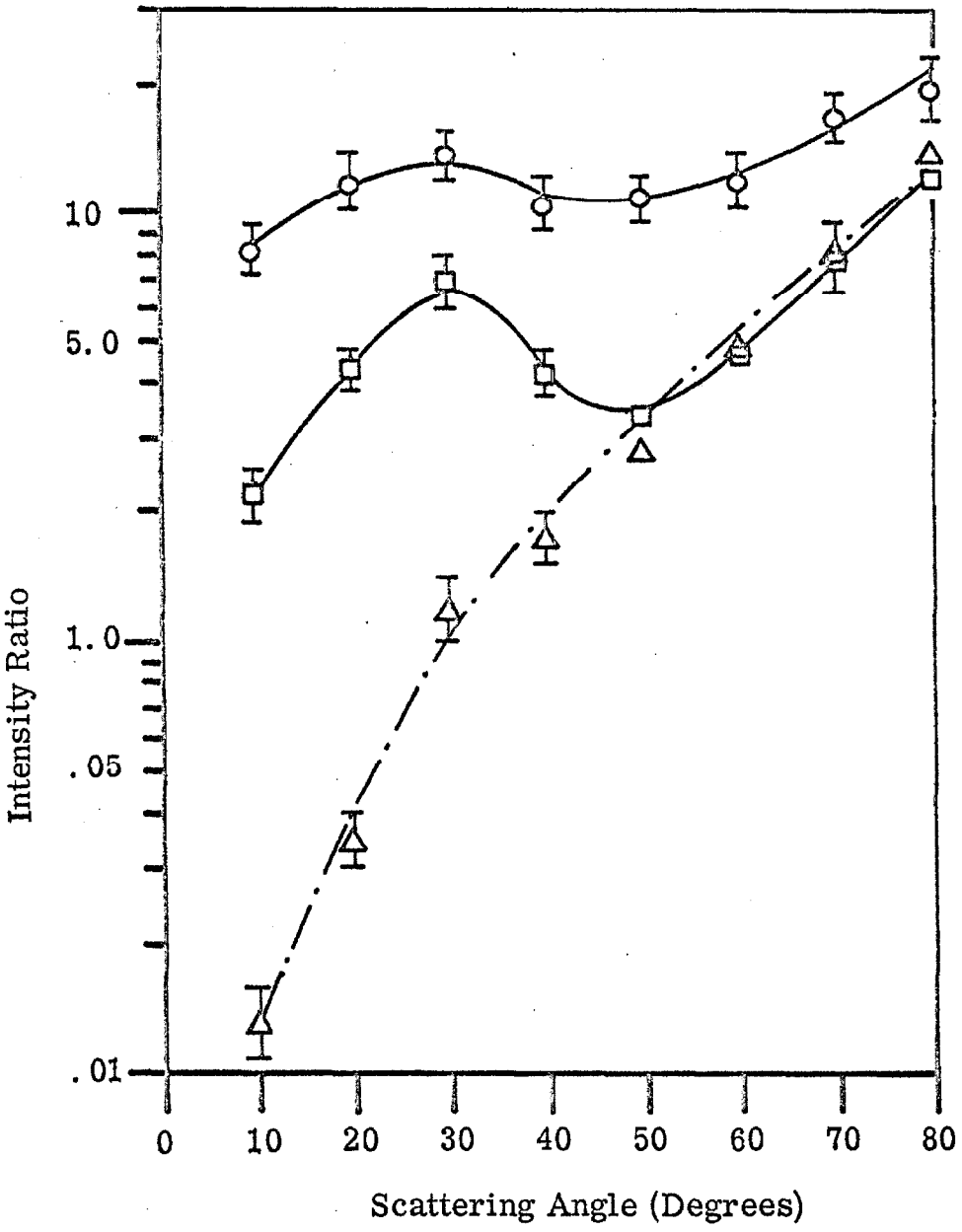

Figure 5.3-6. Ratios of intensities of the $X^1\Sigma_g^+ - B^3\Pi_g$ ($\nu' = 4$), △; $a^1\Pi_g$ ($\nu' = 3$), □; and $p'^1\Sigma_u^+$ (peak), ○ transitions with respect to that of the $b^1\Pi_u$(peak) one in N_2. E_o = 40 eV. Each data point is an average of three scans.

$X \rightarrow p'$ and $X \rightarrow a$ transitions are $g \rightarrow u$, $\Delta\Lambda = 0$, $\Delta S = 0$ and $g \rightarrow g$, $\Delta\Lambda = 1$, $\Delta S = 0$, respectively, while the $X \rightarrow {}^1\Sigma_g^+$ one is $g \rightarrow g, \Delta\Lambda = 0, \Delta S = 0$.

Figure 5.3-7 contains the DCS (in arbitrary units) for the transitions in figure 5.3-4 (35 eV) while figure 5.3-8 presents them for the transitions in figure 5.3-6 (40 eV). Notice that as expected all of the singlet DCS are more sharply peaked forward than any of the triplet ones.

These DCS cannot be placed on an absolute scale primarily because there is no absolute determination of $Q^T_{b\,{}^1\Pi_u}(E)$ with which the $Q^{Arb}_{b\,{}^1\Pi_u}(E)$ can be normalized for E less than about 100 eV[140]. Also, the lack of equal vibrational resolution of the various electronic bands (i.e., the vibrational structure of the $a\,{}^1\Pi_g$ state is resolved while that of the $b\,{}^1\Pi_u$ one is not) complicates the relation of peak intensity ratios to DCS ratios. The first difficulty could be overcome by using a mixture of He and N_2 (of known concentration) in the scattering chamber. The N_2 DCS could then be determined using He as a standard.

5.4. Carbon Monoxide

5.4.1. Introduction

CO is isoelectronic with N_2 and as expected exhibits a somewhat similar energy-loss spectrum under electron impact. Table 5.4-1 summarizes the electronic and vibrational transitions we can observe below an excitation energy of about 12 eV. Transitions from the $X\,{}^1\Sigma^+$ ground state to the $a\,{}^3\Pi$ and $b\,{}^3\Sigma^+$ states are spin-forbidden

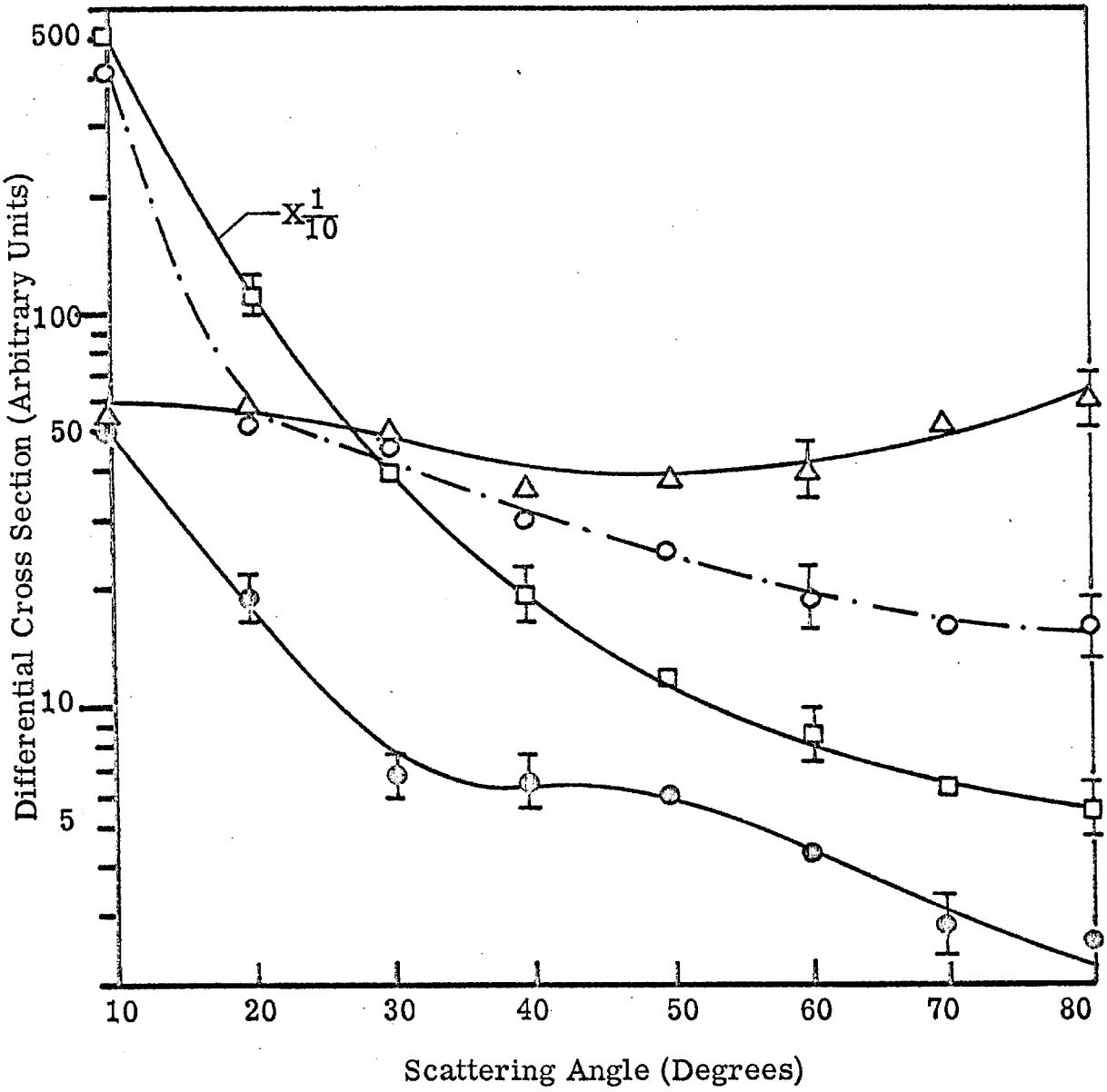

Figure 5.3-7. Differential cross section (arbitrary units) for excitation of the $E\,^3\Sigma_g^+$, ●; $^1\Sigma_g^+$, ○; $C\,^3\Pi_u$, △; and $b\,^1\Pi_u$, □ states in N_2. E_o = 35 eV. For clarity, only a few representative error bars are shown.

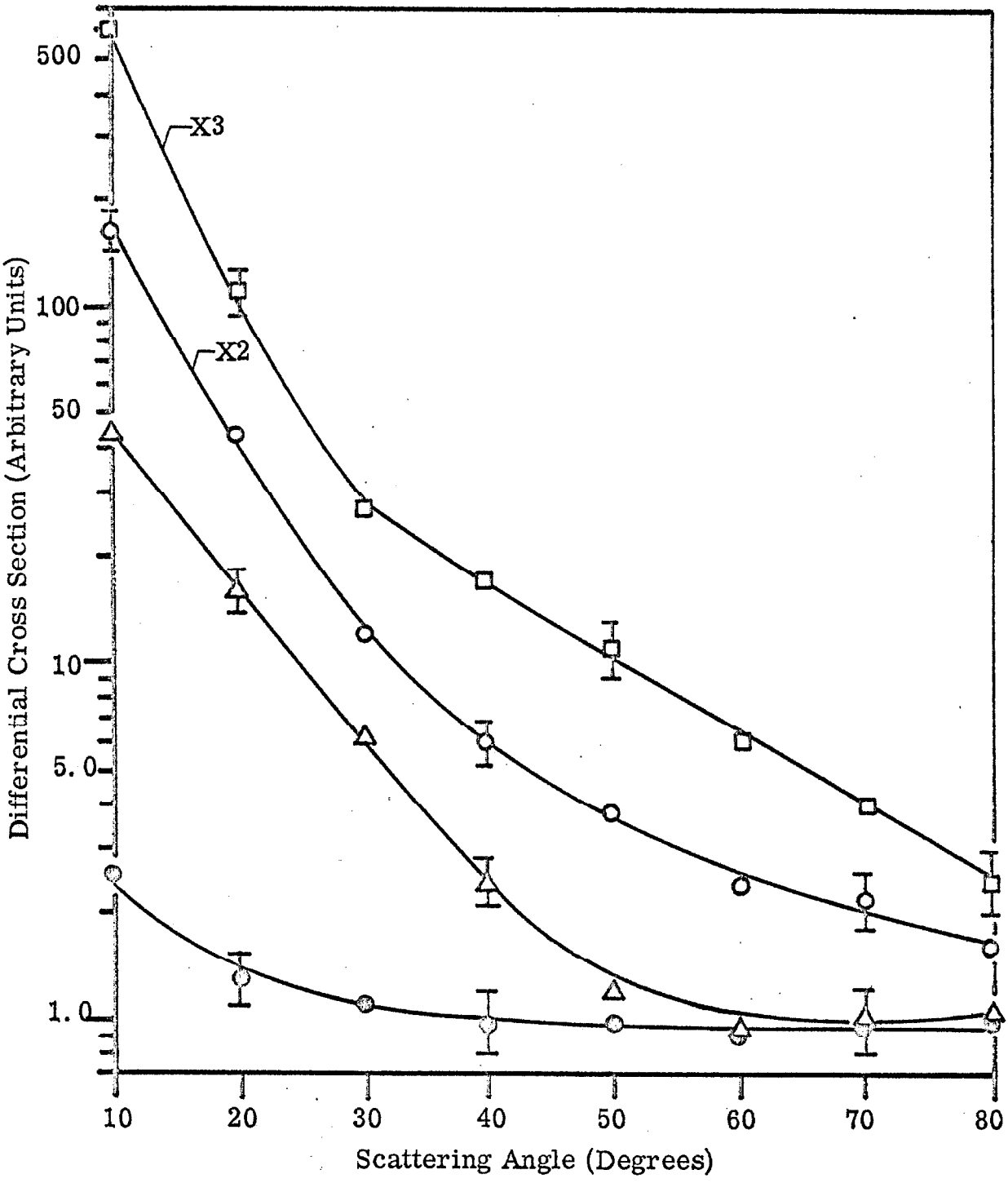

Figure 5.3-8. Differential cross section (arbitrary units) for excitation of the $B^3\Pi_g(\nu' = 4)$, ⊙; $a^1\Pi_g$ ($\nu' = 3$), △; $p'^1\Sigma_u^+$, ○; and $b^1\Pi_u$, □ states in N_2. E_o = 40 eV.

TABLE 5.4-1

Transitions from the $X^1\Sigma^+$ ($\nu = 0$) ground state of CO to various electronic and vibrational states below 12 eV. The abbreviations are defined in table 5.3-1.

UES[a]	UVS	OPT. EE[b] (eV)	OBS. EE[c] (eV)
$a^3\Pi$	0	6.01	6.01
	1	6.22	6.22
	2	6.43	6.43
	3	6.63	6.64
	4	6.84	6.85
$A^1\Pi$	0	8.03	8.03
	1	8.21	8.21
	2	8.39	8.39
	3	8.56	8.57
	4	8.74	8.73
	5	8.90	8.90
	6	9.06	9.07
	7	9.22	-
$b^3\Sigma^+$	0	10.39	10.40
	1	10.67	-
	2	10.94	-
$B^1\Sigma^+$	0	10.78	10.77
	1	11.03	11.03
	2	11.29	-
$C^1\Sigma^+$	0	11.40	11.40
	1	11.66	
$(E^1\Pi)$[d]	0	11.52	(11.50)[e]
	1	11.78	

[a] State designations are from reference (2b), pp 520-522.

[b] Calculated from the data of reference (a) above.

[c] The values are believed to be accurate to about ± .01 eV.

[d] This state designation is given by S. G. Tilford, J. T. Vanderslice,

TABLE 5.4-1 (continued)

and P. G. Wilkinson, Can. J. Phys., 43, 450 (1965).

[e] Observed as a shoulder on the $C^1\Sigma^+$ ($\nu' = 0$) peak.

while all other transitions in table 5.4-1 are optically allowed. Potential energy curves for these states and a summary of available optical data on CO can be found in the review of Krupenie[141].

The electron-impact excitation spectrum of CO was first obtained by Schulz[9a] using the trapped-electron technique. Transitions to the $a^3\Pi$ state (Cameron bands) were the most intense feature in his spectrum. Brongersma and Oosterhoff[11], with an improvement of this same technique, were able to resolve some vibrational structure in the $a^3\Pi$ state. Transitions to the $A^1\Pi$ state were not observed while those to the $B^1\Sigma^+$ and $b^3\Sigma^+$ ones were relatively intense.

Lassettre and coworkers[142] first studied the X → A transition in the energy-loss spectrum of CO at an incident energy of 500 eV and $\theta \leq 15°$. Lassettre and Silverman[143] expanded this study to the angular dependence of the X → B and X → C transitions ($\theta \lesssim 15°$). In a later publication[144] they compared the envelope shape of the unresolved X → A transition with theoretically calculated Franck-Condon factors. The agreement was quite good. Meyer, et al.[21] were able to resolve the X → A vibrational structure with an improved spectrometer. They again compared the relative intensities within this band to calculated Franck-Condon factors. However, noticeable discrepancies were found for higher vibrational levels. This led them to suggest that the intensity distributions within the $A^1\Pi$ band might be energy-dependent, approaching the calculated values at higher (> 200 eV) impact energies. Skerbele,

et al.[145] reinvestigated the $A^1\Pi$ band at 200 eV and 400 eV incident energy ($\theta \lesssim 6°$). They found that the relative intensities of the vibrational levels were independent of angle but differed from calculated Franck-Condon values at higher v'. Also a slight trend in the relative intensity distribution as a function of impact energy was noted.

Recently, Skerbele, et al.[22b] reported a high resolution study of CO at 50 eV impact energy in which excitations of the $a^3\Pi$ and $b^3\Sigma^+$ states were observed in addition to those of the $A^1\Pi$, $B^1\Sigma^+$, $C^1\Sigma^+$, $E^1\Pi$, and $F^1\Pi$ ones. The relative vibrational intensities within the $a^3\Pi$ band agreed well with the calculations of Nicholls[146].

5.4.2. Results and Discussion

Figures 5.4-1 and -2 show electron energy-loss spectra of CO at an impact energy of 25 eV (uncalibrated) and $\theta = 10°$ and 75°, respectively. Since the vibrational structure of both the $a^3\Pi$ and $A^1\Pi$ states is clearly resolved, we can compare the relative peak intensities within these bands with calculations[146] and the results of other investigators[21, 22b, 145]. Table 5.4-2 summarizes the results obtained at 25 eV and 35 eV for the $A^1\Pi$ band. Since we observed no angle dependence in the relative intensities (within the error of this data), all of the scans at each energy are averaged together. However, from equation (3-72) (section 3.3.7.1), we would expect a rather significant difference in the distribution of relative intensities at $\theta = 0°$ from those at $\theta = 80°$. In particular

Figure 5.4-1. Energy-loss spectrum of CO. $E_o = 25$ eV, $I_o = 1 \times 10^{-8}$ A, $\theta = 10°$, S.R. = .01 V/sec, TC = 1 sec, $P = 2 \times 10^{-3}$ torr.

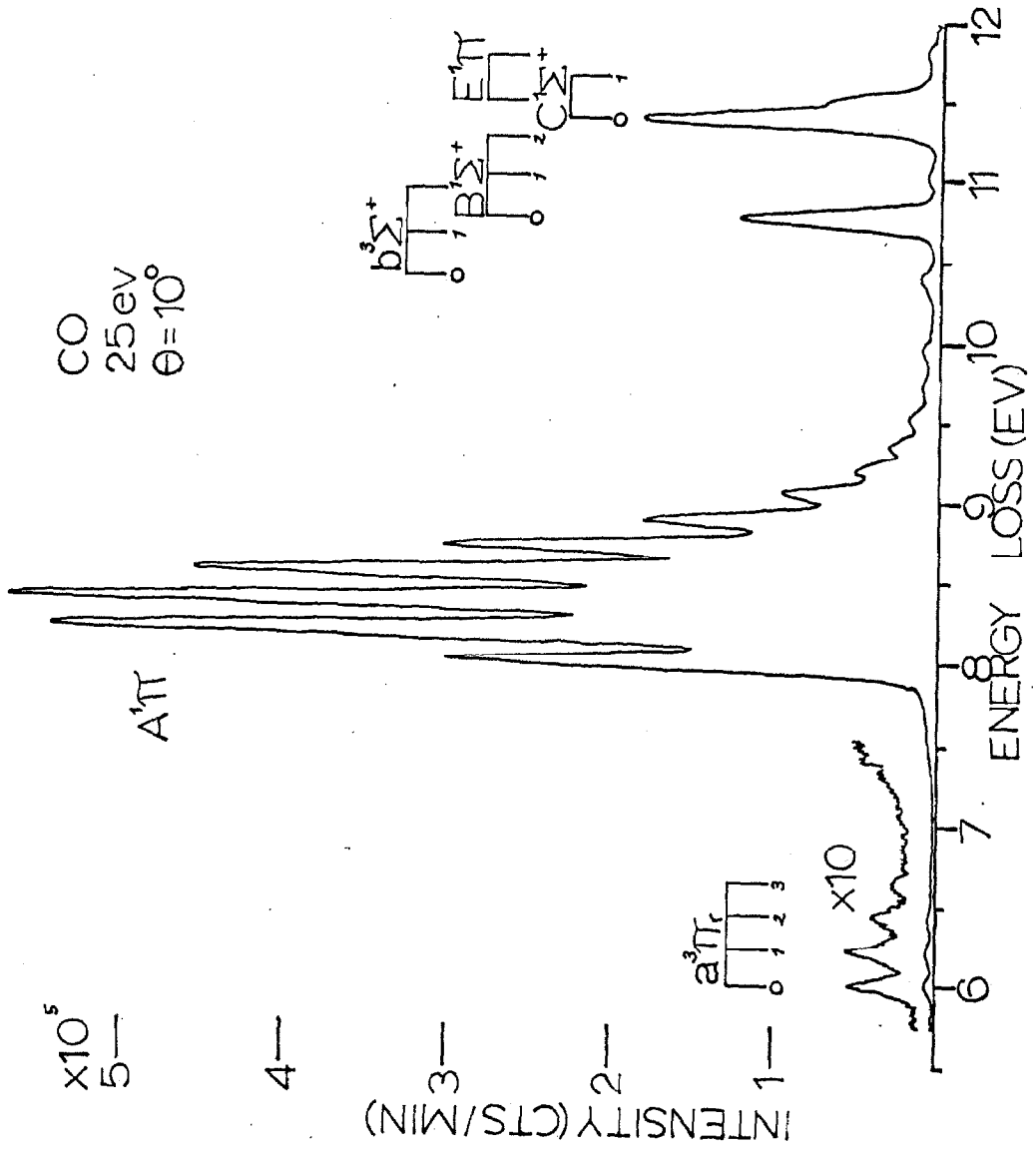
CO
25ev
θ=10°
A¹Π
b³Σ⁺
B¹Σ⁺
C¹Σ⁺
E¹Π
a³Π
×10
×10⁵
INTENSITY (CTS/MIN)
ENERGY LOSS (EV)

Figure 5.4-2. Energy-loss spectrum of CO. $E_o = 25$ eV, $I_o = 1 \times 10^{-8}$ A, $\theta = 75°$, S.R. = .002 V/sec, TC = 10 sec, $P = 2 \times 10^{-3}$ torr.

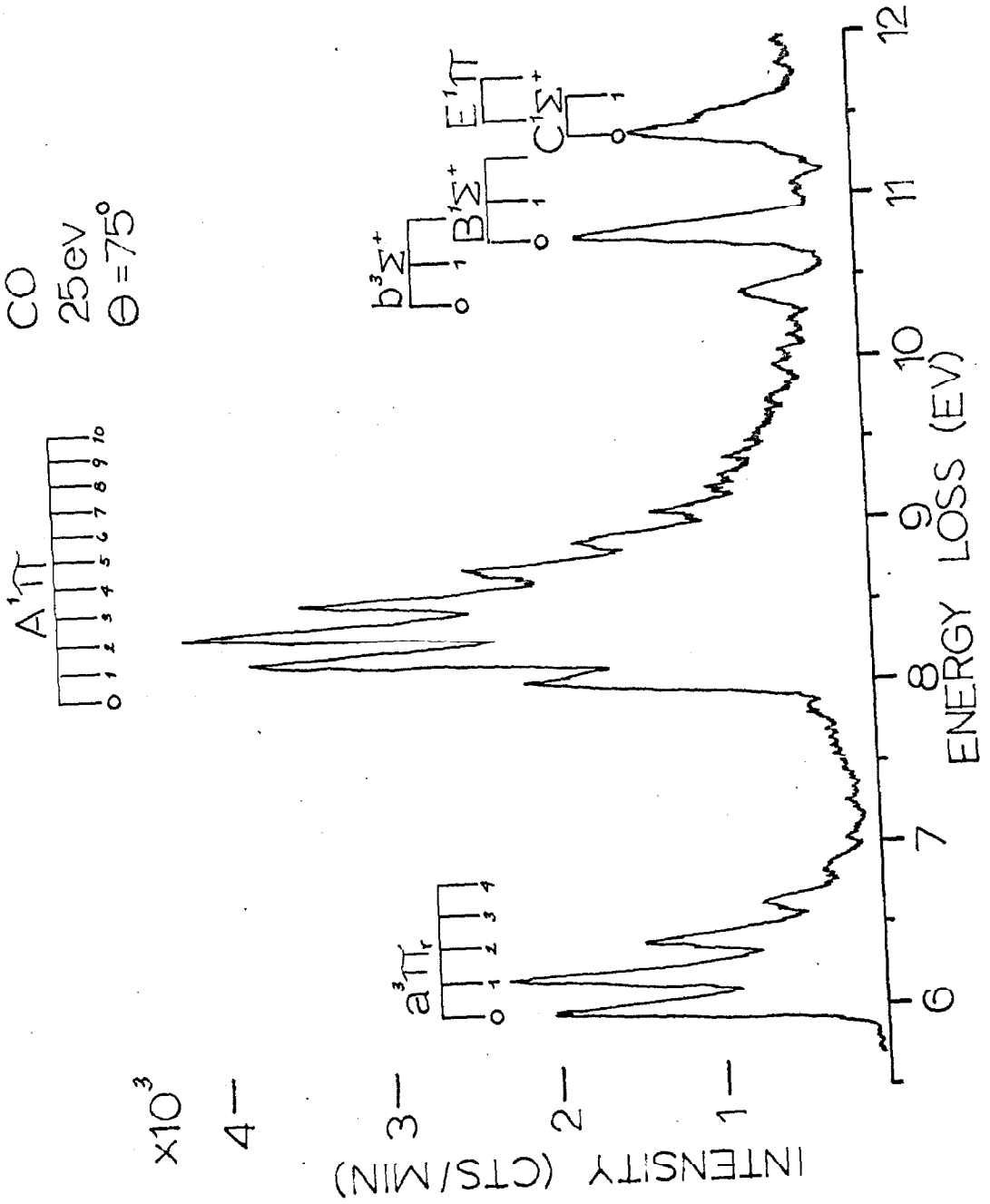
CO
25eV
θ=75°
A¹Π
0 1 2 3 4 5 6 7 8 9 10
a³Π
0 1 2 3 4
b³Σ⁺
0 1
B¹Σ⁺
0 1
C¹Σ⁺
0 1
E¹Π
INTENSITY (CTS/MIN)
x10³
4
3
2
1
6 7 8 9 10 11 12
ENERGY LOSS (EV)

TABLE 5.4-2

Relative vibrational intensity distribution in the $A^1\Pi$ band of CO. The $X^1\Sigma^+$ ($\nu = 0$) → $A^1\Pi$ ($\nu' = 2$) transition intensity is normalized to 1.

ν'	Incident Energy (eV)					Calculations[f]
	400[a]	200[b]	50[c]	35[d]	25[e]	
0	.44 ± .02	.45 ± .02	.55	.48 ± .02	.51 ± .02	.492
1	.87 ± .02	.89 ± .02	.94	.95 ± .03	.94 ± .02	.940
2	1.00	1.00	1.00	1.00	1.00	1.00
3	.83 ± .03	.88 ± .02	.80	.81 ± .04	.78 ± .03	.788
4	.56 ± .03	.62 ± .02	.52	.54 ± .03	.52 ± .03	.517
5	.34 ± .01	.39 ± .02	.32	.34 ± .04	.31 ± .02	.299
6	.20 ± .01	.24 ± .02	.17	-	.16 ± .02	.159

[a] Reference (145).

[b] Reference (21).

[c] Derived from the spectrum of reference (22b).

[d] This research, average of 8 scans.

[e] This research, average of 11 scans.

[f] Reference (146).

equation (3-72) predicts that, at $\theta = 0°$

$$C_{02}^{DD} = 1.092 \text{ and } C_{62}^{DD} = .857 \text{ while at } \theta = 80°$$

$$C_{02}^{DD} = 1.005 \text{ and } C_{62}^{DD} = .991.$$

The fact that the angular resolution is only about 2° will not change these numbers (to 3 significant digits). Although the data do not indicate the trend predicted by equation (3-72), their precision is barely adequate for a valid comparison. It is interesting to note that the low-energy data of this research and reference (22b) agree much better with the calculations than do the high-energy data[21,145]. ($C_{\nu 2}^{DD}$ is essentially 1.00 under the high-energy conditions.)

Table 5.4-3 presents the relative intensities with the $a^3\Pi$ band. The "correction" factor predicted by equation (3-74) is not shown since it exhibits even less deviation from 1.00 than that predicted for the $C^3\Pi_u$ state of N_2. Again, the relative intensities were independent of angle and the average is presented in the table. It is noteworthy that the agreement of these relative intensities with calculations[146] is good even for impact energies within .05 eV of threshold (trapped-electron results[11]). To make equation (3-74) consistent with the trapped-electron method, q^2 and q_o^2 must be integrated over all angles before dividing them. This yields a vibrational level peak intensity ratio of

$$R_{\nu o}^{\nu} = \tilde{C}_{\nu\nu o} \frac{G_{oo}^{n\nu}}{G_{oo}^{n\nu o}} \qquad (5\text{-}13)$$

TABLE 5.4-3

Relative vibrational peak intensities in the $a^3\Pi$ (Cameron) band of CO. The $X^1\Sigma^+$ ($\nu = 0$) – $a^3\Pi$($\nu' = 1$) transition intensity is normalized to 1.

ν'	Incident Energy (eV)				Calculations[e]
	50[a]	Threshold[b] (+.05 eV)	35[c]	25[d]	
0	.84 ± .03	$1._0$	.88 ± .07	.84 ± .04	.835
1	1.00	1.00	1.00	1.00	1.00
2	.74 ± .03	$.6_8$	.75 ± .10	.64 ± .04	.686
3	.39 ± .10	$.3_4$	.44 ± .12	.34 ± .04	.357
4	-	.2	-	.16 ± .02	.158

[a] Reference (22b).

[b] Derived from the trapped-electron spectrum of reference (11) without an overlap correction.

[c] This research, average of angles from 0° to 75°, 8 scans.

[d] This research, average of angles from 0° to 80°, 15 scans.

[e] Reference (146).

where

$$\tilde{C}_{\nu\nu o} = \frac{k_\nu (k^2 + k_\nu^2)}{k_{\nu o}(k_o^2 + k_{\nu o}^2)} \quad ,$$

k^2 is proportional to the incident energy which excites the ν^{th} vibration, and k_o^2 is proportional to that for the νo^{th} one. However, each peak in the excitation spectrum of reference (11) corresponds approximately to the same electron energy after the scattering event. Thus, with $k_\nu = k_{\nu o} \equiv \lambda$, $\tilde{C}$ of equation (5-13) becomes

$$\tilde{C}_{\nu\nu o} \cong \frac{k^2 + \lambda^2}{k_o^2 + \lambda^2} \quad . \tag{5-14}$$

Since $\frac{\hbar^2 \lambda^2}{2m}$ is approximately .05 eV while $\frac{\hbar^2 k_o^2}{2m}$ and $\frac{\hbar^2 k^2}{2m}$ are ~ 6 eV,

$$\tilde{C}_{\nu\nu o} \cong \frac{k^2}{k_o^2} \cong \frac{W_\nu}{W_{\nu o}} \quad . \tag{5-15}$$

Consequently, the high-energy form of the Ochkur approximation predicts only a ~10% distortion in the relative peak intensities at threshold. (Of course, it is very doubtful that this set of approximations has any validity whatsoever at threshold.)

Figures 5.4-3 and -4 show the relative angular dependence of the DCS for excitation of the $a^3\Pi(\nu' = 0 + 1 + 2)$, $b^3\Sigma^+$ $(\nu' = 0)$, $B^1\Sigma^+$ $(\nu' = 0)$, and $C^1\Sigma^+(\nu' = 0)$ states with respect to that of the $A^1\Pi(\nu' = 0 + 1 + 2)$ one at incident energies of 35 eV and 25 eV, respectively. The a/A intensity ratio is quite characteristic of a

Figure 5.4-3. Ratios of intensities of the $X^1\Sigma^+(\nu = 0) \rightarrow C^1\Sigma^+$ ($\nu' = 0$), curve (a); $B^1\Sigma^+$ ($\nu' = 0$), curve (b); $a^3\Pi(\nu' = 0,1,2)$, curve (c); and $b^3\Sigma^+$ ($\nu' = 0$), curve (d) transitions to that of the $X \rightarrow A^1\Pi$ ($\nu' = 0,1,2$) one in CO. $E_0 = 35$ eV. Each data point is an average of three to four scans at each angle.

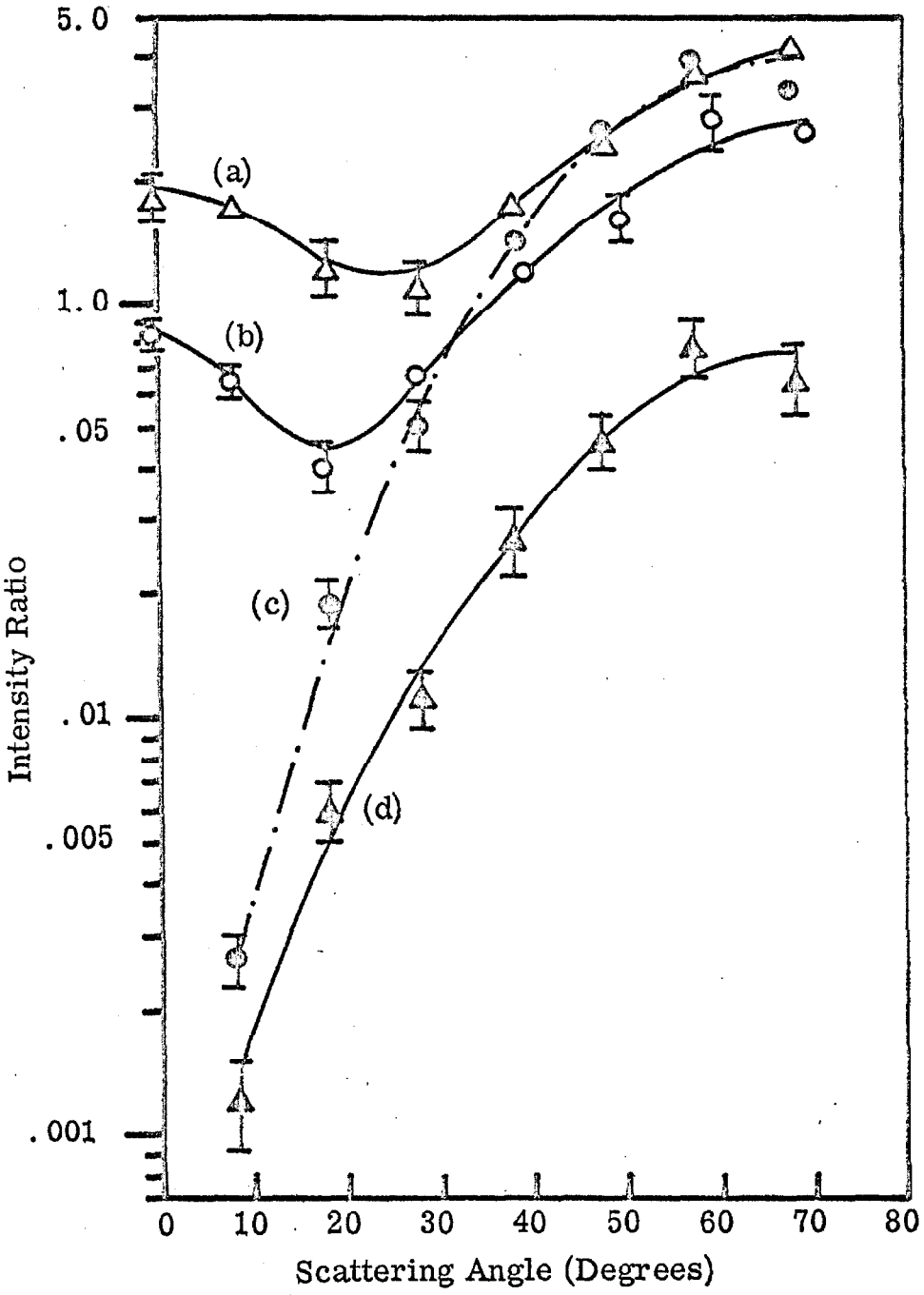
5.0
1.0
.05
.01
.005
.001
Intensity Ratio
(a)
(b)
(c)
(d)
0
10
20
30
40
50
60
70
80
Scattering Angle (Degrees)

Figure 5.4-4. Ratios of intensities as defined in figure 5.4-3. E_o = 25 eV. Each data point is an average of four scans at each angle.

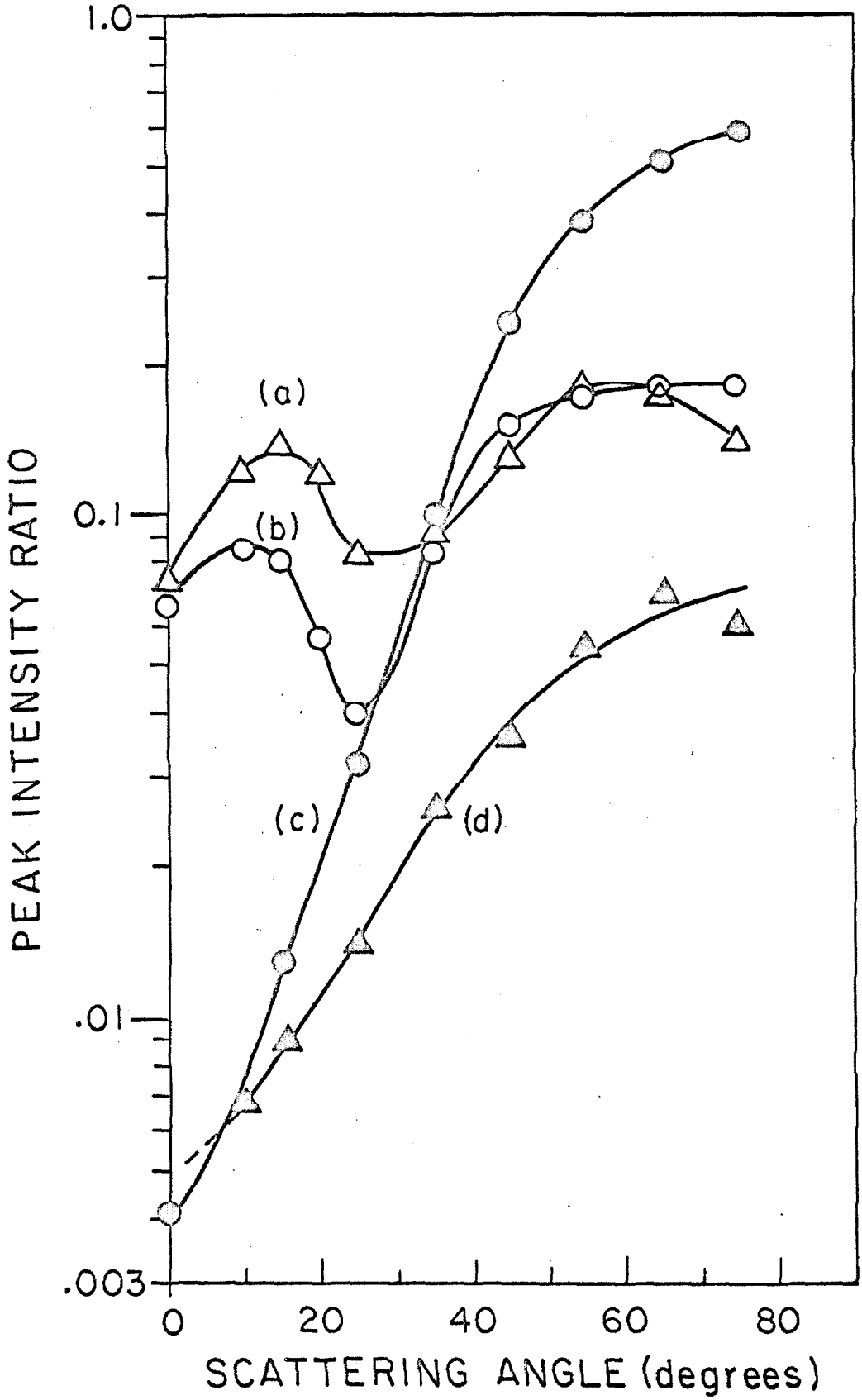
1.0
0.1
.01
.003
PEAK INTENSITY RATIO
(a)
(b)
(c)
(d)
0
20
40
60
80
SCATTERING ANGLE (degrees)

(singlet → triplet)/(singlet → singlet) ratio as evidenced by the $2^3P/2^1P$ ratio of helium and the $B^3\Pi_g/b^1\Pi_u$ and $C^3\Pi_u/b^1\Pi_u$ ratios of N_2. Also the b/A intensity ratio is quite similar to the $E^3\Sigma_g^+/b^1\Pi_u$ one of N_2 and the $2^3S/2^1P$ ratio of helium. This striking similarity with the E/b ratio of N_2 provides an additional confirmation of the triplet designation of that E state. The B/A and C/A intensity ratios exhibit a more complex behavior. At 35 eV they closely resemble the $^1\Sigma_g^+/b^1\Pi_u$ ratio of N_2 while at 25 eV they are more like the $a^1\Pi_g/b^1\Pi_u$ and $p'^1\Sigma_u^+/b^1\Pi_u$ ratios of N_2. In any case, they exhibit the oscillatory behavior which seems characteristic of ($\Delta S = 0$, $\Delta\Lambda = 0$, symmetry-forbidden)/($\Delta S = 0$, $\Delta\Lambda = 1$, allowed) intensity ratios.

Herzberg[2b] lists a $c^3\Sigma^+$ state with a 0 → 0 excitation energy of 11.415 eV. Also, Brongersma[11] observes a relatively intense feature at 11.42 eV in the threshold excitation spectrum. This transition is practically coincident with the $C^1\Sigma^+$ ($\nu' = 0$) transition (11.396 eV) which we observe and which may be responsible for the peak in reference (11). If excitation of the $c^3\Sigma^+$ state were important under our experimental conditions, we would expect the measured $C^1\Sigma^+/A^1\Pi$ ratio to increase abnormally (compared to the B/A ratio, for example) at larger scattering angles. This behavior is not evident in the data (figures 5.4-3 and -4). (A case in which a singlet → singlet transition intensity is distorted by an underlying singlet → triplet one is discussed in section 5.5).

Figure 5.4-5 gives the DCS at 25 eV(in arbitrary units) for the

Figure 5.4-5. Differential cross section (arbitrary units) for excitation of the $A^1\Pi(\nu' = 0, 1, 2)$, ○; $a^3\Pi$ $(\nu' = 0, 1, 2)$, ◉; $b^3\Sigma^+$ $(\nu' = 0)$, △; and $B^1\Sigma^+$ $(\nu' = 0)$, □ states of CO. $E_0 = 25$ eV.

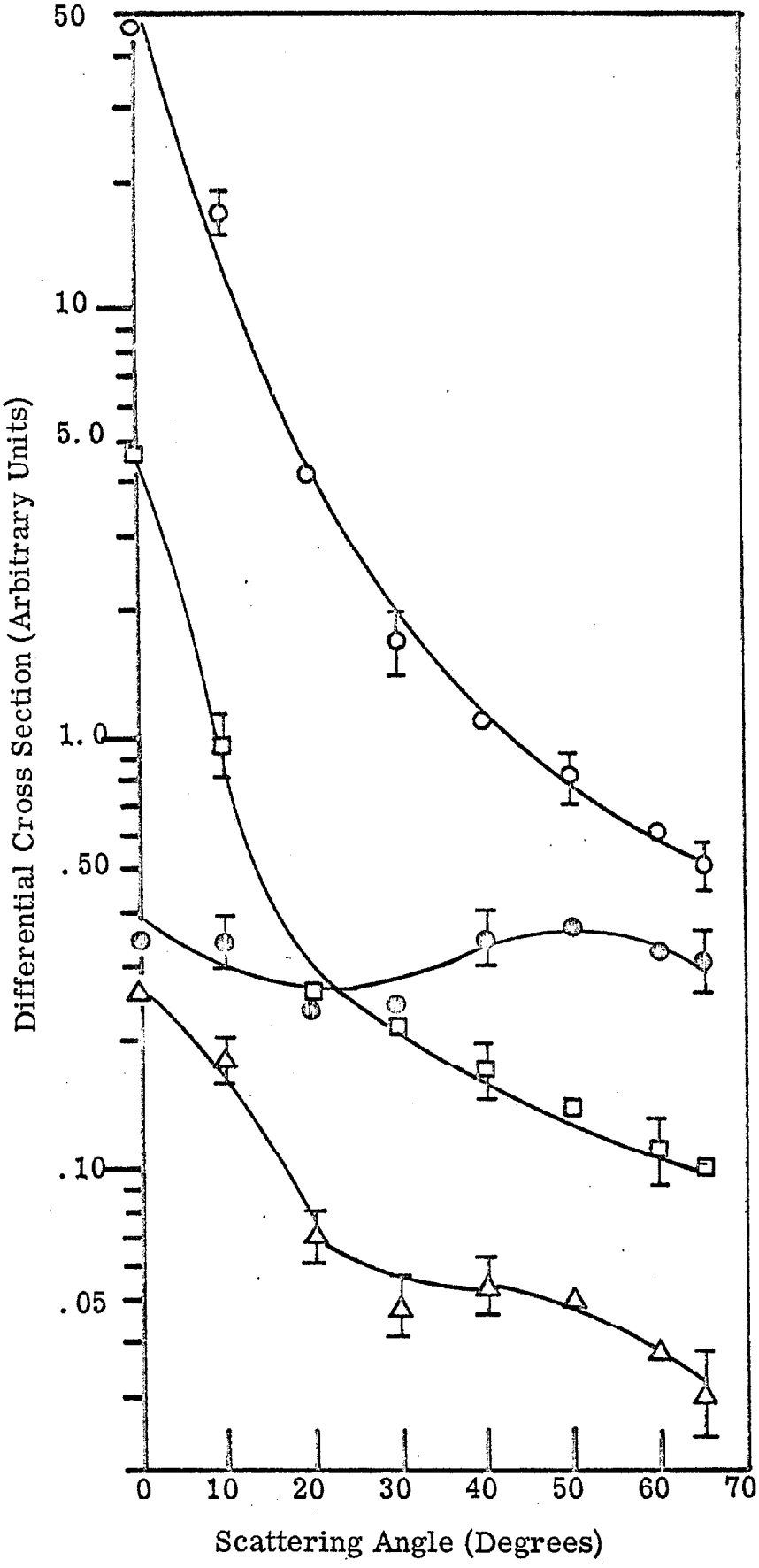
50
10
5.0
1.0
.50
.10
.05
Differential Cross Section (Arbitrary Units)
0
10
20
30
40
50
60
70
Scattering Angle (Degrees)

transitions of figure 5.4-4. The singlet DCS are sharply peaked forward while the $a^3\Pi$ DCS is relatively isotropic. The $b^3\Sigma^+$ DCS is quite similar to that of the $E^3\Sigma_g^+$ state of N_2. All of these comparisons are as expected.

5.5. Hydrogen

5.5.1. Introduction

H_2 has been exhaustively studied by optical methods (reference (2b), pp 530-32). Relatively few electron-impact studies of H_2 have been reported, although excitations from the $X^1\Sigma_g^+$ ground state to the $b^3\Sigma_u^+$, $B^1\Sigma_g^+$, $C^1\Pi_u$, $c^3\Pi_u$, and $D^1\Pi_u$ have been observed.

Schulz[149] used a trapped-electron technique to observe excitations to the $b^3\Sigma_u^+$ (repulsive) state and a second band, peaked at about 12 eV, which he assigned as X → B, C, D (singlets). In view of the recent high-resolution trapped-electron work of Dowell and Sharp[12], this 12 eV peak probably contained substantial contributions from the $c^3\Pi_u$ state.

Kuppermann and Raff[35a] observed transitions to $b^3\Sigma_u^+$ state as well as several of the unresolved singlets using a retarding field method of energy analysis and the collection of electrons scattered between $22° \leq \theta \leq 112°$ (with the $\theta = 90°$ direction being preferred). Lassettre and coworkers[147,148] have reported unresolved energy-loss spectra at impact energies from 300 eV to 500 eV and $0° < \theta < 5°$. No forbidden excitations were observed, nor was any vibrational structure in the B, C, D, etc. states resolved.

Kuyatt, et al.[150] and Heideman, et al.[30] were able to resolve many vibrational levels in the B, C, and D states at incident energies from 90 eV to 13.7 eV at $\theta \cong 0°$. They did not observe excitation of the $b^3\Sigma_u^+$ state. However, below about 30 eV, transitions to the $c^3\Pi_u$ and/or $a^3\Sigma_g^+$ state (unresolved) were noted.

At an incident energy of 25 KeV ($\theta \approx 0°$), Geiger[151] reported a well-resolved energy-loss spectrum of H_2. Transitions to the singlet states (B, C, and D) are clearly evident but no forbidden excitations were observed (nor are they expected to be at this high energy).

5.5.2. Results and Discussion

Our results on the exchange excitation of the lowest triplet state of H_2 ($b^3\Sigma_u^+$) are given in the attached preprint (appendix III). However, there are a number of additional aspects of this study which will be discussed below. (Figures 5.5-1 through -6 are in the attached preprint.) Table 5.5-1 gives the observed excitation energies of H_2 in the same format as used for N_2 and CO.

Since we were able to resolve several vibrational members of the $B^1\Sigma_u^+$ and $C^1\Pi_u$ states at 40 eV, it is of interest to compare the relative vibrational peak heights within each band to the Franck-Condon factor ratios as discussed in section 3.3.7.1. However, H_2 presents an extremely unfavorable case in which to obtain a meaningful comparison. As is evident from figures 5.5-1, -2, and -3, transitions from the $X^1\Sigma_g^+$ ground state to the $b^3\Sigma_u^+$ state overlap those to the $B^1\Sigma_u^+$, which in turn overlap those to the $C^1\Pi_u$ state.

TABLE 5.5-1

Excitation energies in H_2 for transitions from the $X^1\Sigma_g^+$ ($\nu = 0$) ground state. The abbreviations are defined in Table 5.3-1.

UES[a]	UVS	OPT. EE[b] (eV)	OBS. EE[c] (eV)
$b^3\Sigma_u^+$	(repulsive)	-	$10.0 \pm .2$[d]
$B^1\Sigma_u^+$	0	11.18	11.18
	1	11.34	11.35
	2	11.50	11.50
	3	11.66	11.65
	4	11.81	11.81
	5	11.96	11.95
	6	12.10	12.10
$C^1\Pi_u$	0	12.29	12.29
	1	12.58	12.58
	2	12.85	12.85
	3	13.10	13.10
	4	13.34	13.35
	5	13.56	13.55
$a^3\Sigma_g^+$	0	11.79	(11.80)[e]
	1	12.10	(12.08)
	2	12.40	
	3	12.68	
	4	12.94	
	5	13.19	
$c^3\Pi_u$	0	11.75	(11.80)
	1	12.04	(12.08)
	2	12.32	
	3	12.58	
	4	12.82	
	5	13.05	

[a] Reference (2b) pp. 530-32.

[b] Optical excitation energies for the $C^1\Pi_u$, $c^3\Pi_u$, and $a^3\Sigma_g^+$ are from table I of reference (12). Those for the $B^1\Sigma_u^+$ are from reference (154).

TABLE 5.5-1 (continued)

[c] This research. Accurate to within ± .01 eV except as indicated.

[d] Energy-loss corresponding to the peak intensity.

[e] Values in parentheses refer to excitations which were observed as abnormal increases in the $B^1\Sigma_u^+$ ($\nu' = 4, 6$) intensities.

In addition, transitions to the $a^3\Sigma_g^+$ and $c^3\Pi_u$ states overlap part of the $B^1\Sigma_u^+$ band and all of the $C^1\Pi_u$ one. Consequently, each particular peak height is proportional to the sum of a number of DCS, each one contributing an amount which depends on the resolution and scattering angle. It would require a resolution which is well beyond the present "state of the art" to separate all of these excitations.

The results discussed below are for an impact-energy of 40 eV (uncalibrated). This value is chosen because (1) our highest resolution (FWHM = .04 eV) data were obtained at this energy and (2) excitations to the a, b, and c triplet states, although observable, cause relatively little distortion of the strong X → B, C transitions. This latter condition is required if we are to make any meaningful Franck-Condon factor comparisons.

First, let us examine the relative peak intensities within the $C^1\Pi_u$ band. The intensity ratios should be related to the ratio of respective Franck-Condon factors according to equation (3-72) (Bethe-Born approximation). If the X → C (ν') peak intensities are determined relative to that of the X → C ($\nu' = 1$), the $C^{DD}_{\nu'1}$ (of equation (3-72)) differs from unity by less than ~ 5% over the range of ν' we can measure. Since the relative precision of the data is only ~ 5-10%, $C^{DD}_{\nu'1}$ will be neglected. The relative peak intensities were measured for scattering angles from $\theta = 0°$ to $\theta = 80°$. No change in relative intensity was noted (within the accuracy of these measurements). If the transitions to the triplet states (a, c) were

contributing significantly to the $C^1\Pi_u$ band intensity, we would expect some distortion of the relative intensity distribution in this band. Such affects would presumably become more noticeable at higher angles since the ratio of triplet to singlet DCS generally increases markedly with angle (see sections 5.2, 5.3, 5.4). The distortion of the $C^1\Pi_u$ (ν') relative intensities due to the incompletely resolved $B^1\Sigma_u^+$ vibrational peaks should be less dependent on angle since the $B^1\Sigma_u^+/C^1\Pi_u$ DCS ratio does not change much with this variable (see below).

Table 5.5-2 summarizes the average (over all θ's) relative intensities and presents as a comparison the high-energy data of Geiger[151] and the calculations of Hutchisson[152]. The agreement in all cases is quite good, with the exception of the $\nu' = 0$ relative intensity. This is to be expected since the $B^1\Sigma_u^+$ ($\nu' = 7$) level is practically coincident with the $C^1\Pi_u$ ($\nu' = 0$) one.

The measurement and interpretation of the relative vibrational intensity distribution within the $B^1\Sigma_u^+$ band is somewhat more complicated. From figure 5.5-3 it is quite clear that at $\theta = 80°$ the intensities of both the $\nu' = 4$ and 6 levels are strongly enhanced by the $a^3\Sigma_g^+$ ($\nu' = 0,1$) and/or $c^3\Pi_u$ ($\nu' = 0,1$) levels, respectively. Further the intensity of the lower ν' members of the $B^1\Sigma_u^+$ state may be significantly increased at higher angles by the $b^3\Sigma_u^+$ state (see figure 5.5-1). Apparently, the least affected level (which we can observe) will be the $B^1\Sigma_u^+$ ($\nu' = 5$) one. Thus, table 5.5-3 presents the relative vibrational intensities within the $B^1\Sigma_u^+$ state

TABLE 5.5-2

Relative vibrational peak intensity distribution for the $X^1\Sigma_g^+ (\nu = 0) \rightarrow C^1\Pi_u (\nu' = 0 \text{ to } 5)$ transitions. The intensity of the $X(\nu = 0) \rightarrow C(\nu' = 1)$ transition is normalized to 1.00. The data from all angles have been averaged together (16 scans).

Investigator	ν'					
	0	1	2	3	4	5
This research (40 eV)	.72 ± .02	1.00	.91 ± .03	.67 ± .03	.43 ± .02	.26 ± .02
Geiger[151] (25 KeV)	.62	1.00	.96	.62	.40	.23
Hutchisson[152] (calculation)	.635	1.00	.961	.697	.411	.236

TABLE 5.5-3

Relative vibrational peak intensity distribution for the $X^1\Sigma_g^+$ ($\nu = 0$) → $B^1\Sigma_u^+$ ($\nu' = 0$ to 6) transitions. The intensity of the X($\nu = 0$) → B($\nu' = 5$) transition is normalized to 1.00. The scans for $\theta = 0°$ to 10° and 15° to 20° have been averaged together as indicated.

	ν'							No. of
θ	0	1	2	3	4	5	6	Scans
<0°-10°>	.08 ± .01	.24 ± .02	.47 ± .03	.72 ± .03	.91 ± .04	1.00	1.06 ± .05	4
<15°-20°>	.08 ± .01	.22 ± .03	.51 ± .03	.72 ± .04	.92 ± .04	1.00	1.09 ± .05	4
30°	.08	.25	.47	.73	.95	1.00	1.2_0	2
40°	.12 ± .02	.25 ± .04	.52 ± .04	.74 ± .03	.95 ± .04	1.00	1.19 ± .04	3
50°	.16	.32	.57	.78	.90	1.00	1.2	1
60°	.21	.33	.63	.79	1.2_5	1.00	1.4_5	2
80°	.22	.36	.56	.73	1.2	1.00	1.3_5	2
Geiger[151] (25 KeV, $\theta = 0°$)	.10	.19	.38	.59	.84	1.00	1.06	
Hutchisson[152] (calculation)	.082	.345	.860	1.246	1.316	1.00	.556	

(with respect to that of the $\nu' = 5$ level) obtained from this research, the work by Geiger[151], and calculations[152]. (Since Geiger used 25 KeV incident electrons, only singlet → singlet transitions were observed.)

It is clear that neither the results of Geiger[151] nor of this research agree with the calculations[152] (except fortuitously perhaps at $\nu' = 0$). We would expect the agreement of this work with that of Geiger to be best at the lowest angles, since the ratio of triplets to singlets is smallest there. Our results seem consistently high by about 10% (except $\nu' = 0$ and 6) for $\theta \lesssim 20°$. This is probably not due to the overlapping $b^3\Sigma_u^+$ state since the b/B DCS ratio changes by more than a factor of 10 in the same angular range (see below). (Further, below $\theta \approx 30°$ we did not observe excitation of the $b^3\Sigma_u^+$ state in these high resolution scans.) This discrepancy cannot be accounted for by the correction factor $C^{DD}_{\nu\nu 0}$ of equation (3-72) since $C^{DD}_{\nu\nu 0}$ is within about 5% of unity at these angles. In any case, for angles greater than $\sim 40°$, the enhancement of the $\nu' = 0$ and 1 peak intensities (due to excitation of the $b^3\Sigma_u^+$ state); the $\nu' = 4$ intensity (due to transitions to the $a^3\Sigma_g^+$ ($\nu' = 0$) and/or $c^3\Pi_u$ ($\nu' = 0$) levels); and the $\nu' = 6$ peak intensity (due to excitation of the $a^3\Sigma_g^+$ ($\nu' = 1$) and/or $c^3\Pi_u$ ($\nu' = 1$) states) is clearly evident. This distortion with angle of the relative vibrational intensity distribution within an electronic band can presumably be used to detect forbidden transitions which are strongly masked by overlapping allowed ones[153].

Let us next consider the variation with scattering angle of the relative DCS for excitation of the $b^3\Sigma_u^+$, $B^1\Sigma_u^+$, and $C^1\Pi_u$ states. Figure 5.5-7 shows the peak intensity ratios of the $X^1\Sigma_g^+$ ($\nu = 0$) → $b^3\Sigma_u^+$ and $B^1\Sigma_u^+$ ($\nu' = 5$) transitions with respect to that of the $X^1\Sigma_g^+$ ($\nu = 0$) → $C^1\Pi_u$ ($\nu' = 1$) one. The $B^1\Sigma_u^+$ ($\nu' = 5$)/$C^1\Pi_u$ ($\nu' = 1$) intensity ratio was determined from the same high-resolution data used to obtain the results presented in tables 5.5-2 and -3. The $b^3\Sigma_u^+/C^1\Pi_u$ ($\nu' = 1$) intensity ratio was obtained from lower resolution (FWHM ≈ .10 eV) scans (at the same 40 eV impact energy). Both the b/C ($\nu' = 1$) and B ($\nu' = 5$)/C ($\nu' = 1$) peak intensity ratios are directly proportional to the corresponding DCS ratios. Since the proportionality constant depends somewhat on the resolution, but not on the angle, the magnitude of the ratios are not directly comparable although their relative angular dependencies are. As expected, the b/C intensity ratio increases rapidly with angle while the B/C one is practically constant (within the errors of this determination). The angular variation of the b/C ratio is quite similar to the $^3\Sigma^+/\Pi$ ratios already noted (N_2, CO). This tends to reinforce the tentative hypothesis (see section 5.3)) that for $\Delta S = 1$, the value of $\Delta\Lambda$ (0 or 1) is more important in determining the relative angular distribution than is the g → g or u nature of the transition. The $B^1\Sigma_u^+/C^1\Pi_u$ intensity ratio does not exhibit the oscillations noted in the previous $^1\Sigma/\Pi$ ratios. Although the $X^1\Sigma_g^+ \rightarrow B^1\Sigma_u^+$ transition in H_2 is the only case we have examined of a $\Delta\Lambda = 0$, g → u, $\Delta S = 0$ transition, the fact that its intensity, relative to that of the $^1\Pi_u$ one, does not

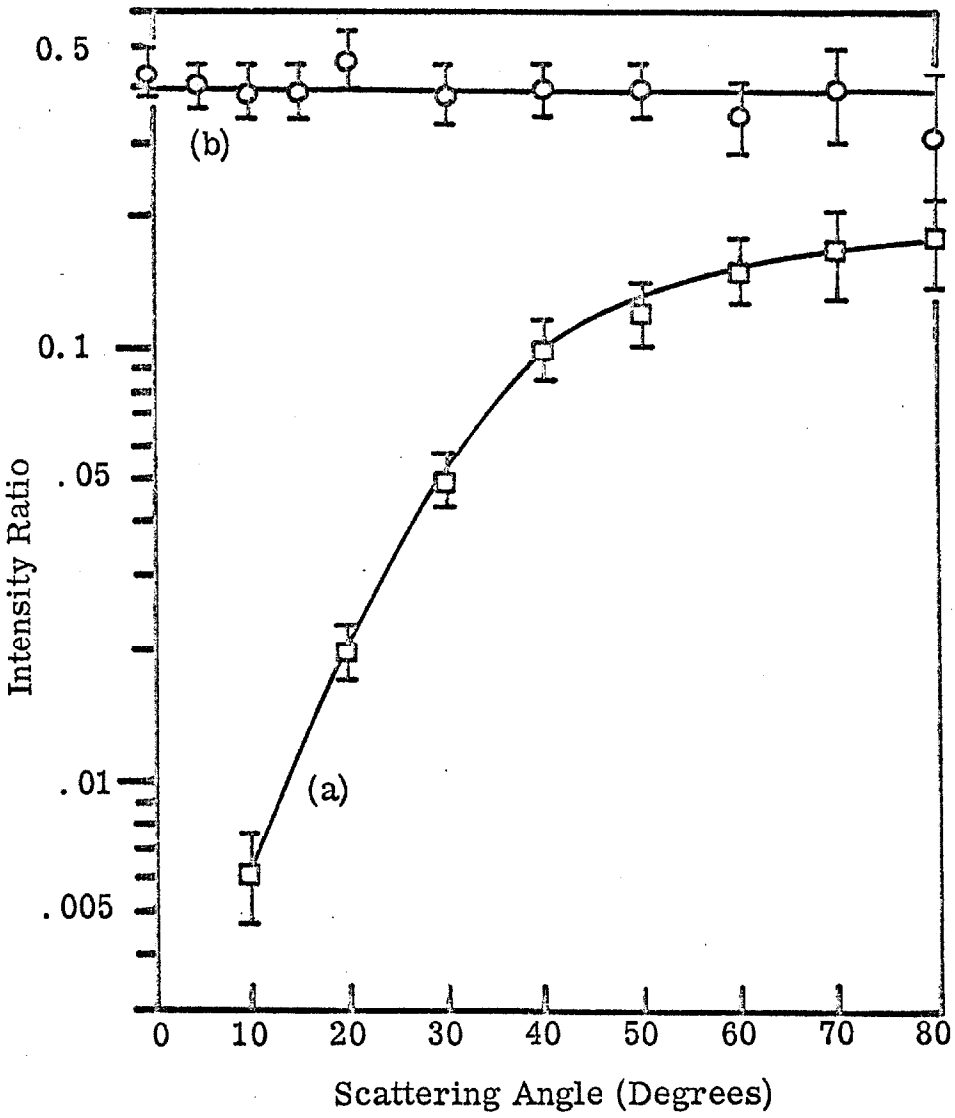

Figure 5.5-7. Ratios of intensities of the $X^1\Sigma_g^+ \rightarrow b^3\Sigma_u^+$ (peak) curve (a) and $B^1\Sigma_u^+$ ($\nu' = 5$) curve (b) transitions to that of the $X \rightarrow C^1\Pi_u$ ($\nu' = 1$) one in H_2. $E_0 = 40$ eV. Each data point is an average of two to four scans at each angle.

oscillate as do those of the $\Delta\Lambda = 0$ or 1, $g \rightarrow g$, $\Delta S = 0$ transitions (N_2) is consistent with the conjecture (section 5.3) that for $\Delta S = 0$, the $g \rightarrow g$ or u nature of the transition is more important in determining the relative angular distribution than is the $\Delta\Lambda$ value.

Finally, figure 5.5-8 shows the DCS (in arbitrary units) for excitation of the $C^1\Pi_u$ ($\nu' = 1$) and $b^3\Sigma_u^+$ states at 40 eV for $\theta = 10°$ to 80°. As expected, the singlet → singlet DCS is sharply forward peaked, while the singlet → triplet one is more isotropic.

5.6. Acetylene

5.6.1. Introduction

Since acetylene (C_2H_2) is isoelectronic with N_2 and CO. we might expect that it would exhibit a similar energy-loss spectrum. The only previous electron-impact study of C_2H_2 was reported by Bowman and Miller[10] using the trapped-electron method. A comparison of their result with those of Schulz[155] for CO and N_2 does indeed show this similarity. However, the tentative state assignments of reference (10) do not reflect this similarity, particularly with regard to the feature peaking at 6.2 eV. In both N_2 and CO a low-lying triplet state ($B^3\Pi_g$ in N_2 and $a^3\Pi$ in CO) was responsible for the peak which appears to correspond to the 6.2 eV transition observed by Bowman and Miller. Ingold and King[156] had observed a weak singlet → singlet transition ($\tilde{X}^1\Sigma_g^+ \rightarrow \tilde{A}^1A_u$) in absorption peaking at about 6 eV. Since the observation of a trapped-electron excitation spectrum is not sufficient to identify a transition as singlet → singlet or triplet[157], Bowman and Miller apparently

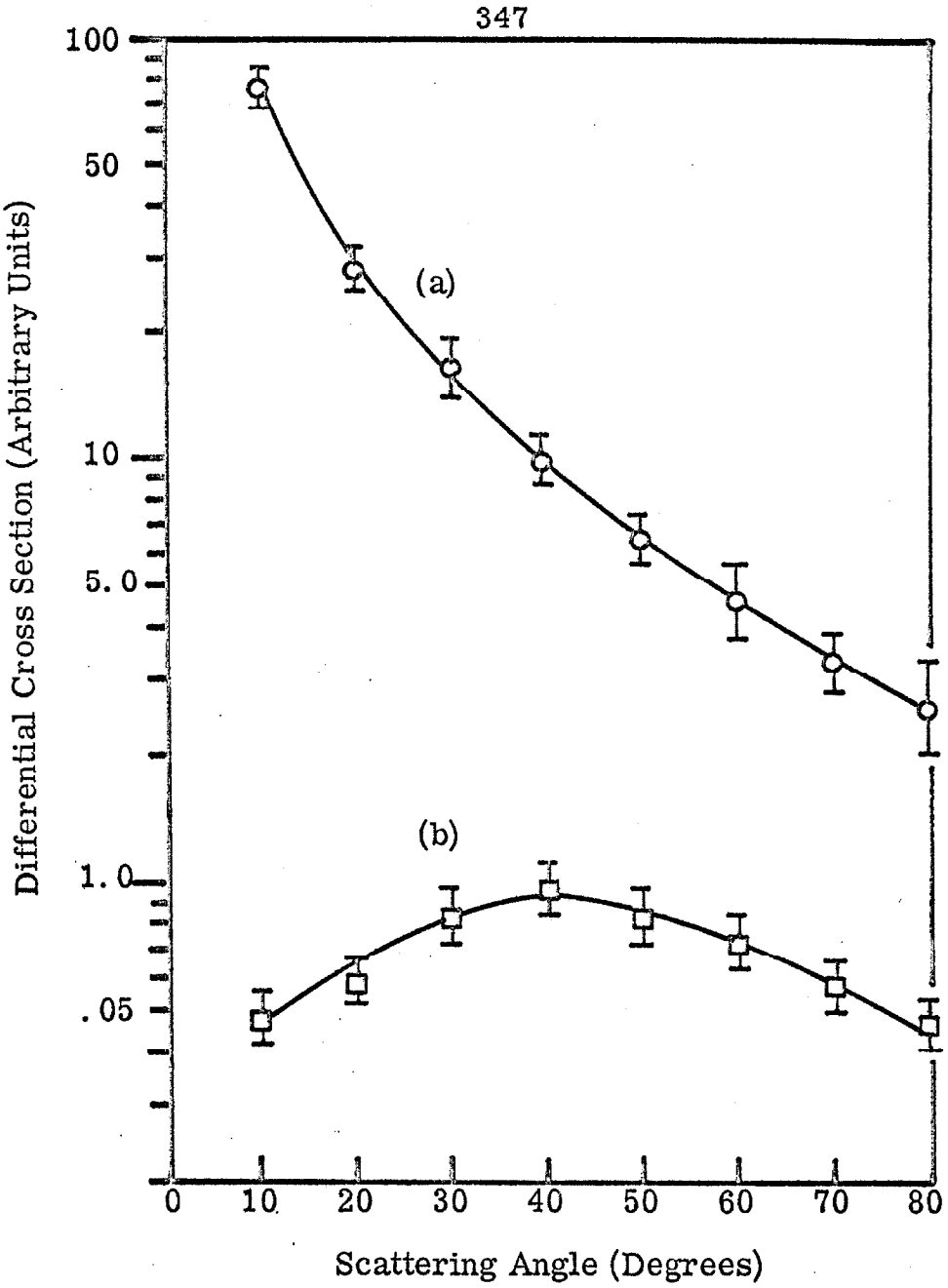

Figure 5.5-8. Differential cross section (arbitrary units) for excitation of the $C^1\Pi_u$ ($\nu' = 1$) curve (a) and $b^3\Sigma_u^+$ curve (b) states in H_2. E_o = 40 eV.

assumed that they were observing the $\tilde{X} \rightarrow \tilde{A}$ excitation.

The attached reprint (appendix IV) discusses our investigation of the energy-loss spectrum of C_2H_2 (from about 1 eV to 9.5 eV) and identification of two singlet → triplet transitions, with peak intensities at 5.2 eV and 6.1 eV. Some additional aspects of this study are discussed below.

5.6.2. Additional Results and Discussion

Figure 5.6-3 (figures 5.6-1 and -2 are in the reprint) shows an energy-loss spectrum of acetylene from about 5 eV to 12 eV for an impact energy of 45 eV and a scattering angle $\theta = 10°$. It is similar in appearance to the optical absorption spectrum obtained by Nakayama and Watanabe[158]. The energy-losses of the main features of figure 5.6-3 are listed in table 5.6-1 along with possible state assignments. Beyond 9 eV the UV absorption spectrum is too complex for these correspondences to be more than tentative.

Figure 5.6-2 (see appendix IV) contains the peak ratios of several states at 25 eV. Similar measurements were made at 35 eV as shown in figure 5.6-4. As before (preprint) the singlet → triplet/singlet → singlet ratios are sharply increasing functions of angle while the singlet → singlet/singlet → singlet ones vary much more slowly.

Note that in both figures 5.6-2 and -4 the $\tilde{C}^1\Pi_u$ ($\nu_2 = 1$)/$\tilde{C}^1\Pi_u$ ($\nu_2 = 0$) intensity ratios gradually increase with angle. This is not expected, since these peaks arise from transitions to two vibrational members of the same electronic state. The 70% change

Figure 5.6-3. Energy-loss spectrum of acetylene. E_o = 45 eV, $I_o = 5 \times 10^{-8}$ A, $\theta = 10°$, SR = .010 V/sec; TC = .5 sec, P = 1.2×10^{-3} torr. The excitation energies for the numbered features are listed in table 5.6-1.

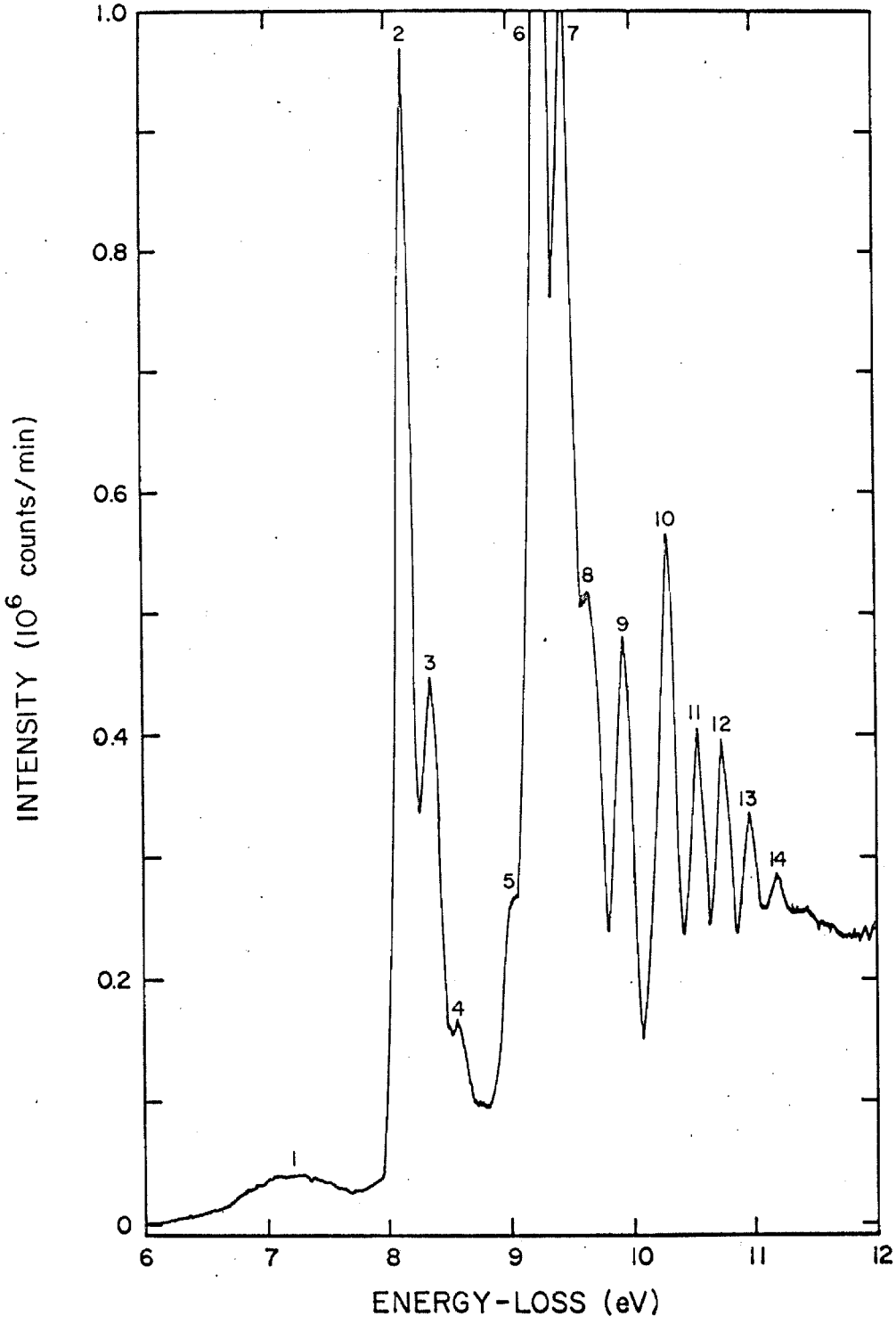
1.0
0.8
0.6
0.4
0.2
0
INTENSITY (10^6 counts/min)
6
7
8
9
10
11
12
ENERGY-LOSS (eV)
1
2
3
4
5
6
7
8
9
10
11
12
13
14

TABLE 5.6-1

Excitation energies observed in the electron impact spectrum of acetylene. The first column is the peak identification number from figure 5.6-3. The second column is the energy-loss at which the peak is observed in the present work, the third column is the most likely corresponding optical excitation energy, and the fourth column is the assignment of the upper state (the ground state is $\tilde{X}\,^1\Sigma_g^+$, point group $D_{\infty h}$).

Peak Number	Energy Loss (eV)	Optical Excitation Energy[a]	Assignment[b]		
			Point Group	State	Vibrational Level
	$5.2 \pm .1$[c]			$\tilde{a}$ (triplet)	unresolved
	$6.1 \pm .1$[c]			$\tilde{b}$ (triplet)	unresolved
1	$7.2 \pm .1$	(7.3) (broad)		$\tilde{B}$	(diffuse, unassigned bands)
2	$8.16 \pm .01$	8.16	$D_{\infty h}$	$\tilde{C}(^1\Pi_u)$, [3R]	ν_{00}
3	$8.37 \pm .01$	8.38	$D_{\infty h}$	$\tilde{C}(^1\Pi_u)$, [3R]	ν_2
4	$8.61 \pm .01$	8.62	$D_{\infty h}$	$\tilde{C}(^1\Pi_u)$, [3R]	$2\nu_2$
5	$9.02 \pm .02$				
6	$9.26 \pm .01$	9.24	$D_{\infty h}$	$\tilde{D}$, [3R′]	ν_{00}

TABLE 5.6-1 (continued)

Peak Number	Energy Loss (eV)	Optical Excitation Energy[a]	Assignment[b]		
			Point Group	State	Vibrational Level
		9.25	C_{2h}	$\tilde{E}, \{B\}$	ν_{oo}
		9.27	C_{2h}	$\tilde{F}, \{C\}$	ν_{oo}
7	9.47 ± .01	9.46	$D_{\infty h}$	$\tilde{D}, [3R']$	ν_2
		9.48	C_{2h}	$\tilde{F}, \{C\}$	ν_2
8	9.66 ± .02	9.68	$D_{\infty h}$	$\tilde{D}, [3R']$	$2\nu_2$
		(9.68)	C_{2h}	$\tilde{F}, \{C\}$	$2\nu_2$
9	9.94 ± .01	(9.93)	$D_{\infty h}$	[4R]	ν_{oo}
10	10.29 ± .01	(10.28)	$D_{\infty h}$	[4R']	ν_{oo}
11	10.54 ± .02	(10.52)	$D_{\infty h}$	[4R']	ν_2
12	10.74 ± .02				
13	10.96 ± .02	Probably Rydberg states [nR] , [nR'].			
14	11.19 ± .03				

TABLE 5.6-1 (continued)

[a] Optical excitation energies in parentheses were determined from fig. 1 of reference (158).

[b] States in square brackets [ ] are from Price[164], those in { } are from Wilkinson[165], the other designations are from Herzberg[2c].

[c] Refer to figure 1 of the reprint, appendix IV.

Figure 5.6-4. Peak intensity ratios in acetylene for E_o = 35 eV. The peak ratios are labelled according to their number designations in figure 5.6-3. The curves labelled $\tilde{a}/2$ and $\tilde{b}/2$ are the triplet intensity ratios (with respect to peak 2) times 10. For clarity, only a few representative error bars are shown for each ratio. Each data point is an average of three scans.

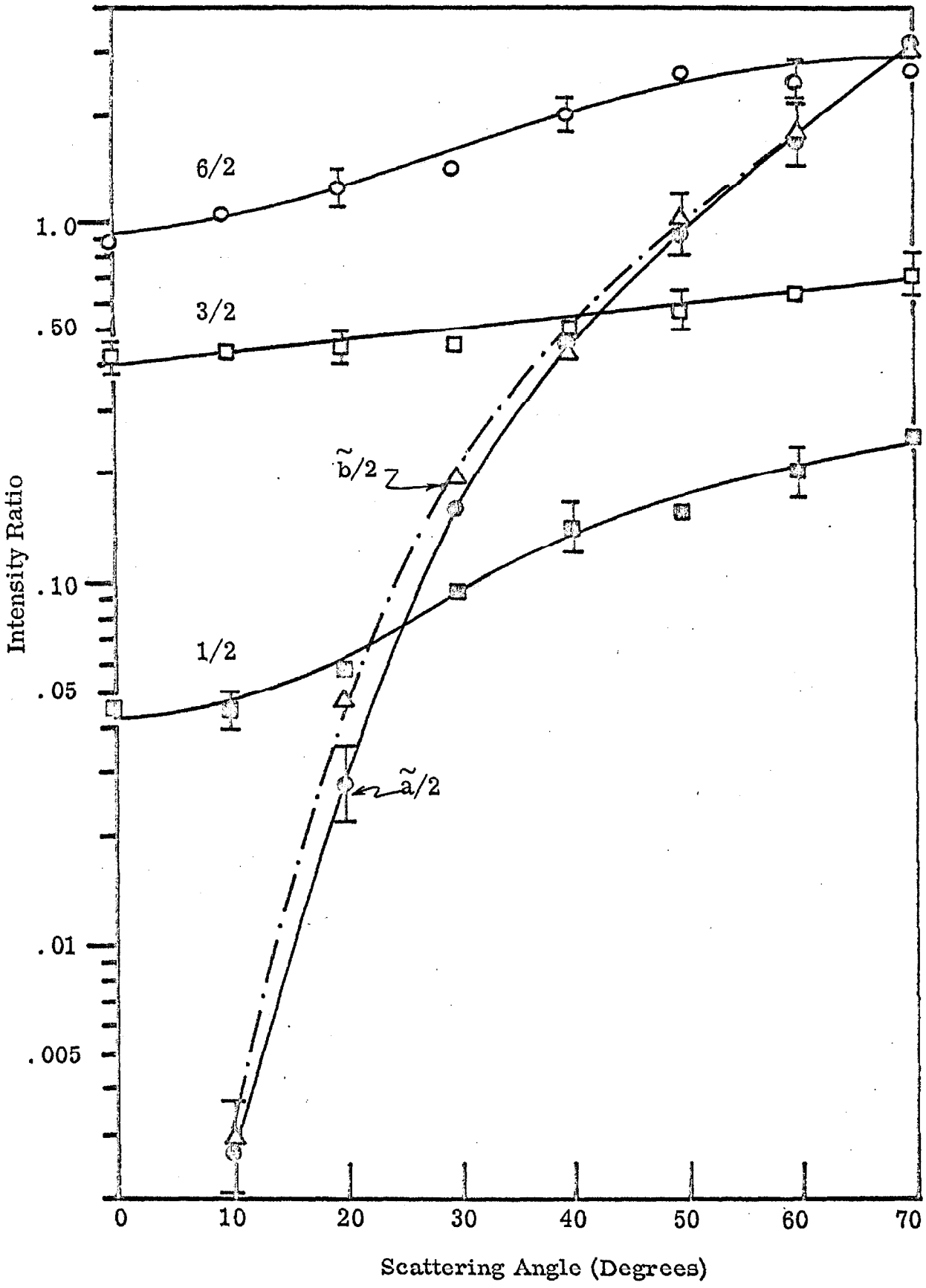
6/2
3/2
1/2
b̃/2
ã/2
1.0
.50
.10
.05
.01
.005
Intensity Ratio
0
10
20
30
40
50
60
70
Scattering Angle (Degrees)

at both E_o = 35 eV and 25 eV for θ = 0° to 70° is well outside the reasonable error limits of the data. This leaves two possible explanations: (1) the Franck-Condon factor considerations of section 3.3.7.1 are not valid[159], and (2) there is an underlying excitation (probably forbidden) which enhances the $\nu_2 = 1$ peak relative to the $\nu_2 = 0$ one. As to the first possibility, we can only point out that in all reported cases (only six transitions, including the present work), no significant ($>\sim 5\%$) deviations in relative vibrational intensities have been noted as a function of angle. The second possibility has been clearly demonstrated for one case in H_2 (refer to section 5.5). Based on this evidence (meager though it is), the second explanation seems to be the most likely one. Referring to reference (10), we note that the most intense excitation occurs at ~ 8.2 eV. From the results of Schulz[9a] and Brongersma[11], we note that the most intense features (excluding negative ion formation) in the trapped-electron spectra of both CO and N_2 are due to singlet → triplet transitions. In particular, the $X \rightarrow B^3\Pi_g$ and $X \rightarrow E^3\Sigma_g^+$ transitions are the most intense in N_2 while the $X \rightarrow a^3\Pi$ and $X \rightarrow b^3\Sigma^+$ are the most intense in CO. In view of these comparisons, it is not unlikely that the excitation observed at 8.2 eV in reference (10) is due to a singlet → triplet transition, analogous to the $^1\Sigma \rightarrow {}^3\Sigma$ transitions of N_2 and CO. In order to explain the intensity ratio variation we have observed in the $\tilde{C}^1\Pi_u$ band of C_2H_2, the maximum transition intensity for this hypothetical triplet state should lie somewhat higher than 8.16 eV, in agreement with reference (10). Without additional data, further speculation seems unwarranted.

The steeply rising (with increasing θ) $\tilde{a}/\tilde{C}$ and $\tilde{b}/\tilde{C}$ intensity ratios are quite similar in behavior to the previously observed intensity ratios for which the singlet → triplet transitions have $\Delta S = 1$ and $\Delta\Lambda = 1$. (All of the reference excitations for the intensity ratios have been chosen to be transitions in which $\Delta S = 0$, $\Delta\Lambda = 1$, and g → u (where applicable).) Thus, we tentatively suggest that $\tilde{a}$ and $\tilde{b}$ are Π states (Λ of ground state = 0, plus $\Delta\Lambda = 1$ implies Λ of excited state = 1). In analogy with N_2, they might correspond to the $B\,^3\Pi_g$ and $C\,^3\Pi_u$ states. These would be states of a linear C_2H_2 configuration. It is also possible that the excited state is "bent" (a possibility which does not exist for N_2). In this case a $^3\Pi_{g(u)}$ state of the linear molecule (point group $D_{\infty h}$) would correlate with $^3A_{g(u)} + {}^3B_{g(u)}$ states of the "trans-bent" (point group C_{2h}) molecule[160]. (We have neglected the "cis-bent" configuration and the possibility of spin-orbit coupling mixing singlets with triplets.) Essentially, the potential function for the degenerate Π electronic state of the linear molecule splits into two when the molecule is bent. The magnitude of this splitting depends on the magnitude of the vibronic interaction (Renner-Teller effect)[161].

From the present data, we cannot decide between the possibilities of (1) excitation of the two $^3\Pi$ states of the linear molecule (probably a $^3\Pi_g$ and a $^3\Pi_u$), or (2) excitation of a single $^3\Pi_{g(u)}$ state of the linear molecule which splits into an $^3A_{g(u)}$ and $^3B_{g(u)}$ state of the "bent" system.

The transitions we observe do not seem to be of the type $^1\Sigma \rightarrow {}^3\Sigma$. The $\tilde{a}$ and $\tilde{b}$/singlet ratios are sharply rising functions of θ as are the $^3\Pi$ and ^3P/singlet ratios already discussed. In particular, all of these ratios are much steeper than are the $^3\Sigma$/singlet ratios we have observed. This apparently eliminates the possibility that we observed a $\pi \rightarrow \pi^*$ transition, since the resulting electron configuration ($\pi^3\pi$) leads only to Σ and Δ states[162]. Π states can be obtained by either promoting an electron from a σ orbital into a π orbital or viceversa. Since MO calculations[163] predict that a $^3\Sigma$ is the lowest triplet state (as in N_2), apparently we have not observed the lowest triplet in C_2H_2. Bowman and Miller's tentative assignment of the lowest triplet state at 2.0 eV is not inconsistent with the present work, even though we failed to observe an energy-loss feature at 2.0 eV.

Figures 5.6-5 and -6 present the DCS (in arbitrary units) for the excitations shown (in ratio form) in figures 5.6-2 and -4, respectively. The $\tilde{a}$ and $\tilde{b}$ DCS are quite similar to the 2^3P (He), $a^3\Pi$(CO), and $C^3\Pi_u$ (N_2) ones, as expected. The singlet cross sections are sharply peaked forward, more so at 35 eV than at 25 eV incident energy (recall the discussion of section 3.4).

As already noted in table 5.6-1, the peak labelled 6 in figure 5.6-3 could contain substantial contributions from the non-Rydberg $\tilde{E}$ (ν_{00}) and $\tilde{F}$ (ν_{00}) states. Likewise, peak 7 could be a composite of $\tilde{D}$ ($\nu_2 = 1$) and $\tilde{F}$ ($\nu_2 = 1$) excitations. Thus, it is of interest to compare the relative intensity of these two peaks as a

Figure 5.6-5. Differential cross sections (arbitrary units) for excitation of the $\tilde{a}$, $\tilde{b}$, $\tilde{B}$ (1), $\tilde{C}$ ($\nu_2 = 0$) (2), and $\tilde{D}$ ($\nu_2 = 0$) (6) states of acetylene. $E_o = 25$ eV. Each data point is an average of three scans.

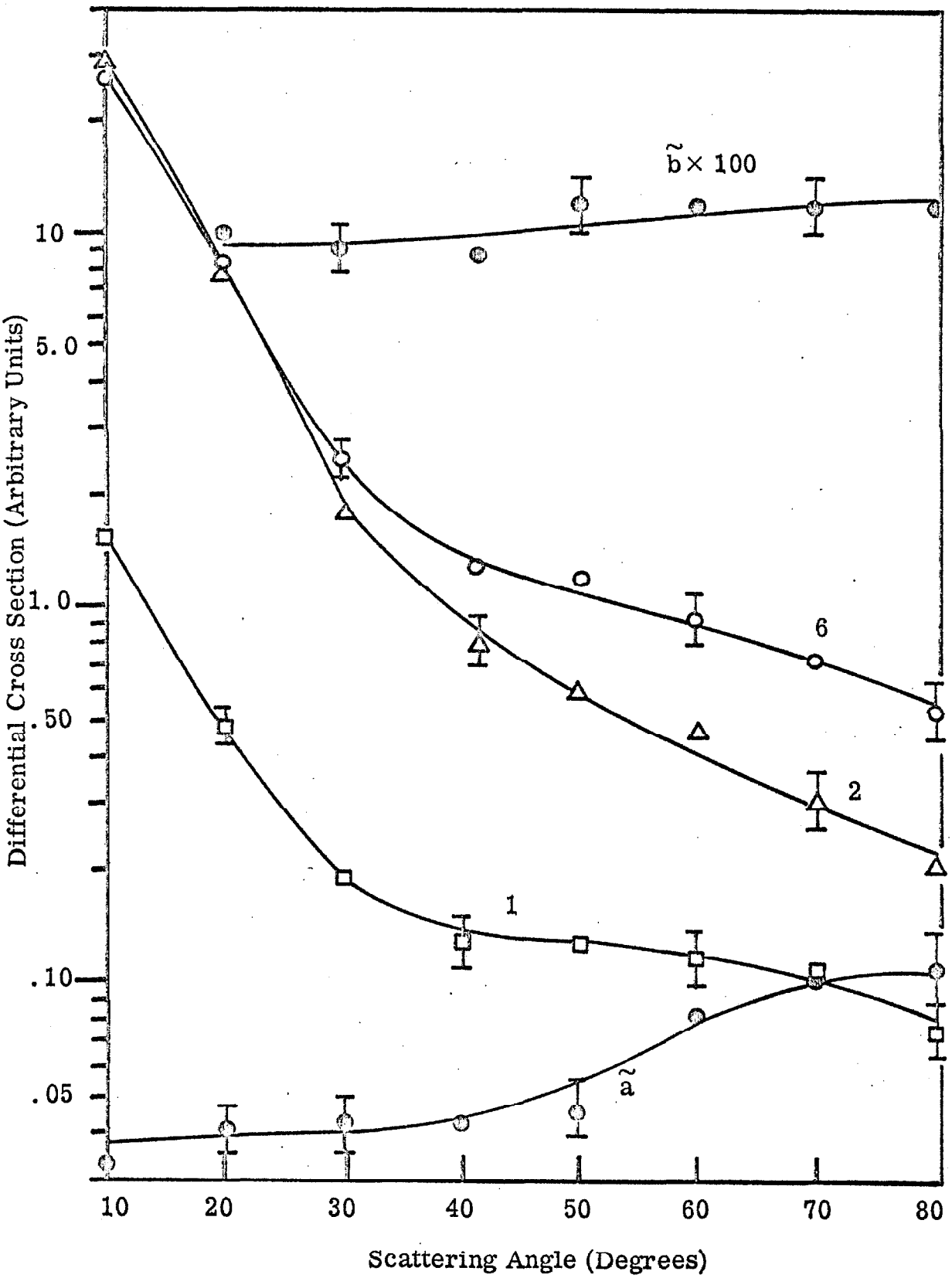
Differential Cross Section (Arbitrary Units)
10
5.0
1.0
.50
.10
.05
10
20
30
40
50
60
70
80
Scattering Angle (Degrees)
b̃ × 100
6
2
1
ã

Figure 5.6-6. Differential cross sections (arbitrary units) for excitation of the $\tilde{a}$, $\tilde{b}$, $\tilde{B}$ (1), $\tilde{C}$ ($\nu_2 = 0$) (2), and $\tilde{D}$ ($\nu_2 = 0$) (6) states of acetylene. $E_o = 35$ eV. Each point is an average of three scans.

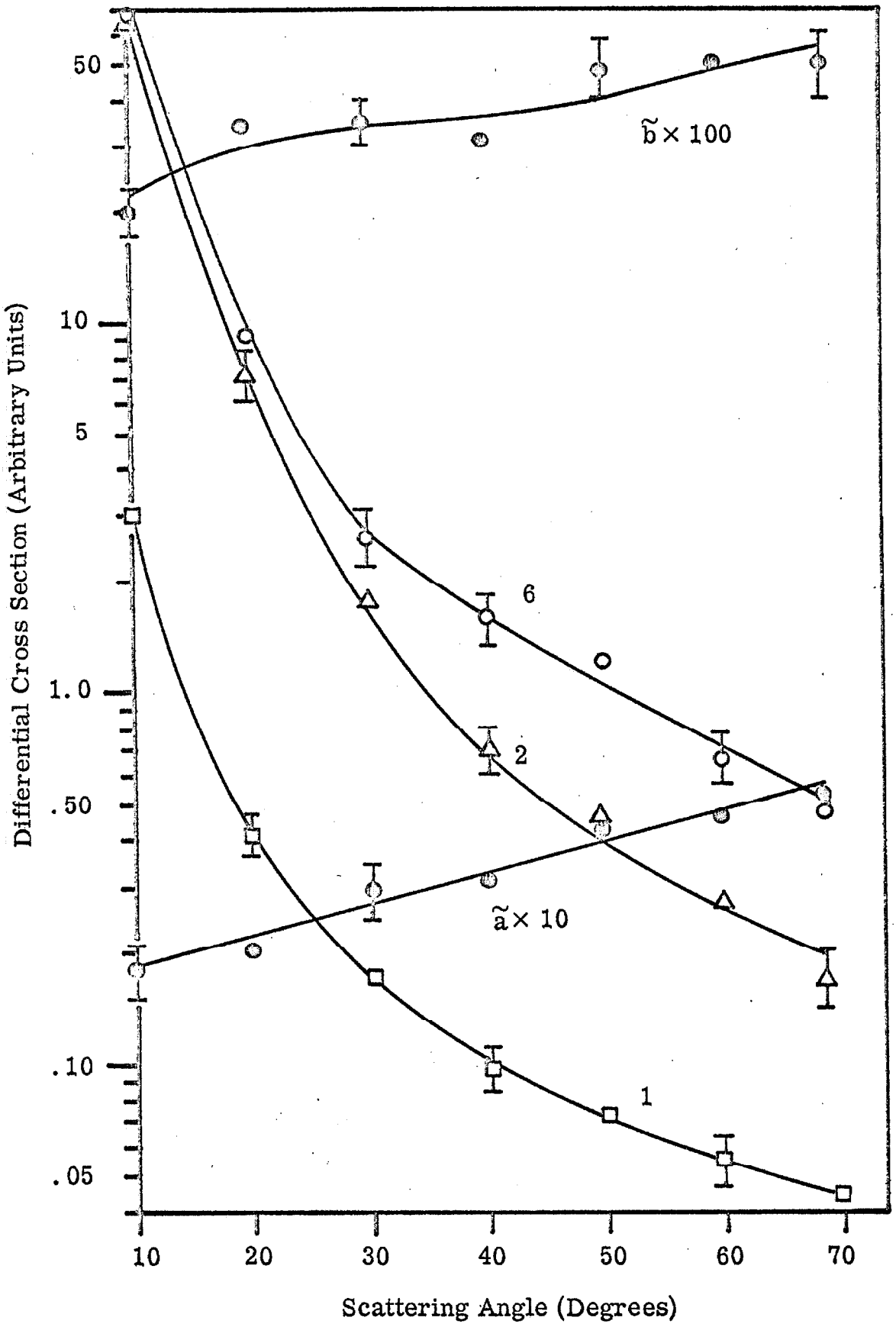
50
10
5
1.0
.50
.10
.05
Differential Cross Section (Arbitrary Units)
$\tilde{b} \times 100$
6
2
$\tilde{a} \times 10$
1
10
20
30
40
50
60
70
Scattering Angle (Degrees)

function of angle. Table 5.6-2 presents the results of such a comparison for an impact energy of 35 eV. $C^{DD}_{\nu\nu o}(\theta)$ has been included in the table, primarily because in this one case it seems to improve the constancy of the ratio (perhaps fortuitously). The invariance of this peak intensity ratio with angle indicates that either the three electronic states mentioned above vary with angle in nearly the same way or that we only observe transitions to one of the states (either $\tilde{F}$ or $\tilde{D}$). Without higher-resolution studies, we cannot decide between these alternatives.

5.7. Ethylene

5.7.1. Introduction

Ethylene is a molecule of considerable interest to both theoretical and experimental chemists. Since C_2H_4 is an example of the simplest pi-electron system, it has been used extensively as a model for testing theoretical calculations. Unfortunately, the overlapping nature of its electronic bands has complicated experimental investigations[166] while ab initio calculations have as yet been somewhat limited by the computational effort involved[167].

The optical absorption spectrum of ethylene has been studied by a number of investigators in the solid[168], liquid[82], and gaseous state[169]. The optically observed transitions (from the $\tilde{X}\,^1A_g$ planar ground state, N state of Mulliken[170]) can be briefly summarized as follows:

(1) At long wave lengths (low energy), a progression of extremely weak diffuse bands, beginning at about 3.6 eV and peaking

TABLE 5.6-2

Ratio of the peak intensity of peak number 7 (figure 5.6-3) to that of peak number 6 as a function of scattering angle θ. E_o = 35 eV.

θ (degrees)	7/6 Peak Intensity Ratio (I_R)	C_{10}^{DD}	$\frac{I_R}{C_{10}^{DD}}$	No. of Scans Used
0°	.85 ± .05	.958	.89	2
10°	.87 ± .05	.979	.89	2
20°	.86 ± .04	.991	.85	2
30°	.90 ± .04	.995	.90	3
40°	.86 ± .03	.997	.86	3
50°	.88 ± .04	.998	.88	2
60°	.90 ± .05	.999	.90	2
70°	.88 ± .04	.999	.88	3
Average of all angles	.88 ± .02		.88 ± .01	19

at ~ 4.6 eV is observed[171]. The upper state for this system is the lowest triplet $\tilde{a}^3B_{1u}$[172] (Mulliken's T state[170]).

(2) A stronger absorption consisting of a progression of diffuse bands beginning at about 5 eV, merging into a continuum at about 7 eV, and reaching a flat maximum at ~ 7.6 eV occurs next. It is generally agreed[172] that the upper state is the first excited singlet, $^1B_{1u}$ (V state of Mulliken[170]).

(3) At 7.11 eV, the first Rydberg transition is observed[173] (R state of Mulliken). Nearly all features observed at higher energies can be attributed to additional Rydberg transitions[166].

(4) The first ionization potential is found to be 10.50_7 eV[173]. The relative intensities and order of these transitions from 6.2 eV to 11.64 eV are conveniently shown in the figures of Zelikoff and Watanabe[174].

Kuppermann and Raff[35] were the first to observe electronic excitation of ethylene via electron-impact. The peaks they observed at 4.6 eV and 7.7 eV correlate well with the N → T and N → V (or R) transitions observed optically. Trapped-electron spectra reported by Brongersma[87] and Bowman and Miller[10] show peaks at nearly these same locations as well as one at ~ 9.2 eV (and negative ion formation at lower energies). Docring's[36c] investigations at large scattering angles (θ = 90°) and low energies (down to 10.9 eV) revealed approximately these same features (4.4 eV, 7.7 eV, and 9.3 eV). At somewhat higher energies (50 eV) and θ = 0°, Simpson and Mielczarek[26] observed energy-loss peaks which coincided

with several Rydberg transitions. The 4.4 (4.6) eV transition was not observed and the broad peak near 7.7 (actually peaking at 7.5 eV) was clearly due to the lowest N → R transition. The energy-loss spectrum of Lassettre and Francis[147], obtained at an incident energy of ~ 400 eV and $\theta \approx 0°$, was quite similar to that of reference (26) (except that the resolution of the former was about 0.6 eV while that of the latter was 0.1 eV).

Significantly higher resolution studies have been reported by Geiger and Wittmaack[40] (FWHM ≈ .025 eV, $E_0 \approx$ 33 KeV, $\theta \approx 0°$) and Ross and Lassettre[23] (FWHM ≈ .03, $E_0 \approx$ 150 eV, $\theta \approx 0°$). Neither the N → T nor N → V transitions are observed, but the N → R and higher Rydberg transitions are clearly evident. The highest energy results[40] agreed in detail[175] with optical absorption data[174]. However, the data of references (26) and (147) indicate a maximum in the N → R (plus underlying N → V) transition intensity at 7.5 eV whereas the optical absorption reaches a maximum at 7.28 eV. Ross and Lassettre[23] have attributed this anomaly to an underlying quadrupole-allowed (but dipole-forbidden) electronic transition.

In summary, electron-impact and optical absorption studies generally agree, with the exceptions that (1) the N → V transition, which is distinctly observed in absorption, has not been seen explicitly via electron-impact (i.e., it is masked by the stronger overlapping N → R transition) and (2) there is electron-impact evidence for an $\tilde{X}\,^1A_g \rightarrow (^1B_{1g})$[176] (quadrupole-allowed) transition

which has not been observed optically. It is generally agreed[177] that no other features have been revealed by electron-impact.

5.7.2. Results and Discussion

Figure 5.7-1 shows an energy-loss spectrum of ethylene under low resolution (FWHM of elastic peak = 0.15 eV) at $\theta = 40°$ and $E_o = 40$ eV. The N → T and N → R (or V) transitions are clearly evident as well as higher Rydberg transitions. Figure 5.7-2 shows the energy-loss region from about 7 eV to 10 eV under relatively high resolution (FWHM $\approx$ .05 eV) at $E_o = 40$ eV and $\theta = 10°$. The peaks observed in these figures along with their probable assignment are listed in table 5.7-1 (all peaks except that of the N → T transition were taken from figure 5.7-2). These spectra agree quite well with the previous results. In particular, the relative intensities within the N → R band agree with those of Ross and Lassettre[23], although the resolution is not as good. Unfortunately, the signal level at this resolution (FWHM = .05 eV) was not sufficient to scan a very large range of angles. The R band relative intensities are summarized in table 5.7-2. Our low angle results at 40 eV are the same (within the error limits)as the $\theta = 0°$, 150 eV results of Ross and Lassettre[23]. At higher angles, the enhancement of the peaks of the $\nu_2 = 2$ and 3 levels relative to that of the $\nu_2 = 1$ is quite clear. This reinforces the hypothesis[23] that at least one forbidden transition (hereafter labelled as N → Z) underlies the N → R transition at about 7.5 eV energy-loss (and higher). The energy-dependence

Figure 5.7-1. Energy-loss spectrum of ethylene. E_o = 40 eV, I_o = 3×10^{-8} A, θ = 40°, SR = .002 V/sec, TC = 5 sec, P = 1.0×10^{-3} torr. FWHM of the elastic peak = 0.15 eV.

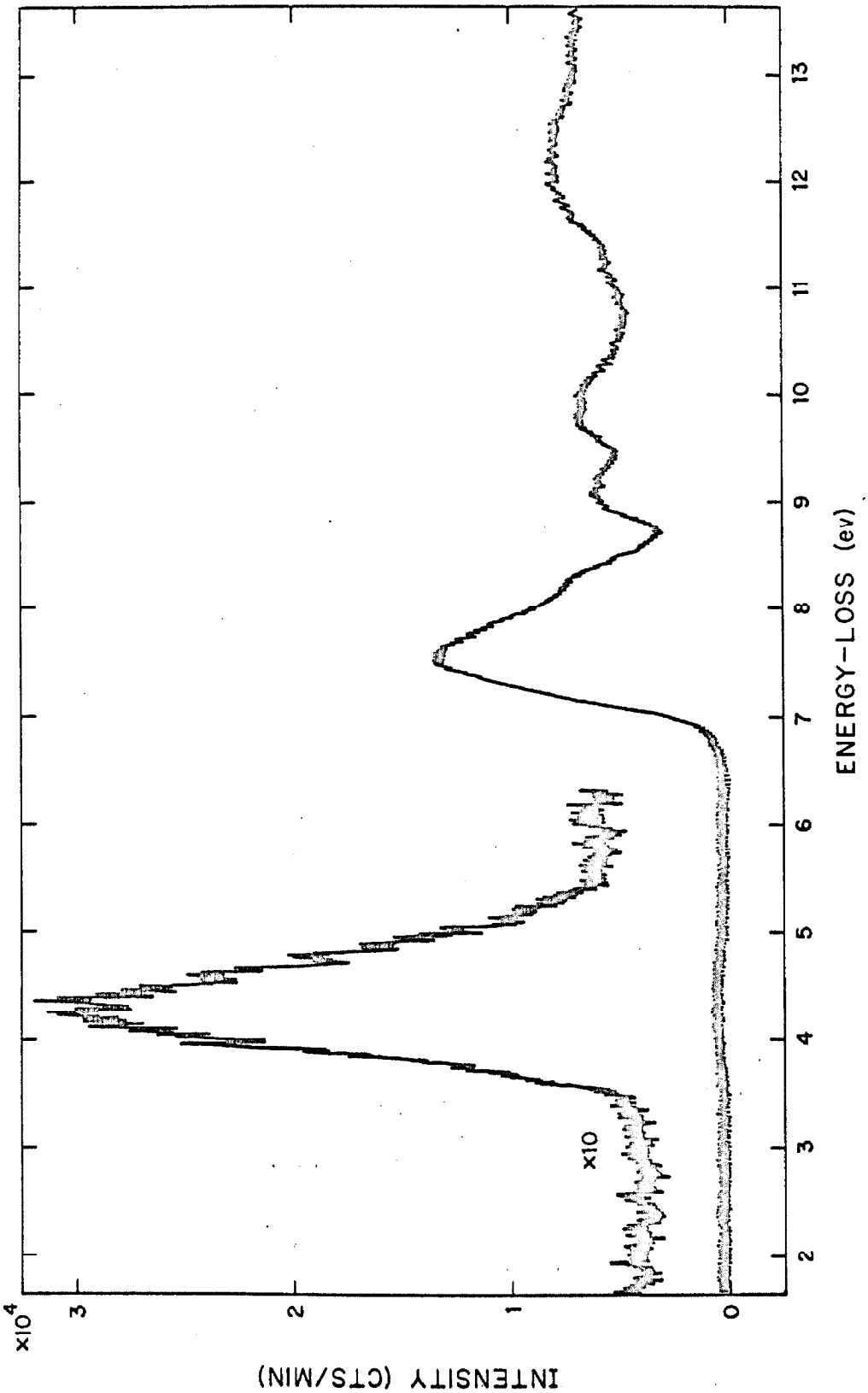
INTENSITY (CTS/MIN)
×10⁴
3
2
1
0
×10
2
3
4
5
6
7
8
9
10
11
12
13
ENERGY-LOSS (eV)

Figure 5.7-2. Energy-loss spectrum of ethylene. E_o = 40 eV, I_o = 1×10^{-9} A, θ = 10°, SR = .008 V/sec, TC = 1 sec, P = 1.2×10^{-3} torr. FWHM of the elastic peak is .05 eV.

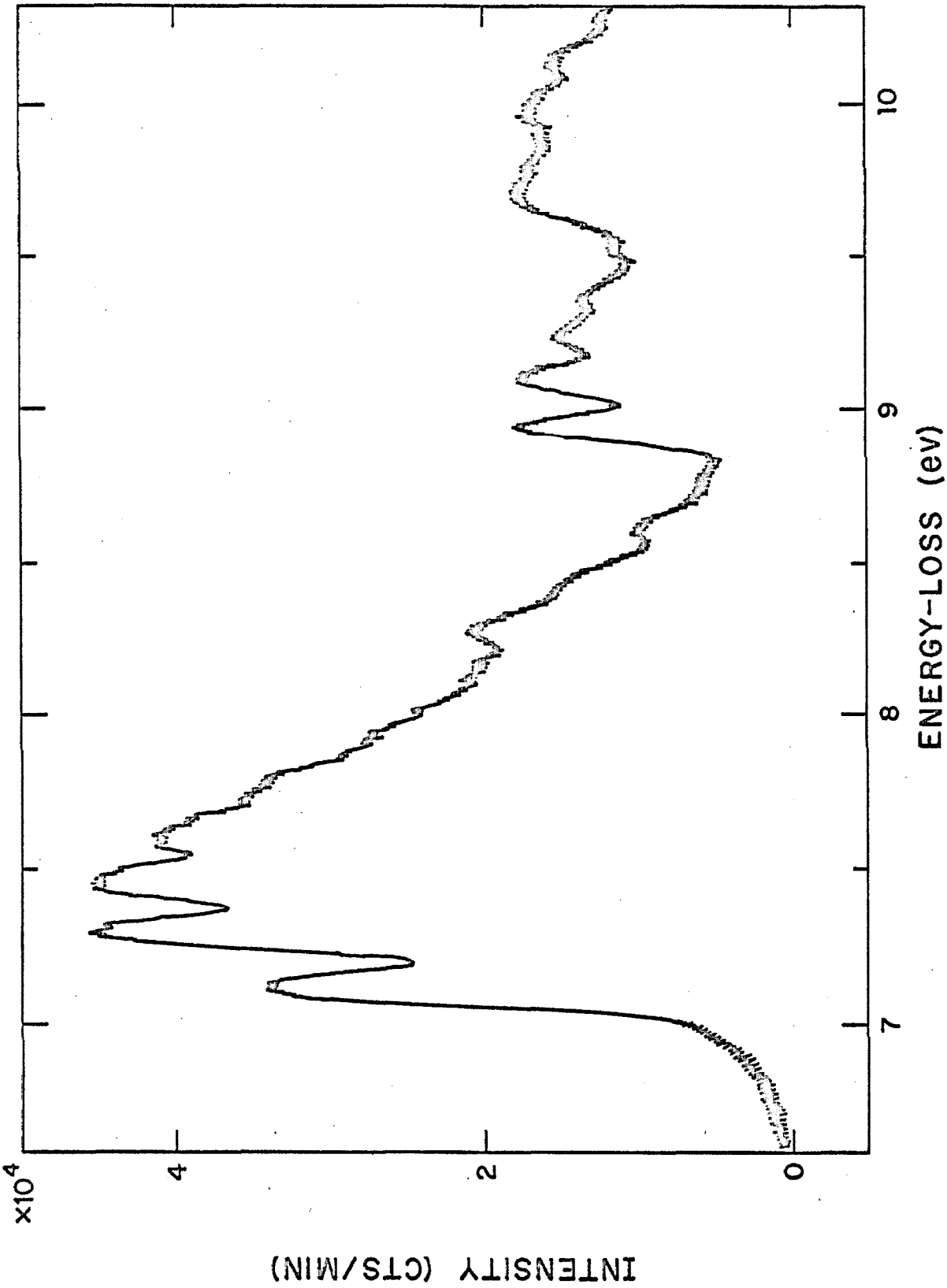
INTENSITY (CTS/MIN)
×10^4
0
2
4
7
8
9
10
ENERGY-LOSS (eV)

TABLE 5.7-1

Energy-loss peak locations in the electron-impact spectrum of C_2H_4. The first column lists the excitation energies (below ionization) of the peaks in figure 5.7-2; the second column lists the corresponding optical values; and the third column presents the upper state assignment corresponding to the optical values. The ground electronic state of ethylene is $\tilde{X}\,^1A_g$ (point group D_{2h})

Excitation Energy From This Research (eV)	Optical Excitation Energy[a] (eV)	Assignment of Upper State		
		Electronic[b]	Vibration[c]	
			ν_2	ν_4
4.4 ± .1		$\tilde{a}\,^3B_{1u}$		
(onset : 3.4 ± .1	<3.6)			
7.12 ± .01	7.11	$\tilde{B}$, (2R)	0	0
	7.17		0	2
7.30 ± .01	7.28		1	0
	7.34		1	2
7.46 ± .01	7.45		2	0
	7.50		2	2
7.59 ± .02	7.61		3	0
	7.67		3	2
(7.79)[d]	7.77		4	0

TABLE 5.7-1 (continued

Excitation Energy From This Research (eV)	Optical Excitation Energy[a] (eV)	Assignment of Upper State		
		Electronic[b]	Vibration[c]	
			ν_2	ν_4
8.27 ± .01	8.26	$\tilde{C}$, (3R′)	0	0
	8.32		0	2
(8.41)[d]	8.42		1	0
8.60 ± .02	8.62	$\tilde{D}$, (3R″)	0	0
8.93 ± .01	8.90	$\tilde{E}$, (3R)	0	0
	8.95		0	2
9.08 ± .02	9.08		1	0
	9.13		1	2
9.24 ± .02	9.25		2	0
9.36 ± .02	9.36	(4R′)	0	0
9.70 ± .02				

[a] Optical excitation energies for the $\tilde{a}$ state are from reference (84), those for the $\tilde{B}$ from reference (169), and all others from reference (166).

[b] Electronic states in parentheses are from references (169) and (266); the others are from reference (2c), p. 629.

[c] The vibrational assignments are from references (169) and (166).

[d] Shoulder.

TABLE 5.7-2

Relative intensity distribution for the first Rydberg transition (N → R) in ethylene. The third, fourth, and fifth columns are the results of other investigators. These authors resolved the ν_2 and $2\nu_4$ excitations, but to compare with our results (column six), in which they are not resolved, these peaks have been averaged together.

ν_2	ν_4	$(I/I_{\nu_2 = 1})^{(a)}$	$(I/I_{\nu_2 = 1})^{(b)}$	$(I/I_{\nu_2 = 1})^{(c)}$	$(I/I_{\nu_1 = 1})^{(d)}$	
					$\theta = 10°$	$\theta = 40°$
0	0	.88	.78	.76 ± .05	.75 ± .06	.72 ± .05
0	2					
1	0	1.00	1.00	1.00	1.00	1.00
1	2					
2	0	.85	.90	1.00 ± .02	1.00 ± .05	1.15 ± .05
2	2					
3	0	.74	.80	.92 ± .02	.91 ± .06	1.10 ± .05
3	2					

[a] Reference (174). [b] Reference (40). [c] Reference (23). [d] Present results, $E_0 = 40$ eV, average of three scans.

of this increase in the $\nu_2 = 2$ (and $\nu_2 = 3$) relative intensity can provide a clue to the nature of the N → Z transition. To this end, the intensity ratios of the $\nu_2 = 2$ to $\nu_2 = 1$ peaks from Geiger[40], Ross[23], and Simpson[26] are listed below:

θ =	0°	0°	0°
E_0 =	33,000 eV	150 eV	50 eV
(I_2/I_1) =	.90	1.00	(1.09)[178]

Ross argued that the ratio increase from 33,000 eV to 150 eV is consistent with an underlying quadrupole transition, but did not point out that Simpson's data are quantitatively in agreement with this suggestion[179].

Our angular measurements (meager though they are) may also provide an indication of the nature of this N → Z transition. Let us assume that the 7.46 eV transition intensity is the sum of three components: the N → R ($\nu_2 = 2$) intensity (IR_2), the N → V continuum intensity (IV_2), and the N → Z intensity (IZ_2). Presumably, the 7.12 eV and 7.30 eV peak intensities are equal to $IR_0 + IV_0$ and $IR_1 + IV_1$, respectively. Although IR_0/IR_1 and IV_0/IV_1 are expected to be independent of angle from our previous Franck-Condon factor considerations, $IR_0 + IV_0/IR_1 + IV_1$ will depend on θ if the N → R and N → V DCS have different angular dependencies. The latter ratio will be independent of θ if $IV_0 \ll IR_0$ and $IV_1 \ll IR_1$ (a likely case). Since the data (Table 5.7-2) indicate that this ratio is nearly constant between $\theta = 10°$ and 40°, we can

tentatively conclude that (1) the N → R and N → V DCS behave in nearly the same way with angle or (2) the N → V DCS is negligible compared to the N → R one. For simplicity we shall assume the latter to be true (although the following arguments do not depend on this assumption). Thus, from the data of table 5.7-2 we have:

$$\frac{IR_2 + IZ_2}{IR_1} \cong 1.00 \text{ at } \theta = 10°$$

and

$$\cong 1.15 \text{ at } \theta = 40°.$$

But $IR_2/IR_1 \cong .90$ from the 33 KeV data of Geiger for which IZ is certainly negligible. (Recall that IR_2/IR_1 is most likely independent of angle and energy since it is a relative intensity within a single electronic band.) Thus,

$$\frac{IZ_2}{IR_1} \cong 0.1 \text{ at } \theta = 10°$$

and

$$\cong 0.25 \text{ at } \theta = 40°.$$

This factor of 2.5 increase from 10° to 40° is not inconsistent with a "quadrupole"/"dipole" intensity ratio (e.g., $^1\Sigma_g^+/b^1\Pi_u$ of N_2), but it is also similar to a "spin- and symmetry forbidden"/"dipole allowed" ratio (e.g., $E^3\Sigma_g^+/b^1\Pi_u$ of N_2). These results are certainly not definitive, but they indicate the utility of angular measurements as well as a need for more complete high resolution studies as a function of angle. In summary, we can only note that all of the arguments above are consistent with Z being either a "singlet" or "triplet" "g" state[180].

Figure 5.7-3 shows the intensity ratios for the peaks of the N → T, N → R, and N → 3R′ ($\nu_2 = 0$) transitions to that of the N → 3R ($\nu_2 = 0$) one. These data were obtained from scans of intermediate resolution (FWHM = .10 eV). The N → 3R ($\nu_2 = 0$) peak intensity was used as a reference because: (1) the resolution was not sufficient to use the N → R ($\nu_2 = 0$) peak intensity as a reference (the most "logical" choice), (2) the peak of the N → R transition could not be used since the N → Z transition might enhance it at higher angles, (3) the N → 3R′($\nu_2 = 0$)/N → 3R ($\nu_2 = 0$) intensity ratio is nearly constant with angle, indicating that both transitions are most likely "isolated" from underlying forbidden transitions and (4) the N → 3R ($\nu_2 = 0$) transition is not strongly overlapped as is the N → 3R′ one.

As expected, the singlet/singlet ratios are relatively flat while the triplet/singlet one increases markedly with angle. The latter ratio is quite characteristic of those for which transitions to the upper state have $\Delta S = 1$, $\Delta\Lambda = 0$. Since this transition is a $\pi \rightarrow \pi^*$ type, our conclusion concerning the acetylene triplets (i.e., they are not $\pi \rightarrow \pi^*$) is consistent with these results. The $\tilde{a}$ (or $\tilde{b}$)/$\tilde{C}$ ratio in acetylene increased by a factor $>10^2$ from $\theta = 10°$ to 80° while the $\tilde{a}$/3R ratio in ethylene only increases by a factor of about 30 over the same angular range and at nearly the same incident energy above threshold.

The (N → R)/(N → 3R ($\nu_2 = 0$)) intensity ratio is not enhanced at higher angles as we might expect from the higher resolution data.

Figure 5.7-3. Peak intensity ratios in ethylene for E_o = 25 eV. The peak labels can be correlated with energy-losses from table 5.7-1. Each data point is an average of three scans. The FWHM of the elastic peak was 0.10 eV for these data.

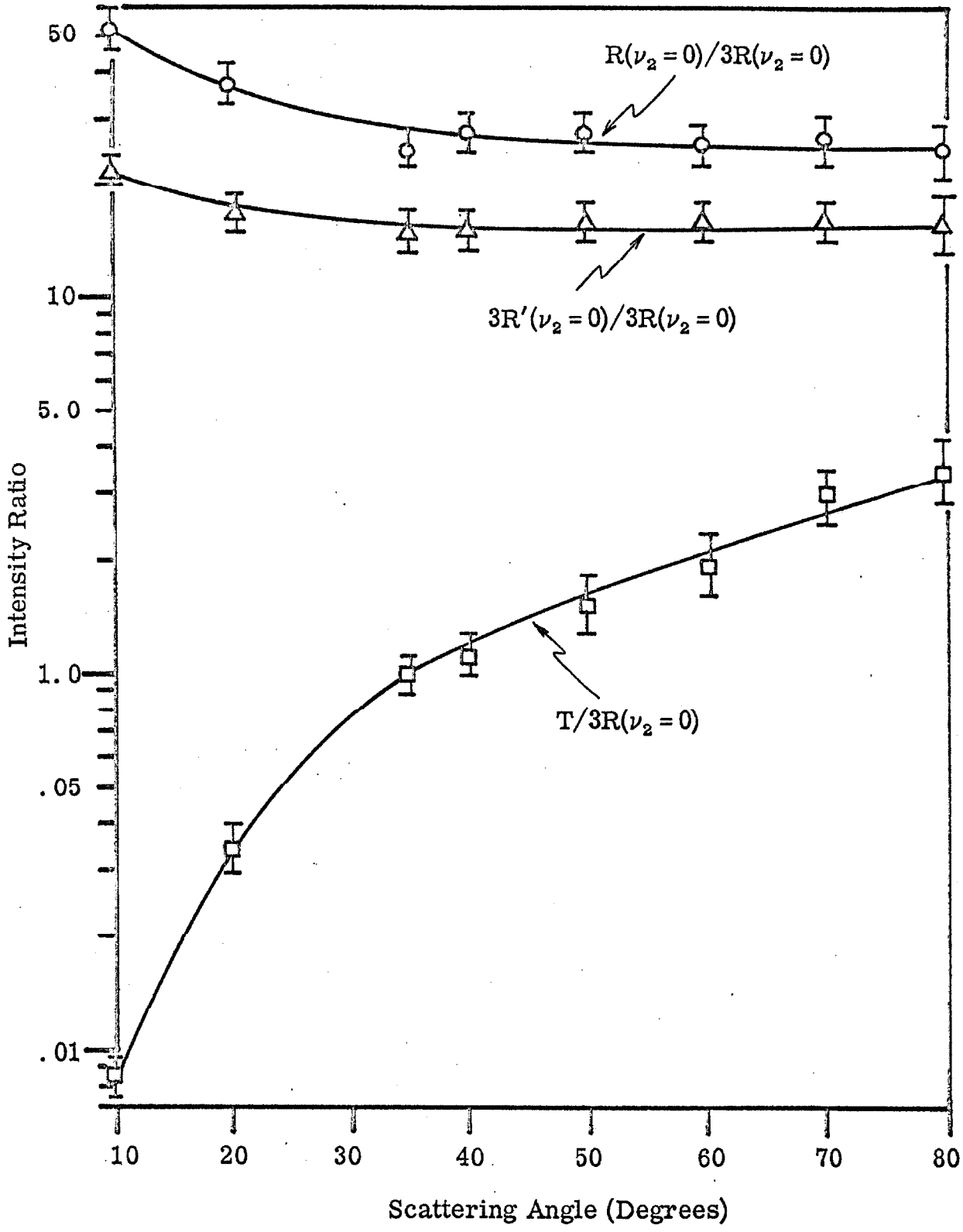
50
10
5.0
1.0
.05
.01
Intensity Ratio
R(ν2 = 0)/3R(ν2 = 0)
3R'(ν2 = 0)/3R(ν2 = 0)
T/3R(ν2 = 0)
10
20
30
40
50
60
70
80
Scattering Angle (Degrees)

However, there is a noticeable shift in the location of the N → R peak from 7.46 ± .01 eV at θ = 10° to 7.58 ± .05 eV at θ = 80° which attests to an underlying forbidden transition. The location of the N → 3R′ (ν_2 = 0) peak does not change with angle.

Figure 5.7-4 shows a comparison of the shape of the N → T DCS calculated in section 3.3.7.2 with that of the experimentally determined one at 25 eV. The agreement is not very good. This is not unexpected since rather crude approximations have been used in the calculation. Figure 5.7-5 shows the calculated distributions at a few additional energies simply to indicate the predicted trends with energy and angle. The curves exhibit a rather unusual shape compared to other calculations on helium and hydrogen[66] using the same approximation. This is probably an artifact of the simple wave functions used in the present case. Inspection of equation (3-92a) shows that the DCS is zero whenever $q \cong 1.453\ a_o^{-1}$. Thus, if $K_o < .843\ a_o^{-1}$ ($E_o < 9.66$ eV), then the DCS will not be zero in the 0° to 180° angular range; if $R_o = .843$, then the DCS is zero at $\theta = 180°$; and if $k_o > .843$, the zero in the DCS moves toward smaller angles, varying as $\theta \approx \frac{1.45}{k_o}$ for $k_o \gg 1.45\ a_o^{-1}$ ($E_o \gg$ 28.6 eV).

Figure 5.7-6 gives the DCS (in arbitrary units) for the N → R (peak), N → 3R (ν_2 = 0), and N → 3R′ (ν_2 = 0) transitions at 25 eV. As expected, these singlet → singlet Rydberg transitions are strongly peaked in the forward direction with very similar shapes. (The latter, of course, was evident from the ratios.)

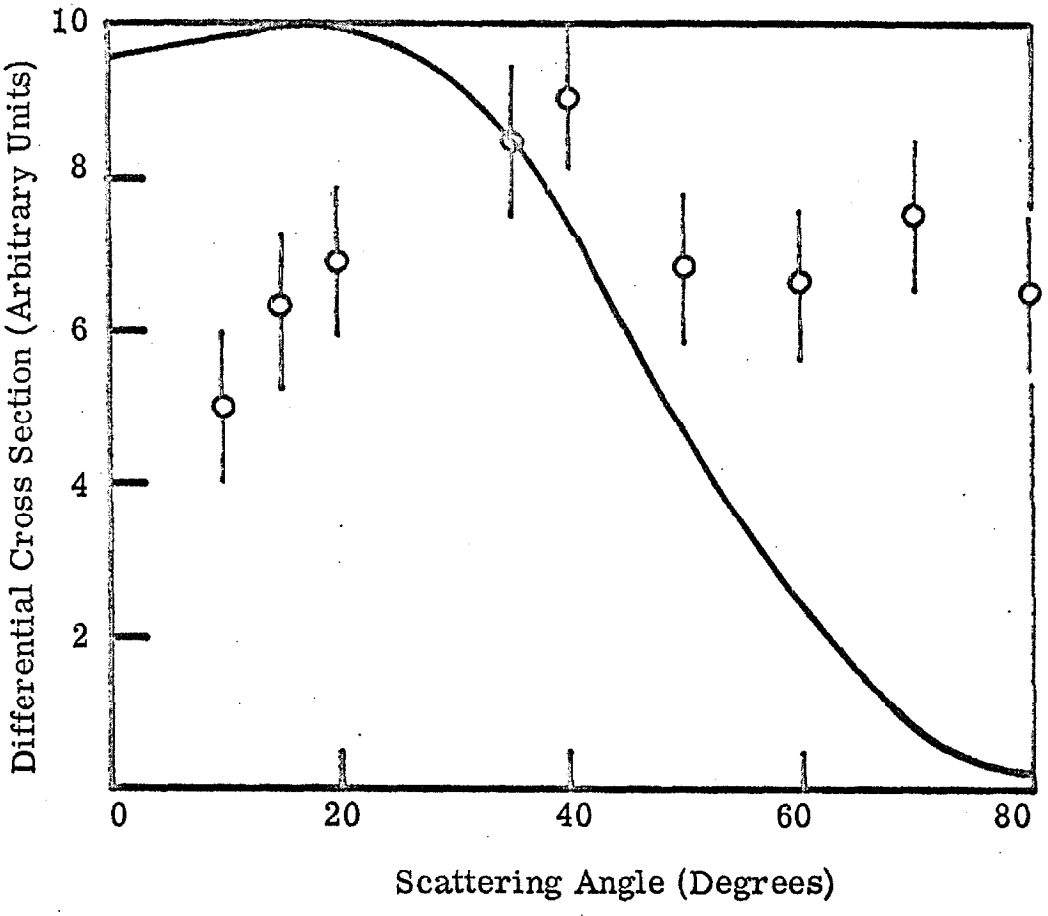

Figure 5.7-4. Differential cross section (arbitrary units) for the N → T transition in ethylene. The circles are experimental points for E_0 = 25 eV (average of three scans). The solid line was calculated according to section 3.3.7.2. The data and calculations are normalized to the same value at $\theta = 35°$.

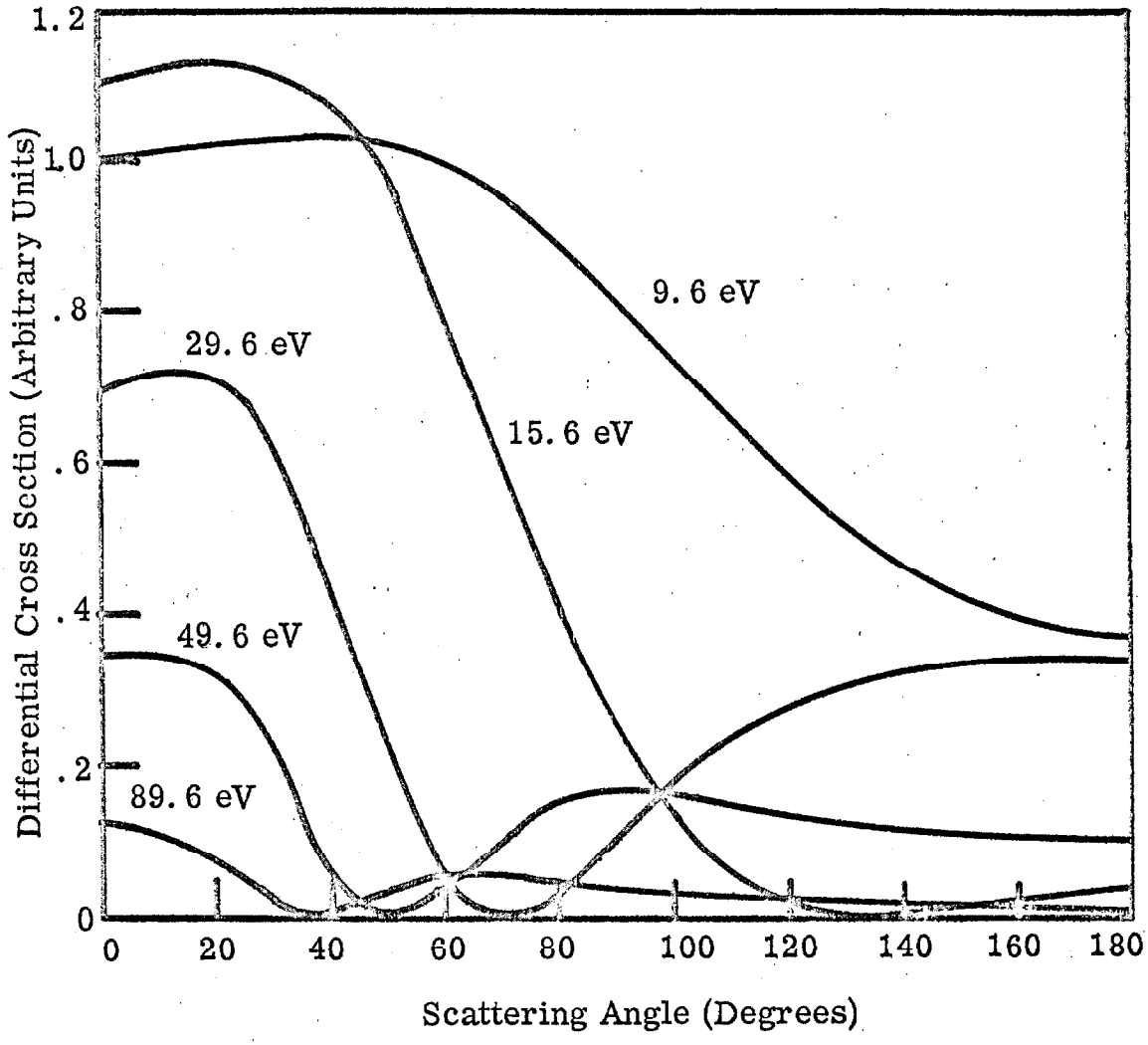

Figure 5.7-5. Differential cross section (arbitrary units) for the N → T transition in ethylene calculated according to section 3.3.7.2 for several incident energies. The relative scale for all of the curves is determined by normalizing the DCS at E_o = 9.6 eV and θ = 0° to 1.0.

Figure 5.7-6. Differential cross section (arbitrary units) for several transitions in ethylene. E_0 = 25 eV. Each data point represents an average of three scans.

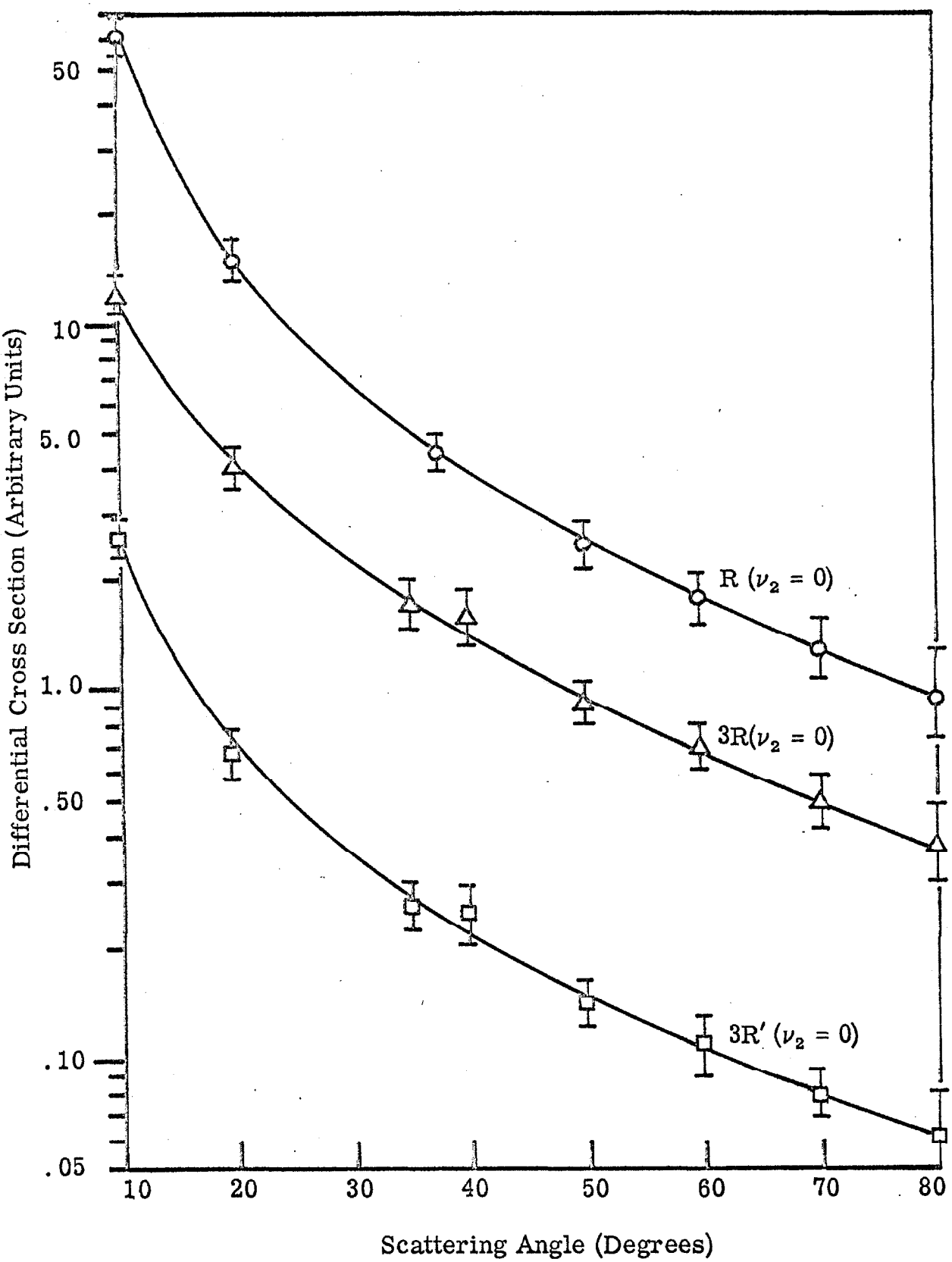
Differential Cross Section (Arbitrary Units)
50
10
5.0
1.0
.50
.10
.05
10
20
30
40
50
60
70
80
Scattering Angle (Degrees)
R (ν_2 = 0)
3R(ν_2 = 0)
3R′ (ν_2 = 0)

6. CONCLUSIONS

The work described in this thesis represents the first use of the measurement of electron-impact differential cross sections (DCS) as a function of scattering angle (θ) to characterize and identify singlet → triplet (spin-forbidden) transitions. We are hampered in our endeavor to draw general "spectroscopic rules" for the identification of such transitions from these DCS measurements by two things:

(1) The theory of electron-molecule scattering, though formally well developed, has not been applied with much success to DCS in the low-energy region (a few tens of eV's above threshold) in which exchange excitations are important; and

(2) practically all of the available experimental measurements of DCS angular dependencies (in this low-energy region) have been made by us during the course of this research on the few systems reported here. These handicaps mean that our "rules" are a self-consistent set of generalizations based primarily on a limited set of empirical results. Nevertheless, it is worth reiterating the consistent trends we have noted in sections 5.2 through 5.7.

The character of an excited state (of the target molecule) is reflected in the corresponding DCS. Differences in the behavior with θ of the DCS for the excitation of states of different character can be enhanced by comparing cross section ratios. This has been done for all of the transitions we studied. The DCS for an optically-allowed transition (usually the lowest lying such transition) in each

molecule was used consistently as a "standard" for ratio comparisons. Let DCSA be the DCS for excitation of the optically-allowed "standard" state (A) of some molecule and DCSB be the DCS for excitation of some other state (B) of the same molecule. Then, we will designate the quantity "DCSB/DCSA" (DCS ratio as used before in sections 5.2 through 5.7) simply by "the B ratio."

Table 6-1 presents a summary of some of the ratio data already discussed in sections 5.2 through 5.7 for singlet → triplet ($\Delta S = 1$) transitions. An examination of this table and the actual behavior with θ of various triplet state ratios leads us to the following conclusions:

(1) Triplet state ratios increase markedly with increasing $\theta (0° \leq \theta \leq 80°)$ for impact energies that are 20 to 30 eV above threshold. This behavior clearly distinguishes them from singlet state ratios.

(2) The magnitude of the triplet state ratio increase is sensitive to the value of $\Delta\Lambda$ associated with the singlet → triplet transition. Notice that the ratios for which $\Delta\Lambda = 1$ increase sharply by about two orders of magnitude over the angular range above in a manner that is independent of the g → g (or u) nature of the transition. On the other hand, triplet state ratios for which $\Delta\Lambda = 0$ increase by about one order of magnitude. From the examples of this latter type, those which are symmetry- allowed (SA) increase by about a factor of five more than those which are symmetry-forbidden (SF). Further, these $\Delta S = 1$, $\Delta\Lambda = 0$ ratios tend to reach a plateau at

TABLE 6-1

Summary of some pertinent data on all of the singlet → triplet transition ratios we have investigated. The first column lists the molecule (atom) and the transition whose DCS is used as a reference for the ratio determination (state A). The second column gives the B state associated with the factor increase (B ratio at high angle limit divided by B ratio at low angle limit) listed in the third column. The fourth, fifth, and sixth columns give the value of $\Delta\Lambda$, the impact-energy above threshold, and the limits of the angular range used to determine the factor increase, respectively.

Molecule (Atom)	B State	Factor Increase	$\Delta\Lambda$	Impact Energy Above Threshold (eV)	Angular Range (degrees)
He	2^3S	6	0	24	0 - 70
$1^1S \rightarrow 2^1P$	2^3P	60	1	23	0 - 70
N_2	$E^3\Sigma_g^+$	6	0	23	10 - 80
$X^1\Sigma_g^+ \rightarrow b^1\Pi_u$	$C^3\Pi_u$	100	1	24	10 - 80
	$B'^3\Pi_g$	100	1	32	10 - 80
CO	$b^3\Sigma^+$	30	0	25	10 - 80
$X^1\Sigma^+ \rightarrow A^1\Pi$	$a^3\Pi$	100	1	29	10 - 80

TABLE 6-1 (Continued)

Molecule (Atom)	B State	Factor Increase	$\Delta\Lambda$	Impact Energy Above Threshold (eV)	Angular Range (degrees)
C_2H_2	$\tilde{a}$	1000	(1)[a]	30	10 - 80
$\tilde{X}^1\Sigma_g^+ - \tilde{C}^1\Pi_u$	$\tilde{b}$	1000	(1)[a]	29	10 - 80
C_2H_4	T	35	0	21	10 - 80
(N - 3R)					
H_2	$b^3\Sigma_u^+$	30	0	30	10 - 80
$X^1\Sigma_g^+ - C^1\Pi_u$					

[a] Presumably, $\Delta\Lambda = 1$ for these two transitions. See text, section 5. 6.

intermediate angles, in contradistinction to the $\Delta S = 1$, $\Delta\Lambda = 1$ ratios.

In summary, triplet state excitations as a whole can be clearly identified by their ratio behavior (11 examples). The determination of $\Delta\Lambda$ from the ratio behavior also seems reasonably reliable (5 examples of $\Delta\Lambda = 0$ and presumably 6 examples of $\Delta\Lambda = 1$). There is no apparent difference in the ratio dependencies of SA and SF ratios for $\Delta\Lambda = 1$ (at least 1 SF example and 2 SA examples), while for $\Delta\Lambda = 0$, the SF ratios seem to increase less than do the SA ones (1 SF example and 3 SA examples). The reliability of these generalizations can be judged by the number of examples.

For singlet state ratios ($\Delta S = 0$), the situation seems more complex. In particular, these ratios do not exhibit any general trend with angle as do the triplet ones (this in itself, however, points up the $\Delta S = 0$ character of the former). Some singlet ratios are practically constant while others oscillate with either positive or negative slopes at small θ. In the case of CO, the signs of the initial slopes of the $^1\Sigma^+$ ratios change from negative to positive as the impact energy is lowered from 35 eV to 25 eV while a similar singlet state ratio ($p'\,^1\Sigma_u^+$) in N_2 has the same behavior at 25 eV that it has at 40 eV.

Consequently, we do not feel that any meaningful correlations between the ratio behavior and the value of Λ or the symmetry of the excited state can be derived from these investigations without additional data.

One diatomic molecule of special interest for future work is O_2. Since it has a triplet ground state, transitions to singlet states are spin-forbidden. This, of course, is simply the reverse of the excitations we have studied so far. In addition, O_2 has a low-lying singlet state with $\Lambda = 2$ (i. e., $a^1\Delta_g$) which, if we could observe it, would provide information about $\Delta S = 1$, $\Delta\Lambda = 2$ transitions (we have observed no other $\Delta\Lambda = 2$ transitions). The list of interesting polyatomic molecules is practically endless since the scattering from none other than those reported here have been studied as a function of angle at low energy. The study of methyl substituted ethylenes may help elucidate the nature of the olefinic "mystery band"[181]. Also the search for the low-lying triplet states of small molecules such as H_2O, CO_2, formaldehyde, etc. is worthwhile for future investigation.

APPENDIX I

OVERLAP OF TWO GAUSSIANS

Consider one energy analyzer (monochromator) for which $f(E)\,dE$ is the fraction of electrons of energy E transmitted in the energy range $E - E + dE$ and a second analyzer (selector) for which $g(E - T)$ is the fraction of electrons of energy E transmitted per unit energy range. We assume that $f(E)$ and $g(E - T)$ have maxima at $E = 0$ and $E = T$, respectively, and are normalized so that

$$\int_{-\infty}^{\infty} f(E)\,dE = \int_{-\infty}^{\infty} g(E - T)\,dE = 1. \qquad \text{(I-1)}$$

If the output of the monochromator is directed into the selector, the fraction of electrons per unit energy range $F(T)$ that will be collected, apparently with energy T, at the selector output is

$$F(T) = \int_{-\infty}^{\infty} f(E)\, g(E - T)\,dE \ . \qquad \text{(I-2)}$$

For the present analyzer system, f and g can be adequately approximated by Gaussians (see section 4. 4. 3. 3) as

$$f(E) = \frac{1}{A\sqrt{\pi}}\ e^{-E^2/A^2} \qquad \text{(I-3)}$$

and

$$g(E - T) = \frac{1}{B\sqrt{\pi}} \; e^{-(E - T)^2/B^2} \qquad \text{(I-4)}$$

where

$$A = \frac{\Delta E_{\frac{1}{2}}^{m}}{2\sqrt{\ell n 2}} \qquad \text{and}$$

$$B = \frac{\Delta E_{\frac{1}{2}}^{s}}{2\sqrt{\ell n 2}} \quad .$$

$\Delta E_{\frac{1}{2}}^{m}$ and $\Delta E_{\frac{1}{2}}^{S}$ are the full-width at half-maximum (FWHM) of the monochromator and selector transmission functions, respectively.

Substitution of (I-3) and (I-4) into (I-2) and integration over E yields

$$F(T) = \frac{1}{\sqrt{\pi(A^2 + B^2)}} \; e^{-T^2/(A^2 + B^2)} \quad . \qquad \text{(I-5)}$$

Consequently, the overall transmission function of this two analyzer system is Gaussian with a FWHM of

$$\Delta E_{\frac{1}{2}} = \left[(\Delta E_{\frac{1}{2}}^{m})^2 + (\Delta E_{\frac{1}{2}}^{S})^2 \right]^{\frac{1}{2}} \quad . \qquad \text{(I-6)}$$

If both analyzers are operated with the same resolution (FWHM), then the FWHM of the beam leaving the monochromator as observed by the selector is $\sqrt{2}\,\Delta E_{\frac{1}{2}}^{m}$.

APPENDIX II

SPECIFICATIONS OF THE 1024 CHANNEL NUCLEAR DATA ANALYZER SYSTEM

1. Introduction

The system is a modified version of the ND-181 FM-ITB system described in Nuclear Data Inc.'s brochures entitled:

a. - ND-180 512 Channel Analyzer System
ND-181 1024 Channel Analyzer System

b. - Instruction Manual, ND-180 FM Pulse Height Analyzer System (November, 1964)

c. - Model ND-180 ITB Integrator and Time Base Unit Instruction Manual (February, 1965)

The main standard features are described in those brochures and are summarized below. The modifications of this system which are desired are described in Section 3 following. Section 4 lists the main components of the system.

2. General Description

2.1 Modes of Operation: A. Pulse Height Analysis (PHA)
B. Multi Channel Scaling (MCS)
C. Signal Averaging (SA). Wave Form Comparison Method

2.2 Number of channels: 1024

2.3 Count capacity per channel: 10^6

2.4 Count rate up to 10^6 per second in MCS.

2.5 Memory dividable into halves and quarters.

2.6 Capability of 2 and 4 detector operation by external routing in Modes PHA, Normal MCS, and Mode B-IV.

2.7 Transfer from any quadrant to any quadrant, bidirectional.

2.8 Coincidence and anticoincidence operation in all modes except in SA. Jacks on front panel for monitoring coincidence or anticoincidence and detector output signals to determine their time relationships.

2.9 Upper and lower level discriminator.

2.10 Display: Analog: CRT and X-Y Recorder.
Digital: Serial Print and Paper Punch.

2.11 Horizontal display position control on front panel to allow user to look at last portion of spectrum when spectrum is greatly expanded on external oscilloscope.

2.12 Auto repeat capability.

2.13 Time Base Unit with channel dwell times, 50, 100, 200, 500, 1000, 2000 μ sec., 5, 10, 20, 50, 100, 200 m sec., 0.5, 1, 2 seconds for MCS and SA.

2.14 Magnetic core memory "Live Time."

2.15 Live Time in steps of 1, 2, 4, 8, 10, 20, 40, 80, 100, 200, 400, 800, 1000 and infinity (minutes) in PHA. Possibility of use of external oscillator. Live Time is always printed in first channel of memory.

2.16 Sweep triggering (MCS and Averaging): Internal, Recurrent, External. Plus or Minus, AC or DC triggering.

2.17 Sweep delay: 0, 1, 2, 4, or 8 times the selected sweep period.

2.18 Data and address lights.

2.19 Dead time meter.

2.20 Test mode.

2.21 Capability of overlapping quarters and halves.

2.22 Capability of normalizing data in each half of memory when in overlapping position.

2.23 Calibration capability to add 1000 counts to all memory channels.

2.24 Manual address advance (one channel at a time) for digital readout of channels of interest.

3. Modifications

In addition to the standard features mentioned in Sections 1 and 2 above, the following modifications are included.

3.1 Forward and Forward-Backward Address Scaler. Either type of operation can be selected in modes of operation PHA and MCS.

3.2 In Multi-Channel Scaling Mode, besides the normal operation mode, called hereafter MCS-I, an additional mode is required, labeled MCS-II.

3.2.1 Mode MCS-II

In this mode the Nuclear Data System will be attached to an electron scattering apparatus. This apparatus has an electron detector system (ED), an electron beam chopper (EBC), and an

electrostatic energy analyzer (EA).

3.2.1.1 General Description of MCS-II Mode

The Time Base Generator (TBG) in the Nuclear Data ITB Unit supplies appropriate pulses to Square Wave Generator (SWG). SWG makes the voltage across terminals P_1 and P_2 change alternately between 0 and 10 volts at a frequency determined by the dwell time (Δt) selected by the ITB. (P_1 and P_2 are not grounded.) TBG also supplies the appropriate pulses to Translator (TR) in such a way that when the electron beam is on (voltage difference between P_1 and P_2 (V_1) is zero), the incoming counts are routed into the first half of the memory of ND-181 FM and when the electron beam is off (V_1 = 10 V), the incoming counts are routed into the second half of the memory.

The Raytheon DAC-20-10 Unit (incorporated by Nuclear Data as part of the analyzer system) supplies an analog voltage (range 0-10 V) which is proportional to the channel number in the first half of the memory if First/Direct Switch (FD-S), incorporated into the system by Nuclear Data, is in First position, and strictly proportional to the channel number into which counts are being accumulated if FD-S is in Direct position. For Mode MCS-II this switch is in the First position. During the time in which counts are being accumulated in channel 1 (first half of the memory) and then into the matching channel 513 (in the second half of the memory) the analog voltage has the same value. A differential amplifier system (supplied by Nuclear Data as part of the system) with an amplification range of

0-10 (with steps 1.0, 2.0, 3.0, 4.0, 5.0, 6.0, 7.0, 8.0, 9.0, and 10.0) amplifies the analog signal supplied by the DAC. The amplified signal, V_2, is available for external use across terminals P_3 and P_4. (P_3 and P_4 are not grounded.) The stability and reproducibility for these voltages are given later in this Section.

A block diagram of this mode is shown in Figure II-1. Figure II-2 shows the various voltages and time relations.

3.2.1.2 Step by Step Description of MCS-II Mode

Step 0. System is not counting (standby position), but TBG is operating and the square wave signal appears across P_1 and P_2. Operator command (manual setting of control switch to start position) causes counting to begin as per Step 1 without disturbing the square wave in any way.

Step 1. When counting is initiated, counts are accumulated in channel number i (i = 1 to start) in the first half of the memory for time Δt, beginning precisely (within 1 μ sec.) when the square wave on terminals P_1 and P_2 goes to zero. The analog voltage across P_2 and $P_3(V_2) = 0$.

Step 2. Counts are accumulated in channel 513 for time Δt beginning precisely (within 4 μ sec.) when $V_1 = 10$ volts. V_2 is left unchanged.

Step 3. i is increased by one and Steps 1 and 2 are repeated until channel 1024 is reached. When channel 1024 is reached, a Full cycle has been completed.

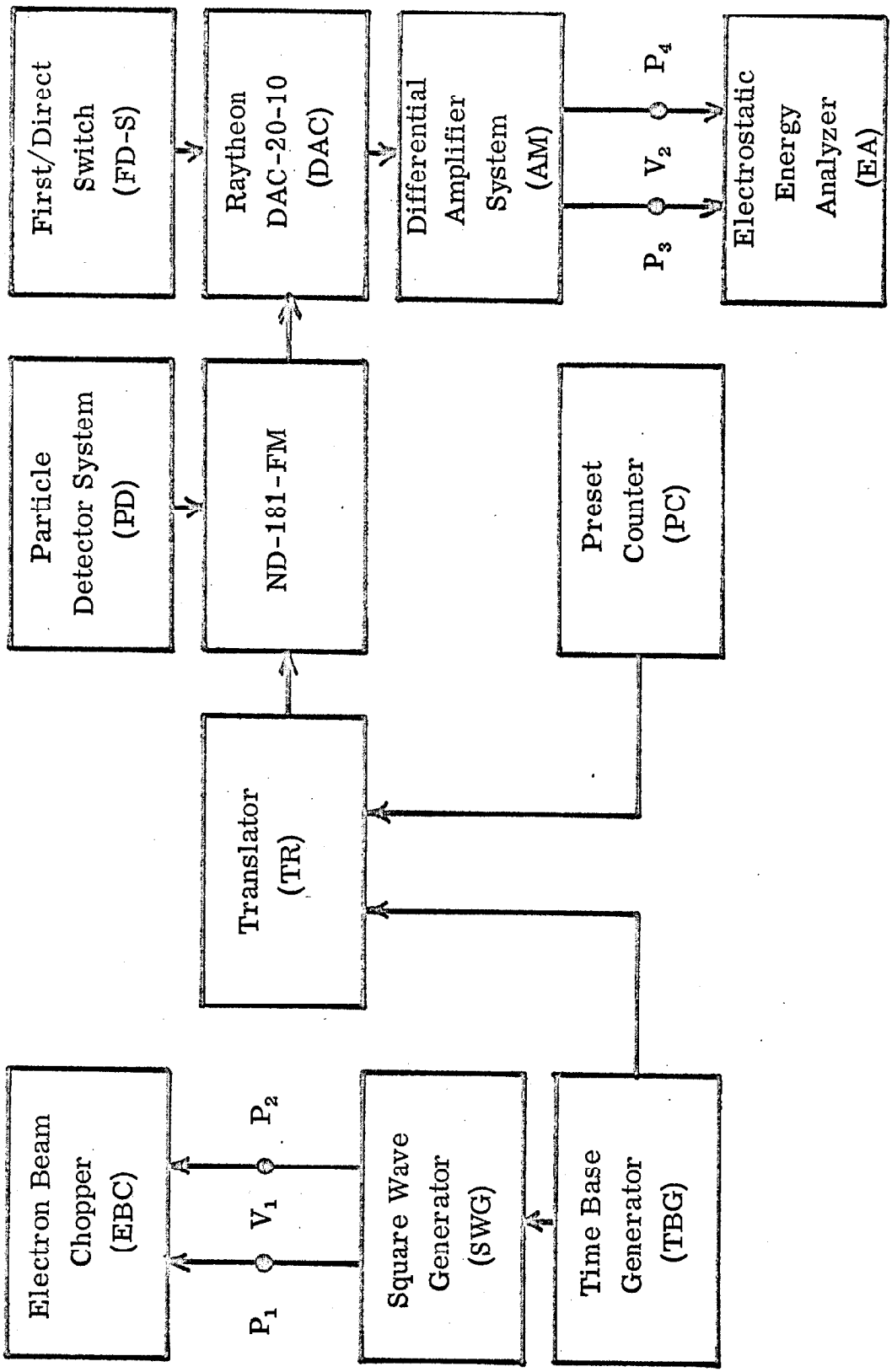

Figure II-1. Block schematic diagram for Mode MCS-II.

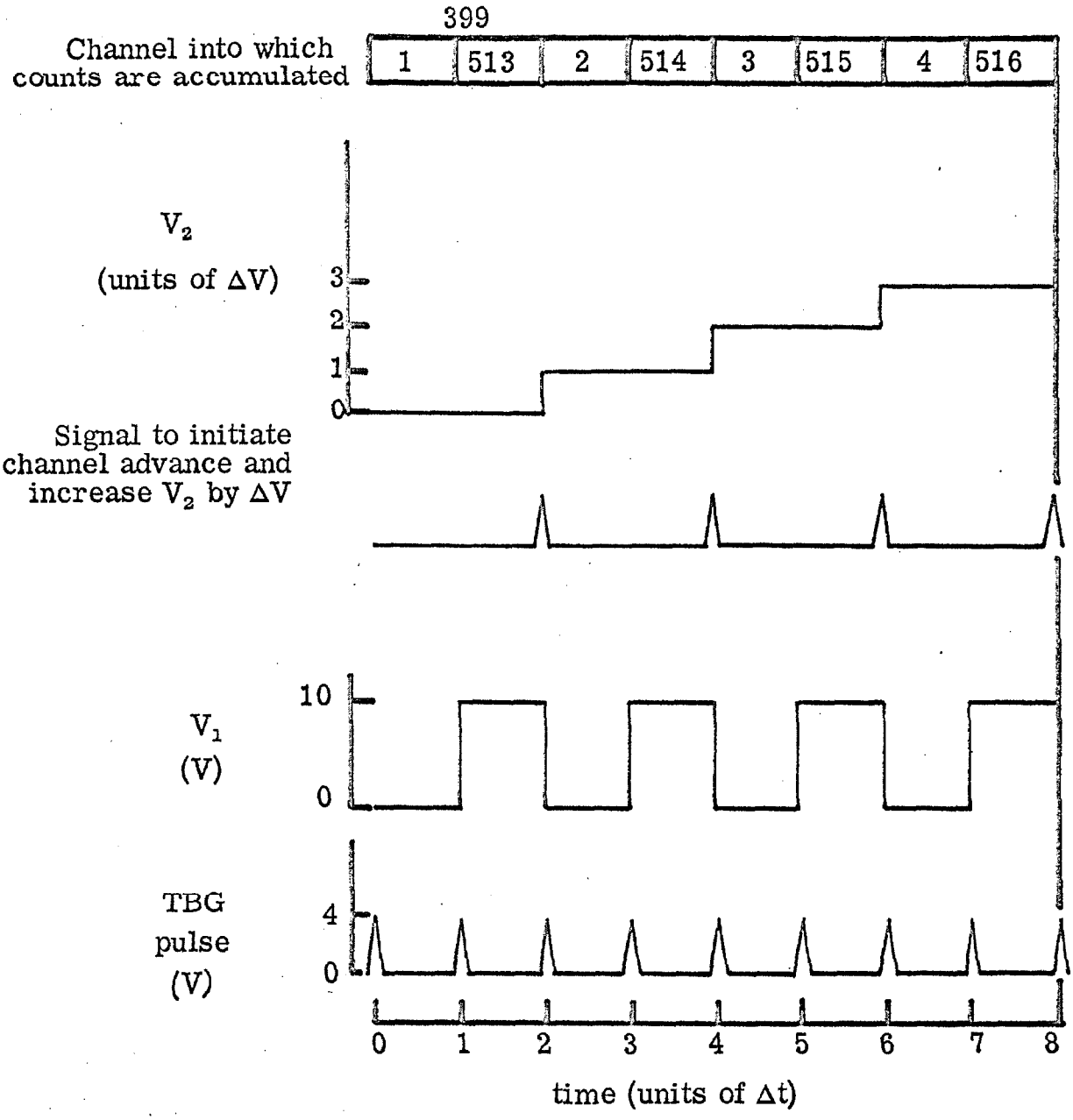

Figure II-2. Time signal relations for Mode MCS-II.

Step 4. Full cycle is repeated as many times as selected on the 5-digit present counter (PC) incorporated into the system by Nuclear Data.

3.2.1.3 Specifications for Mode MCS-II

a. - V_1 is 0 or 10 volts within 0.1 volts. The rise time and decay time for switching between these two values is less that 4 μ sec.

b. - V_2 is proportional to the channel number in the first half of the memory or to the channel number into which counts are being accumulated depending on whether FD-S in in First or Direct position, respectively. When the differential amplifier is set at gain 1, the range of V_2 is 0.000 to 10.240 V with a deviation from linearity that is less than 1 mV and reproducibility better than 1 mV in the entire range. When the amplifier gain is 10, the range is 0.00 to 102.40 V and deviation from linearity and reproducibility is less than 10 mV in the entire range. As the channel address is increased by one, the time for V_2 to reach its new value (to within 0.01%) is 1 μ sec. or less. As this address is switched from 1024 to 1, the time for V_2 to drop to less than 1 mV is 10 μ sec. or less.

c. - Δv, the voltage step, is 10, 20, 30, 40, 50, 60, 70, 80, 90, or 100 mV corresponding to gain 1, 2, 3, 4, 5, 6, 7, 8, 9, or 10 of the differential amplifier.

d. - Δt, the dwell time selected on ITB: see Section 2.13.

e. - DAC-20-10 Unit: see Raytheon Booklet SP-171C, pp. 6 and 7.

f. - Output impedence is $\leq$ 1000 ohms for both V_1 and V_2.

g. - Synchronization between ITB pulses and changes in V_1 and V_2 is 1 μ sec.

h. - Dwell times in corresponding channels of two halves of the memory (for example, channels 2 and 514) are equal to within 0.25 microseconds or 1 part in 10^5, whichever is larger.

4. Components

The major components of which the system is composed are:

a. - ND-181-F

b. - ND-181-M

c. - ND-180-ITB

d. - ND-312 Teletype

e. - Raytheon DAC-20-10

f. - Differential Amplifier System

g. - Translator

h. - Preset Counter

i. - Modification of ITB

APPENDIX III

Angular Dependence of Low-Energy Electron Impact Excitation Cross Section of the Lowest Triplet States of H_2

by

S. Trajmar,* D. C. Cartwright,†‡ J. K. Rice,† R. T. Brinkmann,* and A. Kuppermann†

California Institute of Technology, Pasadena, California

(Received 12 July 1968)

ABSTRACT

The differential cross sections for the electron impact excitation of the lowest triplet states of molecular hydrogen ($b^3\Sigma_u^+$, $a^3\Sigma_g^+$) have been calculated from threshold to 85 eV impact energy using the Ochkur-Rudge theory. For the $X^1\Sigma_g^+ \rightarrow b^3\Sigma_u^+$ transition, the relative differential cross sections

---

*Jet Propulsion Laboratory. Work supported in part by the National Aeronautics and Space Administration, Contract NAS7-100.

†Albert Amos Noyes Laboratory of Chemical Physics, contribution number 3705. Work supported in part by the U. S. Atomic Energy Commission. Report Code CALT 532-33.

‡Present address: The Max Planck Institute for Physics and Astrophysics, Institute for Extraterrestrial Physics, 8046 Munich, Germany.

were measured with a low-energy, high-resolution electron impact spectrometer from 10° to 80° scattering angle and impact energies of 25, 35, 40, 50, and 60 eV. Theory and experiment are in good agreement for the shape of the differential cross section for energies of 35 eV and above. However, at 25 eV, the theory continues to predict a rather well developed maximum in the cross section at around 40° while the experimental cross sections are more isotropic. An appreciable contribution to the inelastic scattering in the energy loss region from 11 to 14 eV due to excitation to the $a^3\Sigma_g^+$ and/or $c^3\pi_u$ states is definitely established from the observed angular distributions. A quantitative evaluation of the individual angular behavior of the excitations in this region, however, would require a resolution higher than the presently available one of 0.030 eV.

1. INTRODUCTION

Low-energy electron impact spectroscopy has been found to be a very powerful tool for locating and identifying energy levels of molecules, especially those to which transitions from the ground state are forbidden by optical selection rules.[1-9] (The low-energy range as defined here is from a few eV up to 100 eV. This corresponds to the binding energy of outer electrons in atoms and molecules and is a very important region from the point of view of spectroscopy, photochemistry, plasma physics, and for many atmospheric phenomena.) Both the energy and angular dependencies of the differential cross section are important in identifying a given transition. The energy dependence of the differential cross section has been investigated to some degree in the past.[1-9] However, there is very little information available on the angular dependence of excitation cross sections at low impact energies. The Born-Oppenheimer approximation is not valid at these impact energies; in fact, no theory has proved reliable in predicting the energy and angular dependencies of differential cross sections for even the simplest system of electron-atomic hydrogen.

Recent studies of He,[9a] C_2H_2,[9b] H_2, N_2, CO, CO_2, H_2O, and C_2H_4,[10] indicate that the measurement of the differential cross section at a fixed incident energy and variable scattering angle yields more information about the nature of the electronic excitation than does the measurement of the energy dependence of the differential cross section at a fixed scattering angle. In order to learn more about the angular behavior of differential cross sections for different types of electronic

excitations, it is important to carry out experiments on transitions of known character. The information obtained from such studies is useful in the evaluation of different approximate theories and may lead to rules for assigning unknown transitions.

The hydrogen molecule, being the molecule most amenable to theoretical calculation, was the natural selection for comparison between theory and experiment. Cartwright and Kuppermann[11] have calculated total cross sections for the electron impact excitation of the two lowest triplet states of molecular hydrogen using the Ochkur-Rudge (OR) theory.[12] These cross sections agree well with Corrigan's experimental electron impact dissociation cross sections[13] from threshold to about 50 eV. A comparison between the theoretical and experimental angular distributions as functions of incident energy provides an additional and more sensitive test of the theory, since integration of the differential cross section may conceal a failure of the theory while still leading to the correct total cross section. Green[14] has pointed out that the arguments of Rudge[12c,d] and Crothers[12e] justifying Rudge's modification of the Ochkur theory are of doubtful validity and the best test of these theories is comparison with experimental differential cross sections. Hence, the (OR) approximation has been used to calculate the differential cross sections for the $X^1\Sigma_g^+ \rightarrow b^3\Sigma_u^+$ and $X^1\Sigma_g^+ \rightarrow a^3\Sigma_g^+$ excitations for comparison with the equivalent experimental measurements. The singlet-triplet transition provides an unambiguous test of rearrangement scattering theories since they are due entirely to exchange excitation with no contribution from direct process.

A broad feature in the electron impact spectrum of H_2 corresponding to the $X^1\Sigma_g^+ \rightarrow b^3\Sigma_u^+$ transition has been observed by Schulz[2a] and Dowell and Sharp[15] using the trapped-electron method. By this method the total cross section is measured very near threshold energy. Kuppermann and Raff[4c] also observed the $X^1\Sigma_g^+ \rightarrow b^3\Sigma_u^+$ transition at 60 eV impact energy with an apparatus which collected scattered electrons from 22° to 112°, the collection efficiency being highest at 90°. To our knowledge there are no experimental or theoretical differential cross sections for electron-exchange processes in molecular hydrogen to which our results can be compared.

2. THEORY

Most previous calculations of the exchange excitation of atoms by low energy electrons have been performed in the Born-Oppenheimer (BO) approximation.[16] The results of such calculations, however, indicate that the (BO) approximation fails badly for incident electron energies below about 100 eV.[17] The calculation of similar exchange processes involving diatomic molecules has been limited by the mathematical difficulty of treating the noncentral molecular force field and the nuclear motion. Ochkur[12b] and Rudge[12c] have proposed modifications of the (BO) approximation which have been found to give reliable total cross sections for exchange processes in atomic systems. Recently, this (OR) approximation was employed to calculate total cross sections for excitation of the $(b^3\Sigma_u^+)$ and $(a^3\Sigma_g^+)$ states of molecular hydrogen.[11] The methods used in the cross section calculations reported here are very similar to the ones used in the total cross section calculations and consequently are only briefly outlined.

Within the framework of the (BO) separation of nuclear and electronic motion [18] and the (OR) approximation to the exchange scattering amplitude of an electron by a diatomic molecule, the differential cross section for exchange excitation from initial state $i(n,\nu,J,M)$ to final state $f(n',\nu',J',M')$ can be written as

$$I_i^f(k_o,\theta,\varphi) = \frac{3k'}{k_o} \left| \int_{R,\Omega} \xi_{n'\nu'J'}^{*}(R)\, Y_{J'}^{M'*}(\chi,\phi)\, T_i^f\, \xi_{n\nu J}(R)\, Y_J^M(\chi,\phi) R^2 dR d\Omega \right|^2, \quad (1)$$

where

$$T_i^f(k_o,\theta,\varphi;R,\chi,\phi) \equiv \frac{2a_o}{\left[a_o k' - i\left(I_n/\mathcal{R}\right)^{\frac{1}{2}}\right]^2}$$

$$\times \int e^{i\vec{q}\cdot\vec{r}_1}\, \psi_{n'}^{*}(\vec{r}_1,\vec{r}_2;R)\, \psi_n(\vec{r}_1,\vec{r}_2;R) d\vec{r}_1\, d\vec{r}_2 \quad (2)$$

In Eqs. (1) and (2), ψ,ξ, and Y are the spatial electronic vibrational and rotational wave functions; I_n is the ionization energy of state n; $\mathcal{R}$ is the Rydberg energy; a_o is the Bohr radius; R the internuclear distance; χ,ϕ the polar orientation angles of the internuclear axis with respect to a space-fixed coordinate system; $d\Omega$ is the element of solid angle in the direction of the internuclear axis; θ and φ are polar angles defining the direction of scattering with respect to the direction of the incoming free electron; $\vec{r}_1$ and $\vec{r}_2$ are the coordinates of the bound electrons in the molecule fixed coordinate system; n,ν, and J are the electronic, vibrational and rotational quantum numbers; $\vec{k}_o$, $\vec{k}'$ are the initial and final wave number vectors of the free electron which are related by

$$k'(k_o,i,f) = \left[k_o^2 - (2m/\hbar^2)(E_f - E_i)\right]^{\frac{1}{2}} \quad (3)$$

where E_i and E_f represent the total energy of the molecule before and after collision, and finally

$$\vec{q} = \vec{k}_o - \vec{k}'$$

The factor of 3 in Eq. (1) comes from integration over spin variables. Since the presently available experimental energy resolution is not sufficient to resolve rotational transitions, only rotationally averaged differential cross sections will be considered here. If the temperature of molecular hydrogen is appreciably higher than its rotational characteristic temperature (174°K), then the rotationally averaged differential cross section for a gaseous thermal target is given by

$$I_{n\nu}^{n'\nu'}(k_o,\theta,\varphi) = \frac{3k''}{k_o}\int_\Omega \left|\int_R \left[R\xi_{n'\nu'}(R)\right]^* T_{n\nu}^{n'\nu'}(k_o,\theta,\varphi;R,\chi,\phi)\left[R\xi_{n\nu}(R)\right]dR\right|^2 \frac{d\Omega}{4\pi} \quad (4)$$

where

$$k''(k_o,n,\nu,n',\nu') = \left[k_o^2 - (2m/\hbar^2)(E_{n'\nu'} - E_{n\nu})\right]^{\frac{1}{2}} \quad (5)$$

In the derivation of (4), the vibrational wave functions and the wave number of the scattered electron were assumed independent of J and J'. This assumption is consistent with present experimental energy resolution capabilities.

The excited $(b^3\Sigma_u^+)$ state is unbound and hence there is a continuum of ν'-vibrational states. The differential cross section for excitation to all final vibrational states is formed from (4) by "summing" over ν'. Application of the delta-function approximation[19] to (4) leads to a rotationally averaged differential cross section for excitation from the

ground vibrational state to all excited vibrational states which is given by

$$I^{(1)}(k_o,\theta,\varphi) = \frac{3k''}{k_o} \int_{D_o}^{E_o} P^{(1)}(E_1) \langle |T_{\nu'}^{(1)} R^{(1)}(E_1)|^2 \rangle dE_1 \qquad (6)$$

where

$$P^{(1)}(E_1) \equiv \frac{|R^{(1)}(E_1)\xi_o^{(o)}[R^{(1)}(E_1)]|^2}{\int_{D_o}^{\infty} |R^{(1)}(E_1)\xi_o^{(o)}[R^{(1)}(E_1)]|^2 \, dE_1} \qquad (7)$$

In the above, D_o is the dissociation energy of the ground electronic state; E_o is the energy of the incident electron; $\xi_o^{(o)}$ is the lowest vibrational wave function of the ground electronic state; and the angular brackets represent an average over all orientations of the internuclear axis with respect to the incident electron beam. The integration over the internuclear distance R has been transformed to an integration over the corresponding potential energy E_1. E_1 (R) is the expression for the potential energy of the $b^3\Sigma_u^+$ state as a function of internuclear distance and $R^{(1)}(E_1)$ is the inverse of this function.

The $a^3\Sigma_g^+$ state is bound (dissociation energy 2.91 eV) and has about 16 vibrational states and no continuum whose left classical turning points fall within the Frank-Condon vertical band from the ground electronic-vibrational state. The calculation of the differential cross section for this state is performed similarly to that of the $b^3\Sigma_u^+$ state.

In the calculations reported here, the electronic wave functions used were those of Weinbaum[20] for the ground state, Phillipson-Mulliken[21] for the $b^3\Sigma_u^+$ state, and a two parameter Hartree-Fock wave function for the

$a^3\Sigma_g^+$ state. The numerical methods used were similar to those discussed previously[11] and the results reported here are believed to have computation errors of less than 10%.

3. MEASUREMENT OF THE CROSS SECTIONS

3.1 Apparatus

The low-energy electron-impact spectrometer used in these experiments is basically the same type as the one described by Simpson[22] and Kuyatt and Simpson.[23] It consists of a low-energy electron gun, a scattering chamber, two hemispherical electrostatic analyzers (for generating a monochromatic electron beam and energy-analyzing the scattered electrons), and a detector. The resolution of each of the two electrostatic analyzers is variable in the 0.030 to 0.300 energy range by appropriately adjusting the sphere potentials. The scattering chamber is a welded-bellows cylinder which allows a variation in scattering angle from -30° to +90°. The convolutions of the bellows have an "s" shape and form an electron trap which reduces the effect of wall scattering which could seriously interfere with the measurements at higher angles. The scattering chamber sample pressure is normally in the 10^{-5} to 10^{-2} torr region. The pressure is measured with miniature ion and thermocouple gauges and is kept constant during an experiment by a variable leak and a pressure controlling system. Temperature control of the target gas is possible by introducing cooling or heating media into the area between the scattering chamber and a second bellows which surrounds it. The second electrostatic energy analyzer is tuned to pass electrons with the same energy as the first energy selector. A sweep voltage is applied between scattering chamber and center of the second analyzer.

When this voltage is zero, electrons that did not lose any energy during the scattering will pass this analyzer and reach the detector, a twenty stage electron multiplier. The multiplier output can be coupled to a count-rate-meter or a 1024 channel scaler. As the sweep voltage is gradually increased, electrons that have lost the corresponding energy in exciting the molecular target will reach the detector. The number of electrons counted per unit time versus the sweep voltage furnishes an energy-loss spectrum. The energy-loss sweep voltage is controlled either by a sweep generator or by the multichannel scaler whose memory channel number (into which counting occurs) is converted to an analog voltage. External field effects are eliminated with appropriate radio frequency and magnetic shielding. The entire apparatus is bakable to 400° C. A more detailed description of the system is given elsewhere.[24]

3.2 Experimental

In these experiments the electron current scattered into a given solid angle of approximately 10^{-3} steradian was measured as a function of energy loss at a fixed electron impact energy. A typical energy-loss spectrum is shown in Fig. 1. It is an X-Y recording of the count-rate-meter output. The X-axis represents the energy-loss of the electrons and the Y-axis corresponds to the number of electrons per minute reaching the detector with each particular energy loss. This spectrum was obtained with an electron impact energy of 50 eV and a scattering angle of 40°. The elastic peak shown on the left-hand side determines the zero energy loss point.

The apparatus for the $b^3\Sigma_u^+$ excitation was tuned to about 0.2 eV resolution (full width at half-maximum FWHM of the elastic peak). This was a reasonable choice to insure high signal level and partial resolution of the vibrational structure of the $X^1\Sigma_g^+ \rightarrow C^1\pi_u$ transition. Most of the measurements were made with a count-rate-meter with a time constant that varied from 0.5 sec for the elastic peak to 10 sec for the triplet transition at high angles. The energy-loss sweep-rate was adjusted accordingly to give an undistorted reproduction of the features. The energy-loss scale is absolute, being measured with a digital voltmeter with respect to the center of the elastic peak. Its accuracy (about 10 meV) is verified by the optical values of the portions of the vibrational bands of the $C^1\pi_u$ excitation.

For the experiments in the 11-14 eV energy loss region the instrument was retuned to obtain an overall resolution of about 0.040 eV (FWHM). Typical spectra at this resolution are shown on Figs. 2 and 3 and discussed below.

In order to monitor the conditions at different angles during the experiment, and check the overall instrument stability, the pressure and the beam current in the scattering chamber were measured and the elastic peak was scanned before and after each energy loss spectrum was taken. The pressure of H_2 was kept constant (to within about 5%) at a value between 1 and 2 millitorr during each experiment and the linearity of the scattered current with pressure was established from 0.1μ up to 2μ.

3.3 Scattering Volume Correction and Error Estimation.

Measurements taken at different scattering angles correspond to different scattering geometry. If one wants to compare cross sections at different angles, a normalization of all measurements to the same

scattering geometry is necessary. It is customary[25] to carry out this normalization by multiplying the scattered current by sin θ where θ is is the scattering angle. This procedure yields proper normalization only if the electron beams entering the scattering chamber and the electron optics of the detector system have small diameter and angular divergence.

In our instrument circular apertures are used for collimating and focusing the electron beam. The scattering geometry is shown on Fig. 4. Both the electron beam entering the scattering chamber and the directions viewed by the electron optics at the exit of this chamber are represented by cones. Typical values for the incident beam and exit viewing cone half angles are 3° and 4.5° respectively. The intersection of these two cones defines the volume from which scattered particles can reach the detector. The solid angle extended by the detector varies from point to point within this volume in fact it drops to zero at the extremes. One has to average therefore, the solid angle over this volume to get an effective value of (scattering length) x (solid angle) $\equiv (\ell d\Omega)_{eff}$. This problem has been discussed by G. Breit, H. M. Thaxton and L. Eisenbud[26a] and by C. L. Critchfield and D. C. Dodder.[26b] Every differential volume element within this volume has to be properly weighted for electron density and solid angle subtended at the entrance of the detector optics. For normalizing our measurements, the incoming beam was considered as a cone with a truncated Gaussian electron density distribution having its maximum along the cone axis. The density weighted volume elements of the beam cone were integrated within the limits defined by the surface of the view cone. Each element was also weighted by the inverse square of the distance from the entrance aperture of the detector to allow for the solid angle of the detector at the volume element. The value of $(\ell d\Omega)_{eff}$ at

each angle was normalized to the value at 90°. The differential scattering cross section for a particular excitation is proportional to the peak height (after correction for scattering geometry) provided that the cross section is independent of angle within the range defined by the view cone and that the line shape is independent of angle. At $\theta = 10°$, the difference between these calculations and the approximate $\sin\theta$ correction is about 10%.

The errors inherent in the reduced measurements are of three types:

1. Random fluctuations and background noise. If the number of counts per second reaching the detector is N, then from the statistical nature of the counting process, the uncertainty in N (one standard deviation) is $\pm\sqrt{N/\tau}$ where τ is the time constant (in sec) of the rate meter.[27] This fluctuation was always less than 5% for the $X^1\Sigma_g^+ \rightarrow b^3\Sigma_u^+$ peak. In addition, there is a background noise due to stray electrons, electronic noise, and cosmic rays. This noise is relatively independent of scattering angle and amounts to about 2 counts per sec.

2. Effective scattering volume correction. Another source of error arising from the effective volume correction is due to the ±1° uncertainty in the scattering angle and the uncertainties in the beam and view cone angles. These latter angles cannot be determined directly with the present experimental setup. The latter, however, can be estimated from the electron optics with satisfactory accuracy. The beam cone angle is then obtained from the direct beam intensity profile as measured on the first dynode of the multiplier as a function of scattering angle. (The peak position of this curve defines the zero scattering angle.)

3. Instrumental error. This includes all effects associated with the variation of pressure, beam intensity, and overall instrument detection efficiency during the measurements. The constancy of these quantities is monitored during each energy-loss sweep but a significant change of instrument detection efficiency with scattering angle could go undetected. The fact that the optimum tuning conditions are found to be the same at any angle and that the scattering intensity is symmetric around zero angle, indicates that this effect is negligible.

The error bars assigned to the measurements include estimated contributions from these three sources of error.

4. RESULTS AND DISCUSSION

As seen in Fig. 1, the inelastic feature corresponding to the $X^1\Sigma_g^+ \rightarrow b^3\Sigma_u^+$ transition has a maximum at about 10 eV energy loss. Since the $b^3\Sigma_u^+$ state of H_2 is unstable with respect to dissociation into two hydrogen atoms, the transition is represented by a broad feature whose shape seems to be determined[11] by the Frank-Condon overlap integrals.[28a] In the 11 to 14 eV energy loss region several singlet and triplet transitions overlap.[28b] The optical vibrational band progression for the $X^1\Sigma_g^+ \rightarrow C^1\pi$ transition is shown.

To determine the angular dependence of the differential cross section for this transition, the corresponding maximum ordinate was read off the energy loss spectrum at each angle and normalized to the same scattering volume with the calculated effective scattering volume described above. Using this peak height instead of the area under the band does not introduce any error if the line shape is the same at all

angles. We found that this was indeed the case for both the elastic and inelastic features of the energy loss spectra. In order to compare the absolute theoretical and relative experimental cross sections, the latter are multiplied at each energy, by a factor which is the average of the ratios of the calculated absolute and experimental relative cross sections at each angle. The possibility of appreciable contribution from the strong $C^1\Pi_u$ tail was eliminated by plotting the cross sections obtained not only from the maximum ordinate measurements, but from measurements at 0.5 and 1.0 eV away from that maximum. No change in the shape of the curves of relative cross section versus scattering angle was observed.

Figure 5 compares the theoretical and experimental differential cross sections at 25, 35, 40, 50, and 60 eV impact energies. The solid curves are the calculated ones. Each experimental point was obtained from a spectrum similar to the one shown in Fig. 1.

At 50 and 60 eV the calculated and observed curves agree quite well. As one goes to lower impact energies, however, the disagreement between theory and experiment increases. While the theory predicts well-formed maxima at around 40° for low impact energies, the experiment shows fairly isotropic scattering below 35 eV. Although the measured differential cross sections are in arbitrary units, the absolute values obtained from them by the procedure described above should be close to the correct ones at 50 and 60 eV impact energies, since for them the experimental and calculated differential cross sections agree very well and the total cross section obtained from the integration of the calculated differential cross sections agrees approximately with Corrigan's measurement.[11,13] In

calculating the total cross section, Cartwright and Kuppermann[11] neglected the contribution from the excitation to the $c^3\Pi_u$ state. Inclusion of this contribution may improve this agreement.

The validity of the Ochkur (O) and (OR) theories of electron exchange scattering can be tested only in a very few cases due to the lack of experimental data and/or more accurate theoretical calculations. The (O) approximation may be considered as an (OR) approximation with improper normalization of the wave function. For the 2^3S excitation of He the shape of the experimental differential cross section of Ehrhardt and Willman[7b] agrees with the OR predictions at 24 eV from 20° to 120°.[29] The experimental data of Simpson, Menderez, and Mielczarek[6b] at 56.5 eV (5°-50°) and Vriens, Simpson, and Mielczarek[25] in the 100 to 225 eV energy range (5° - 15°) are in complete disagreement with the (OR) and (O) curves for the same excitation. In the case of atomic hydrogen, a comparison of the (OR) differential exchange cross sections for elastic scattering and the 1s → 2s excitation to the accurate close coupling calculation of Burke, Shey and Smith[30] has been made by Truhlar, Cartwright, and Kuppermann.[31] They find that the (OR) angular distributions are in qualitative agreement with the close coupling results at intermediate energies but at low energies the agreement is very poor.

It is somewhat surprising, especially in light of the above discrepancies, that the (OR) approximation predicts as well as it does the shape of the angular distribution for the $X^1\Sigma_g^+ \rightarrow b^3\Sigma_u^+$ transition in H_2 for energies as low as 40 eV. Since the theory is based on first order perturbation principles, the above comparison between theory and experiment implies that for the angular regions and impact energies considered

here the deviation of the interactions from first order are not important or that the agreement is simply an accident. It is important therefore to do additional comparisons between experiment and theory before the usefulness of the (OR) approximation can be determined.

Figures 2 and 3 show the energy loss spectrum of H_2 in the 11 to 14 eV region with a resolution (FWHM) of about 0.040 eV at 20° and 80° respectively. The electron impact energy was 40 eV for these experiments. Many of the vibrational features of the $B^1\Sigma_u^+$ and $C^1\pi_u$ excitation are separated and they account practically for all the intensity at 20°. At higher angles, however, contribution to the inelastic scattering from the $a^3\Sigma_g^+$ and/or $c^3\pi_u$ state is definitely observable. The intensity envelope of the $B^1\Sigma_u^+$ vibrational bands is easily recognized on Fig. 2. The intensity of consecutive vibrational features follows this envelope smoothly. At 80° however the bands with $\nu' = 4$ and 6 are much more intense than they should be according to this intensity envelope. The extra intensity comes from the contribution of the $\nu' = 0$ and 1 bands of the $a^3\Sigma_g^+$ and/or $c^3\pi_u$ excitations. Dowell and Sharp[15] argue that in their electron-trap threshold spectra the dominant features in H_2 are associated with the $c^3\pi_u$ excitation and that all other contributions are negligible. It is not possible to tell from our spectra whether the $a^3\Sigma_u^+$ or $c^3\pi_u$ scattering is responsible for the intensity enhancement we observe. At 40 eV electron energy the singlet bands are stronger than the triplet ones even at high angles and their interference prohibits a definite conclusion. It would require a much better resolution to separate the $a^3\Sigma_u^+$ and $c^3\pi_u$ features from the overlapping singlet ones.

The differential cross sections calculated for the $X^1\Sigma_g^+ \rightarrow a^3\Sigma_g^+$ excitation are shown in Fig. 6. No experimental data are available for comparison, for the reasons just given.

5. *ACKNOWLEDGMENT*

The authors are grateful to Drs. J. A. Simpson and C. E. Kuyatt for valuable advice concerning the design of the instrument and to Mr. G. Steffensen for his help in carrying out the measurements. They would also like to acknowledge helpful discussions with Professors R. M. Pitzer and W. A. Goddard, and Mr. D. G. Truhlar of the California Institute of Technology concerning certain aspects of the theoretical work.

REFERENCES

1. For a review of early work in this field see H. S. W. Massey and E. H. S. Burhop, Electronic and Atomic Impact Phenomena (Oxford University Press, London, 1952).
2. a) G. J. Schulz, Phys. Rev. 112, 150 (1958); b) G. J. Schulz and J. W. Philbrick, Phys. Rev. Letters 13, 477 (1964).
3. a) E. N. Lassettre, Rad. Res. Supplement 1, 530 (1959); b) A. Skerbele, M. A. Dillon, and E. N. Lassettre, J. Chem. Phys. 46, 4161 (1967); c) ibid, 46, 4162 (1967).
4. a) A. Kuppermann and L. M. Raff, J. Chem. Phys. 37, 2497 (1962); b) ibid, 39, 1607 (1963); c) Discussions of the Faraday Soc. 35 30 (1963).
5. a) F. H. Read and G. L. Whiterod, Proc. Phys. Soc. 82, 434 (1963); b) ibid, 83, 619 (1964); c) ibid, 85, 71 (1965).
6. a) H. G. M. Heideman, C. E. Kuyatt, and G. E. Chamberlain, J. Chem. Phys. 44, 355 (1966); b) J. A. Simpson, M. G. Menendez and S. R. Mielczarek, Phys. Rev. 150, 76 (1966); c) G. E. Chamberlain, Phys. Rev. 155, 46 (1967).
7. a) H. Ehrhardt and F. Linder, Z. Naturfosschg. 22a, 11 (1967); b) H. Ehrhardt and K. Willman, Z. Physik, 203, 1 (1967).
8. J. P. Doering and A. J. Williams III, J. Chem. Phys. 47, 4180 (1967).
9. a) J. K. Rice, A. Kuppermann, and S. Trajmar, J. Chem. Phys. 48, 945 (1968); b) S. Trajmar, J. K. Rice, P. S. P. Wei, and A. Kuppermann, Chem. Phys. Letters 1, 703 (1968).
10. Under investigation in our laboratories.

11. D. C. Cartwright and A. Kuppermann, Phys. Rev. 163, 861 (1967).

12. a) R. A. Bonham, J. Chem. Phys. 36, 2360 (1964); b) V. I. Ochkur, Soviet Physics-JETP 18, 503 (1964); c) M. R. H. Rudge, Proc. Phys. Soc. 85, 607 (1965); d) ibid. 86, 763 (1965); e) D. S. F. Crothers, Proc. Phys. Soc. 87, 1003 (1966).

13. S. J. B. Corrigan, J. Chem. Phys. 43, 4381 (1965).

14. T. A. Green, Proc. Phys. Soc. 92, 1144 (1967).

15. J. T. Dowell and T. E. Sharp, J. Chem. Phys. 47, 5068 (1967).

16. J. R. Oppenheimer, Phys. Rev. 32, 361 (1928).

17. D. R. Bates, A. Fundaminsky, J. W. Leech, and H. S. W. Massey, Trans. Roy. Soc. A243, 117 (1950).

18. M. Born and R. Oppenheimer, Ann. Physik 84, 457 (1927).

19. a) A. S. Coolidge, H. M. James, and R. D. Present, J. Chem. Phys. 4, 193 (1936); b) H. M. James and A. S. Coolidge, Phys. Rev. 55, 186, (1939).

20. C. Weinbaum, J. Chem. Phys. 1, 593 (1933).

21. P. E. Phillipson and R. S. Mulliken, J. Chem. Phys. 28, 1248 (1958).

22. J. A. Simpson, Rev. Sci. Instr. 35, 1698 (1964).

23. C. E. Kuyatt and J. A. Simpson, Rev. Sci. Instr. 38, 103 (1967).

24. S. Trajmar, J. K. Rice, and A. Kuppermann, JPL Tech. Memo. No. 33-373.

25. L. Vriens, J. A. Simpson, and S. R. Mielczarek, Phys. Rev. 165, 7 (1968).

26. a) G. Breit, H. M. Thaxton, and L. Eisenbud, Phys. Rev. 55, 1018 (1939); b) C. L. Crithfield and D. C. Dodder, ibid. 75, 419 (1949).

27. R. D. Evans, The Atomic Nucleus, p. 807 (McGraw-Hill, 1955).

28. a) G. Herzberg, Spectra of Diatomic Molecules, 2nd ed., p. 387 (Van Nostrand, 1953); b) ibid. p. 530.

29. D. C. Cartwright, thesis, California Institute of Technology, Pasadena, California (June 1967), unpublished.

30. a) P. G. Burke, H. M. Schey, Phys. Rev. 126, 147 (1962); b) P. G. Burke, H. M. Schey, and K. Smith, ibid., 129, 1256 (1963).

31. D. C. Truhlar, D. C. Cartwright and A. Kuppermann (to be published).

FIGURE CAPTIONS

Fig. 1. (5.5-1) Electron impact energy-loss spectrum of molecular hydrogen at 50 eV impact energy and 40° scattering angle. Ion gauge reading (uncalibrated): 2×10^{-3} torr. Incident beam current: 2.8×10^{-8} A. Elastic peak FWHM: 0.22 eV.

Fig. 2. (5.5-2) Electron impact spectrum of H_2 in the 11 to 14 eV energy-loss range at 40 eV impact energy and 20° scattering angle. Incident beam current: 1.0×10^{-8} amps. Elastic peak FWHM: 0.040 eV.

Fig. 3. (5.5-3) Electron impact spectrum of H_2 in the 11 to 14 eV energy-loss region at 80° scattering angle. The experimental conditions are the same as for Fig. 2.

Fig. 4. See figure 4.4-10 of thesis.

Fig. 5. (5.5-5) Differential cross section of $X^1\Sigma_g^+ - b^3\Sigma_u^+$ transition in H_2 as a function of scattering angle. Solid curves are theoretical and points are experimental. Different symbols indicate different experiments, conducted over a period of seven months. Incident energies are: (a) 25 eV: ●, ■, ▲. (b) 35 eV: +. (c) 40 eV: ○, □, △. (d) 50 eV: ⊙, ⊡, ◬. (e) 60 eV: ×.

Fig. 6. (5.5-6) Differential cross sections calculated for the $X^1\Sigma_g^+ - a^3\Sigma_g^+$ excitation. The numbers over the curves represent the electron impact energy in eV.

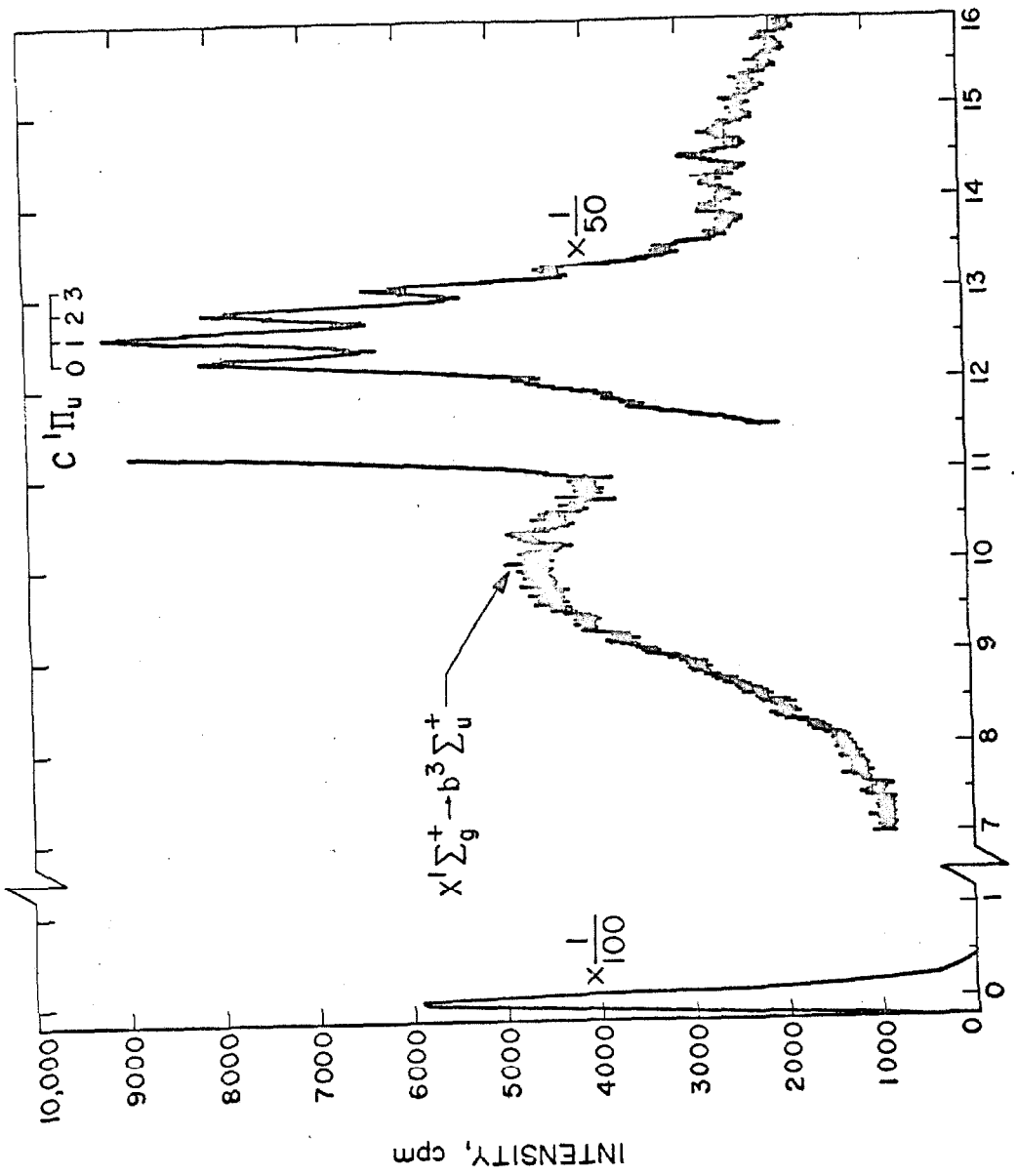
INTENSITY, cpm
ENERGY LOSS, ev
$C\ ^1\Pi_u$ 0 1 2 3
$X\ ^1\Sigma_g^+ \rightarrow b\ ^3\Sigma_u^+$
$\times\frac{1}{100}$
$\times\frac{1}{50}$

Figure 1.

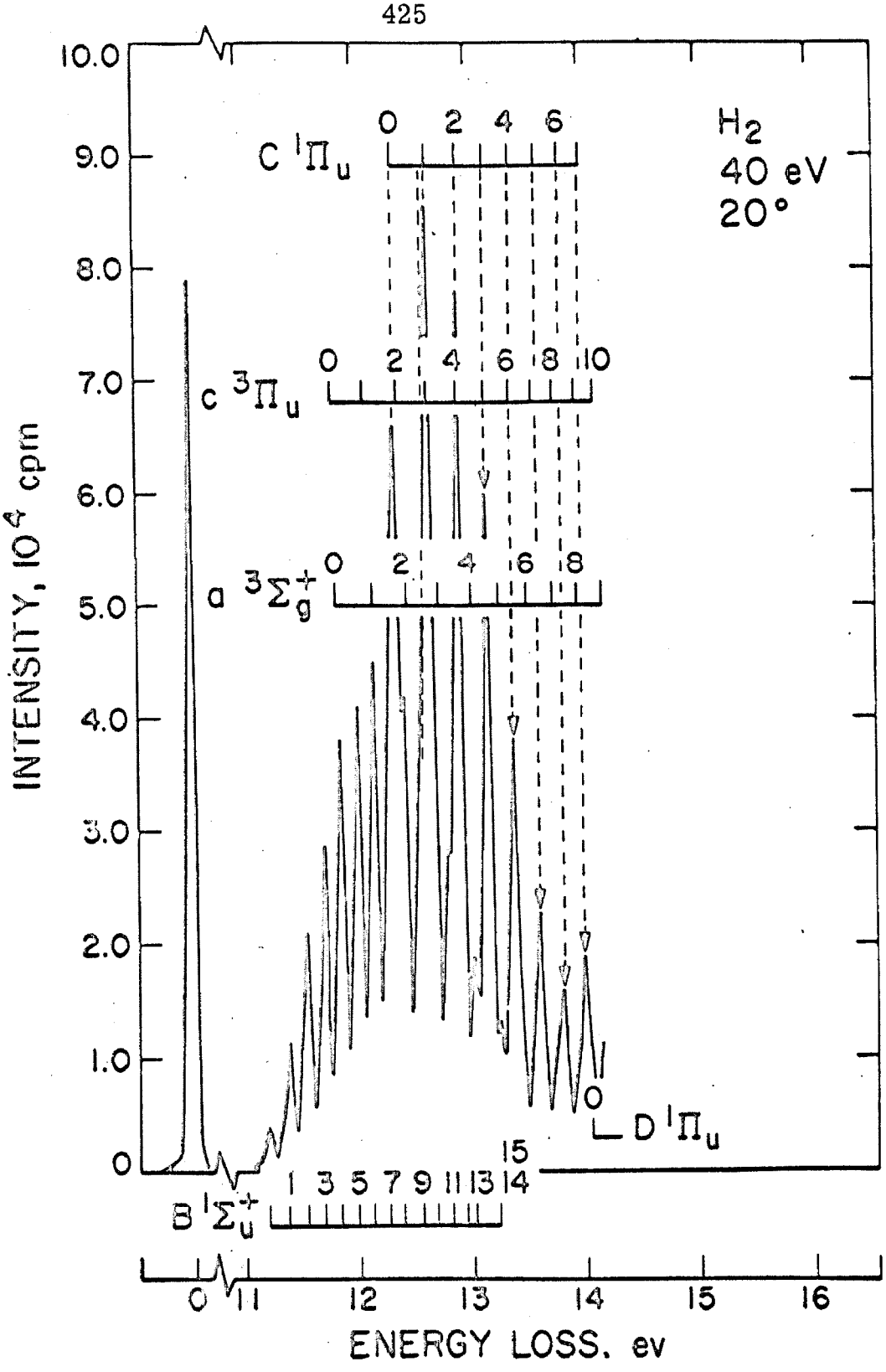
H2
40 eV
20°
C ¹Πu
c ³Πu
a ³Σg+
B ¹Σu+
D ¹Πu
INTENSITY, 10⁴ cpm
ENERGY LOSS. ev

Figure 2.

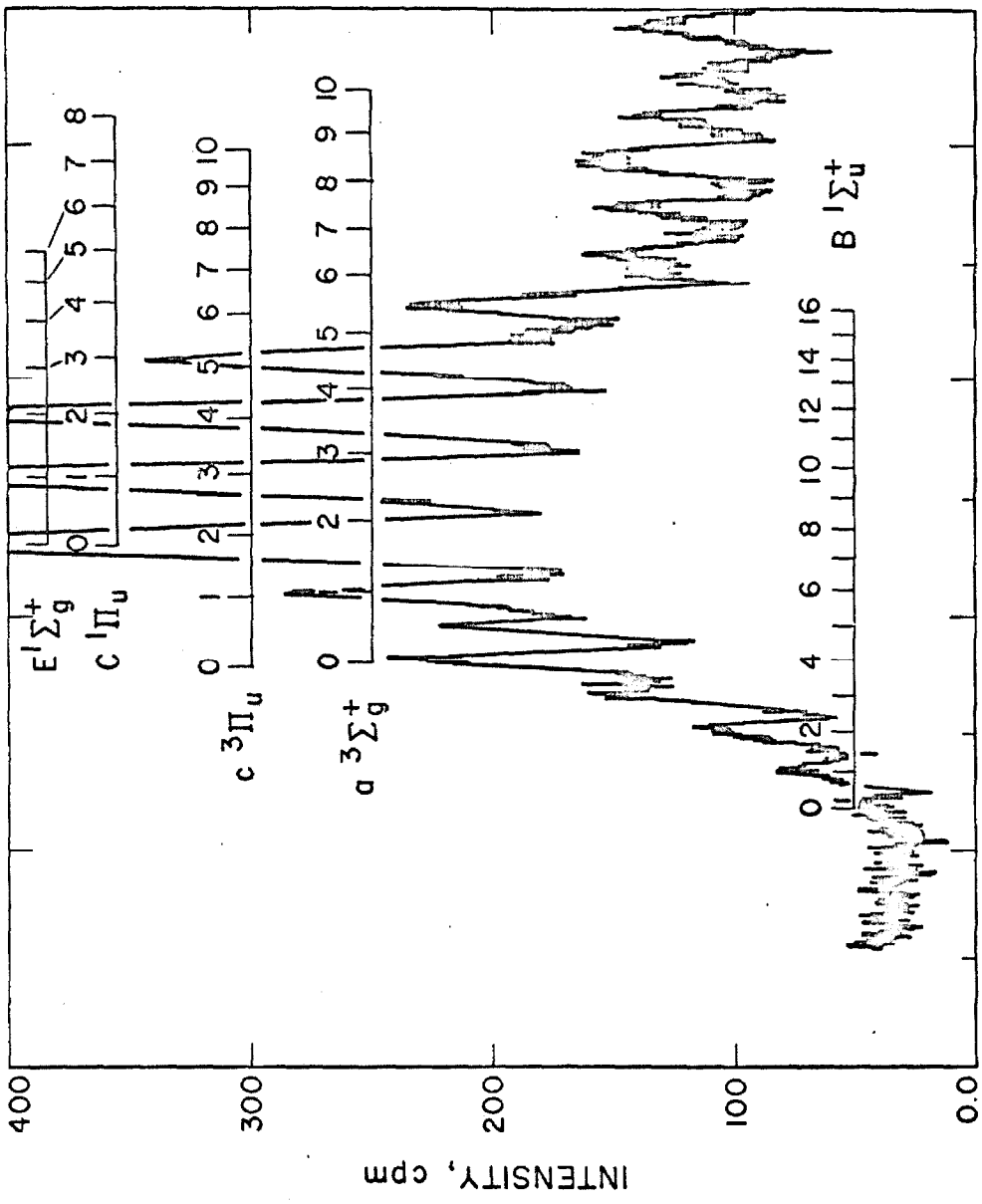
INTENSITY, cpm
400
300
200
100
0.0
ENERGY LOSS, ev
11
12
13
14
$E\,^1\Sigma_g^+$
$C\,^1\Pi_u$
$c\,^3\Pi_u$
$a\,^3\Sigma_g^+$
$B\,^1\Sigma_u^+$

Figure 3.

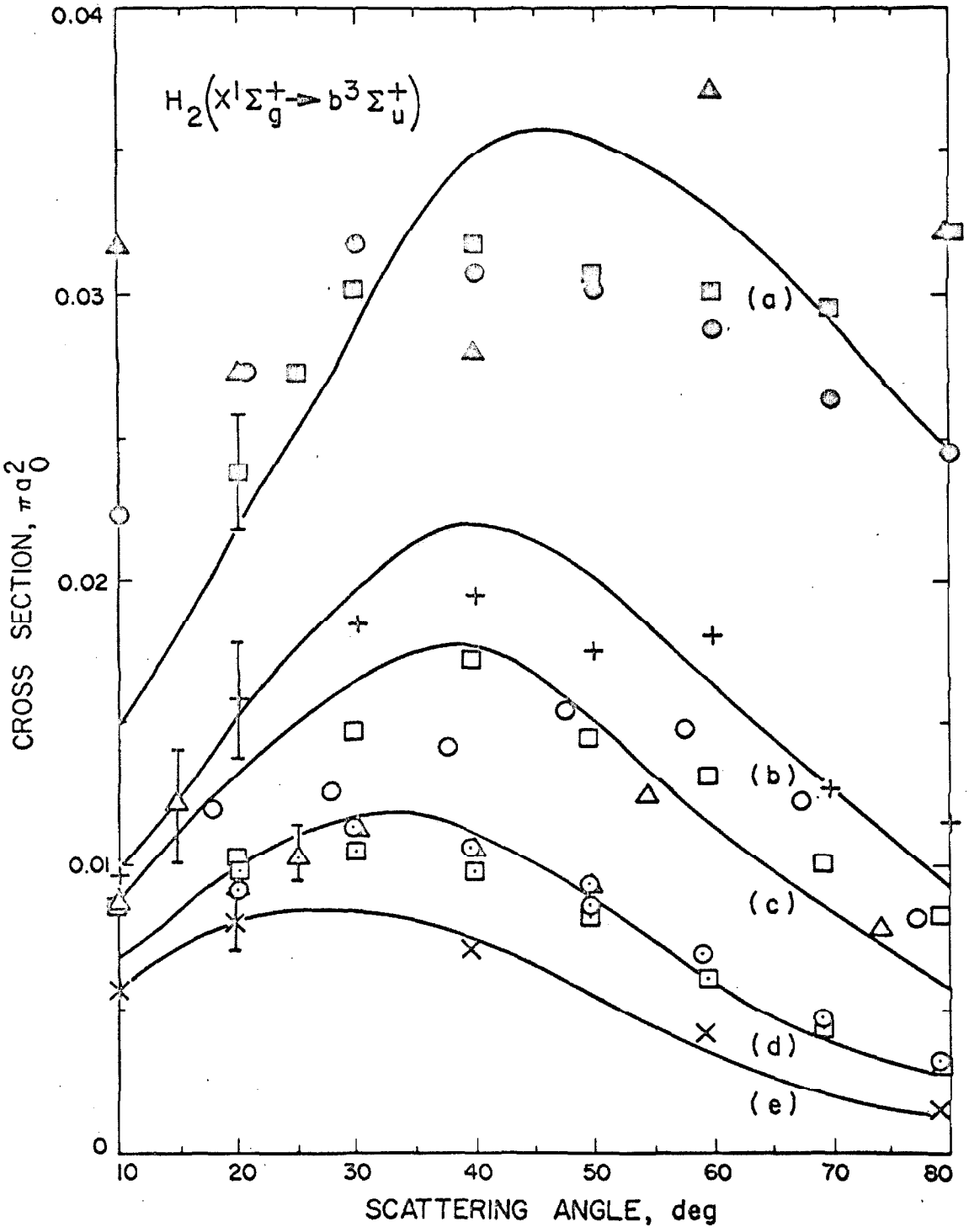
$H_2(X^1\Sigma_g^+ \rightarrow b^3\Sigma_u^+)$
(a)
(b)
(c)
(d)
(e)
CROSS SECTION, πa_0^2
SCATTERING ANGLE, deg
0.04
0.03
0.02
0.01
0
10
20
30
40
50
60
70
80

Figure 4.

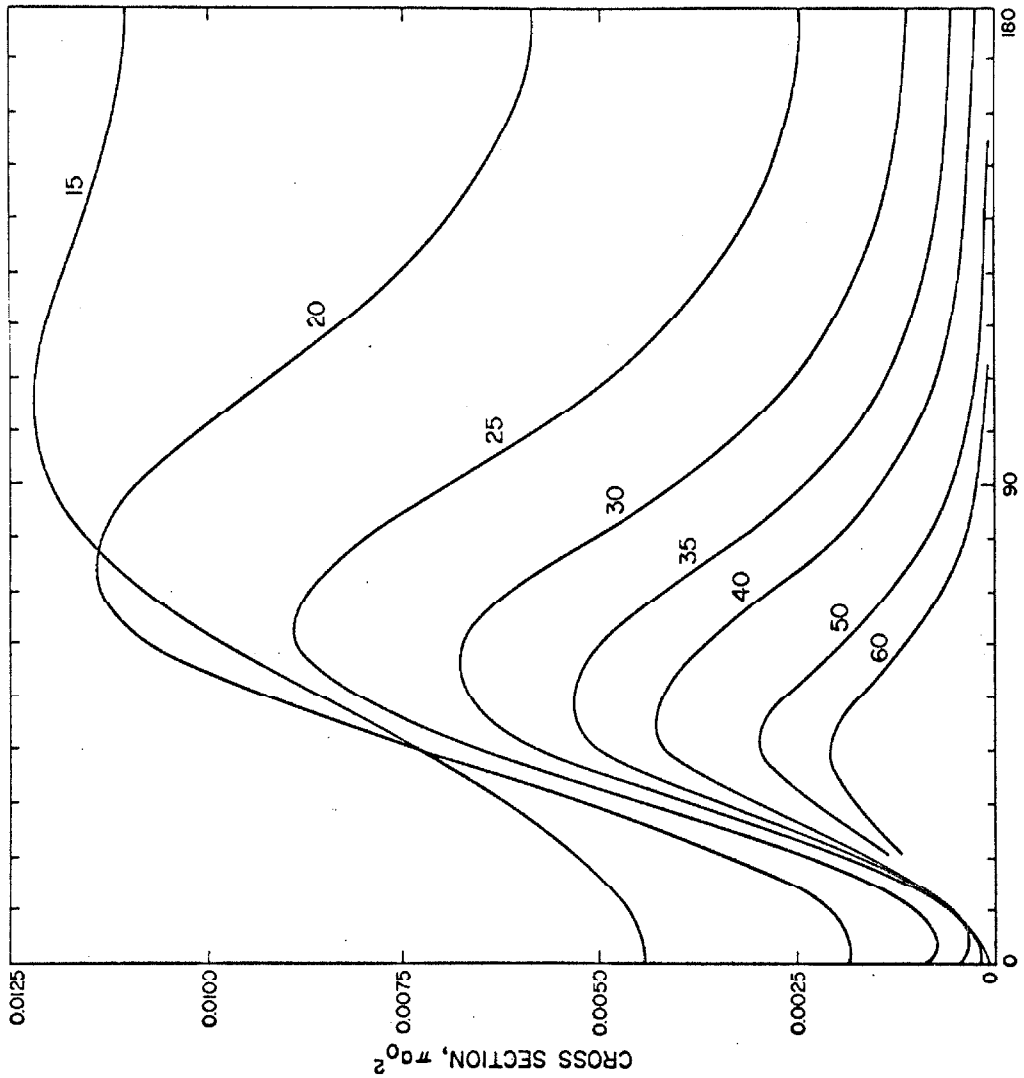
0.0125
0.0100
0.0075
0.0050
0.0025
0
CROSS SECTION, πa_0^2
0
90
180
SCATTERING ANGLE, deg
15
20
25
30
35
40
50
60

Figure 6.

CHEMICAL PHYSICS LETTERS 1 (1968) 703-705. NORTH-HOLLAND PUBLISHING COMPANY, AMSTERDAM

TRIPLET STATES OF ACETYLENE BY ELECTRON IMPACT *

S. TRAJMAR**, J. K. RICE, P. S. P. WEI*** and A. KUPPERMANN
Gates and Crellin Laboratories of Chemistry †,
California Institute of Technology, Pasadena, California 91109, *USA*

Received 18 March 1968

Low-energy electron-impact spectroscopy has revealed two previously unknown low-lying triplet states in acetylene at 5.2 eV and 6.1 eV. The basis for this identification and the disparity in the electron energy-loss and optical absorption spectra are discussed.

The triplet states of acetylene have long eluded detection [1]. A study of the electron-impact energy loss spectrum of C_2H_2 as a function of scattering angle and incident electron energy with an instrument described previously [2] has now unequivocally revealed at least two low-lying triplet states with maximum transition intensities at 5.2 eV (onset at 4.5 eV) ($\tilde{a}$) and 6.1 eV ($\tilde{b}$) (see fig. 1). This identification is based on

* Work supported in part by the U.S. Atomic Energy Commission, Report Code No. CALT-532-24.
** Jet Propulsion Laboratory; supported by the National Aeronautics and Space Administration, Contract No. NAS-7-100.

*** Present address: Bell Telephone Laboratories, Murray Hill, New Jersey 07971.
† Contribution No. 3638.

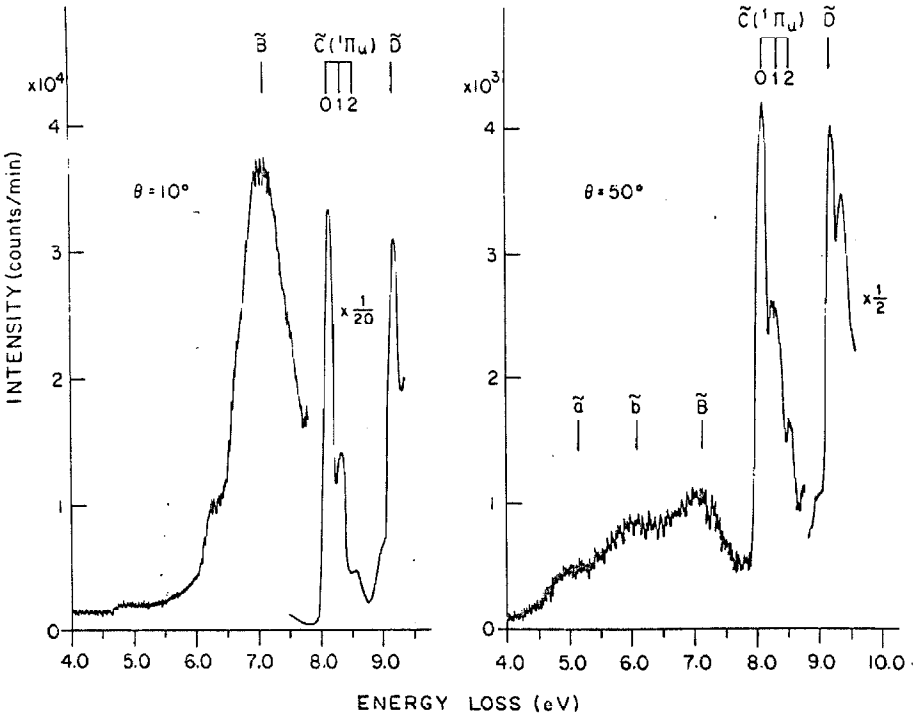

Fig. 1. Energy loss spectra of acetylene at 10° and 50° scattering angles. Pressure gauge reading 8 millitorr; impact energy 25 eV; incident electron current 1×10^{-8} A. The $\times \frac{1}{20}$ and $\times \frac{1}{2}$ are the factors by which intensities were multiplied before plotting.

rules derived from our investigation of the energy and angular dependencies of differential scattering cross sections for 10 singlet ← singlet and 9 triplet ← singlet known transitions in He [2], H_2 [3], N_2 [4], and CO [4].

Fig. 2 shows peak intensity ratios as a function of angle for the indicated states of acetylene [5]. It also illustrates one of the characteristic differences between the angular dependence of singlet/singlet and triplet/singlet intensity ratios. The latter are much steeper functions of angle than the former. Another distinguishing feature we observed is that decreasing the impact energy toward threshold enhances the triplet/singlet ratio over most of its measured angular range (0° to 80°) significantly more than any singlet/singlet ratio. The $\tilde{a}$ or $\tilde{b}$/singlet intensity ratios exhibit both of these characteristic "fingerprints" and, hence, $\tilde{a}$ and $\tilde{b}$ are identified as triplet states.

The UV absorption spectrum begins at 5.23 eV with a weak absorption ($f \sim 0.8 \times 10^{-4}$) [6] peaking at ~ 6 eV. Ingold and King [7] have shown that the upper state has A_u symmetry (trans-"bent"). Its singlet nature seems certain from the absence of Zeeman splitting [8] and several observations of Hougen and Watson [9]. The weakness of the absorption is attributed to unfavorable Franck-Condon overlap.

In this case, optical triplet ← singlet transitions are probably much weaker than even the $\tilde{A}^1A_u \leftarrow \tilde{X}^1\Sigma_g^+$ transition due to the absence of appreciable spin-orbit coupling and, as a consequence, excitation to the $\tilde{a}$ and $\tilde{b}$ states have not been observed in the optical absorption spectrum. It has been shown, however, that low-energy electron-impact is quite effective in causing triplet ← singlet transitions but that relative Franck-Condon factors are independent of incident energy and scattering angle [10] even for impact energies low enough for the Born approximation to fail. Since the optical $\tilde{A} \leftarrow \tilde{X}$ transition is 10^{-3} to 10^{-4} times as intense as an ordinary electric-dipole transition (e.g., $\tilde{C} \leftarrow \tilde{X}$) for "geometrical" reasons [7], we would expect this same relative intensity in the electron energy-loss spectrum at any scattering angle. Thus, the electron-impact differential scattering cross sections for excitation of the spin-forbidden $\tilde{a}$ and $\tilde{b}$ states are much larger than that for excitation of the spin-allowed but "Franck-Condon forbidden" $\tilde{A}$ state at scattering angles greater than 10°. For this reason transitions to the $\tilde{a}$ and $\tilde{b}$ states but not to the $\tilde{A}$ one are seen by low-energy electron scattering, whereas in optical absorption spectroscopy the reverse is

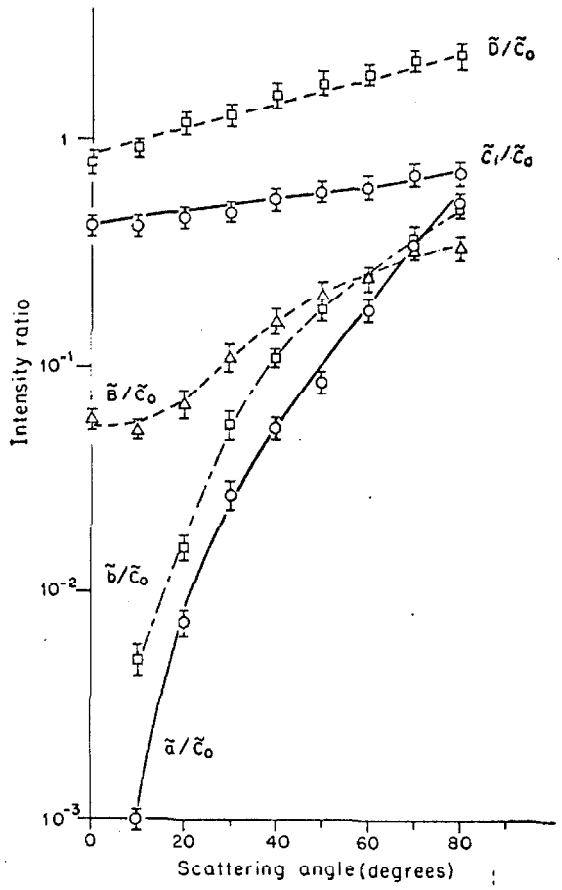

Fig. 2. Peak intensity ratios. $\tilde{C}_0$ refers to the $v=0$ vibrational level of the $\tilde{C}$ state. $\tilde{C}_1$ refers to the $v=1$ level.

true. This interpretation would predict that a careful analysis of the optical lines of the $\tilde{A}^1A_u$ state might reveal perturbations due to interaction with the triplet $\tilde{b}$ state. In addition, electron impact at incident energies above 100 eV should make transitions to $\tilde{a}$ and $\tilde{b}$ much weaker than those to $\tilde{A}$.

Bowman and Miller [11] have studied the excitation spectrum of acetylene by the trapped-electron technique. They observed a broad excitation peaking at 6.2 eV which they assigned as $\tilde{A}^1A_u \leftarrow \tilde{X}^1\Sigma_g^+$. This feature might actually be due to transitions to the $\tilde{a}$ and $\tilde{b}$ states. They also reported a transition peaking at 2.0 eV which was tentatively assigned to a low-lying triplet state. We searched carefully for a transition in that region, but found none. The sensitivity of our instrument was sufficient to have revealed features as small as 1/30 of the $\tilde{a}$ and $\tilde{b}$ peaks.

The transition peaking at 7.15 eV has been assigned by Herzberg [1] as $\tilde{B} \leftarrow \tilde{X}$ in analogy to the quadrupole allowed a $^1\Pi_g \leftarrow X^1\Sigma_g^+$ transition in N_2. An extension of this analogy suggests a possible correlation of $\tilde{a}$ and $\tilde{b}$ with the $A^3\Sigma_u^+$ and $B^3\Pi_g$ states of N_2, respectively. The location of these two triplet states should be useful in the evaluation of theoretical energy level calculations in acetylene [12-15].

References

[1] G. Herzberg, Molecular spectra and molecular structure, Vol. III, Electronic spectra and electronic structure of polyatomic molecules (D. Van Nostrand Co., New York, 1966).
[2] J. K. Rice, A. Kuppermann and S. Trajmar, J. Chem. Phys., in press.
[3] S. Trajmar, D. C. Cartwright, J. K. Rice and A. Kuppermann, 20th Annual Gaseous Electronics Conference, October, 1967.
[4] Forthcoming.
[5] See ref. 1 for identification of these states.
[6] G. W. King and C. K. Ingold, Nature 169 (1952) 1101.
[7] C. K. Ingold and G. W. King, J. Chem. Soc. 1953 (1953) 2702.
[8] A. E. Douglas, unpublished, see ref. 1, p. 517.
[9] J. T. Hougen and J. K. G. Watson, Can. J. Phys. 43 (1965) 298.
[10] A. Skerbele, M. A. Dillon and E. N. Lassettre, J. Chem. Phys. 46 (1967) 4162;
A. Skerbele, V. D. Meyer and E. N. Lassettre, ibid. 44 (1966) 4069.
[11] C. R. Bowman and W. D. Miller, J. Chem. Phys. 42 (1965) 681.
[12] I. G. Ross, Trans. Faraday Soc. 48 (1952) 973.
[13] (a) J. Serre, J. Chim. Phys. 52 (1955) 331; (b) C. R. Acad. Sci., Paris, 242 (1956) 1469.
[14] M. J. S. Dewar and N. L. Hojvat, Proc. Roy. Soc., London. A264 (1961) 431.
[15] M. Barfield, J. Chem. Phys. 47 (1967) 3831.

APPENDIX V

LIST OF VENDORS AND/OR MANUFACTURERS

Allied Electronics
2085 E. Foothill Boulevard
Pasadena, California

Assembly Products, Inc.
5770 N. Rosemead Boulevard
Temple City, California

Beckman Instruments
Helipot Division
2400 Harbor Boulevard
Fullerton, California

Carl Herman Associates Industries
1245 E. Walnut Street
Pasadena, California
Representative of Granville-Phillips, F.J. Cooke, and Hastings.

C. E. Howard Corporation
9001 Rayo Avenue
South Gate, California

Centralab
6446 Telegraph Road
Los Angeles, California

Ceramaseal Incorporated
New Lebanon Center
New York, New York

Chester Paul Company
1605 Victory Boulevard
Glendale, California
Representative of Hanson Manufacturing Company.

Dow Radio
1759 E. Colorado Boulevard
Pasadena, California

Dynamics Associates
2615 South Senta Street
Los Angeles, California

Edwards High Vacuum Corporation
6151 W. Century Boulevard
Los Angeles, California

Electronics Measurement Company
Eatontown, New Jersey

Fairchild Instrumentation
5410 West Imperial Boulevard
Los Angeles, California

Fibros Seal
Culver City, California
Representative of United Aircraft Products, Incorporated.

General Electric Company
Vacuum Products Operation
Schenectady, New York

General Radio Corporation
1000 N. Seward Street
Los Angeles, California

Hasco
8318½ W. Third Street
Los Angeles 48, California

Hewlett-Packard
Neely Sales Division
3939 Lankershim Boulevard
North Hollywood, California

Hoskins Manufacturing Company
5935 E. Sheila Street
Los Angeles, California

Industrial Tectronics, Incorporated
3686 Jackson Road
Ann Arbor, Michigan

Kenneth C. Holloway, Incorporated
135 North Halstead Avenue
Pasadena, California

Ladish Pacific Division
3321 East Slauson
Los Angeles, California

Leeds and Northrop Company
5111 Via Corona Avenue
Los Angeles, California

Metal Bellows Corporation
20977 Knapp Street
Chatsworth, California

Miniature Precision Bearings, Incorporated
Precision Park
Keene, New Hampshire

Molycote Corporation
65 Harvard Avenue
Stamford, Connecticut

Mycalex Corporation of America
125 Clifton Boulevard
Clifton, New Jersey

Nuclear Chicago
1053 West Colorado Boulevard
Los Angeles, California

Nuclear Data, Incorporated
P. O. Box 88
San Rafael, California

Nuclide Corporation
642 East College Avenue
State College, Pennsylvania

Pace Engineering Company
13035 Saticoy Street
North Hollywood, California

Parker Seal Company
10567 Jefferson Boulevard
Culver City, California

Paul Nurches Company
2396 Foothill Boulevard
Pasadena, California
Representative of Pamona Electronics and Bell.

Photocon Research
421 North Altadena Drive
Pasadena, California

PIC Design Corporation
East Rockaway, New York

Picker-Nuclear
Los Angeles, California

Princeton Applied Research Corporation
Box 565
Princeton, New Jersey

Ratron
P. O. Box 282
Northridge, California

Radio Corporation of America
Electronic Components and Devices
Lancaster, Pennsylvania

Scientific Atlanta, Incorporated
Box 13654
Atlanta, Georgia

The Carborundum Company
Electronics Division
2240 South Yates Avenue
Los Angeles, California

The Wilkinson Company
P. O. Box 303
Santa Monica, California

T. L. Snitzer Company
5354 West Pico Boulevard
Los Angeles 19, California
Representative of Keithley Instruments.

U. S. Flexible Metallic Tubing Company
454 East Third Street
Los Angeles, California

Vacuum Accessories Corporation of America
P. O. Box 134
Greenlawn, Long Island, New York

Vacuum Research Corporation
420 Market Street
San Francisco 11, California

Varian Associates
Vacuum Products Division
611 Hansen Way
Palo Alto, California

Veeco
86 Denton Avenue
New Hyde Park, Long Island, New York

V. T. Rupp Company
307 Park Avenue
Los Angeles, California
Representative of Kepco, Incorporated

W. D. Wilson
1118 Mission Street
South Pasadena, California
Representative of Swagelok, Cajon, Nupro, and Whitey.

REFERENCES

1. A. Messiah, Quantum Mechanics, Vols. I and II (John Wiley and Sons, Inc., New York, 1961): (a) p. 833; (b) p. 836; (c) p. 867; (d) p. 348.
2. The optical selection rules for atomic systems are summarized in:
   (a) G. Herzberg, Atomic Spectra and Atomic Structure (Dover Publications, New York, 1944), pp. 27-28, 50-54, 153-159.
   Those for diatomic molecules are presented in:
   (b) G. Herzberg, Spectra of Diatomic Molecules (Second Edition, D. Van Nostrand, Inc., 1950), pp. 240-280.
   Those for polyatomic molecules are discussed in:
   (c) G. Herzberg, Electronic Spectra of Polyatomic Molecules (D. Van Nostrand, Inc., 1966), pp. 128-142.
3. J. Franck and G. Hertz, Verk. dtsh. Physik Ges., 16, 457 (1914).
4. E. G. Dymond, Phys. Rev., 29, 433 (1927).
5. J. R. Oppenheimer, Phys. Rev., 32, 361 (1928).
6. H. S. W. Massey and E. H. S. Burhop, Electronic and Ionic Impact Phenomena (Clarendon Press, Oxford, 1952): (a) p. 146, (b) pp. 93-99, (c) p. 189, (d) p. 91, (e) p. 10.
7. E. W. McDaniel, Collision Phenomena in Ionized Gases (John Wiley and Sons, Inc., New York, 1964).
8. G. J. Schulz, Phys. Rev., 112, 150 (1958).

9. G. J. Schulz, (a) Phys Rev., 116, 1141 (1959); (b) 125, 229 (1962); (c) 135, A988 (1964); (d) 136, A650 (1964): (e) J. Chem. Phys., 33, 1661 (1960); (f) 34, 1778 (1961): (g) Phys. Rev. Letters, 10, 104 (1963); (h) 13, 583 (1964).

10. C. R. Bowman and W. D. Miller, J. Chem. Phys., 42, 681 (1965).

11. H. H. Brongersma and L. J. Oosterhoff, Chem. Phys. Letters, 1, 169 (1967).

12. J. T. Dowell and T. E. Sharp, J. Chem. Phys., 47, 5068 (1967).

13. R. N. Compton, R. H. Huebner, P. W. Reinhardt, and L. G. Christophorou, J. Chem. Phys., 48, 901 (1968).

14. Their early work (prior to 1959) has been reviewed by:
(a) E. N. Lassettre, Rad. Res. Supplement, 1, 530 (1959).
A later series of 10 papers appeared in 1964:
(b) E. N. Lassettre, et al., J. Chem. Phys., 40, 1208-1275 (1964).

15. S. M. Silverman and E. N. Lassettre, J. Chem. Phys., 40, 1265 (1964).

16. E. N. Lassettre and M. E. Krasnow, J. Chem. Phys., 40, 1248 (1964).

17. (a) V. D. Meyer and E. N. Lassettre, J. Chem. Phys., 44, 2535 (1966).
(b) A. Skerbele and E. N. Lassettre, J. Chem. Phys., 42, 395 (1965).

(c) E. N. Lassettre, A. Skerbele, and V. D. Meyer, J. Chem. Phys., 45, 3214 (1966).

18. K. Dressler and B. L. Lutz, Phys. Rev. Letters, 19, 1219 (1967).

19. V. Cermák, J. Chem. Phys., 44, 1318 (1966).

20. H. G. M. Heideman, C. E. Kuyatt, and G. E. Chamberlain, J. Chem. Phys., 44, 355 (1966).

21. V. D. Meyer, A. Skerbele, and E. N. Lassettre, J. Chem. Phys., 43, 805 (1965).

22. A. Skerbele, M. A. Dillion, and E. N. Lassettre, (a) J. Chem. Phys., 46, 4161 (1967); (b) 46, 4162 (1967).

23. K. J. Ross and E. N. Lassettre, J. Chem. Phys., 44, 4633 (1966).

24. J. A. Simpson, Rev. Sci. Instr., 35, 1698 (1964).

25. C. E. Kuyatt and J. A. Simpson, Rev. Sci. Instr., 38, 103 (1967).

26. J. A. Simpson and S. R. Mielczarek, J. Chem. Phys., 39, 1606 (1963).

27. G. E. Chamberlain, H. G. M. Heideman, J. A. Simpson, and C. E. Kuyatt, Fourth International Conference on the Physics of Electronic and Atomic Collisions, Abstracts (Science Book Crafters, Inc., Hastings-on-Hudson, New York (1965)), pp. 378-381.

28. C. E. Kuyatt, J. A. Simpson, and S. R. Mielczarek, Bull. Am. Phys. Soc., 9, 266 (1964).

29. H. G. M. Heideman, C. E. Kuyatt, and G. E. Chamberlain, J. Chem. Phys., 44, 355 (1966).

30. H. G. M. Heideman, C. E. Kuyatt, and G. E. Chamberlain, J. Chem. Phys., 44, 440 (1966).

31. J. A. Simpson, M. G. Menendez, and S. R. Mielczarek, Phys. Rev., 150, 76 (1966).

32. L. Vriens, J. A. Simpson, and S. R. Mielczarek, Phys. Rev., 165, 7 (1968).

33. A recent study containing references to their earlier work is: F. M. J. Pichanick and J. A. Simpson, Phys. Rev., 168, 64 (1968).

34. Refer to section 4.1 of this thesis.

35. (a) A. Kuppermann and L. Raff, J. Chem. Phys., 37, 2497 (1962).

(b) A. Kuppermann and L. Raff, Disc. Farad. Soc., 35, 30 (1963),

(c) A. Kuppermann and L. Raff, J. Chem. Phys., 39, 1067 (1963).

36. (a) J. P. Doering, J. Chem. Phys., 45, 1065 (1966).

(b) J. P. Doering, J. Chem. Phys., 46, 1194 (1967).

(c) J. P. Doering and A. J. Williams, IV, J. Chem. Phys., 47, 4180 (1967).

37. (a) D. Andrick and H. Ehrhardt, Z. Phys., 192, 99 (1966).

(b) H. Ehrhardt and K. Willmann, Z. Phys., 203, 1 (1967).

(c) H. Ehrhardt and K. Willmann, Z. Phys., 204, 462 (1967).

38. J. Geiger, Z. Phys., 180, 415 (1964).

39. J. Geiger and W. Stickel, J. Chem. Phys., 43, 4535 (1965).

40. J. Geiger and K. Wittmaack, Z. Naturforsch, 20A, 628 (1965).

41. A discrepancy between the optical data of R. E. Huffman, Y. Tanaka, and J. C. Larrabee [J. Chem. Phys., 39, 910 (1963)] and the electron impact data of E. N. Lassettre, F. M. Glaser, V. D. Meyer, and A. Skerbele [J. Chem. Phys., 42, 3429 (1965)]; V. D. Meyer, A. Skerbele, and E. N. Lassettre [J. Chem. Phys., 43, 3769 (1965)]; Lassettre, et al.[17c]; and Geiger and Stickel[39] had been noted in the relative intensities of the $X^1\Sigma_g^+$ ($\nu = 0$)→ $b^1\Pi_u(\nu' = 2)$ and $b^1\Pi_u(\nu' = 3)$ transitions in N_2. However, this anomaly has been resolved by the recent optical work of G. M. Lawrence, D. L. Mickey, and K. Dressler [J. Chem. Phys., 48, 1989 (1968)].

42. D. R. Bates, A. Fundaminsky, J. W. Leech, and H. S. W. Massey, Trans. Roy. Soc., A243, 93 (1950).

43. J. D. Jobe and R. M. St. John, Phys. Rev., 164, 117 (1967).

44. N. F. Mott and H. S. W. Massey, The Theory of Atomic Collisions (Clarendon Press, Oxford (1965)): (a) p. 421, (b) p. 463, (c) pp. 19-28, (d) p. 420, (e) p. 28, (f) Chp. I § 7, etc., (g) p. 593, pp. 571-573.

45. T. Y. Wu and T. Ohmura, Quantum Theory of Scattering (Prentice Hall, Inc., New Jersey (1962)).

46. M. L. Goldberger and K. M. Watson, Collision Theory (John Wiley and Sons, Inc., New York (1964)).

47. L. J. Kieffer, "Bibliography of Low Energy Electron Collision Cross Section Data," National Bureau of Standards Miscellaneous Publication 289, March 10, 1967.

48. We have ignored the explicit consideration of nuclear spin since low-energy electrons are not effective in causing nuclear spin "flips." However, it is important to note that the nuclear spin state of homonuclear diatomic molecules (such as H_2) may affect the excitation probability of certain rotational levels.

49. L. Pauling and E. B. Wilson, Introduction to Quantum Mechanics (McGraw-Hill Book Company, Inc., New York 1935): (a) Chpt. VIII, (b) p. 210, (c) p. 138.

50. It has been pointed out be F. S. Levin, Phys. Rev, 140, B1099 (1965) that the expansion (3-15) and asymptotic form (3-12) do not correctly define the scattering amplitude which determines the cross section of equation (3-13). This can be seen by considering the projection $\langle \underset{\sim}{\psi_0} \mid \Psi_I \rangle$ as $r \to \infty$. This quantity should yield only $\underset{\sim}{G_0}$ in the limit. However, the continuum states of the target will also contribute. The same is true for all inelastic channels. In all practical applications, the expansion (3-15) is truncated before the inclusion of continuum states is necessary and this problem does not arise.

51. P. G. Burke, S. Ormande, and W. Whitaker, Phys. Rev. Letters, 17, 800 (1966); Proc. Phys. Soc. (London), 92, 319 (1967).

52. P. G. Burke, J. W. Cooper, and S. Ormande, Phys. Rev. Letters, 17, 345 (1966).

53. B. L. Moiseiwitsch and S. J. Smith, Rev. Mod. Phys., 40, 238 (1968).

54. S. Khashaba and H. S. W. Massey, Proc. Phys. Soc. (London), 71, 574 (1958).

55. (a) H. S. W. Massey and B. L. Moiseiwitsch, Proc. Roy. Soc. (London) 227, 38 (1954); (b) 258, 147 (1960).

56. The usual Born approximation becomes the Born-Oppenheimer one for indistinguishable particles. This was first pointed out in reference (5).

57. D. G. Truhlar, D. C. Cartwright, and A. Kupperman, Phys. Rev. 1968 (in press).

58. (a) V. I. Ochkur, Soviet Physics - JETP 18, 503 (1964) {Zh. Eksperim. i Teor. Fiz. 45, 734 (1963)}
(b) V. I. Ochkur and V. F. Bratsev, Opt. Spectry. USSR, 19, 274 (1965). {Opt. i Spectroskopiya, 19, 490 (1965b).}
(c) V. I. Ochkur and V. F. Bratsev, Soviet Astron. A J 9, 797 (1966). {Astron. Zh., 42, 1035 (1965a).}

59. R. A. Bonham, J. Chem. Phys., 36, 3260 (1962).

60. H. Bethe, Ann. der Physik, 5, 325 (1930).

61. M. Born and J. R. Oppenheimer, Ann. der Physik, 84, 457 (1927).

62. M. R. H. Rudge, Proc. Phys. Soc., 85, 607 (1965); 86, 763 (1965).

63. Y. N. Demkov, Variational Principles in the Theory of Collisions (Pergamon Press, London, 1963), pp. 97-102.

64. O. Bely, Il Nuovo Cimento, 49, 66 (1967).

65. L. D. Landau and E. M. Lifshitz, Quantum Mechanics, second edition (Pergamon Press, Oxford, 1965), (a) p. 553, (b) p. 411.

66. D. C. Cartwright, Ph.D. Thesis, California Institute of Technology, 1967.

67. K. J. Miller and M. Krauss, J. Chem. Phys., 48, 2611 (1968).

68. S. Trajmar, D. C. Cartwright, J. K. Rice, R. T. Brinkman, and A. Kuppermann, J. Chem. Phys. 1968 (in press). A copy of this paper can be found in Appendix III.

69. S. P. Khare [Phys. Rev. 149, 33 (1966)] has calculated the DCS for excitation of the B and C states of H_2 at 25 KeV incident energy including exchange. However, the effect of exchange is negligible at this incident energy.

70. K. L. Bell, H. Eissa, and B. L. Moiseiwitsch, Proc. Phys. Soc. (London), 88, 57 (1966).

71. D. J. T. Morrison and M. R. H. Rudge, Proc. Phys. Soc. (London), 91, 565 (1967).

72. A theoretical discussion of the applicability of the Born approximation has been presented by H. S. W. Massey [Rev. Mod. Phys., 28, 199 (1956)] while an experimental

test was carried out by S. M. Silverman and E. N. Lassettre [J. Chem. Phys., 40, 1242 (1964)].

73. H. G. M. Heideman and L. Vriens, J. Chem. Phys., 46, 2911 (1967).

74. H. B. Dwight, Tables of Integrals and Other Mathematical Data, (The Macmillan Company, New York (1961)): (a) p. 132, (b) p. 235.

75. Reference (2b), p. 18.

76. D. C. Cartwright and A. Kuppermann, Phys. Rev., 163, 86 (1967).

77. Reference (2b), p. 200.

78. Reference (2b), p. 203.

79. Reference (2b), p. 193.

80. Reference (2c), p. 629.

81. A. Streitwieser, Molecular Orbital Theory for Organic Chemists (John Wiley and Sons, Inc., New York, 1961): (a) p. 207, (b) p. 33, (c) p. 165, (d) p. 10, (e) p. 16.

82. C. Reid, J. Chem. Phys., 18, 1299 (1950).

83. D. F. Evans, J. Chem. Soc., 1735 (1960).

84. See references (10), (35a), (36c), and this research section 5.7.

85. R. S. Mulliken, J. Chem. Phys., 3, 375 (1935).

86. J. D. Roberts, Molecular Orbital Calculations (W. A. Benjamin, Inc., New York, 1962), p. 42.

87. H. H. Brongersma, Ph.D. Thesis, FOM - Institute for Atomic and Molecular Physics, Amsterdam, 1968.

88. I. C. Percival and M. J. Seaton, Proc. Cambridge, Phil. Soc., 53, 654 (1957).

89. H. Wayland, Differential Equations Applied in Science and Engineering (D. Van Nostrand Company, Inc., Princeton, 1957), p. 199.

90. For example, see reference (31) and this research, sections 5.2-5.7.

91. Compare the angular distributions of reference (32) with those of (31). This effect has been noted in this research, sections 5.2-5.7.

92. (a) A computer program for the calculation of these symbols is available from: R. S. Gaswell and L. C. Maximon, "Fortran Programs for the Calculation of Wigner 3_j, 6_j, and 9_j Coefficients for Angular Momenta $\leq$ 80" NBS Technical note 409, November 15, 1966, Superintendent of Documents, Government Printing Office, Washington, D. C. 20402 (40 cents).

(b) A compilation of these symbols for angular momenta ≤ 8 is given by M. Rotenberg, R. Bivans, N. Metropolis, and J. K. Wooten, Jr., The 3_j and 6_j Symbols (Technology Press, Cambridge, 1959).

93. P. S. Hoeper, W. Franzer, and R. Grysta, Phys. Rev., 168, 50 (1968).

94. R. B. Leighton, Principles of Modern Physics (McGraw-Hill Book Company, Inc., New York, 1959), (a) p. 356, (b) pp. 350 ff.

95. W. B. Nottingham, Phys. Rev., 55, 203 (1939).

96. H. Boersch, J. Geiger, and H. Hellwig, Physics Letters, 3, 64 (1962).

97. W. Legler, Z. Physik, 171, 424 (1963).

98. S. N. Foner and B. H. Nall, Phys. Rev., 122, 512 (1961).

99. E. M. Clarke, Can. J. Phys., 32, 764 (1954).

100. A. Ll. Hughes and J. H. McMillen, Phys. Rev., 34, 291 (1929).

101. P. Marmet and L. Kerwin, Can J. Phys., 38, 787 (1960).

102. E. M. Purcell, Phys. Rev., 54, 818 (1938).

103. K. R. Spangenberg, Vacuum Tubes (McGraw-Hill Book Company, Inc., New York, 1948).
(a) This effect is discussed in chapter 8, (b) Chapt. 4.

104. J. R. Pierce, Theory and Design of Electron Beams, Second ed. (D. Van Nostrand Book Co., New York, 1934) (a) Chapt. 9, (b) Chapt. 8.

105. K. Spangenberg and L. M. Field, Elec. Comm., 21, 194 (1943).

106. J. A. Simpson and C. E. Kuyatt, J. of Res. of NBS, 67C, 279 (1963).

107. J. A. Simpson and C. E. Kuyatt, Rev. Sci. Instr., 34, 265 (1963).

108. E. A. Soa, Jenaer Jahrbuch, 1, 115 (1959).

109. D. B. Langmuir, Proc. IRE, 25, 977 (1937).

110. C. E. Kuyatt, Lectures at the National Bureau of Standards, Washington, D. C. (April-May, 1967).

111. See, for example, reference (94), p. 409.

112. E. R. Peck, Electricity and Magnetism (McGraw-Hill Book Company, Inc., New York, 1953), pp. 441-442. We have used formulae 12.102 and 12.109 and have assumed a total power of 50,000 watts emanating from a transmitter located about $2\frac{1}{2}$ kilometers from the apparatus.

113. M. Pirani and J. Yarwood, Principles of Vacuum Engineering (Chapman and Hall, London, 1961), Chapter 1.

114. C. Kittel, Introduction to Solid State Physics, Second ed. (John Wiley and Sons, Inc., New York, 1956), Chpt. 10.

115. W. B. Nottingham, Phys. Rev., 49, 78 (1936).

116. A. R. Hutson, Phys. Rev., 98, 889 (1955).

117. G. G. Belford, A. Kuppermann, and T. E. Phipps, Phys. Rev., 128, 524 (1962).

118. J. A. Simpson and C. E. Kuyatt, J. Appl. Phys., 37, 3805 (1966).

119. See for example, W. Hume-Rothery, The Metallic State (The Clarendon Press, Oxford, 1931), pp. 148-157.

120. See for example, J. A. Simpson and U. Fano, Phys. Rev. Letters, 11, 158 (1963).

121. G. E. Chamberlain, J. A. Simpson, S. R. Mielczarek, and C. E. Kuyatt, J. Chem. Phys., 47, 4266 (1967).

122. For example, the DCS for elastic scattering varies as q^{-4}, while that for optically dipole-allowed transitions varies as q^{-14} for large q^2 ($q^2 = k_o^2 + k_n^2 - 2k_o k_n \cos\theta$, see section 3 for the definitions of k_o and k_n). Refer to E. N. Lassettre [J. Chem. Phys., 43, 4479 (1965)] for a further discussion of this "Born approximation" behavior.

123. This phenomenon is adequately discussed in references (124) through (126) and will not be reiterated here.

124. E. B. Jordan and R. B. Brode, Phys. Rev., 43, 112 (1933).

125. C. L. Critchfield and D. C. Dodder, Phys. Rev., 75, 419 (1949).

126. R. J. Carbone, E. N. Fuls, and E. Everhart, Phys. Rev., 102, 1524 (1956).

127. R. T. Brinkman, private communication.

128. A detailed discussion of this approximation is given by J. D. Craggs and H. S. W. Massey, Handbuch der Physik, ed. by S. Flügge (Springer-Verlag, Berlin, 1959), Vol. 37, p. 314.

129. For example, refer to the work of Lassettre and coworkers[14,15] and Simpson[26,28].

130. For example, refer to the work of Doering[36] and Kuppermann[35].

131. S. M. Silverman and E. N. Lassettre, J. Chem. Phys., 44, 2219 (1966).

132. C. E. Moore, "Atomic Energy Levels," Vol. 1, National Bureau of Standards, Circular No. 467 (U. S. Government Printing Office, 1949), p. 4.

133. J. Todd, Survey of Numerical Analysis (McGraw-Hill Book Company, Inc., New York, 1962), p. 48.

134. This decrease can be understood from the data of reference (43) which show that the total cross section for excitation of the 2^3P state is lower at 26 eV than at 34 eV.

135. G. E. Chamberlain and H. G. M. Heideman, Phys. Rev. Letters, 15 (1965).

136. F. R. Gilmore, J. Quant. Spectr. Rad. Transfer, 5, 369 (1965).

137. W. Benesch, J. T. Vanderslice, S. G. Tilford, and P. G. Wilkinson, Astrophys. J., 143, 236 (1966).

138. Y. Tanaka, M. Ogawa, and A. S. Jursa, J. Chem. Phys., 40, 3690 (1964).

139. Such a comparison can be found in reference (17c).

140. K. Takayanagi and T. Takahashi, Report of Ionosphere and Space Research in Japan, 20, 357 (1966).

141. P. H. Krupenie, "The Band Spectrum of Carbon Monoxide," NBS reference data series, US NBS, 5, 1 (1966).

142. E. N. Lassettre, A. S. Berman, S. M. Silverman, and M. E. Krasnow, J. Chem. Phys., 40, 1232 (1964).

143. E. N. Lassettre and S. M. Silverman, J. Chem. Phys., 40, 1256 (1964).

144. S. M. Silverman and E.N. Lassettre, J. Chem. Phys., 41, 3727 (1964).

145. A. Skerbele, V. D. Meyer, and E. N. Lassettre, J. Chem. Phys., 44, 4069 (1966).

146. R. W. Nicholls, J. Quant. Spectry. and Radiative Transfer, 2, 433 (1962).

147. E. N. Lassettre and S. A. Francis, J. Chem. Phys., 40, 1208 (1964).

148. E. N. Lassettre and E. A. Jones, J. Chem. Phys., 40, 1222 (1964).

149. G. J. Schulz, Phys. Rev., 112, 150 (1958).

150. C. E. Kuyatt, S. R. Mielczarek, and J. A. Simpson, Phys. Rev. Letters, 12, 293 (1964).

151. J. Geiger, Z. Physik, 181, 413 (1964).

152. E. Hutchisson, Phys. Rev., 37, 45 (1931).

153. The discrepancies between relative intensitites observed via electron impact and those observed optically have been used to propose the existence of a forbidden transition in ethylene by Ross and Lassettre[23].

154. G. H. Dieke, J. Mol. Spectry., 2, 494 (1958).

155. Reference (9a). Note that the $A^3\Sigma_u^+$, $a^1\Pi_g$ and $C^3\Pi_u$ state assignments in figure 5 of this reference are incorrect as pointed out by Brongersma and Oosterhoff[11].

156. C. K. Ingold and G. W. King, J. Chem. Soc., 1953, 2702 (1953).

157. This point is discussed by Dowell and Sharp[12].

158. T. Nakayama and K. Watanabe, J. Chem. Phys., 40, 558 (1964). (1050 Å to 2000 Å.)

159. As in the previous cases, $C^{DD}_{\nu\nu 0}$ changes too slowly with angle to account for this ratio behavior. At $E_0 = 25$ eV, $C^{DD}_{10}(\theta = 0°) \cong .95$ while $C^{DD}_{10}(\theta = 70°) \cong 1.00$.

160. Reference (2c), p. 516.

161. Reference (2c), p. 26.

162. Reference (2b), p. 337.

163. References (12) through (15) of C_2H_2 preprint, also R. J. Buenker and S. D. Peyerimhoff., J. Chem. Phys., 48, 354 (1968).

164. W. C. Price, Phys. Rev., 47, 44 (1934). (1050 - 1520 Å.)

165. P. G. Wilkinson, J. Mol. Spec., 2, 387 (1958). (1280 - 1520 Å.)

166. P. G. Wilkinson, Can. J. Phys., 34, 643 (1956).

167. T. H. Dunning and V. McKoy, J. Chem. Phys., 47, 1735 (1967).

168. A. Lubezky and R. Kopelman, J. Chem. Phys., 45, 2526 (1966).

169. A summary of this work has been presented by P. G. Wilkinson and R. S. Mulliken, J. Chem. Phys., 23, 1895 (1955).

170. R. S. Mulliken, J. Chem. Phys., 33, 1596 (1960).

171. First observed in liquid ethylene by Reid[82] and then later by Evans[83] in ethylene-oxygen mixtures.

172. Reference (2c), p. 533 and p. 629.

173. W. C. Price and W. T. Tutte, Proc. Roy. Soc., 174A, 207 (1940).

174. M. Zelikoff and K. Watanabe, J. Opt. Soc. Amer., 43, 756 (1953).

175. Except, of course, for the N → T transition, which is spin-forbidden, and the N → V one which is masked by the much stronger N → R transition.

176. Ross and Lassettre[23] suggest a ^1A_g assignment for this state. However, M. Yaris, A. Moscowitz, and R. S. Berry, "On the Low-Lying Excited States of Mono-Olefins," (to be published) present plausible arguments for the $^1B_{1g}$ designation.

177. A low-lying "singlet → singlet transition" at 6.5 eV was reported by Kuppermann and Raff[35]. Since this feature has not been observed by any other investigator (not even by P. S. Wei [Ph.D. Thesis, California Institute of Technology, 1967] on an improved version of the Kuppermann-Raff apparatus), it is considered a spurious result.

178. This ratio was measured from the lower resolution (FWHM ≈ 0.1 eV) spectrum of reference (26).

179. Ross and Lassettre[23] did note the qualitative agreement, i.e., the intensity at 7.45 eV was greater than at 7.28 eV in the work by Simpson[26]. The discussion of the expected energy dependence given in reference (23) will not be repeated here.

180. Recall that for N_2, the X → $E^3\Sigma_g^+$ and X → $^1\Sigma_g^+$ transitions were observed at relatively high impact energies and $\theta \approx 0°$, leading Lassettre (see section 5.3) to an erroneous

assignment of the E state. A similar situation may exist in this case.

181. M. B. Robin, R. R. Hart, and N. A. Kuebler, J. Chem. Phys., 44, 1803 (1966).

PROPOSITION I

An infrared absorption experiment is proposed to measure directly transitions between the translational energy levels of H_2 molecules dissolved in liquid rare gases. The selection rules for such transitions are derived assuming isotropic harmonic oscillator wave functions and a quadrupole-induced dipole interaction potential.

The induced infrared absorption spectra of H_2 in the liquid and solid state[1], foreign gas mixtures[2], and solutions[3-5] have exhibited broad absorption features ($\nu_{\frac{1}{2}} \sim 100\ cm^{-1}$) on the high and low energy side of the fundamental vibrational absorption line, Q_Q. These absorptions, Q_R and Q_P, had been attributed to summation and difference tones, $\nu_0 \pm \nu_\kappa$, where ν_0 is the vibration frequency of the hydrogen molecule and $h\nu_\kappa$ is the continuum of kinetic energies of the relative motion of the absorbing molecule and its nearest neighbors[1].

Recently Ewing and Trajmar[4] have assigned the Q_R and Q_P features in the induced infrared absorption spectra of H_2 and D_2 in liquid argon to vibration-translation combination bands involving changes in the quantized translational energy levels of H_2 (or D_2) in solution. If the vibrational and translational quantum numbers are v and n, respectively; Q_P arises from the transition $v' = 1,\ n' = 0 \leftarrow v'' = 0,\ n'' = 1$; Q_Q from $v' = 1,\ n' = 0 \leftarrow v'' = 0,\ n'' = 0$; and Q_R from $v' = 1,\ n' = 1 \leftarrow v'' = 0,\ n'' = 0$ (there is no change in the rotational quantum number). Assuming a cell model of the liquid state and

that the potential interaction of the solute (H_2 or D_2) with its solvent cage is $V = \frac{1}{2}kr^2$ (isotropic harmonic oscillator) where r is the displacement of H_2 from the center of the cage and k is the interaction force constant, they predict

$$[\nu_{Q_R} - \nu_{Q_Q}]_{H_2} = \sqrt{2}\,[\nu_{Q_R} - \nu_{Q_Q}]_{D_2} . \qquad (1)$$

Their experimental results agree with this interpretation.

Rather than attempt to characterize the translational energy levels available to H_2 (or D_2) in solution from the vibrational-rotational spectra, an experiment is proposed to observe directly, in the far-infrared ($\nu \geq 50\ cm^{-1}$), transitions between these translational levels for H_2 molecules in their ground electronic, vibrational, and rotational states. This information would be of use in determining intermolecular potentials and in understanding the quantum effects which influence the thermodynamics of these systems[6,7].

The selection rules for translational transitions are determined by the dipole matrix elements

$$\langle \mu_i \rangle \equiv \langle \psi^*_{N'} | \mu_i | \psi_{N''} \rangle \quad . \qquad (2)$$

μ_i is the component of the induced dipole moment function μ along the i^{th} coordinate axis (x, y, or z) and the ψ_N are assumed to be isotropic harmonic oscillator wave functions[8].

$$\psi_N = \Phi_{n\ell}(r)\, Y_{\ell m}(\theta, \varphi) \tag{3}$$

where

$$\Phi_{n\ell} = N_{n\ell}\, L_p^{\alpha}(\rho^2)\, \rho^{\ell}\, e^{-\rho^2/2} \quad ,$$

$$p = \tfrac{1}{2}(n - \ell) \; , \; \alpha = \ell + \tfrac{1}{2},$$

$$\rho = \left[\frac{4\pi^2 M k}{h^2}\right]^{\frac{1}{4}} r \quad ,$$

$L_p^{\alpha}(\rho^2)$ is the associated Laguerre polynomial, $Y_{\ell m}$ is the spherical harmonic, $N_{n\ell}$ is a normalization constant, and M is the mass of H_2. If we assume that the dipole moment induced in the rare gas system is due to the effect on the rare gas of the permanent quadrupole moment of H_2, then

$$\mu(R) \cong \frac{K}{R^4} \quad .^{(9)} \tag{4}$$

R is the distance separating H_2 and the nearest solvent molecule and K is a constant depending on the solvent but independent of H_2 orientation. To calculate the total induced dipole of this solute-solvent interaction, we must average (4) over the cell (refer to figure 1).

Consider an H_2 molecule displaced a distance r from the center of a spherical cage of radius a. The S nearest neighbor solvent molecules are assumed to be uniformly distributed

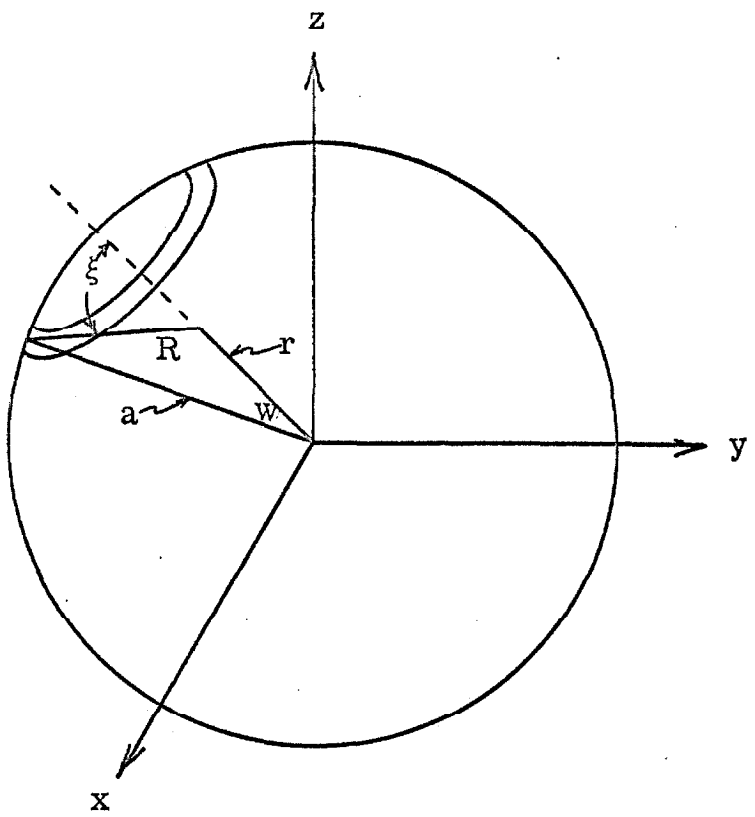

Figure 1. Coordinate system used for the calculation of the selection rules.

over the cavity wall. The dipole induced along R due to the fraction of molecules in the ring of area $2\pi a^2 \sin w\, dw$ is

$$d\mu_R = \frac{SK}{4\pi a^2}\left[\frac{2\pi a^2 \sin w\, dw}{R^4}\right] . \tag{5}$$

The moment induced along r by these molecules is

$$d\mu_r = \cos\xi\, d\mu_R . \tag{6}$$

Then, the total dipole moment induced along r by all of the surrounding molecules is

$$\mu_r = \frac{SK}{2}\int_{w=0}^{\pi} \frac{\cos\xi \sin w}{R^4}\, dw . \tag{7}$$

Changing variables and performing the integration over R yields

$$\mu_r = \frac{2\,SK}{3\,a^5}\left[\frac{r}{(1 - r^2/a^2)^2}\right] . \tag{8}$$

The component of μ_r along a space fixed coordinate axis (μ_i of equation (2)) is

$$\mu_i = \alpha_i(\theta, \varphi)\, \mu_r(r) \tag{9}$$

where α_i is the i^{th} direction cosine of the coordinate system.

The induced dipole matrix elements for transitions from the ground translational state $n'' = m'' = \ell'' = 0$ are

$$\langle \mu_i \rangle = \langle \Phi^*_{n'\ell'} \mu_r \Phi_{oo} \rangle \langle Y_{\ell'm'} \alpha_i(\theta,\varphi) Y_{oo} \rangle \quad . \qquad (10)$$

The "r" integral is in general non-zero, but the "θ,φ" one is zero unless $\ell' = 1$. This can only occur for $n' = 1, 3, 5$, etc.[8]. Translational transitions of $n'' = 0 \rightarrow n' = 2, 4, 6$, etc. are forbidden.

It is suggested that the initial experiments be done with H_2 dissolved in liquid argon to compare with experimental work already done[4]. It would then be of interest to examine heavier (Kr, Xe) and lighter solvents (Ne, He). In the argon systems the experimentally observed ($\nu_{Q_R} - \nu_{Q_Q}$) which have been assigned to the $n'' = 1 \leftarrow n' = 0$ transition are on the order of 100 cm^{-1}. To cover the desired spectral region (50 cm^{-1} to 1000 cm^{-1}) there are commercial instruments available[10]. A block diagram of a possible arrangement is shown in Figure 2. The entire optical path, except for the sample itself, should be kept under high vacuum to eliminate water vapor, which absorbs strongly in the far-infrared. Diamond is a good transparent window material in this region and, if 1 to 2 mm thick, has the required mechanical strength to hold a vacuum. All windows, mirrors, and gratings should be coated with a material such as turpentine soot to decrease the transmission of visible and near-infrared light. A convenient cell length for the study of vibrational-rotational transitions in dilute solutions of liquid H_2 was 0.5 meters[4]. Since the magnitude of the induced dipole allowing the pure translational transitions is not known, it is difficult to

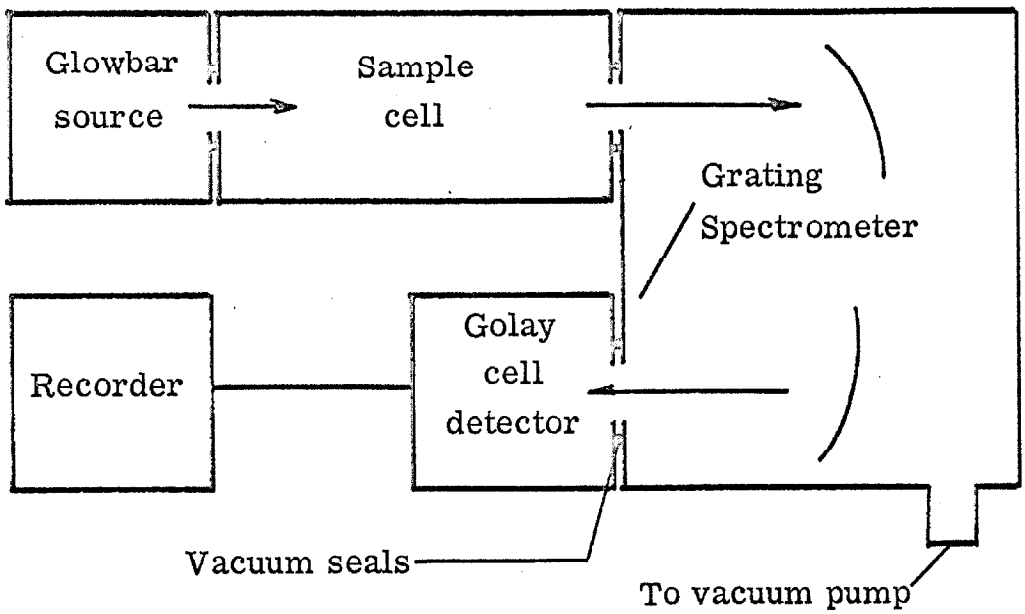

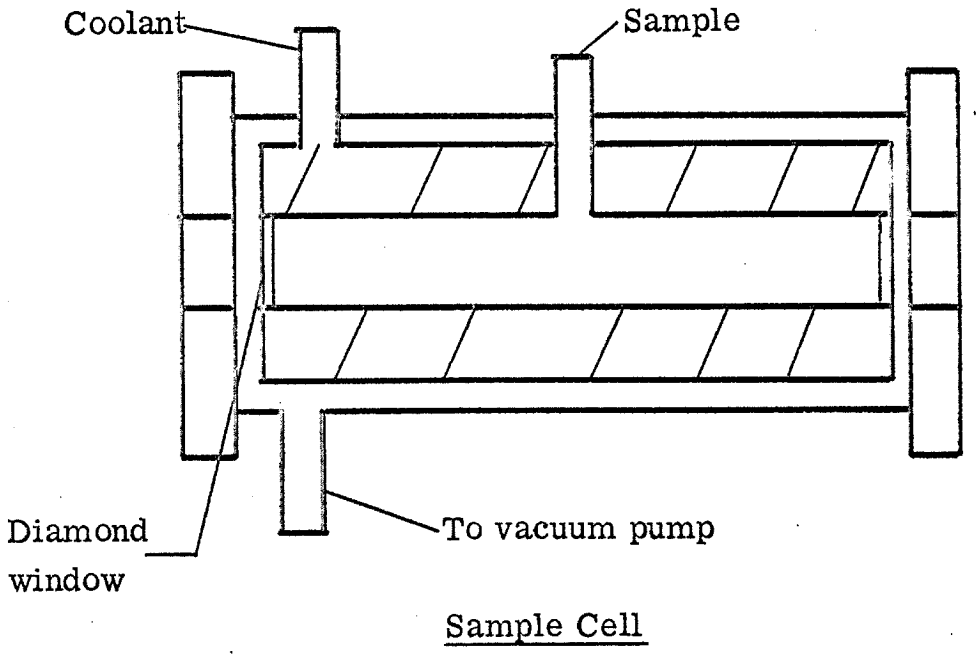

Figure 2. Experimental arrangement.

estimate the required cell length. Assuming an intensity 1/10 of that in the vibration-translation combination bands, a cell of approximately 5 meters is required. The cell dimensions could be reduced with no decrease in optical path length by using gold mirrors at each end of the cell for multiple reflections.

Since this proposition was first advanced, H_2 vibration-translation combination bands have been observed in liquid neon[11] and rotation-translation combination bands have been seen in liquid argon[12]. Because of the complications introduced by the attendent vibrational or rotational transitions, these further studies[11, 12] point out the desirability of direct observation of the translational transitions.

REFERENCES

1. H. P. Gush, W. F. J. Hare, E. T. Allin, and H. L. Welsh, Can. J. Phys., 38, 176 (1960).
2. D. A. Chisholm and H. L. Welsh, Can. J. Phys., 32, 291 (1954).
3. M. O. Bulanin and N. D. Orlova, Opt. Specty., 11, 298 (1961).
4. G. E. Ewing and S. Trajmar, J. Chem. Phys., 41, 814 (1964).
5. H. Vu, M. R. Atwood, and E. Staude, Compt. Rend., 257, 1771 (1963).
6. H. Volk and G. Halsey, J. Chem. Phys., 33, 1132 (1960).
7. M. Simon, Physica, 29, 1079 (1963).
8. J. Powell and B. Crasemann, Quantum Mechanics (Addison-Wesley Publishing Co., Inc., Reading, Mass., 1961).
9. J. Van Kranendonk, Physica, 17, 968 (1951).
10. R. A. Smith, F. E. Jones, and R. P. Chasman, The Detection and Measurement of Infrared Radiation (Oxford University Press, London, 1957).
11. G. E. Ewing and S. Trajmar, J. Chem. Phys., 42, 4038 (1965).
12. G. W. Holleman and G. E. Ewing, J. Chem. Phys., 47, 571 (1967).

PROPOSITION II

It is proposed that the techniques of low-energy, variable angle, high-resolution electron impact spectrometry be applied to the investigation of the polarization of light emitted from helium atoms excited via electron-impact at incident energies near threshold. One possible experimental arrangement is suggested and the expected signal level is calculated.

In 1926 Skinner[1] observed that various lines emitted when an electron beam struck a low-pressure mercury sample were polarized parallel or perpendicular with respect to the beam. Subsequently, Skinner and Appleyard[2] investigated the variation of this polarization with electron velocity in mercury. In this study and later ones on helium[3,4] the observed percent polarization at 90° (P) with respect to the electron beam had a value close to zero at or just above the threshold energy for the excitation and rose to a maximum value at higher energy[5].

$$P = 100\,(I^{\parallel} - I^{\perp})/(I^{\parallel} + I^{\perp}) \qquad (1)$$

$I^{\parallel}$ and $I^{\perp}$ are the emitted light intensities at 90° polarized parallel and perpendicular to the beam axis, respectively. In the case of D states of helium, the rise to maximum takes place within the energy spread of the electron beams used, about 1 eV. Theoretical investigations, however, predicted that polarizations in many cases should be as high as 100% at threshold[6]. Recently, McFarland[7] has attributed the failure of experimental verification of theory to

radially directed electrons elastically scattered from the electron beam. In his refined experiments, the electron energy resolution was about 0.1 eV and the threshold polarization measurements approached the theoretically expected magnitudes.

It is proposed that the techniques of low-energy, variable angle, high-resolution electron impact spectrometry be applied to the measurements of polarization effects near threshold in helium. High resolution ($\Delta E = \pm$ 0.03 eV) is quite important near threshold as evidenced by the calculated variation in polarization with energy of Lyman-alpha due to collisional 1s → 2p transitions in H[5]. As the energy of the electron beam approaches threshold from above, the polarization P dips sharply at about 0.1 eV above threshold and then rises to about 45% at threshold. In other cases, the percent polarization is theoretically predicted to be a maximum at threshold and a sharply decreasing function of beam energy a little above threshold (for example He $3^1D \rightarrow {}^1P$)[6]. These low energy dips were not observed in the earlier work of McFarland and Soltysik[4] due to poor electron energy resolution.

To help determine if high-resolution variable angle investigations are feasible, the expected signal intensities will be computed. Assume a simple three energy level system; an initial level "a" (usually the ground state), an upper level "b" populated by electron collision, and a final level "c" reached after photon emission. If Q_{ab} is the total cross-section for electron-impact excitation of level b; N_e and N_a are the number densities of the electron beam and

the particles in state a, respectively; and v_e is the velocity of the electron beam, the transition rate from a to b equals $v_e N_e N_a Q_{ab}$. Assuming that the only method of deexcitation of state b is through spontaneous photon emission (note that this assumption ignores stimulated emission, cascade effects, and collisional energy transfer in the gas) and equating the rate of excitation to the rate of emission imply that the total number of photons emitted per cc per sec (I_T) equals $v_e N_e N_a Q_{ab}$. If i and A are the electron beam current (electrons/sec) and cross-sectional area, respectively, the number of photons originating in a volume V emitted into a given solid angle $S(\theta, \varphi)$ per second is

$$I_p(\theta, \varphi) = \frac{i N_a V Q_{ab}}{A} S \frac{3(100 - P\cos^2\theta)}{4\pi (300 - P)} , \qquad (2)$$

and

$$I_T = \int I_p(\theta, \varphi)\, d\Omega .$$

With the following estimates of the various parameters in a typical experiment:

$N_a = 3.2 \times 10^{18}$ particles/cc (10^{-3} torr at 300°K)

$Q_{ab} = 10^{-16}$ cm^2

$V/A = 10^{-2}$ cm

$P = 20$ percent

$S = 10^{-2}$ steradians

$\theta = 90°$

$$i = 6 \times 10^{10} \text{ electrons/sec}$$

equation (2) implies that $I_p(\theta) = 1.6 \times 10^3$ photons/sec. If the photons pass through a filter of 50% transmission and are detected by a photomultiplier of 20% efficiency there would be about 160 counts/sec. This is a practical level for standard counting techniques.

A schematic representation of a possible experimental arrangement is shown in figure 1. Although Smit[8] has verified the angular distribution law (equation 2) in helium, Fite and Brackman[9] have noted some discrepancies in atomic hydrogen. Thus, it is imperative to check this angular distribution at higher resolution. This would require the direct measurement of P at a given energy and the measurement of the variation in $I_p(\theta)$ with angle at this same energy. A polaroid filter could be used to determine $I^{\parallel}$ and $I^{\perp}$. Then subsequent measurements of P (at different impact energies) could be made by determining $I_p(\theta)$ at two different angles and applying the known distribution law.

There are a number of refinements in the method, such as cooling the photomultiplier, phase sensitive detection, and circular grids to reduce the effects of radially scattered electrons which may be required.

Since this proposition was first suggested, McFarland[10] has reinvestigated the polarization of the helium 4922 Å radiation as a function of incident energy. He used a cross-beam configuration which eliminated many of the previous experimental uncertainties.

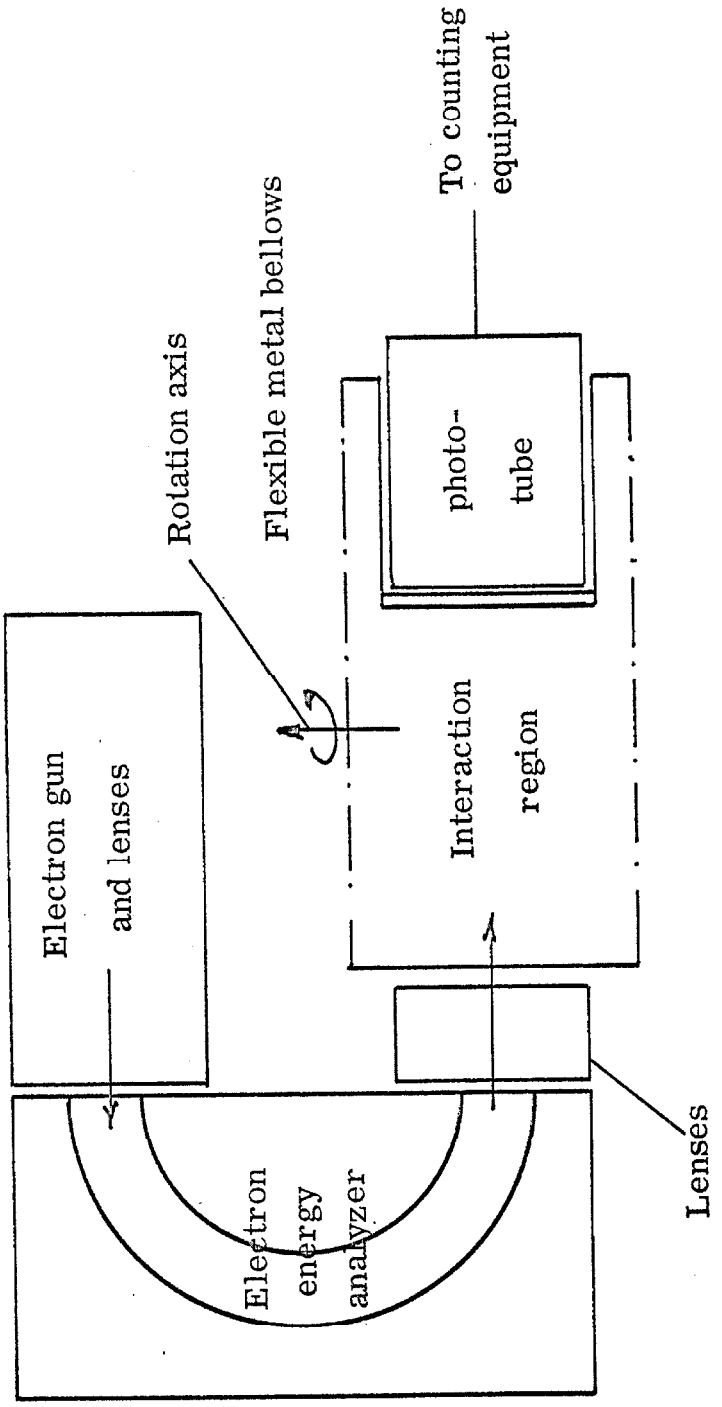

Figure 1. Experimental arrangement.

Although his experimentally determined threshold polarization agreed well with the theoretical value, a near threshold minimum was observed--a feature that has not been predicted by theory. However, these experiments[10] were performed at a fixed angle (90°) under low resolution ($\Delta E \approx 0.2$ eV). More detailed studies, as a function of angle and with better resolution, would still be of interest.

REFERENCES

1. H. W. B. Skinner, Proc. Roy. Soc. London, A112, 642 (1926).
2. H. W. B. Skinner and E. T. S. Appleyard, ibid, A117, 224 (1927).
3. R. H. McFarland and E. A. Soetysik, Phys. Rev., 128, 1758 (1962).
4. R. H. McFarland and E. A. Soltysik, Phys. Rev., 127, 2090 (1961).
5. D. W. O. Heddle and M. J. Seaton, Atomic Collision Processes, Proc. of the Third Int. Conf on the Phys. of Elec. and Atomic Collisions, 137 (1964).
6. I. C. Percival and M. J. Seaton, Phil. Trans., 251, 113 (1958).
7. R. H. McFarland, Phys. Rev., 133, 986 (1963).
8. J. A. Smit, Physica, 2, 104 (1935).
9. W. L. Fite and R. T. Brackman, Phys. Rev., 112, 1157 (1958).
10. R. H. McFarland, Phys. Rev., 156, 55 (1967).

PROPOSITION III

An experiment is proposed to measure the vibration-rotation infrared absorption of the 2326 cm^{-1} asymmetric stretching fundamental in H_3^+ produced in a microwave discharge of H_2. The conditions for which the concentration of H_3^+ is a maximum are discussed and an estimate of the pertinent experimental parameters is given.

In a recent article Huff and Ellison[1] have calculated the fundamental vibration frequencies and absorption intensities of H_3^+ using a theoretically obtained potential energy surface and associated electronic state wavefunctions. Although the existence of H_3^+ was established by Bleakney[2] in 1930, there is very little experimental data available[3-5]. Thus, an experiment is proposed to measure the vibration-rotation infrared absorption of the 2326 cm^{-1} asymmetric stretching fundamental in H_3^+ produced in a microwave discharge of H_2 to provide some experimental results to compare with recent theory[1,6].

Following the notation of Huff and Ellison, the integrated molar absorption coefficient, A", can be expressed as;

$$A'' = (1/\ell C) \int \ell n[I_0/I(\nu)]\, d\nu \qquad (1)$$

where ℓ is the cell path length in centimeters; C is the number of moles per liter of H_3^+; I_0 and $I(\nu)$ are the incident and transmitted intensities, respectively; ν is the frequency in wavenumbers; and A" is calculated[1] to be 7069 darks. The integration is over all frequencies of the vibration-rotation band.

From these calculations we can estimate the feasibility of an absorption experiment. To get an approximate idea of the H_3^+ ion density needed (N), assume $I(\nu)$ has an average value of I_{av} and a band width of 50 cm^{-1} and that $I_{av}/I_o = .95$ results in a detectable absorption. Performing the integral in equation (1), one finds that;

$$\ell N = 2.1 \times 10^{17} \text{ ions/cm}^2 \qquad (2)$$

A microwave discharge in H_2 at pressures greater than a few mm Hg initially produces H^+ and H_2^+. After a millisecond the predominating ionic species are H_2^+ and H_3^+ with most of the H^+ gone (p. 577)[7]. Typical ion densities in moderate power microwave discharges range from 10^9 to 10^{12} ions/cc (p. 560)[7]. The average power (P_{av}) that must be supplied by the oscillating electric field per unit volume to sustain a given total ion density (N_i) is given as[8];

$$P_{av} = \frac{\frac{1}{2} c N_i (X_o e)^2}{m (c^2 + w^2)} \qquad (3)$$

where e and m are the electronic charge and mass, respectively; c is the collision frequency; X_o and w are the amplitude and frequency, respectively, of the applied field. This formula applies in cases for which c is greater or equal to w; i.e., for frequent electron collisions with the gas molecules for each oscillation of the electric field. This condition will prevail in the proposed experiment since pressures on the order of 100 mm Hg and microwave frequencies

of about 1000 Mc/sec are suggested. Goodyear and von Engel[9] report $c = 2.3 \times 10^{8}$ sec^{-1} at 30 microns pressure and 400°K in H_2. At 100 mm Hg and 400°K, c would be approximately 7×10^{11} sec^{-1}. With $w/2\pi$ equal to 1000 Mc/sec (10^{9} sec^{-1}), c is greater than w and the formula (3) applies. Using Goodyear and von Engel's value of $X_o = 1.8$ volts/cm as representative of microwave sources, and substituting the values of the various parameters into equation (3) implies that the power necessary to sustain a discharge of 10^{14} ions/cc is approximately 0.075 watts/cc. If much higher electron (ion) densities are attempted by increased power input, the probable result is more H^+ formation as observed in high electron density spark discharges (10^{17} electrons/cc) rather than an increased H_3^+ density (pp. 501-502)[7]. Varney[10] indicates that at pressures above 1 mm Hg the preponderant ionic species measured by mass spectrographic tests is H_3^+. Assuming N of relation (2) is on the order of 10^{14} ions/cc, the required path length ℓ is 21 meters.

At this stage we can make an estimate of the apparatus required. The reflectivity of silver for radiation of 2300 cm^{-1} can be 98%[11]. If 55 reflections are made there will be about 33% of the incident IR source radiation transmitted, which should be sufficient. The physical cell length needed is then about .4 meters. If the cell cross-section is circular with a radius of 1.8 cm (cross-sectional area of 10^{2} cm^{2}) the volume would be 4,000 cc and the required power would be 300 watts. Suitable microwave sources are commercially available to supply this power but a cavity to contain the sample cell would have to be designed.

Figure 1 is a schematic representation of a possible experimental arrangement. At the wattages anticipated, the sample tube and gas will heat up and radiate in the IR. To discriminate between this IR signal and the source signal, a phase sensitive detection system should be used. The output of the Nernst glower could be chopped by a rotating sectored disc before entering the sample cell. The frequency of rotation can be monitored by a photo-cell and only the component of the detector signal in phase with the photo-cell output would be recorded. There are many commercial IR spectrometers and phase sensitive detection circuits available for this application.

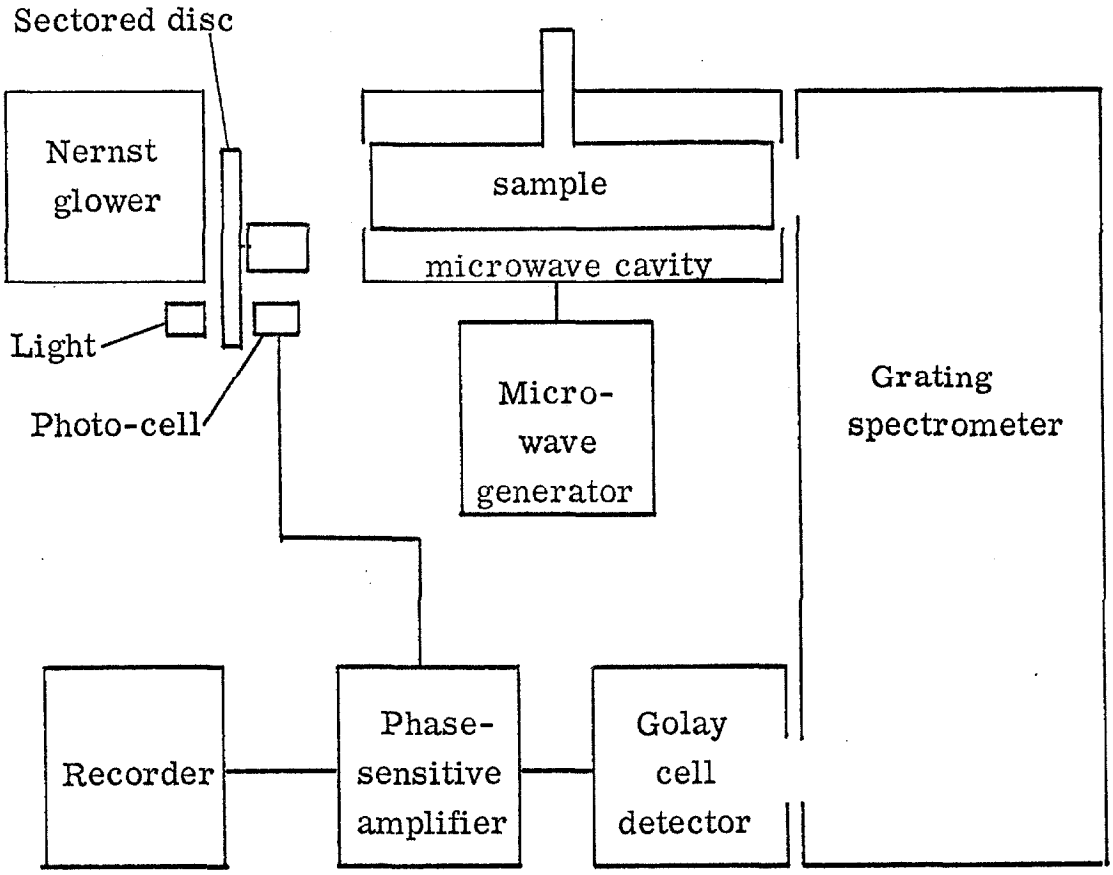

Figure 1. Experimental arrangement

REFERENCES

1. N. T. Huff and F. O. Ellison, J. Chem. Phys., 42, 364 (1965).
2. W. Bleakney, Phys. Rev., 35, 1180 (1930).
3. D. P. Stevenson, J. Chem. Phys., 29, 282 (1958).
4. R. N. Varney, Phys. Rev. Letters, 5, 559 (1960).
5. J. A. R. Samson and G. L. Weissler, U. S. Dept. Com. Office Tech. Serve. PB Report 45,(1961).
6. R. E. Christoffersen, J. Chem. Phys., 41, 960 (1964).
7. L. B. Loeb, Basic Processes of Gaseous Electronics (University of California Press, Berkeley, Calif., 1955).
8. G. Francis, Ionization Phenomena in Gases (Butterworths, London, 1960) p. 87.
9. C. C. Goodyear and A. von Engel, Proc. of Fifth Int. Conf. on Ionization Phenom. in Gases, I, 203 (1961).
10. R. N. Varney, ibid., p. 43.
11. R. A. Smith, F. E. Jones, and R. P. Chasmar, The Detection and Measurement of the Infrared Radiation (Oxford University Press, London, 1957).

PROPOSITION IV

It is proposed that an ion cyclotron resonance mass spectrometer be utilized to investigate the photoionization of gaseous alkali metals (particularly cesium) by light at wavelengths longer than those corresponding to the ionization potential with and without added gases (particularly NH_3).

It has been known for a long time that gaseous cesium can be photoionized by photons which have an energy less than that corresponding to the atomic ionization potential[1,2]. This early work indicated that the ionization mechanism is as follows:

$$Cs\,(6S) + h\nu \rightarrow Cs^*(nP) \qquad (1)$$

$$Cs^* + Cs \rightarrow [Cs\,Cs]^* \rightarrow Cs_2^+ + e^- . \qquad (2)$$

Lee and Mahan[3] have shown that an additional ionization process probably should be considered when $n \geq 12$,

$$Cs^*(nP) + Cs \rightarrow Cs^+ + Cs^- . \qquad (3)$$

Recently, it has been observed[4] that the addition of ammonia vapor alters the photoionization spectrum of cesium by decreasing the ion current for wavelengths longer than 3400 Å and increasing it for shorter ones. This has led Williams and Naiditch[4] to propose an ionization mechanism analogous to that of (2), i.e.,

$$Cs^*(nP) + NH_3 \rightarrow [Cs\,NH_3]^* \rightarrow Cs\,NH_3^+ + e^- . \qquad (4)$$

It should be pointed out that in none of these experiments have any of the ions produced been positively identified. In most cases[1,2,4] the total ion current was measured, while in one case[3] ions of different mobilities (presumably Cs_2^+ and Cs^+) were detected. Thus, it is proposed that the photoionization of gaseous cesium (and other alkali metals) with and without added gases be studied using an ion cyclotron resonance mass spectrometer[5] to detect and identify the ionic species. This method of detection enables one to unambiguously identify all of the ions formed and to monitor their currents independently. Such studies can be used to confirm or deny the ionization mechanisms already suggested.

In order to calculate the rate of formation of a particular ion, a few additional processes must be considered.

$$Cs^* \rightarrow Cs + h\nu \tag{5}$$

$$Cs^* + NH_3 \rightarrow Cs + NH_3^* \tag{6}$$

where (5) and (6) represent spontaneous emission and electronic energy transfer, respectively. The rate of Cs^* formation (due to reaction (1)) is proportional to the incident photon flux ρ times the Cs concentration ([Cs]). The net rate of Cs^* formation (considering only reactions (1) through (6)) is

$$\frac{d[Cs^*]}{dt} = \rho B[Cs] - A[Cs^*] - (k_2 + k_3)[Cs^*][Cs]$$

$$- (k_4 + k_6)[Cs^*][NH_3]$$

where A and B are the Einstein transition probabilities[6] of spontaneous emission and absorption, respectively, and k_2 through k_6 are the rate constants associated with reactions (2) through (6). Under steady state conditions, the net formation rate of Cs^* is zero which implies a concentration of

$$[Cs^*] = \frac{\rho B[Cs]}{A + (k_2 + k_3)[Cs] + (k_4 + k_6)[NH_3]} .$$

Thus, the Cs_2^+, Cs^+ (Cs^-), and $CsNH_3^+$ ion currents will be given by

$$I(Cs_2^+) = k_2[Cs^*][Cs]$$

$$= \frac{\rho B k_2 [Cs]^2}{A + (k_2 + k_3)[Cs] + (k_4 + k_6)[NH_3]}$$

$$I(Cs^+) = \frac{k_3}{k_2} I(Cs_2^+) \text{ , and}$$

$$I(CsNH_3^+) = \frac{k_4}{k_2} [NH_3][Cs]^{-1} I(Cs_2^+) .$$

k_3/k_2 and k_4/k_2 can then be determined from measurements of these ion currents. Further, if the Cs_2^+ ion current when $[NH_3] = 0$ is denoted $I_0(Cs_2^+)$, then

$$\frac{I_0(Cs_2^+)}{I(Cs_2^+)} = 1 + \frac{(k_4 + k_6)[NH_3]}{A + (k_2 + k_3)[Cs]}$$

$$= 1 + \frac{(k_4/k_2 + k_6/k_2)[NH_3]}{A/k_2 + (1 + k_3/k_2)[Cs]} \quad .$$

The measurement of I_o/I as a function of [Cs] and $[NH_3]$ can then be used to determine A/k_2 and k_6/k_2. (Note that in reality A includes the deexcitation of Cs^* by wall collisions as well as spontaneous emission.) The k's are expected to be slowly varying functions of temperature but to depend strongly on the particular Cs^* excited state. In particular, the investigations already mentioned indicate that k_4 has an apparent energy threshold at 3400Å while k_2 has one at 3888Å.

The apparatus required to perform these experiments is for the most part commercially available. The usual ion cyclotron resonance spectrometer cell[5] must be modified to allow its operation at elevated temperatures (~ 200° C). Also, the electron beam ionizer should be replaced by a suitable light source (a high-pressure mercury lamp, for example) and a monochromator.

REFERENCES

1. F. L. Mohler and C. Boeckner, J. Res. Natl. Bur. Std., 5, 51 (1930).
2. F. L. Mohler and C. Boeckner, J. Res. Natl. Bur. Std., 5, 399 (1930).
3. Y. Lee and B. H. Mahan, J. Chem. Phys., 42, 2893 (1965).
4. R. A. Williams and S. Naiditch, J. Chem. Phys., 47, 343 (1967).
5. J. D. Baldeschwieler, Science,159, 263 (1968).
6. G. Herzberg, Spectra of Diatomic Molecules (Second Edition, D. Van Nostrand, Inc., 1950), p. 20.

PROPOSITION V

An experiment is proposed to measure the energy distribution of electrons thermionically emitted from single crystals of tungsten in order to rationalize theory and experiment. A number of suggestions to correct inadequacies of prior investigations are given.

The increasing interest in electron scattering phenomena has led to a reexamination of the energy profiles of electron beams from thermionic sources. From the assumptions of the free electron theory of metals[1], the current distribution is expected to be[2a]

$$I(E)\,dE = \frac{4\pi me}{h^3} e^{-W_f/kT} E\, e^{-E/kT}\, dE \quad . \qquad (1)$$

IdE is the current carried by electrons in the energy range $E \rightarrow E + dE$, h is Planck's constant, e and m are the electron charge and mass, respectively, W_f is the work function of the metal, k is Boltzmann's constant, T is the cathode temperature, and E is the electron energy. The integral of (1) over all energies E gives the Richardson-Dushman equation for the total temperature limited current

$$I_T = \frac{4\pi me}{h^3} (kT)^2 e^{-W_f/kT} \quad . \qquad (2)$$

Equation (2) has been found to be a valid description of thermionic emission when written in the form

$$I_T = KT^2 e^{-W_f/kT} \qquad (3)$$

where K is an experimentally determined parameter for a given metal[1b].

However, experimental attempts to verify even the shape of the distribution given by equation (1) have not been successful. Hutson[3] observed an apparent "reflection coefficient" at the surface of single crystals of tungsten which resulted in a measured deficiency of low energy electrons. On the other hand, Simpson and Kuyatt[4] have noted an anomalous broadening of the distribution (1) as a function of beam current which appears to increase the relative number of low energy electrons. Although the experimental arrangements of these two investigations are basically similar (i.e., a thermionic cathode followed by an energy analyzer), there are a number of differences in the cathode preparation and operation and method of energy analysis which may significantly affect the results. It is therefore proposed that systematic experimental measurements of the electron energy distribution from a thermionic source be made in an attempt to clear up this somewhat muddled situation.

There are a number of restrictions on the experimental arrangement which are necessary in order to eliminate as many of the complicating factors as possible from the previous investigations[3,4]. These requirements and the methods proposed for obtaining them are outlined below. Figure 1 shows the proposed experimental set up.

Planar, indrectly heated, single crystals of tungsten will be used as the thermionic emitter. Robinson[5] has described a simple

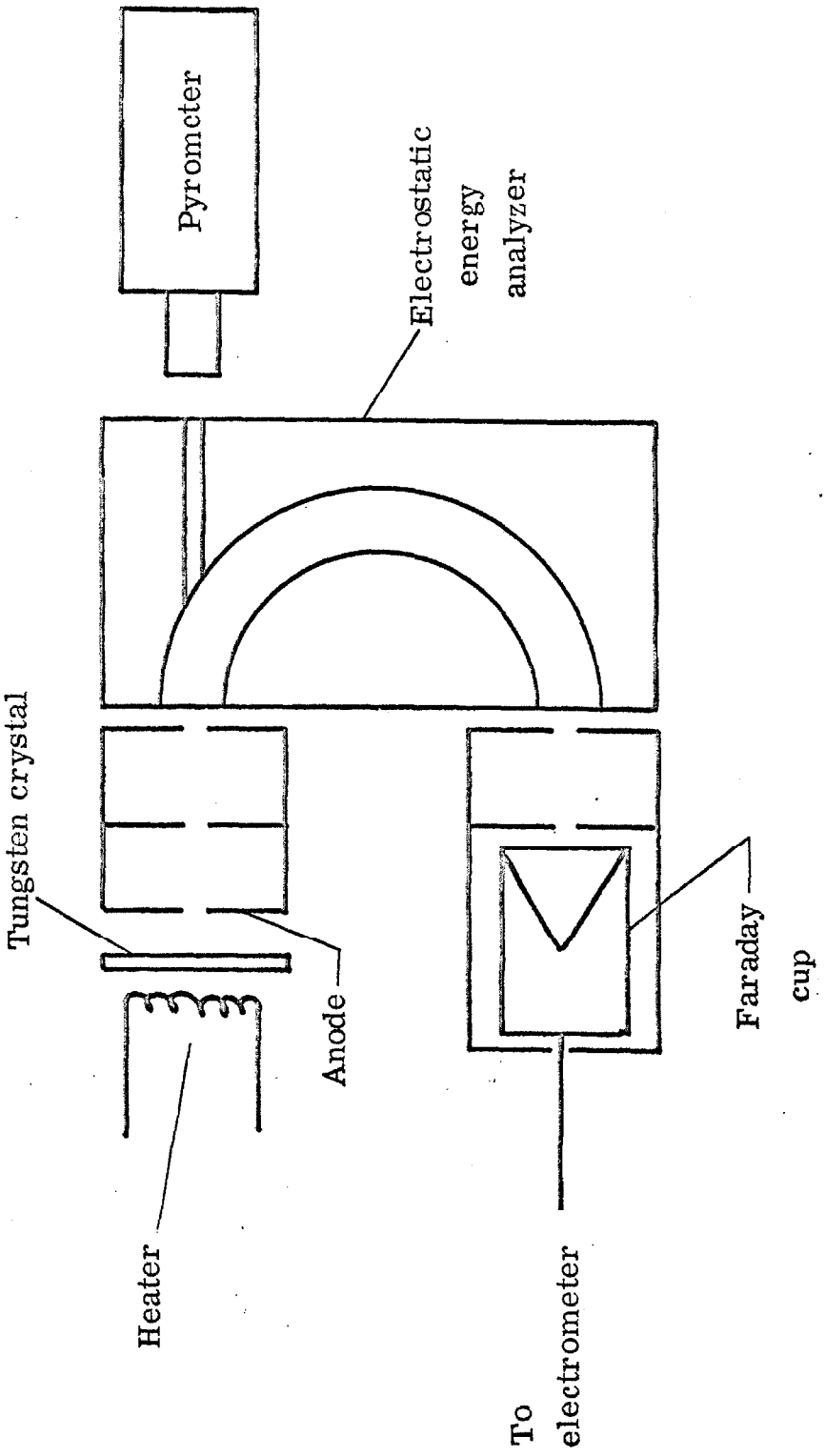

Figure 1. Experimental arrangement

procedure for obtaining such crystals and the particular exposed crystal face can be determined by X-ray scattering[6]. The use of indirect heating will eliminate the possibility of IR drops in the source. Also, it is imperative that a means of measuring the crystal temperature be provided. Commercial optical pyrometers are available with an accuracy of $\frac{1}{2}\%$ (10°K @ 2000°K).

The electron gun itself will consist of the tungsten source (cathode) and an aperture (anode). The potential between the cathode and anode provides the necessary draw-out voltage to direct the electron beam into an energy analyzer. The gun can be operated under space-charge or temperature limited conditions depending on the value of this potential.

The electron gun is followed by two apertures, equi-potential with the anode, and a hemispherical electrostatic energy analyzer[2b]. The apertures are needed to collimate the beam before its entrance into the analyzer. The region between the anode and analyzer is kept free of electric fields to eliminate the possibility that lens effects may distort the electron energy distribution. Likewise, magnetic shielding can be provided by Helmholtz coils[2c].

The analyzer is followed by two apertures (equi-potential with the anode) and a Faraday cup current collector. The energy profile of the beam can be obtained by recording the current reaching the Faraday cup versus the voltage across the hemispheres with all other voltages constant. This method of sweep has the disadvantage that the resolution is a function of the electron energy. This is not

a serious handicap since that function is known[2d].

Finally, the electron source and analyzer are enclosed in a high vacuum chamber (residual pressure less than 10^{-7} torr) to eliminate any interference from ionization or gas scattering phenomena.

Let the experimentally determined energy profile be $I_{exp}(E)$ and the "real" one be $I_{real}(E)$. Then

$$I_{exp}(E + U) \cong C I_{real}(E)$$

(provided the resolution of the analyzer is adequate) where C is an energy independent constant and U is a contact potential correction (generally unknown) that represents a shift in the energy origin but not a change in shape. Since T is known, I_{exp} can be compared with the theoretical prediction for I_{real} (i. e., equation (1)) simply by normalizing them to the same peak position (and height). These experimental energy distributions should be obtained for $E = 0$ to $E \gg kT$ as a function of the cathode temperature, total beam current, space charge conditions in the gun, and draw-out voltage.

There is an additional experimental complication that has been ignored in all previous investigations--the production of low energy secondary electrons by electron collisions with the apertures. Since the importance of this effect is not known, it is suggested that several sets of apertures, with different secondary electron yield characteristics[7], be used in the apparatus. In this way, distortions in the measured electron energy distribution due to

aperture scattering might be identified.

REFERENCES

1. R. B. Leighton, Principles of Modern Physics (McGraw-Hill Book Company, Inc., New York, 1959), (a) pp. 352-357, (b) p. 357.
2. J. K. Rice, Ph.D. Thesis, California Institute of Technology, 1969; (a) section 4.4.3.1, (b) sections 4.1.1 and 4.2.4.3, (c) section 4.1.3.2, (d) section 4.1.1.2, equations (4-19) and (4-29).
3. A. R. Hutson, Phys. Rev., 98, 889 (1955).
4. J. A. Simpson and C. E. Kuyatt, J. Appl. Phys., 37, 3805 (1966).
5. C. S. Robinson, Jr., J. Appl. Phys., 13, 647 (1942).
6. M. J. Buerger, Crystal Structure Analysis (John Wiley and Sons, Inc., New York, 1960).
7. E. W. McDaniel, Collision Phenomena in Ionized Gases (John Wiley and Sons, Inc., New York, 1964), pp. 658-670.